Report No. SFIM-AEC-ET-CR-95041

U.S. Army Environmental Center

Ground Penetrating Radar for Ordnance Contaminated Site Restoration

DTIC
SELECTE
JUN 2 2 1995
F

14 March 1995

Prepared by Battelle/The Ohio State University ElectroScience Laboratory

Distribution Unlimited; Approved for Public Release

AEC Form 45, 1 Feb 93 replaces THAMA Form 45 which is obsolete.

GROUND PENETRATING RADAR FOR ORDNANCE CONTAMINATED SITE RESTORATION

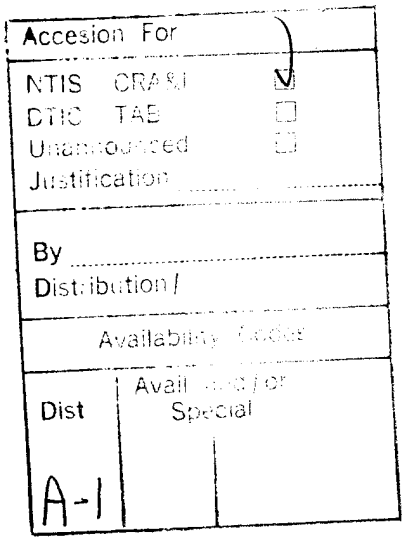

19950620 009

REPORT DOCUMENTATION PAGE

Form Approved
OMB No. 0704-0188

Public reporting burden for this collection of information is estimated to average 1 hour per response, including the time for reviewing instructions, searching existing data sources, gathering and maintaining the data needed, and completing and reviewing the collection of information. Send comments regarding this burden estimate or any other aspect of this collection of information, including suggestions for reducing this burden to Washington Headquarters Services, Directorate for Information Operations and Reports, 1215 Jefferson Davis Highway, Suite 1204, Arlington, VA 22204-4302, and to the Office of Management and Budget, Paperwork Reduction Project (0704-01881, Washington, DC 20503.

1. AGENCY USE ONLY (Leave Blank)	2. REPORT DATE	3. REPORT TYPE AND DATES COVERED
	14 March 1995	Final Report March 1993 - March 1995

4. TITLE AND SUBTITLE

Ground Penetrating Radar for Ordnance Contaminated Site Restoration

5. FUNDING NUMBERS

6. AUTHOR(S)

7. PERFORMING ORGANIZATION NAME(S) AND ADDRESS(ES)

Naval Explosive Ordnance Disposal Technology Division
Project Manager: Gerard Snyder 301/743-6855
2008 Stump Neck Road
Indian Head, Maryland 20640-5070

8. PERFORMING ORGANIZATION REPORT NUMBER

9. SPONSORING / MONITORING AGENCY NAME(S) AND ADDRESS(ES)

U.S. Army Environmental Center
Project Officer: Kelly Rigano 410/612-6868
SFIM-AEC-ETP
Aberdeen Proving Ground, Maryland 21010-5401

10. SPONSORING / MONITORING AGENCY REPORT NUMBER

SFIM-AEC-ET-CR-95041

11. SUPPLEMENTARY NOTES

Supporting Contractors:

Battelle
505 King Avenue
Columbus, Ohio 43201

The Ohio State University ElectroScience Laboratory
1320 Kinnear Road
Columbus, Ohio 43212

Contract Number N00174-93-C-0047

12a. DISTRIBUTION / AVAILABILITY STATEMENT

Unlimited Distribution

12b. DISTRIBUTION CODE

"A"

13. ABSTRACT (Maximum 200 words)

The main purpose of this document is to apply ground penetrating radar (GPR) technology to the problem of locating and identifying buried ordnance at military sites. The emphasis of the research applied GPR technology to an airborne system that will allow very large parcels of land to be processed. This contract represents one portion of an overall U.S. Government program to clear former and present military ordnance ranges of all unexploded ordnance and other buried devices that pose a threat to the public.

DTIC QUALITY INSPECTED 3

14. SUBJECT TERMS

Unexploded Ordnance, Detection and Identification, Target Discrimination, Complex Reconnaissance

15. NUMBER OF PAGES

16. PRICE CODE

17. SECURITY CLASSIFICATION OF REPORT	18. SECURITY CLASSIFICATION OF THIS PAGE	19. SECURITY CLASSIFICATION OF ABSTRACT	20. LIMITATION OF ABSTRACT
Unclassified	Unclassified	Unclassified	Unlimited

Contents

Figures

Tables

1.0 Introduction

1.1 Background

This document is the Final Technical Report (CLIN A016) for contract N00174-93-C-0047 between the Naval Surface Warfare Center (NSWC) and Battelle. This research was funded through BAA-92-01 as presented by NSWC and was monitored by the Naval Explosive Ordnance Disposal Technology Division (NEODTECHDIV). The main purpose of the contract was to apply ground penetrating radar (GPR) technology to the problem of locating and identifying buried ordnance at military sites. The emphasis of the research applied GPR technology to an airborne system that will allow very large parcels of land to be processed. This contract represents one portion of an overall U.S. government program to clear former and present military ordnance ranges of all unexploded ordnance (UXO) and other buried devices that pose a threat to the public.

This report summarizes work done by Battelle and the only subcontractor, The Ohio State University ElectroScience Laboratory (ESL).

The goal of this first phase of this research program was to design such an airborne radar through the use of a test-bed GPR system that provides feed-back concerning the critical parameters that include data rates, antennas, discrimination algorithms, and total system implementation. The second phase of this program will result in a GPR system prototype, further developed using lessons-learned from the first phase, capable of being flown and tested under field conditions. The design goal for the system is that it be capable of acquiring data and generating maps of buried ordnance at the rate of approximately 5 acres per hour with maximum probability of detection and minimum false alarm rate. This document contains data concerning Phase 1 of this program. This phase resulted in a system design based on a test-bed GPR system that will be used to generate actual data on buried

ordnance and to test design options. During the second phase of the program, the design will be evolved into a brassboard prototype capable of acquiring data from a height of 100 feet or higher above the ground and processing the raw data into maps showing the location of buried ordnance with probabilities assigned to each location. It is anticipated that these maps will be combined with data from other sensor systems for the purpose of providing increased detection probabilities with decreased false alarm rates.

1.2 Report Data

The basis for the design data described in this document was the System/Design Trade Study Report (CLIN A009) submitted to NAVEODTECHDIV in March 1994 and the Conceptual Drawings and Associated Lists (CLIN A011) submitted in February 1995. The design items submitted to trade-off in that study are included in this report in their final design form. The primary items presented in this report are the airborne platform, the GPR antenna, the receiver architecture, signal processing, and navigation options. Certainly many subsystem decisions were also made and are presented here. We were also bound, of course, by the needs and assets of our customers, namely, NAVEODTECHDIV and the Army Environmental Center. While we expended considerable time and energy investigating receiver architectures, for example, the follow-on second phase of this program is a system demonstration program and therefore is not funded to fabricate and test our high-speed receiver described below. Instead, we will use an existing ESL stepped-chirp radar. We did not investigate navigation and positioning information systems as part of this task. As part of another program, however, we worked with the Ohio State University Center for Mapping (CFM). As part of that study, for PRC Inc. and NAVEODTECHDIV, CFM investigated options for optimum navigation and positioning of an airborne GPR system. In the follow-on effort, CFM will be providing the navigation and positioning information. A design drawing and components list of the navigation system is also included in this document.

1.3 Report Organization

This report is divided into 13 sections with this Introduction being the first. Section 2.0 presents data processing methods used and Section 3.0 provides details on the SAR simulation that was developed as part of this program. Section 4.0 provides details on the antennas considered and Section 5.0 discusses the effects of soil conditions on underground radar propagation. Section 6.0 provides information on our techniques for extracting complex resonances from radar data and examples of such extraction on data generated on this program. Section 7.0 summarizes our findings on GPR receiver design alternatives and includes our recommendations. Section 8.0 includes information on positioning and navigation necessary for the airborne GPR. Section 9.0 provides a short discussion of RF safety levels with regard to GPR systems. Section 10.0 comprises information compiled during the literature review conducted as part of this program. Section 11.0 includes information on airborne platforms from the airborne GPR perspective. Section 12.0 provides a summary of the report and the program. An Appendix is included as Section 13.0.

2.0 Signal Processing

This section briefly explains two of the critical signal processing procedures we will use to detect objects and then to discriminate between clutter objects and target objects. Synthetic Aperture Radar (SAR) processing is used to aid in detection. Target discrimination is achieved by exploiting the complex natural resonance frequencies of known ordnance items. Both of these topics are examined in more detail in subsequent chapters.

2.1 Synthetic Aperture Radar Processing

One very important factor in the airborne GPR system is the antenna beamwidth. Because of the low frequencies being used (and their accompanying large wavelengths), the antenna gain will be small and the main beam will be very wide. This large beam causes several problems, namely, the gain is low, return is obtained not only from a target of interest but also from clutter and other targets, and if a target is identified, its position is not known with much precision.

Relatively low frequencies are used because of the requirements of the target discrimination techniques used (explained in detail in Section 6.0) and because lower frequencies have better propagation properties in the ground (explained in Section 5.0). Frequencies between 50 and 500 MHz are used with our proposed system. The percentage bandwidth used is 100 percent, that is, nearly 500 MHz information bandwidth centered at 250 MHz.

Because of the enormous percentage bandwidth involved with this UWB radar, antenna patterns are difficult to define and describe. However, because of the small aperture at the lower frequencies, we know that the gain will be small and the main beam will be large.

SAR processing can be used to lessen the effects of using low frequencies. Figure 1 shows the helicopter moving across a large distance and what its wide beamwidth looks like at each position. If the data from many positions across this distance are processed together in the proper way, the effective synthetic aperture of the system can be much larger, the antenna gain is increased, and the main beam becomes smaller. The processing is done continuously and many smaller beams are processed where only one existed before this SAR processing step.

The relationship between aperture and beam size is completely analogous to Fourier transform processing in the time and frequency domains. In the case of a short pulse in the time domain, the frequency domain spectrum of the system must be wide (large bandwidth).

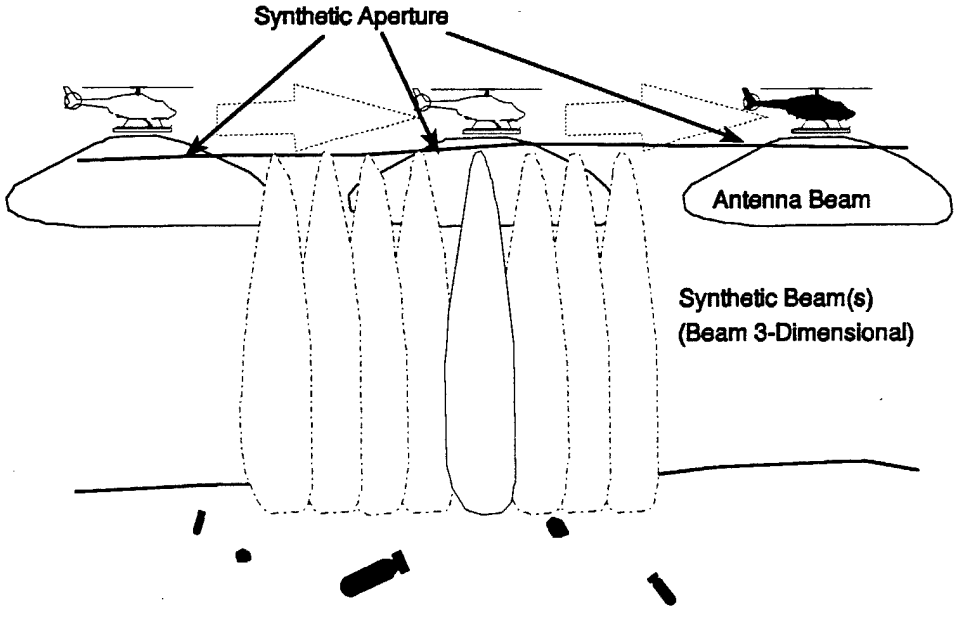

Figure 1 Two-Dimensional view of the synthetic aperture.

In this analogy, the aperture corresponds to the frequency domain spectrum and the beam corresponds to the time-domain pulse. The wider the spectrum, the narrower the pulse. The wider the aperture, the narrower the beamwidth.

Note that the antenna beam in Figure 1 is actually three-dimensional. It is wide coming out of the paper. In Figure 1, the synthetic beam shown in the center is narrow from left to right but still wide coming in and out of the paper.

Figure 2 attempts to depict the three-dimensional nature of that synthetic beam. For the helicopter flying to the right and slightly out of the paper, the three-dimensional beam is orthogonal to the direction of flight. The ground is not shown but it can be any place within the beam. The beam actually defines a volume. Figure 2 shows the way range resolution is formed. Range resolution cell size is inversely proportional to bandwidth. The wider the bandwidth, the smaller the resolution cell. A resolution cell formed by the beam and by range forms a volume that is shaped like a tube. This tube will actually be very strangely shaped in the airborne GPR because of the presence of the ground and resulting refraction. This drawing does not go into that detail.

The use of an antenna with a null below the aircraft (which is the case with some of the antennas described in Section 4.0) does not alter the SAR processing. Less energy will be directed from the vertical position but as the aircraft moves, this effect is minimized because each voxel in the ground is excited when the aircraft is in positions where the voxel is not directly below the aircraft. The voxel still influences the overall process. Figure 3 depicts the vertical antenna pattern and synthesized pattern.

While the creation of this smaller resolution cell is very useful, its width still causes problems. The width of the beam can be decreased in a similar way by flying the helicopter in an orthogonal direction, as depicted in Figure 4, or along multiple offset paths in the same direction. The same SAR processing creates a large aperture in this orthogonal direction with its corresponding narrow beams. The resolution cell is no longer a tube but some

strangely-shaped cube-like volume. Through these three processing steps, the beam size has decreased (increasing the gain) and the resolution cell can be small enough to place a UXO target in one cell and a problematical clutter object in another cell. In fact, the helicopter does not need to fly in the orthogonal direction. Instead, the data acquired while flying in the single direction can be processed in the orthogonal direction to create the same effect of narrower antenna beams in the orthogonal direction.

Section 3 presents the detailed derivation of the SAR simulation that was compiled during the course of this effort. Some examples, presenting the use of the simulation are included with the derivation.

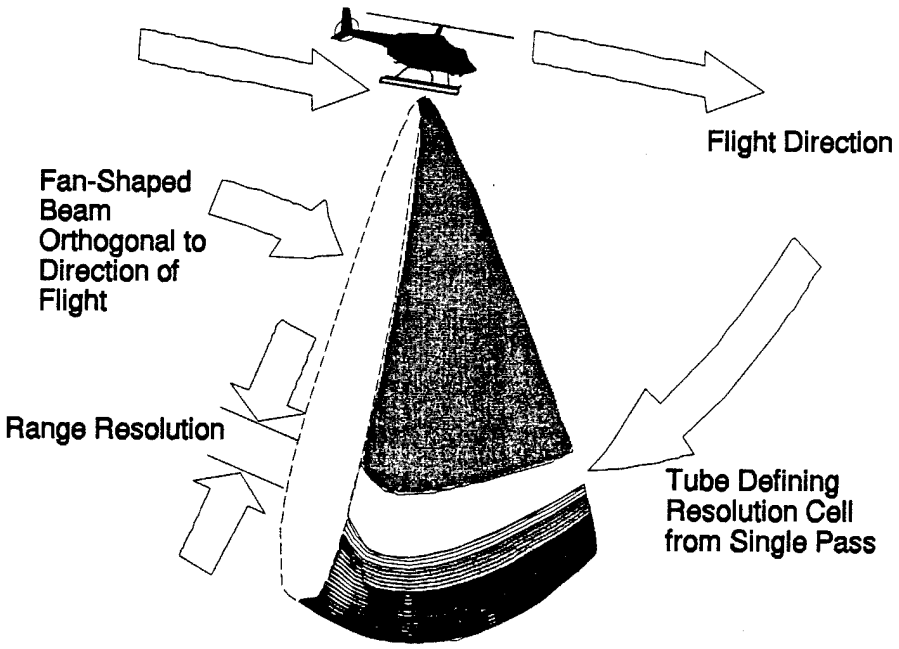

Figure 2 Three-Dimensional view of the synthetic aperture

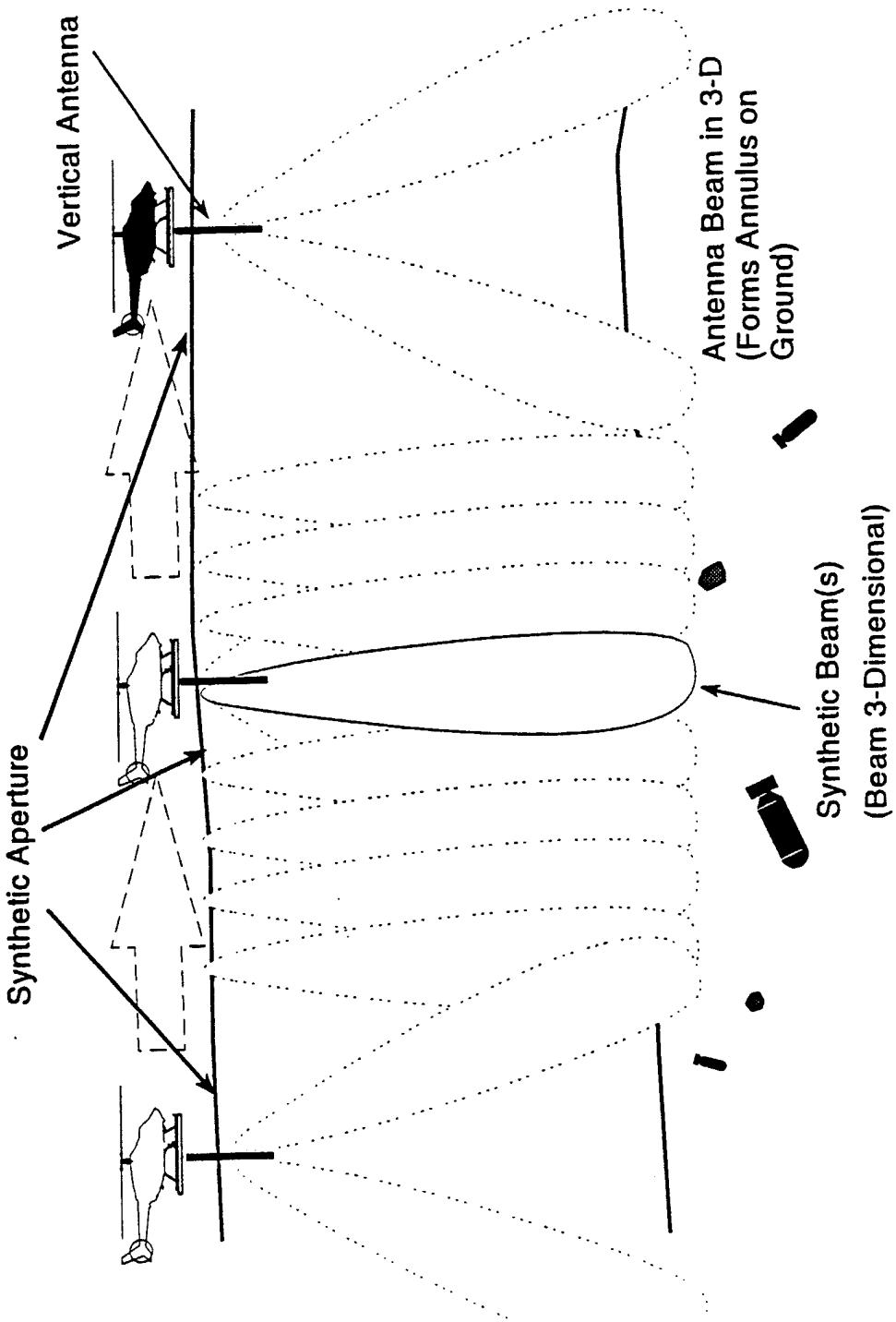

Figure 3 Drawing depicting the pattern from the vertical dipole and the resulting SAR pattern

2.2 Target Discrimination

This section describes the complex natural resonance-based discrimination procedures in generic terms. It is described in more detail in Section 6, along with new techniques and analysis developed at ESL over the course of this effort.

Complex natural resonances will play the critical role in discriminating between items of interest and clutter. Numerous organizations over the years have shown systems or techniques with the ability to *detect* objects below the surface using GPR. People have generated very interesting images showing an object below the surface. Often, however, they have not been able to say whether that object is an item of interest or debris or a rock. Equally important as detection, then, is the ability to *discriminate* between a target of interest and clutter. In any discrimination methodology, one needs some property that is different for a target of interest than the surrounding clutter. Researchers at Ohio State ESL began using

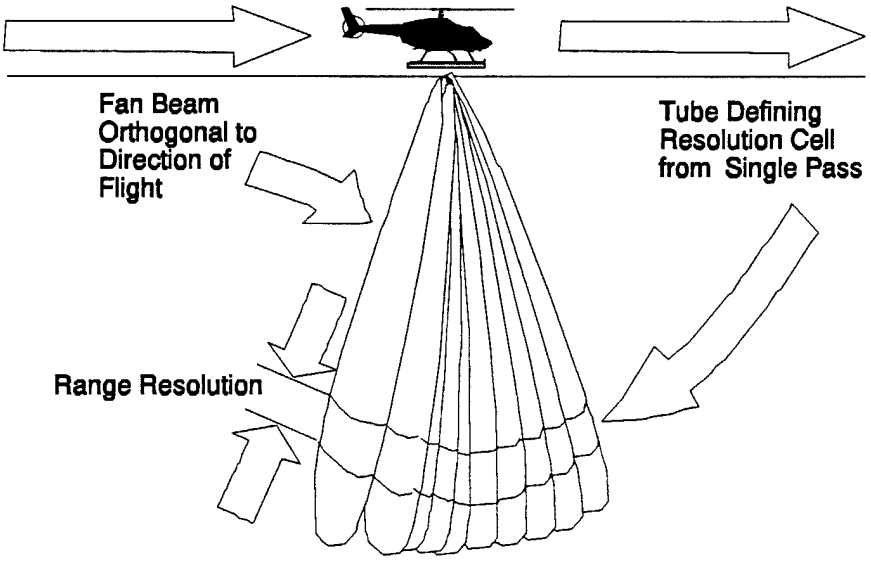

Figure 4 The final resolution volume formed by two directions of travel and bandwidth.

the scattering target's *complex natural resonances* 20 years ago as the unique property that can be exploited to discriminate between targets of interest and clutter. These complex resonances function much as finger prints do to aid in discrimination between individuals.

An excellent introduction into the complex resonances of scattering objects was presented by Mains and Moffatt[1]; a short, simplified summary of portions of that report is included here. They drew an analogy between circuit theory and scattering by examining the transfer admittances, $Y_{ij}(s)$ $(i \neq j)$ of a linear, bilateral, lumped, passive network in the complex frequency, s, domain. They cited the fact that for this type of network, the $Y_{ij}(s)$ expressions all contain the same denominator, say, $D(s)$. The admittances, $Y_{ij}(s)$, can be written as

$$Y_{ij}(s) = \frac{N_{ij}(s)}{D(s)}, \quad \text{for all } i, \quad \text{for all } j,$$

where $N_{ij}(s)$ is the numerator.

The function $D(s)$ depends only on the lumped elements of the network and is independent of which pair of ports one chooses to examine. The zeros of $D(s)$ are the poles of all of the $Y_{ij}(s)$ functions. These poles are the complex natural resonances of this network. Their effects are seen regardless of how you examine the network. If one wanted to discriminate between two networks, then, a measure of the network's poles offers an excellent discriminant, regardless of which two ports one examined. It must be said that in some cases, for a given i,j pair, a zero in the numerator of $Y_{ij}(s)$ (the numerator changes with aspect angle) could cancel the effect of one or more poles.

The analogy to circuit theory is not exact but the case is made by Mains and Moffatt that the same phenomenology occurs in radar target scattering. A radar target can be

---

[1] R.K. Mains and D.L. Moffatt, "Complex Natural Resonances of an Object in Detection and Discrimination," The Ohio State University ElectroScience Laboratory Technical Report 3424-1, prepared for Electronic Systems Division, Hanscom Field, June 1974.

described in many ways but one way, for a given aspect angle, is to define a transfer function, $F(s)$, in the complex frequency domain. This transfer function could be the ratio of the scattered to the incident field, for example. Such an expression can be approximated by a rational function of the form

$$F(s) = \frac{a_0 + a_1 s + a_2 s^2 + \cdots + a_M s^M}{1 + b_1 s + b_2 s^2 + \cdots + b_N s^N} . \quad (1)$$

The a_m and b_n are chosen to achieve a best fit to empirical or analytical data over some frequency range. The zeros of the denominator, which is similar to $D(s)$, described previously, are the approximate complex natural resonances of the scattering target. Over the years, several methods have been proposed to find these resonances of known targets. The specific means of obtaining the resonances is not of interest here, only the knowledge that they can be found analytically is important.

Two properties of these resonances must be proved. First, they must be aspect invariant; their values should be nearly constant regardless of the aspect angle of the incoming and outgoing radar energy. Second, they must be unique for a given target. Mains and Moffatt investigated the invariance of the resonances with aspect angle by changing the position of the generator on a thin-wire model, which was analyzed using the Moment Method[1]. They found that the positions of the complex resonances changed very little as the position was moved. For some aspect angles, some resonances were not found but this fact was consistent with the fact that at some aspect angles, a particular resonance would not be excited by an incident waveform so the received waveform would not contain any evidence of that resonance. Mains and Moffatt also presented three interesting data sets based on thin-wire model calculations. Figure 5 shows a plot of the complex resonances of a bent wire structure in the s-plane. The structure is shown to have an included angle of 2α

[1] The Moment Method is a widely-accepted and widely-used method of calculating the electromagnetic scattering from a given target when the target is about the same size as a wavelength or smaller. This low frequency method is useful in the GPR situation because high frequency energy is attenuated in the ground.

and the plot shows the movement of each of the resonances as α changes from 5° to 90° (a straight wire). The first and second even and odd mode resonances are shown. The even modes exhibit an even number of sinusoidal maxima; the odd modes exhibit an odd number. The abscissa represents the normalized real part of the complex frequency. All complex resonances (poles) must have negative real parts to correspond to damped sinusoids[1]. The ordinate axis represents the normalized imaginary part of the complex frequency. For this simple example, it is clear that the resonances are distinct for different targets. They also provided data on two simple wire models of aircraft. Their data are reproduced in Figure 6. The differences in the configurations of the two aircraft models are minimal but a clear difference exists in the locations of some of the complex resonances. The lowest frequency resonances (in the bottom right corner of both plots) are identical because they are associated with the overall length of the models. The next two lowest resonances are clearly in different positions. These types of differences provide the basis for discrimination.

Predictor-Correlator Discrimination Procedure Mains and Moffatt also presented a discrimination procedure which has been used successfully in many discrimination problems. They found an automated method for discriminating between the two wire models of Figure 6, for example. The method revolves around a difference equation presented by Corrington[2]. The difference equation is

$$R(t) = \sum_{i=1}^{M} (-1)^{i+1} A_{M,i} R(t - i\,\Delta t). \qquad (2)$$

This equation just states that, given the right coefficients, a point on the transient response curve, $R(t)$, can be predicted from preceding points. Mains and Moffatt also gave a formula that can be used to find the $A_{M,i}$ in terms of the complex resonances. Given a measured ramp response of some unknown target, $F_{Rm}(t)$, (the ramp response is the second integral of the

---

[1] This plot appears as it does in Mains and Moffatt's report and is in error. All values on the horizontal axis should be negative, i.e. from left to right the labels should be -0.5, -0.4, ..., -0.1, 0.

[2] M.S. Corrington, "Simplified Calculation of Transient Response," Proceedings of the IEEE, Vol. 53, No. 3, March 1965, pp. 287-292.

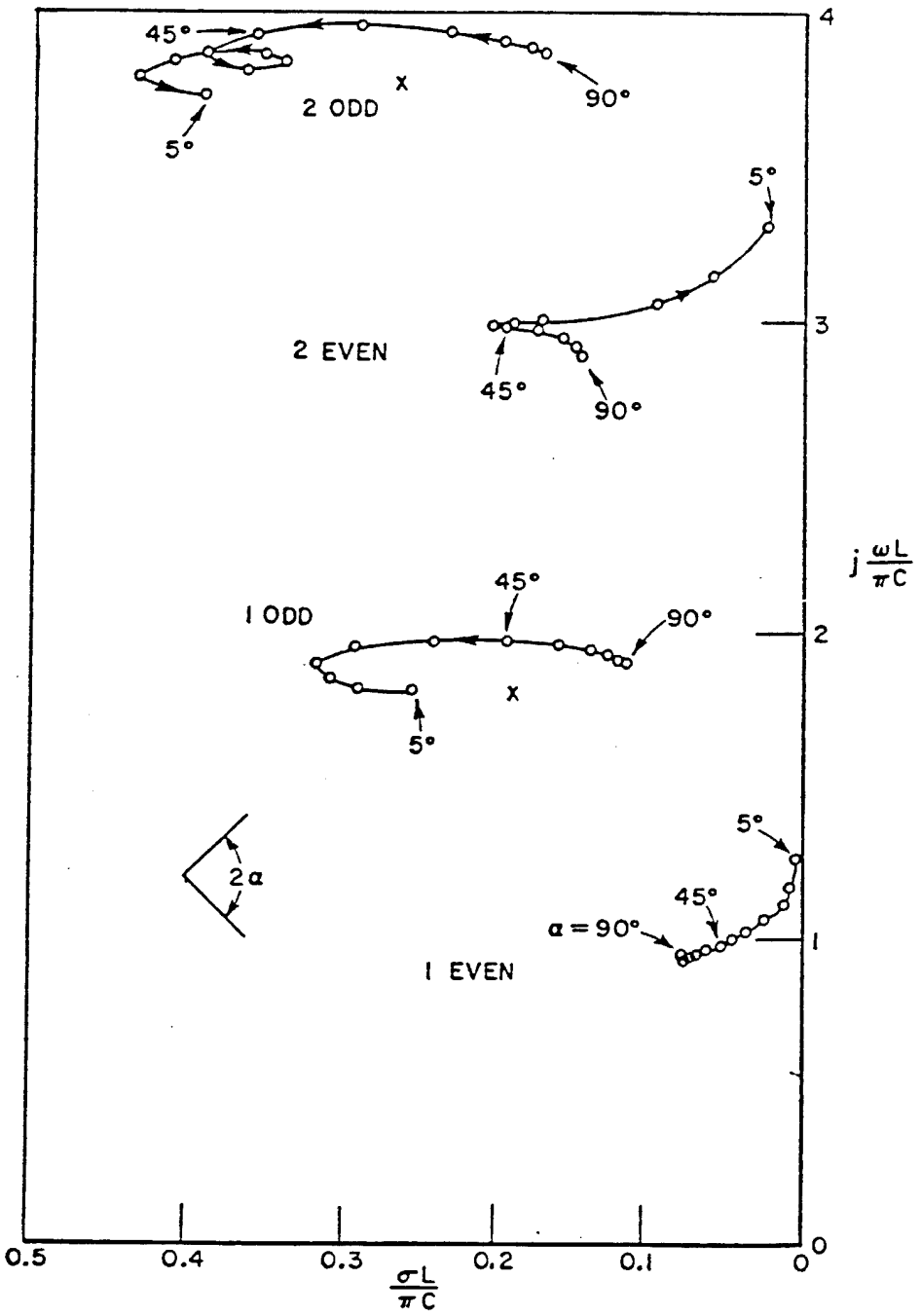

Figure 5 Natural resonances of bent wire with variable included angle (from Mains and Moffatt).

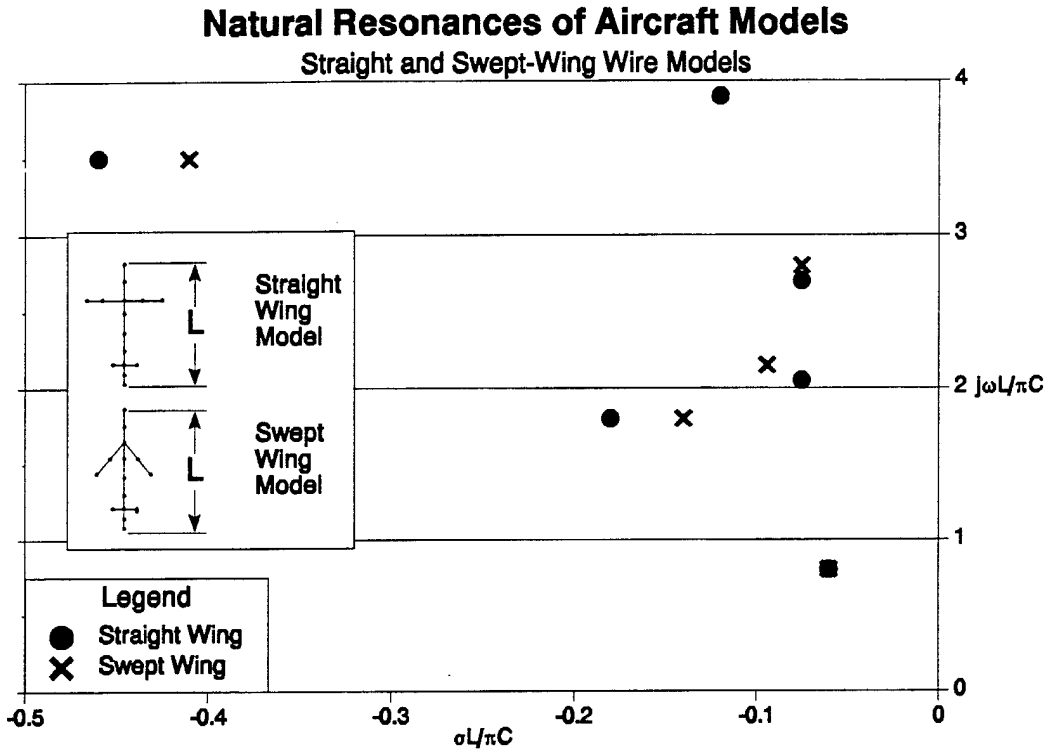

Figure 6 Natural resonances of straight and swept wing aircraft models (from Mains and Moffatt).

impulse response), equation (2) shows how to calculate a predicted ramp response, $F_{RC}(t)$ using the complex natural resonances (and corresponding $A_{M,i}$) of some *known* target. The function $F_{RC}(t)$ can then be calculated for each of the targets for which the $A_{M,i}$ are known. A measure of the fidelity of each of these predicted ramp responses can then be made by comparing each calculated ramp response to the original *measured* ramp response. One means of quantitatively performing this comparison is described below.

Figure 7 depicts the predictor-correlator methodology. Prior to performing any discrimination, a library of complex resonances of possible targets must be compiled through analytical or empirical means. In the discrimination procedure, a measured ramp response is tested with one of several candidate sets of complex resonances from the library. First, a predicted ramp response is generated using the postulated resonances and the measured ramp response. If the postulated complex resonance set matches the target associated with the measured ramp response, $F_{Rm}(t)$, then the predicted response, $F_{RC}(t)$, should be equivalent to the measured response. Mains and Moffatt suggested correlation as a measure of the equivalency of the two waveforms. This correlation, ρ', is given by

$$\rho'(\Delta t) = 1 - \frac{\sum_{n}^{N} [F_{Rm}(n\,\Delta t) - F_{RC}(n\,\Delta t)]^2}{\sum_{n}^{N} [F_{Rm}(n\,\Delta t)]^2} \qquad (3)$$

where ρ' is a function of the time interval Δt, which can be varied. The measured and predicted ramp responses will be equivalent if ρ' is unity, which indicates the measured ramp response waveform matches the candidate complex resonance set.

Mains and Moffatt tested this discrimination technique on the thin wire models of Figure 6 (straight-wing and swept-wing models). The results are given in Figure 8 for radar return from two aspect angles. These plots show ρ' plotted as a function of (normalized) Δt for both aircraft models when the complex resonances used were those of the straight-wing model. A threshold set at a ρ' value of 0.75 would insure that the discrimination technique

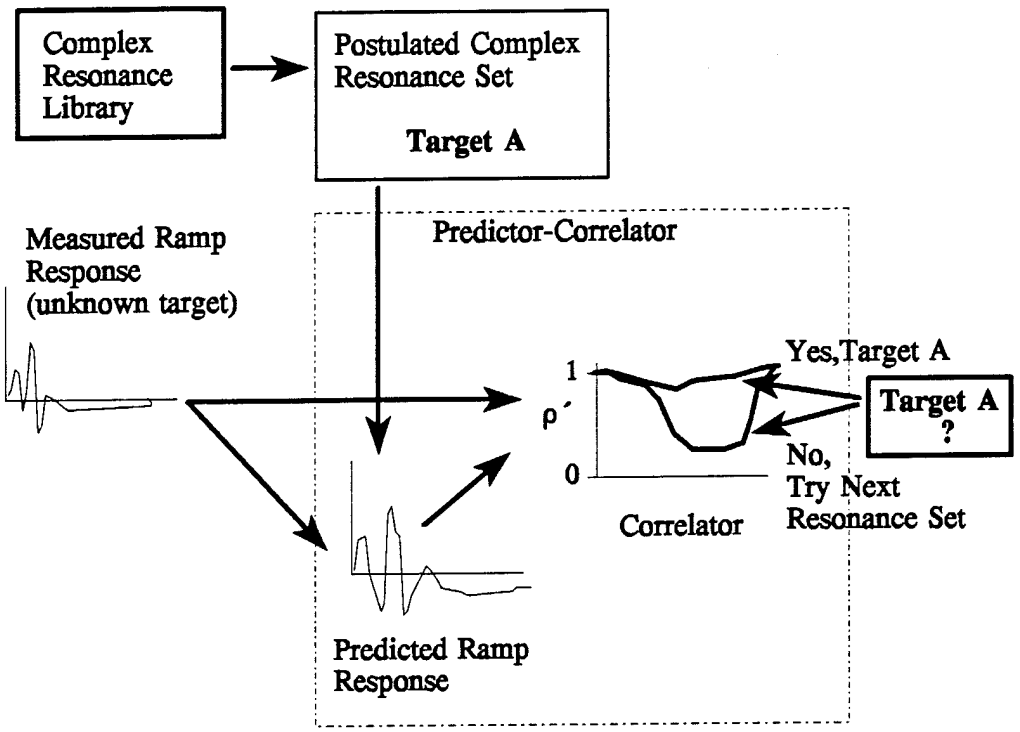

Figure 7 Predictor-Correlator methodology.

would choose the straight-wing model as the correct candidate. Mains and Moffatt present many more curves for different aspect angles and for the cases where the swept-wing resonances were employed. The curves presented dramatic confirmation of the utility of this predictor-correlator scheme for these two fairly similar targets.

While use of the predictor-correlator proved successful, other techniques could be used. The important aspect of the preceding discussion is the confirmation that the complex natural resonances are a useful set of target descriptors that are both unique and aspect invariant. Specific to this research program, it is important to note that these resonances occur at frequencies where the wavelength is on the order of the size of the scatterer. For the size of the objects of interest to this program, these frequencies are fairly low. The ability to rely on low frequency energy is fortunate because high frequency energy is greatly attenuated in the ground. The frequency of the resonances are dictated by the target

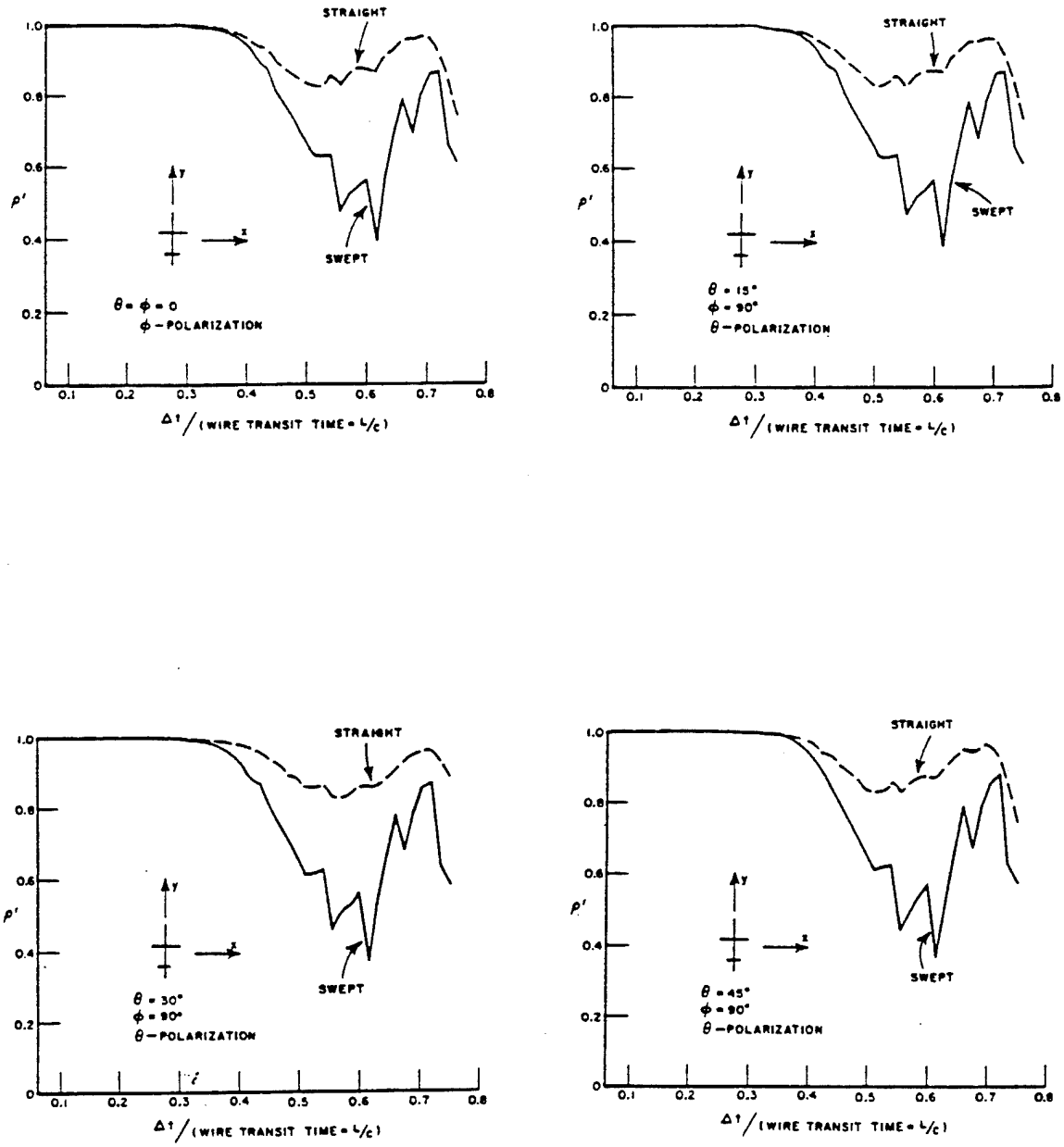

Figure 8 Calculation of ρ' for the straight and swept-wing thin-wire models using the resonances of the straight-wing model (from Mains and Moffatt).

geometry (and the ground media, as discussed in the following section). Gross length generally determines the frequency of the lowest order resonance. This size/resonance frequency relationship then determines the frequency range that the GPR must use if this resonance identification scheme is to be applied. The size of the largest anticipated UXO item dictates the low frequency end and the smallest item dictates the highest required frequency.

2.3 Complex Resonances in Distinct Ground Media

One area of investigation was the use of the complex resonances using experimental and computer-generated scattering data. As part of this analysis, two methods for predicting the value of the resonance in an arbitrary medium were investigated. These techniques rely on knowledge of the resonance values in free space and the constitutive parameters of the medium. One method, suggested by Carl Baum[1], gives the new complex resonance as

$$s_\alpha = -\frac{\sigma}{2\epsilon} + \left[\left[\frac{\sigma}{2\epsilon}\right]^2 + \frac{1}{\epsilon_r} s_\alpha^{(0)^2}\right]^{\frac{1}{2}} \tag{4}$$

where s_α is the complex resonance in the arbitrary medium, $s_\alpha^{(0)}$ is the value of the resonance in free space and ϵ is equal to the product of ϵ_0 (free space) and ϵ_r (the relative dielectric constant of the medium). An alternative method for long cylinders was suggested by Dr. Luen Chan[2] where

$$\alpha_1 = -\frac{\sigma}{2\epsilon_1} - 0.0828\frac{\pi c}{\sqrt{\epsilon_r} L} \tag{5}$$

---

[1] Carl E. Baum, "The SEM Representation of Scattering from Perfectly Conducting Targets in Simple Lossy Media," Interaction Note 492, Published by Phillips Laboratory, Air Force Weapons Laboratory, April 21, 1993.

[2] Luen C. Chan, "Subsurface Electromagnetic Target Characterization and Identification," Ph.D. Dissertation, The Ohio State University, 1979.

and

$$f_1 = \frac{0.925\,c}{2\,L\sqrt{\epsilon_r}} \tag{6}$$

where c is the speed of light in free space and L is the length of the cylinder. Table 1 shows the calculated results for 1 foot, 2 foot, and 3 foot cylinders in sand using the two methods. The sand resonance values were calculated using free space Moment Method resonances and Chan's and Baum's equations. They can be compared to Moment Method data calculated with sand as the surrounding medium. A quick analysis shows that the error for the real part of the complex resonance (α) for the 1 foot cylinders is unreasonably high (60-80 percent). For the remaining five values, the average of the absolute error is about 18 percent for Chan's equations and about 8 percent for Baum's equations.

Table 1 Complex Resonance in Sand Calculations for Three Long Cylinders.

Cylinder Length	Free Space $\epsilon_r = 1, \sigma = 0$ mmho				Sand $\sqrt{\epsilon_r} = 2.3, \sigma = 4.1$ mmho				Sand Chan's Equations		Sand Baum's Equations	
	α_c^0	f_c^0	α_m^0	f_m^0	α_c^s	f_c^s	α_m^s	f_m^s	α_L	f_L	α_B	f_B
1′	-0.09	0.410	-0.10	0.414	-0.21	0.185	-0.10*	0.170*	-0.16	0.199	-0.18	0.181
2′	-0.13	0.210	-0.17	0.208	-0.15	0.098	-0.12	0.080	-0.10	0.099	-0.13	0.091
3′	-0.26	0.150	-0.30	0.136	-0.14	0.066	-0.10	0.058	-0.08	0.066	-0.09	0.060

Notes:

1. Actual value = table value $\times 10^9$

2. α_m, $2\pi f_m$ are the real and imaginary parts of the complex poles obtained from processing the measured data using 4 foot long crossed dipoles

3. α_c, $2\pi f_c$ are the real and imaginary parts of the complex poles obtained from processing the moment method scattered field data for a cylinder immersed in a homogeneous medium.

4. α_L, f_L are the predicted poles in the sand obtained by plugging the α_m^0, f_m^0 into Chan's equation.

5. α_B, f_B are the predicted poles in the sand obtained by plugging the α_m^0, f_m^0 into Baum's equation.

* These data were measured by using 1 foot long crossed dipoles.

2.4 Description of UXO's Studied on this Effort

The UXO samples studied in this report are described here. They weight from 0.55 lbs. to 86 lbs. Their lengths range from 39 mm to 1 m. Table 2 lists these ordnance items and their average penetration depth characteristics. These data were prepared by NEODTECHDIV for the US Army Corps of Engineers in March, 1990. Photographs of most of these UXO's are also shown in Figure 9 and Figure 10. If one plots the average penetration depth versus weight from this table, the results are plotted in Figure 11. It is clear that the depth is approximately proportional to the weight for most UXO's below 20 lbs. For UXO's heavier than 20 lbs, the depths in clay are greater than 9 feet.

From the data of Figure 12, a 9 foot depth (total travel distance 18 feet) and a loss of 33 mmhos/m at 10 MHz, the attenuation is calculated as about 54 dB using

$$\text{Attenuation (dB)} = 20 \log_{10} \left(e^{-\sqrt{\frac{\omega \mu \sigma}{2}} x} \right)$$

where x is in meters.

SAR processing must be capable of separating the surface clutter from the UXO item return in the presence of this 54 dB attenuation. This capability will be influenced by the site where the UXO's are to be detected. There is one other factor. For a dielectric constant of 16 (common in clay), the reflection from a 9 foot deep UXO item would be delayed 72 ns from a reflection at the surface. This separation allows time for any antenna resonance remaining to be damped out and will increase the likelihood of target detection.

Table 2. List of UXO's under study.

Estimated Target Ordnance Item Depth Characteristics
(including Data from Range Clearance Technology Assessment Report[1])

NEODTC Inert Number (or from Report)	Description	Approx. Aspect Ratio	Weight in Pounds	Depth of Penetration in Feet							
				Sandstone		*Sand and Gravel*		*Chalk*		*Clay*	
				Avg	Prob. Max	Avg	Prob. Max	Avg	Prob. Max	Avg	Prob. Max
Report	20 mm	-	0.25	0.2	0.5	0.3	0.6	0.3	0.6	0.5	1.0
2075	30 mm	4.9:1	0.8	0.2	0.5	0.3	0.6	0.4	0.8	0.6	1.2
2076	40 mm	2:1	0.55	0.1	0.4	0.2	0.5	0.2	0.5	0.3	0.8
Report	37 mm	-	2.0	0.3	0.6	0.4	0.8	0.5	0.9	0.8	1.5
2077	37 mm	5.4:1	3.05[2]	0.45	0.9	0.6	1.2	0.75	1.35	1.2	2.25
2078	60 mm	4.8:1	3.15	0.3	0.5	0.3	0.7	0.4	0.8	0.7	1.2
2079	81 mm	3.5:1	10.5	0.5	1.0	0.5	1.5	1.1	2.8	2.8	4.0
2082	USSR 160 mm	7.5:1	69	4	9	8	11	10	13	12	17
2083	2.75 in	9.5:1	17	1	2	1	3	2	4	4	6
2084	3 in	4:1	12	0.8	1.6	0.8	2.4	1.6	3.2	3.2	4.8
2085	7 mm	4.1:1	8.7	0.5	1	0.5	1.5	1.1	2.8	2.8	4
2086	155	4.3:1	80	3.5	8	7	10	9	11	11	15
2087	USSR 82	4.1:1	5.75	0.4	0.8	0.5	1.2	0.7	1.4	1.1	1.8
2088	105 mm	3.8:1	14	1	2	1	3	2	4	4	6
2089	39	sphere	0.3	0.2	0.5	0.3	0.6	0.3	0.6	0.5	1
2090	USSR 85 mm	9:1	25	2	3	4	6	6	9	10	13
report	155 mm	-	90	4	9	8	11	10	13	12	17
report	-	-	100	8	17	9	19	11	19	14	25

Notes:

1. "Range Clearance Technology Assessment (Revision 1)", Final Report, Table 2, p. 2-14, Prepared by NEODTC for U.S. Army Corps of Engineers, March 1990.

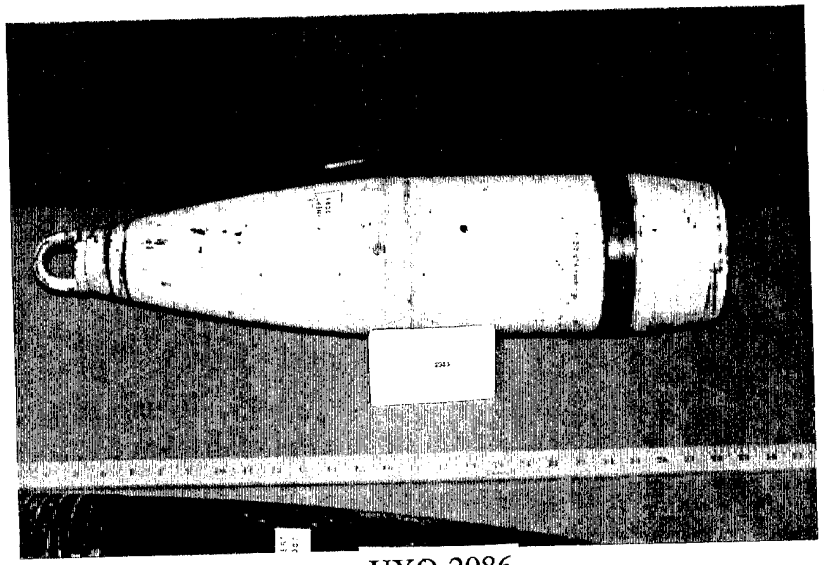

UXO 2086

UXO 2090

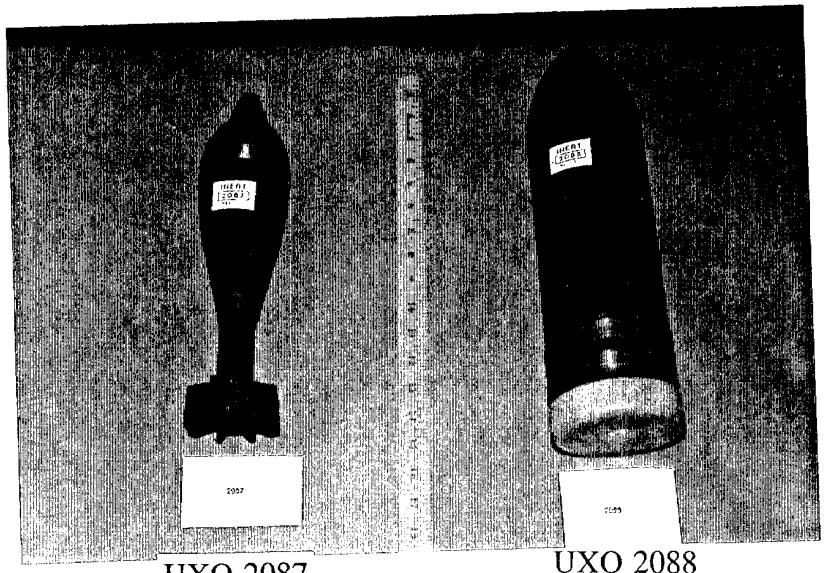

UXO 2087 UXO 2088

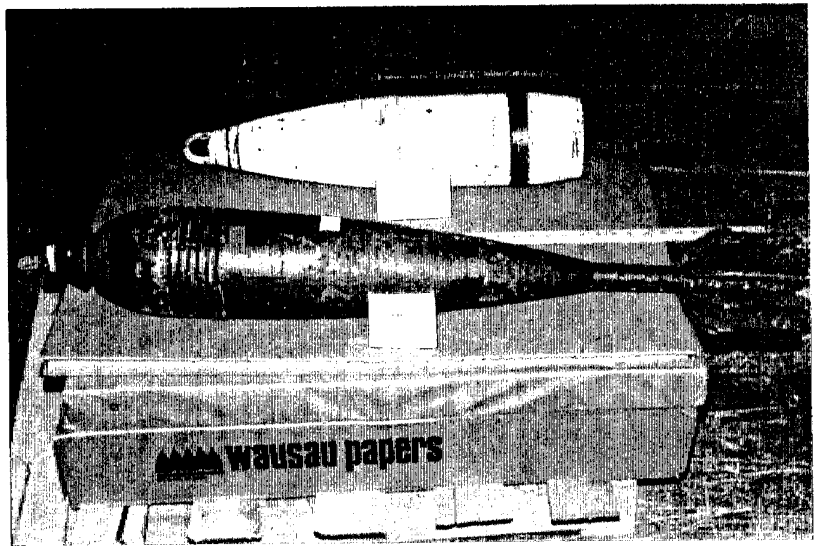

UXO 2082

Figure 9. Photos of UXO's under study.

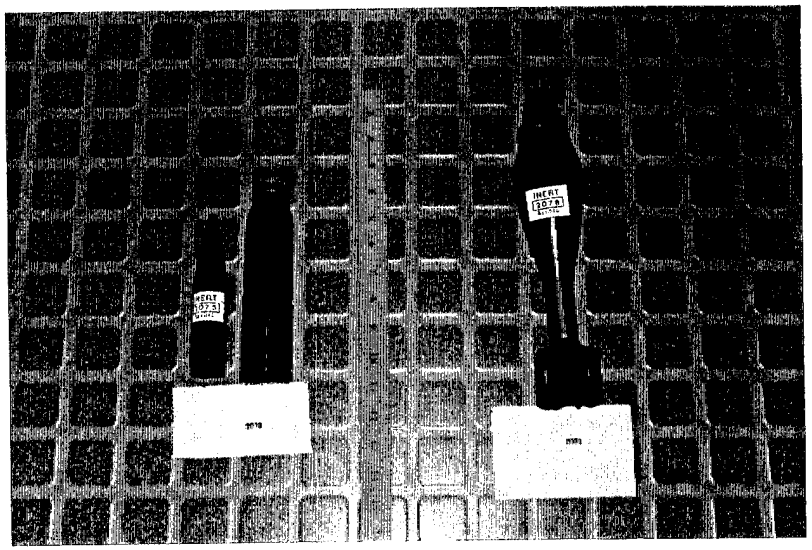

UXO 2075 UXO 2078

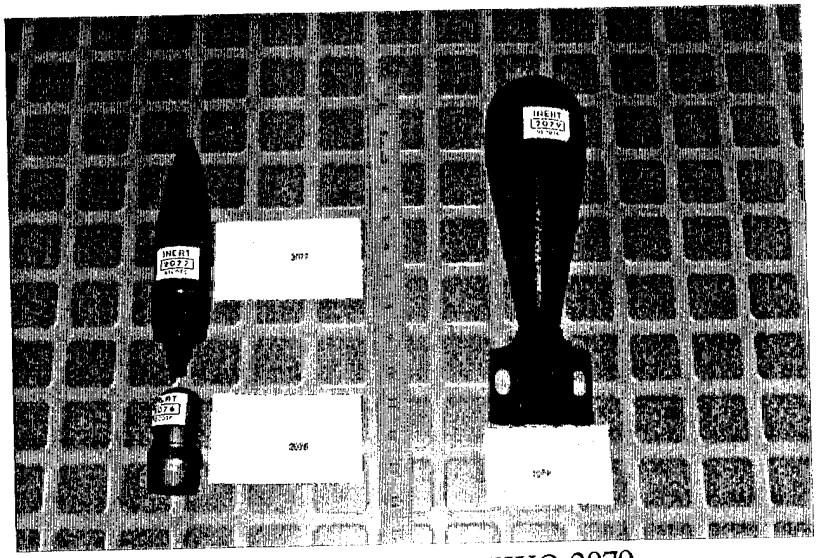

UXO 2077 UXO 2079

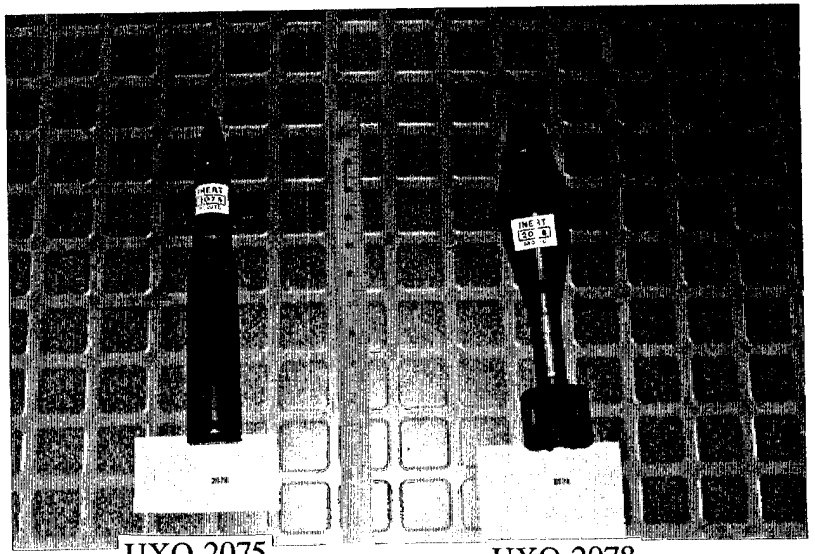

UXO 2075 UXO 2078

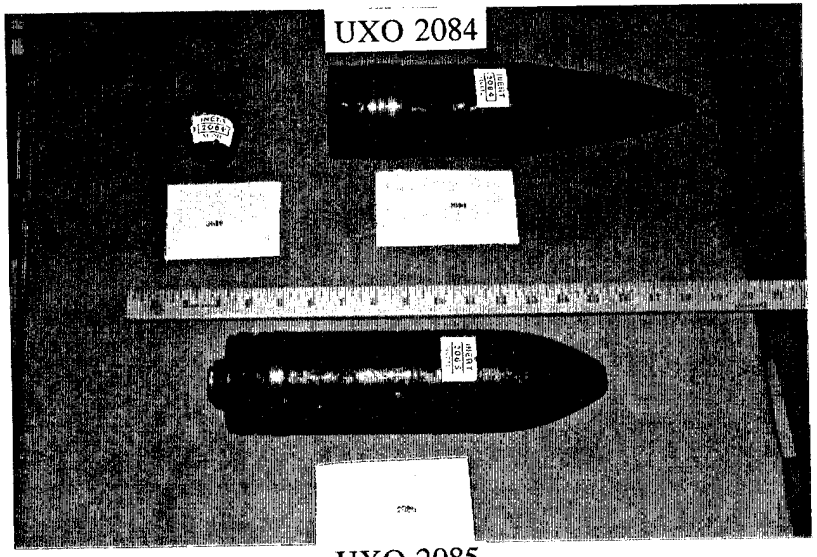

UXO 2084

UXO 2085

Figure 10. Photos of UXO's under study.

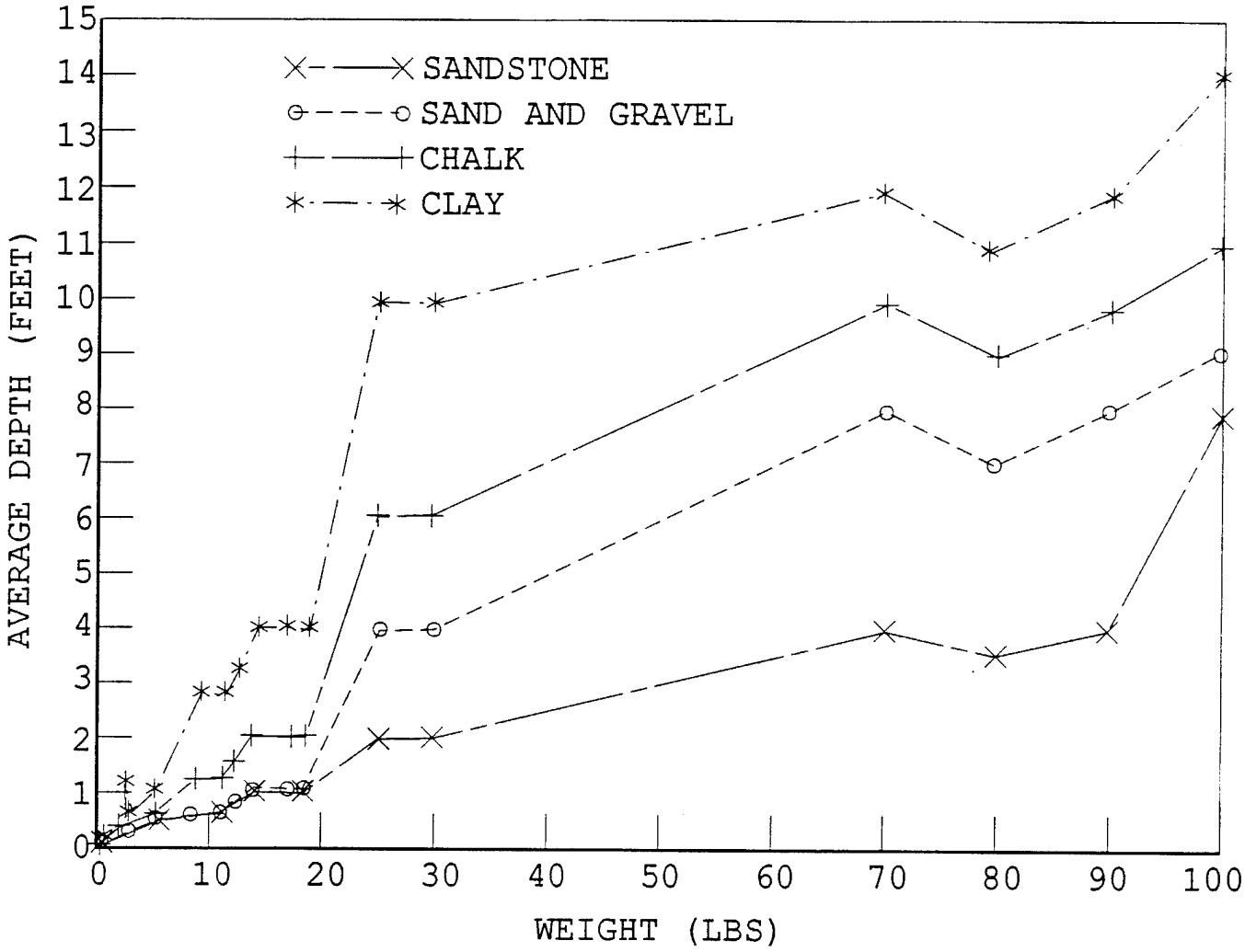

Figure 11. Penetration depth characteristics of UXO's of different weights.

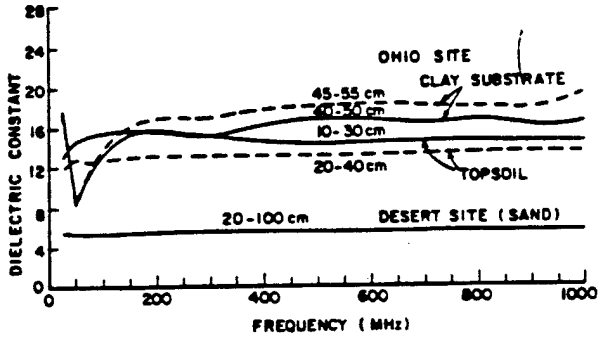

ϵ_r values for topsoil, clay substrate, and a desert site.

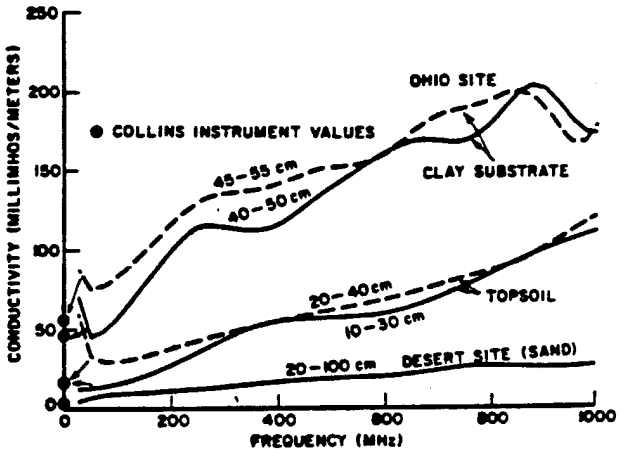

σ values for topsoil, clay substrate, and a desert site.

Figure 12. Electrical properties of soils as a function of frequency.

Polarization Properties of UXO's

Most UXO's under consideration here have elongated shapes, (i.e, L/D >> 1). This geometry makes them electrically polarized targets. Typically, the scattering from an electric field aligned parallel to the to the UXO's axis is at least 20 dB higher than the orthogonal polarization, at GPR frequencies. This scattering property of UXO's is very different from most natural GPR clutter sources such as rocks and soil layers. Table 3 shows the calculated difference of backscatter radar cross section (RCS) between parallel and perpendicular polarizations for different UXO's listed in Table 2. Note that the complete calculated response of these UXO's, for frequencies below 1 GHz, can also be found in Appendix A.

Table 3. Parallel ($\parallel$) and perpendicular ($\perp$) normal incidence backscatter RCS (dBsm) of different UXO's at 100 MHz and 300 MHz in free space.

No.	$\parallel$ RCS 100 MHz	$\perp$ RCS 100 MHz	$\parallel$ RCS 300 MHz	$\perp$ RCS 300 MHz
2075	-40	-69	-17	-50
2077	-50	-72	-38	-60
2078	-40	-68	-17	-48
2079	-38	-58	-15	-41
2082	+2	-35	-1	-18
2083	-18	-52	-2	-33
2084	-35	-58	-11	-39
2085	-34	-57	-11	-39
2086	-15	-40	-1	-21
2088	-27	-48	-2	-30
2090	-5	-42	-2	-24

From these examples, it is clear that radar detection and identification ability is strongly dependent on the UXO's polarization. This polarization property of these UXO's also suggests two guiding requirements for the radar designed to detect and identify them: (1) linear polarized antennas, and (2) dual polarization capability. Condition (1) can optimize the UXO's response when the antenna's polarization is aligned with the target. Condition (2) provides complete polarization information about targets and also avoids the low target response situation when the polarization of a single antenna is orthogonal to a UXO's axis. An example is the crossed-dipole (or crossed-slot) antenna arrangement operated in both co-polarization and cross-polarization modes. The advantages of cross-polarization mode are the reduction of antenna mutual coupling and reflections from the layered structure such as the ground surface.

Longitudinal Complex Natural Resonances

When the UXO is excited by the incoming wave from the radar, there will be an induced current flowing on the surface. The physical dimension of the UXO will limit the current flow and force it to bounce back and forth on the body, that is, it resonates. Because the current is continuously radiating while it is flowing, the scattered field received by the radar will show the same resonance behavior. This type of resonance, due to the physical nature of the target, is known as the complex natural resonance of the target. Note that each CNR has both a resonance frequency and a damping factor which are closely related to the target's dimensions as well as the environmental properties. Therefore, one can use CNR's to identify a certain desired target. As mentioned earlier, most UXO's of interest for this study have an elongated shape which means that the dominant resonant frequency is such that the UXO's length is about one-half wavelength. The damping factor is also related to the L/D ratio of the UXO. Table 4 lists the dominant CNR's of the UXO's under study. More information can also be found in Appendix A. One can see from this table that the longer the UXO's the lower the dominant resonant frequency. Also, the higher the resonance frequencies the larger the damping factor. It has been found that these observations hold for most situations.

Table 4. The dominant CNR of UXO's in free space.

UXO Number	Calculated Resonance		Measured Resonance	
	f(MHz)	α (1.0e9)	f(MHz)	α (1.0e9)
2075	450	0.57	457	0.12
2077	640	1.11	***	***
2078	390	0.48	366	0.23
2079	430	0.61	429	0.46
2082	120	0.12	121	0.10
2083	150	0.22	190	0.16
2084	350	0.64	368	0.18
2085	395	0.64	397	0.40
2086	195	0.32	206	0.11
2088	300	0.49	362	0.39
2090	150	0.16	139	0.07

*** No resonances were found.

Signatures of UXO's via CNR's

The theoretical CNR's of each UXO considered here were obtained by applying the modified SVD Prony's method (which is explained in detail in Section 6) to the calculated responses from its numerical 3-D models (see Figure 13). The 30 mm UXO, 2075, (see Figure 9), is used here as an example to show how to find its CNR's. The normal incidence backscatter RCS for both polarizations is calculated using the moment method for a body of revolution and is plotted in Figure 14. By doing an inverse Fourier transform (IFFT), one can obtain the corresponding time response, as shown in Figure 15. The last step is to process the obtained waveform to find the CNR's. A processing package has been developed

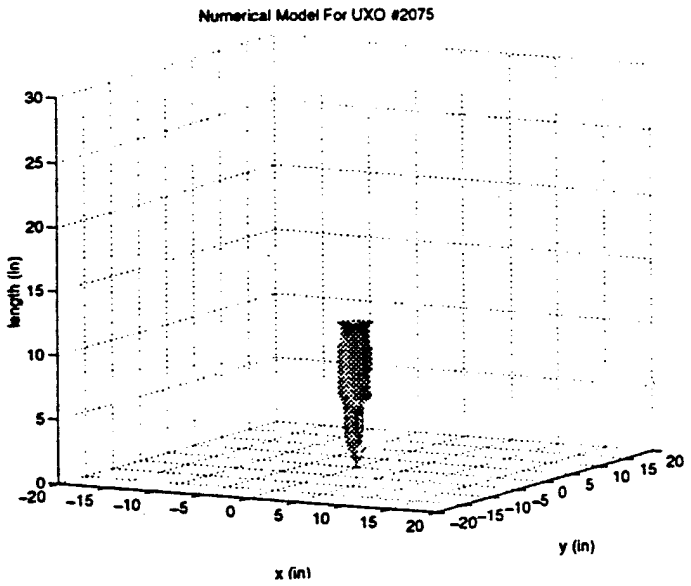

Figure 13. 3-D model of UXO 2075.

in this project to perform the CNR's extraction and present the resultant CNR's, which can be displayed in different useful formats: (1) time-frequency plot of resonant amplitude, (2) time-frequency plot of damping factor, (3) frequency versus damping factor, and (4) complex pole plot. This processing package is developed using the well-known commercial signal processing package MATLAB.

Figure 16 shows one type of the processed output where the CNR's are plotted in frequency versus damping factor coordinates. Two significant resonances corresponding to the first and second resonant modes of UXO 2075 were found in this case. The dominant resonance usually exhibits a smaller damping factor and lower resonance frequency. The CNR's removed waveform (solid line) is compared with the original waveform (dotted line) in the lower figure. A flat solid line indicates a good prediction of the original waveform using the obtained CNR's. Figure 17 plots the amplitude of each CNR as function of time and frequency in gray scale. It is clear that the dominant resonance is stronger and lasts longer in time. The CNR's of other UXO's under consideration were obtained in the same way and are tabulated in Appendix A.

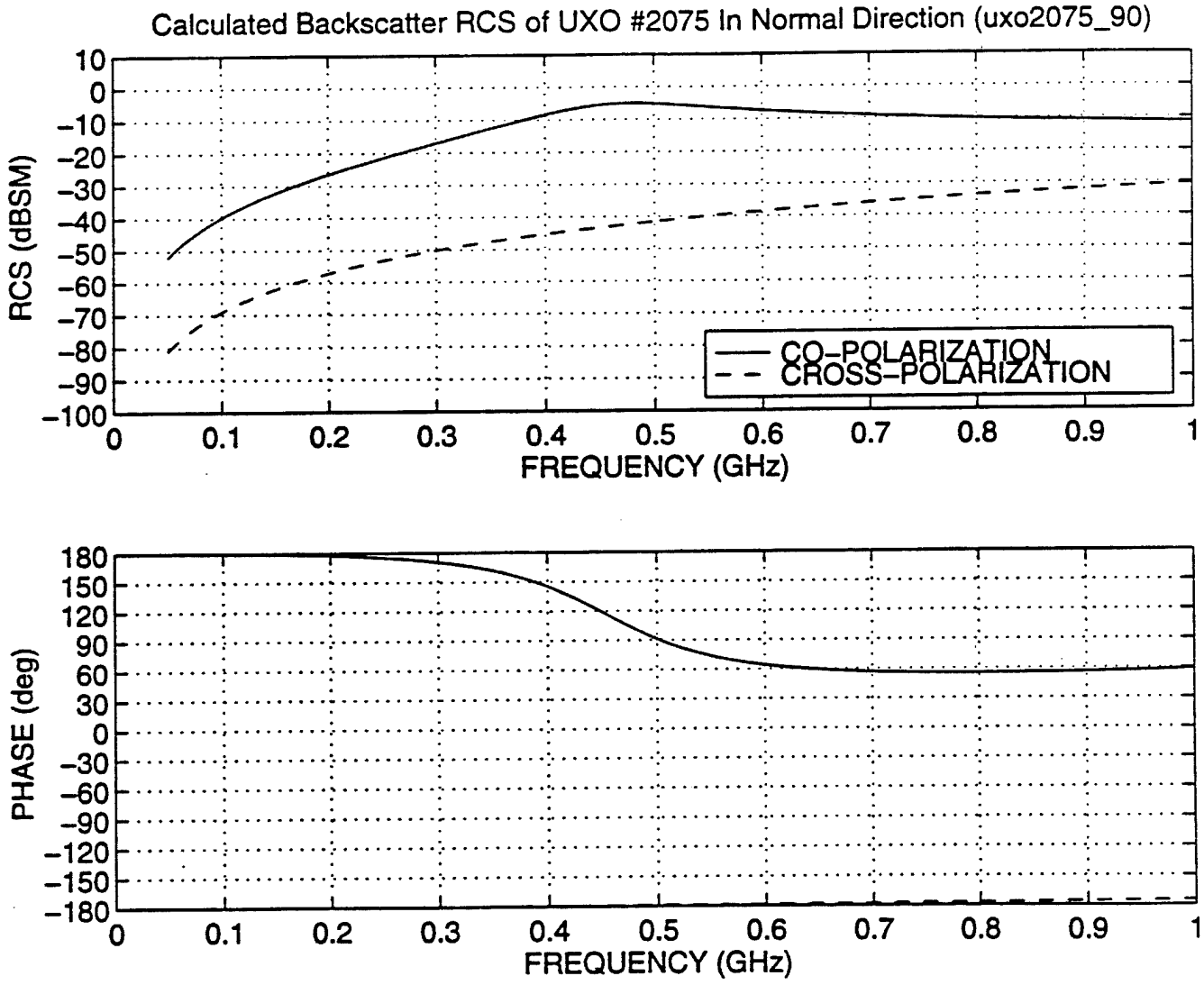

Figure 14. Backscatter RCS of UXO 2075.

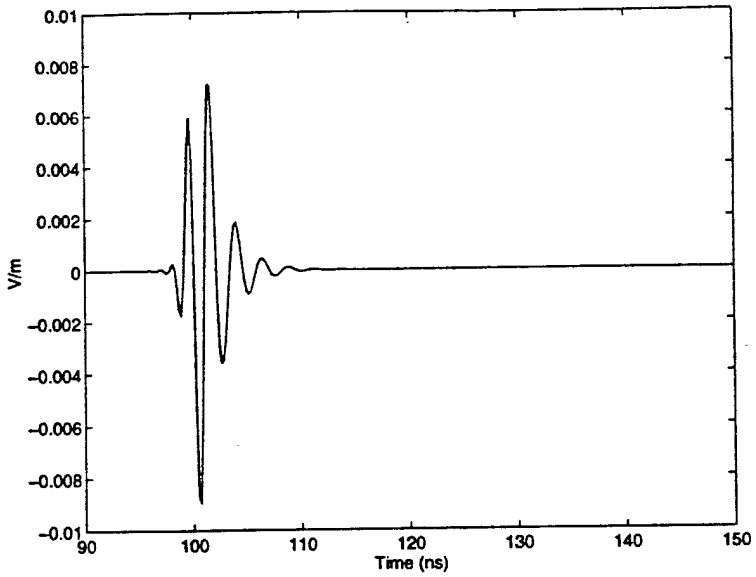

Figure 15. Time waveform of the backscatter field from UXO 2075.

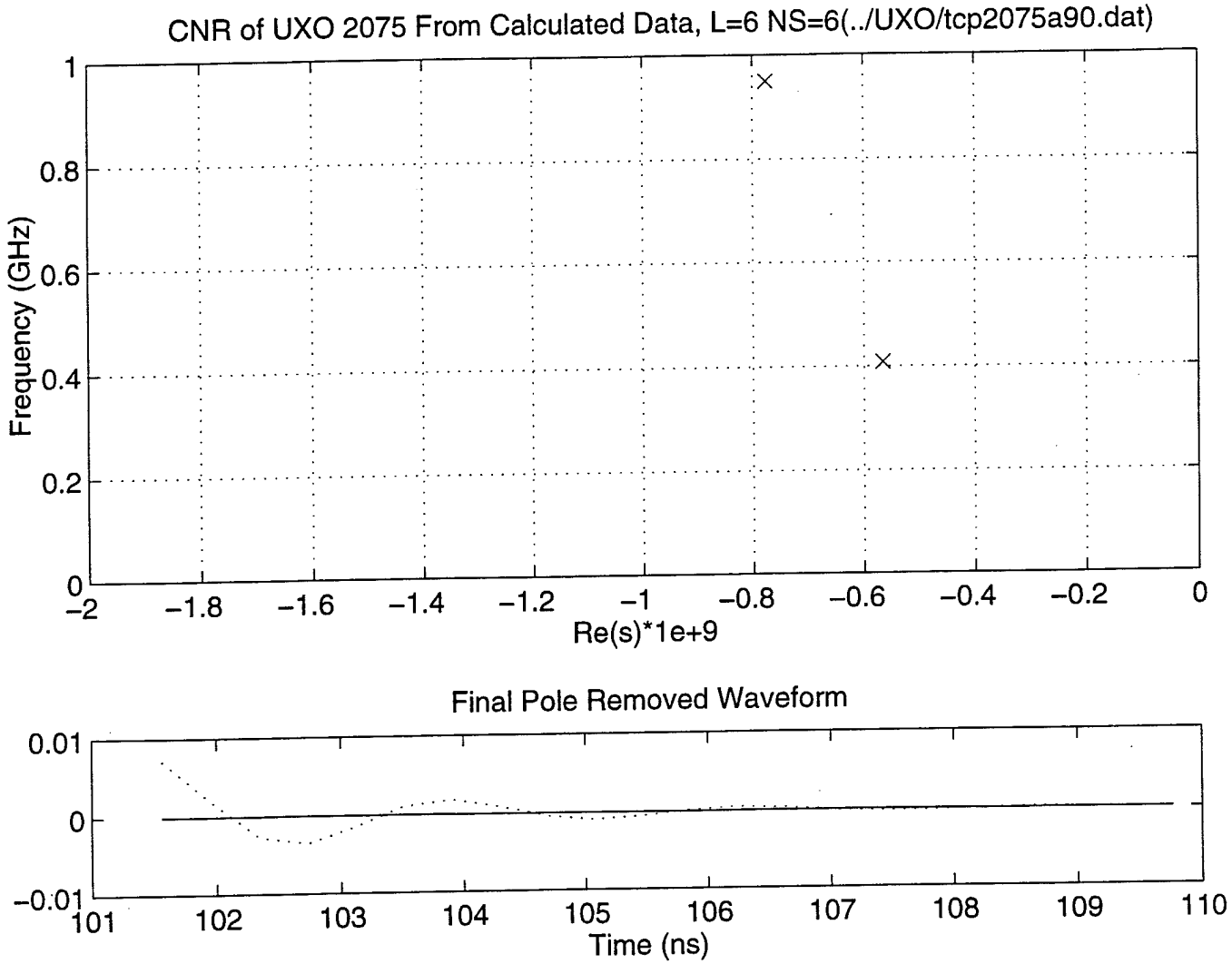

Figure 16. CNR's obtained for UXO 2075.

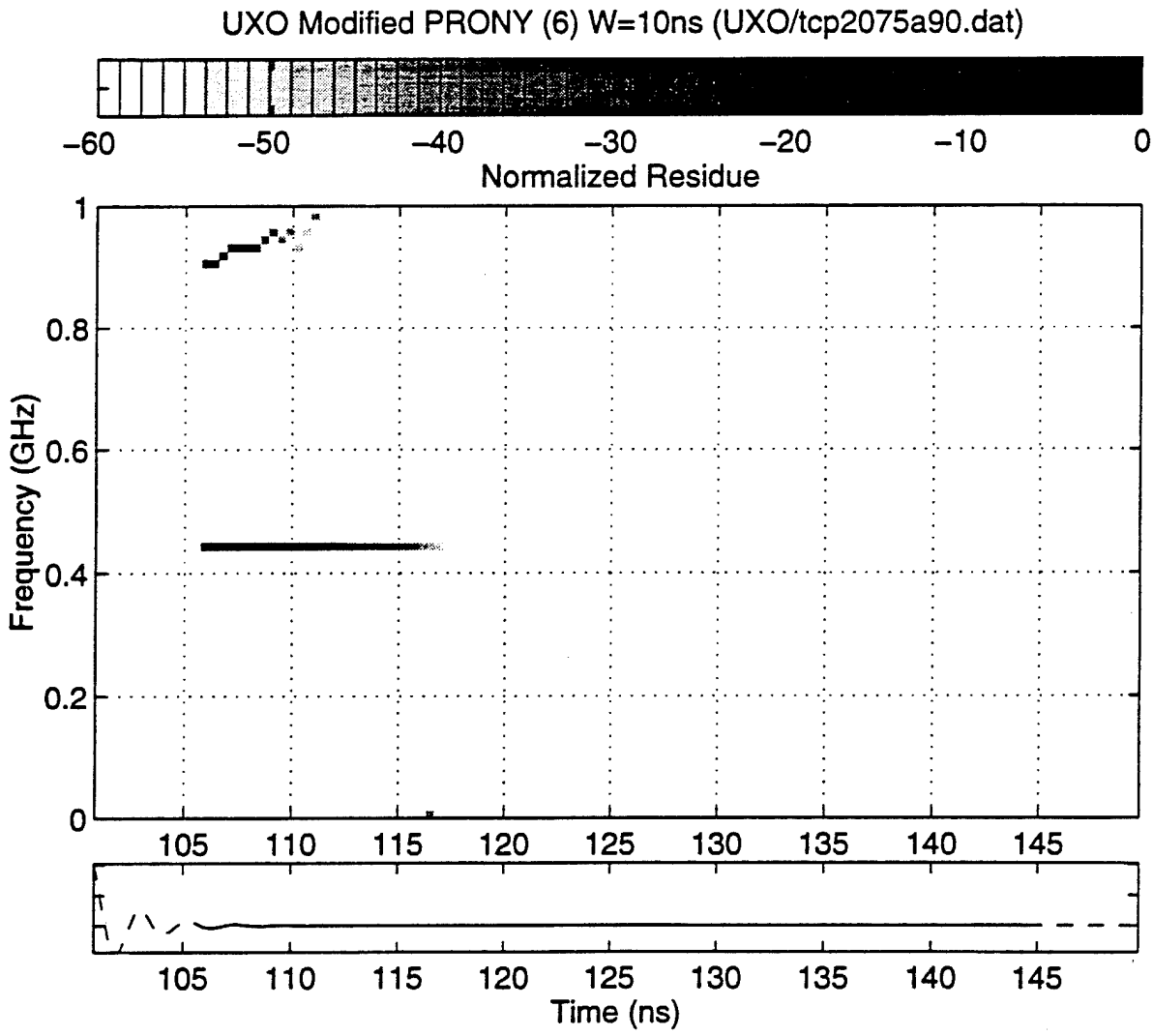

Figure 17. Time-frequency plot of magnitude of CNR's obtained for UXO 2075.

2.5 Inert Target Measurements

Finite Length Cylinder Approximations

Conducting cylinders are good approximations for most of the UXO's in the study of their CNR's. This approximation provides an easier way to predict a UXO's scattering properties in different media. Furthermore, thin wire models can also be used to model conducting cylinders if their length to diameter ratios are not too small. For the data in this section, a thin-wire computer code using the moment method was applied to calculate the scattered fields from the conducting cylinders and then the CNR information was extracted from these calculated results. Figure 18 shows the calculated RCS of 1 foot, 2 foot, and 3 foot conducting cylinders in free space. The wires are tilted at 45° with respect to the incident waves. The "peaks" in these responses indicate the locations of possible CNR's. Note that, at a 45° incident angle, the specular reflection will not be received. Therefore, the resonant fields and the tip diffractions are dominating the response. The CNR's of these cylinders are extracted from the corresponding time domain response, which are obtained by applying the IFFT to the frequency domain data. The calculated CNR's with resonance frequencies below 1 GHz are shown in Figure 19, Figure 20, and Figure 21. All the CNR's are fairly stable due to that fact that there is no other noise or clutter signals as discussed in Section 6.0. The comparison of the first CNR's between the calculated data and the measured data is also shown in Table 5. One can see a very good agreement in these data.

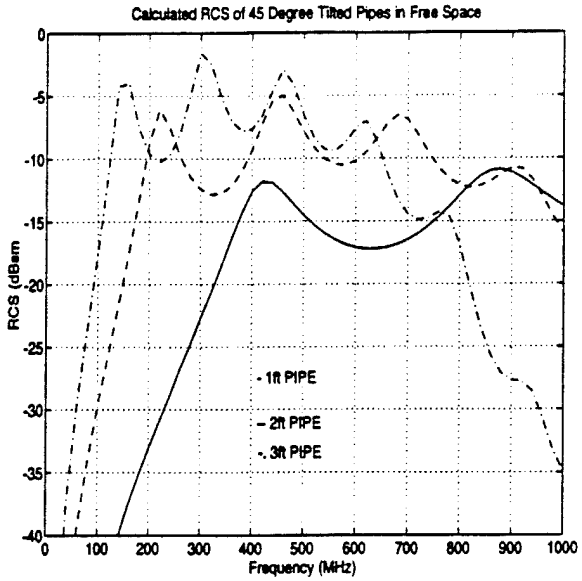

Figure 18. Calculated backscattered RCS of conducting cylinders of 1 foot, 2 foot, and 3 foot length with 45 degrees incident angle.

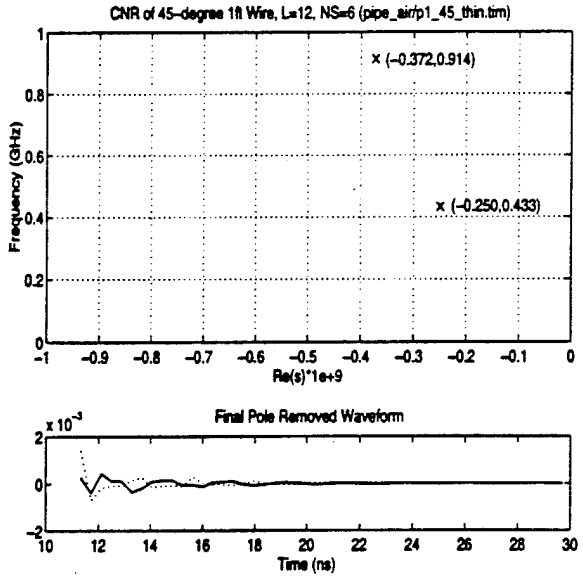

Figure 19. Extracted CNR's of 1 foot cylinder.

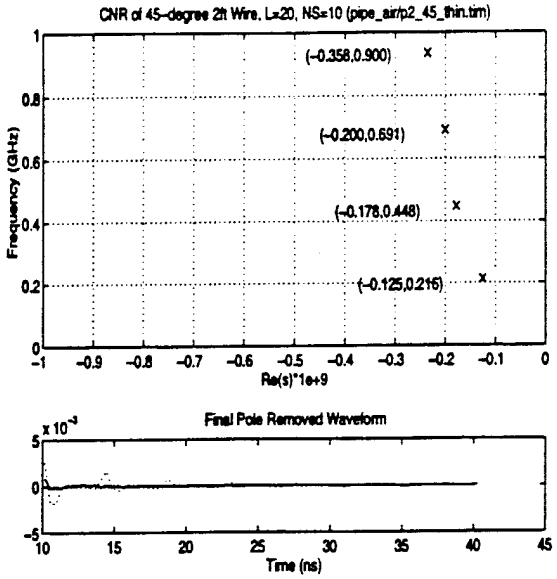

Figure 20. Extracted CNR's of 2 foot cylinder.

Table 5. The dominant CNR's of pipes in free space.

Pipe	Calculated Resonance		Measured Resonance	
	f (MHz)	α (1E9)	F (MHz)	α (1E9)
1 foot pipe	433	0.25	439	0.28
2 foot pipe	216	0.13	208	0.17
3 foot pipe	134	0.06	137	0.05

Scattering from UXO's

As stated previously, the UXO's were easily modeled due to their circular symmetry. A body of revolution code using the moment method was used to calculate the scattering fields of the UXO devices. The results are provided in Appendix A. The next step was to extract the CNR's of the UXO's from these calculated data. The resultant CNR's were provided in Table 4. In the same table, the first order CNR's extracted from the measured data with all UXO's in free space are also listed for comparison. The "***" indicates that no CNR's were found. This lack of a resonance occurred because the measurement system frequency band is below 500 MHz and the resonance for this target is above 500 MHz. It is clear that the resonance frequencies found from the measured data are very close to those obtained from the calculated ones, whereas the damping factors α's show greater differences. It is well known that the damping factor is a sensitive parameter and is very unstable compared to the resonance frequency. This sensitivity can be understood from the fact that the resonance frequency is determined by the zero-crossing rate and the damping factor is determined by the waveform amplitude variation. Therefore, if there are other small signals added to the desired resonance signal, the zero-crossing rate will not change much but the damping factor will be affected more significantly. A second error source lies in the fact that the body of revolution code has less accuracy when the incident wave is away from the head-on direction. This lack of precision could also cause the difference between the calculated and the measured data. Note that the first order resonance frequency is mainly determined by the UXO's length, regardless of its shape. However, different shapes will cause different damping factors. At resonance, the length of a UXO is about one-half wavelength, as is the case with a conducting cylinder. This similarity explains why inert 2082 has a resonance frequency close to the 3 foot cylinder and inert 2075 has a resonance close to that of a 1 foot cylinder.

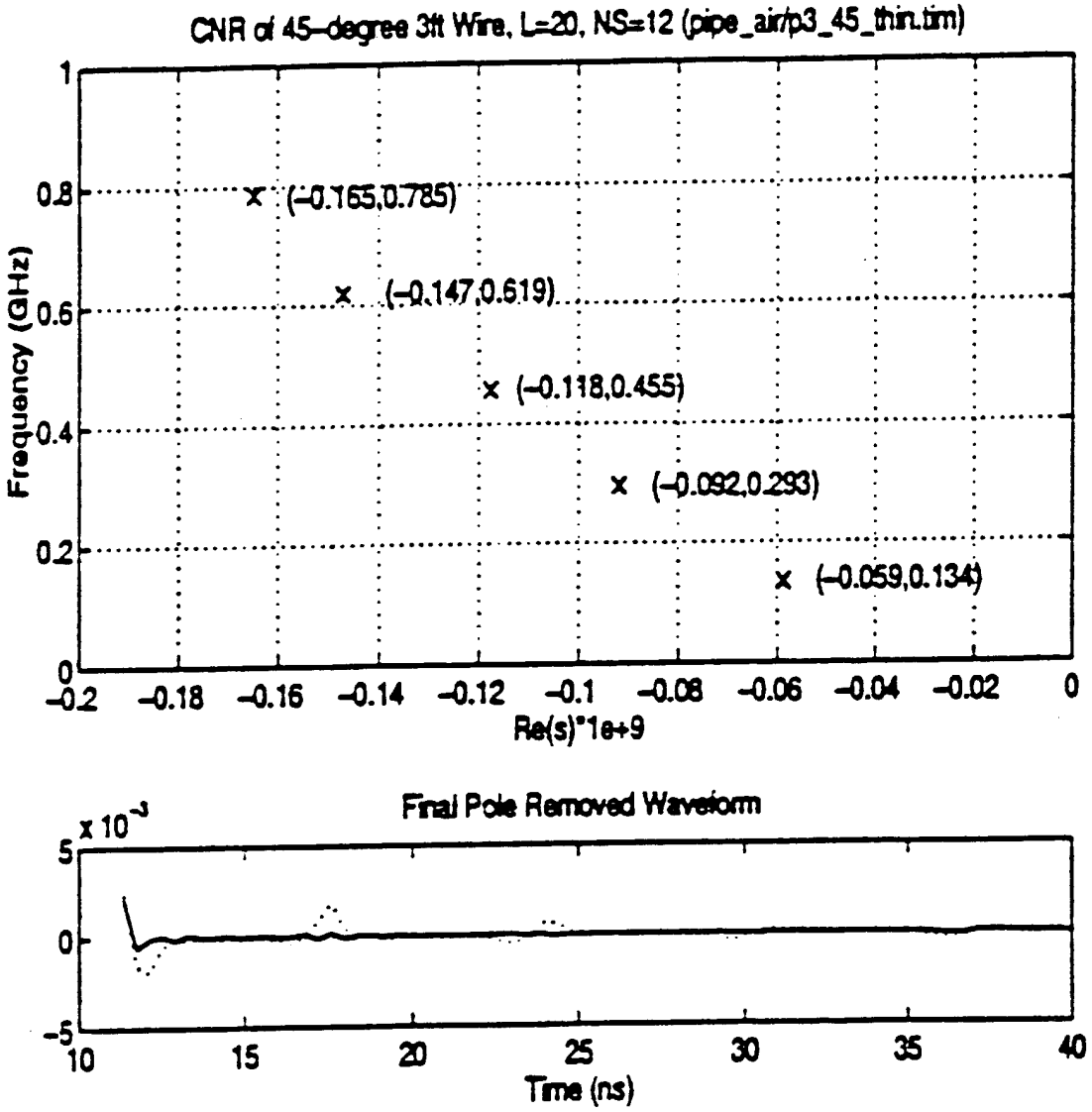

Figure 21. Extracted CNR's of 3 foot cylinder.

2.6 Measurement Methodology

The UXO targets and other metal cylinders were measured using a variety of GPR antennas and in a variety of soils. Table 6 shows a summary of all measurements. For each target, the code indicates the antenna, radar system, oreientation, and burial depth. There are separate columns for free space, sand, and clay soil media.

As shown in the tables, the largest set of data was acquired using a sampling scope, which uses a time-domain impulse source. Crossed-dipole antennas were used in most cases. These antennas have 20 dB or better transmit-receive isolation than same-sense polarized antennas and they sense the cross polarized echo of the target. The crossed-polarized return still contains all characteristic resonance features but with approximately 6 dB less excitation than the same-sense antennas. The use of two antenna sizes, namely, 1 foot and 3 foot elements, allows us to sense the resonances over a wider range of frequencies.

Figure 22 shows a diagram of the measurement setup for the targets buried in sand. The impulse generator is connected to the transmitting antenna and the sampling oscilloscope is connected to the orthogonal receive antenna. The antenna is positioned on the flat sand surface directly above the target and the target is oriented at 45 degrees to the axis of the antennas. After the target was measured, the antena was picked-up, rotated 90 degrees, and a second measurement was taken. For a crossed-dipole, the target echo will reverse polarity in this situation, but antenna coupling and non-coherent surface clutter do not. Therefore, processing of the data included subtracting the 0 and 90 degree data to double the target return and cancel-out coupling and clutter.

For the free space tests, the antenna was positioned upside down above the ground and the targets were mounted on a foam support directly above the antenna. The target orientation was the same as for buried targets. In the free space measurements, a no-target waveform was recorded first and then this error energy was coherently subtracted from all the target measurements as a part of the waveform processing before calibration.

Table 6 Matrix of experimental data.

CODE: SYSTEM ANTENNA ORIENTATION DEPTH

	Free Space		Sand		Clay	
	Code	File	Code	File	Code	File
UXO2075	S1M1	3210	S1M1	3211		
	S1M1	3320	S1M1	3212		
	S3M1	3216	S4M1	3313		
	S3M1	3320	S5M1	3313		
			D2M1	3211		
UXO2076	S1M1	3210	S1M1	3211		
	S1M1	3320	S1M1	3212		
	S3M1	3216	S4M1	3313		
	S3M1	3320	S5M1	3313		
			D2M1	3211		
UXO2077	S1M1	3210	S1M1	3211		
	S1M1	3320	S1M1	3212		
	S3M1	3216	S4M1	3313		
	S3M1	3320	S5M1	3313		
			D2M1	3211		
UXO2078	S1M1	3210	S1M1	3211		
	S1M1	3320	S1M1	3212		
	S3M1	3216	S4M1	3313		
	S3M1	3320	S5M1	3313		
			D2M1	3211		
UXO2079	S1M1	3210	S1M1	3211		
	S1M1	3320	S1M1	3212		
	S3M1	3216	S4M1	3313		
	S3M1	3320	S5M1	3313		
			D2M1	3211		
UXO2082	S1M1	3210	S1M1	3211		
	S1M1	3320	S1M1	3212		
	S3M1	3216	S4M1	3313		
	S3M1	3320	S5M1	3313		
			D2M1	3211		
UXO2083	S1M1	3210	S1M1	3211		
	S1M1	3320	S1M1	3212		
	S3M1	3216	S4M1	3313		
	S3M1	3320	S5M1	3313		
			D2M1	3211		
UXO2084	S1M1	3210	S1M1	3211		
	S1M1	3320	S1M1	3212		
	S3M1	3216	S4M1	3313		
	S3M1	3320	S5M1	3313		
			D2M1	3211		
			F6O0	4072		

SYSTEM
S = Sampling Scope
D = Digitizer
G = GPR Box
F = CW

ANTENNA
1 = 1′ Cross Dipole
2 = 3′ Green Cross
3 = 4′ Orange Cross
4 = 4′ Mono Cancel
5 = 4′ Mono Bistatic
6 = 8′ Rombic On Roof
7 = Slot-Dipole
8 = Cross-Slot
9 = Cross-Dipole

ORIENTATION
M = Normal Incidence
O = Offset
S = Scan

DEPTH
(Units = feet)

Table 6. Continued

UXO2085	S1M1	3210	S1M1	3211		
	S1M1	3320	S1M1	3212		
	S3M1	3216	S4M1	3313		
	S3M1	3320	S5M1	3313		
			D2M1	3211		
UXO2086	S1M1	3210	S1M1	3211		
	S1M1	3320	S1M1	3212		
	S3M1	3216	S4M1	3313		
	S3M1	3320	S5M1	3313		
			D2M1	3211		
UXO2088	S1M1	3210	S1M1	3211		
	S1M1	3320	S1M1	3212		
	S3M1	3216	S4M1	3313		
	S3M1	3320	S5M1	3313		
			D2M1	3211		
UXO2090	S1M1	3210	S1M1	3211		
	S1M1	3320	S1M1	3212		
	S3M1	3216	S4M1	3313		
	S3M1	3320	S5M1	3313		
			D2M1	3211		
1′ pipe	S1M2	3215	D3M1	3217	G4M2	3288
	S3M1	3216	S1M1	3211	G4M1	3287
	D3O1	3223	D2M1	3211	G4M3	3287
	D4O2	3231	D1M1	3217	G4M5	3287
			S4M1	3313		
			S5M1	3313		
			S1M1	3312		
			S3O1	3336		
			S3O2	4013		
			F6O0	4072		
			F3M1	4172		
			F3M1	4173		
			F3M1	4174		
2′ pipe	S1M2	3215	D3M1	3217	G4M1	3288
	S3M1	3216	D1M1	3217	G4M2	3288
	S1M1	3216	S3O2	3343	D3M1	3288
	D3O1	3223	S3O2	4013		
	D4M2	3231				
	D4O2	3231				
			F6O0	4072		
			F3M1	4172		

SYSTEM
S = Sampling Scope
D = Digitizer
G = GPR Box
F = CW

ANTENNA
1 = 1′ Cross Dipole
2 = 3′ Green Cross
3 = 4′ Orange Cross
4 = 4′ Mono Cancel
5 = 4′ Mono Bistatic
6 = 8′ Rombic On Roof
7 = Slot-Dipole
8 = Cross-Slot
9 = Cross-Dipole

ORIENTATION
M = Normal Incidence
O = Offset
S = Scan

DEPTH
(Units = feet)

Table 6. Continued

3′ pipe	S1M2	3215	D3M1	3217	G4M1	3287
	S3M1	3216	D1M1	3217	G4M3	3287
	S1M1	3216	S3O2	4013	G4M5	3287
	D3O1	3223				
	D4M2	3231				
	D4O2	3231				
			F6O0	4072		
5′ pipe					G4M1	3287
					G4M3	3287
					G4M5	3287
2.5′ pipe			D4M1	3278		
			D3M1	3278		
			D2M1	3278		
3′ pipe varying depth	D5M*	3232				
Trench					G4M1	3288
			G4S*	a4244		
			G3S*	a4244		
Trihedral			S3O1	3341		
Trihedral			S3O1	3341		
Metal Plate			F3M1	4188		
Plastic Mine			F3M1	4188		
Metal Sphere			F3M1	4188		
Wood Block			F3M1	4188		
2′ log			F3M1	4188		
Rock Block			F3M1	4188		
ESL Pipe Farm	G3S*	a4189				
	G3S*	a4192				
	G4S*	a4194				
	G4S*	a4196				
	G4S*	a4220				
	G4S*	a4222				
	G4S*	a4272				
	G7S*	a4314				
	G4S*	a4321				
	G8S*	a5018				
	G9S*	a5018				
	G8S*	a5017				
	G9S*	a5029				
	G9S*	a5030				
	G9S*	a5031				
	G9S*	a5033				
ESL Slant Pipe	G4S*	a4199				
	G4S*	a4214				
	G4S*	a4228				

SYSTEM
S = Sampling Scope
D = Digitizer
G = GPR Box
F = CW

ANTENNA
1 = 1′ Cross Dipole
2 = 3′ Green Cross
3 = 4′ Orange Cross
4 = 4′ Mono Cancel
5 = 4′ Mono Bistatic
6 = 8′ Rombic On Roof
7 = Slot-Dipole
8 = Cross-Slot
9 = Cross-Dipole

ORIENTATION
M = Normal Incidence
O = Offset
S = Scan

DEPTH
(Units = feet)

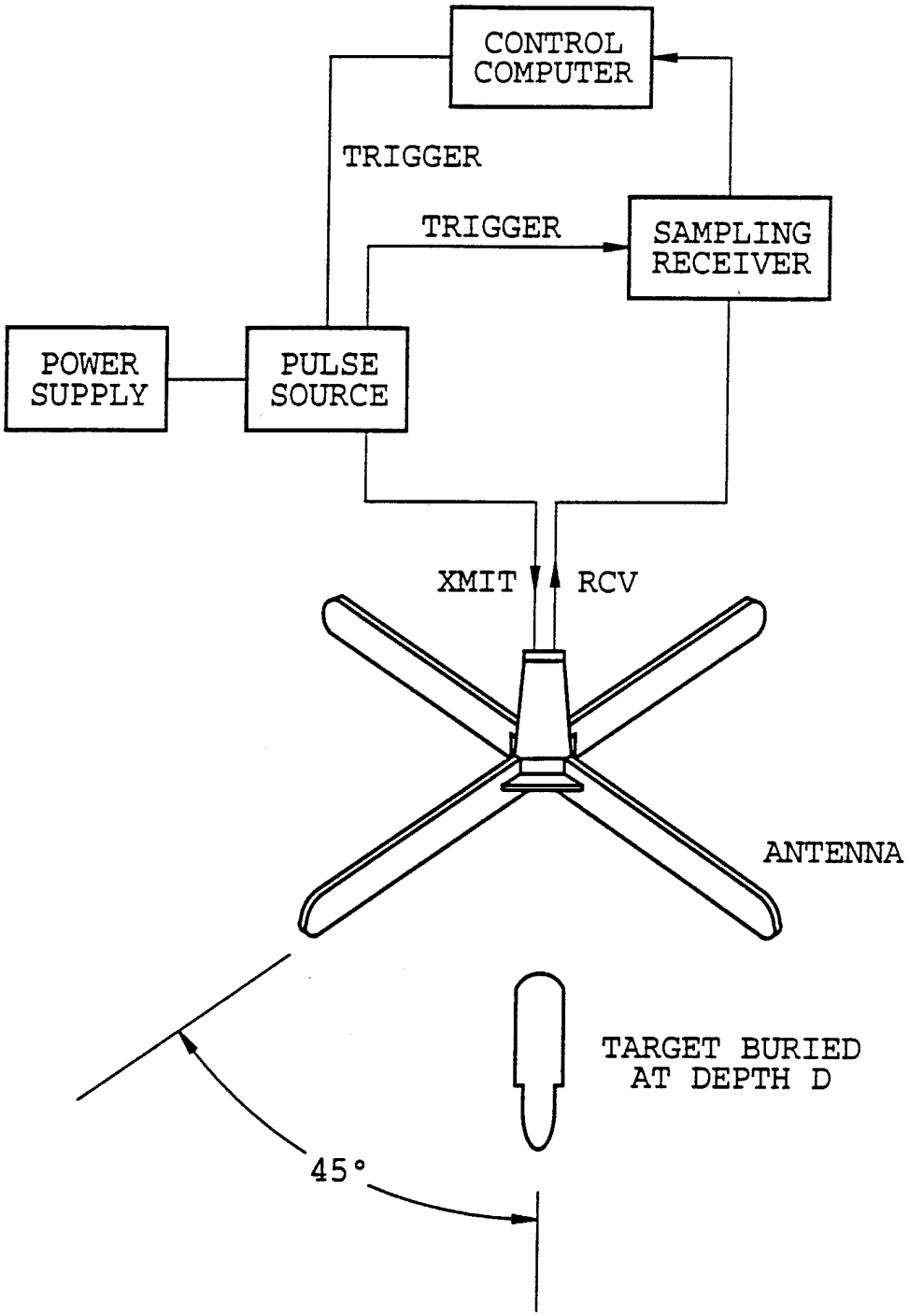

Figure 22 Buried target measurement geometry.

The measurements verified that conducting cylinders having the same length-to-width ratio as the UXO targets reproduce the same characteristic resonances with good accuracy. Because of this similarity, we did not bury the UXO targets in clay for measurement. There were existing cylinder targets buried in the clay since 1971; these cylinders were measured. Because they have been buried so long, these targets will not have nearly as strong a trench effect return as for recently buried targets. The data from the cylinders do a better job of simulating data from UXO targets buried years ago, in our opinion.

The targets in clay were measured using the same procedure as for targets in sand.

For the antennas referenced in Table 6, both the 3 foot green and 4 foot orange are crossed-dipole antennas with absorber loading. The orange antenna was manufactured by M/A-COM and is illustrated in Figure 22. The green antenna was constructed at ESL with antenna elements being 4 inch wide top and bottom walls of a rectangular tube.

3.0 SAR Modeling

3.1 SAR Simulation

The goal of the SAR Simulation Program is to simulate the response of an airborne synthetic aperture ground penetrating radar. If we can accurately model the responses from expected targets, underground clutter, and the air-to-ground interface, we can predict the necessary dynamic range, synthetic aperture length, system sampling rate, and other system variables required for a real system. We will also be able to predict the effectiveness of a GPR given the electrical characteristics of the soil. Table 7 contains a list of the variable parameters in the SAR Simulation Program. Section 3.5 on page 92 discusses model fidelity.

Description of the System

The airborne synthetic aperture radar is flying straight at a constant velocity v and altitude h above the surface. The main beam of the antenna is pointed normal to the surface. The soil is characterized by a homogeneous dielectric constant and conductivity. Relative permeability is 1. Conductivity should be in the range of 0.01 to 0.001 mhos/m. The targets below the surface are modeled as perfectly conducting small ellipsoids, large cylinders, or point targets. The targets may be oriented in any direction. The transmitting and receiving antennas may be either horizontal or vertical infinitessimal dipoles.

Impulse and Stepped-Frequency Models

The SAR Simulation Program models two types of synthetic aperture radar systems: an impulse radar and a step-frequency radar.

In the impulse radar model, an impulse is transmitted at each position of the radar. Each impulse is modelled as N frequencies being transmitted simultaneously at each

transmission point. The number of impulses is M. M is determined by the requirement that the spacing between samples be $\lambda/2$ at the highest transmitted frequency, 500 MHz. If L is the length of the synthetic aperture, or the distance over which data is recorded, M is equal to $L/(\lambda/2)$.

In the step-frequency radar model, only one of the N frequencies from 50 MHz to 500 MHz will be transmitted at each position of the radar. The frequencies are stepped through, one frequency at a time, as the radar moves along the flight path. The sequence of frequencies is repeated M times for a given image. Using the step-frequency model, we can examine the effects of changing the number of frequencies transmitted, the number of times a given frequency is transmitted per image, and the sampling rate or spacing.

Table 7 SAR Simulation Parameters

SAR Simulation Variables
Impulse Model or Step-Frequency Model
Source and Receiver Polarization
Windowing Functions
Radar Velocity
Radar Altitude
Soil Parameters (Homogeneous only)
Number of Frequencies
Number of Samples per Frequency
Sample Spacing
Length of Synthetic Aperture
Image Size, Position, and Pixel Size
Number of Targets
Target Position
Target Size and Shape (sphere, cylinder, ellipsoid, or point)
Target Orientation

The impulse model and the step-frequency model are fundamentally equivalent when the number of impulses in the impulse model is equal to the number of times the frequency sequence is repeated in the step-frequency model. The bandwidth and number of frequencies used in each model must also be the same. Figure 23 and Figure 24 show examples of the SAR simulation of an impulse system and a step-frequency system, respectively, for point targets.

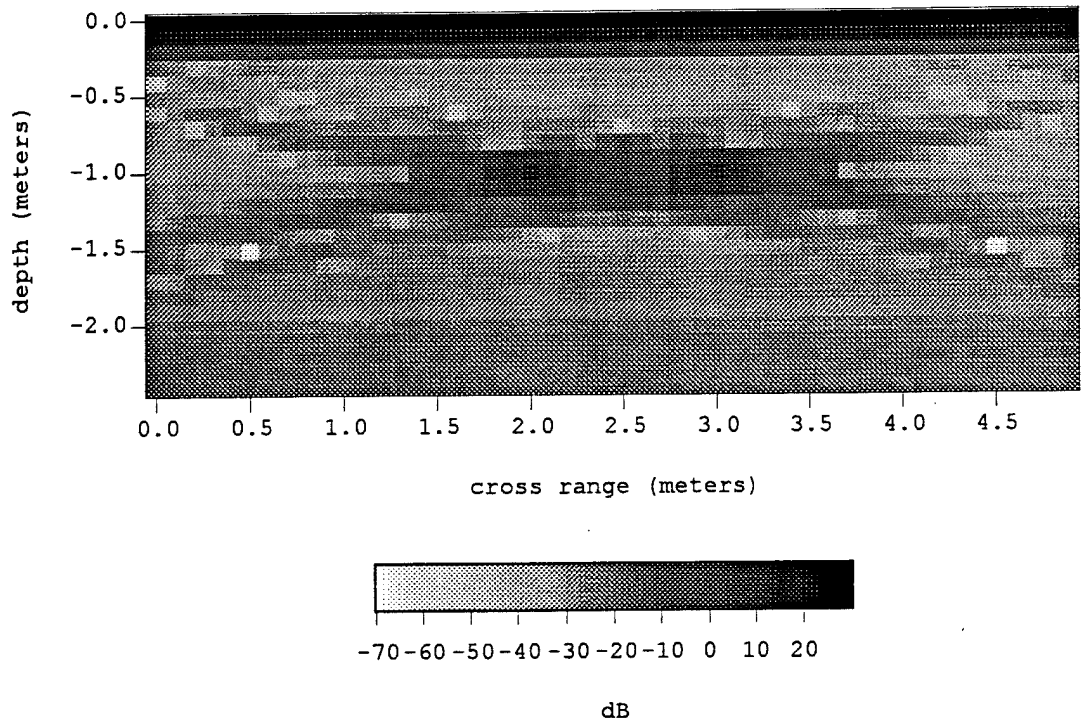

Figure 23 SAR Image using the Impulse Model, 105 Frequency Terms, Sample Spacing of 0.3 m. [9614]

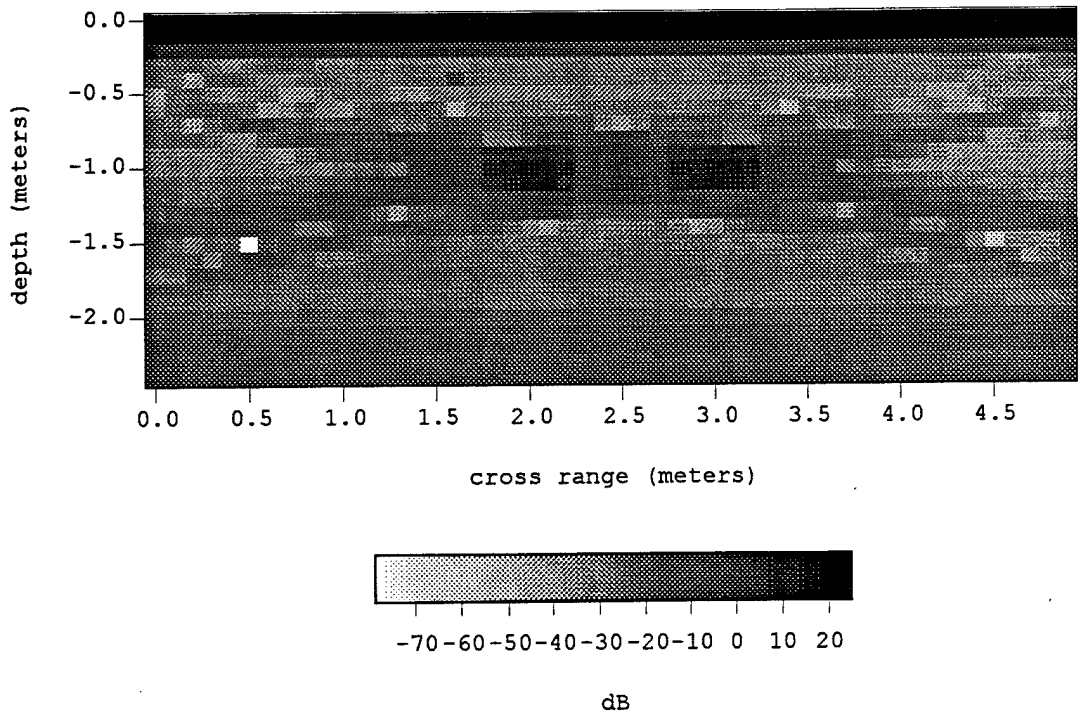

Figure 24 SAR Simulation using the Step-Frequency Model, 105 Frequency Terms, Sample Spacing of 0.3 m. [9636]

Simulation of the Radar Response

In the simulation, we must first simulate the response of the system to the ground, the surface, and the targets below the surface. To construct the received signal the response from each pixel in the image must be calculated for each frequency and each transmit/receive position. The only pixels from which there will be a response are those on the surface or those containing targets.

The transmitting and receiving antennas are modeled as infinitessimal horizontal or vertical dipoles using the far field approximations. The polarization of the incident fields depends on the orientation of the transmitting infinitessimal dipole antenna. Infinitessimal dipoles are used because the signal returned from the surface is calculated for an infinitessimal dipole.

Referring to Figure 24, Figure 25, the dipole antenna may be parallel to x, y, or z axis. The target orientation is defined by the angle of rotation Ψ about the target local z-axis and the angle of rotation η that the axis of the cylindrical target makes with the target local x-y plane.

The transmitting antenna pattern factor for the vertical infinitessimal dipole is:

$$A_{T\theta} = \frac{i\omega\mu}{4\pi}\sin\theta \qquad A_{T\phi} = 0 \tag{9}$$

The transmitting antenna pattern factor for the horizontal infinitessimal dipole is:

$$A_{T\theta} = \frac{-i\omega\mu}{4\pi}\cos\theta\cos\phi \qquad A_{T\phi} = \frac{i\omega\mu}{4\pi}\sin\phi \tag{10}$$

$A_{T\theta}$ and $A_{T\phi}$ represent the components that are parallel and perpendicular to the plane of incidence, respectively. θ is the plane wave angle of incidence and ϕ is the angle that the horizontal projection of the plane wave propagation vector makes with the horizontal dipole.

The receiving antenna pattern factor for the vertical infinitessimal dipole is:

$$\begin{aligned} A_{R\theta} &= \sin\theta \\ A_{R\phi} &= 0 \end{aligned} \tag{11}$$

The receiving antenna pattern factor for the horizontal infinitessimal dipole is:

$$\begin{aligned} A_{R\theta} &= \cos\theta\,\cos\phi \\ A_{R\phi} &= \sin\phi \end{aligned} \tag{12}$$

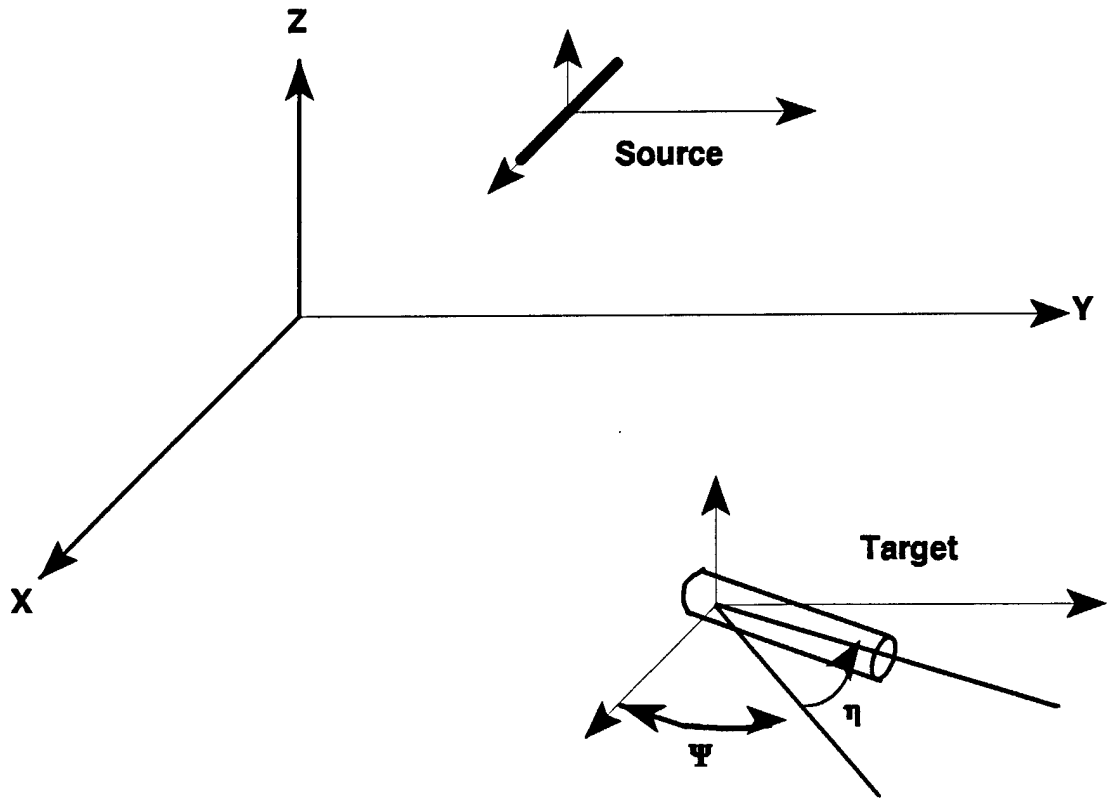

Figure 25 SAR Simulation Orientation of Targets and Antennas

Due to the cross polarization terms in the bistatic scattering function, there may be both a vertically and horizontally polarized component to the received signal. For example, if the incident field is vertically polarized, the scattered field may have both vertical and horizontal polarization components. Each polarization will be treated separately when the SAR image is constructed from the raw data arrays.

The received signal *s(m,n)* is a sum of the responses from each pixel of the image that contains a target plus the return from the surface. *m* is the radar position index and *n* is the frequency index.

$$s(m,n) = S_{surface} + \sum_{all\ targets} A_T(\theta_1,\phi_1)\ \frac{e^{-jk_1r_1}\ e^{-jk_2r_2}}{r_1 + r_2}\ T_{12}(\theta_1)\ S_{target}\ T_{21}(\theta_3)\ \frac{e^{-jk_2r_3}\ e^{-jk_1r_4}}{r_3 + r_4}\ A_R(\theta_4,\phi_4) \quad (13)$$

T_{12}, T_{21} = ratio of transmitted electric field to incident electric field according to Fresnel's equation, region 1 to 2 and 2 to 1, respectively.

$S_{surface}$ = scattering function of the surface.

S_{target} = scattering function of the target.

A_R = antenna pattern of the receiving antenna.

A_T = transmitting antenna pattern.

k_1, k_2 = complex propagation constant in medium 1, 2

r_1 = distance from the transmitter to the surface

r_2 = distance from the surface to the target

r_3 = distance from the target to the surface

r_4 = distance from the surface to the receiver

θ_1,ϕ_1 = angles of incidence in medium 1

θ_2,ϕ_2 = angles of refraction in medium 2

θ_3,ϕ_3 = angles of scattering in medium 3

θ_4,ϕ_4 = angles of scattering in medium 4

Calculation of Range and Angle of Incidence

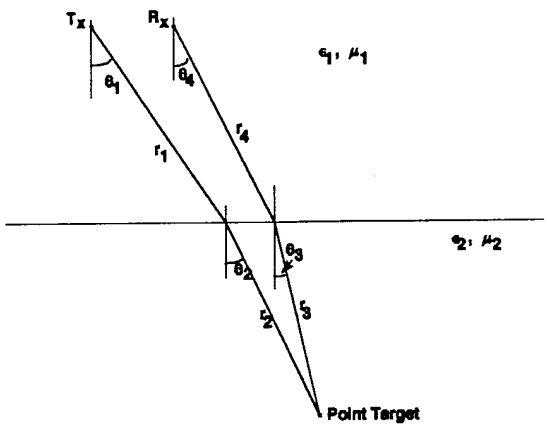

Figure 26 SAR Geometry

The ranges, r_1, r_2, r_3, and r_4, (see Figure 26) must be calculated from the transmitter to each target and back to the receiver for each sample received. The angles and ranges can be calculated from the soil characteristics and the coordinates of the transmitter, receiver, and each target. Let (x_1, y_1, z_1) be the coordinates of the transmission point and let (x_2, y_2, z_2) be the coordinates of the image point (or target point). r_1 is the range from the transmission point to the surface, r_2 is the range from the surface to the image point. θ_1 is the plane wave angle of incidence in air and θ_2 is the angle of incidence in the soil. We experimented with several techniques for calculating the ranges in each medium from the transmitting antenna to the image point and back to the receiving antenna. The following method is from Roy, et al.[1] From Snell's Law,

$$\sin\theta_2 = \frac{\sin\theta_1}{\eta(\theta_1)} \tag{15}$$

where

θ_1 = angle of incidence in medium 1
θ_2 = angle of incidence in medium 2

[1]Roy, S., R.S. Berkowitz, W.J. Graham, and D. Carlson, "Applications of Subsurface Radar for Mine Detection," Final Report, December 31, 1990, Appendix.

$$\eta\ (\theta_1) = \frac{1}{\sqrt{2}} \sqrt{\epsilon_r + \sin^2\theta_1 + \sqrt{(\epsilon_r - \sin^2\theta_1)^2 + (\frac{18\ \sigma}{f})^2}} \qquad (17)$$

ϵ_r = relative permittivity of medium 2
σ = conductivity of medium 2
f = frequency in gigahertz

From the geometry,

$$x_2 - x_1 = y_1 \tan\theta_1 - y_2 \tan\theta_2 \qquad (19)$$

We use an iterative procedure on this equation and Snell's Law to solve for θ_1, then we find the angle θ_2 and ranges r_1 and r_2:

$$r_1 = \frac{y_1}{\cos\theta_1} \qquad (20)$$

$$r_2 = \frac{-y_2}{\cos\theta_2} \qquad (21)$$

A similar calculation is performed to find r_3, r_4, θ_3, and θ_4. r_3 is the range from the image point to the surface and r_4 is the range from the surface to the receiver. θ_3 is the angle from which the plane wave is scattered from the target in the soil and θ_4 is the angle at which the scattered plane wave propagates in air.

Fresnel Transmission Coefficients

The Fresnel transmission coefficients are being used to account for the reflection/refraction at the air-to-soil interface. The fields are approximated as plane waves. If the electric field is perpendicular to the plane of incidence:

$$T_{12\phi}(\theta) = \frac{2\mu_2 k_1 \cos\theta}{\mu_2 k_1 \cos\theta + \mu_1 \sqrt{k_2^2 - k_1^2 \sin^2\theta}} \tag{22}$$

If the electric field is parallel to the plane of incidence:

$$T_{12\theta}(\theta) = \frac{\mu_2 k_1}{k_2 \mu_1} \frac{2\mu_1 k_2^2 \cos\theta}{\mu_1 k_2^2 \cos\theta + \mu_2 k_1 \sqrt{k_2^2 - k_1^2 \sin^2\theta}} \tag{23}$$

Similar expressions are used for $T_{21}(\theta)$.

Target Scattering

We have included three types of targets in the SAR Simulation: isotropic point scatterers, small ellipsoids, and large cylinders.

Isotropic Point Scatterer

The isotropic point scatterer is used in this model in many cases to compare the effects of changing parameters of the model without worrying about the effects of the target model. The field scattered from the isotropic point scatterer is defined in this simulation as 10 dB less than the incident field. This ideal scatterer scatters equally in all directions. The value 10 dB was an estimate. This value is a parameter that can be modified.

Ellipsoids

The bistatic scattering of an ellipsoidal target is found by considering each target to be a perfectly conducting ellipsoid with axes dimensions of $2a$, $2b$, and $2c$. If $a=b=c$, the target is a sphere. The target position, dimensions, and orientation can be varied. The bistatic scattering depends on the incident and scattered angles and the incident polarization. This model is valid when the target is small compared to a wavelength,

$$ka < \lambda \tag{24}$$

The scattering coefficients for the electric fields for perpendicularly polarized incident fields are:

$$S_{\theta\perp} = \left[\frac{2}{3}\right] k^2 \left(- \frac{\sin\phi \cos\theta' \cos\phi}{I_a} + \frac{\cos\phi \cos\theta' \sin\phi'}{I_b} + \frac{\cos\phi \cos\theta \sin\phi'}{I_b + I_c} \right. \tag{25}$$

$$\left. - \frac{\sin\phi \cos\theta \cos\phi'}{I_a + I_c} \right)$$

$$S_{\phi\perp} = \left[\frac{2}{3}\right] k^2 \left(\frac{\sin\phi \sin\phi'}{I_a} + \frac{\cos\phi \cos\phi'}{I_b} + \frac{\cos\phi \cos\theta \cos\theta' \cos\phi'}{I_b + I_c} \right. \tag{26}$$

$$\left. + \frac{\sin\phi \cos\theta \cos\theta' \sin\phi'}{I_a + I_c} + \frac{\sin\theta \sin\theta'}{I_a + I_b} \right)$$

I_a, I_b, and I_c are the ellipsoid polarization parameters, dependent on the dimensions of the target. The unprimed angles, θ and ϕ , are the incident plane wave angles. The primed angles are the scattered plane wave angles.

The scattering coefficients for the electric fields for parallel polarized incident fields are:

$$S_{\phi\parallel} = \left[\frac{2}{3}\right] k^2 \left(- \frac{\cos\theta \cos\phi \sin\phi'}{I_a} + \frac{\cos\theta \sin\phi \cos\phi'}{I_b} \right. \tag{27}$$

$$\left. + \frac{\sin\phi \cos\theta \cos\phi'}{I_b + I_c} - \frac{\cos\phi \cos\theta' \sin\phi'}{I_a + I_c} \right)$$

$$S_{\theta|} = \left[\frac{2}{3}\right] k^2 \left(\frac{\cos\theta\cos\phi\cos\theta'\cos\phi'}{I_a} + \frac{\cos\theta\sin\phi\cos\theta'\sin\phi'}{I_b} \right. \tag{28}$$

$$\left. + \frac{\sin\theta\sin\theta'}{I_c} + \frac{\sin\phi\ \sin\phi'}{I_b + I_c} + \frac{\cos\phi\cos\phi'}{I_a + I_c} \right)$$

Cylinders

To model cylindrical targets whose length, h, is greater than a wavelength in the soil, we calculate the scattering coefficients from the diffraction cross section of a cylinder for backscattering only. The diffraction scattering model is valid when the target is a perfectly conducting cylinder and

$$h \geq \frac{\lambda_0}{2n_2}, \tag{29}$$

where n_2 is the refractive index of the soil and λ_0 is the free space wavelength. The ratio of the scattered electric field to the incident electric field is calculated as a function of incident angle, frequency, and ground characteristics. The backscattered field is a function of the angle θ that the incident plane wave makes with the long axis of the cylinder. The radius of the cylinder is a.

The backscattered fields for a cylinder are given by equations (34) and (36). These equations appear more concise if the following constants are defined (the functions J_n are Bessel functions of the first kind of order n):

$$C = \cos\left[\frac{2}{3}\pi\right]$$

$$S = \frac{2}{3}\sin\left[\frac{2}{3}\pi\right] \tag{30}$$

$$SN = \frac{\sin\left[\frac{2}{3}\pi\right]}{\cos\left[\frac{2}{3}\pi\right] - 1}$$

$$CP = \cos\left[\frac{4}{3}\left[\frac{\pi}{2} + \theta\right]\right]$$

$$CM = \cos\left[\frac{4}{3}\left[\frac{\pi}{2} - \theta\right]\right] \tag{31}$$

$$CT = \cos\left[\frac{4}{3}\theta\right]$$

$$x = 2ka\sin\theta$$

$$y = 2kh\cos\theta \tag{32}$$

$$A_{-} = a(J_1(x) - i\,J_o(x))\,S$$

$$A_{+} = a(J_1(x) + i\,J_o(x))\,S \tag{33}$$

$$B = i\frac{2}{3}a\,SN\,(J_o(x) + i\,J_2(x))$$

Then for an incident electric field perpendicular to the plane of incidence, the scattered field is:

$$\frac{E(\theta)}{E_i} = \frac{i}{2}\left[A_- \left(\frac{1}{C-1} - \frac{1}{C-CM}\right) + 2B\right] e^{iy/2} \qquad (34)$$

$$+\frac{i}{2}\left[- A_+ \left(\frac{1}{C-1} - \frac{1}{C-CP}\right) - A_+ \left(\frac{1}{C-1} - \frac{1}{C-CT}\right) e^{iy} + Be^{iy}\right] e^{iy/2}$$

For an incident electric field parallel to the plane of incidence, the scattered field is:

$$\frac{H(\theta)}{H_i} = \frac{i}{2}\left[A_- \left(\frac{1}{C-1} + \frac{1}{C-CM}\right) + 2B\right] e^{iy/2} \qquad (36)$$

$$+ \frac{i}{2}\left[- A_+ \left(\frac{1}{C-1} + \frac{1}{C-CP}\right) - A_+ \left(\frac{1}{C-1} + \frac{1}{C-CT}\right) e^{iy} + Be^{iy}\right] e^{iy/2}$$

Surface Scattering

To simulate the scattering from the surface, the electric field at the point of the receiver is calculated due to an infinitessimal dipole at the point of the transmitter in the presence of a conducting half space.

The electric field at the receiver due to the scattering at the surface is a function of the radar frequency, ground conductivity and permittivity, radar transmitter and receiver position, and orientation of the dipole. A rigorous and exact approach to the scattering from a conducting half-space is presented by Sommerfeld, originally in several papers and subsequently in Volume VI of the books *Lectures on Theoretical Physics* republished in English by Academic Press, 1964.

For a vertical dipole located at a height h above a finitely conducting ground, the Hertzian potential for the scattered field is given by

$$\pi^{vert} = \pi_z^{vert} = \int_0^\infty F^V(\lambda) I_0(\lambda\rho) e^{\nu(z+h)} d\lambda$$

where z, ρ are the field point coordinates. In the above equation

$$\nu = \sqrt{\lambda^2 - k^2}, \quad \nu_g = \sqrt{\lambda^2 - k_g^2}$$

and

$$F^V(\lambda) = \frac{\lambda}{\nu} \frac{1-2\nu}{\epsilon_g \nu + \nu_g},$$

with ϵ_g = the complex dielectric constant for the ground and k_g the ground wavenumber. From the Hertzian potential the scattered electric and magnetic fields can be obtained. A direct solution of the complex integral for the scattered field Hertzian potential is not possible, and thus either approximate solutions or numerical integration must be used. Either of these approaches is quite complex and error prone.

For an x-directed horizontal dipole, the situation is more complex than for the vertical dipole since the Hertzian potential has two components, both an x-directed and a z-directed component. Thus,

$$\begin{aligned} \pi^{horz} &= \pi_x^{horz} + \pi_z^{horz}, \ with \\ \pi_x^{horz} &= \int_0^\infty F^H(\lambda) I_0(\lambda\rho) e^{-\nu(z+h)} d\lambda \end{aligned} \tag{41}$$

with

$$F^H(\lambda) = \frac{\lambda}{v}\left[-1 + \frac{2v}{v+v_g}\right] \quad (42)$$

where the integration path w is not along the real axis but runs from $-\infty$ to ∞ in the complex plane. The z-directed Hertzian dipole component is obtained from a similar expression involving the first order modified Bessel function, $I_1(v)$. Again, as for the vertical dipole, only approximate solutions or numerical integration can be used to obtain actual scattered field values.

A numerical solution approach to the Sommerfeld integrals (in the complex plane) has been outlined by Miller, et al.,[1, 2, 3] and previously programmed and validated at Battelle. Although, providing essentially exact results independent of dipole height to wavelength relationships or ground dielectric constant parameter, the numerical computation of the Sommerfeld integral is very slow and thus not suitable for use in the SAR simulation due to the excessive computer time required. Approximate solutions to the Sommerfeld equations have been developed by Norton,[4] and others which are computationally very efficient and were used as the basis for the surface scattering computations in the SAR simulations.

Figure 27 provides a comparison of the effective total specular surface return as an equivalent radar cross section computed using both the approximation method and the exact Sommerfeld method for a horizontal dipole antenna. Good agreement is achieved between the approximate and exact solutions with the approximate solution being several orders of magnitude faster to compute.

---

[1] Sommerfeld, A., *Lectures in Theoretical Physics — Vol. VI — Partial Differential Equations*, pp. 246, Academic Press, NY, 1964.

[2] Lytle, R.J. and Lager, D.L., "Numerical Evaluation of Sommerfeld Integrals", Lawrence Livermore Laboratory, RPT UCRL-51688, Oct. 1974.

[3] Miller, E.K., et.al., Canadian Jour. of Physics, 50, pp. 879, and pp. 2614, 1972.

[4] Norton, K.A., Proc. IRE, 24, #10, pp. 1667, 1936) and 25, #9, pp. 1203, 1937.

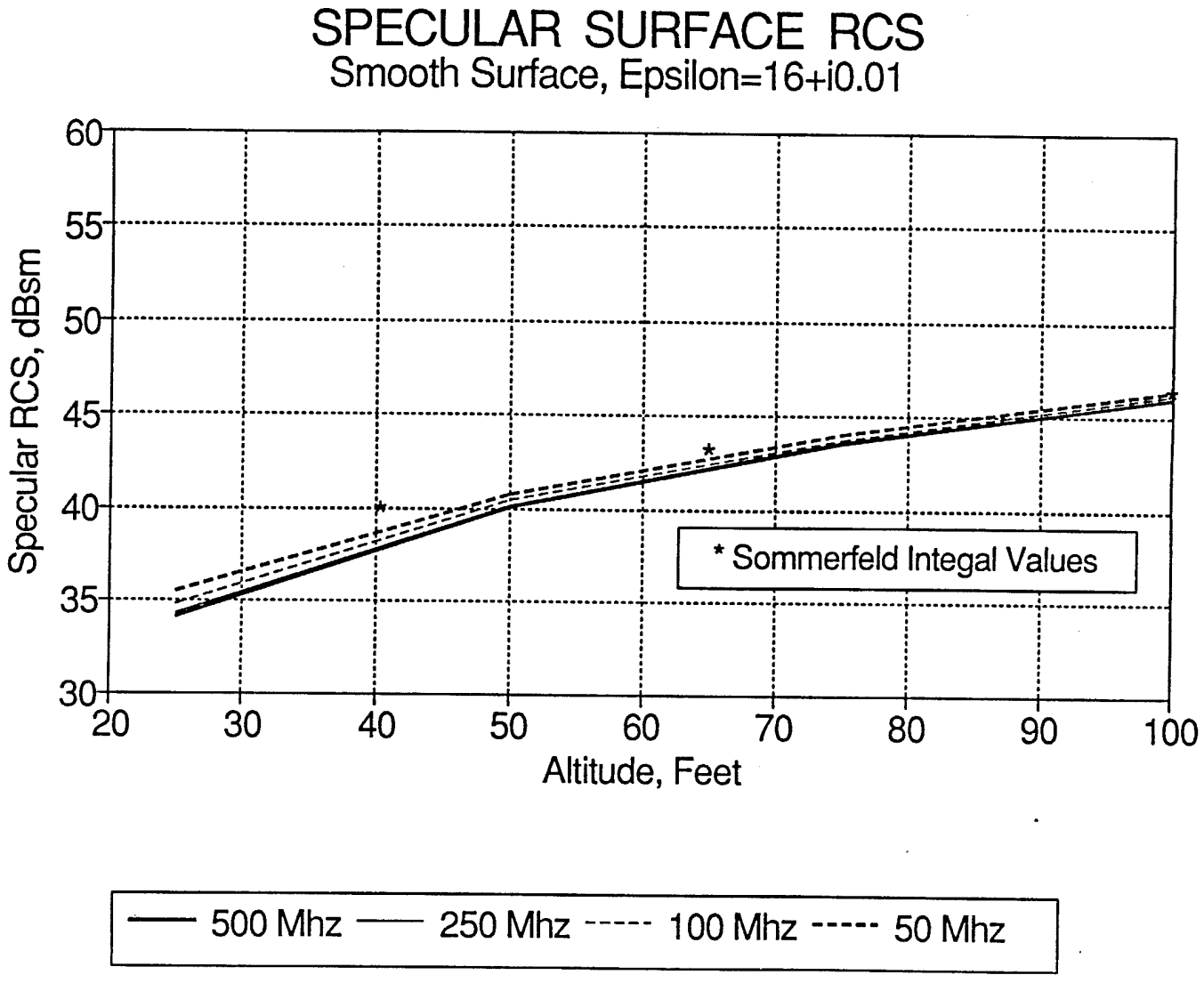

Figure 27 Specular Surface RCS Comparison

3.2 Synthetic Aperture Radar Processing

The process that we use to create the SAR image from the simulated return signal is described below. First we will describe the processing of the data for the impulse model, then the procedure used in the step-frequency model.

Impulse Model

In the time domain, the transmitted signal is a series of impulses transmitted at times $t=t_m$, $m=1...M$, as the SAR flies over the targets. The transmitted signal is represented in the frequency domain by the fourier sum of N frequencies:

$$\delta(t-t_m) = \frac{1}{N}\sum_{n=1}^{N} e^{j2\pi f_n(t-t_m)} \tag{41}$$

The frequencies, f_n , are

$$f_n = f_{\min} + (n-1)\frac{f_{\max}-f_{\min}}{N-1} \tag{42}$$

To construct the SAR image, we first perform the SAR phase correction on the frequency domain return signal function, $s(m,n)$, for each pixel of the image. i indicates the row (depth) and j indicates the column (cross range) of the image:

$$p(i,j,n) = \frac{1}{M}\sum_{m=1}^{M} s(m,n)\, e^{j\, k_1 R_{ijm}} \tag{43}$$

where

$$R_{ijm} = r_{1ijm} + \frac{k_2}{k_1} r_{2ijm} + \frac{k_2}{k_1} r_{3ijm} + r_{4ijm} \tag{44}$$

M is the number of impulses. r_{1ijm} is the distance from the transmitter to the surface, r_{2ijm} is the distance from the surface to the pixel, r_{3ijm} is the distance from the pixel to the surface, and r_{4ijm} is the distance from the surface to the receiver. To get the image value for each pixel we sum over the frequency index, n. This is equivalent to taking the t=0 term in the time domain.

$$P(i,j) = \frac{1}{N} \sum_{n=1}^{N} p(i,j,n) \tag{45}$$

$|P(i,j)|^2$ is plotted in dB in the SAR simulation images in this report.

Step-Frequency Model

The step-frequency model simulates a radar that transmits N frequencies, one at a time from f_{min} to f_{max} as it moves in space. The transmission of the N frequencies is repeated M times over the aperture. So, using the step-frequency model, there is also a received signal function, $s(m,n)$, the mth reception of the nth frequency. The image value for the pixel in the ith row and jth column is:

$$P(i,j) = \frac{1}{M} \sum_{m=1}^{M} \frac{1}{N} \sum_{n=1}^{N} s(m,n)\, e^{jk_1 R_{ijmn}} \tag{46}$$

The only difference between the Impulse Model processing and the Step-Frequency Model processing is that in the Step-Frequency Model there are M times N transmit positions for the radar and M times N receive positions for the radar. Therefore, additional ranges, R_{ijmn}, must be calculated.

Windowing Functions

Windowing functions have been applied to the SAR processing to reduce the sidelobes in the image. With no windowing functions, which is equivalent to a rectangular window, the image in Figure 28 is created. We can implement a Hanning window function or a Blackman-Harris window function in the raw data processing. The Hanning Window function is

$$w(m) = 1 - \cos(\frac{2\pi m}{M}) \quad \text{for } m=0,1,2,3,...M-1 \tag{47}$$

and the 4-term Blackman-Harris[1] Window with sidelobes at -74 dB is

$$w(m) = a_0 - a_1 \cos(\frac{2\pi}{M}m) + a_2 \cos(\frac{2\pi}{M}2m) - a_3 \cos(\frac{2\pi}{M}3m) \tag{48}$$

where

$$\begin{aligned} a_0 &= 0.40217 \\ a_1 &= 0.49703 \\ a_2 &= 0.09392 \\ a_3 &= 0.00183 \end{aligned} \tag{49}$$

for m=0,1,2,...M-1.

[1]F.J. Harris, "On the Use of Windows for Harmonic Analysis with the Discrete Fourier Transform," Proceedings of the IEEE, Vol. 66, No. 1, January 1978, pp.51-83.

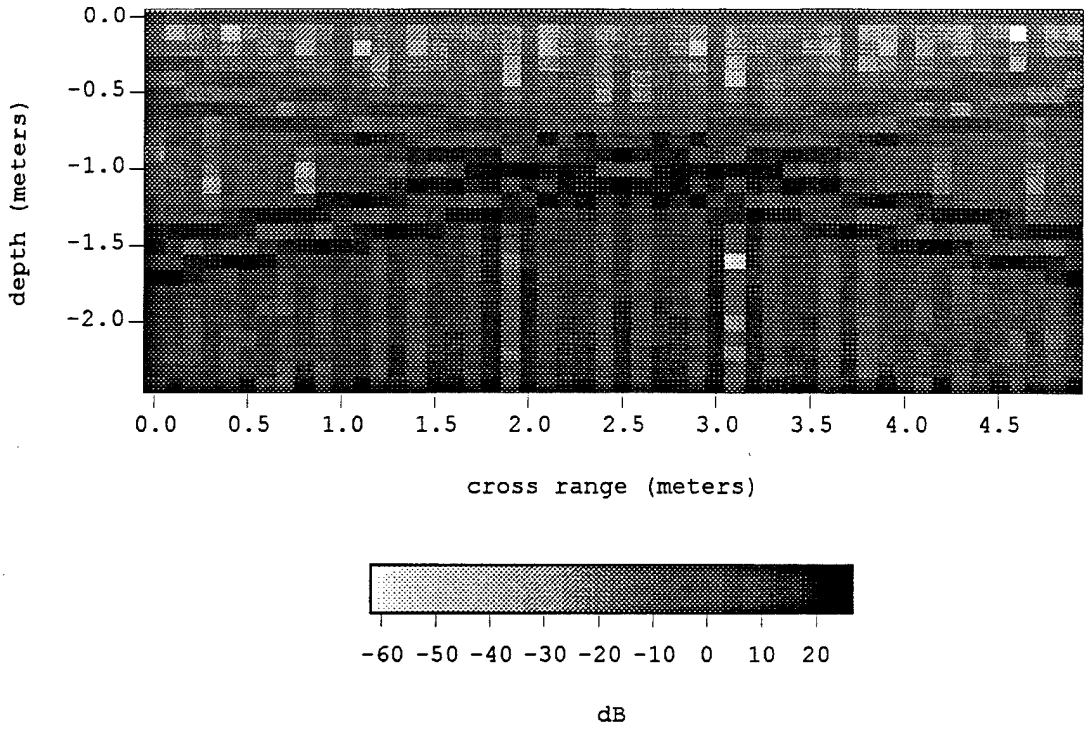

Figure 28 SAR Image for a Vertical Antenna with No Windowing Functions. [9633]

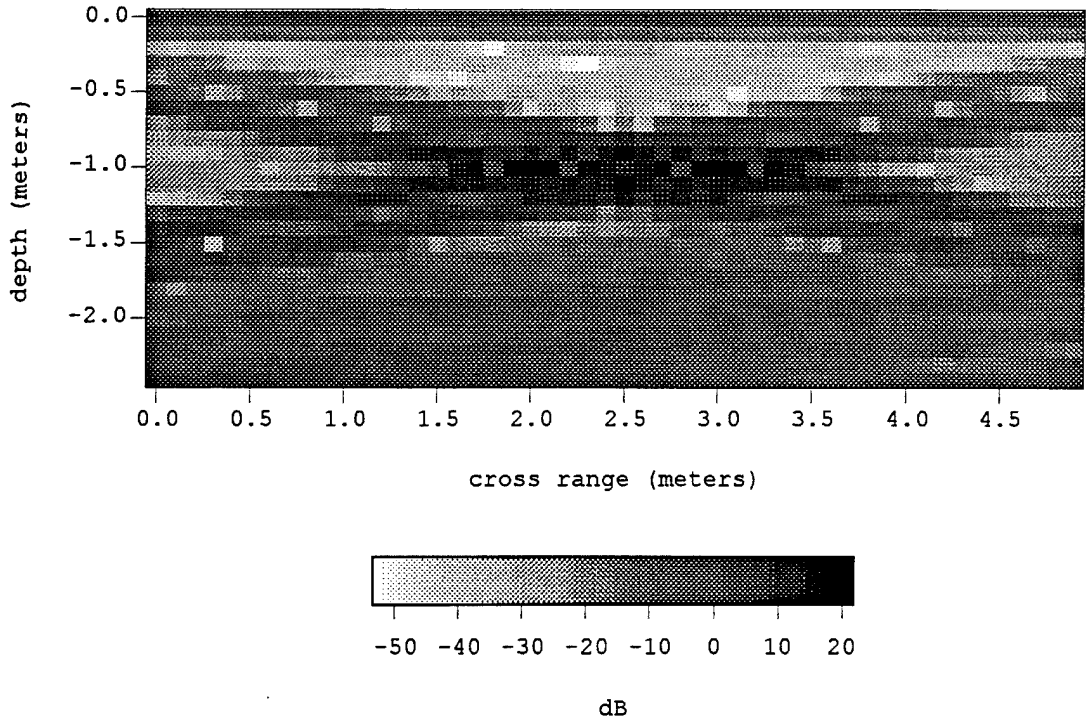

Figure 29 SAR Image for Vertical Dipole Antenna with Hanning Windows. [9632]

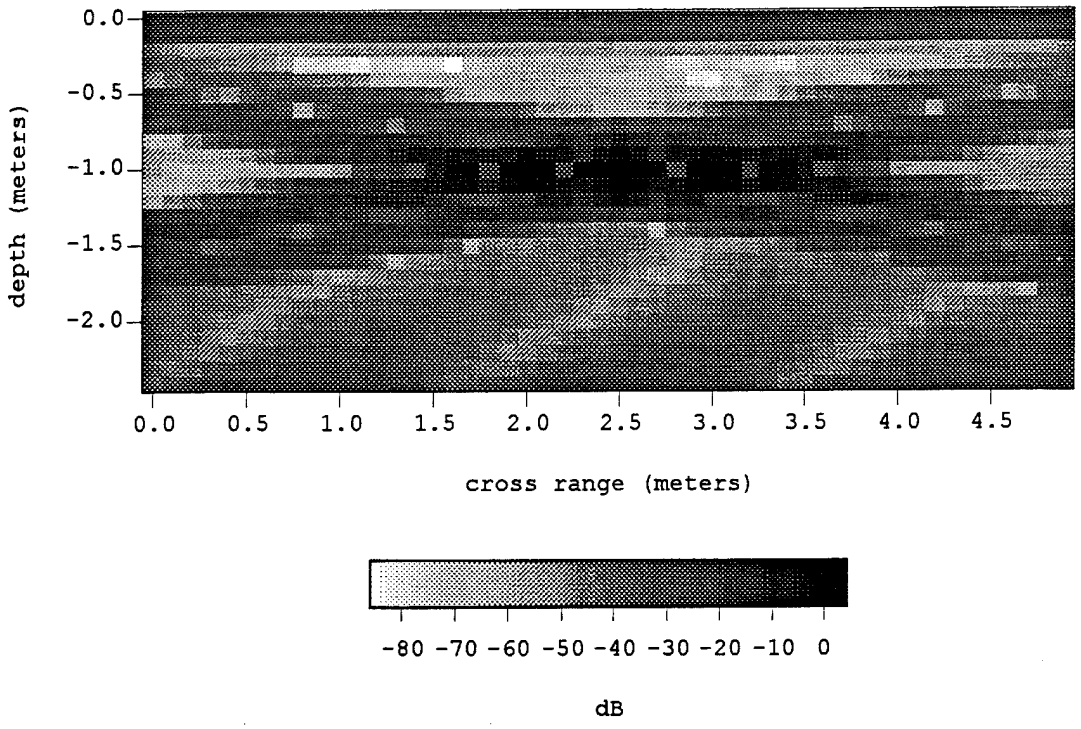

Figure 30 SAR Image for a Vertical Dipole Antenna using Blackman-Harris Windows. [9628]

We use the window functions in the spatial and frequency domain. The windowing reduces the sidelobes due to the surface return, allowing the lower return targets to be seen. With the windowing functions, the equation for the image becomes:

$$P(i,j) = \frac{1}{M} \sum_{m=1}^{M} \frac{1}{N} \sum_{n=1}^{N} w(m-1)\, w(n-1)\, s(m,n)\, e^{j k_1 R_{ijmn}} \qquad (52)$$

w(m-1) is the spatial windowing function. *w(n-1)* is the frequency domain windowing function. Figure 28 shows an image using no windowing function. Figure 29 shows an image using the Hanning windows and Figure 30 shows an image using the Blackman-Harris windows.

3.3 Results

Soil Characteristics

The soil is characterized in the SAR Simulation Program as a homogeneous medium with a dielectric constant and a conductivity. To examine the effects of increasing the soil dielectric constant compare Figure 31 and Figure 32, which show the results for a soil with a dielectric constant of 16, and Figure 33 and Figure 34, which show the results for a soil with a dielectric constant of 25. Increasing the dielectric constant alone does not seem to affect the result by much except to increase the background noise in the image. The number of frequencies required to simulate the impulse increased from 109 in Figure 31 to 116 in Figure 33.

As we increase the conductivity, targets below a certain depth are obscured. Figure 35 shows an image where the conductivity is 0.01 mho/m. Figure 31 shows an image where the conductivity is 0.02 mho/m. Most of the examples shown in this report have a conductivity of 0.02 mho/m. Figure 37 and Figure 38 show the results for soil with a conductivity of 0.05 mho/m. Figure 38 shows that the background level in the image is increasing and targets deeper than 1.5 m would not be visible under these conditions.

Figure 39 shows the image for 5 targets at increasing depths in soil with conductivity of 0.02 and dielectric constant of 16. As the targets get deeper, they are more difficult to distinguish from the increased background level.

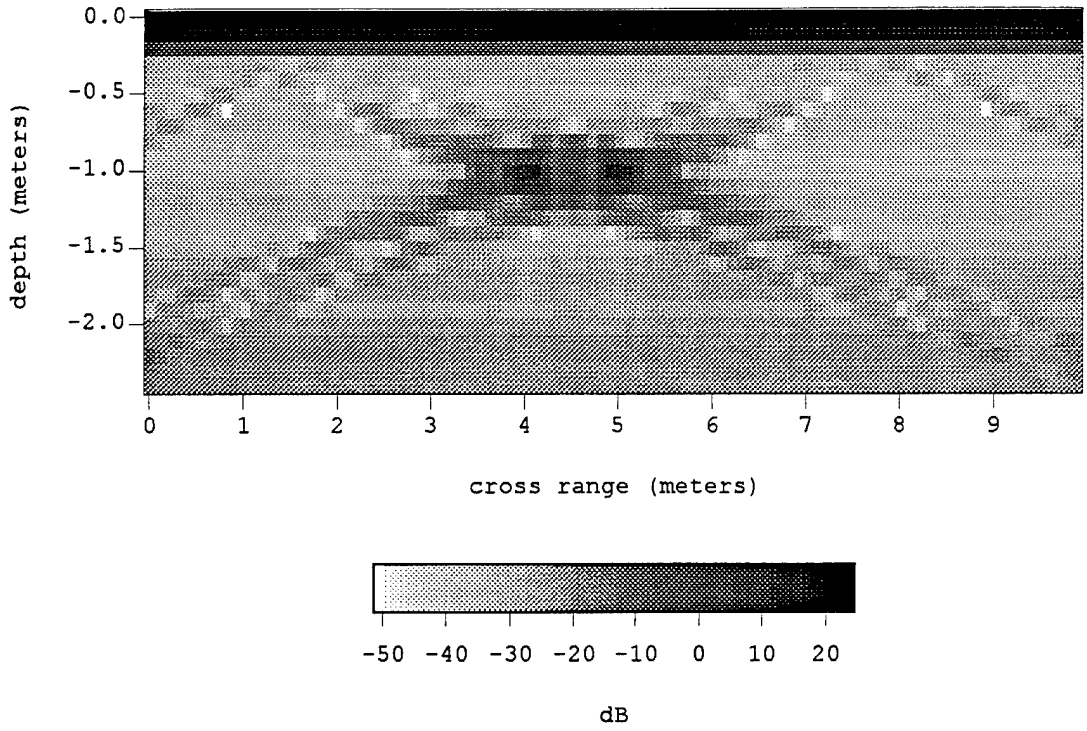

Figure 31 SAR Image for Two Point Targets in Homogeneous Soil with Dielectric Constant of 16, Conductivity of 0.02 mho/m [9608]

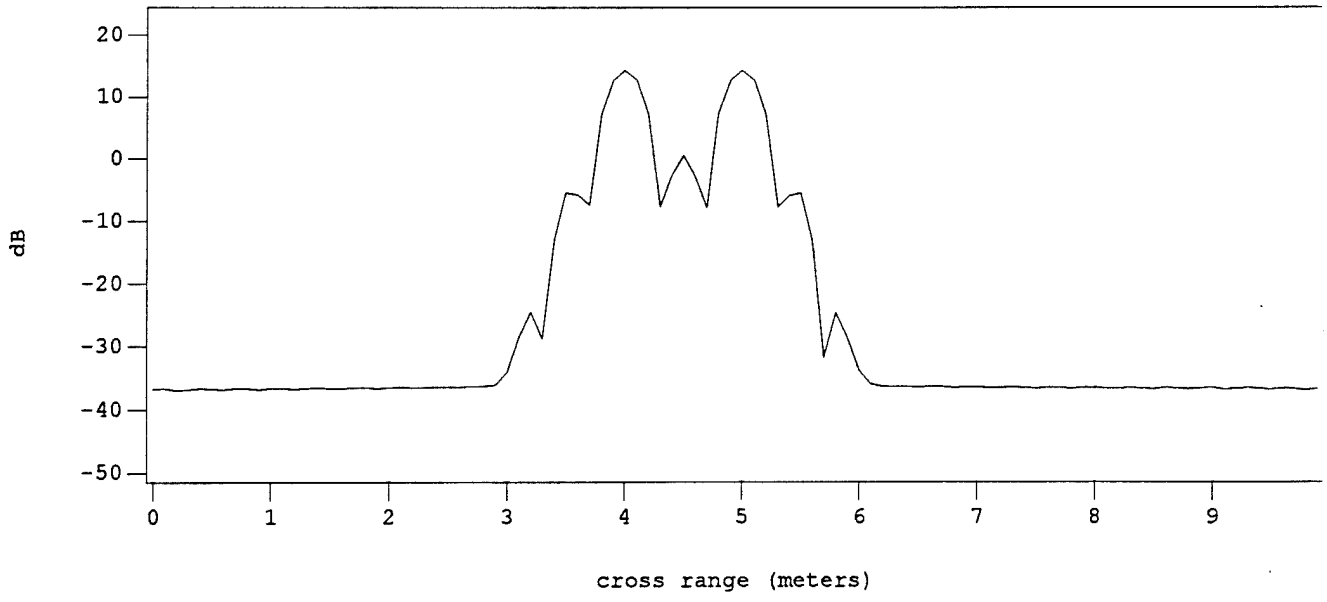

Figure 32 SAR Image 1 m Below the Surface for Two Point Targets in Homogeneous Soil with Dielectric Constant of 16, Conductivity of 0.02 mho/m [9608]

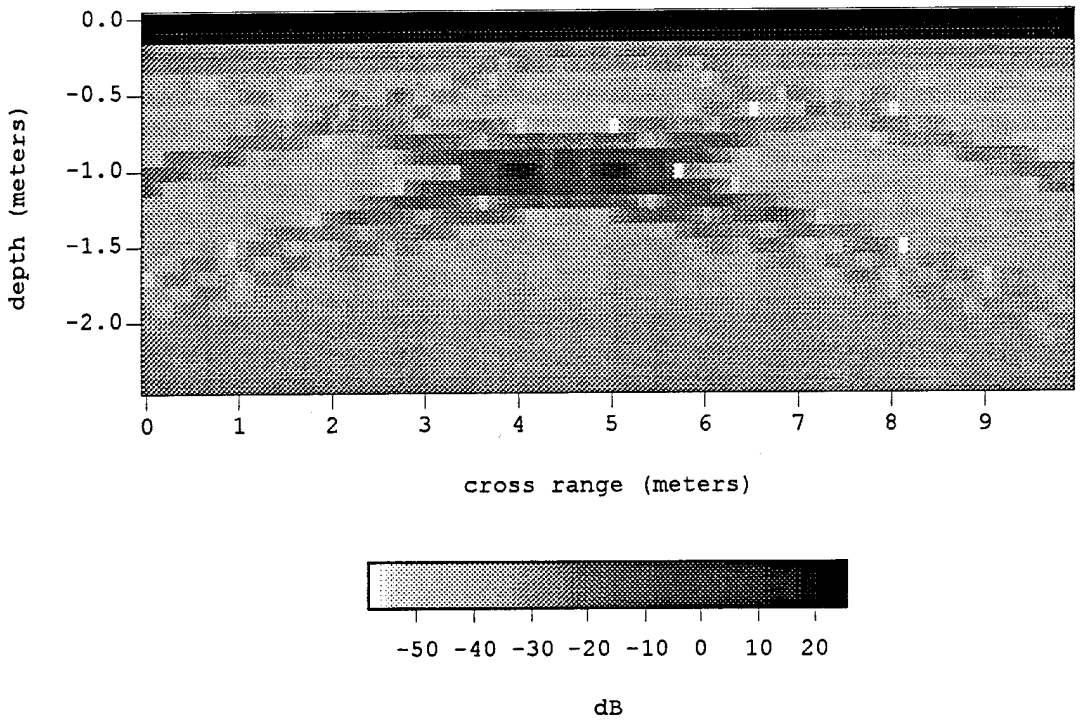

Figure 33 SAR Image for Two Point Targets in Homogeneous Soil with Dielectric Constant of 25, Conductivity of 0.02 mho/m [9609]

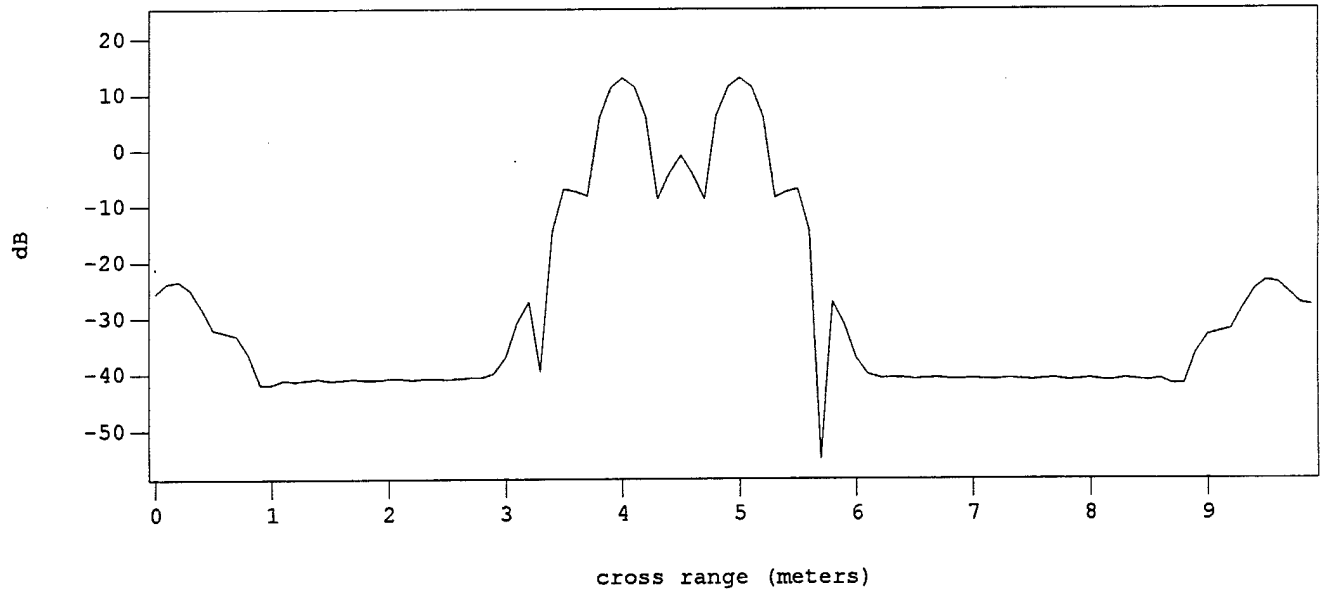

Figure 34 SAR Image 1 m Below the Surface for Two Point Targets in Homogeneous Soil with Dielectric Constant of 25, Conductivity of 0.02 mho/m [9609]

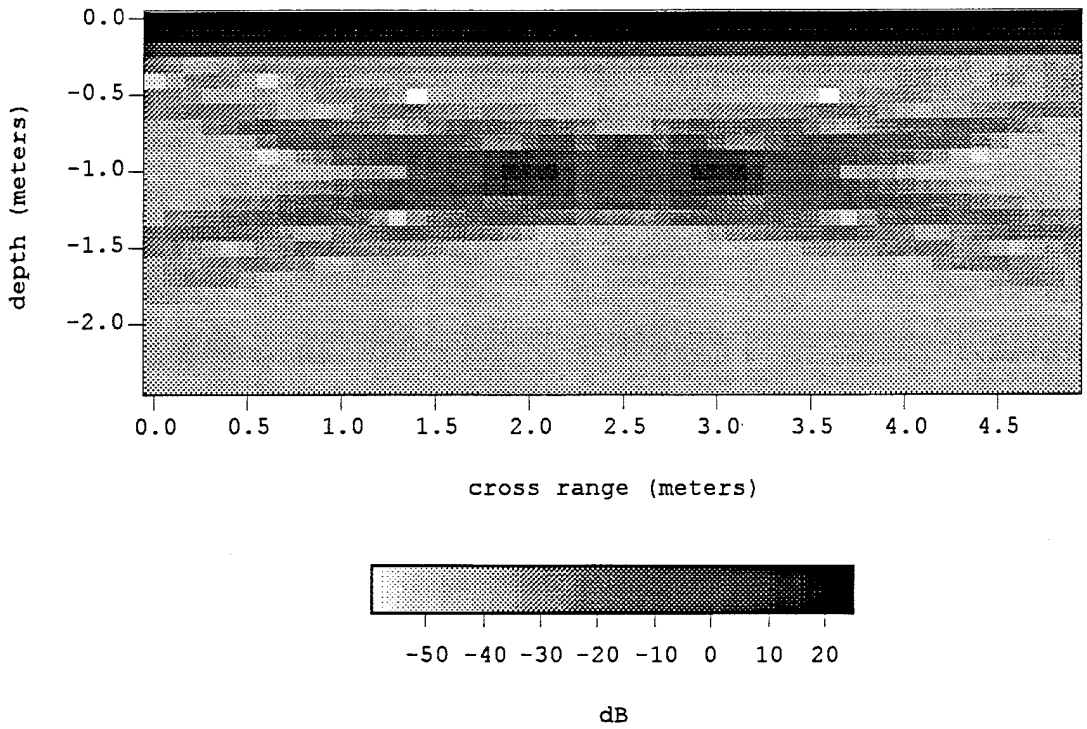

Figure 35 SAR Image of Two Point Targets in Homogeneous Soil with Conductivity of 0.01 mho/m and Dielectric Constant of 16 [9620]

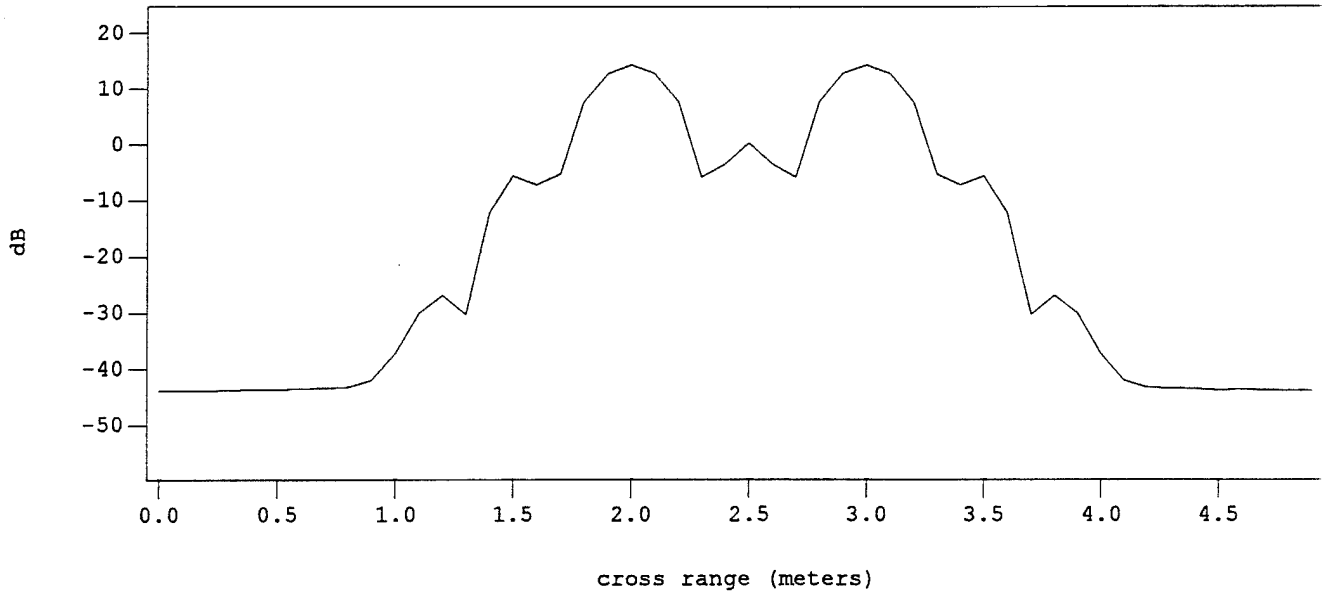

Figure 36 SAR Image 1 m Below the Surface in Homogeneous Soil with Conductivity of 0.01 mho/m and Dielectric Constant of 16 [9620]

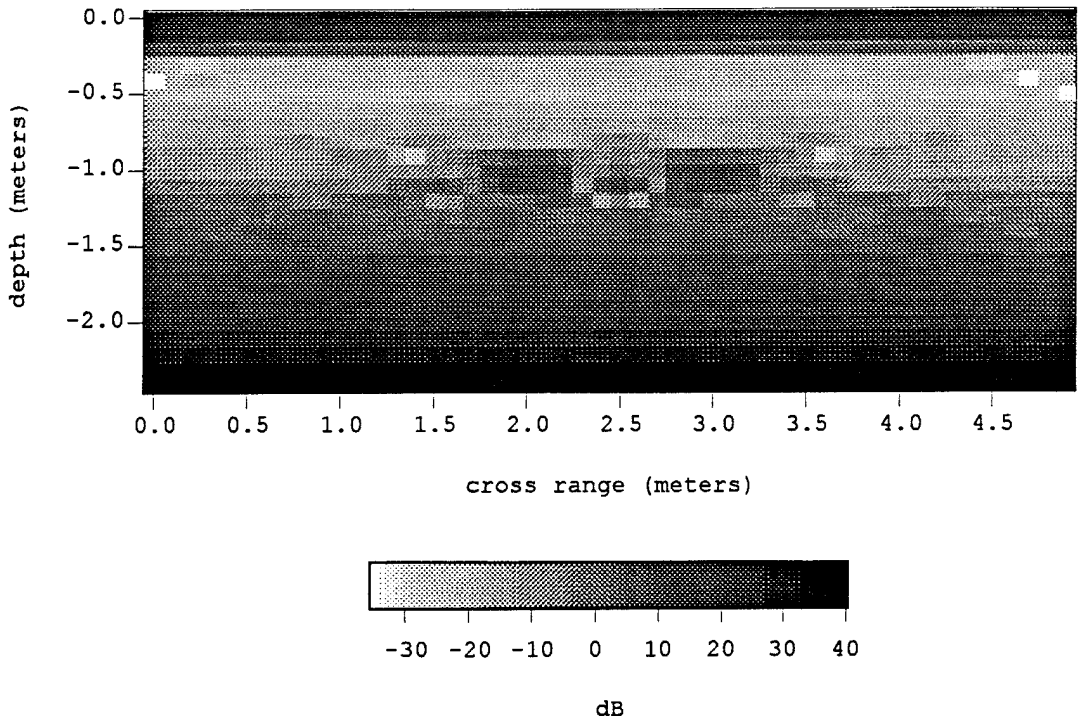

Figure 37 SAR Image of Two Point Targets in Homogeneous Soil with Conductivity of 0.05 mho/m and Dielectric Constant of 16 [9622]

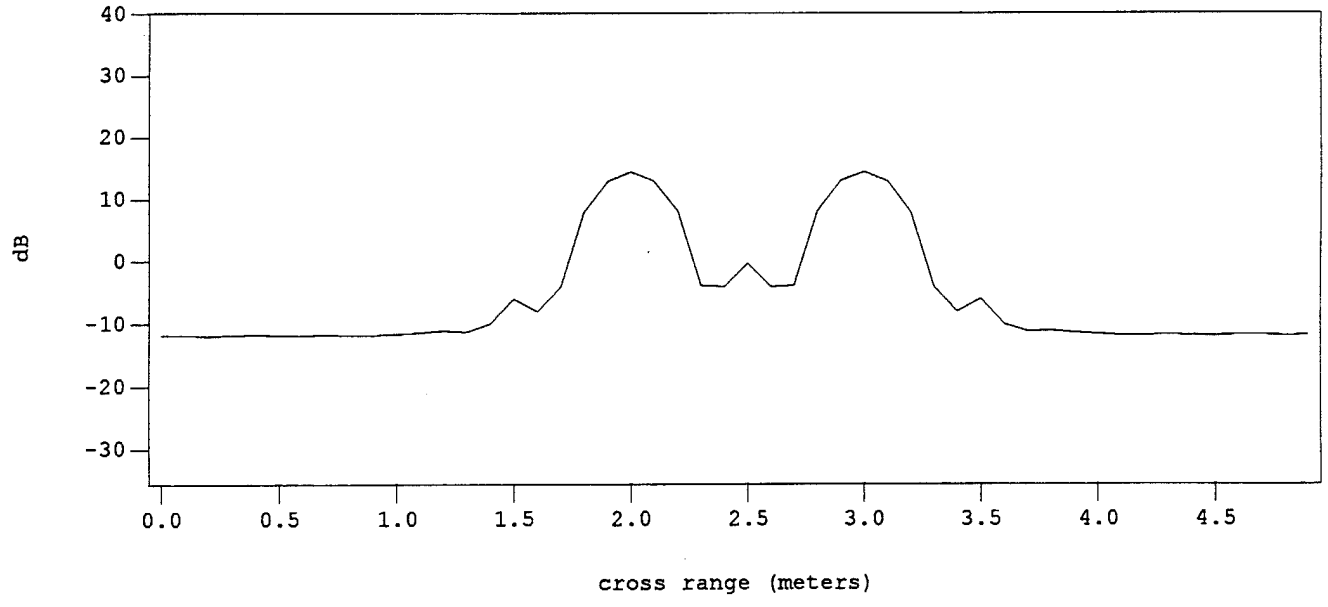

Figure 38 SAR Image 1 m Below the Surface of Two Point Targets in Homogeneous Soil with Conductivity of 0.05 mho/m and Dielectric Constant of 16 [9622]

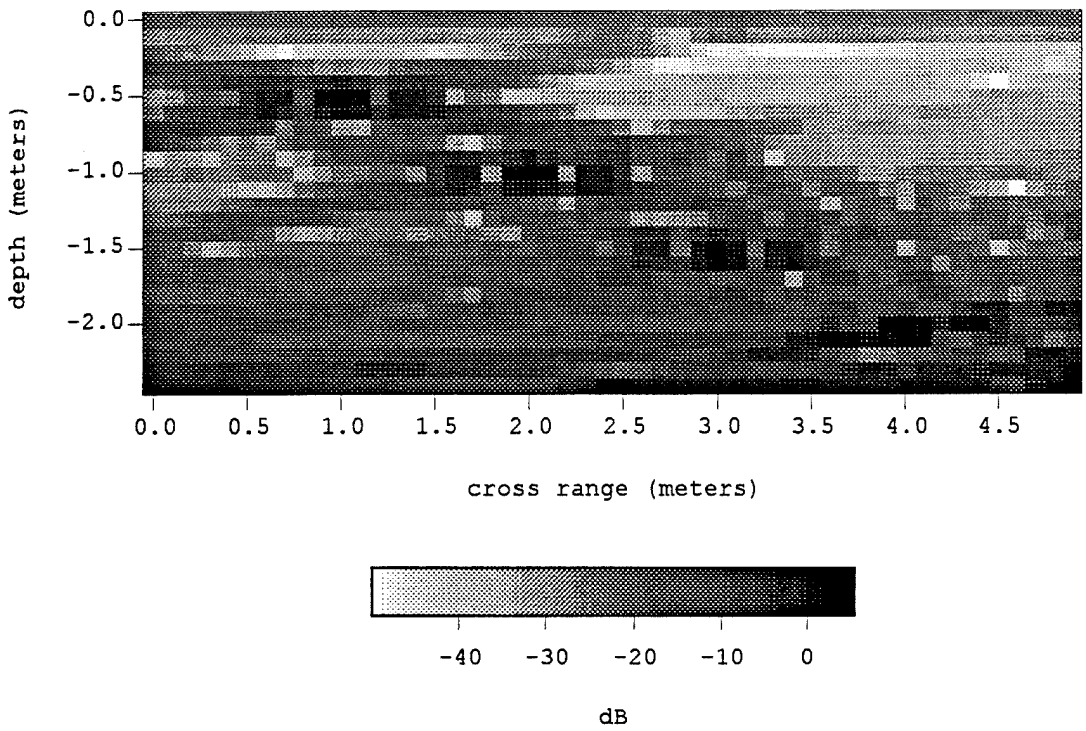

Figure 39 SAR Image of 5 Point Targets at Depths of 0.5 m, 1.0 m, 1.5 m, 2.0 m, and 2.5 m for a Vertical Dipole Antenna [9629]

Target Size

Naturally, increasing a conducting target's size, increases the ability for the SAR to detect and image the target. Figure 40 shows the image for a perfectly conducting sphere of radius 0.01 m using the Rayleigh scattering model. The sphere is centered at cross-range 2 m and is located at a depth of -1 m. The sphere is only 5 dB above the background and the signal is very low. Figure 41 shows the image for a large perfectly conducting cylinder with a length of 2 m and radius of 0.5 m. The cylinder is centered at cross-range 5 m and is 1 m deep. It is positioned as shown below. The diffraction scattering model is used to model target scattering. The signal is strongest from the bottom of the cylinder. The cylinder is lying horizontally in the ground. The dielectric constant is 16 and the conductivity is 0.02 mho/m for the images in Figure 40 and Figure 41.

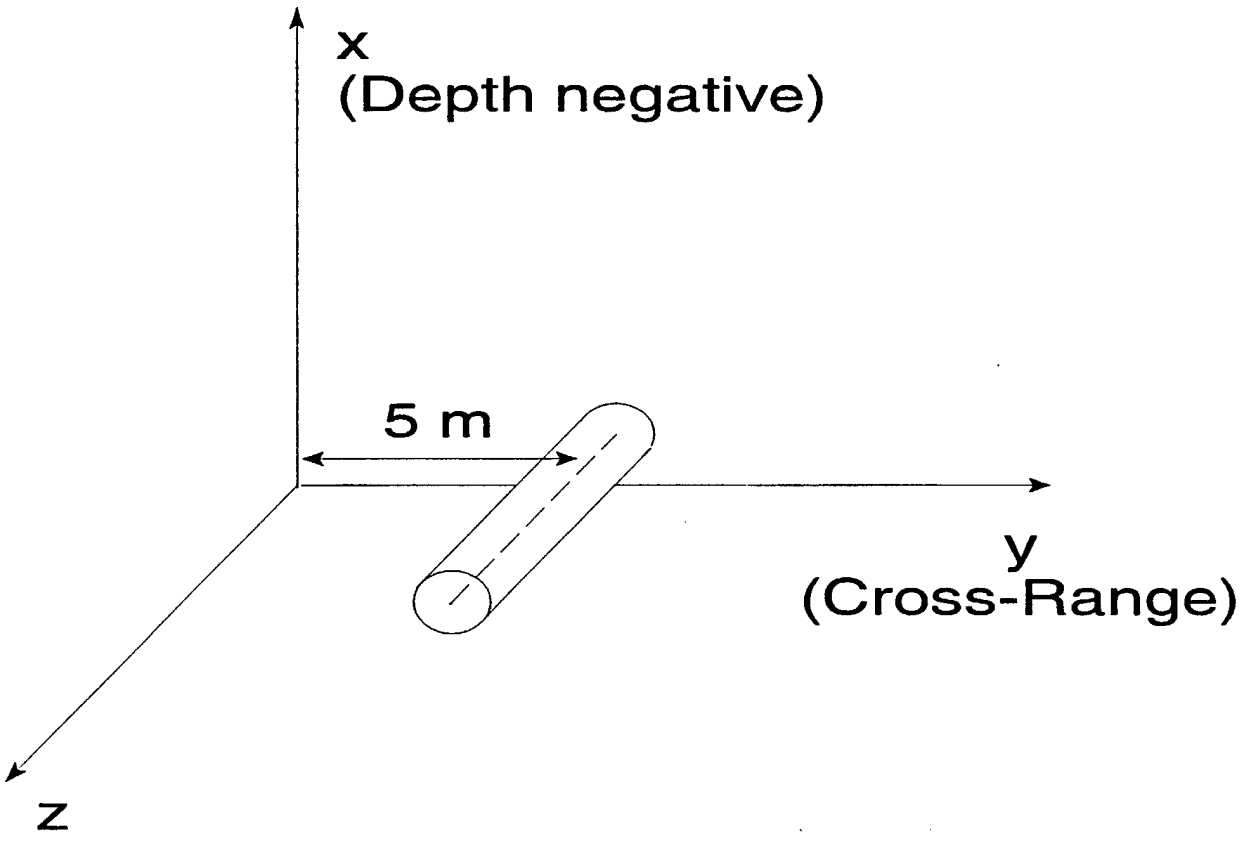

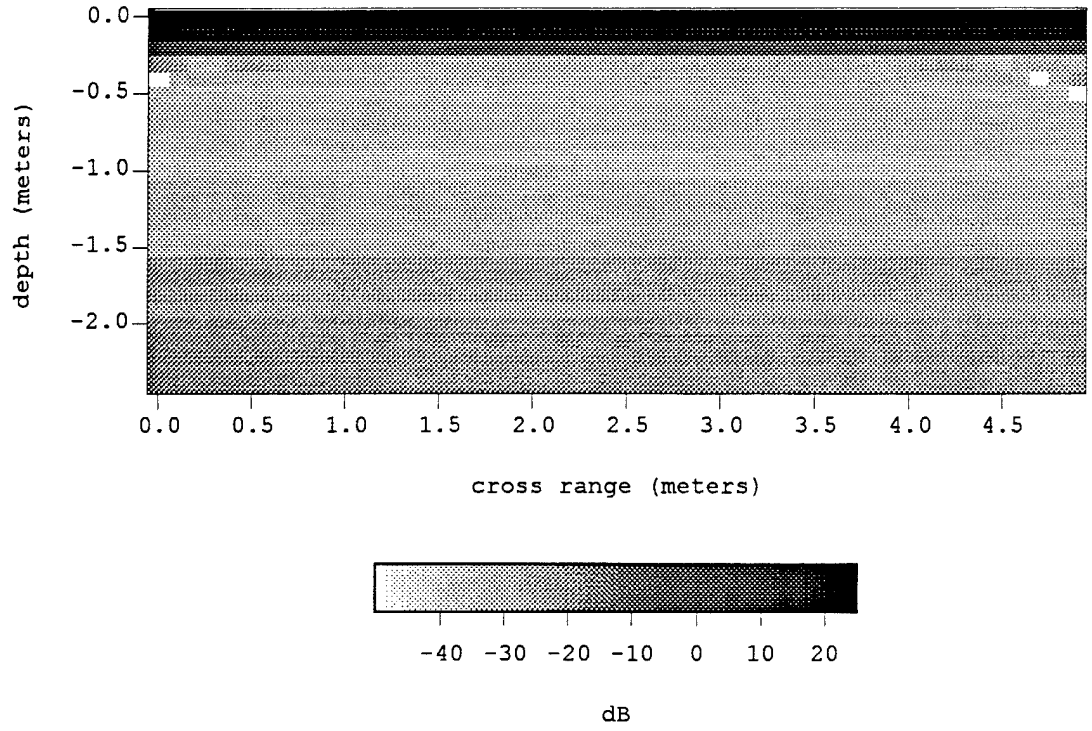

Figure 40 SAR Image for Conducting Sphere of Radius 0.01 m [9623]

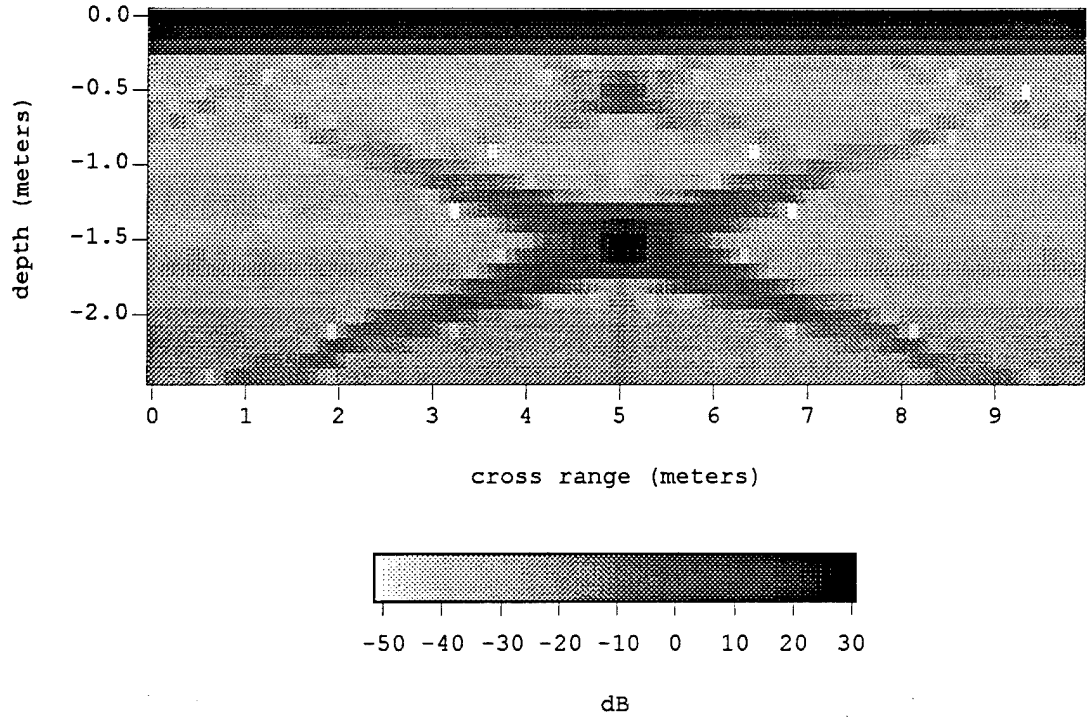

Figure 41 SAR Image for Conducting Cylinder with Length of 2 m and Radius of 0.5 m [9610]

Length of the Synthetic Aperture

We have examined what the length of the synthetic aperture should be for an image. Energy scattered from a pixel below the surface will be refracted due to the change in media and scattered at an angle θ_4, where

$$\theta_4 = \sin^{-1}\left(\frac{n_2}{n_1}\sin\theta_3\right) \qquad (51)$$

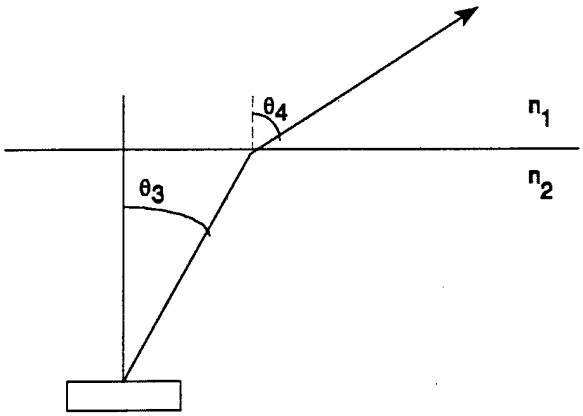

Figure 42 Angle of Refraction for Energy Scattered from a Pixel Below the Surface.

and θ_3 is the angle the energy is scattered from the pixel in the ground (see Figure 42). There is a maximum scattering angle, θ_{3max}, such that any energy scattered from the pixel at angles greater than θ_{3max} will be scattered parallel to the surface or reflected and will not get out of the ground.

$$\theta_{3max} = \sin^{-1}\left(\frac{n_1}{n_2}\right) \qquad (52)$$

At the surface, there is some finite maximum aperture, l, through which the energy from a pixel will pass (see Figure 44).

$$l = 2d\tan\theta_{3max} \qquad (53)$$

d is the depth of the pixel below the surface. To get all of the energy that passes through the aperture, l, at the surface, the length of the synthetic aperture in free space, L, would have to be infinite. However to get a percentage, α, of the aperture at the surface, the length of the synthetic aperture must be, L_α, (see Figure 43)

$$L_\alpha = \alpha l + 2\, a \tan\theta_L \tag{56}$$

$$\theta_L = \sin^{-1}\left(\frac{n_2}{n_1}\sin\theta_\alpha\right) \tag{57}$$

$$\theta_\alpha = \tan^{-1}\left(\frac{\alpha l/2}{d}\right) \tag{58}$$

Figure 45 shows L_α as a function of α for $n_2 = 4$, d=1 m, and a=25 m. Figure 46, Figure 48, Figure 50, and Figure 52 show images with lengths of synthetic apertures of 25 m, 55 m, 110 m and 150 m, respectively. It is obvious that the increased synthetic aperture length increases the cross range resolution. The targets are -10 dB point targets at cross range coordinates of 2 m and 3 m, at a depth of 1 m. They are 1 m apart. Again, $n_2 = 4$, and $a = 25$ m. As stated previously, the value -10 is an estimate and a parameter that can be modified.

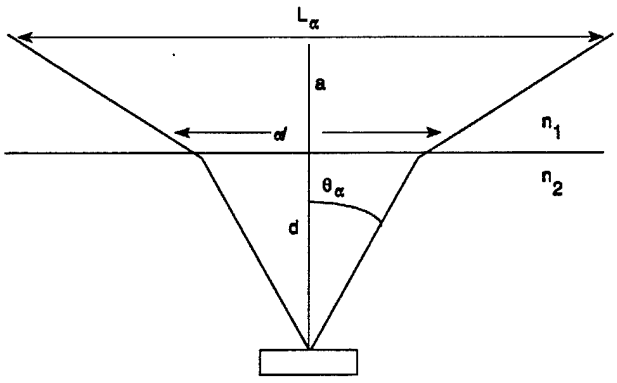

Figure 43 L_α is the length of the Synthetic Aperture Required to get a Percentage, α, of the Total Energy Scattered Out of the Ground

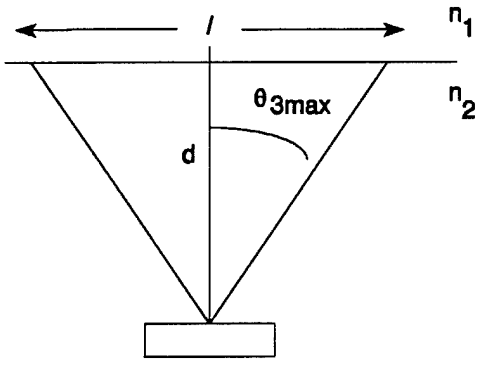

Figure 44 Length of Synthetic Aperture, l, of the Maximum Aperture at the Surface.

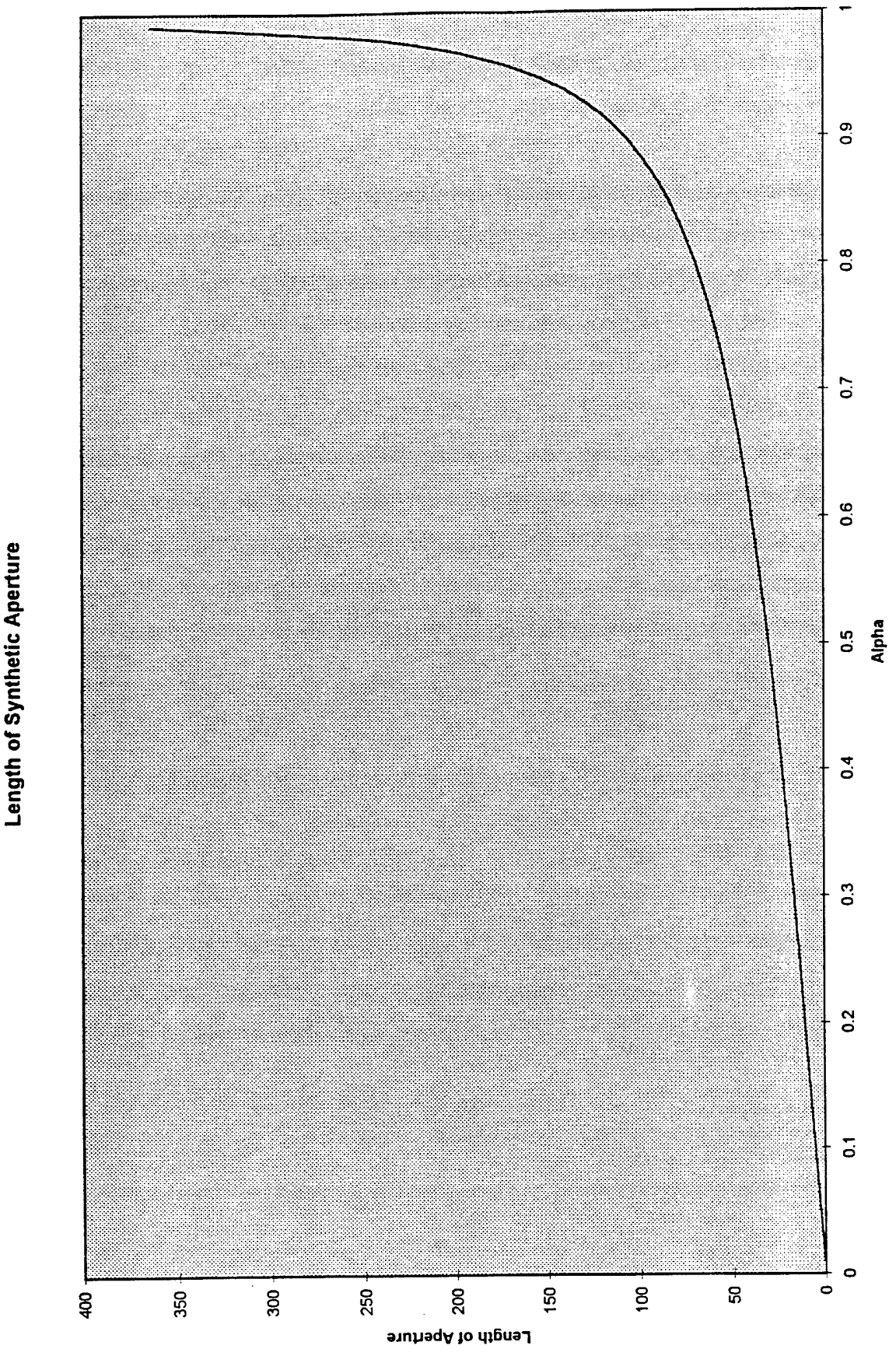

Figure 45 Length of Synthetic Aperture vs. α, n_2=4, d=1 m, a=25 m.

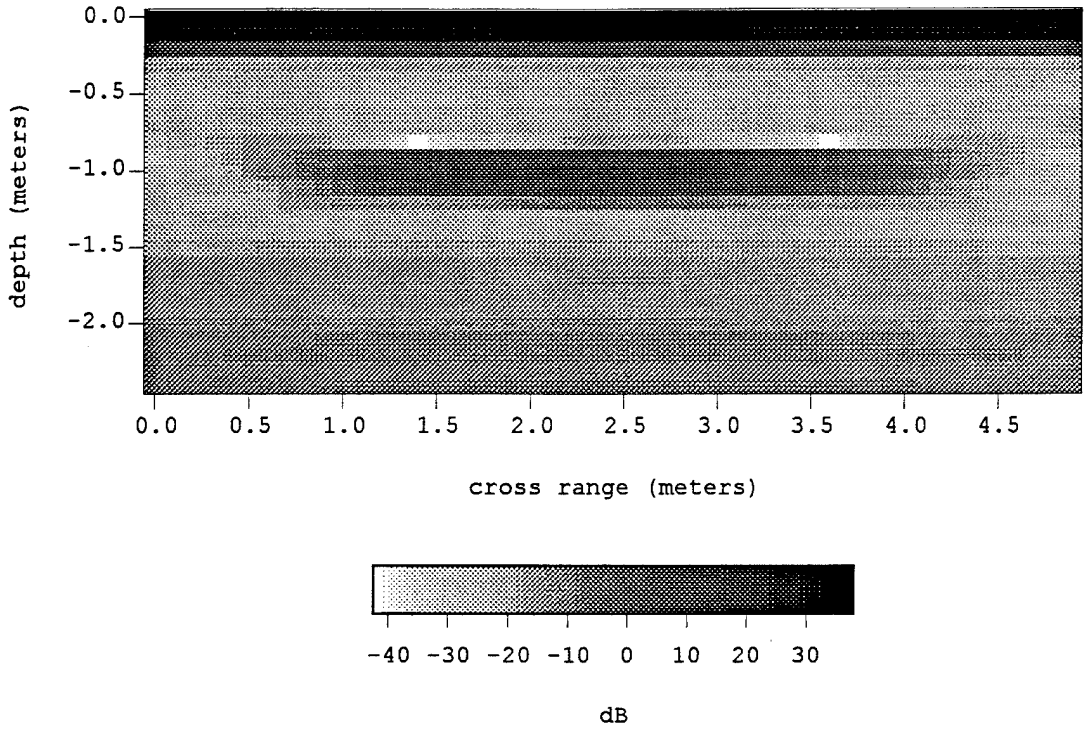

Figure 46 SAR Image of Two Point Targets, Length of Synthetic Aperture=25 m [9619]

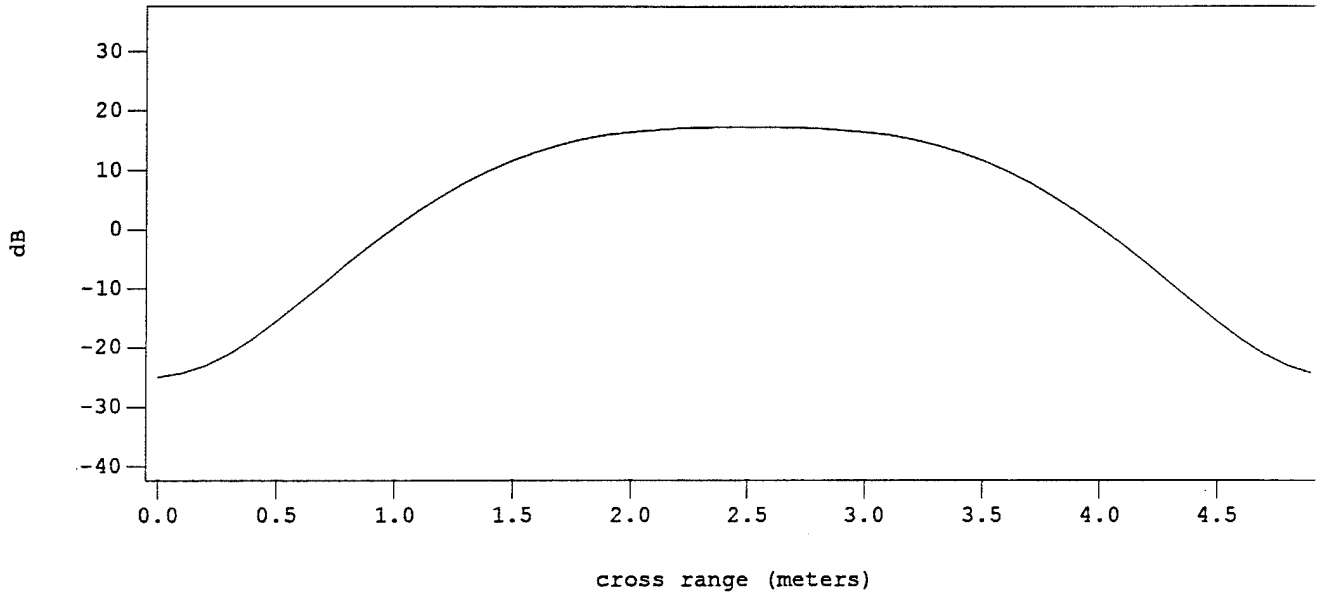

Figure 47 SAR Image 1 m Below the Surface of Two Point Targets, Length of Synthetic Aperture=25 m [9619]

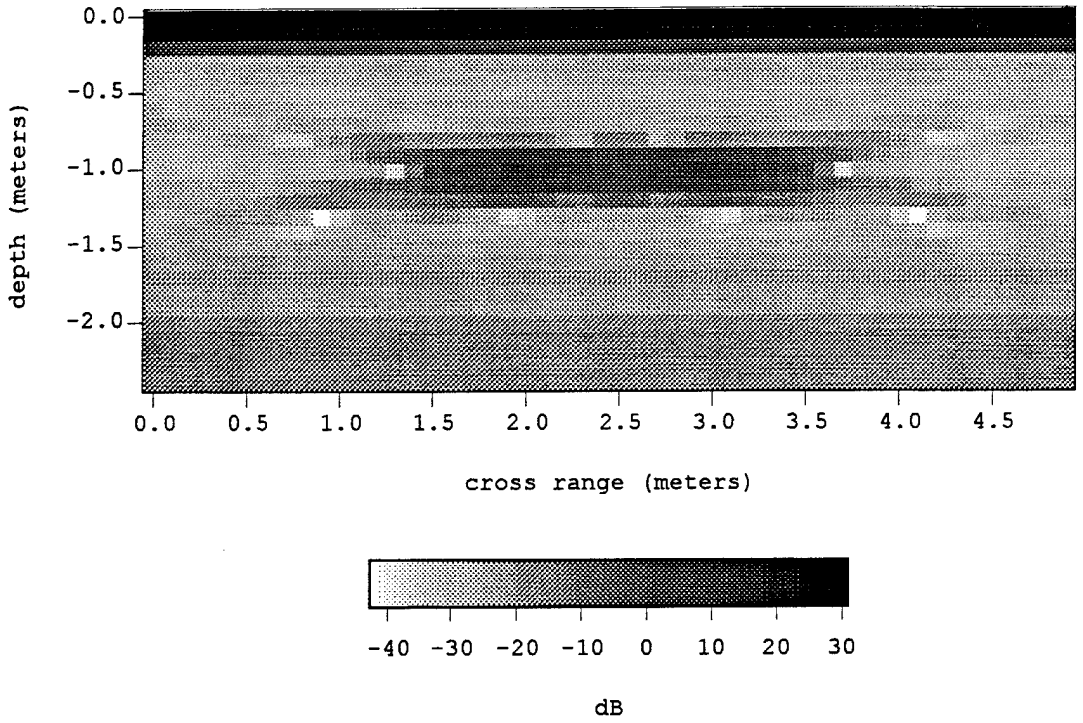

Figure 48 SAR Image of Two Point Targets, Length of Synthetic Aperture=55 m [9618]

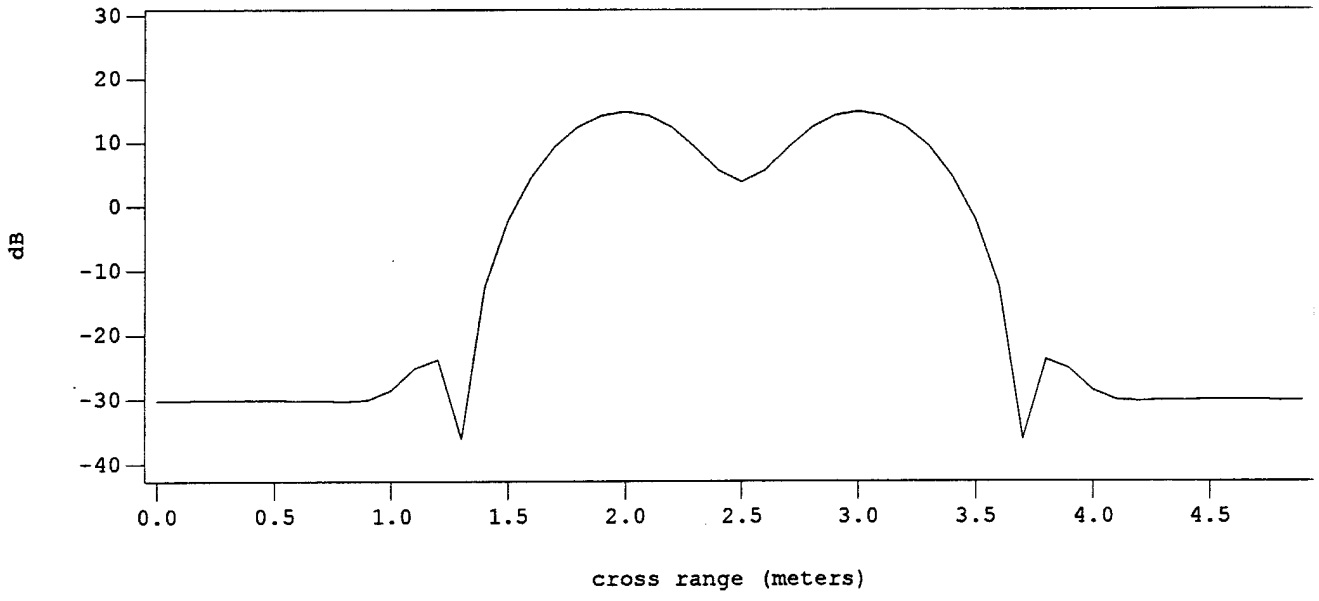

Figure 49 SAR Image 1 m Below the Surface of Two Point Targets, Length of Synthetic Aperture=55 m [9618]

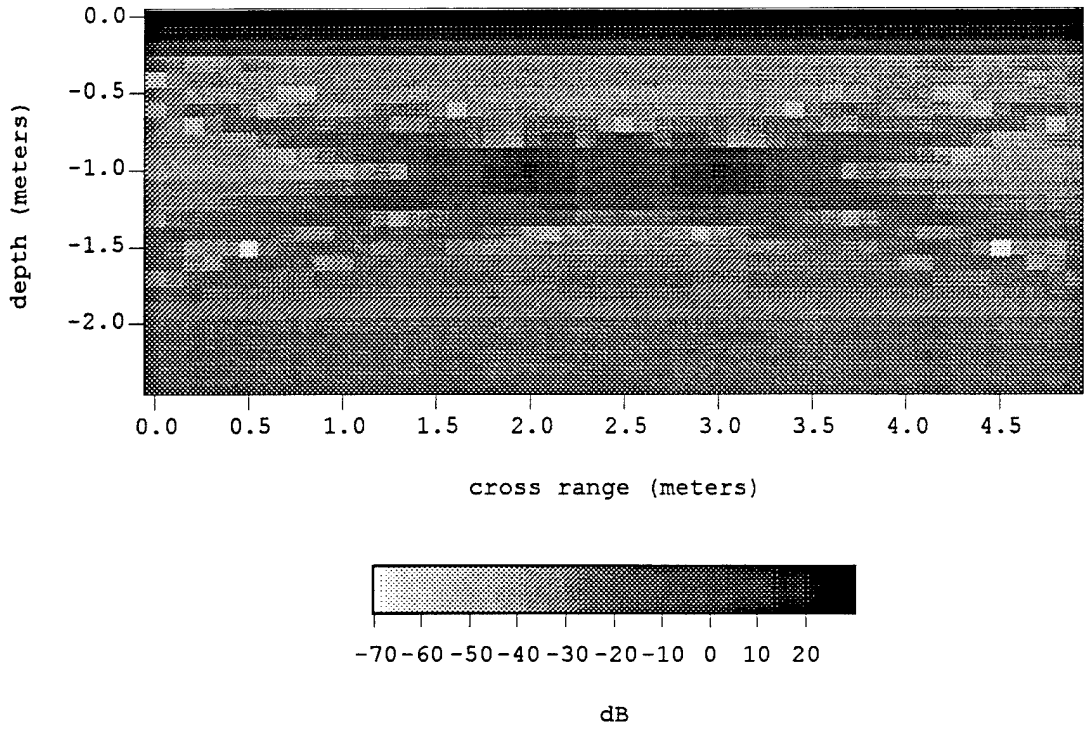

Figure 50 SAR Image of Two Point Targets, Length of Synthetic Aperture=110 m. [9614]

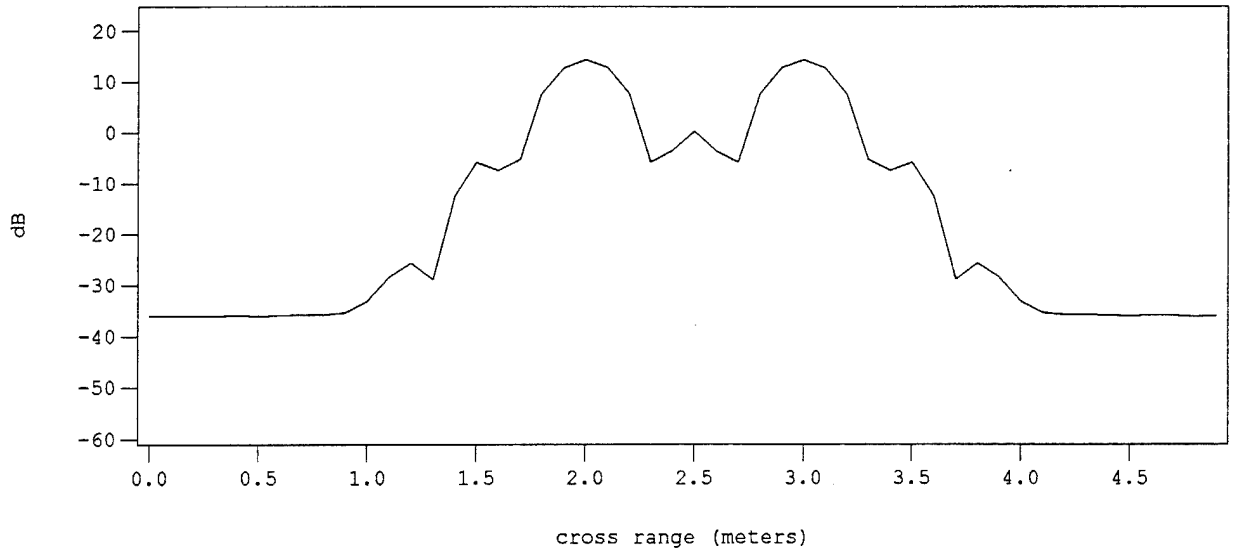

Figure 51 SAR Image 1 m Below the Surface of Two Point Targets, Length of Synthetic Aperture=110 m. [9614]

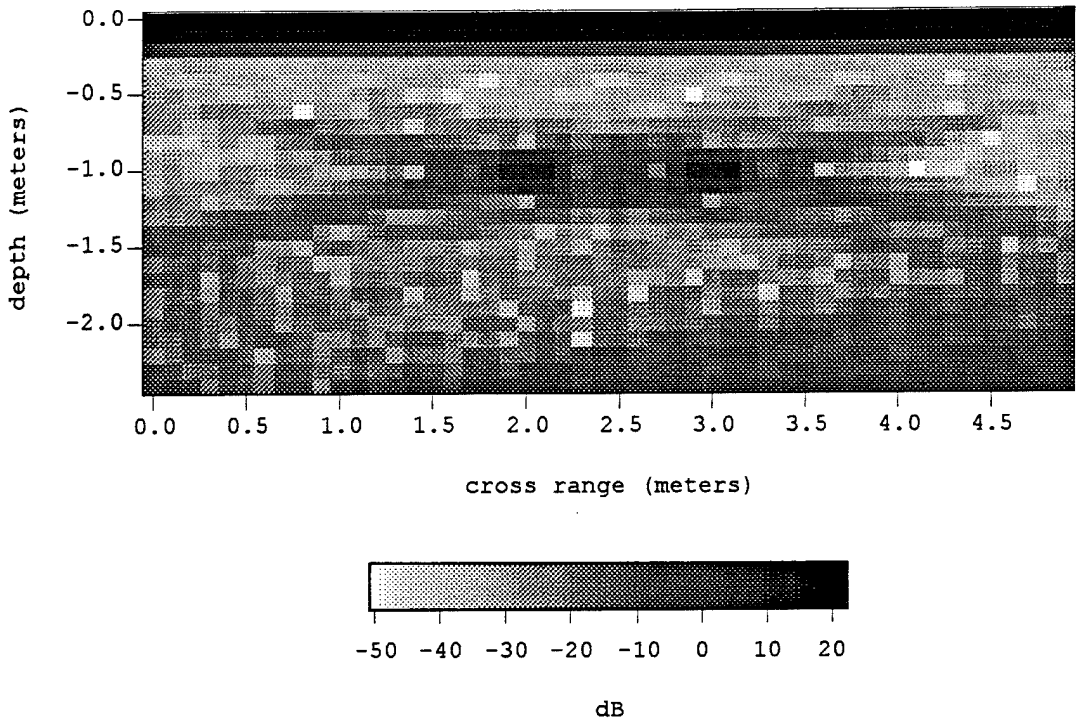

Figure 52 SAR Image of Two Point Targets, Length of Synthetic Aperture=150 m [9631]

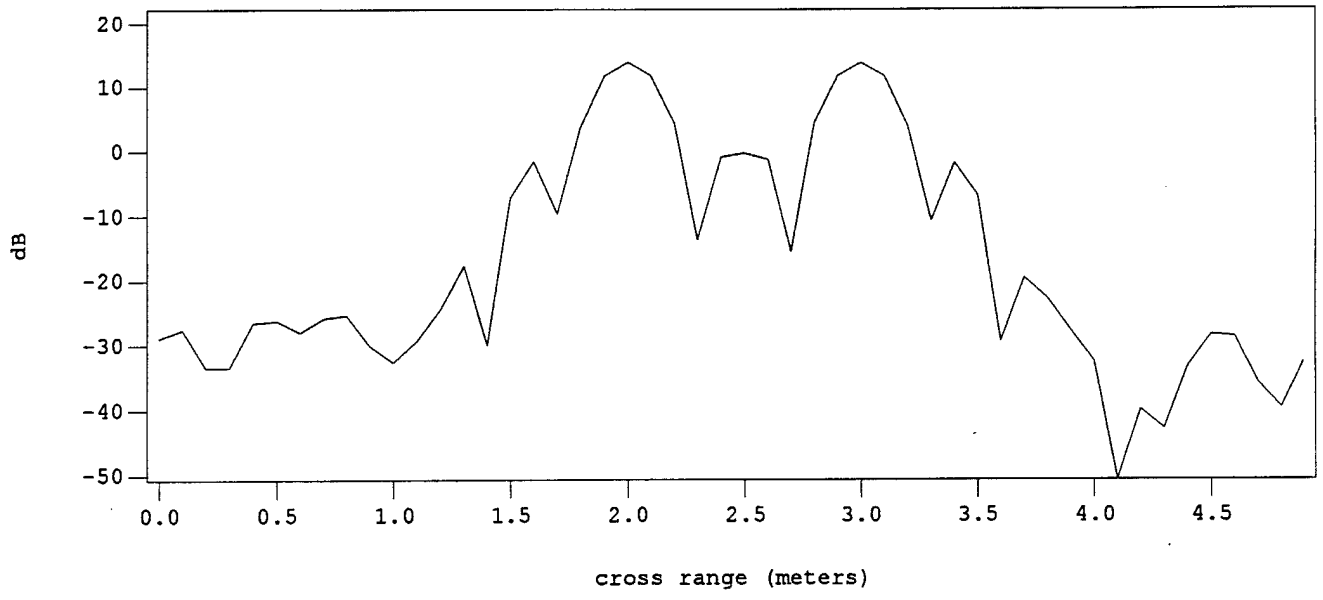

Figure 53 SAR Image 1 m Below the Surface of Two Point Targets, Length of Synthetic Aperture=150 m [9631]

Sample Spacing

According to sampling theory, the spacing between data points should be $\lambda/2$. For the impulse model, this means that the impulses should be transmitted and received at $\lambda/2$ meter intervals. Because our frequency range is 50 MHz to 500 MHz, the sample spacing at the highest frequency should be 0.3 m or less and the sample spacing at the lowest frequency should be 3 m or less. Because of the wide bandwidth of our signal, we can undersample at the high frequencies and oversample at the low frequencies and still get reasonable results. Figure 54, Figure 56, and Figure 58 show images obtained with sample spacing of 0.3 m, 0.6m, and 1.2m, respectively. These cases are for an infinitessimal horizontal dipole antenna and two -10 dB point targets located 1 m below the surface at cross range coordinates of 2 m and 3 m (the targets are separated by 1 m). The targets are still visible as the spacing increases beyond 0.3 m, but the background level begins to increase, making it more difficult to distinguish the targets. Figure 60 shows what happens when the sample spacing is 3 m, when all but the lowest frequency component of the signal is undersampled.

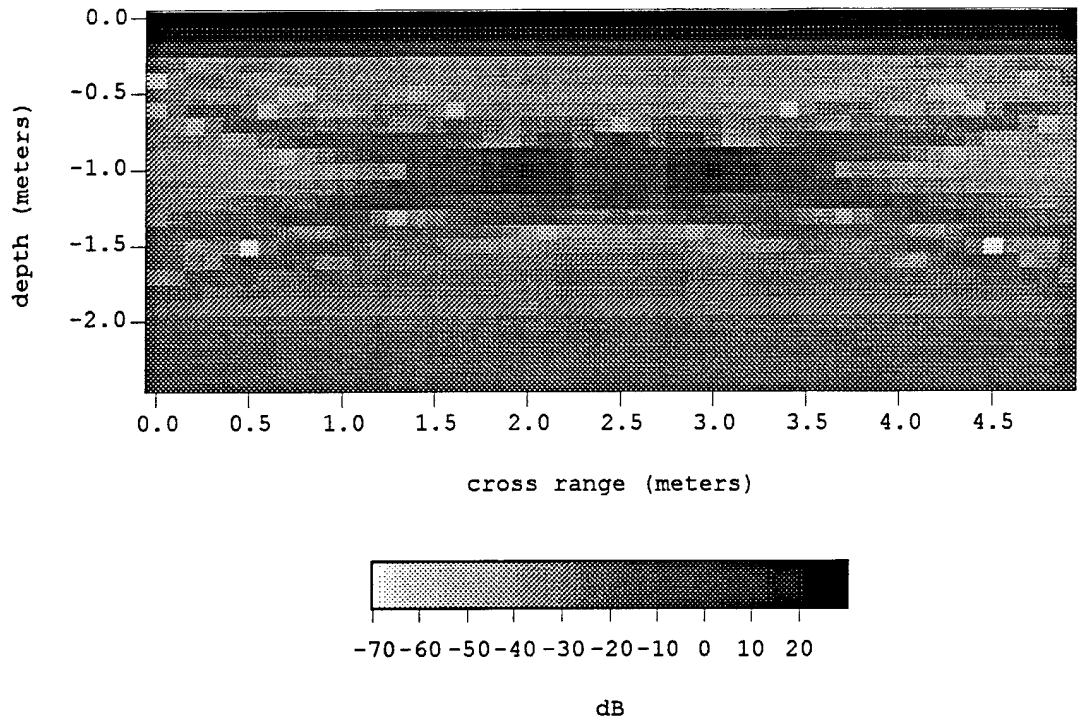

Figure 54 SAR Image with Sample Spacing of 0.3 m. [9614]

*

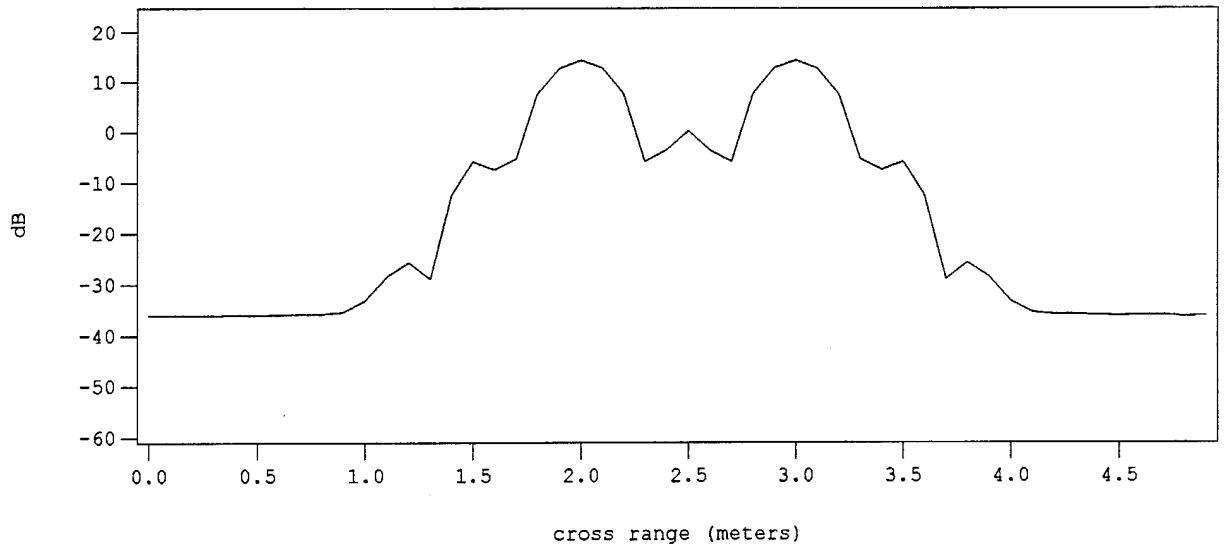

Figure 55 SAR Image at 1m Below the Surface with Sample Spacing of 0.3 m. [9614]

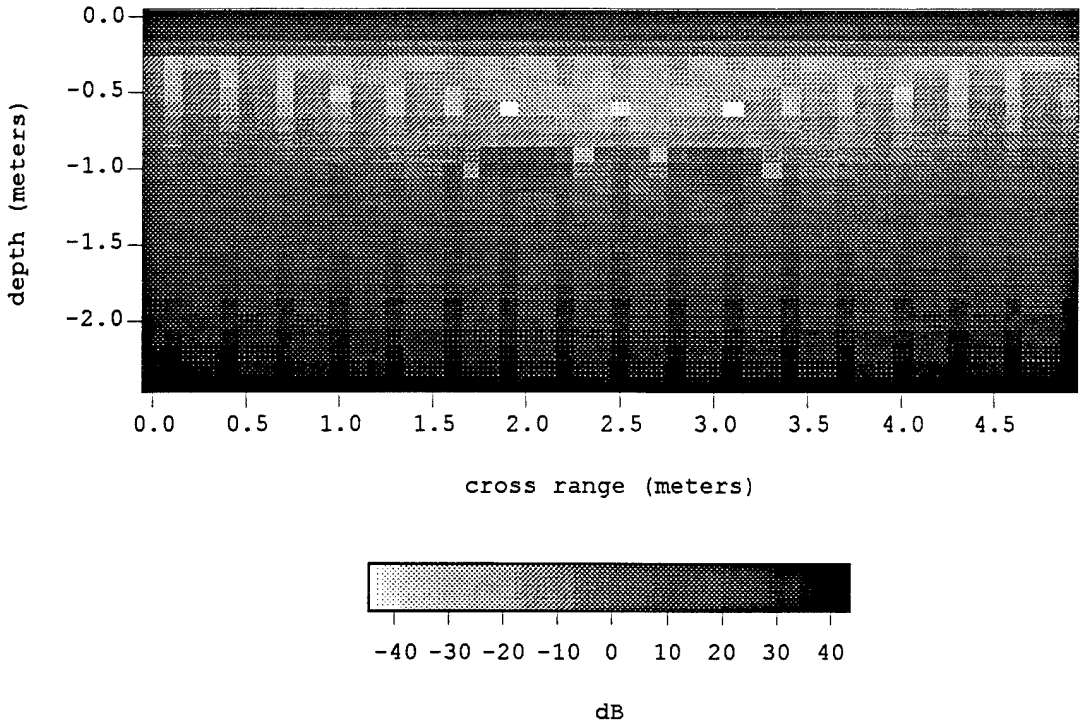

Figure 56 SAR Image for Sample Spacing of 0.6 m [9624]

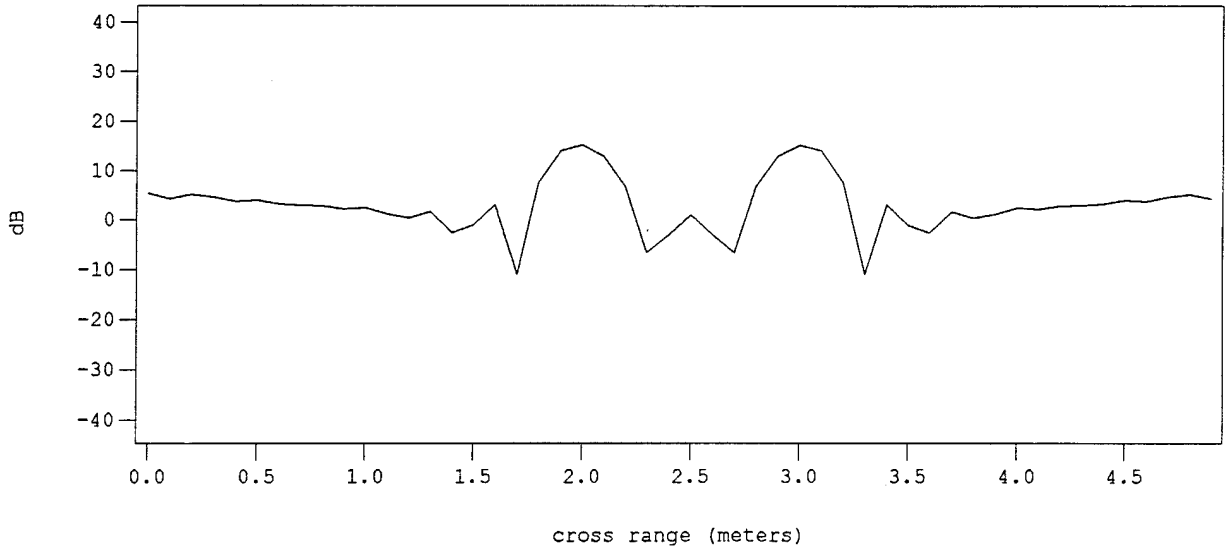

Figure 57 SAR Image at 1 m Below the Surface, Sample Spacing of 0.6 m [9624]

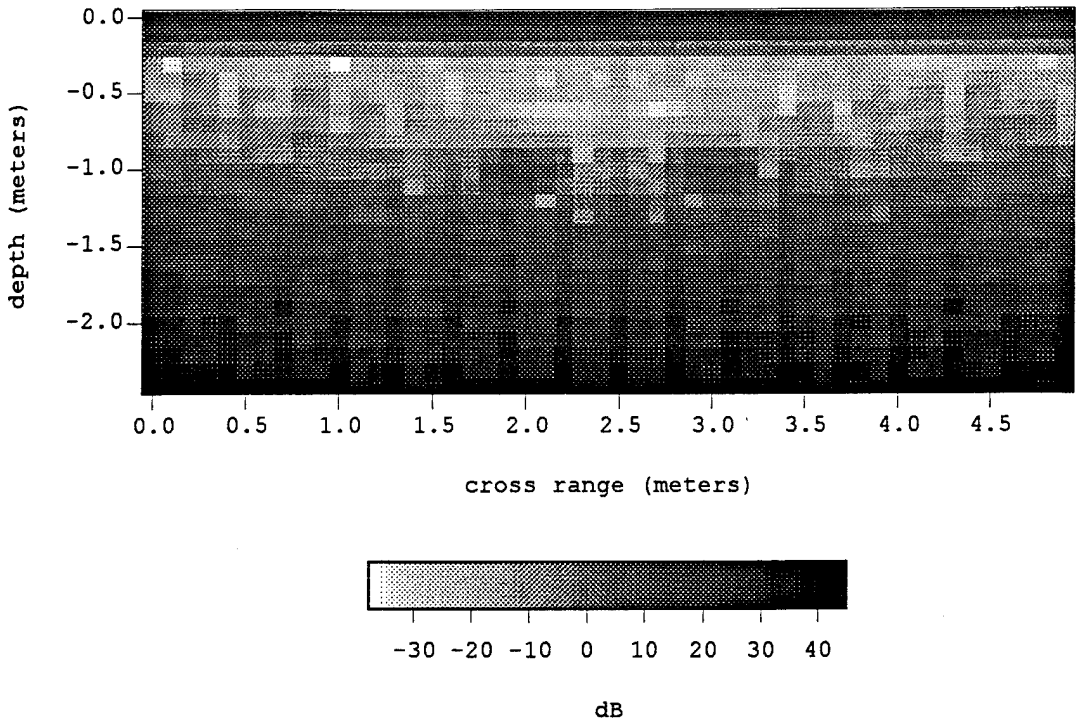

Figure 58 SAR Image for Sample Spacing of 1.2 m [9626]

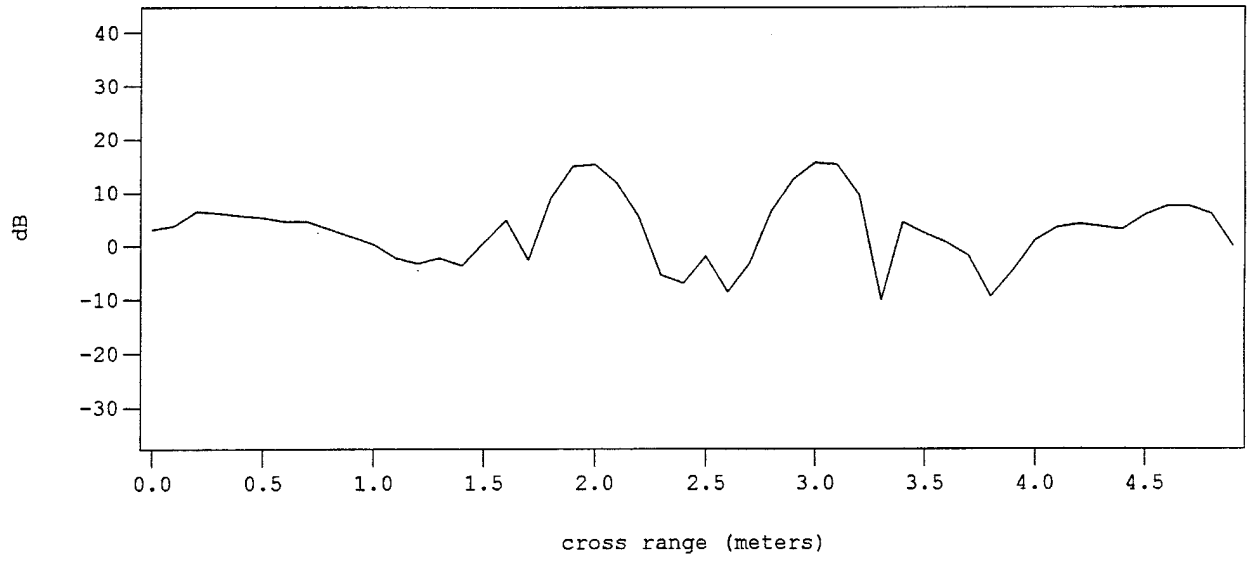

Figure 59 SAR Image at 1 m Below the Surface, Sample Spacing of 1.2 m [9626]

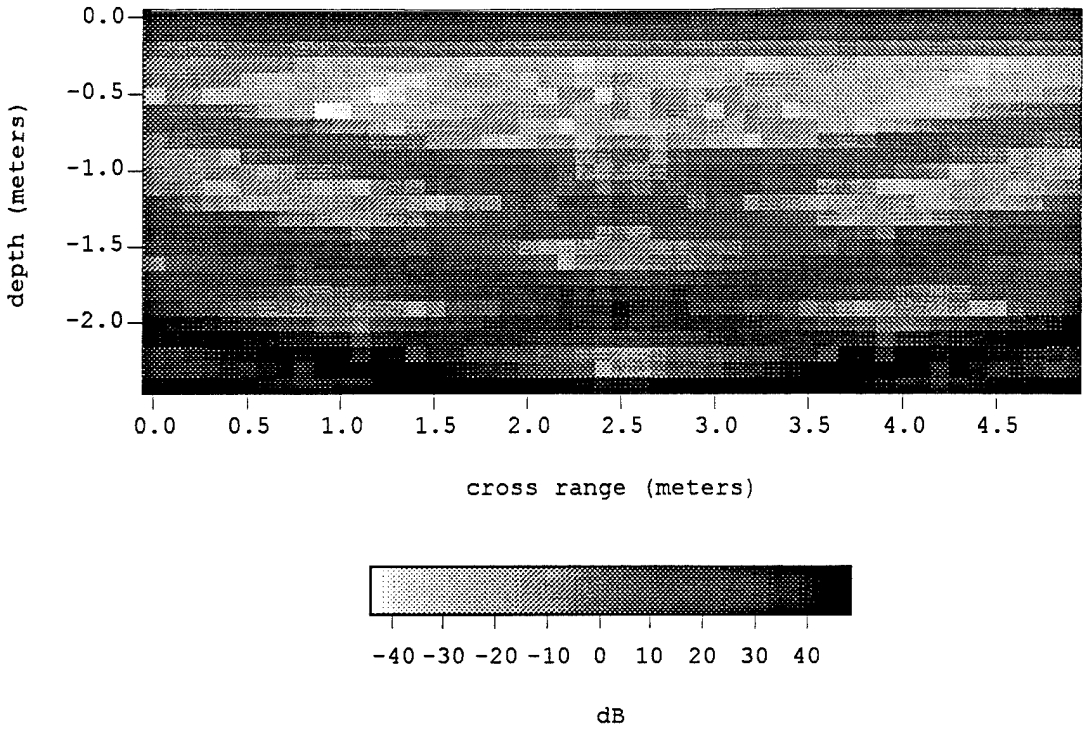

Figure 60 SAR Image for Sample Spacing of 3 m [9630]

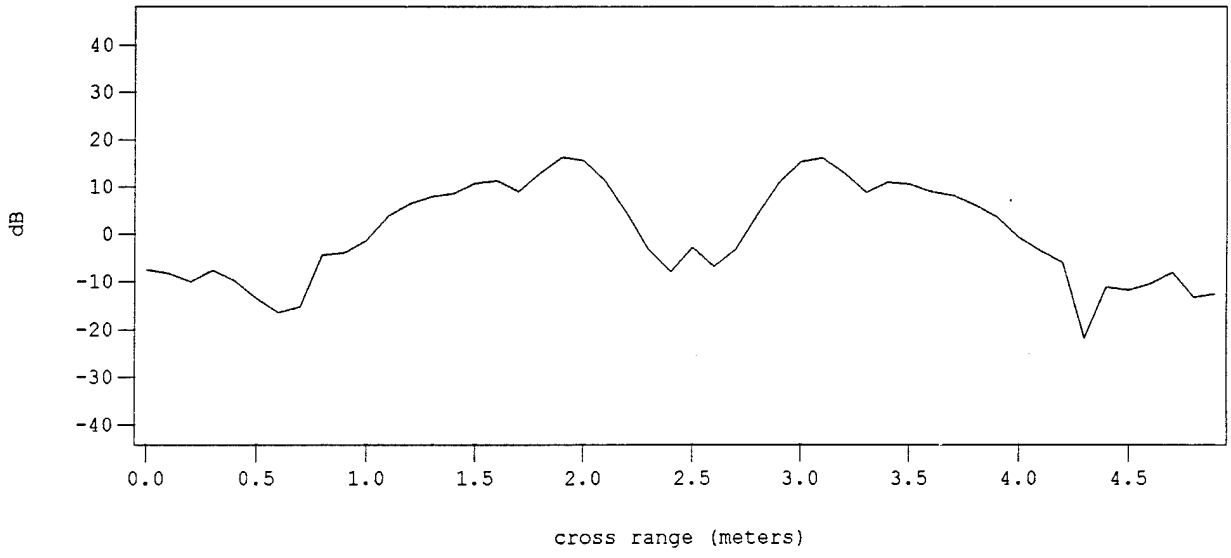

Figure 61 SAR Image at 1 m Below the Surface, Sample Spacing of 3 m [9630]

Antenna Pattern

We have compared horizontal and vertical infinitessimal dipoles and vertical infinitessimal dipoles with a pattern limited to 15° to 75°. Figure 62 is for a horizontal infinitessimal dipole oriented parallel to the surface of the ground and perpendicular to the flight path of the radar. Figure 63 is for an infiinitessimal vertical dipole, oriented normal to the surface of the ground. The signal levels for the vertical dipole are generally lower than the horizontal dipole case because most of the energy from the horizontal dipole is directed toward the surface, while the energy from the vertical dipole is directed toward the horizon. However, the vertical dipole image contains much less reflection from the surface. If the horizontal and vertical dipole antennas are limited to angular ranges of 15° to 75° from the normal, the images resulting are shown in Figure 64 and Figure 65. In these cases it does not appear that much information is lost by limiting the antenna patterns.

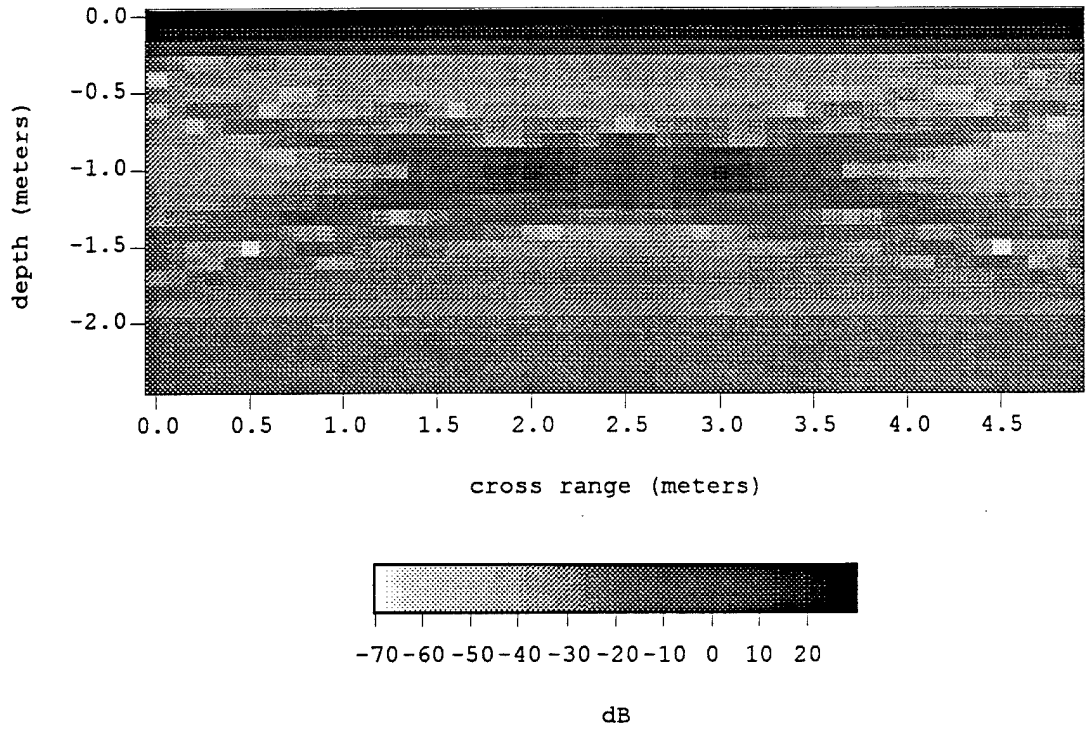

Figure 62 Full Horizontal Infinitessimal Dipole Antenna [9614]

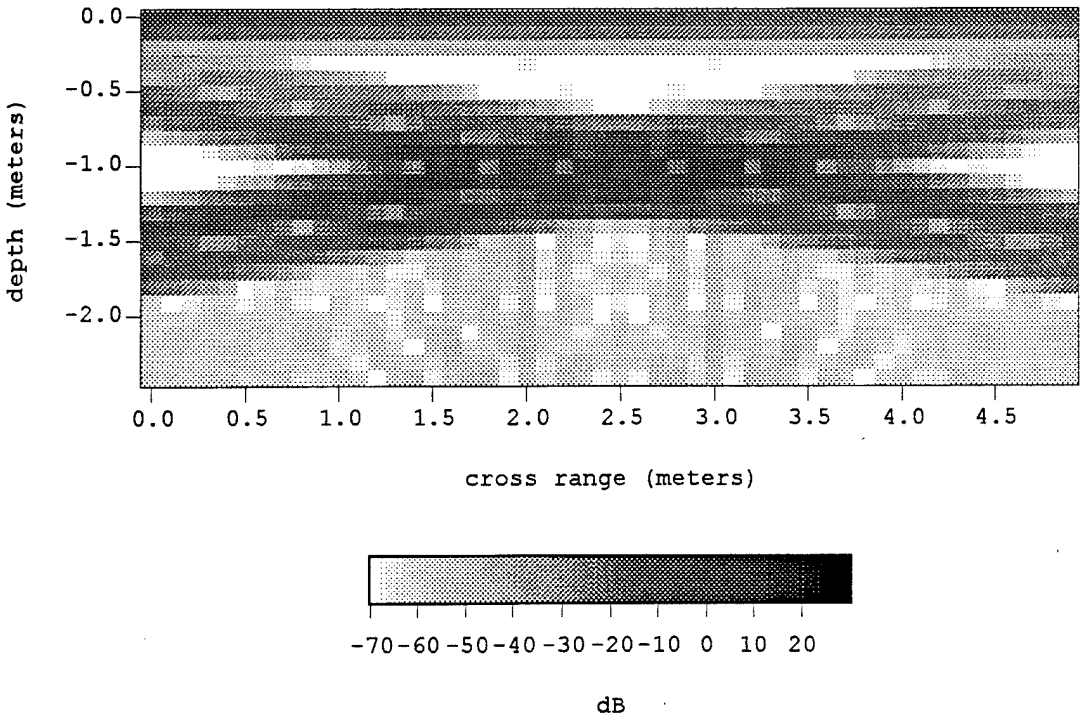

Figure 63 Full Vertical Infinitessimal Dipole Antenna [9615]

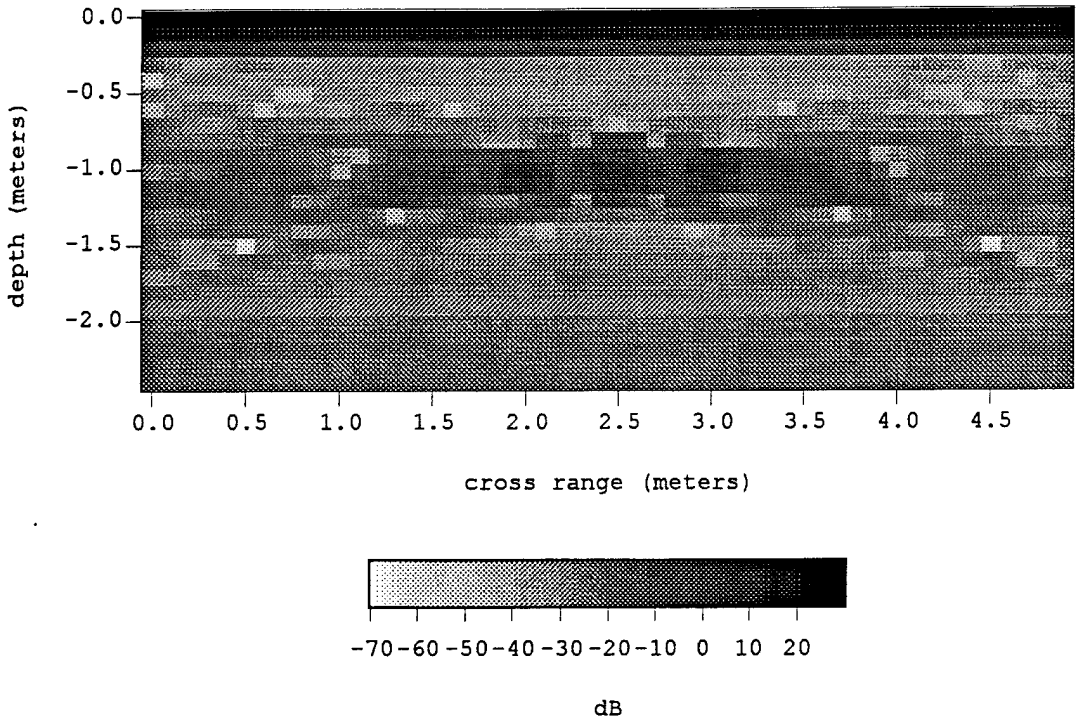

Figure 64 Horizontal Infinitessimal Dipole, Limited to 15° to 75° [9617]

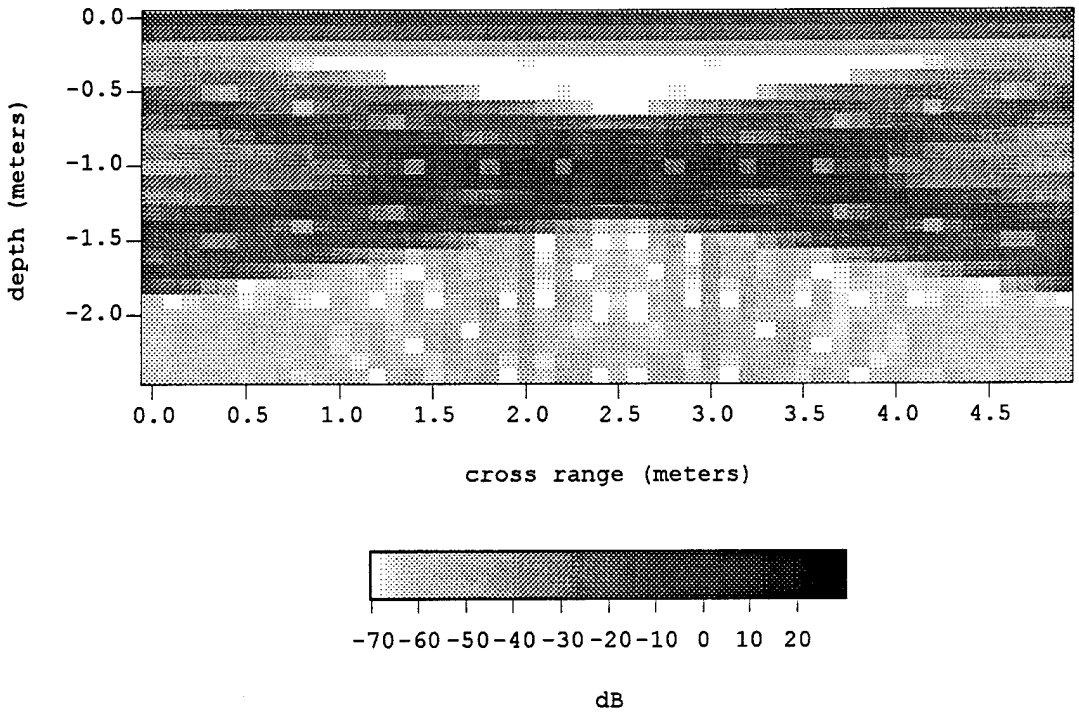

Figure 65 Vertical Infinitessimal Dipole, Limited to 15° to 75° [9616]

Number of Frequency Terms

We can use the step-frequency model to examine what happens to an image if the bandwidth is constant, but the number of frequencies within the bandwidth is reduced. If we decrease the number of frequency terms, N, we can still identify targets, but we begin to get ambiguous results. Figure 66 shows the ambiguous results obtained when only 10 frequency terms are used. The two targets that should appear 1 meter deep and at the 2 m and 3 m range positions also appear 0.2 m deep and 1.7 m deep. Figure 67 shows the same case using 105 frequency terms, which is the number used in most of the examples in this report.

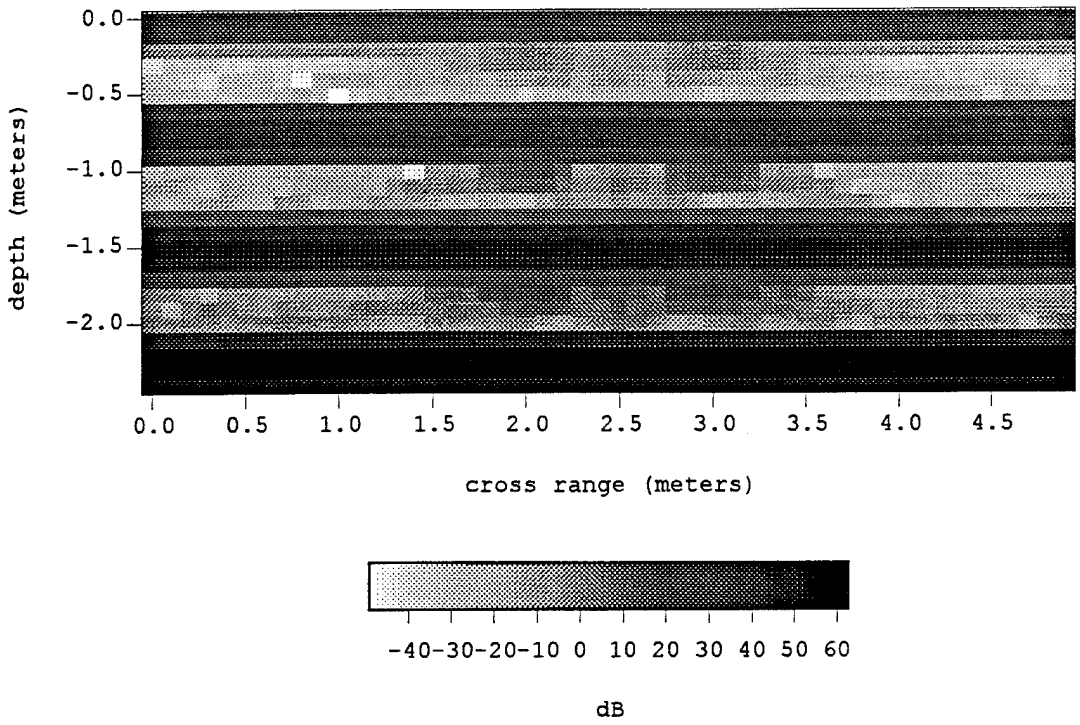

Figure 66 Step-Frequency SAR Image using 10 Frequencies, Horizontal Dipole Antennas [9612]

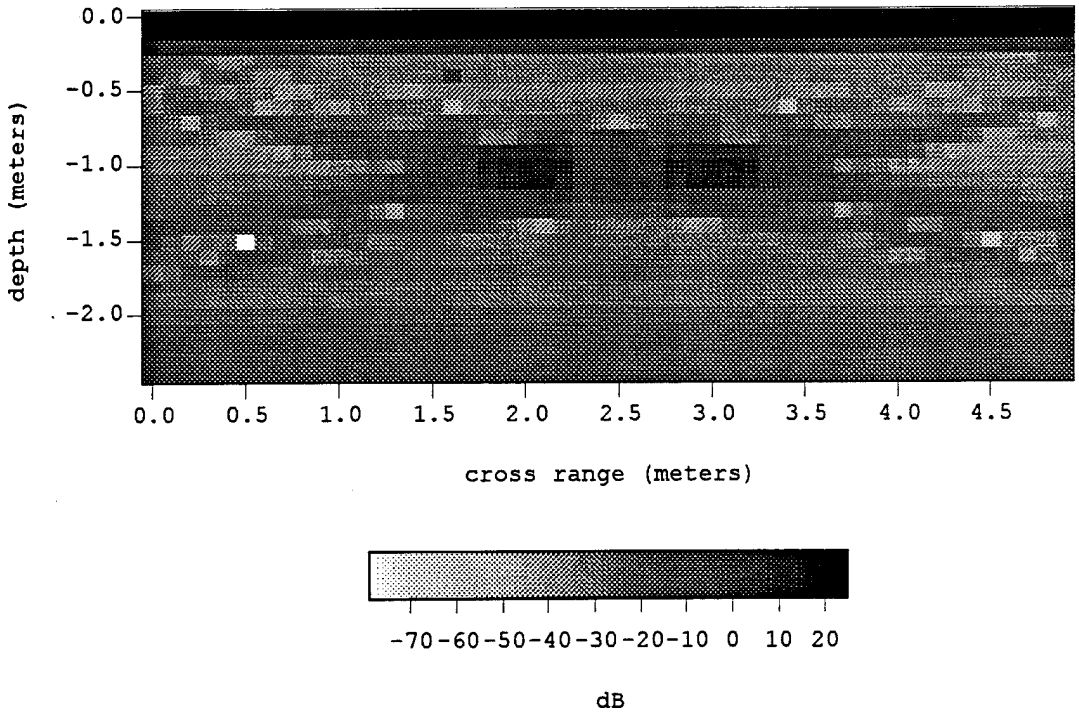

Figure 67 Step-Frequency SAR Image using 105 Frequencies, Horizontal Dipole Antennas [9636]

3.4 Computer Hardware and Software

We used Microway's NDP Fortran and the Microway Number Smasher-860 board to develop and run the SAR Simulation Program. The Number Smasher-860 board allowed us to continue to run the simulation on a 80386 or 80486 PC and have access to 32 MBytes of memory. The NDP Fortran also has a graphics library for screen graphics and the NDP VAST-860 Vectorizer. We can also run the program on a Sun workstation using Sun Fortran. The program can run approximately 3-4 times faster on the Sun workstation than on a 80386 PC with the Number Smasher-860 board. No graphics are available on the Sun with this code.

We wrote a simple user interface for the PC version of the simulation to enter parameters, run the simulation, and display data on the computer screen. The user selects the desired activity from a short menu.

Most of the parameters can be entered from the "Enter Parameters" screen. The parameters include: antenna beamwidth, antenna altitude, antenna velocity, soil index of refraction, soil conductivity, frequency, sampling interval of the received waveform, number of targets, target position, target size, and target orientation. The user may also be prompted to enter additional information, depending on whether the impulse model or step-frequency model is running. The impulse model and step-frequency model are compiled as separate programs, although they share many of the same subroutines.

For a quick view of the image that results from the simulation, the user may view the image on the PC screen using up to 16 colors to represent the magnitude of the signal from each pixel. The user selects "View Simulation" to view the image on the computer screen. The image may be scaled either linearly or logarithmically to the 16 colors.

For a better view of the results, the results of each simulation are saved in a text file. The file can be read by a 2-dimensional visualization software application which displays the

image and the data and can produce a hard copy of the image. The application we use is Spyglass® Transform.

3.5 SAR Model Fidelity

We believe the SAR model to be potentially useful to this program in spite of inherent limitations in the model. For example, the ground is modeled as a single medium with uniform dielectric constant and loss. Rarely, however, will the ground actually have this property of homogeneity. If the model was to be developed further, adding distinct homogeneous layers of arbitrary dielectric constant and loss would probably be the next step. Still, the model is useful in the engineering sense in that it provides a first-order approximation of what the limitations will be at a given site for targets of arbitrary size and depth. The model would be run for several constitutive parameter sets to allow the engineer to understand trends and limitations. It also provides the Battelle/ESL system developers with a clearer understanding of phenomenology and the impact of changing the parameters listed in Table 7.

4.0 Antennas

The form of the antenna or antennas used on the helicopter has been an item of intense scrutiny during this program. Because of the often conflicting wide dynamic range and relatively high speed requirements, it was initially felt, and became more apparent during the study, that the antenna would have to provide some form of analog signal processing. The dynamic range requirements are driven by the very high return from the ground surface and the very low level of return from buried objects. The required dynamic range values are difficult to quantify because the losses in distinct soils can vary over large ranges. ESL's previous experience has been that 60 to 70 dB of dynamic range is required in reasonable soils. A further discussion of dynamic range is included on page 201. The highest surface return is caused by an ill-defined surface patch that is generally directly beneath the airborne platform. If the earth was locally perfectly flat and perfectly level, the area beneath the aircraft would cause a high level of specular reflection. An actual surface, of course, is neither flat nor level so the specular scattering is diffuse but in general, the highest return is from a ground patch beneath the helicopter.

One very useful potential characteristic of the antenna, then, is a null in the pattern directly below the aircraft. This null then provides an analog means for reducing the largest component of the return from the surface. Several antennas were considered that provide this null but a vertical dipole array beneath the aircraft seemed to be the most useful design. It is described subsequently.

The antenna bandwidth, antenna size, and antenna efficiency can influence measurement accuracy and time required for measurements in a significant way. The antenna bandwidth needs to cover the spectrum of the signal reflected from the UXO required for target identification purposes. Since the length of the UXO items can vary from the order of 1 foot to 9 feet, a broadband antenna is essential, even if only the dominant

resonance is used for identification purposes. This problem is compounded by the electrical properties of the soil where the relative dielectric constant ϵ_r can vary from about 5 for some sands to up to 50 for some clays. Because the *electrical* length of a body immersed in the ground is proportional to the square root of the dielectric constant, the first resonance frequency of any given target can vary significantly, depending on the dielectric constant of the soil. Distinct targets (those with distinct shapes) will still have distinct resonances, if immersed in the same soil. Considering the diversity of target shapes supplied by NAVEODTECHDIV and the well-documented diversity of soil types and accompanying dielectric constants, it appears that first resonances of targets of interest can vary between approximately 7.8 MHz and 200 MHz. This large bandwidth places severe requirements on the antenna design. The antenna length is probably going to be about 10 feet to 20 feet with an associated low-frequency resonance of the order of 25 to 50 MHz.

A series of antenna types have been considered in this study. These antennas have all been subject to the constraints that, if possible, they should be operable at frequencies low enough to be able to detect the lowest order resonance of the UXO's. This constraint is tied to the use of Complex Natural Resonances (CNR's) as a target discriminant. This range corresponds to that frequency at which the largest UXO is approximately one-half wavelength long in the media. A worst case might be that of a 3 m long UXO in a media whose permittivity is 50. In this case, the lowest operating frequency would be approximately 7 MHz which is probably below the capability of a realistic airborne antenna.

4.1 Antennas Candidates for the Airborne Platform

The antennas that have been considered for the Airborne GPR system include:

(a) Horizontal Dipole — Dipole Monopulse between Struts
(b) Horizontal Slot Dipole Monopulse between Struts
(c) Horizontal Cross Dipole between Struts
(d) Horizontal Cross Dipole between Struts
(e) Vertical Dipole Array
(f) Vertical Slot Array
(g) Spiral
(h) TEM Horn

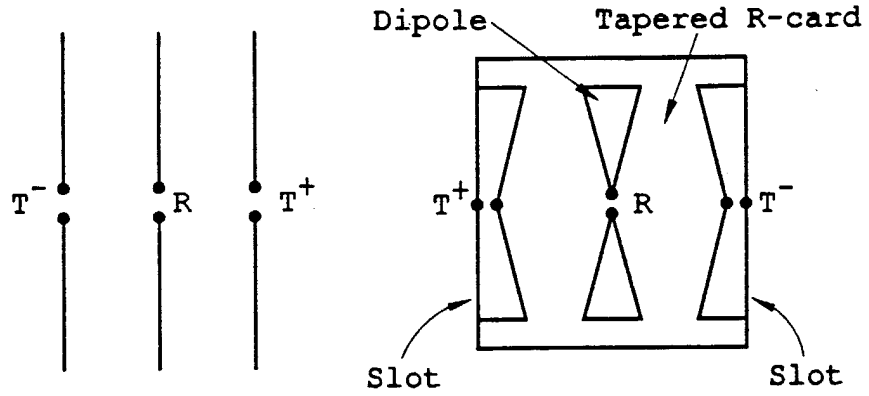

(a) Horizontal Dipole-Dipole Monopulse

(b) Horizontal Slot Dipole Monopulse

(c) and (d) Horizontal Cross Dipole or Slot (see Fig 1.9)

(e) and (f) Vertical Dipole or Slot (see Fig 1.12)

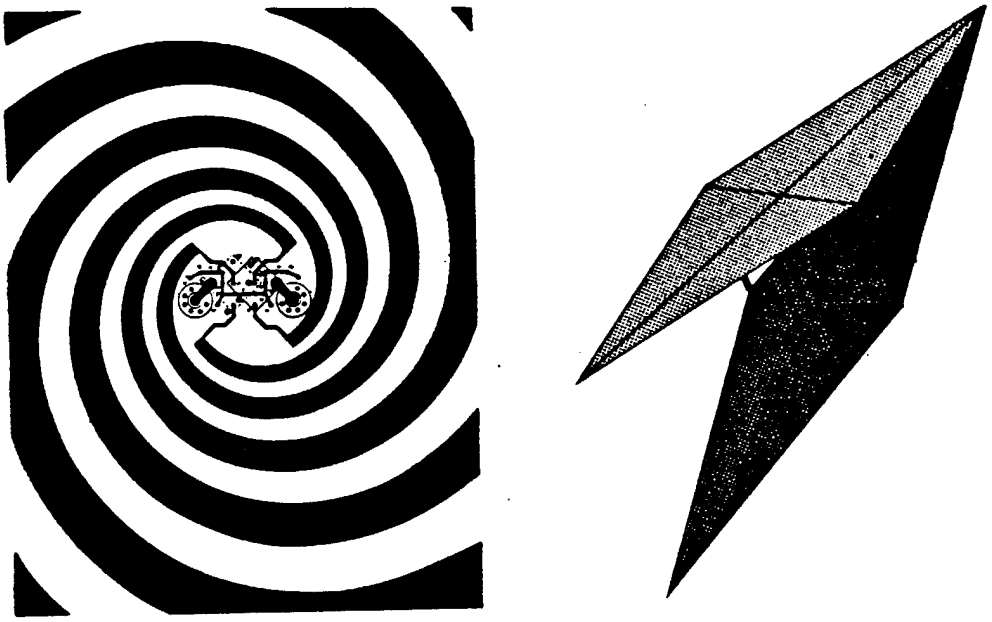

(g) Spiral

(h) TEM Horn

Figure 65. Antenna geometries.

Figure 65 illustrates these antenna configurations.

Many of these antennas proved to be reasonable for a system mounted on the ground primarily because they took advantage of the electrical properties of the ground to provide adequate transmission. However, it seems desirable to be able to detect targets at frequencies as low as possible. We noted earlier that for some media the dominant target resonance can be at 10 MHz or even lower and that this is the dominant signature. The radar range equation does require detection of ever smaller signals as the operational frequencies increase.

Because it is desirable to operate these antennas at as low a frequency as possible the horizontal monopulse antennas may not be satisfactory. Figure 66 shows the two transmit antenna positioned between the skids of the helicopter. The 8 foot separation corresponds to the spacing of the skids (the maximum available spacing). The electrical distance $\beta\ell$ at 10 MHz is

$$\frac{360^\circ}{30} \cdot 2.4 \sin\phi = 28.8^\circ \sin\phi \tag{57}$$

and the radiation pattern in the plane of the paper is given by

$$E = E_1 - E_1 e^{-j28.8\sin\phi} = E_1 e^{-j14.4\sin\phi}\, 2j\sin(14.14\sin\phi) \tag{58}$$

Clearly this will not be an effective antenna at 10 MHz and, in fact, the frequency must be increased to approximately 100 MHz to produce an effective radiator. This antenna would be useful, however, for detecting smaller UXO's in sand where the dielectric constant is approximately equal to 6.

The crossed-dipole geometries can be positioned between the struts and oriented so that an 11 foot (3.5 m) long dipole could be used. It has several advantages. First, it would have reasonable radiation as low as 10 MHz. The crossed-dipole would not receive the

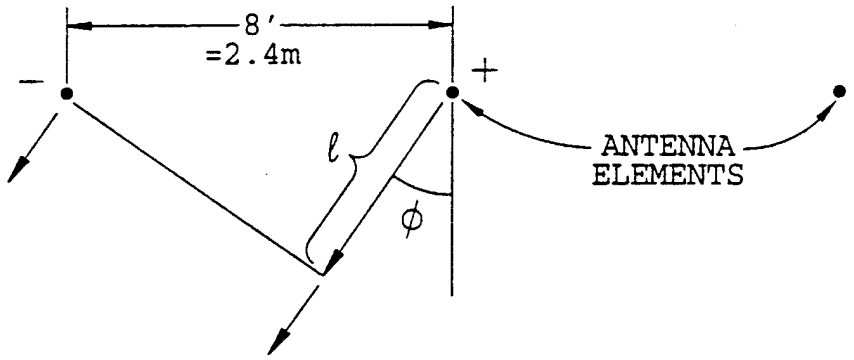

Figure 66. Transmit antennas for monopulse schemes.

specular scatter from the ground below. It would be mounted in a cavity with an absorber layer directly above to shield it from radiation from the helicopter and scattering from the helicopter structure. The struts might represent a source of scatter since they are arranged at 45° with respect to the dipole elements as are the walls of its cavity. Second, the dipoles would be susceptible to signals propagating along the horizon. In a recent discussion with the Ohio Air National Guard (ANG), it was found that hoist facilities are available located at the center of gravity of the helicopter. This device could be used to pull a cross dipole into position in flight. The top of the antenna cavity could be grooved so that the struts would fit into the grooves for stability and thus could be made longer than the previously-mentioned 11 feet.

The crossed-dipoles can also be used to illustrate that the characteristic matching concept is successful. A gray scale plot is included using data generated by a GPR using crossed-dipoles matched approximately by their characteristic impedance. The plot is shown in Figure 67. The target is a 3 foot long cylinder buried 3 feet deep in clay. The antenna resonance (at t=20 ns) and the cylinder resonance (at $t \approx 60$ ns) are distinct and are readily

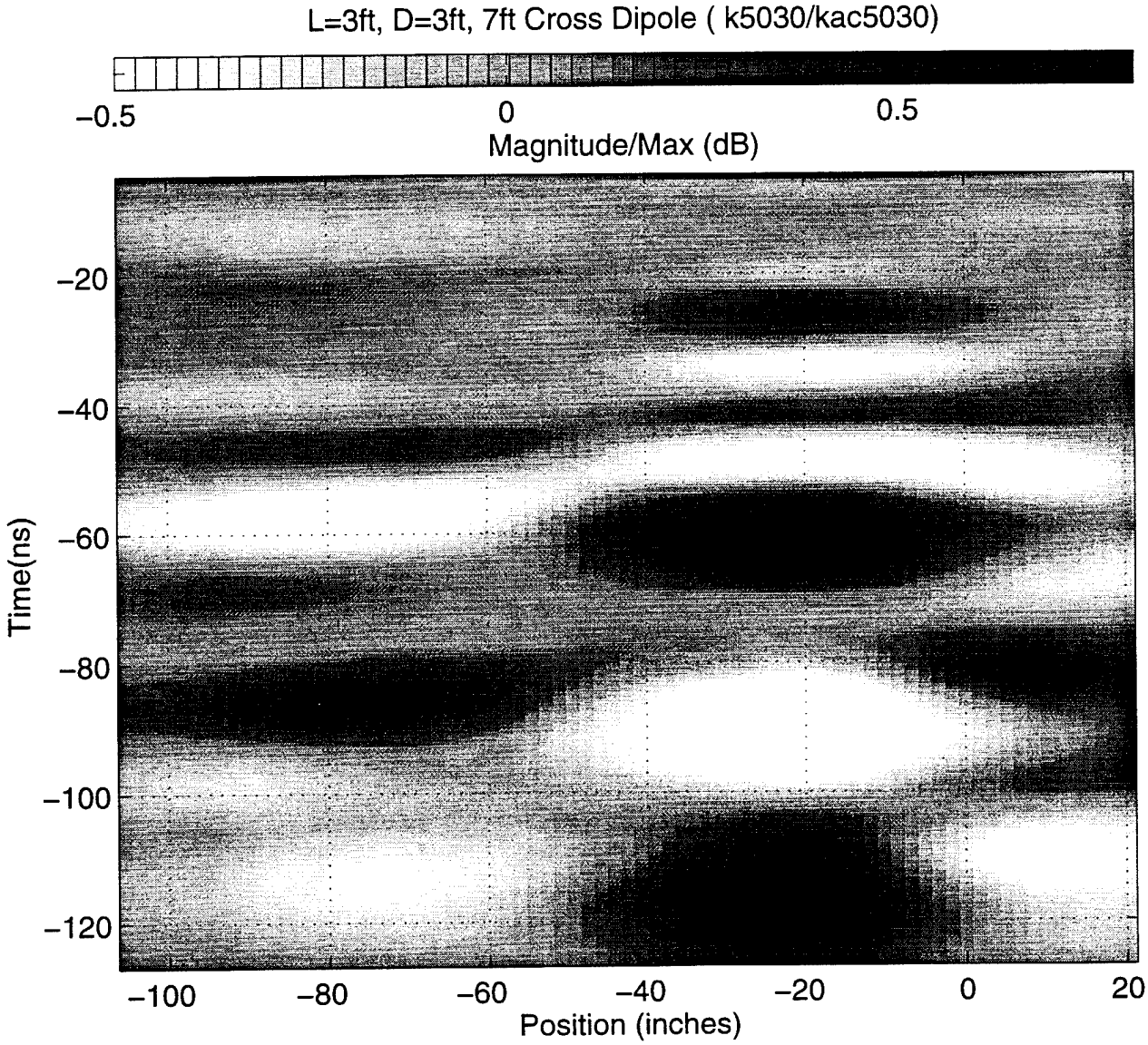

Figure 67. Gray scale map for cross dipole antenna where $Z_g \sim Z_c$ over a 3 foot pipe 3 feet deep in clay.

observable with no further data processing. The gray scale plots are generated by plotting successive measured waveforms as a function of antenna position and time (corresponding to depth). The resonance frequency is found from $f_r = 1/2T$ where T is the time between two successive nulls.

Figure 68 is the gray scale plot for a 5 foot long cylinder at a 3 foot depth. Again, the antenna resonance is clearly observable in the early time frame (i.e., for $t \approx 20$ ns). The expected fundamental resonance of the 5 foot long cylinder is not observable because there is no periodic structure at a lower frequency than that of Figure 67 ($t > 60$ ns). It is noted, however, that the lobe structure from 60 to 90 ns is somewhat broader than that observed in earlier times or from 20 to 40 ns. The fundamental resonance was not observed because it was at approximately 9.8 MHz and was below the operating frequency of that antenna. The observed response in the 60-90 ns region would then be a higher order resonance.

The crossed-slot offers the same features as does the crossed-dipoles. They can both be excited using the same antenna elements as shown in Figure 69 by using hybrids and an approximate switching mechanism to select one or the other. This configuration offers an advantage because a linear scatterer, lined-up with one of the antenna elements, becomes invisible to this antenna configuration. However, such as scatterer could not be invisible to both. This concept is being pursued further for a ground based GPR. This antenna system is a viable antenna for the Airborne GPR.

The spiral is an effective radiator for frequencies where the circumference of the spiral is less than a wavelength. The circumference of a spiral between the struts is 7.6 m or the operating frequencies would be above 40 MHz. Thus, this antenna like the monopulse antenna would perform poorly at frequencies below 40 MHz.

A vertical dipole array is illustrated in a sketch in Figure 70. This antenna is currently being studied using the HARP code that has been developed at OSU [2]. A preliminary computation of the pattern on a single 3 m long element is given in Figure 71. The crossed-

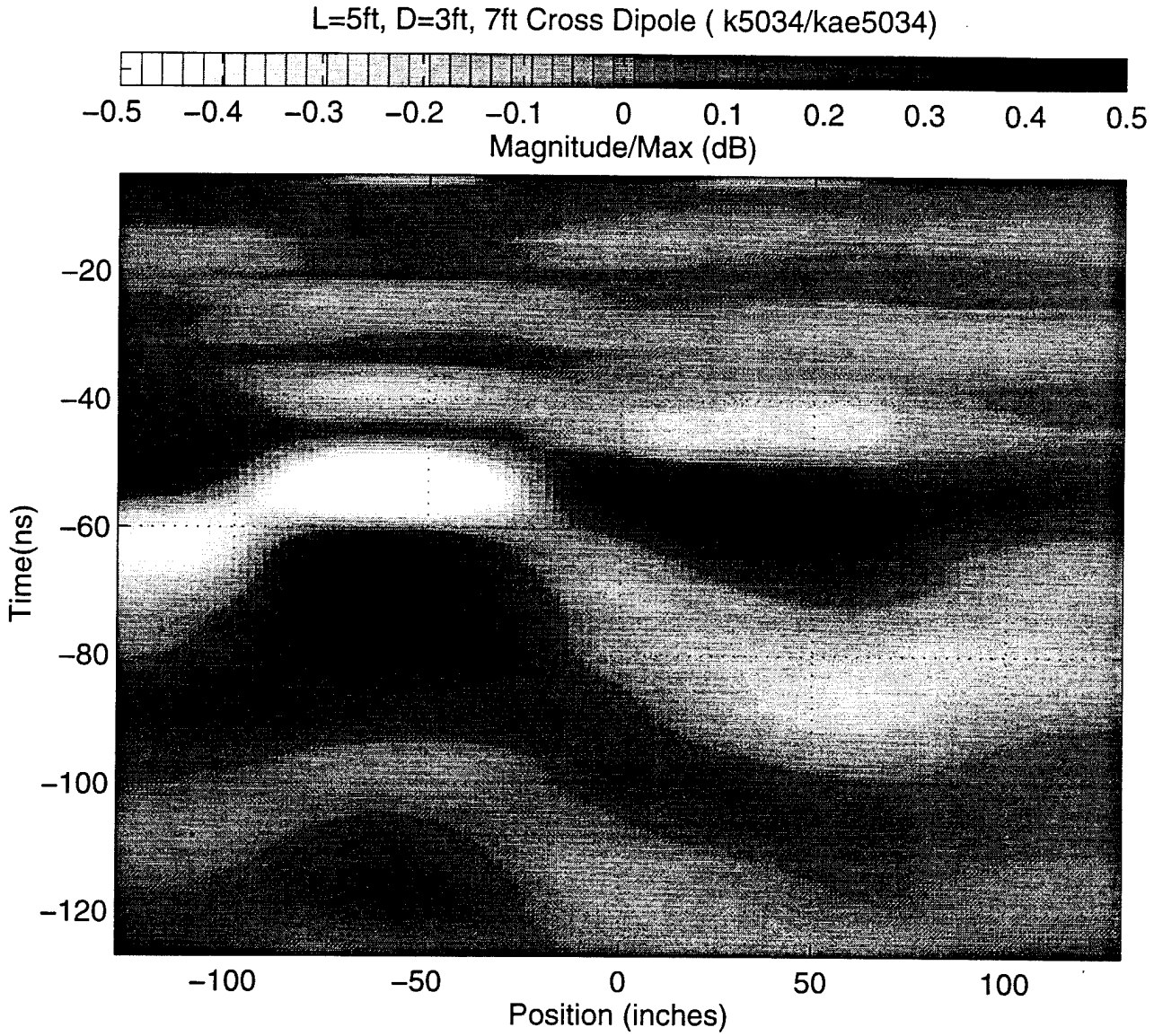

Figure 68. Gray scale map for cross dipole antenna where $Z_g \sim Z_c$ over a 5 foot pipe 3 foot deep in clay.

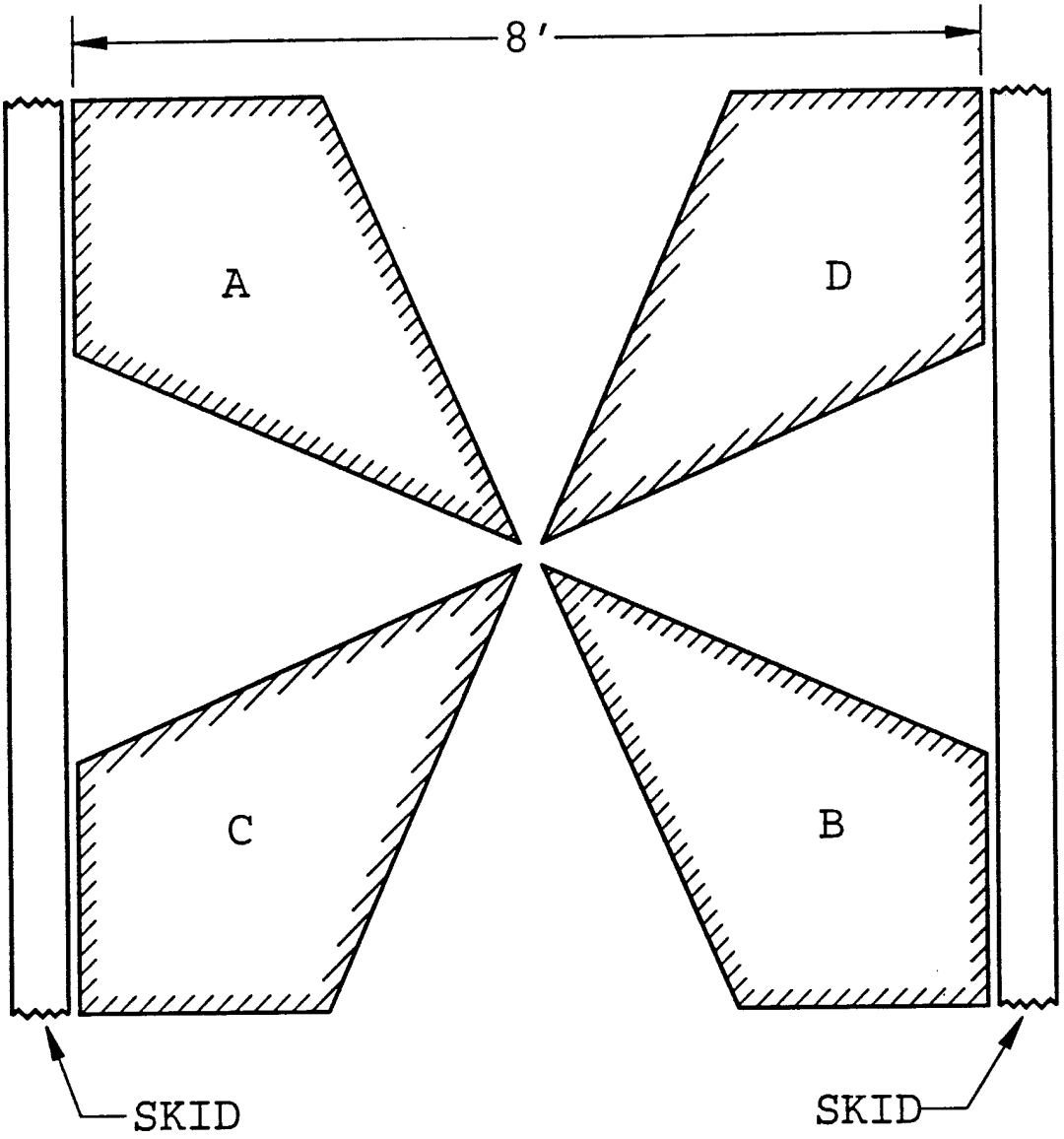

For Dipole Operation	A-B are excited
	C-D are receiver
For Slot Operation	AC-BD are excited
	AD-BC are receivers

Figure 69. Crossed-dipole/slot antenna.

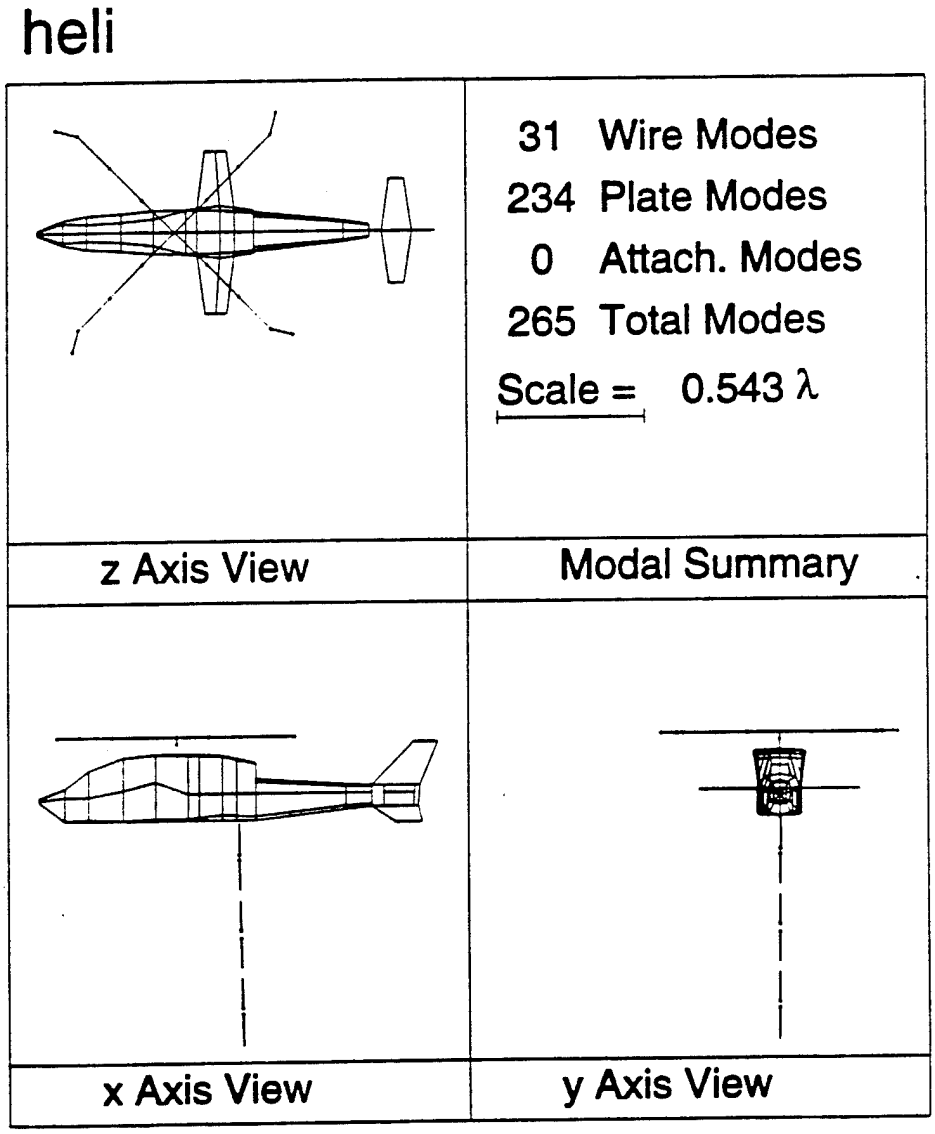

Figure 70. Helical with 3 vertical dipoles.

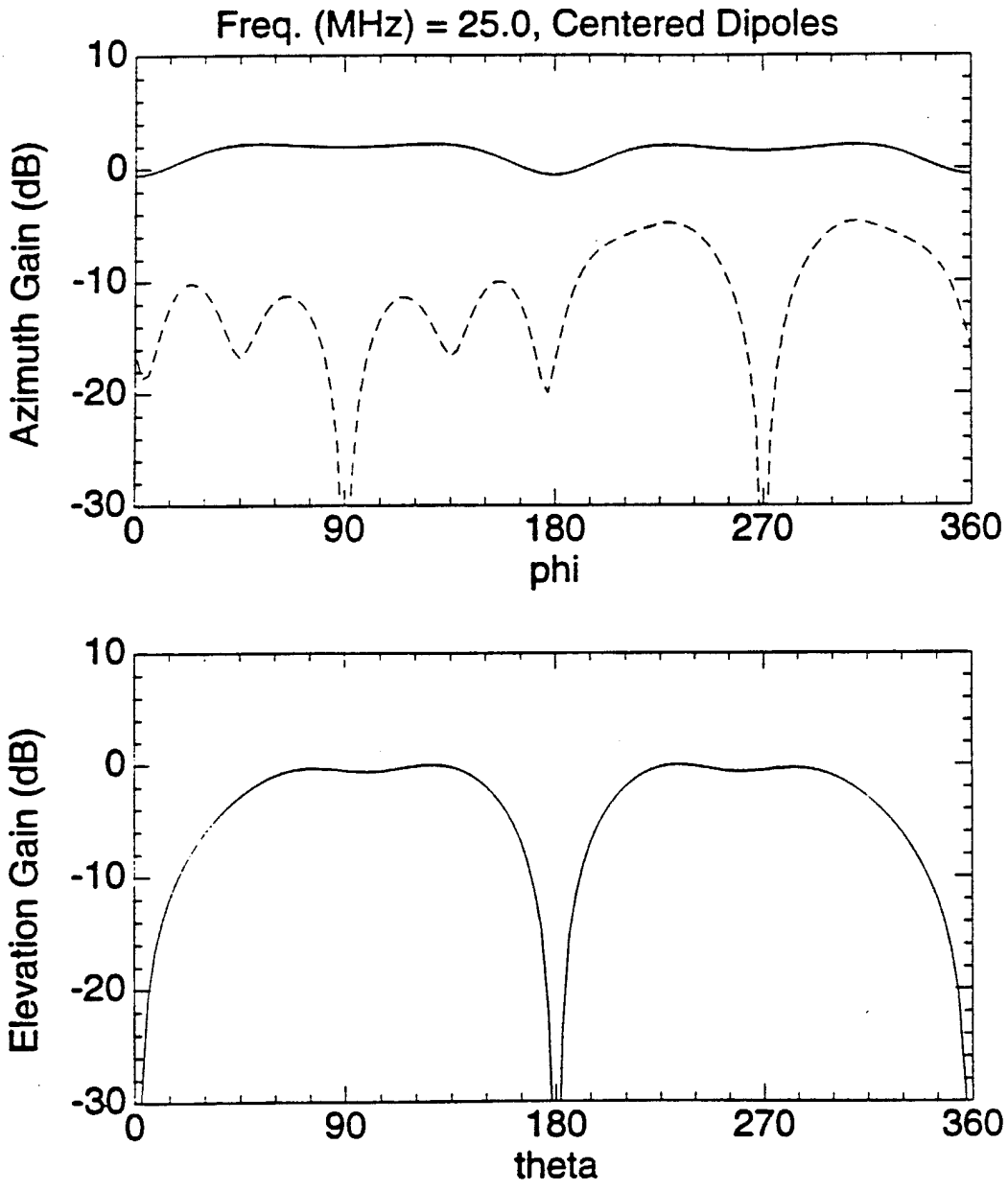

Figure 71. Patterns for center dipole (receiver) Figure 70

polarized component is shown by the dotted line for the horizontal plane pattern. The vertical plane pattern is taken in the plane containing the nose and the tail. These two patterns are at 25 MHz.

While Figure 71 shows the pattern for a single antenna, the actual operation will have the upper and lower antennas excited 180° out of phase. The monopulse pattern without the helicopter (see Figure 72) for this case in the vertical plane at 10 MHz is given by

$$E = 2jE_1 e^{-j33^\circ} \cos\phi \sin(33^\circ \sin\phi) \qquad (59)$$

where the additional cos ϕ factor is the antenna element pattern. At both $\phi=0$ and $\phi=90°$, Equation (1.3) predicts a null will be generated. At $\phi = 45°$, the electric field is reduced by about one-half, i.e., $|E| = 0.55E_1$. The pattern is broad and should be useful for this application.

The vertical dipole system suffers one deficiency; it will not detect a linear scatterer that is perpendicular to the dipole. However, because the helicopter will scan the entire area, this condition will not occur for all antenna positions and this drop in amplitude in itself this could represent an additional target signature.

The vertical monopulse dipole antenna system also has a nearly circular pattern with the array as the axis of symmetry.

The transmitter is used to excite the monopulse system because this geometry projects a null along the horizon. Thus, it minimizes interference with external systems. If one wished to minimize interference with our radar, the receiver would be connected to the monopulse array. In the ANG discussion, it was also noted that there are several hard spots that could be used for additional monopulse antenna positions. For example, horizontal monopoles could be used that are at the midpoint of the fuselage (i.e., of the slide doors). This additional geometry will be examined in terms of pros and cons with respect to the vertical dipole array.

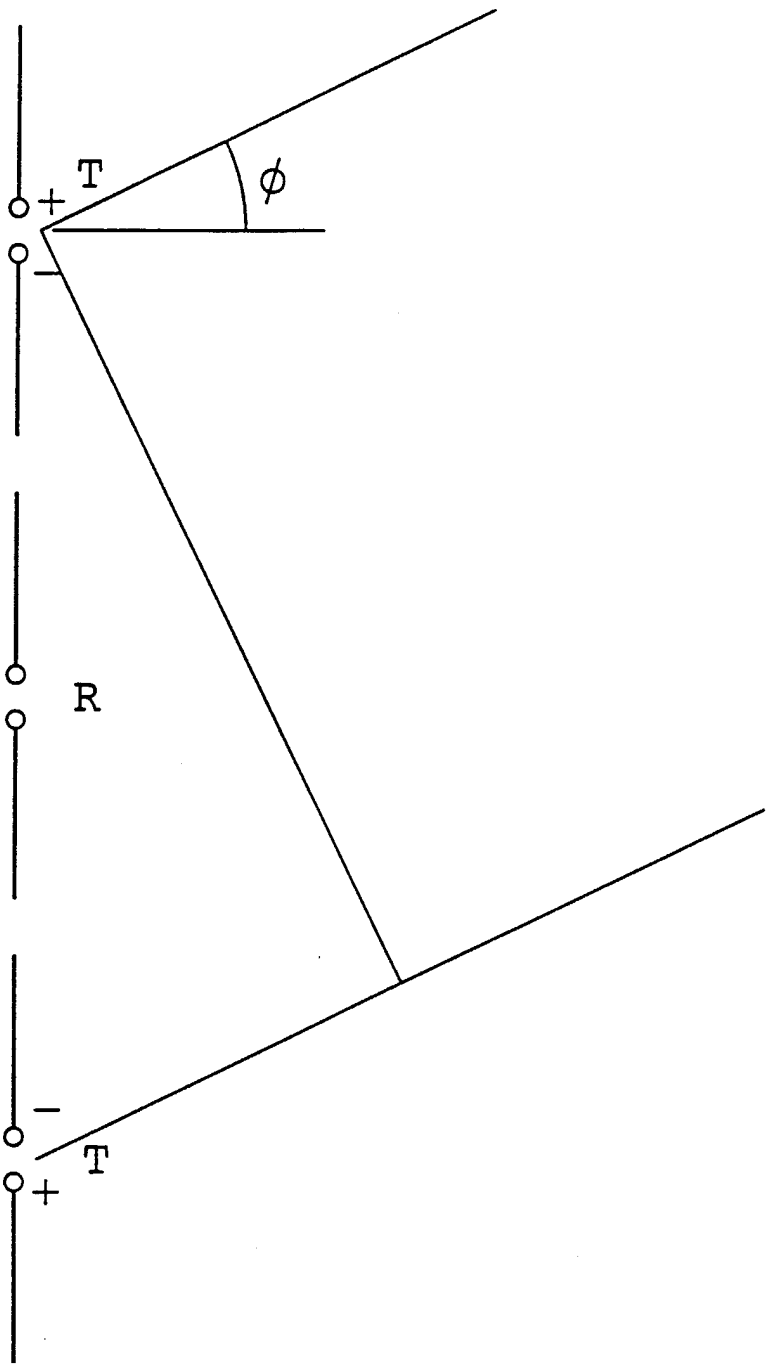

Figure 72. Vertical monopulse GPR antenna.

The vertical slot antenna where the dipoles are replaced by slots has been discarded because it would require too large a ground plane to support a broad-band slot mode.

The TEM horn would be too large a structure to cover the required frequency. The present TEM horn is an effective antenna for frequencies as low as 50 MHz.

At 10 MHz, this antenna would be simple a loaded transmission line.

4.2 Antenna Resonances and Their Influence on GPR

A major problem using broad band GPR systems with antennas that are electrically small in order to detect the strongest CNR is that of antenna ringing. This ringing and means to reduce its influence are discussed in the following paragraphs. Antennas resonances are echoed in any reflection so that if a strong reflection occurs, the resonance produces a strong signal that can mask a weaker desired signal from a deeper target. These reflections could be caused by the ground interface or inhomogeneities in the ground. Experimental surface GPR results are used below to demonstrate the significance of this antenna resonance.

This antenna ringing, as caused by their resonances, can be reduced significantly by the proper antenna impedance matching. If the antenna is matched by its complex conjugate impedance, the ringing will be eliminated. If it is matched in its characteristic impedance, it can be greatly reduced.

Means of reducing the effects of ringing are available via signal processing techniques as discussed in Section 6.

Figure 73 shows a gray scale plot obtained with a GPR unit over a 3 foot cylinder buried one foot deep in a clay medium ($\epsilon_r = 13$, $\sigma = 0.021$). The antenna geometry was

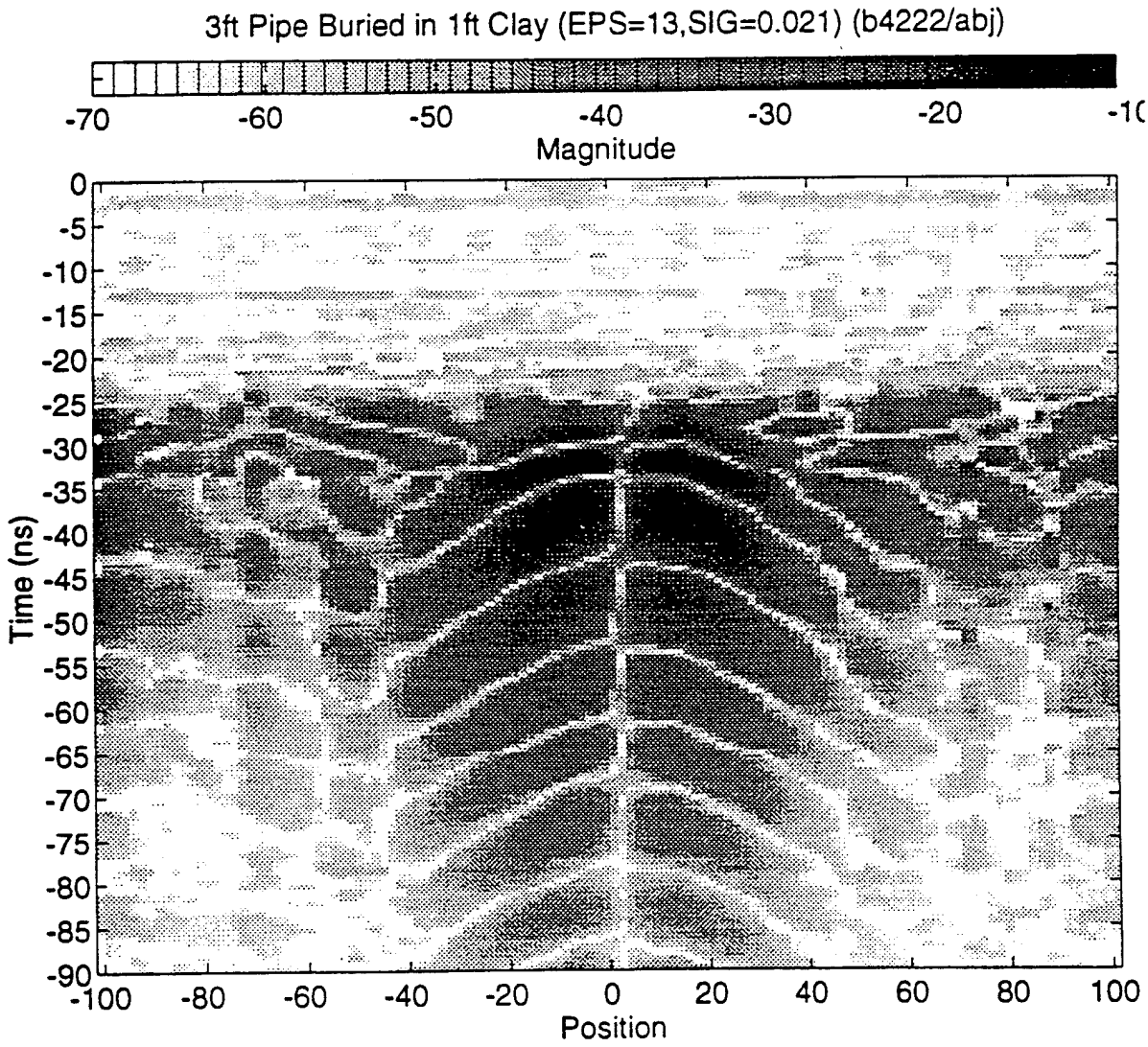

Figure 73. Gray scale map for 3 foot pipe in trench in 1 foot of clay.

generated using the dipole monopulse array [3]. This plot was generated by moving the antenna across the cylinder at the air-ground interface and plotting the absolute value of the received signal as a function of antenna position and time (distance to cylinder). The null at the 0 position is a consequence of the monopulse antenna geometry.

These data sets were used to generate the Complex Natural Resonances shown in Figure 74 via a Prony procedure discussed in Section 6. The resonance at 50 MHz was removed and a new gray scale map is shown in Figure 75. The resonance at 100 MHz was removed to obtain the gray scale map of Figure 76. The data of Figure 76 were processed to obtain the SAR image of Figure 77. The two resonances that were removed were antenna resonances as was confirmed by computing the CNR's at a distance removed from the cylinder. Note that the data maximum of Figure 73 is order of 20 dB higher than the data maximum of Figure 76. Clearly it would have been difficult to detect the cylinder in the gray scale plot of Figure 73.

Some form of additional resistive antenna loading or impedance matching is required to keep the small linear antenna elements from ringing so as to reduce the burden on the signal processing.

The use of resistive antenna loading should be minimized since it leads to lower efficiency.

Reduction of Antenna Resonance Phenomena

There are several methods by which the problems caused by these troublesome antenna resonances can be reduced. They can be represented schematically as shown in Figure 78. A pulse is launched on the antenna. It propagates to the end of the antenna where it is reflected back where it is again reflected. This process continues and at each reflection radiation occurs.

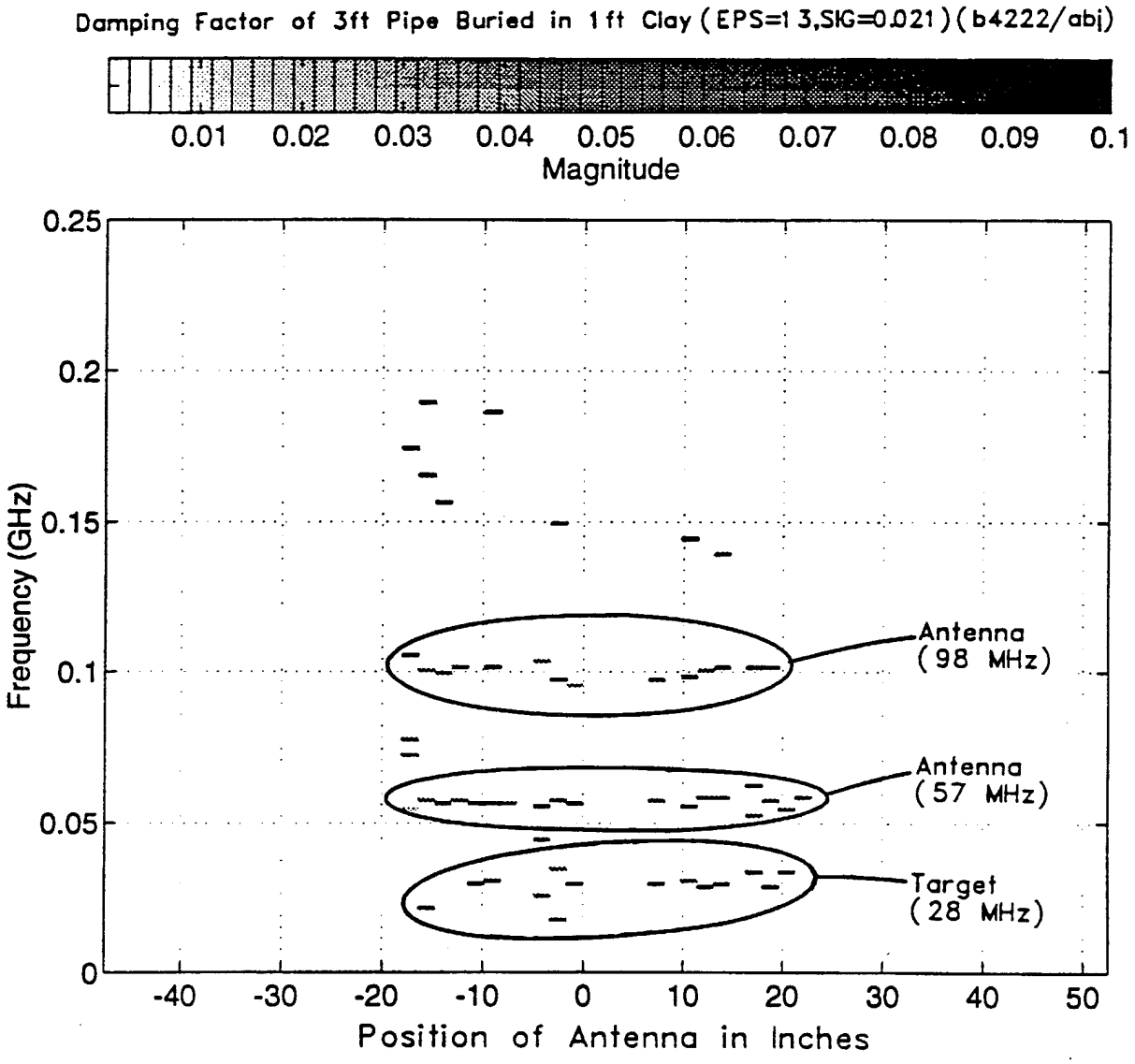

Figure 74. Natural resonances as a function of antenna position.

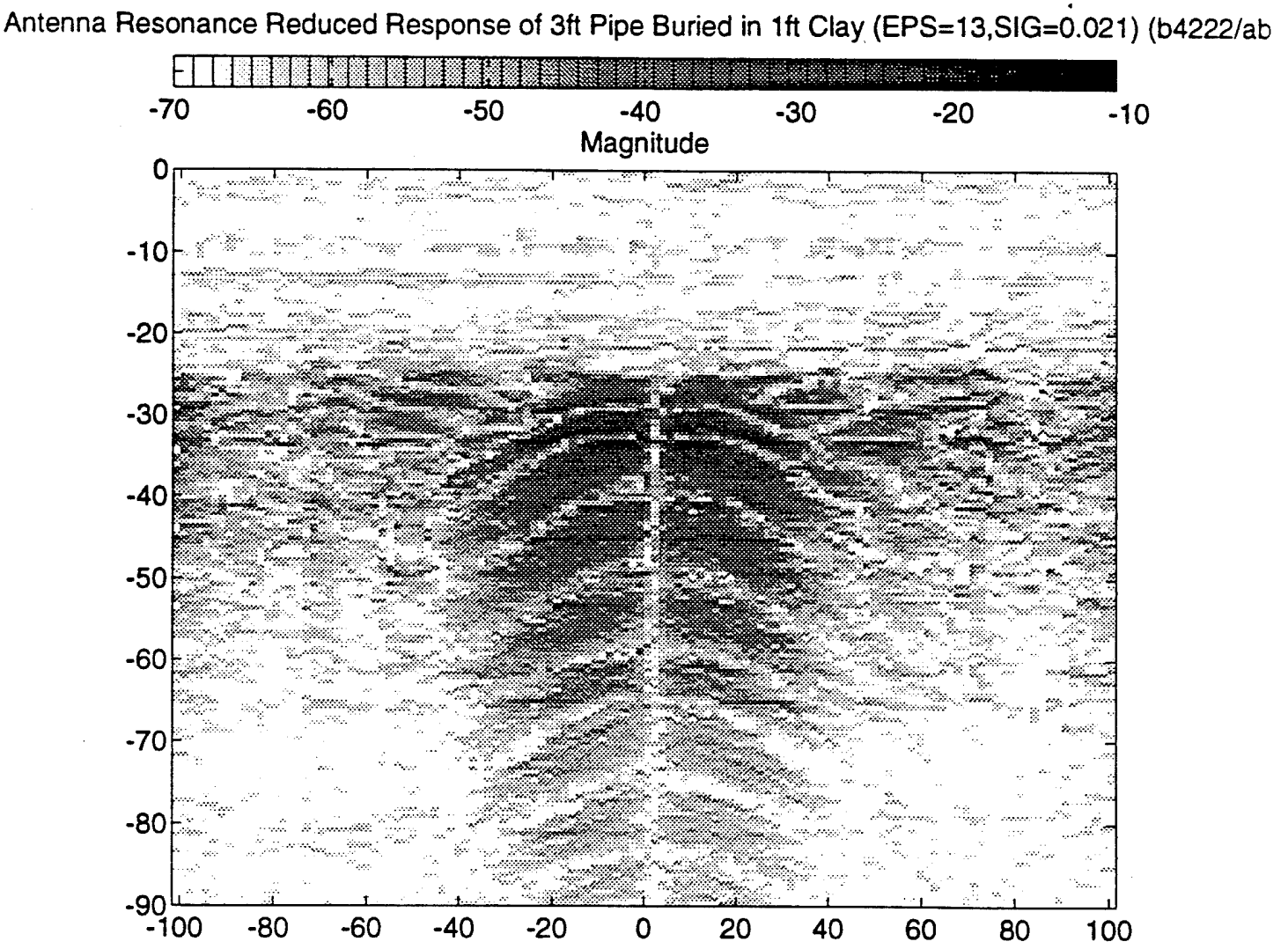

Figure 75. Gray scale map of Figure 74 after first resonance is removed.

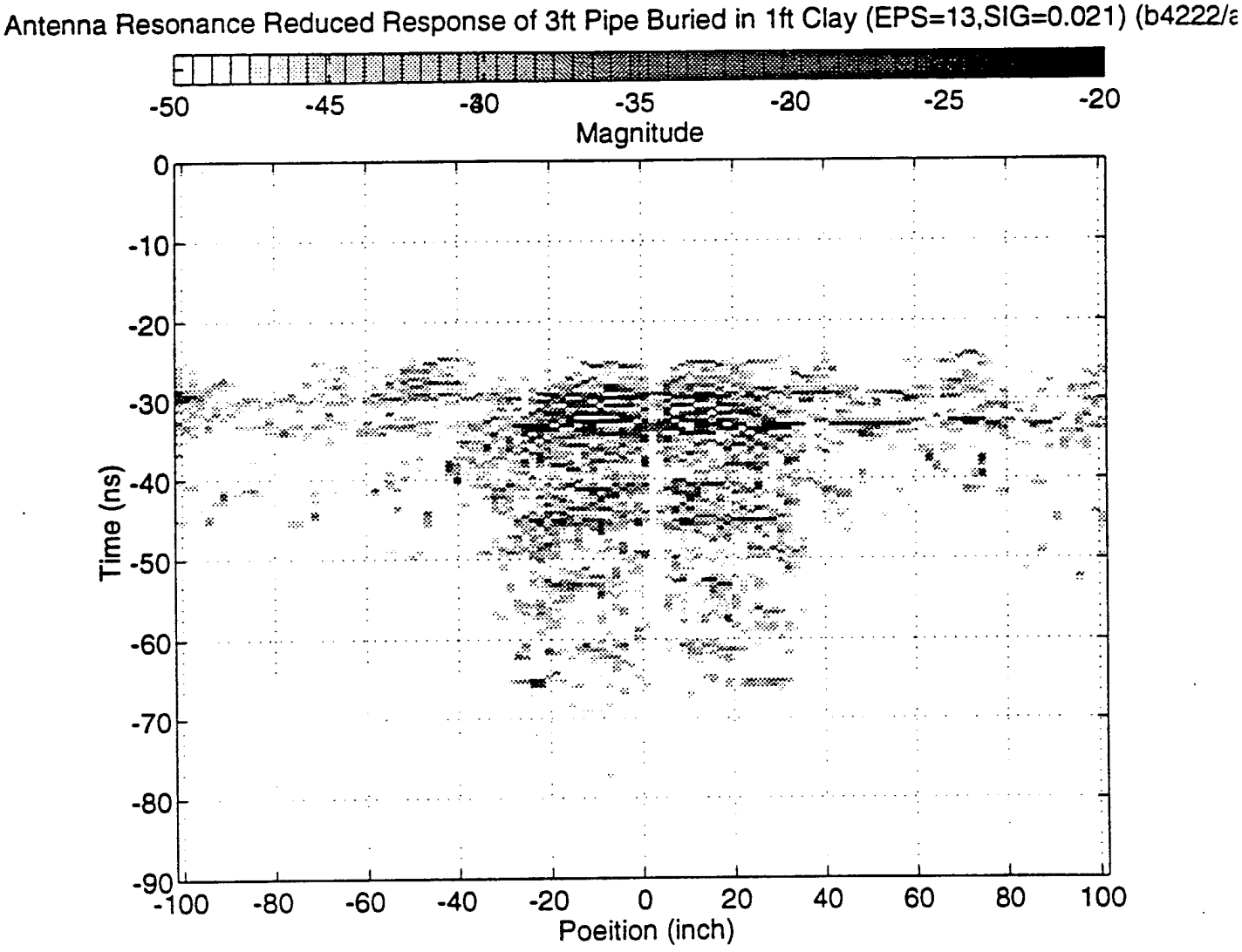

Figure 76. Gray scale map of Figure 74 after two resonances are moved, revealing 3 foot pipe at proper depth and resonant frequency.

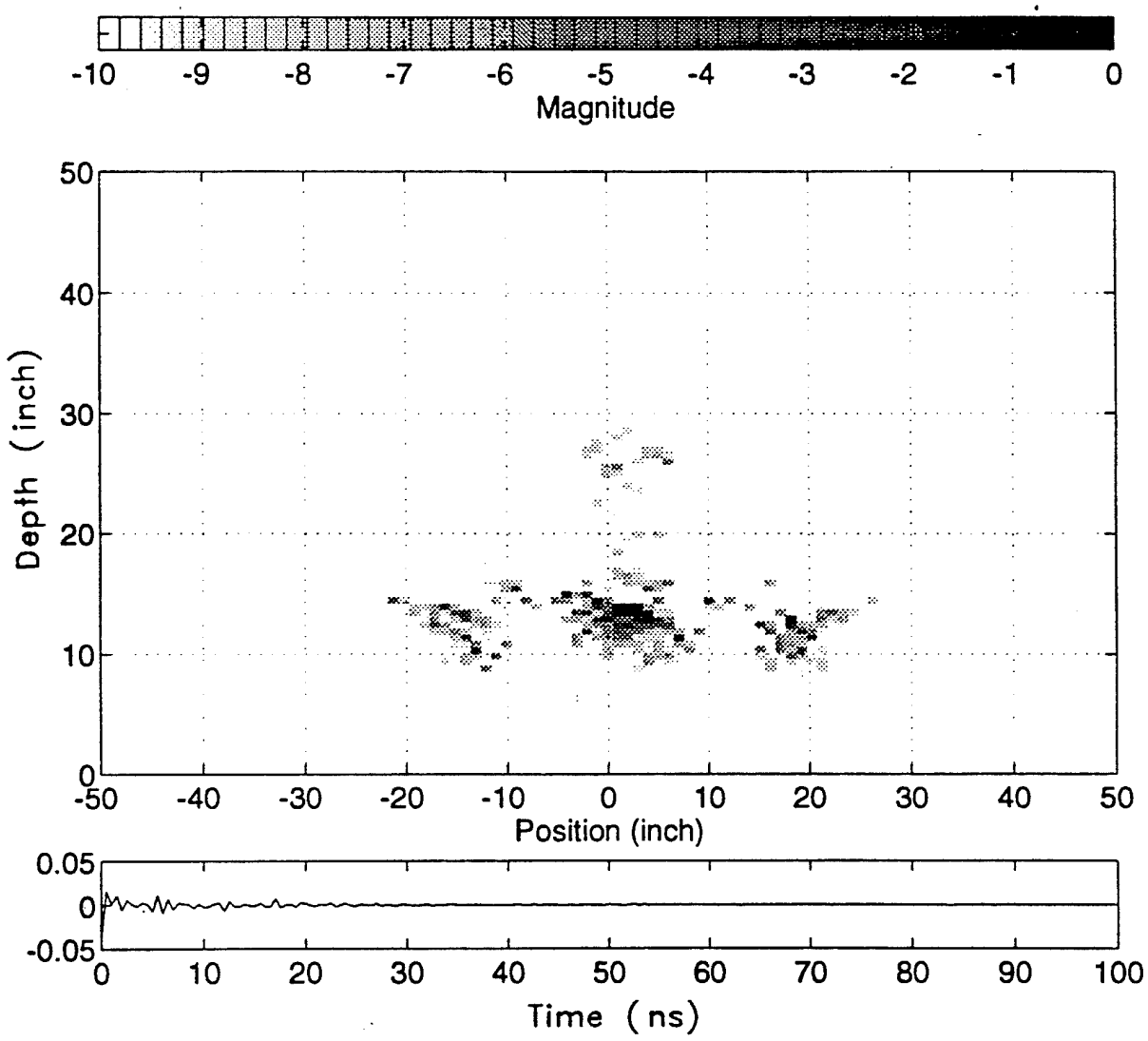

Figure 77. SAR image of Figure 76.

There are several ways these resonances can be treated. The simplest conceptually is to make the generator impedance Z_g equal to the complex conjugate of the antenna impedance. The result is shown in Figure 79 for a 3 m long biconical antenna. There is no evidence of antenna resonance. The pulse that is radiated is a duplicate of the pulse being launched on the antenna.

In this case, the antenna is completely matched at the antenna terminals at every frequency. It is noted that a perfect match cannot be achieved over the wide bandwidth necessary for this GPR application. There are several alternative matching techniques. One is to adjust the terminating impedance Z_L such that there is no reflection from the end of the antenna. Smith [4] and others have used tapered resistive loading to achieve this goal usually using a Wu-King distribution [5]. This technique is highly successful but the antenna efficiency is very low when the antenna is less than a wavelength long. Another approach is to simply match the antenna in its characteristic impedance.

Characteristic Impedance Matching

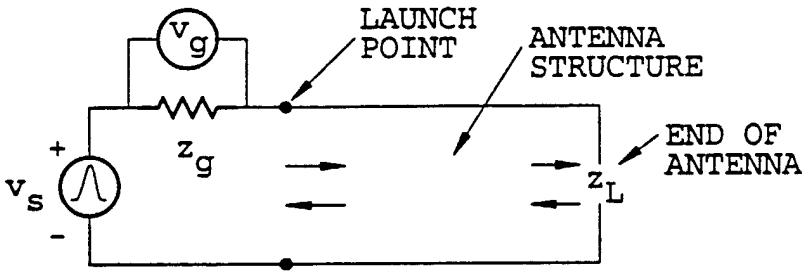

Figure 78. Antenna resonance illustration.

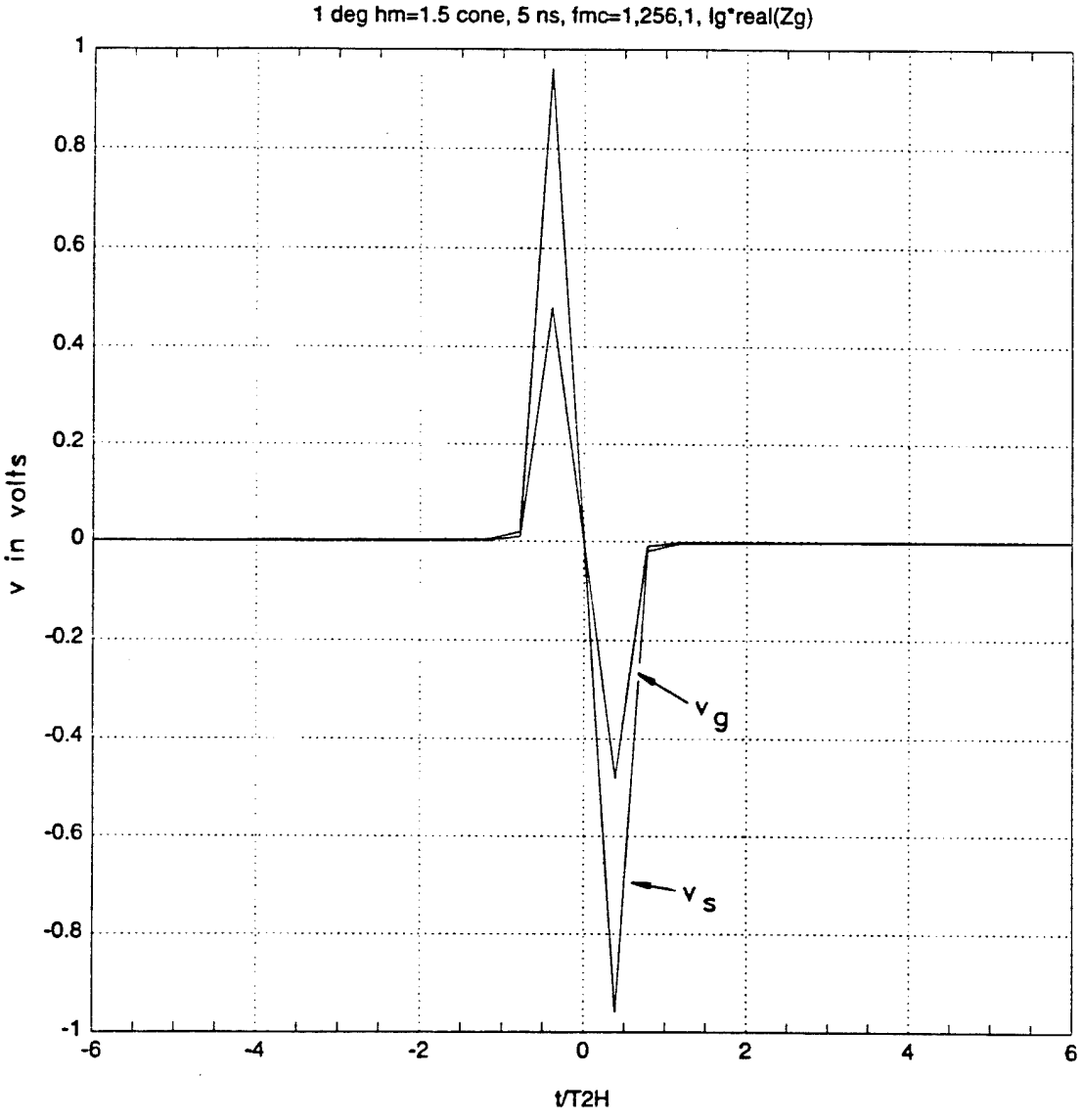

Figure 79. Elimination of resonances via complex conjugate matching.

To demonstrate that setting the source impedance equal to the characteristic impedance will reduce the antenna ringing, a biconical antenna was selected as a model. The main reason for this choice is that a boundary value solution exists for the finite length biconical antenna [6]. The geometry is shown in Figure 80.

To clearly demonstrate the need for improvement a long antenna (L = 10 m) was used. Then the pulses generated by the various mechanisms were separated in time so that they are clearly observable. The biconical half-angle, ϕ, is 1°. A generator impedance Z_g = 1 Ω was used. Figure 81 shows the voltage across the generator impedance. The waveform in this figure is a measure of the current flowing in the antenna at that time. The current waveform being launched on the biconical antenna would have a magnitude V_g/Z_g.

The current waveform being launched on the antenna structure is

$$\frac{V_g}{Z_g(=1\ \Omega)} f(t) \tag{60}$$

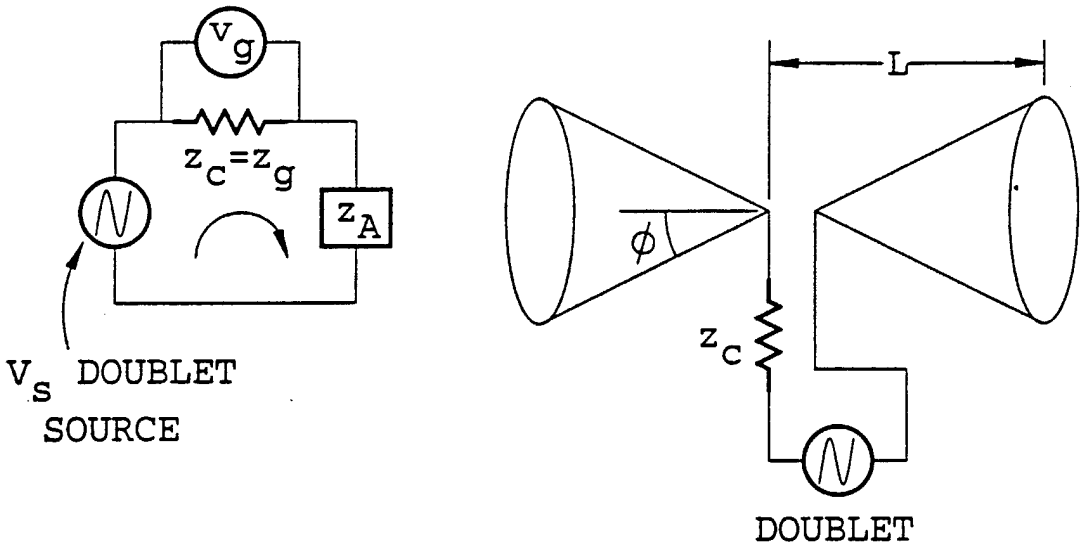

Figure 80. Biconical antenna geometry.

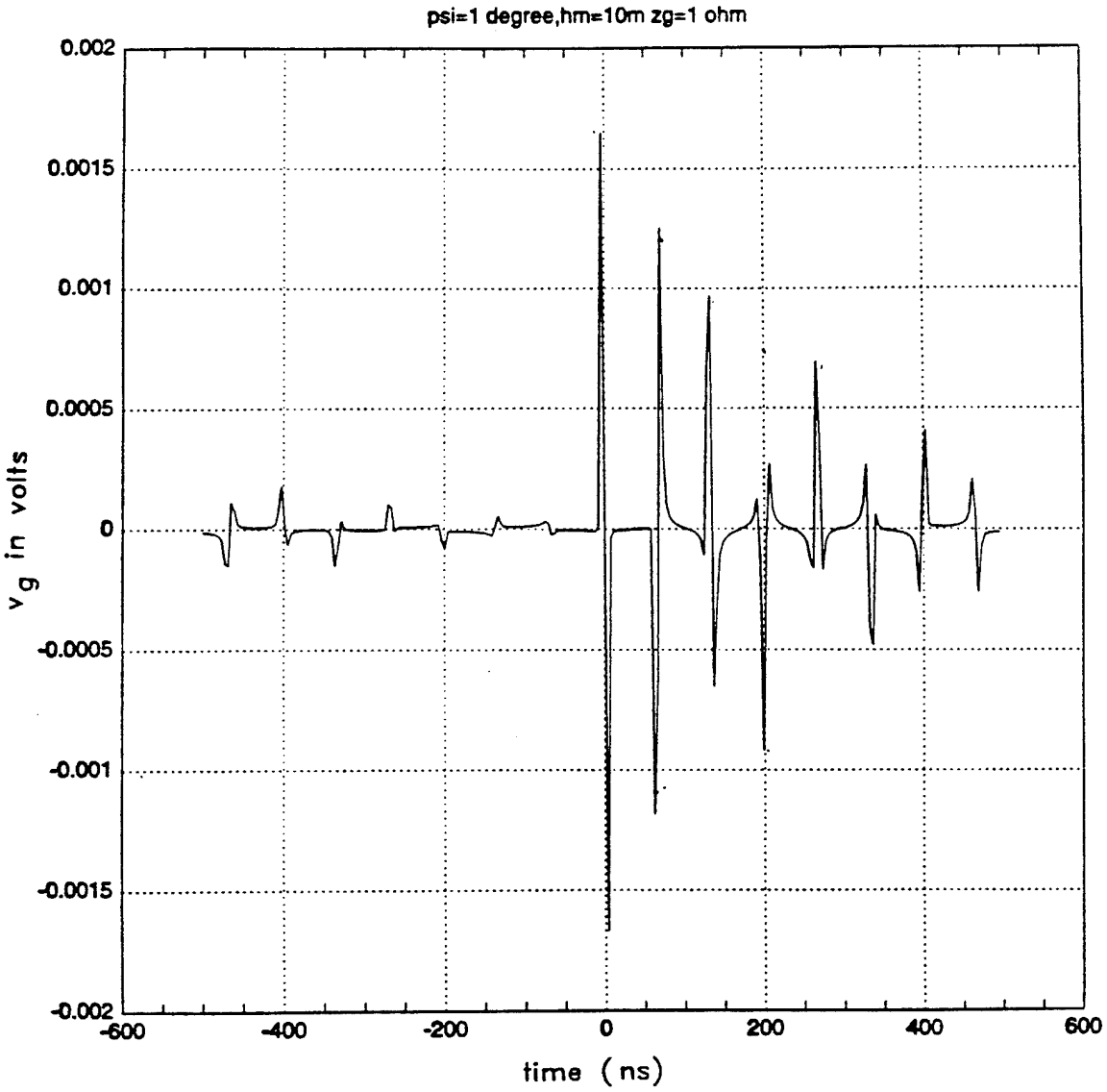

Figure 81. Antenna ringing when $Z_g = 1\Omega$, $\phi = 1°$, L = 10 m, v_s = 5 ns doublet.

where *f(t)* is the waveform of Figure 81. The biconical antenna is considered to be a transmission line with a characteristic impedance [6]

$$Z_c = \frac{Z_0}{\pi} \ln \cot \frac{\phi}{2} \tag{61}$$

where Z_0 is the characteristic impedance of the medium. The current waveform is subsequently reflected at the end of the antenna. The current reflection coefficient is negative because the antenna is approximately an open circuit and consequently produces a reflected pulse of opposite polarity. This reflected pulse is subsequently reflected at the antenna terminals. In this case, the reflection coefficient is positive because $Z_c >> Z_g$. The second measured voltage "doublet" across Z_g is subsequently of opposite polarity from the first doublet. The process is repeated for a large number of reflections as seen in Figure 81.

Next, Z_g is set equal to Z_c and the process is repeated. The resulting waveform is shown in Figure 82. The magnitude of the first "doublet" in Figure 82 is now given by $V_g=0.5$ because $Z_g=Z_c$. Assuming no radiation, the second doublet would be reduced by 6 dB. It is again reversed in polarity as expected. The third doublet is reduced by about 17 dB from the first doublet. It would not exist if the transmission line was a complete model of the antenna. It is not complete because a radiated pulse would result from the antenna-generator discontinuity.

Figure 83 shows the voltage waveform generated across $Z_g = Z_c$ when the biconical half-angle, ϕ, is increased to 39°. In this case, the reflection occurring from Z_L has been reduced because of the larger diameter at the end of the antenna.

In the next sequence of figures, the length of the antenna is reduced to a more practical 3 m and the results are now plotted in dB to include a broader dynamic range.

The abscissa is also normalized by the time it takes the pulse to propagate to the end of the antenna and back to the source region. The units are now the number of bounces. This

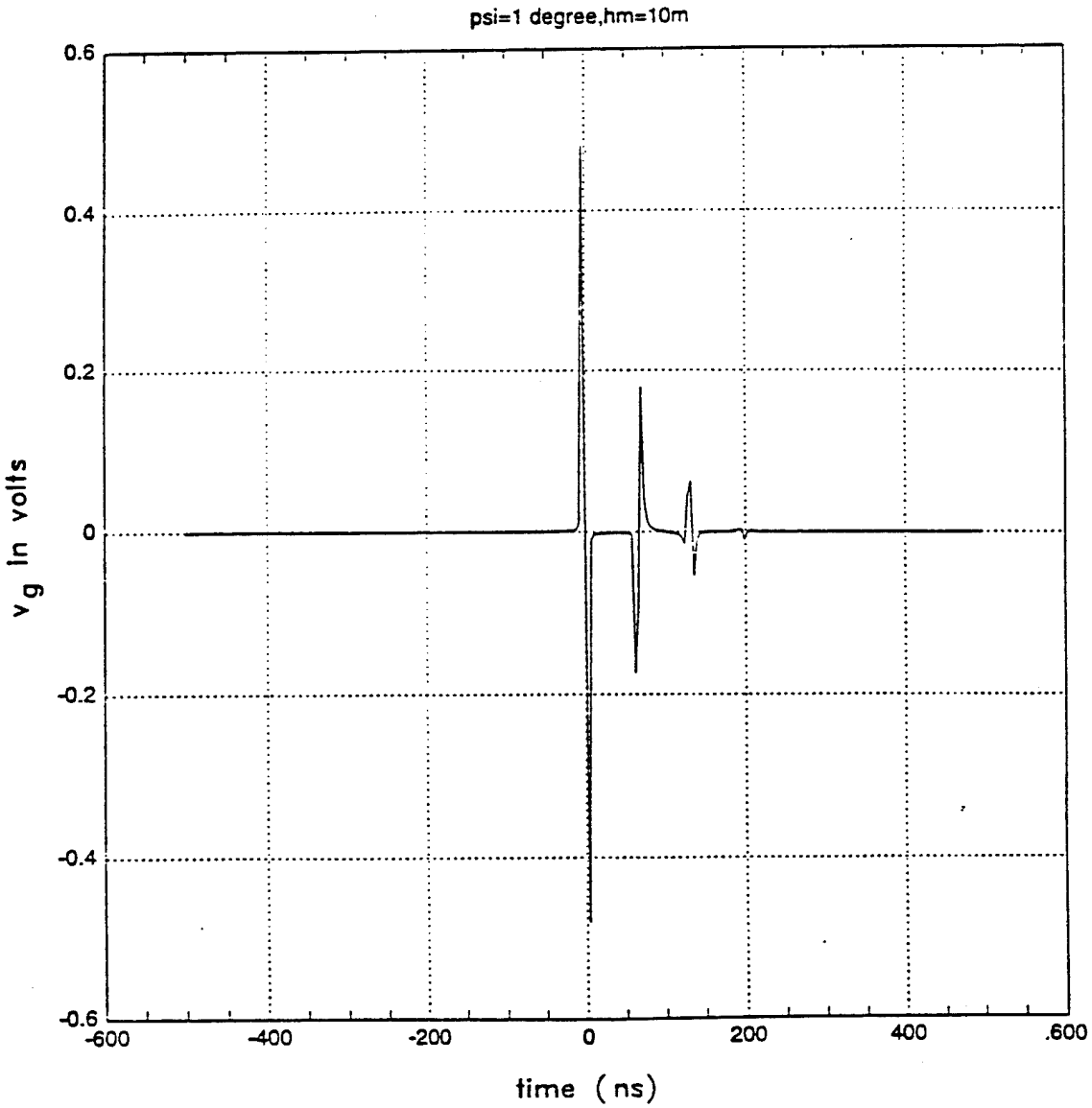

Figure 82. Antenna ringing when $Z_g = Z_c$, $\phi = 1°$, L = 10 m, v_s = 5 ns doublet.

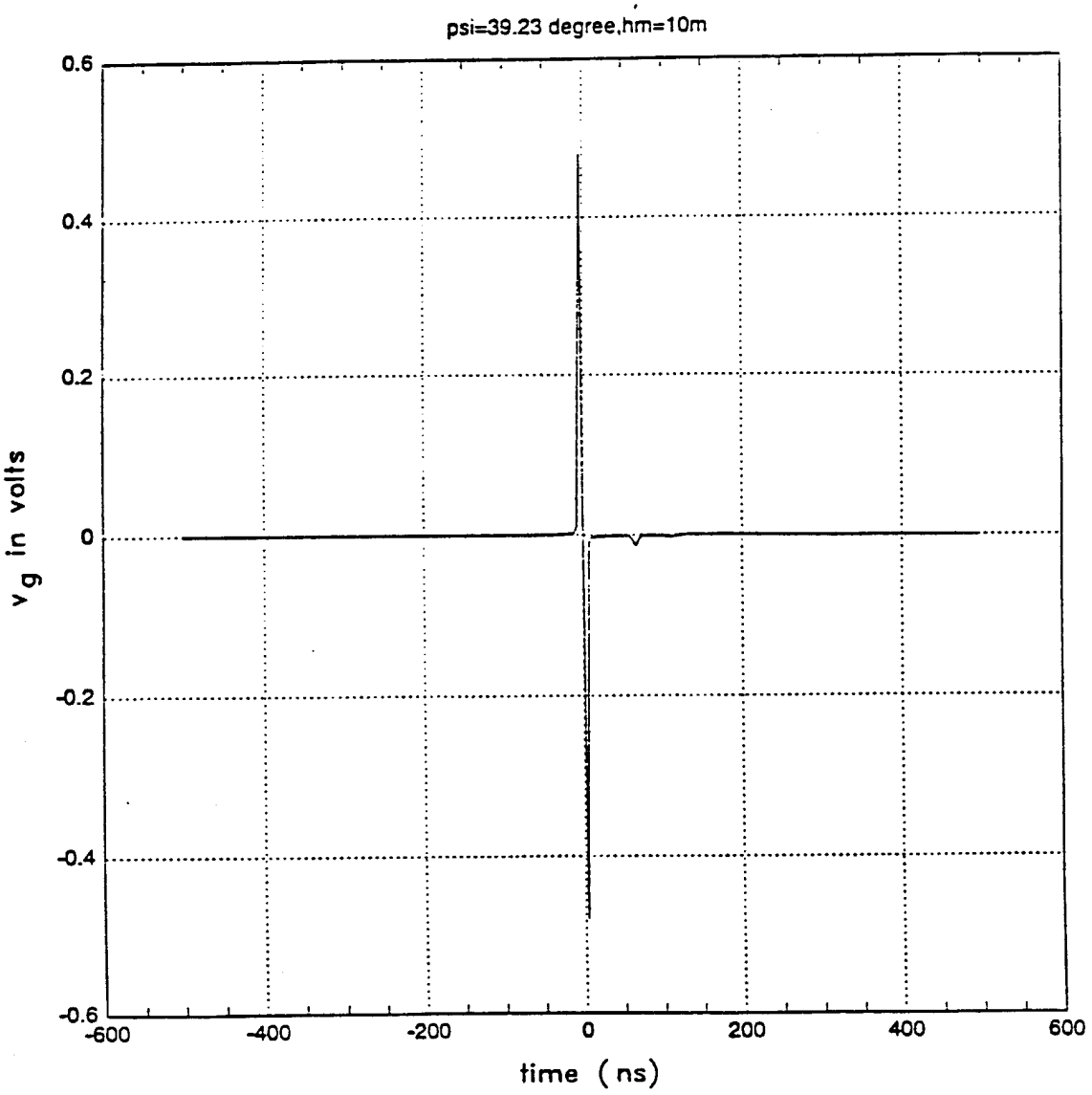

Figure 83. Antenna ringing when $Z_g = Z_c$, $\phi = 39.23°$, L = 10 m, v_s = 5 ns doublet.

normalization is done because the pulse width is now so big that various reflections merge together. Each such unit now corresponds to 9.84 ns.

Figure 84 shows V_g when $\phi = 0.1°$, $Z_g = Z_c = 845\ \Omega$, the antenna length is 3 m and a 5 ns doublet issued. The spectrum included was 265 MHz in 1 MHz steps. The bandwidth can be used to reduce the ringing even further as is shown in Figure 85 where the upper frequency was increased to 512 MHz. Figure 86 gives V_g when $Z_g=500\ \Omega$. The ringing is increased but not by an unreasonable amount. The same result is observed when Z_g is increased to as much as $Z_g=4Z_c$.

Characteristic impedance matching has been incorporated in our ground based radar and much improved measurements have been obtained in the ESL test bed and have been included in the antenna that has been delivered for the SOCS platform.

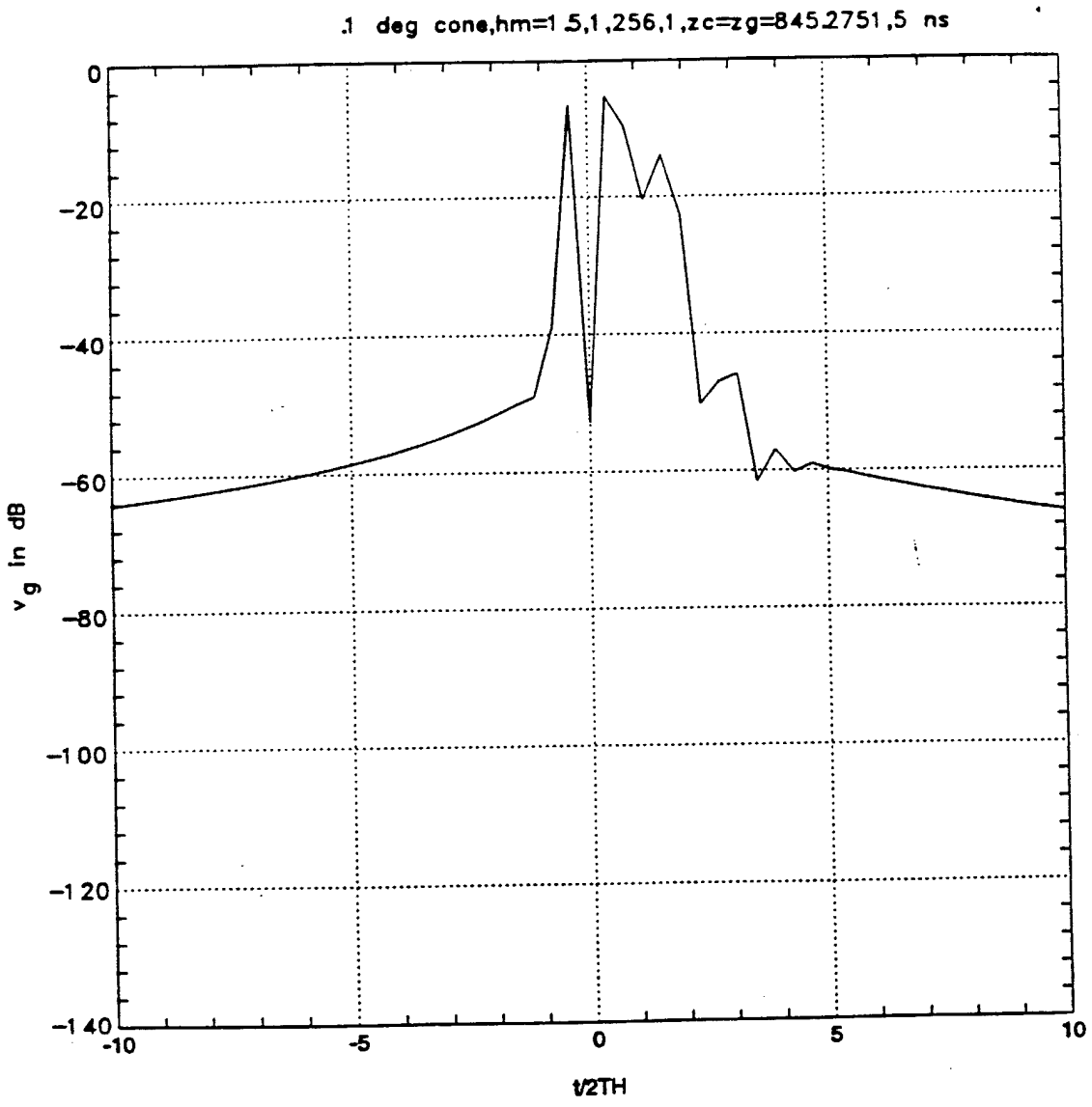

Figure 84. Voltage across Z_g for $\phi = 0.1°$, L = 1.5 m, excited by a 5 ns doublet (1 MHz $\leq$ f $\leq$ 256 MHz spectrum).

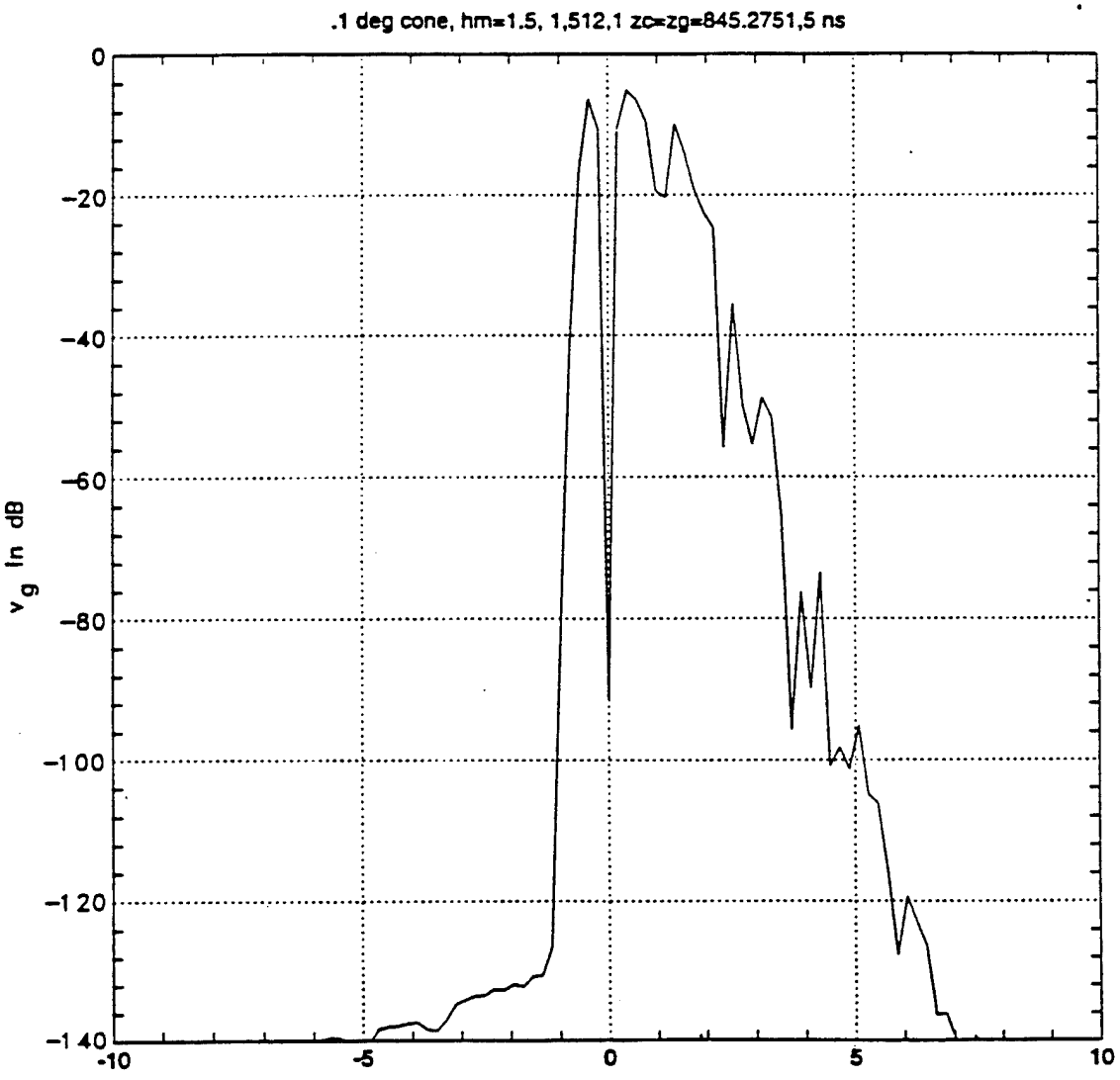

Figure 85. Voltage across Z_g for $\phi = 0.1°$, L = 1.5 m, excited by a 5 ns doublet (1 MHz $\leq$ f $\leq$ 512 MHz spectrum).

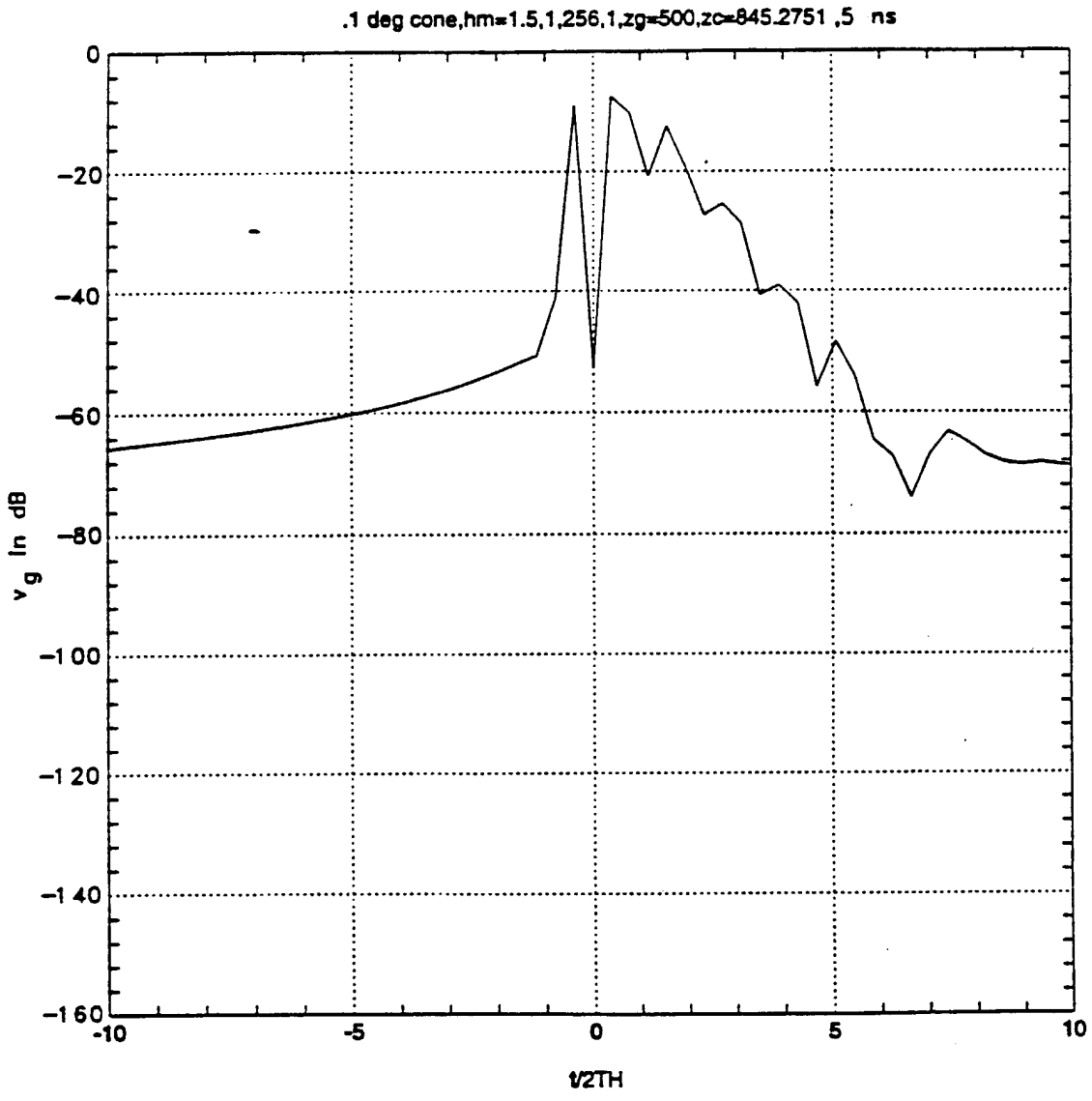

Figure 86. Voltage across Z_g for $\phi = 0.1°$, L = 1.5 m, excited by a 5 ns doublet (1 MHz $\leq$ f $\leq$ 256 MHz spectrum). $Z_g = 500\ \Omega$.

4.3 References for Antennas Section

[1] Peter K. Hayes, "A Single-Probe On-Site Method of Measuring the Dielectric Constant and Conductivity of Soft Earth Media Over a l-GHz Bandwidth," *IEEE Trans. on Geoscience and Remote Sensing,* Vol. GE-20, No. 4, pp. 504-510, October 1982.

[2] E.W. Braeden, F.T. Klevenow, E.H. Newman, R.G. Rojas, K.S. Sampath, J.T. Schiek, and H.T. Shamansky, "Operation of the Helicopter Antenna Radiation Prediction Code," The Ohio State University ElectroScience Laboratory Technical Report 722792-4, June 1993.

[3] Mark Barnes, "Experimental Investigation of Ground Penetrating Radar Antennas," M.Sc. Thesis, The Ohio State University, Dept. of Electrical Engineering, 1991.

[4] J.G. Maloney and G. Smith, "A Study of Transient Radiation from the Wu-King Resistive Monopole-FDTD Analysis and Experimental Measurements," *IEEE Irans. on Antennas and Propagation,* Vol. 41, No. 5, May 1993.

[5] T.T. Wu and R.W.P. King, "The Cylindrical Antenna with Non-Reflective Resistive Loading," *IEEE Irans. on Antennas and Propagation,* Vol. 13, No. 5, May 1965.

[6] James R. Wait, "Electromagnetic Radiation from Conical Structures," Chapter 12, pp. 483-522, in Antenna Theory, Part I, Inter-University Electronics Series, McGraw-Hill 1969.

[7] C. E. Baum, "The SEM representation of scattering from perfectly conducting targets in simple lossy media," Tech. Rep. Note 492, Phillips Laboratory,Interaction, Apr. 1993.

[8] J. D. Young, L. Peters, C. Chen, and F. Paynter, "Radar Signature Measurements of Buried, Unexploded Ordnance Targets," technical report 727388-2, ElectroScience Lab., The Ohio State University, Columbus, Feb. 1994.

5.0 Propagation

Ground parameters will have a major influence on the performance of any GPR system. These parameters include attenuation in the soil due to dielectric loss, an interface loss on transitioning from air to soil, and more subtle effects such as limiting the useful SAR aperture size due to refraction effects at the soil/air boundary and within the soil.

5.1 Soil Attenuation

Soil attenuation can be very severe for media such as clay with a high moisture content. This is very clear when the electric properties of clay are examined more closely. Figure 12 shows *in situ* measurement of these electrical properties of several media as a function of frequency [1]. For clay, these numbers translate to a loss in the media at 400 MHz of approximately 60 dB/m. This loss is in addition to the free space losses as the wave propagates from the airborne platform to the ground.

Assuming that the antenna is 30 m above the ground, the radar range equation gives

$$\frac{P_r}{P_t} = \frac{G^2}{(4\pi)^3}\frac{A_e\lambda^2}{r^4} = G^2\,\sigma\,(3.5x10^{-10})\,|_{400\,\mathrm{MHz}} \qquad (62)$$

where P_r, P_t, are the received and transmitted power, respectively, G is the antenna gain, A_e is the radar cross section and λ is the wavelength. The losses exclusive of antenna gain and radar cross section are of the order of 95 dB at 400 MHz. Thus, the losses introduced when the radar is used to detect a target at 1 meter depth in clay at 400 MHz would be 215 dB.

At 10 MHz, the term in brackets of equation (62) reduces to about 60 dB and the ground losses reduce to 10 dB/m or a net loss of 80 dB.

Figure 87 gives the radar cross section of a linear target in a lossy media as a function of frequency for a fictitious medium where the electrical properties are not a function of frequency. For the longer wire corresponding to the larger UXO, this cross section is somewhat larger than one square meter. Consequently the radar must be able to detect a signal which is of the order of 80 to 100 dB below the transmitter signal and in the presence of clutter.

Given sufficient transmitter power and receiver sensitivity, the free space propagation problems can be overcome. However, the losses caused by ground attenuation represent a more serious problem because clutter reflections from the surface must be separable from the UXO scatter which has been attenuated by the ground loss. The sub-clutter visibility would be determined by the SAR processing gain.

5.2 Interface Loss

In the above discussion we did not include the transmission into and out of the ground. In general, for near normal irradiance, when the product is considered, this interface loss plays a minor role as is demonstrated by the following equation.

$$T_{12}T_{21} = \frac{2\sqrt{\epsilon_r}}{\sqrt{\epsilon_r}+1} \cdot \frac{2\frac{1}{\sqrt{\epsilon_r}}}{\frac{1}{\sqrt{\epsilon_r}}+1} = \left[\frac{4\sqrt{\epsilon_r}}{(\sqrt{\epsilon_r}+1)^2}\right]_{\epsilon_r=50} = 0.37 \qquad (65)$$

where T_{12}, T_{21} are transmission coefficients into and out of the ground respectively for normal incidence, and ϵ_r is the relative permittivity of the earth. As is illustrated for $\epsilon_r = 50$, this corresponds to 0.37 or -8.5 dB. It is also true that the top soil has a lower permittivity than the clay as shown in Figure 88. This top soil layer tends to match the incident wave into the soil, thus reducing the influence of the interface even further.

For angles other than normal incidence, the two-way interface transmission coefficient becomes a function of polarization. This case has been studied, and the results illustrated

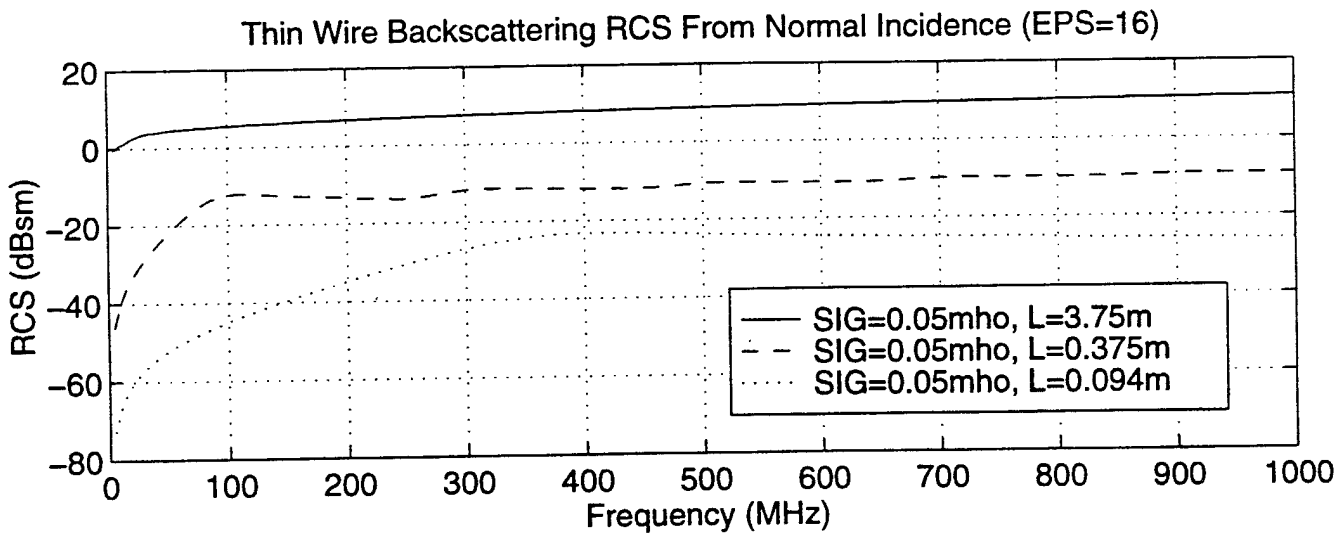

Figure 87. RCS of a wire in a lossy earth.

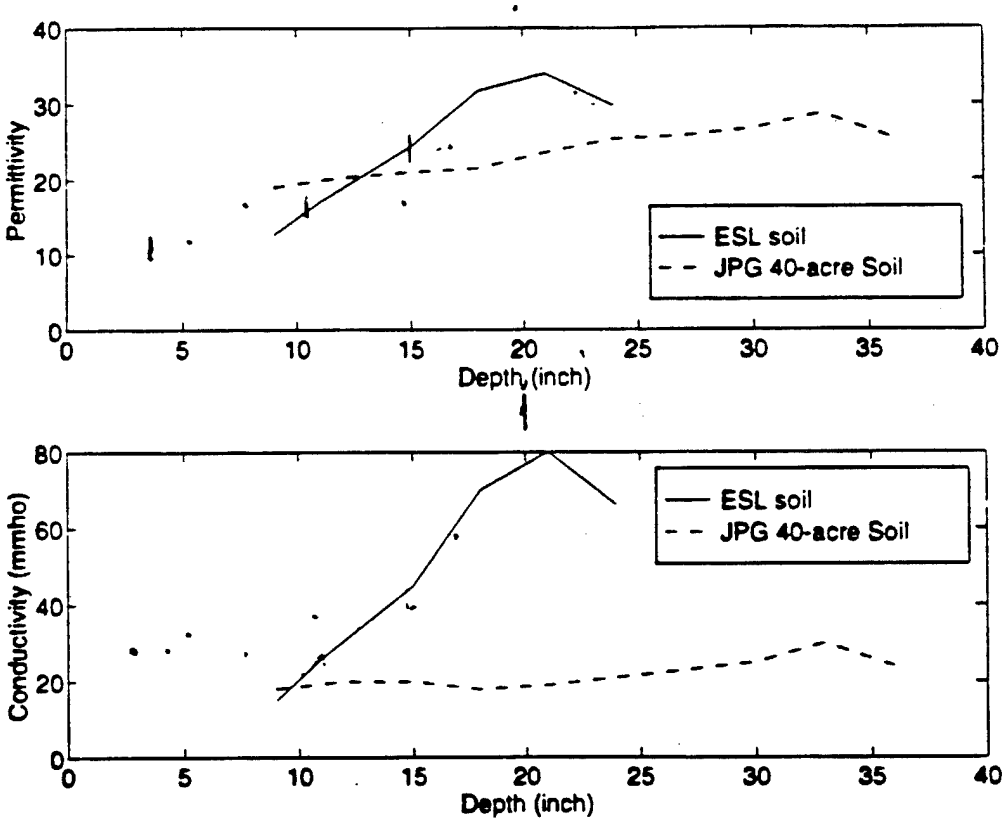

Figure 88. Electrical properties of soil at ESL and JPG.

below. Figure 89 shows the two-way transmission versus dielectric constant and incidence angle for vertical E-field polarization. In this surface, an incidence angle of 0 is normal incidence. The incidence angle/2 goes to 45°, representing an incidence angle of 90 degrees or grazing incidence. Values of relative dielectric constant from 1 to 50/2 are plotted. Note the coefficient is 1 when the dielectric constant is 1 for all incidence angles, and the coefficient is 0 when the incidence angle is 90° (grazing incidence) for all values of dielectric constant.

Figure 90 shows the same data for horizontal polarization. Along the front right edge of the curve where the incidence angle is 0, the horizontal polarization curve is exactly like the vertical polarized curve as we would expect. For other angles, the horizontal polarization in general has a lower two-way transmission coefficient than for vertical polarization, because of the combination of the Brewster and critical angle effects.

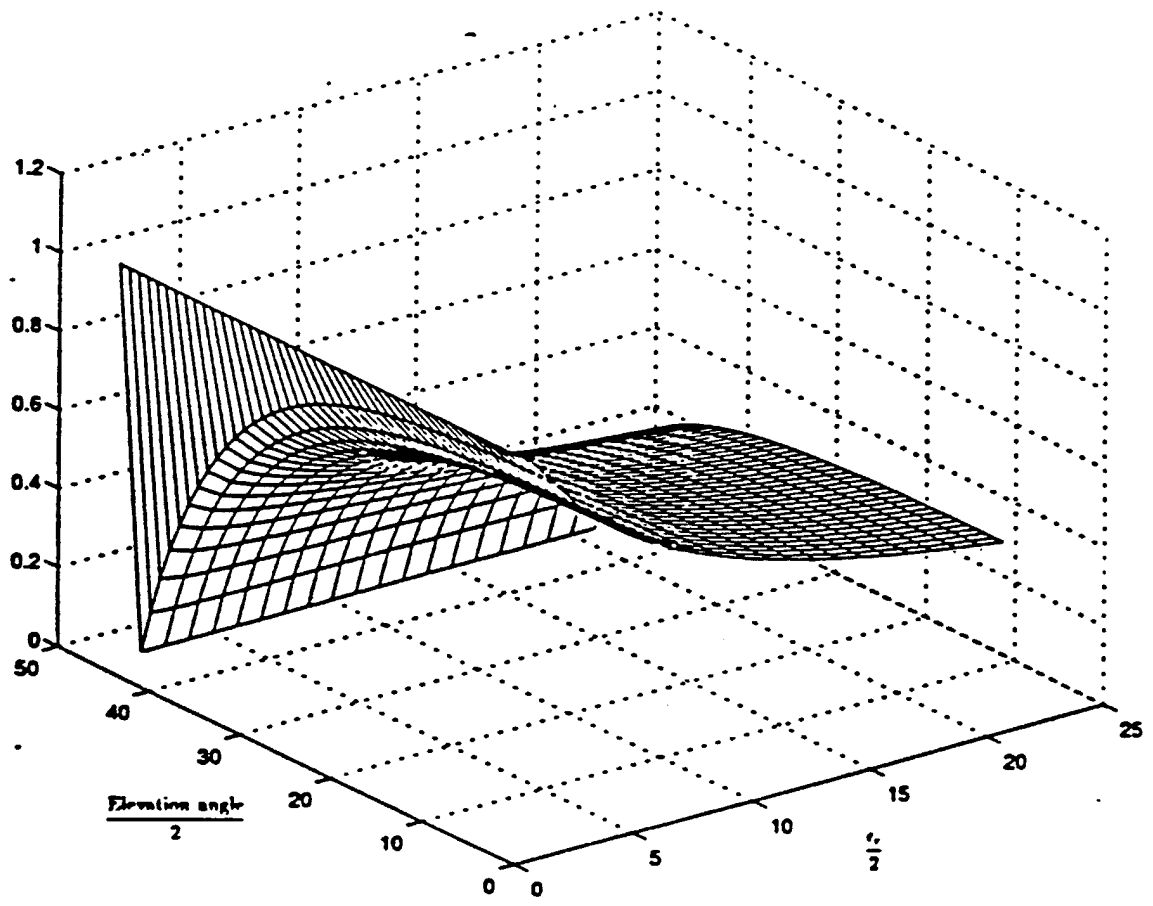

Figure 89. Vertical polarization. Two-way surface transmission coefficient.

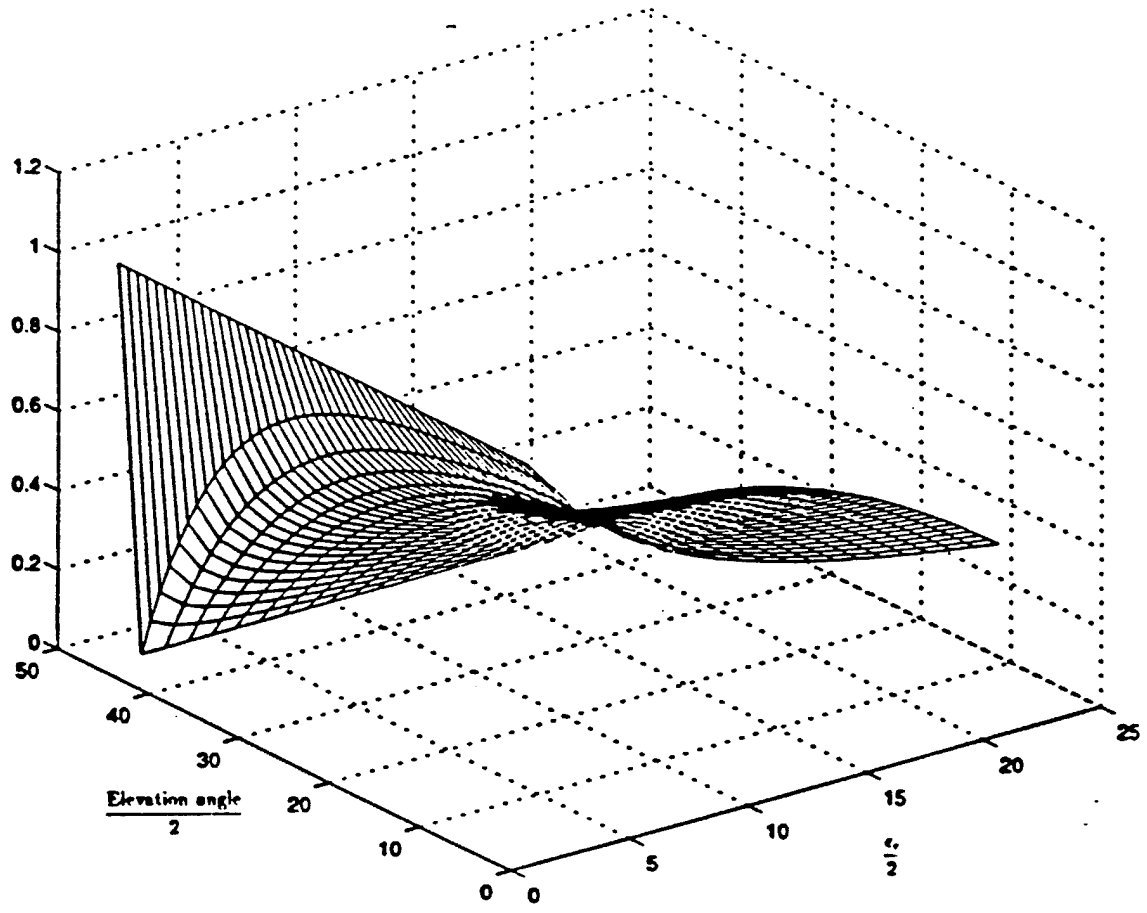

Figure 90. Horizontal polarization. Two-way surface transmission coefficient.

Figure 91 shows the ratio of vertical to horizontal two-way transmission coefficient in dB versus dielectric constant/2 and angle/2. Notice that for angles near normal (approximately 0 degrees) the ratio is near 0 dB. However, as the incidence angle approaches grazing, the vertical polarization is as much as 235 dB stronger than the horizontal for large dielectric constants. For example, the case of 60° incidence angle and a dielectric constant of 40 yields an 11 dB difference. For these angles, polarization is still not the dominant factor in the radar propagation calculation, but is may begin to be worth using vertical polarization provided the polarimetric response of the target is relatively uniform.

The presence of a λ^2 factor in the radar range equation, the ground losses (for clay) and the use of CNR's for target identification tend to emphasize the need for the lower operating frequencies. A fourth factor is the influence of surface clutter which will increase as the frequency is increased because the surface roughness dimensions in wavelengths become larger as the frequency is increased. As an example, a six-inch high hill is 1/20 λ high at 100 MHz and 1/200 λ at 10 MHz. Obviously the lower frequency is preferable.

Because the electrical properties of the earth can vary over very large ranges, it is not practical to give a single number for its attenuation factor. However, Figure 92 gives the attenuation factor in dB/m for range of materials. The attenuation factor

$$\alpha = \frac{1}{2}\sigma\sqrt{\frac{\mu}{\epsilon}} \tag{64}$$

where σ is the conductivity, and μ, ϵ are the permeability and permittivity of the earth, respectively, for the high frequency regime where the material is a loss dielectric

$$\alpha = \sqrt{\frac{\omega\mu\sigma}{2}} \tag{65}$$

for the low frequency regime where the ground is a conductor. For the intermediate region where the ground is neither.

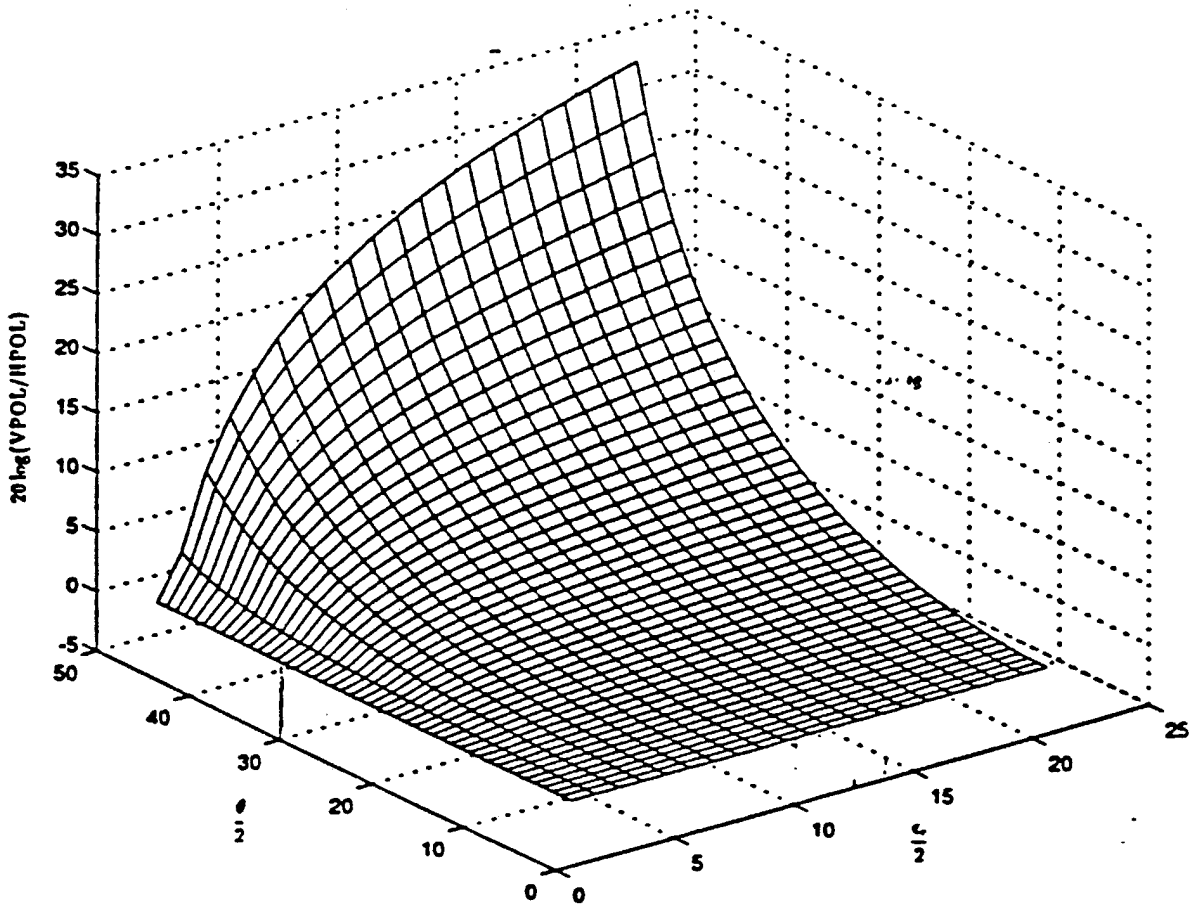

Figure 91. Ratio in dB of vertical to horizontal two-way transmission.

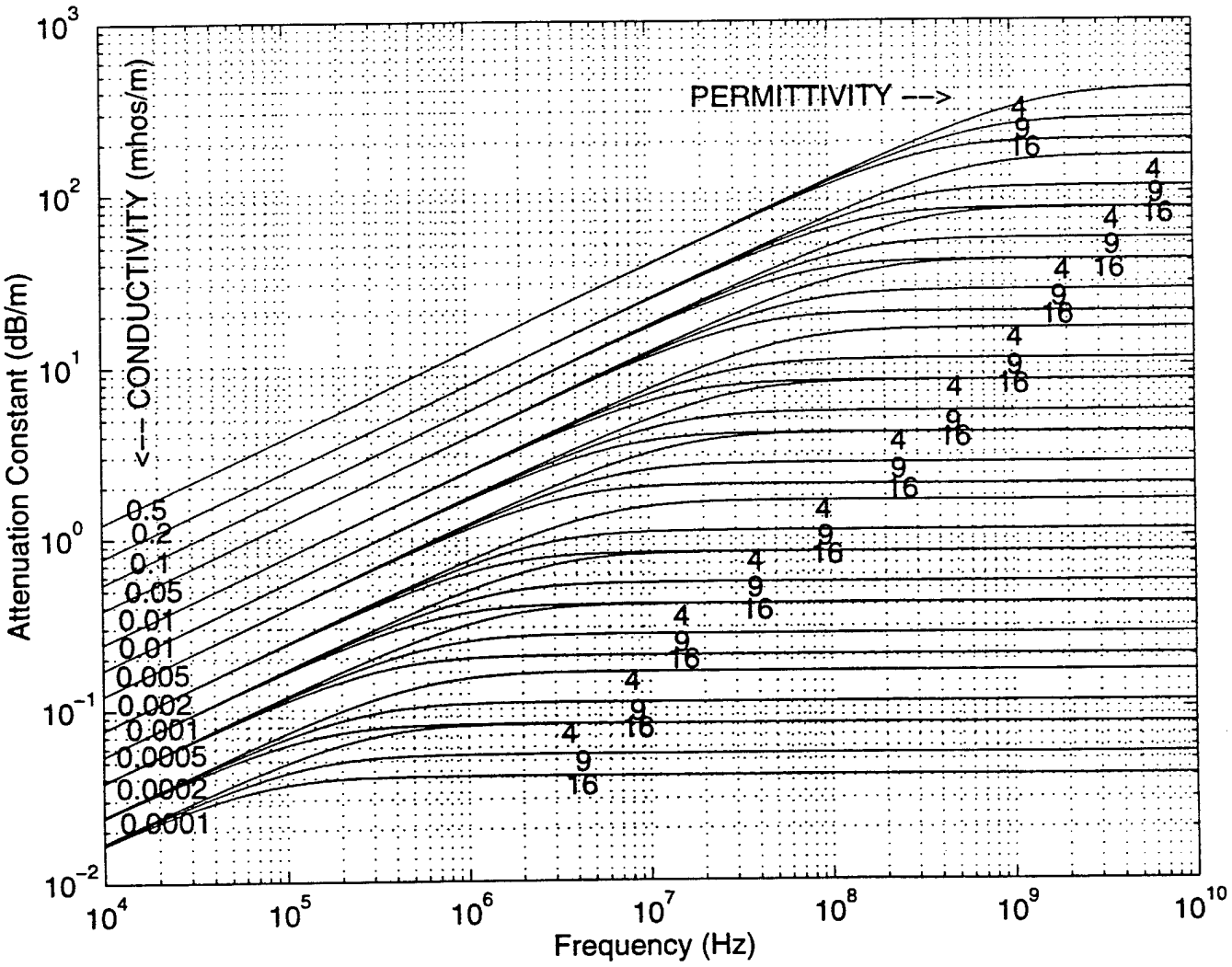

Figure 92. Attenuation constant of lossy soils.

$$\alpha = Re\sqrt{-\omega^2\mu\epsilon + j\omega\mu\sigma} \tag{68}$$

Recall from Figure 88, that the electrical properties of the earth are depth dependent. One can generate an effective attenuation factor α_{eff} as follows. From

$$e^{-\alpha_{eff}Nd} = e^{-\alpha_1 d} e^{-\alpha_2 d} \cdots e^{-\alpha_N d} \tag{69}$$

where the media has been divided into N uniform layers of depth d and α_i is the attenuation at the id depth. Then,

$$e^{-\alpha_{eff}Nd} = e^{\sum_{i=1}^{N} \alpha_i d} \tag{70}$$

or

$$\alpha_{eff} = \frac{1}{N} \sum_{i=1}^{N} \alpha_i \tag{71}$$

There is virtually no data available for clutter levels in the frequency band of interest. However, some clutter data has been extracted from measurements at Jefferson Proving Ground (JPG) in the autumn of 1994. These data included the frequency band from 50 to 750 MHz and was obtained for near grazing incidence. The clutter levels were approximately -25 dBsm/m^2. Assuming the SAR processing can focus to about a meter square surface area or less, then the clutter signal level would be of the order of -25 dBsm. At 10 MHz, the attenuation factor is of the order of 10 dB/m. Thus, a one meter deep one square meter target would produce a signal that would exceed this clutter level.

However, these numbers included frequencies up to 750 MHz and our frequency range is lower. Thus, the clutter level is further reduced. In future studies, the clutter obtained from the JPG data is to be evaluated as a function of frequency.

It will not be possible to generate completely realistic clutter data until additional measurements are made on sites of interest at the appropriate frequency band.

5.3 Refraction Effects

Due to the high dielectric constant of soil relative to air, a plane wave incident on the ground is transitioning from a low dielectric constant to a high dielectric constant and, in addition to the loss resulting from the surface reflection, the wave in the soil will be refracted toward the vertical.

Similarly, the wave scattered by the target is transitioning from a high dielectric constant media to a low dielectric constant medium and it will be refracted away from vertical. In particular, if the angle of incidence at the ground-air interface for the scattered wave exceeds the angle of total reflection, no energy will be transmitted through the interface, it will instead be reflected back into the ground.

Figure 93 gives the angle in the ground versus the free space irradiance angle for various ground dielectric constants. For an ϵ_r value of 9, which was typical of JPG soil at the surface, the angle ranges from 0° at vertical incidence to a maximum of 19.2° at grazing or 90°.

For a dielectric constant of 16 the maximum angle is 14.3°. These refraction effects have several consequences. Although ostensibly one could form a synthetic aperture as large as desired in free space, in reality the target resolution improvement is limited by the angular range over which an underground target is viewable. A point of diminishing returns is reached where additional samples over a longer flight path do not improve the effective SAR resolution on the target.

On the other hand, a longer synthetic aperture is useful in reducing the surface clutter cell size and improving the signal-to-clutter ratio.

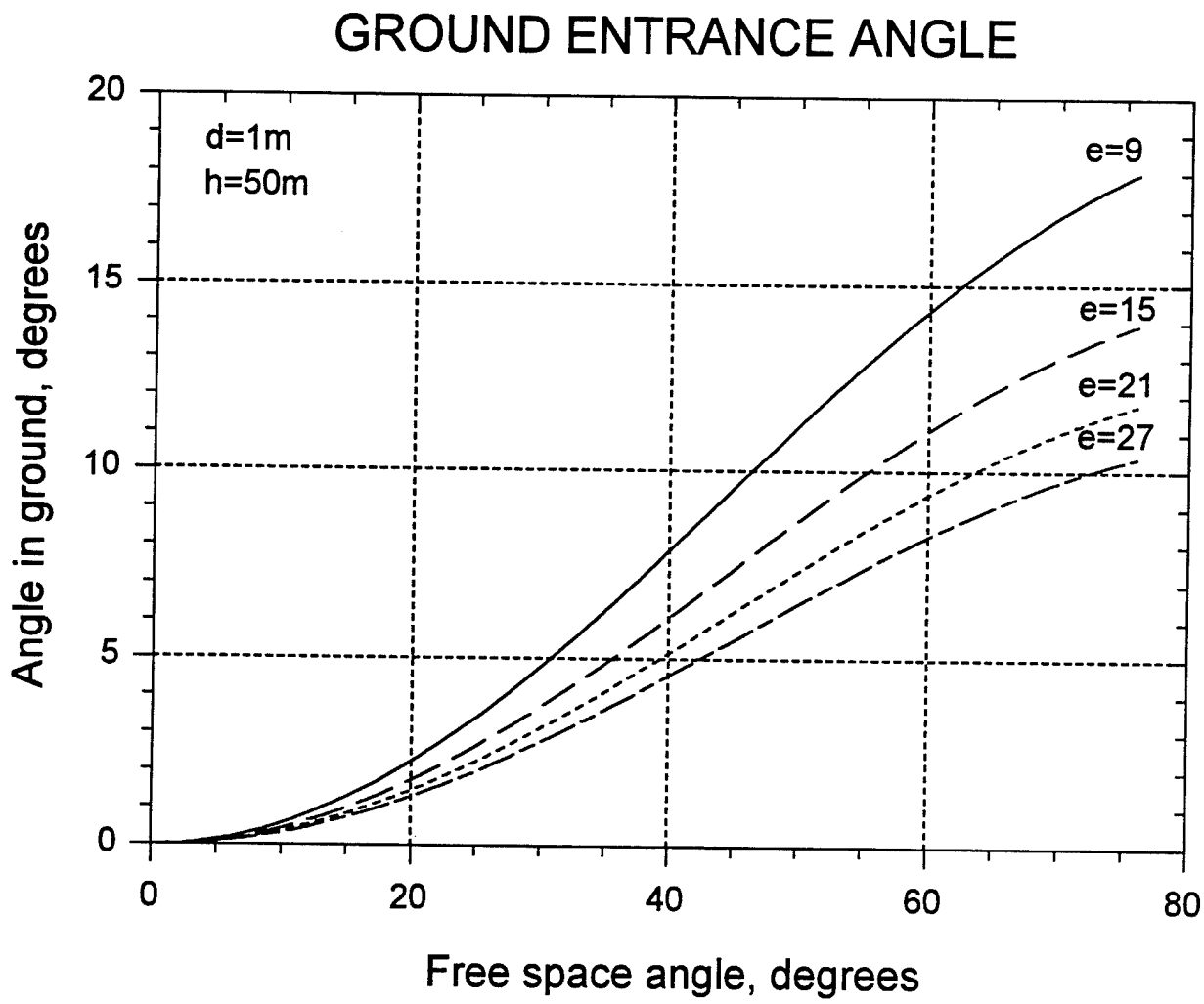

Figure 93. Ground entrance angle versus free space angle for various dielectric constants.

6.0 Resonance Extraction and Target Discrimination

6.1 Introduction

The complex natural resonance (CNR) frequencies of radar targets have been shown to be practical and useful in target discrimination. This use of resonances was pioneered by Hill [1] in 1970. The attractive features of using the CNR frequencies are their independence of the target aspect angle and the small number of characterizing parameters. Baum [2] and Marin [3] showed that the impulse response of a radar target can be modeled as a summation of a finite number of damped sinusoidal resonances. This technique is usually referred to as the singularity expansion method (SEM) since each singularity corresponds to a natural resonant mode of the target excited by the impulse radar. The original CNR concept and formulations were derived in the complex frequency domain, however most of the data were measured in the time domain. Much effort has been directed toward applying the CNR concept directly to the time-domain data. Van Blaricum provided a systematic approach for extracting poles and residues of the CNR's directly from the target's transient response using Prony's method [4], [5], [6]. His calculated CNR's for a dipole agreed with the well-known results obtained by Tesche [7] using the singularity expansion technique. In 1965 Corrington [8] independently found that the transient response of a radar target can be predicted by a special difference equation. The coefficients in his difference equation were obtained by assuming that the Laplace transform of the target impulse response could be represented in a rational polynomial form. This technique turned out to be closely related to the SEM. Because his method is applied to the time-domain data directly, it is more attractive in terms of real time target detection and discrimination. Berni [9] and Moffatt [10] then applied the CNR frequencies concept and the time-domain technique to real target detection and discrimination by correlating the measured response and the response predicted from the difference equation. In 1984, Morgan showed that the Laplace transform of the scattered

fields from a radar target illuminated by an impulse radar was composed of two parts: a forced response and a natural response. The natural response was expressed as a simple pole expansion and each pole corresponds to one natural resonance of the target.

The ElectroScience Laboratory at The Ohio State University has been interested in detecting and discriminating targets immersed in free space via CNR's since the 1970's. In 1975, Berni [9] modeled the late-time transient radar signatures by a summation of natural frequencies of oscillation and then used them for target identification. Moffatt and Mains [10] introduced a time domain predictor-correlator process to discriminate some thin-wire geometry. In 1976, Moffatt and Chuang [11] used the Prony method to extract the CNR's and then used the predictor-correlator process to perform the target identification for simple wire aircraft and some realistic aircraft models. In 1977, Moffatt and Shubert [12] used a rational function to model the complex frequency responses of thin-wire targets and then obtained the complex natural resonances from the poles of the rational function.

In these earlier applications, the targets were measured in free space. At about the same time, Ohio State had also developed GPR systems for subsurface target measurement. Because most subsurface targets of interest have simple geometries, the CNR target discrimination technique would be applicable to these targets. From 1979 to 1981, Chan, Moffatt, and Peters [13], [14], [15] did a series of studies that applied the CNR and predictor-correlator techniques to identify plastic mines and some simple geometric metallic targets buried at shallow depths. These studies also showed that the CNR's for buried metal targets vary with the medium parameters. It was not until 1993 that a transformation for CNR's in different homogeneous, isotropic, lossy, and non-magnetic media was given by Baum [16]. With this transformation, only one database of target CNR's obtained in free space is required. In 1983, Volakis and Peters improved the identification of underground targets by removing the undesired natural resonances associated with the antenna and various form of clutter.

Since 1990, ElectroScience Laboratory has been involved in the detection and identification of unexploded ordnance. This report summarizes the data processing progress achieved between 1993 and 1994 on subsurface target identification. The system and antenna portions are not included in this section. The details of these topics can be found elsewhere in this report and in ESL Technical Reports 727388-2, 727388-3 and 727388-4. Prony's method has been further modified to obtain more accurate and stable CNR's under low signal-to-clutter and signal-to-noise ratio conditions. These conditions are discussed below. The predictor-correlator process previously used for target identification is also re-examined below.

6.2 Extraction of Complex Natural Resonances Using Prony Model

Introduction

The Prony method has been widely used for modeling time-domain signals that can be predicted by its previous-time information. It is used to evaluate the poles that can be used to characterize the damped oscillations. Although it is well known that the Prony method has poor performance for noisy signals, it has been chosen to extract the CNR's in our data processing due to its efficiency and sensitivity. In this chapter, the formulation of the Prony method will be given in the first section. Some difficulties in applying Prony's method such as unknown model order, low-signal-to-noise ratio and multiple delays from multiple targets are also discussed in the following sections. Some techniques, that partially eliminate the problems and thus improve the processing performance, will also be presented.

Prony Model

Formulations

The specific type of function to be discussed in this chapter has the following form,

$$f(t) = \sum_{m=1}^{N} c_m e^{s_m t} u(t) \tag{70}$$

where the s_m are the poles in the complex frequency plane and the c_m are their corresponding residues. The above expansion is also often referred to as a SEM because each pole is also a function singularity [2]. It is noted that the s_m should appear in complex conjugate pairs because $f(t)$ is a real-valued function. The late time portion of the impulse response of a radar target has been shown to contain natural responses with the same form as $f(t)$ [2], [3], [9], [17]. This part of the response is composed of the natural resonance modes of the target when they are excited by an impulse radar. Each resonance mode is characterized by its CNR frequency, s_m which can also be explicitly expressed as

$$s_m = \alpha_m + j2\pi f_m \tag{71}$$

where α_m and f_m are the damping factors and the resonance frequencies of the target natural resonant modes. It should be noted that the α_m are non-positive values for stable systems. A very attractive feature of CNR's is their independence of the target aspect angle. The residue corresponding to each mode is, on the contrary, a function of the excitation. There are two types of CNR's. One is internal CNR's and the other is external CNR's. Internal CNR's occurs in cavity modes or dielectric bodies. External CNR's occur in non-penetrable targets or perfectly conducting bodies. Note that external resonances also exist in dielectric bodies. The internal type of CNR is independent of the medium where the target is located, however, the external type of CNR varies with the properties of the medium. An empirical relation was given by Chan [13] for including medium effects on these external CNR's for long thin targets. More general theoretical analysis by Baum [16] extended this approach to include all perfectly conducting targets. He showed that the CNR in any medium with permittivity ϵ_r and conductivity σ can be found from the corresponding CNR in free space using the following relation:

$$S_\alpha = -\frac{\sigma}{2\epsilon_0\epsilon_r} + \left[\left(\frac{\sigma}{2\epsilon_0\epsilon_r}\right)^2 + \frac{(S_\alpha^{(0)})^2}{\epsilon_r}\right]^{1/2} \tag{72}$$

where S_α and $S_\alpha^{(0)}$ are the poles in the medium and free space, respectively. The above formula has been shown to agree with the measurement results for conducting pipes buried in sand [18].

From the above discussion, one can see the importance of equation (70) in radar target characterization. The discrete version of equation (70) is expressed as

$$f(n\Delta t) = \sum_{m=1}^{N} c_m e^{s_m n\Delta t}, \quad n=0,...,L \tag{73}$$

where Δt is the sampling period which should be chosen such that the Nyquist sampling criteria is satisfied to avoid aliasing. The effect of aliasing will be discussed in more detail in Section C. The above equation will be written in the following simpler form for convenience.

$$f_n = f(n) = \sum_{m=1}^{N} c_m Z_m^n \tag{74}$$

where

$$Z_m = e^{s_m \Delta t}. \tag{75}$$

The above equation was solved by Prony in 1795 [19]. It can be shown that the waveform satisfying Equation (74) can also be generated by the difference equation

$$f(n) = -\sum_{m=1}^{N} a_m f(n-m). \tag{76}$$

where the coefficients a_m can be solved using the $2N$-1 data points, f_o, f_1, ..., f_{2N-1}, and the following matrix equation

$$\begin{bmatrix} f_N & f_{N-1} & \cdots & f_0 \\ f_{N+1} & f_N & \cdots & f_1 \\ \vdots & \vdots & \ddots & \vdots \\ f_{N+(N-1)} & f_{N+(N-2)} & \cdots & f_N \end{bmatrix} \begin{bmatrix} a_1 \\ a_2 \\ \vdots \\ a_N \end{bmatrix} = - \begin{bmatrix} f_{N+1} \\ f_{N+2} \\ \vdots \\ f_{N+N} \end{bmatrix} \tag{77}$$

If more then $2N$ points are used, i.e. the number of rows is greater than the number of columns, one can solve the above equation in a least square error sense, which is equivalent to the covariance method of linear prediction in the modern spectral analysis [20,21]. As will be shown in the next section, using more data points can usually improve the processing performance and reduce the error by at least 12 dB. Taking the Z-transform of the above difference equation, one can easily show that the coefficients a_m are also the coefficients of the Nth order characteristic polynomial

$$1 + a_1 Z^{-1} + a_2 Z^{-2} + \ldots + a_N Z^{-N} = 0. \tag{78}$$

The roots of the above equation then give the poles $Z_m = \exp(s_m \Delta t)$, $m = 1, 2, \ldots, N$. Using equation (74) the residues, c_m can then be found by solving the matrix equation

$$\begin{bmatrix} 1 & 1 & \cdots & 1 \\ Z_1 & Z_2 & \cdots & Z_N \\ \vdots & \vdots & \ddots & \vdots \\ Z_1^{N-1} & Z_2^{N-1} & \cdots & Z_N^{N-1} \end{bmatrix} \begin{bmatrix} c_1 \\ c_2 \\ \vdots \\ c_N \end{bmatrix} = \begin{bmatrix} f_0 \\ f_1 \\ \vdots \\ f_N \end{bmatrix} \tag{79}$$

The above procedures used to find the poles, Z_m, and the residues, c_m are usually referred to as the Prony method. That is

$$\begin{bmatrix} c_1 \\ c_2 \\ \vdots \\ c_N \end{bmatrix} = \begin{bmatrix} 1 & 1 & \cdots & 1 \\ Z_1 & Z_2 & \cdots & Z_N \\ \vdots & \vdots & \ddots & \vdots \\ Z_1^{N-1} & Z_2^{N-1} & \cdots & Z_N^{N-1} \end{bmatrix}^{-1} \begin{bmatrix} f_0 \\ f_1 \\ \vdots \\ f_N \end{bmatrix} \quad (80)$$

For over-determined systems, the singular value decomposition (SVD) method and a least square error solution can be used to obtain the residues. This is usually referred to as the ''modified Prony method'' which provides some improvement in the presence of noise.

Effect of Data Sampling Rate

Assume that a waveform is sampled at a period of Δt and the waveform contains only a pair of complex conjugate poles, $Z=exp(\alpha \pm j2\pi f)\Delta t$ whose positions on the Z-plane are shown in Figure 94.

As Δt varies, the distance between the origin and the angle of each pole will change according to $Z=\exp[(\alpha \pm j2\pi f)\Delta t]$. As Δt keeps increasing and the sampling rate keeps decreasing, two poles will finally merge at the an angle of 180 degrees where aliasing starts to occur. As Δt increases further, two conjugate poles will ''fold'' over. Because the

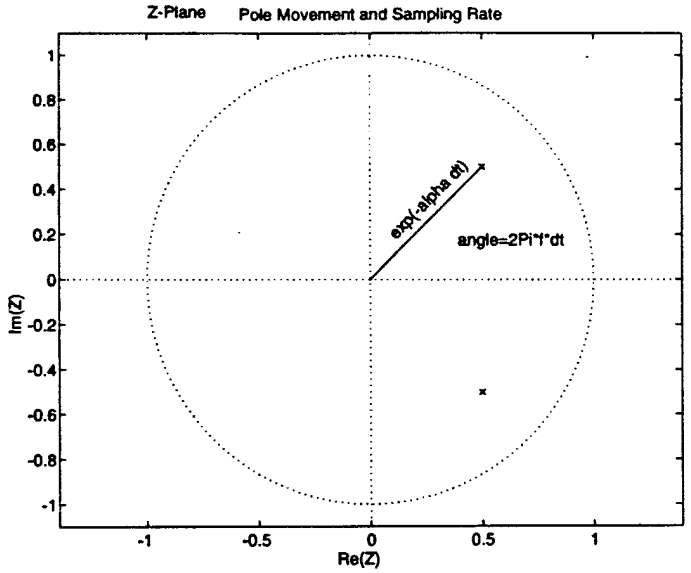

Figure 94 A pair of complex conjugate poles, (0.5±-j0.5), on the Z-Plane.

frequency is determined from the angle of the pole on the upper half plane, i.e. positive theta between 0 and π, when the aliasing occurs (the poles fold over) the angle will decrease as Δt increases. The result is an apparent decrease in the frequency, $f\text{-}1\Delta t$, instead of a constant frequency f. The point where the aliasing starts is when $2\pi f\Delta t$ equals π, i.e., $f\Delta t = ½$. Because the sampling rate, f_s, equals $1/\Delta t$, the aliasing starts at $f_s = 2f$, i.e., the Nyquist rate.

Figure 95 shows the movement of poles extracted from a damped sinusoidal oscillation, (α=-0.3, f=0.3E+9), using the Prony method. As the sampling rate decreases from 2 GHz to 100 MHz, the pole on the upper half-plane rotates counter-clockwise and forms an inward going spiral locus. The conjugate pole also moves correspondingly. The "fold over" points ($f\Delta t = n\pi$) of the poles are clearly seen in this figure and are marked by "P", "Q", "R", "S", etc. Figure 96 shows the resultant resonance frequency (upper-half plane) and the damping factor (lower-half plane) of the same processing. At point P, the sampling rate equals 1.2 GHz, twice that of the signal resonance frequency (0.6 GHz). It is interesting to observe that the damping factor can still be found correctly even from the under-sampled data because it is obtained from the distance between the origin and the pole and is not affected by the "fold over" situation.

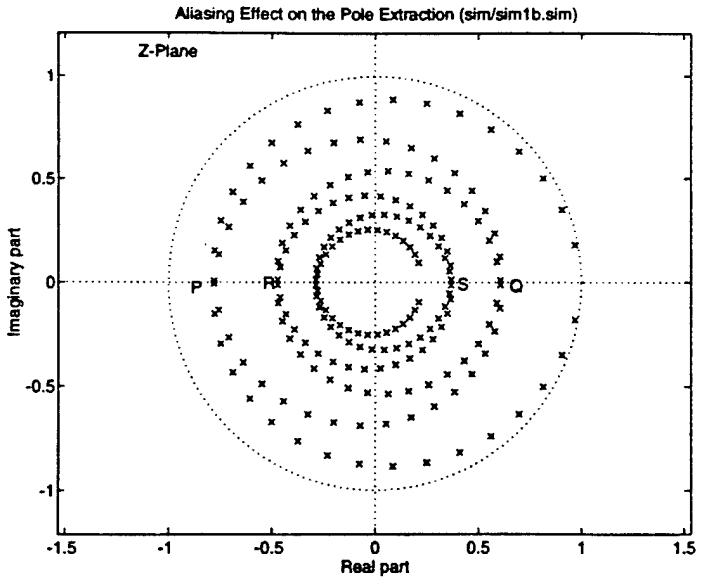

Figure 95 Locus of extracted poles as a function of the sampling rate.

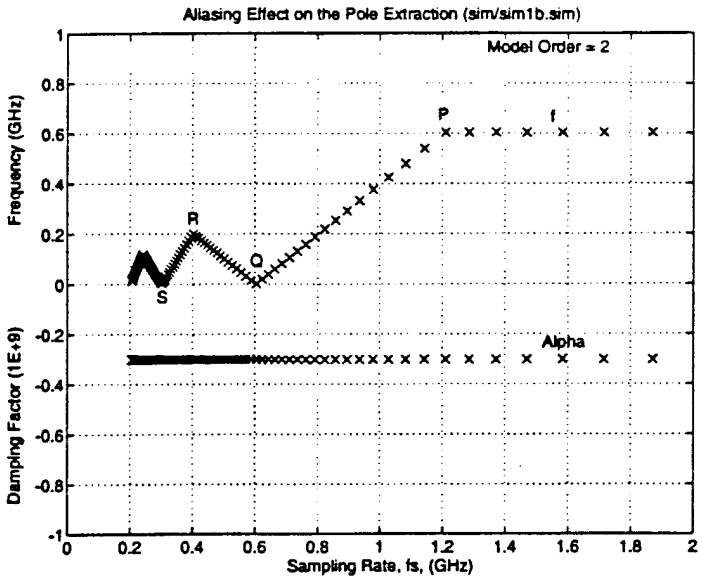

Figure 96 Effect of aliasing on the extracted frequency and damping factor.

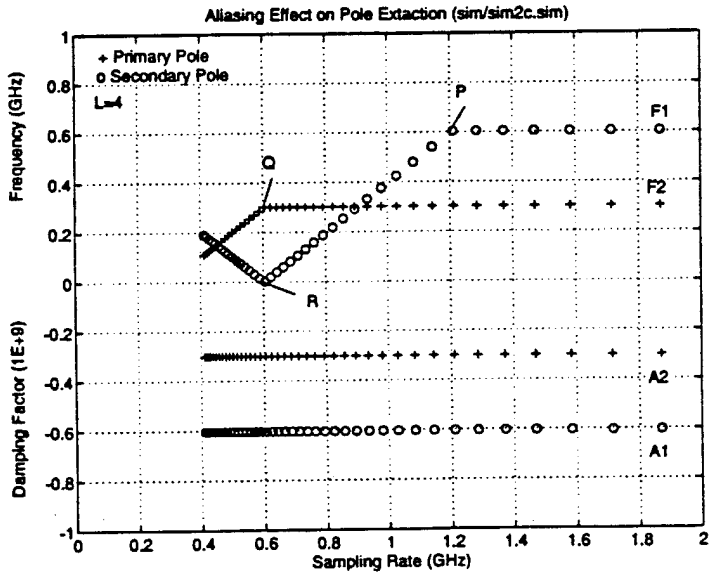

Figure 97 The aliasing effect in multiple CNR's signal processing.

In the next example, a waveform generated by two unit-residue CNR's is processed using the Prony method. The two CNR's are (α=-0.3E+9, f=0.3 GHz) and (α=-0.6E+9, f=0.6 GHz). The results are shown in Figure 97. The primary resonance (+) is chosen to be the one with higher energy. One can see that in order to extract all the resonance frequencies correctly, the data need to be sampled faster than the Nyquist rate associated with the highest resonance frequency. The correspondent residues and energy (defined by Moses) are also plotted in Figure 98 and Figure 99, respectively. It is seen that the residues associated with each pole were also found correctly. Because the primary (+) pole has a smaller damping factor, the wave lasts longer and thus contains more overall energy as shown in Figure 99. As will be shown later, this energy information plays a very important role in separating the true poles and the false poles introduced by an over-estimated model order.

As one can see, the Z-plane concept is very helpful in explaining the behavior of the Prony' processing and will be used often in this report.

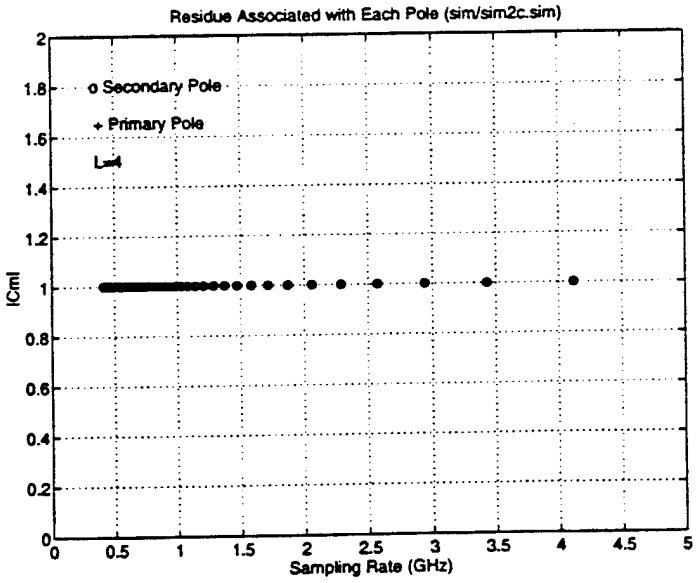

Figure 98 The calculated residue.

Noise Effects on Extracted Poles

In the real world, any measured signal contains noise that appears to be random in time and has a zero mean value. Because the noise signal cannot be modeled by a finite length Prony model, it will cause errors in the CNR extraction process and sometimes a rank deficient problem occurs if the mode order is not high enough. The purpose of this section is to discuss the calculated resonance frequency and damping factor errors caused by noise. White Gaussian noise with zero mean will be assumed. In general, GPR data are corrupted by noise, clutter, and interference. The undesired *noise* signals are Gaussian; the clutter and interference are probably not Gaussian. The signal-to-noise ratio (SNR) will be defined as

$$\text{SNR} = 10\log_{10}\frac{(\text{peak amplitude})^2}{2\sigma^2} \tag{83}$$

where σ^2 is the variance of the white Gaussian noise. It should be noted that for a damped sinusoidal oscillation with damping factor, α, the instantaneous SNR decreases at a rate of $\exp(-2\alpha\Delta t)$. Note also that for undamped signals, the above definition becomes the same as the common definition using an average power concept.

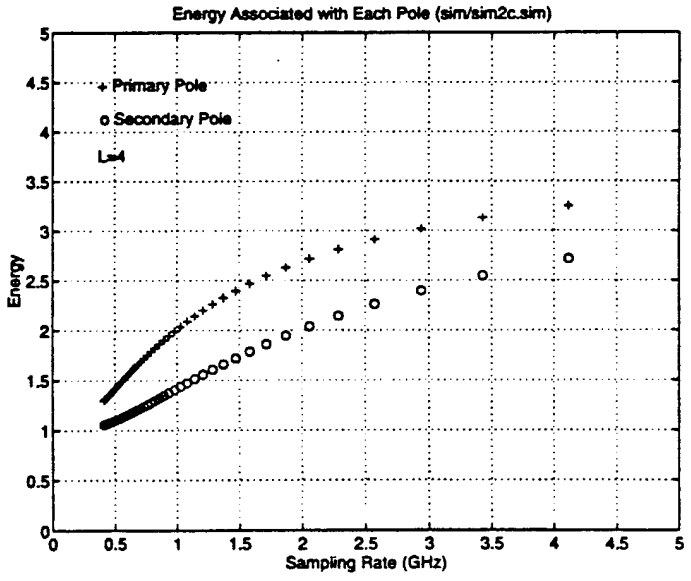

Figure 99 The calculated energy.

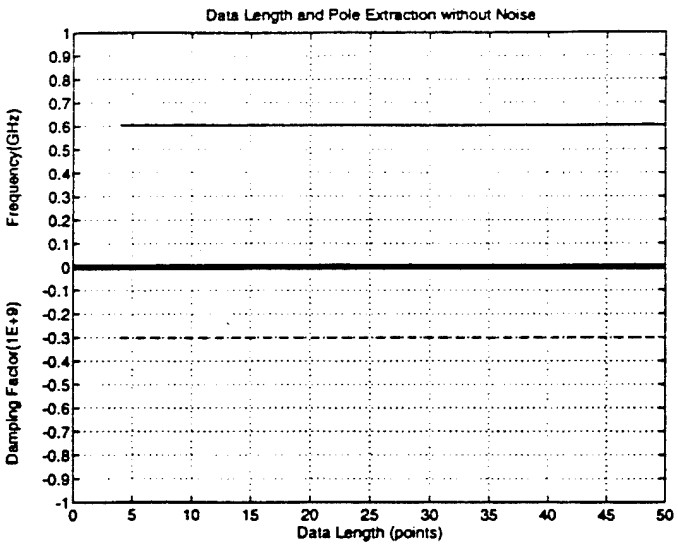

Figure 100 The extracted CNR from data of different lengths. The second order Prony model was used.

Choice of Data Length

As mentioned in the previous chapter, the Prony method is applied in a least square sense for an over-determined system to achieve better performance in the presence of noise. This is illustrated by the following example. A signal containing a single CNR with α=-0.3E9 and f=0.6 GHz is sampled at a rate of 4.1 GHz (or a 0.243 ns time step). The Prony method is used to extract the CNR's from different data lengths. That is, each segment starts from time zero but has a different number of points. The model order is fixed at two in all cases. The results are shown in Figure 100. As one can see, the CNR is obtained correctly for all lengths. Next, zero mean, white, Gaussian noise is added to the previous signal such that the SNR equals 10 dB. The new results are shown in Figure 101 where twenty noisy waveforms are processed and overlaid together as the length is increased. For longer data lengths, the variations of the calculated frequency and the damping factor are reduced. This reduction is achieved by solving the over-determined system in the least square error sense. It is noted that the variation in the damping factor is almost five times greater than that of the frequency. This number varies with the pole position in Z-plane as shown by Steedly and Moses [23]. They also showed that both variations decrease when the poles are close to the unit circle, i.e., $|Z|=1$.

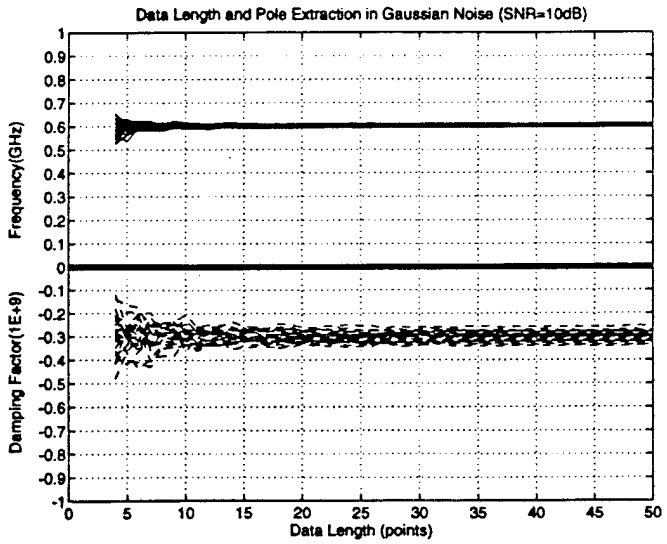

Figure 101 The extracted CNR from data of different length in zero mean white Gaussian noise with SNR of 10 dB, Δt of l0.243, model order 2.

Multiple Waveform Average

It is also interesting to observe the variation of the extracted damping factor and frequency with different SNR values. This variation is shown in Figure 102. Twenty processed results were overlayed. Because white, zero-mean, Gaussian noise has been assumed, averaging over more waveforms can be expected to improve the signal to noise ratio. Figure 103 plots the average values of 20 processes. It is seen that the variations are greatly reduced and the errors are less than 10 percent even for 5 dB SNR. Of course, the price paid here is the additional measurements and additional computation time.

Autocorrelation

It is well known that autocorrelation can reduce uncorrelated white noise. In the autocorrelated waveform, the noise appears as an impulse at $t=0$ and can be removed by ignoring points around $t=0$. This procedure is illustrated in the following example where the noisy data was first autocorrelated before CNR extraction and then processed using the $t>0$ portion of the data. The results are plotted in Figure 104. When compared with Figure 102, less variation in both the frequency and the damping factor are observed at lower SNR. For

SNR greater than 10 dB the reduction is not significant. It is also noticed that the damping factor is biased toward $\alpha=0$ as the SNR decreases.

It has not been shown that the autocorrelation process preserves the poles. This will be shown in the following discussions. The autocorrelation function for a discrete signal *x[n], (n=0, 1, ...,N-1)* is defined as

$$r_{xx}(k) = \frac{\sum_{n=0}^{n=N-1-|k|} x[n]\, x^*[n]}{\sum_{n=0}^{n=N-1} |x[n]|^2} \tag{82}$$

Now, let *x(t)* be a continuous, damped sinusoidal signal containing only one pole, $s=\alpha+j\omega$, $\alpha<0$, i.e.

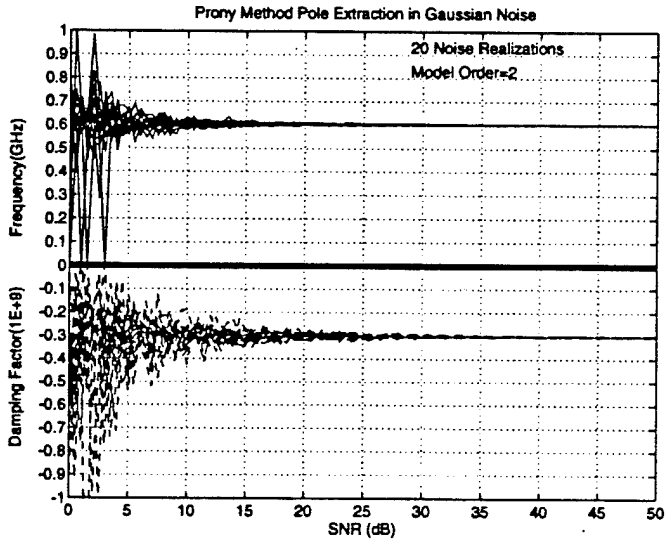

Figure 102 The extracted CNR variation in zero Mean white Gaussian noise of different SNR. Twenty noise realizations are overlayed. The second order Prony model was used.

$$x(t) = ce^{st}u(t). \tag{83}$$

The autocorrelation function of $x(t)$ can then be found to be

$$r_{xx}(\tau) = \frac{|c|^2}{2|\alpha|} s^{s|\tau|}. \tag{84}$$

It is clear that, for $\tau > 0$, r_{xx} has the same pole as $x(t)$. That is, autocorrelation preserves poles. However, the residue associated with the pole is modified. Generally speaking, higher harmonics from a radar target have larger target damping factors, α. Therefore, the autocorrelation process tends to further weaken the higher harmonics and weaker poles (small $|c|$).

A more general $x(t)$ containing two poles is

$$x(t) = c_1 e^{s_1 t} u(t) + c_2 d^{s_2(t-d)} u(t-d), \tag{85}$$

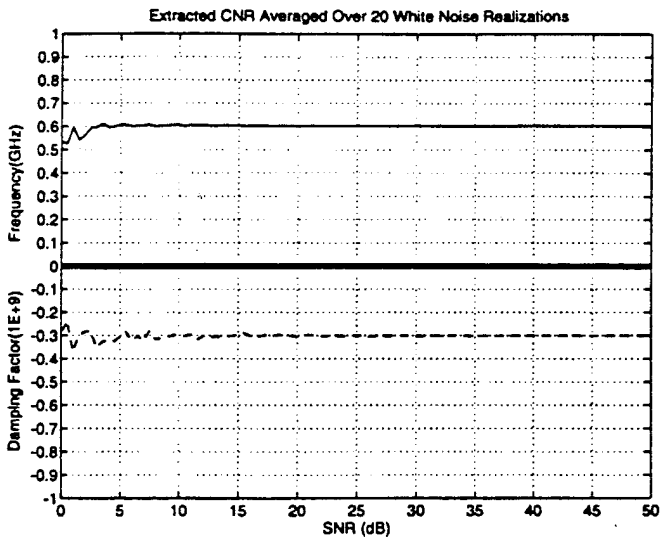

Figure 103 The averaged CNR from twenty noise realizations. The second order Prony model was used.

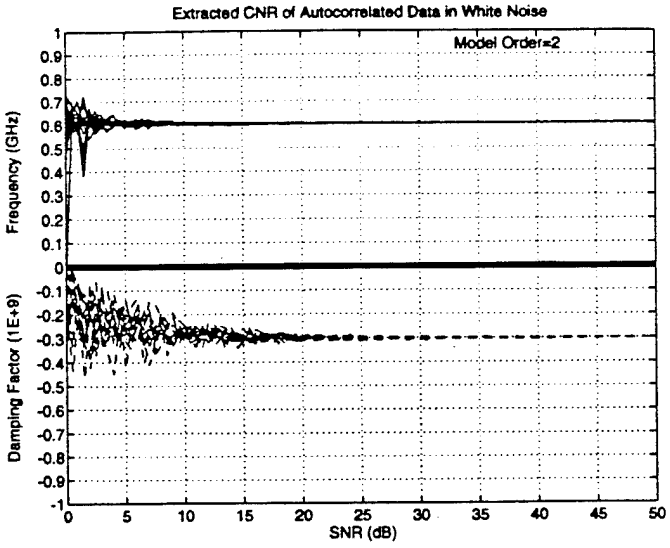

Figure 104 The extracted CNR using autocorrelated data in the presence of white noise (twenty realizations). The second order Prony model was used.

where $d>0$ is the delay of the second signal. After some manipulation, one can obtain

$$r_{xx}(\tau) = \left[\frac{c_1 c_1^*}{2(s_1+s_1^*)} - \frac{c_1 c_2^*}{2(s_1+s_2^*)}\right] e^{s_1\tau} + \left[\frac{c_2 c_2^*}{2(s_1+s_1^*)} - \frac{c_1^* c_2}{2(s_1+s_2^*)}\right] e^{s_2\tau} \qquad (86)$$

$$= Ae^{s_1\tau} + Be^{s_2\tau}, \qquad \text{for } \tau>d.$$

Again the poles have been preserved in the autocorrelation process but the residues have also been modified.

Summary

In this section, we have discussed some of the noticeable effects of Prony processing in the presence of white noise. The variations in the extracted damping factor and resonance frequency are significant for SNR greater than 15 dB. It was also shown that averaging more waveforms greatly reduces these variations and provides accurate CNR's for signal-to-noise ratios as low as 5 dB. It should be noted that the various curve smoothing techniques, used in some situations when noise is present, cannot be applied here. It was found, but not mentioned, that the damping factor is severely biased after smoothing. Although the autocorrelation technique can also reduce some variations, it biases the damping factor. It should be noted that a second order Prony model was used to extracte the CNR's for all cases in this section because the number of poles was known *a priori*. However, in real applications, the order of the model needs to be determined first. The presence of the noise also causes difficulties in finding the correct model order. This situation will be discussed in the following section.

Model Order Selection

The first difficulty one meets in applying the Prony method is to determine the order of the model. This determination requires the knowledge of the number of significant CNR's contained in the data. For some cases, one may have a very good guess but this is usually a trial-and-error process. If the model order is underestimated, the resulting CNR's will be incorrect. On the other hand, over-estimation will create extraneous poles. Because the Prony method is closely related to linear prediction using autoregressive (AR) and autoregressive moving average (ARMA) models [20,21], the criteria developed for selecting the AR and ARMA model order may be applied. Some important criteria are the final prediction error (FPE) by Akaike [24], Akaike information criterion (AIC) [25] and criterion autoregressive transfer (CAT) by [26], etc. However, for short data lengths, none these criteria work well and some may tend to underestimate the order, as shown by Ulrych and Clayton [27]. Two other methods have been used to select the order of Prony model, which have been found to work reasonably well. The first method is the eigenvalue method by Van Blaricum [6]. In this method, the model order is found from the number of significant

eigenvalues of a correlation matrix formed by the sampled data. The eigenvector associated with the minimum eigenvalue gives the coefficients of the difference equation. A similar method was also used by Pisarenko [28]. Moses [22] calculated the energy associated with each pole and then selected the high energy ones. Using the expression in equation (76), the energy P_i associated with the pole Z_k is defined as

$$P_i = \sum_{k=1}^{N} |c_k Z_k|^{2k} = |c_i|^2 \frac{1-c_i^2 N}{1-c_i^2} \tag{90}$$

Both the eigenvalue and the energy methods start by using a large model order and then determine the order by comparing the eigenvalue or the energy with a designated threshold. These two methods also give some physical insight into the problem.

The main purpose of this section is neither to compare nor to re-derive different techniques for model order selection. It is to examine the effects of improper order selection. Therefore, in the following discussion, the eigenvalue and energy methods will be used to study the effects of over-estimation and under-estimation of the model order. We will start with a calculated, noise free, damped, complex exponential sequence with α=-0.3E+9, f=0.6 GHz, and Δt=0.486 ns. After studying the behavior of the extraneous poles and underestimated poles, white noise will be added to the signal.

Model Order Selection for Noise Free Cases

Model order selection, is in general, a difficult task, especially for a low SNR environment. Even for high SNR cases, improper model order also presents problems in interpreting results. In this section, a noise free signal will be considered. The noisy case will be discussed in the following section. In general, under-estimating model order will result in incorrect poles and over-estimating will produce extraneous poles in addition to the true poles. These situations will be illustrated in the following example. Assuming that the poles in simulated data set are to be extracted using SVD Prony's method with the number of the principle eigenvectors equal to the model order. The data have 25 points and contains two complex poles (s_1=-0.1+j2π(0.52), s_2=-0.2+j2π(0.42)) and

$$x[n] = e^{s_1 n} + e^{s_2 n},\ n=0, 1, \ldots, 24. \tag{89}$$

Different model orders were chosen to process the data. The extracted poles (left hand side) and the magnitude of the associated residues (right hand side) are shown in Figure 105. One can see that, as the model order increases, extraneous poles appear along with the two true poles.

Two interesting observations can be made here. First, from the pole locations, it is possible to identify the true poles by choosing two different overestimated model orders and pick the common poles. Second, the magnitude of the residues associated with the true poles are much greater than those associated with the extraneous poles, and thus provide another possible way to identify true poles. For example, on the right hand side of Figure 105, one can see that there are two dominant residues. Therefore, one can estimate the model order to be 2 and reprocess the data to remove the extraneous poles, as shown in the top figure. It should be noted that the first method requires multiple processing while the second method becomes less efficient when noise is present.

A model order selection criterion related to the residue magnitude is given in [22] where the energy associated with pole z_m is defined as

$$P_m = |c_m|^2 \frac{1-|z_m|^N}{1-|z_m|^2}, \tag{90}$$

with c_m the associated residue and N the model order. The eigenvalue method provides another alternative for model order estimation [6]. In terms of model selection, all these methods work equally well for noise free signals. Note that more data points can also improve the ability to identify true poles by reducing the relative residue magnitude

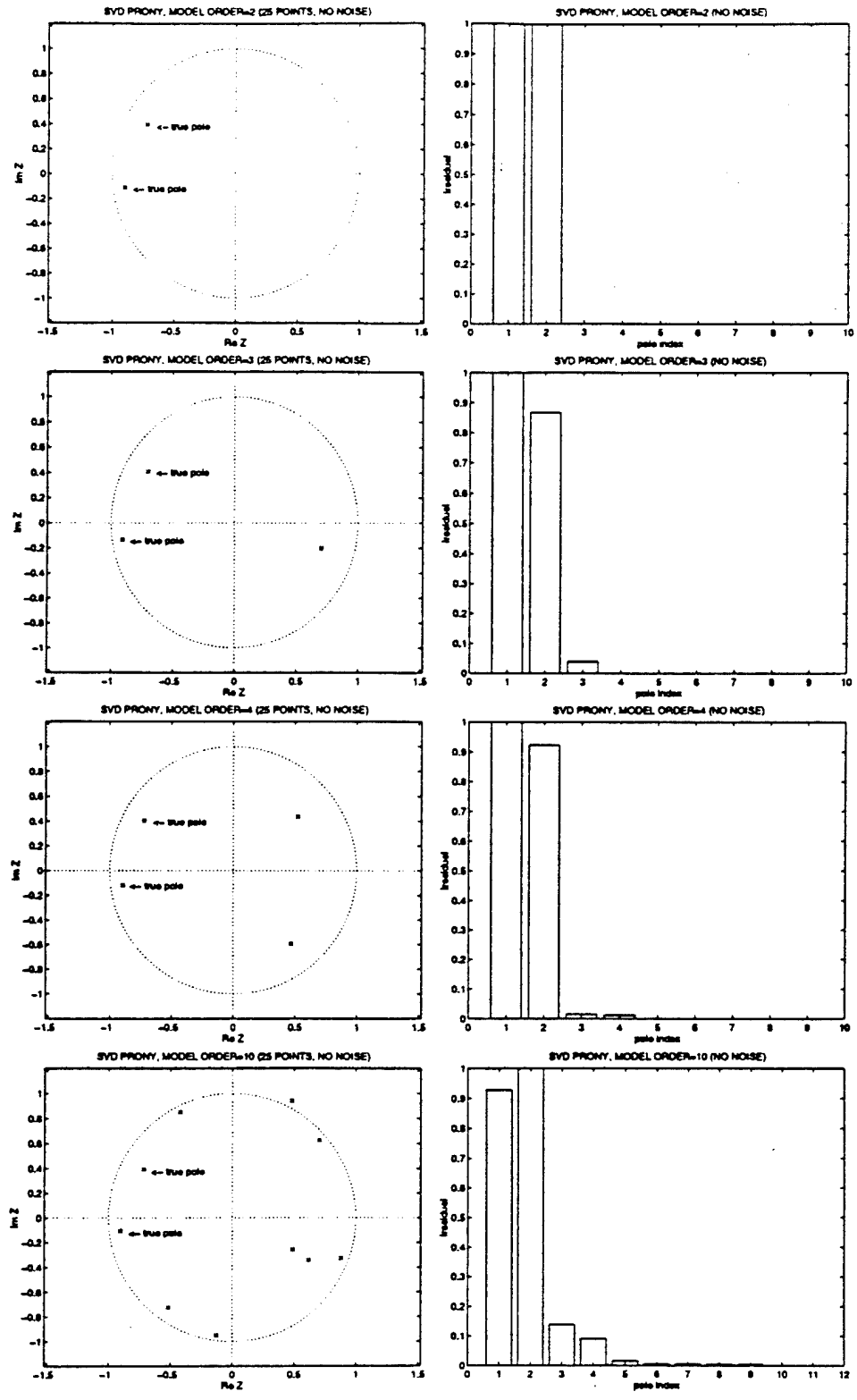

Figure 105 Pole extraction using different model order.

associated with extraneous poles. This concept is illustrated in Figure 106 where 50 data points were used.

Model Order Selection in White Gaussian Noise

In this section, random noise with a Gaussian distribution is added to the previous simulation signal. The effect of noise on the model order selection will be examined for different SNR levels (20 dB, 10 dB, 5 dB, and 0 dB). Model order selection based on the residue magnitudes, energy and eigenvalue methods will be compared.

The following processing is done using 50 independent random noise realizations and an 8th order model. Note that the number of principal eigenvectors in the SVD method is first set to be the same as the model order because the order is not a known *a priori*. The processed results are shown in Figure 107 in dB where the left hand side plots the overlay of poles found in 50 realizations and the right hand side plots the residue magnitude, energy and eigenvalues of each pole averaged over 50 realizations. By comparing these pole plots with the ones in Figure 105, one finds that the effect of the extraneous poles are to make it extremely difficult to identify the true poles, despite the true poles tending to have smaller variance than the extraneous poles. Note that the variance of the poles depend on their locations in the complex plane, as shown by Moses [23]. On the right hand side, it is also

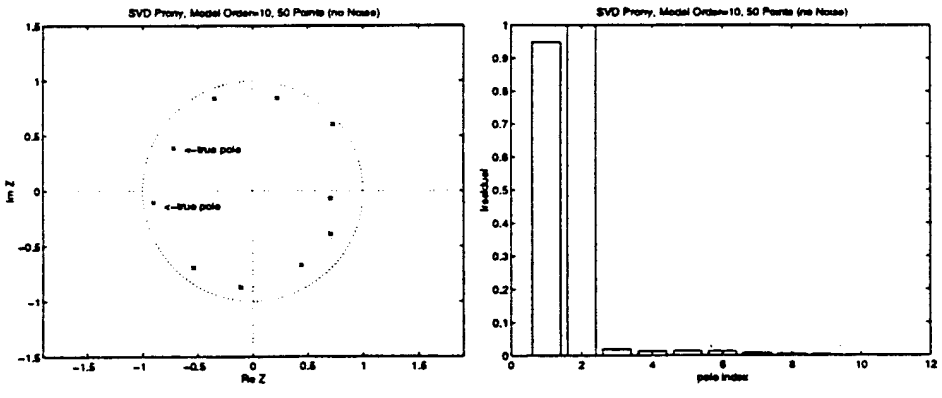

Figure 106 Poles extracted using SVD Prony method with order of ten and 50 data points.

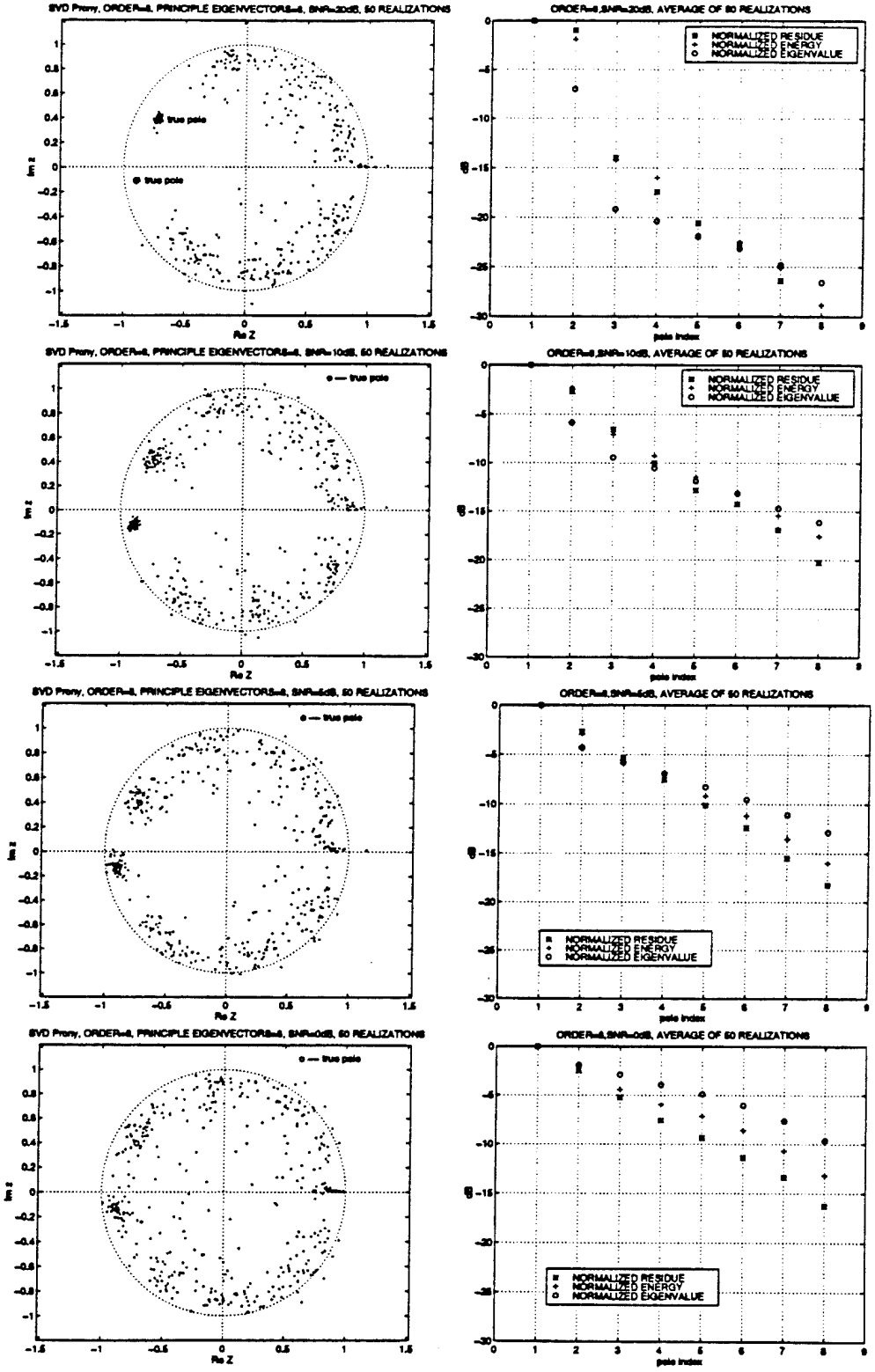

Figure 107 Poles extracted and model order selection from a noisy signal.

noted that, for SNR less than 10 dB, the differences in the magnitudes of the residues, energy, and eigenvalues are no longer obvious. In this case, all three methods fails to estimate the model order. If one ''guesses'' the model order to be 2, then the poles variances can be largely reduced by choosing two principal eigenvectors in the SVD Prony's method. This situation is illustrated in Figure 108. It should be noticed that the model order must be chosen larger than the number of true poles, due to the presence of noise.

Running Window Technique

The Prony model assumes that the signal can be represented by the summation of a finite number of complex exponentials. For most radar targets, the impulse response contains both the forced response and the natural response. The former dominates the earlier time portion of the received signal. The latter is due to the target's CNR's, which contain complex poles and can be well modeled by the Prony model. Theoretical proof of the above observations has been given by Morgan [17]. Similar observations have also been discussed in other papers, [14, 9, 23]. Because the CNR's of a target are independent of target aspect, they can be used to characterize the target for identification and discrimination purposes. It is desirable to avoid the early-time, forced response-dominated signals to achieve greater spectral dynamic range and sensitivity in detecting resonance peaks. This avoidance is also required by the nature of the Prony model. Therefore, only the later time portion of the data is used in pole extraction. However, this portion of a signal usually suffers from poor signal-to-noise and signal-to-clutter ratios. This situation has become one of the major difficulties in applying the Prony method to measured data. Another difficulty related to the previous one is the multiple target case. In this case, more than one impulse response is received at different times. These were introduced by cable mismatch, antenna ringing, different target depths, and so on. Because the Prony model itself also assumes that all the complex exponentials start at time zero, this situation presents some problems. As observed by Berni, it is necessary to choose a starting time point where all the CNR's have been excited.

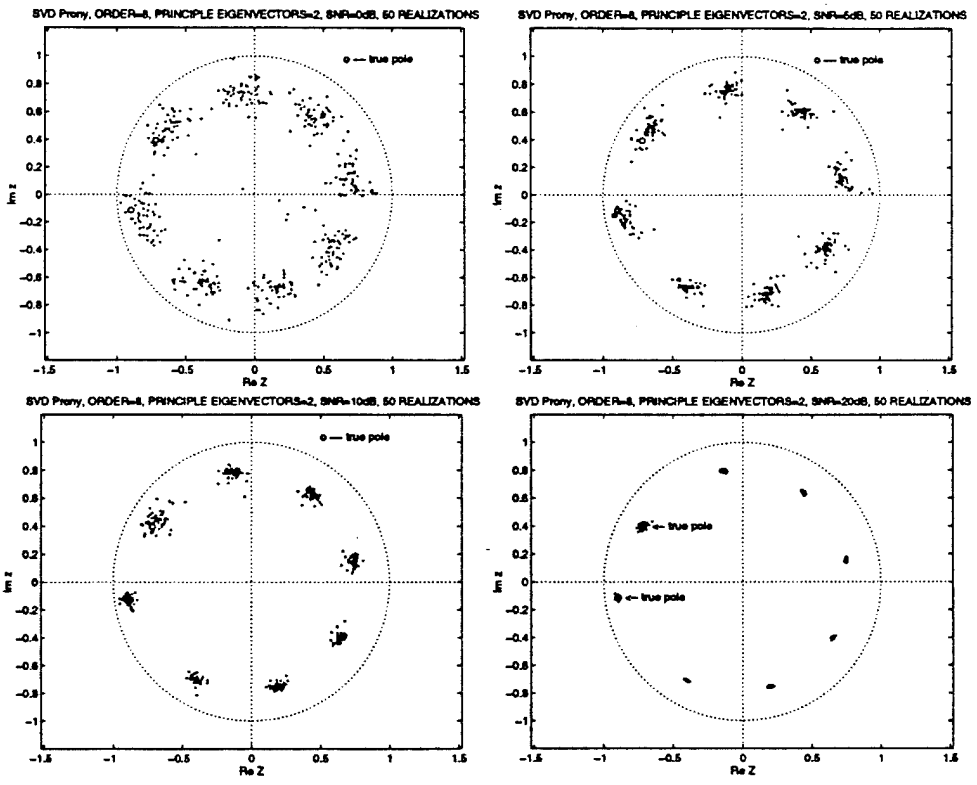

Figure 108 Reduction of pole variance by choosing the right number (2 in this case) of principal eigenvectors.

A running window technique similar to that used in the common time-frequency distribution (TFD) technique has been developed to alleviate these problems. First, the sampled data is truncated from the maximum response position by a window running through the rest of the waveform. Then the window is shifted and the process is repeated. After this processing, the resonance components contained in each window are examined. If the maximum number of poles of interest is N, then each window must have at least $2N$ data points. Some features of this technique are summarized as follows:

1. Smaller window sizes provide better resolution for showing details of CNR migration and better isolation between multiple impulses.

2. Larger window sizes give more stable results in the presence of noise.

3. The window will automatically stop when the variance of pole distributions exceeds the preset limit to avoid the low signal-to-noise and signal-to-clutter ratio tail region.

4. For multiple targets with little isolation, one can process the data backward from a designated tail point.

5. The migration of each resonance may reveal important physical insights.

The following example illustrates the above features. A simulated waveform shown in Figure 109 containing two damped complex exponentials or CNR's is to be processed. The two CNR's are characterized by (α_a=-0.5E+9, f_a=0.5 GHz) and (α_b=-0.3E+9, f_b=0.3 GHz), respectively. One of the CNR's is excited 5 ns later than the first one. The second one also has a residue twice that of the first one. This waveform cannot be processed by the original Prony model. If one decides to process it anyway, one will get the result shown in Figure 110. As expected, the results are wrong! If one now processes the data in the 5 ns to 30 ns segments where both signals have been excited, one can obtain the correct results, as shown in Figure 111.

Next, the running window technique is applied to the waveform. Because the two impulses are only 5 ns apart, the first few forward running windows may lead to the same problem. Therefore, the backward running window was chosen. A 5 ns window size (or 10 points) is used and the center of the window is shifted backward from 30 ns in one point steps (or 0.5 ns). The CNR's were obtained correctly, as shown in Figure 112. Note that the program automatically stopped when it passed the 5 ns time position where the Prony model started to fail and many false poles were generated. This situation suddenly increased the total variance of the pole positions and the threshold set by the user forced the program to stop. Otherwise, the result would contain many false poles.

A time-frequency representation of the magnitudes of residues or the damping factor is also used with a forward running window. The gray levels in Figure 113 and Figure 114 represent the magnitude of the residue and positive damping factor, α*1E+9, respectively. It is clear that the results are unstable close to the 5 ns position. Away from that critical region the frequencies, damping factors, and the residues were accurately obtained. It is

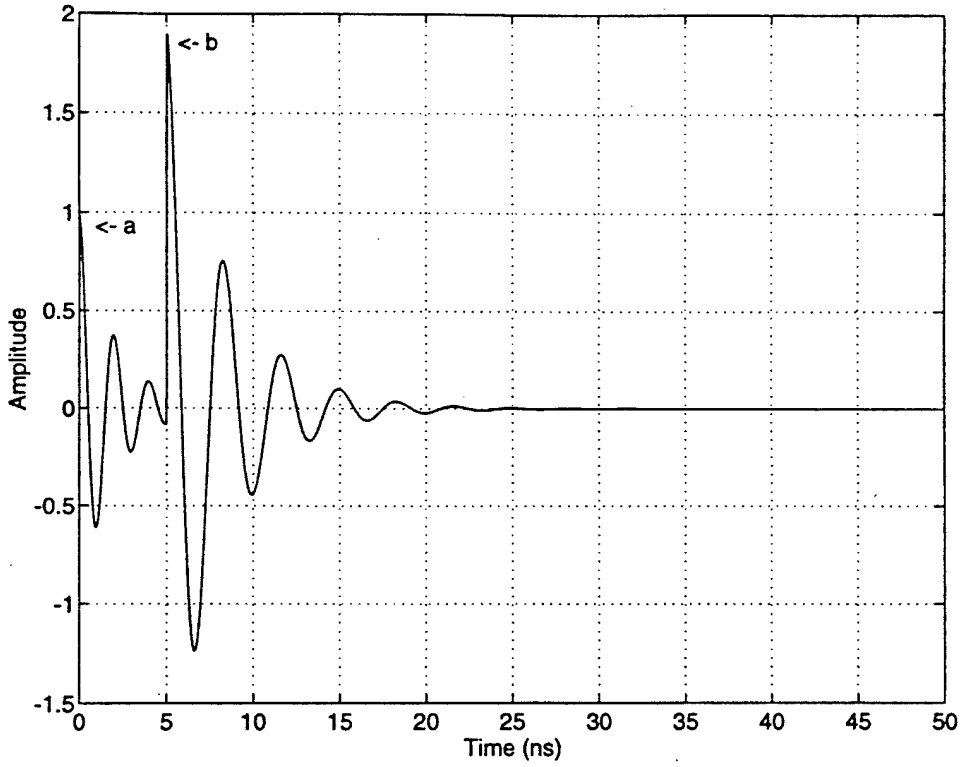

Figure 109 A simulated waveform containing two damped exponentials excited at different time positions. The residue associated with each CNR is 1 and 2, respectively.

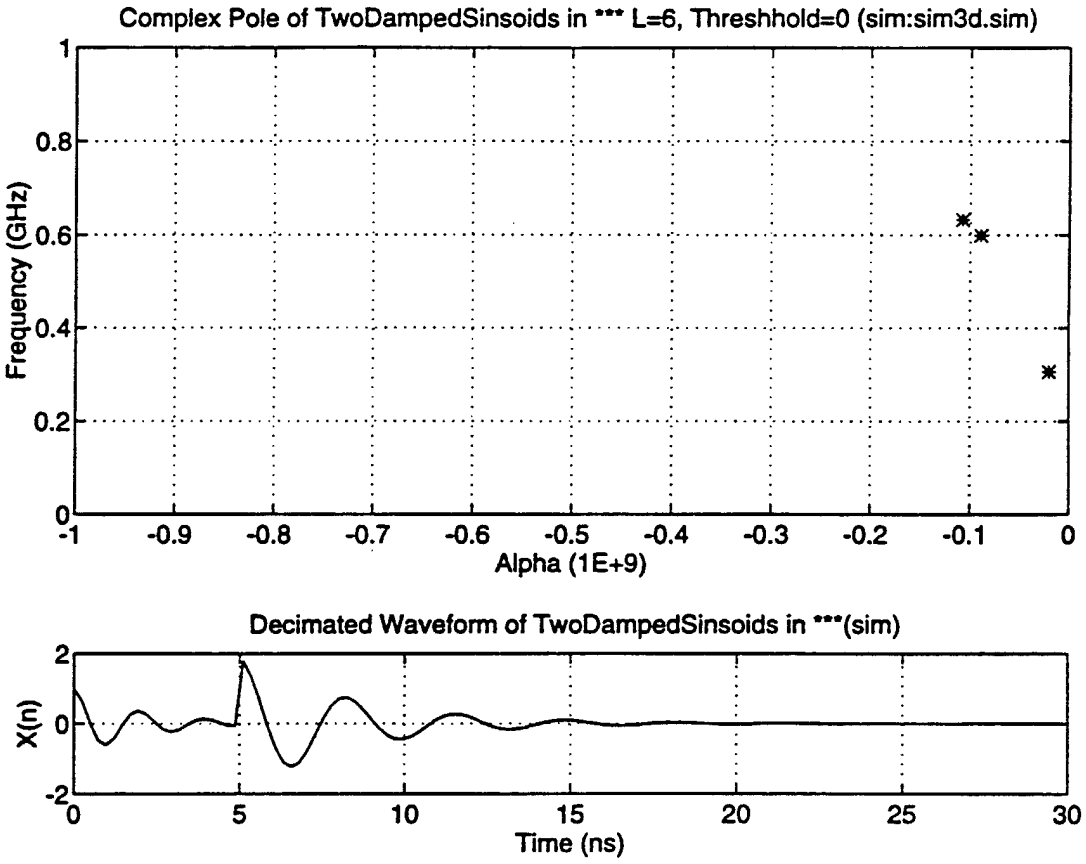

Figure 110 Extracted CNR's using the data segment between 0 ns and 30 ns and the 6th order Prony model.

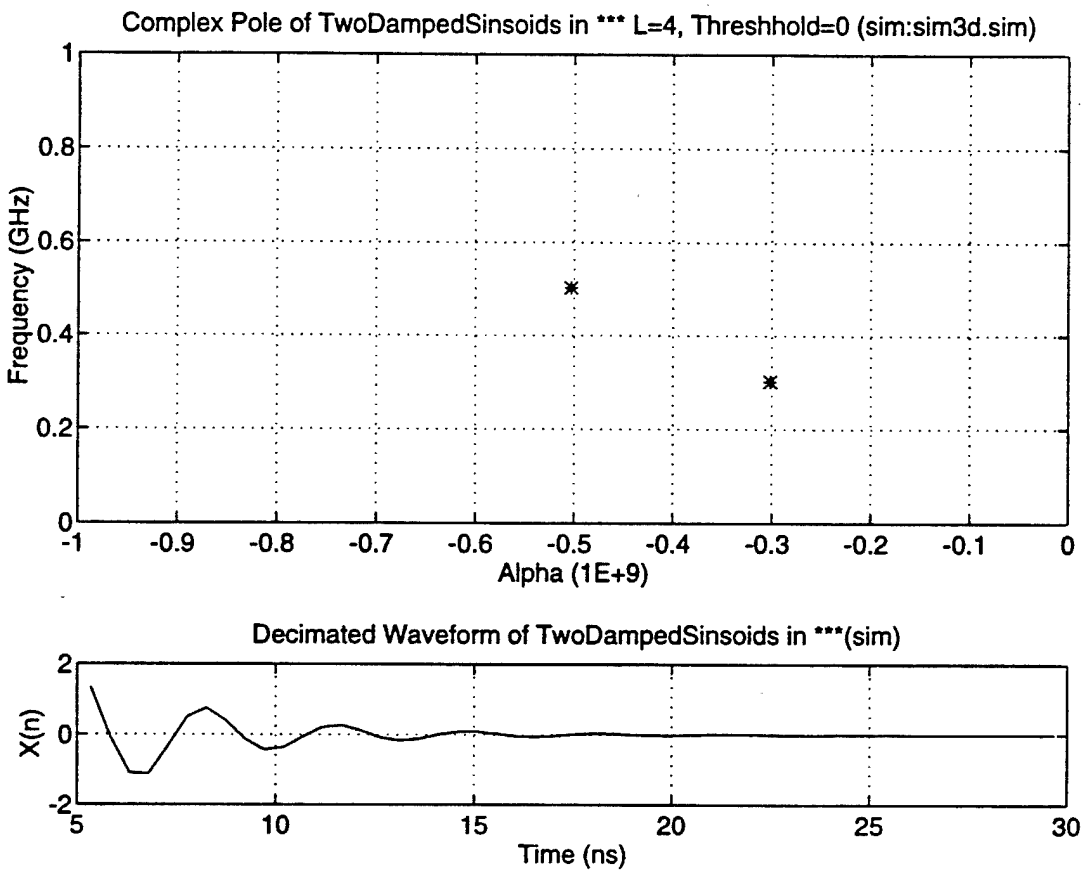

Figure 111 Extracted CNR's using the data segment between 5 and 30 ns and the fourth order Prony model.

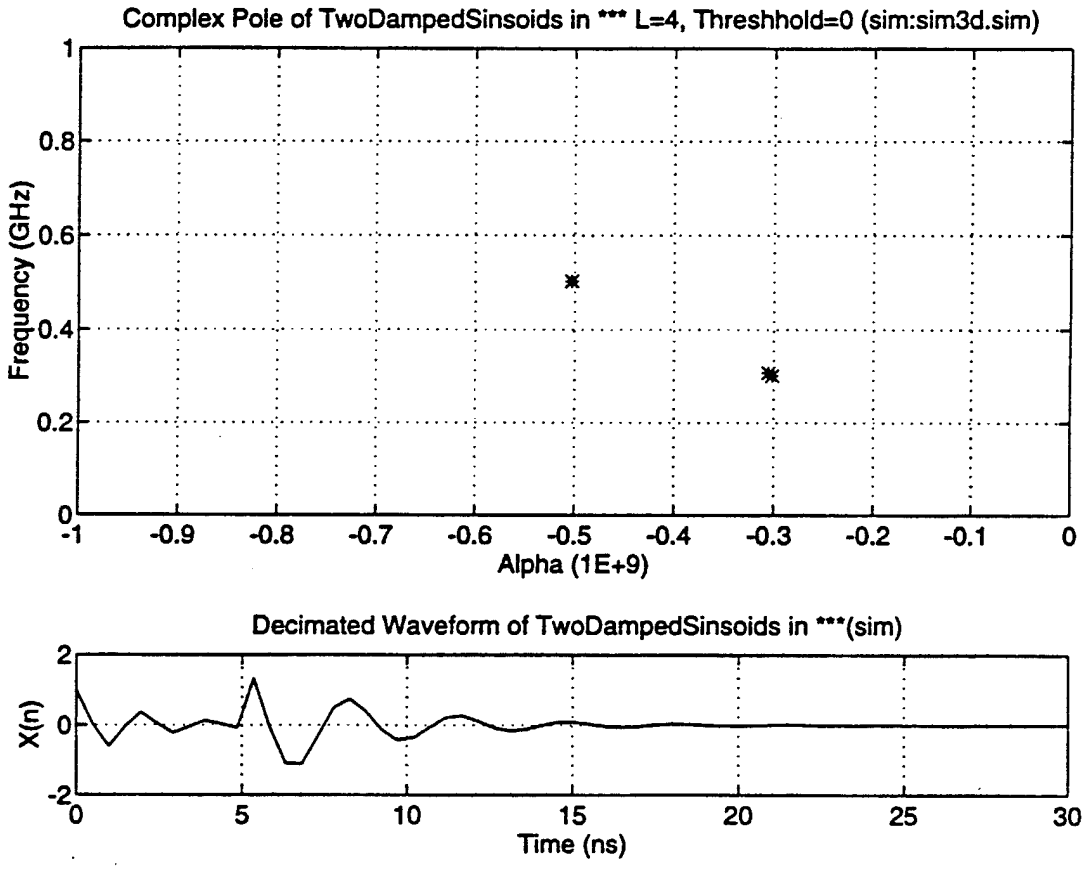

Figure 112 Extracted CNR's for data segment between 0 and 30 ns using 5 ns backward running window and the fourth order Prony model.

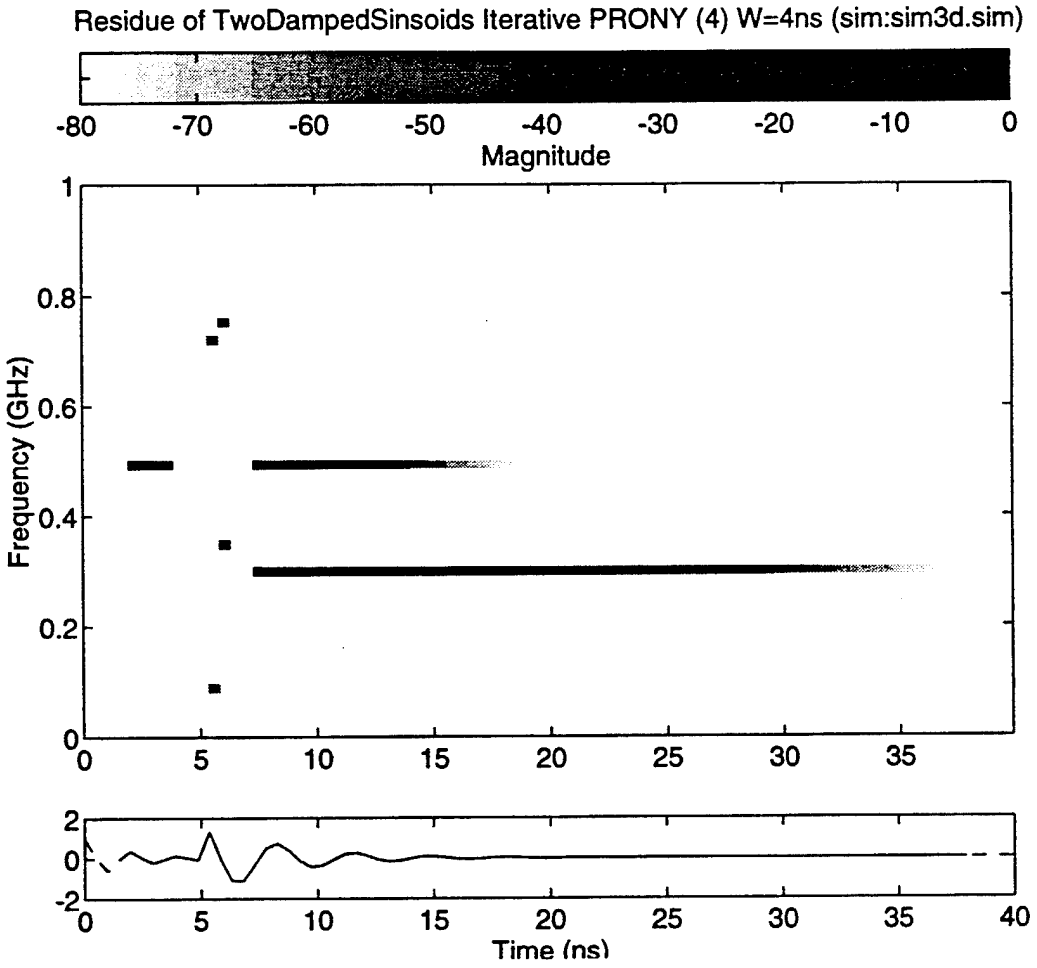

Figure 113 Time-frequency representation of CNR's for data segment between 0 and 30 ns using 4 ns forward running window and 4th order Prony model.

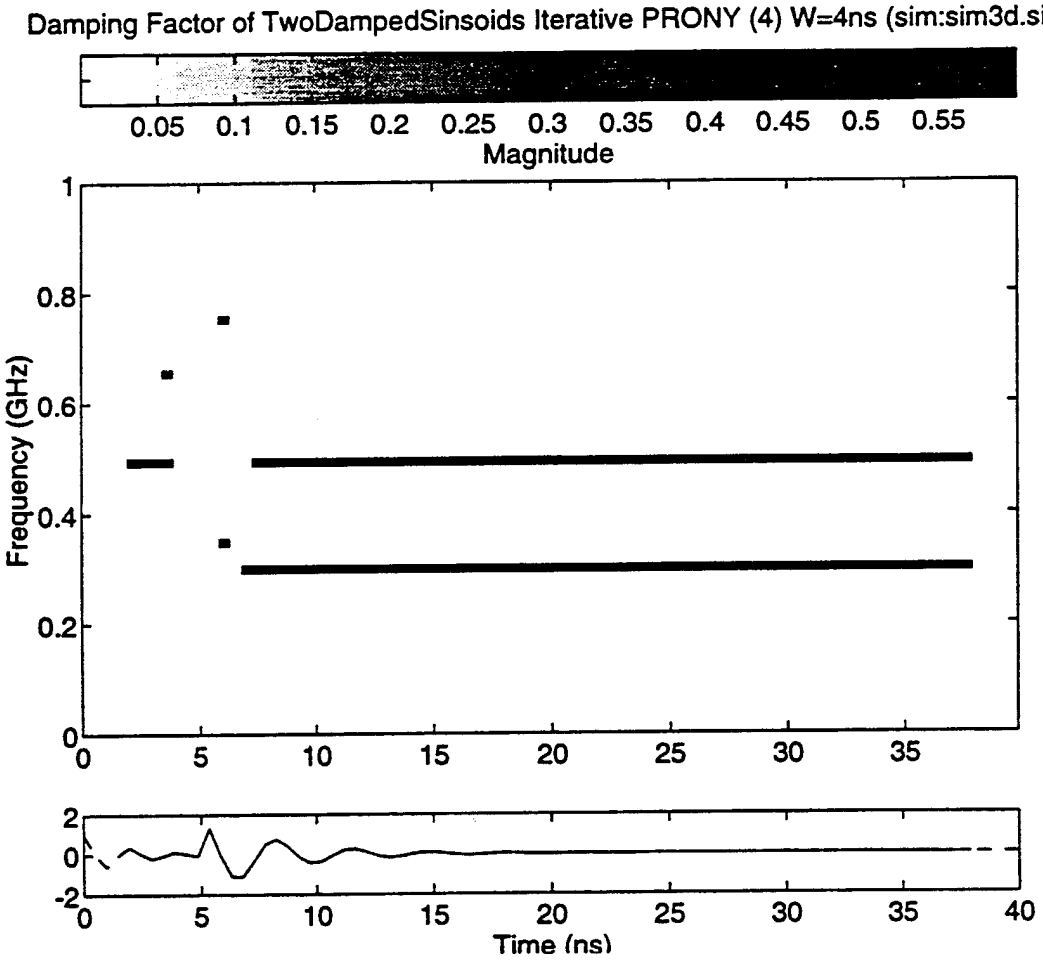

Figure 114 Time-frequency representation of CNR's for data segment between 0 and 30 ns using 4 ns forward running window and 4th order Prony model.

interesting to note that the strength of each resonance decays as time increases, however, the damping factor, which is not time dependent, remains constant.

The Iterative Prony (IP) Method

As discussed in the previous section, the Prony method will fail when there are multiple impulses excited at different time positions. This failure occurs because the model requires all the damped complex exponentials start at time zero. Unfortunately, this assumption cannot be satisfied for multiple targets or for a large target having different natural resonances from different parts of the body. This problem can be partly solved by using the following new technique.

The iterative Prony (IP) method, is designed to improve the performance of the common Prony method (or modified Prony method) in the presence of multiple CNR's from a single target or from multiple targets. It will extract the most dominant CNR, the CNR having the largest residue amplitude, and remove it from the original waveform by subtraction. The new waveform, with its most dominant CNR removed, is then searched for the peak response to determine the new starting point. The data after this new starting point from the new waveform are then used to search for its most dominant CNR. These same procedures are iterated until the number of CNR's found meets the specified model order. The order is often chosen higher than the number of true target CNR's. An energy threshold is then used to select the high energy CNR's as discussed earlier. It is noted that the IP method discussed here processes the whole waveform without using a running window. Of course, both techniques can be combined to deal with long signals.

In order to illustrate this IP method, the same example used in the previous section will be used. Recall that the waveform was composed of two CNR's excited at 5ns time separation. Also recall that the results shown in Figure 110 were incorrect. After using the IP method, it will be shown that both CNR's are correctly extracted. Figure 115 shows the part of waveform to be processed in each iteration. The original waveform is also plotted as a dotted line. The final extracted damping factors and resonance frequencies are shown in

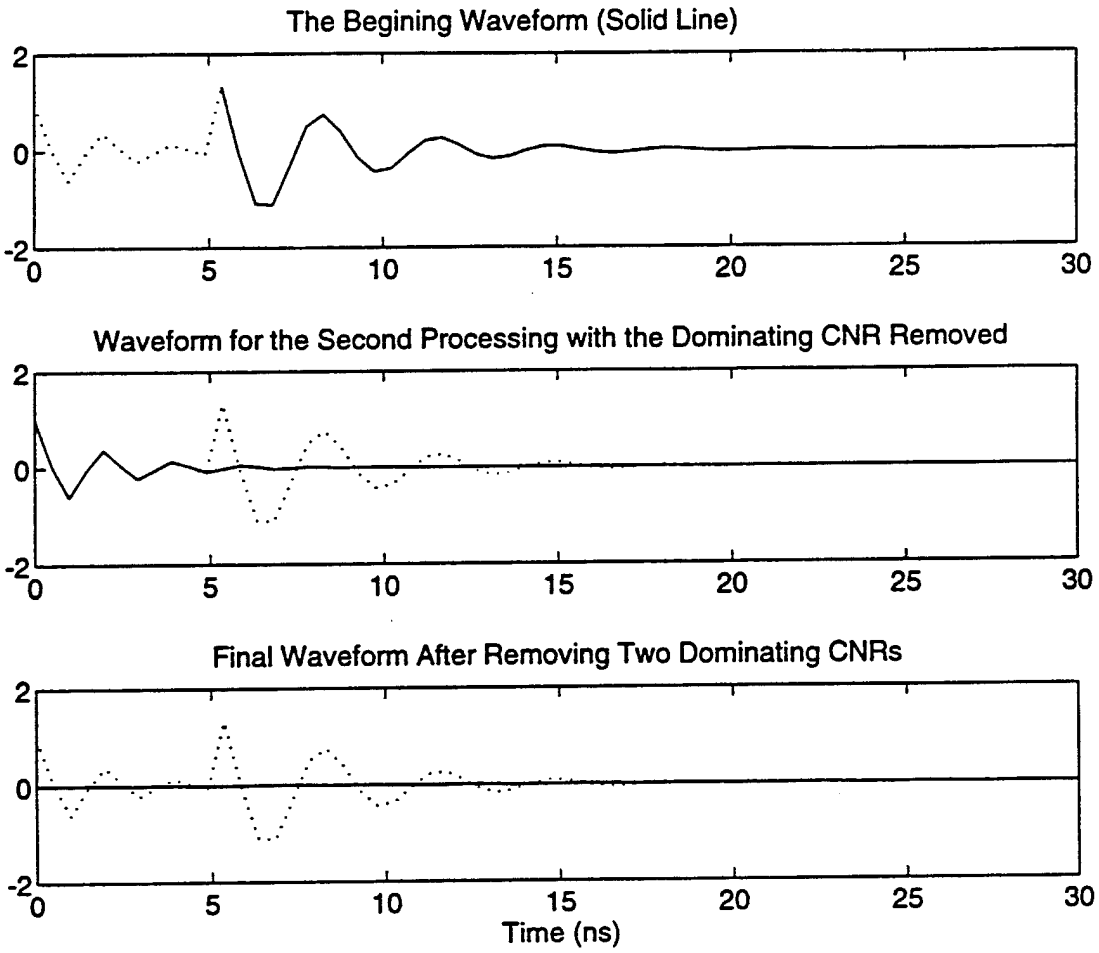

Figure 115 The waveform to be processed in each iteration (solid line) overlayed with the original waveform (dotted line) using the IP method.

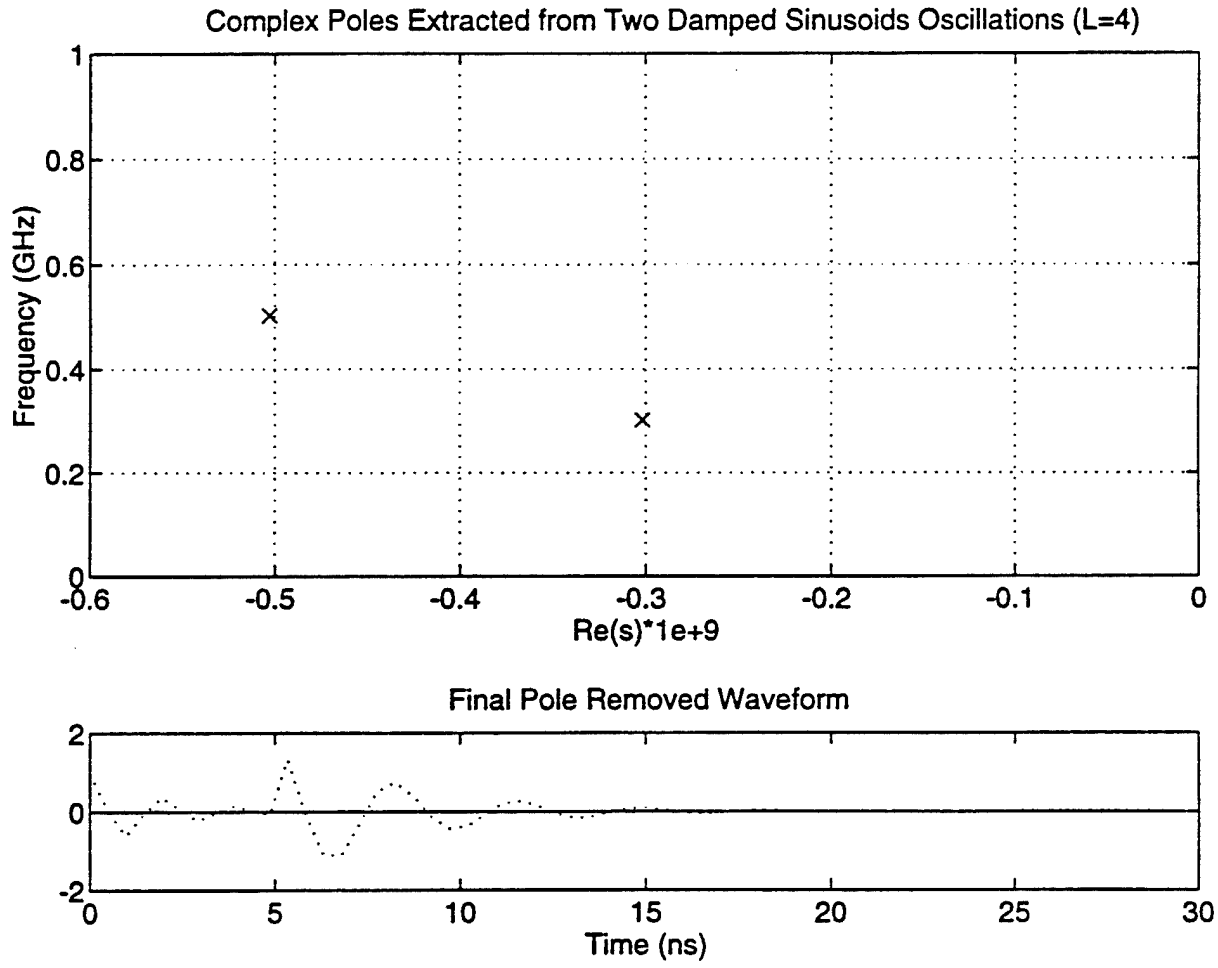

Figure 116 The final extracted CNR's using the IP method.

Figure 116. As one can see, both CNR's have been accurately obtained.

In the previous example, the strongest peak occurs at later time and the whole waveform for the first iteration is dominated by it. This situation occurred by chance. Next, the time position of the two CNR's are reversed to form another new waveform. This case is obviously more challenging because the waveform for the first iteration will start from time zero and contains the second CNR, which is significant in the later time portion. The results are shown in Figure 117 and Figure 118. Indeed, the final waveform is not as clear as the previous case, however, both CNR's are still obtained accurately. As one might expect, if the second CNR has a stronger amplitude then the results will be poorer. In this case, one can start the iteration from the second peak where both CNR's have been excited. This situation was discussed in the previous section.

A very useful new iterative Prony (IP) technique was introduced in this section. The improvement in CNR extraction under multiple impulse situations was illustrated. The IP method can easily be combined with the existing Prony routine and the running window technique.

CNR Resolution

For ideal signals that fit into the Prony model and contain no noise, the extracted poles will be of a fixed point in the complex *Z*-plane, i.e., infinite resolution. If the signal contains white noise, the pole resolution is limited by the variance of the pole position. Statistically, the Cramer-Rao bound, which provides the upper bound of variance for a given model and SNR, can be used to define the resolution. The Cramer-Rao bounds, for pole and residue estimates of damped exponential signals in white noise using the Prony method, have been obtained by Moses [23]. He shows that the variances of the angle, $2\pi f\Delta t$, and amplitude, $\exp(-\alpha\Delta t)$, of each pole or CNR extracted using the modified Prony method are independent. Furthermore, the normalized variances of pole angle and amplitude are equal. This natural bound of angle and amplitude variances in white Gaussian noise determines the resolution of the extracted poles using the Prony method. From the same study, it was shown that the

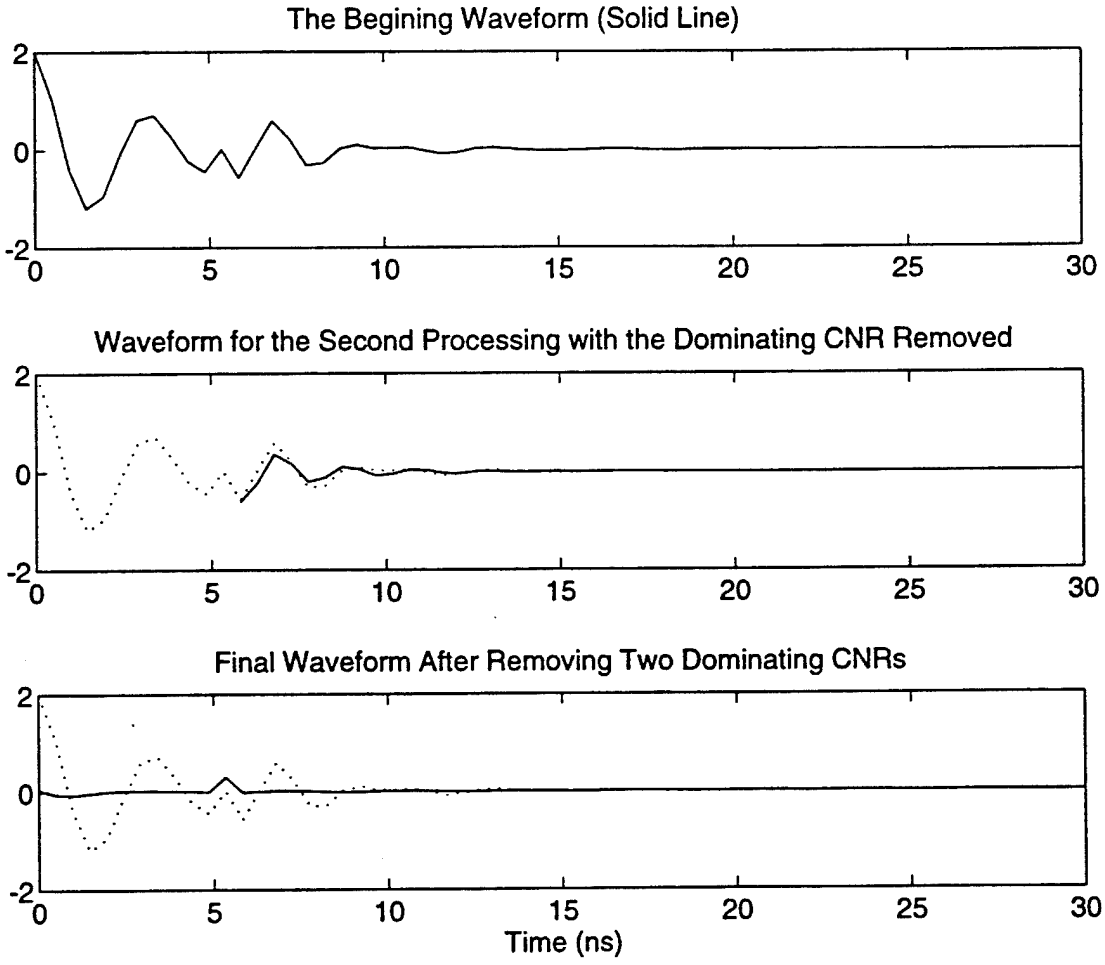

Figure 117 The waveform to be processed in each iteration (solid line) overlayed with the original waveform (dotted line) using the IP method.

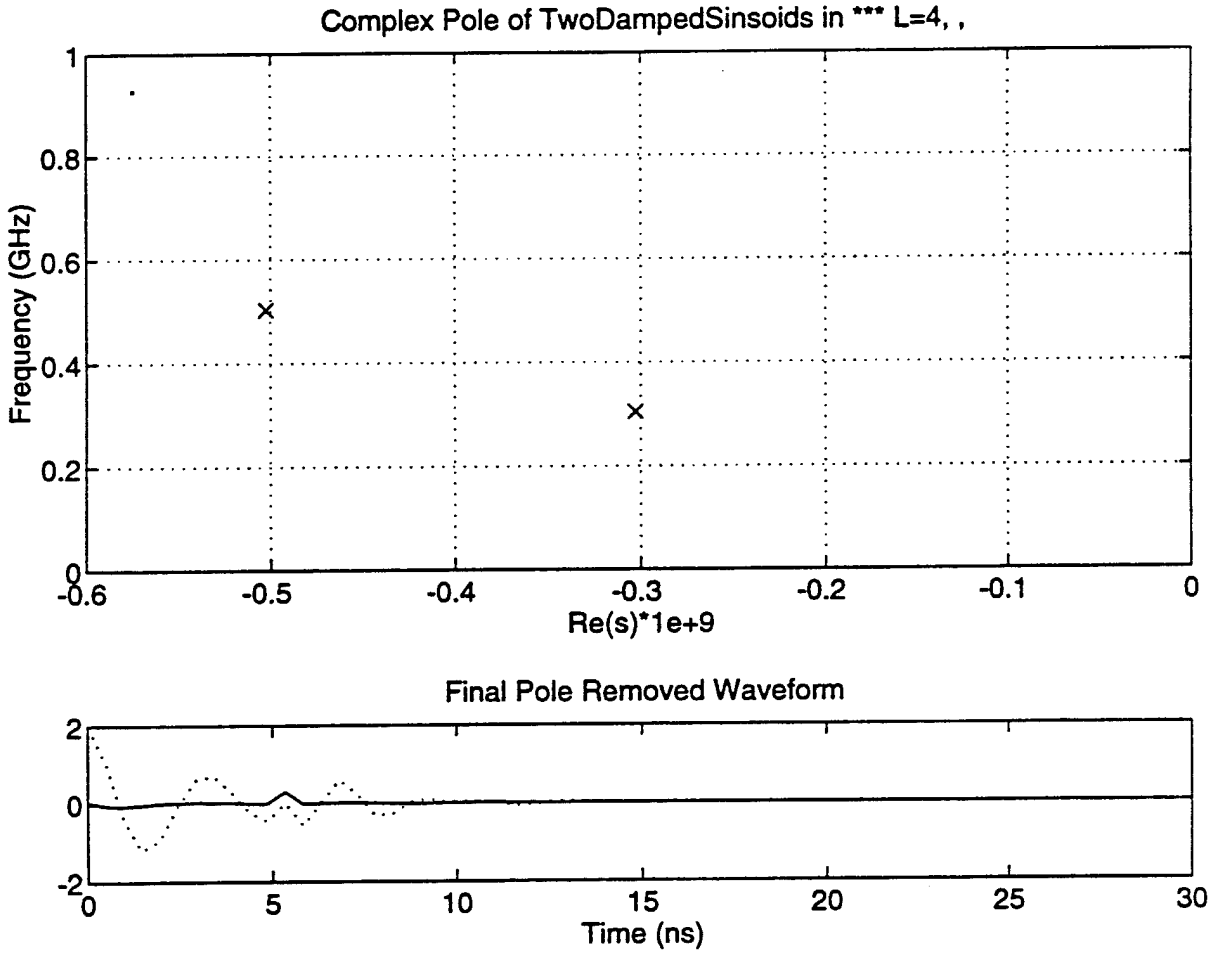

Figure 118 The final extracted CNR's using the IP method.

resolution is higher for pole locations close to the unit circle $|Z|=1$. But, it should be noted that since the combination of extraneous poles and noise will produce many poles near to the unit circle , true poles are difficult to identify in this region.

Summary

In this chapter, CNR extraction techniques have been closely examined. The basic formulation were given in both matrix and difference equation forms. Some difficulties related to the Prony method, such as under-sampling, model order selection, multiple delayed signals, and noise effects, have been studied. New techniques have also been introduced to overcome some of the above difficulties. The final modified Prony subroutine appears to be able to work under less restrictions and give more accurate and stable results.

6.3 Time-Domain Discrimination Using Complex Natural Resonances

Prediction of Waveform Using CNR Information

It is well known that the transient response of a linear, time-invariant lumped-constant circuit can be obtained from its singularities and the associated complex residues by using the SEM:

$$x(t) = \sum_k c_k e^{s_k t}, \quad t \geq 0 \tag{93}$$

where s_k is the singularity in the complex s-plane and c_k is the complex residue associated with each singularity. In general, each singularity can be expressed as $\alpha + j2\pi f$, which corresponds to a simple pole in the s-plane. For a realizable and stable system, α is non-positive and the number of poles is finite. Thus, equation (93) is equivalent to saying that the impulse response can be expressed as a summation of a finite number of exponential sinusoids.

For discrete data that are sampled from the continuous data by satisfying the Nyquist criteria, equation (93) can be rewritten as

$$x(n) = \sum_{k=1}^{N} c_k z_k^n \tag{94}$$

where $z_k = \exp\{s_k \Delta t\}$ and Δt is the sampling time step. It is easy to show that a system characterized by the above equation has the following characteristic polynomial

$$a_0 + a_1 z^{-1} + a_2 z^{-2} + \cdots + a_N z^{-N} = 0 \tag{95}$$

where $a_0 = 1$ and $z_1, z_2, \ldots, z_N$ are the N complex roots. Because this is a real variable system the roots are in complex conjugate pairs. By applying the inverse Z-transformation to the above equation, one can show that the $x(n)$ can predicted from past values. That is

$$x(n) = -\sum_{k=1}^{N} a_k x(n-k). \tag{96}$$

Note that one can also derive the above equations in a reversed fashion by starting from the above difference equation as done in references [8] and [10].

Predictor

Equation (94) can be solved to find the poles s_k and the residues c_k by using the Prony method. It should be noted that special treatment and some modifications need to be incorporated in the Prony method for practical situations such as noisy signals, unknown model order, and multiple targets. These details have been discussed previously. For now, we will assume that the exact poles have been obtained and stored in a data base.

The next step is to find the coefficients $\{a_1, a_2, \ldots, a_N\}$. This search can be easily performed using equation (95). Once the coefficients are found, one can use equation (96) to predict (or extrapolate) the impulse response for the later time from the measured early time data. Equation (96) will be called the *predictor* of the system and will be actually used to construct the waveform from known complex poles.

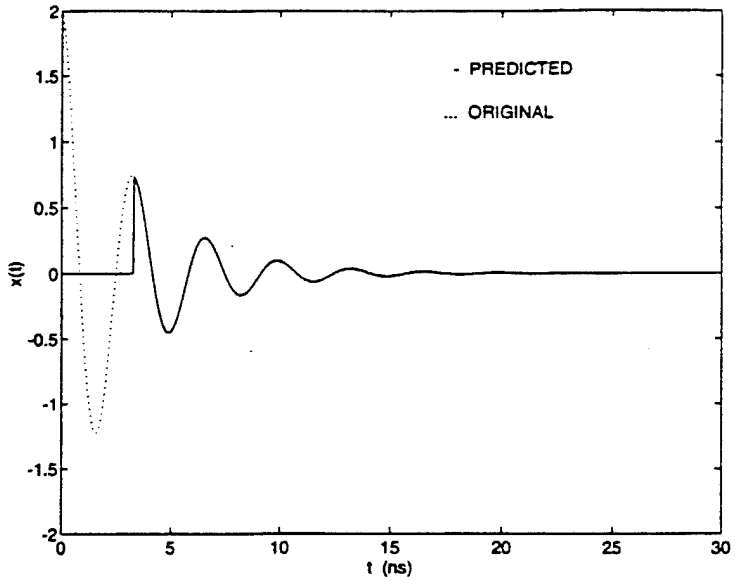

Figure 119 Comparison between the predicted and original data. The data contains poles at (-0.3e9, 0.3e9).

Figure 119 compares the predicted waveform (solid line) and its original waveform (dotted line) by using the technique described above. One can see that the original data have been correctly predicted using the early time data points (non-overlapping section). The waveform was generated using only one CNR pair. It should be noted that we have assumed a noise-free environment and the order of the system is also known *a priori*.

Correlator for Target Identification

The predictor discussed in the previous section can be used to reconstruct a target waveform using target CNR's and early time data. The reconstructed waveform can then be compared with the measured waveform for target discrimination. A time-domain target discrimination technique to be discussed here was developed by Chan et al [13]. The discrimination of targets is based on a single number, the correlation coefficient, defined as

$$\rho(T) = \frac{\sum_{n=0}^{M} 2x_p(t_s+nT)\cdot x_m(t_s+nT)}{\sum_{n=0}^{M} (x_p^2(t_s+nT) + x_m^2(t_s+nT))} \tag{95}$$

where x_p and x_m are the predicted and measured data in the overlapping time section. Note that in the following sections the ''measured waveform'' is actually a simulation rather than a real measurement, however, for discussion purposes, we will still refer to the simulated waveform as a ''measured waveform''. The start time, t_s is where the overlapping begins and is normally chosen to avoid significant forced response. The last time point, t_s+MT, is chosen such that the signal to noise ratio (SNR) is still good enough to provide accurate prediction (usually above 15 dB). Details regarding the choice of starting and ending points are discussed later. The parameter T is the time step used to reconstruct the data from a known CNR. Note, that for perfect prediction where x_m equals x_p , $\rho(T)$ equals 1 for any T. The denominator is the trace of the covariance matrix and the numerator is the sum of the diagonal terms in the covariance. ρ is a measure of similarity between two set of data. It is more obvious if one uses 1-ρ as a measure of the difference between measured and predicted waveforms then

$$1 - \rho(T) = \frac{\sum_{n=0}^{M} (x_p(t_s+nT) - x_m(t_s+nT))^2}{\sum_{n=0}^{M} (x_p^2(t_s+nT) + x_m^2(t_s+nT))} \tag{96}$$

The behavior of the above correlator function and the effect of random white noise will be discussed in the next few sections. It will be shown that this correlator can be used as a

discriminator for target identification under certain conditions. This correlator is less sensitive to the variance of the damping factors and is affected by the presence of noise.

Effect of White Noise

Let the measured waveform, the true target response and the random white noise (mean=0 and variance=σ^2) be denoted as $x_m(i)$, $x_t(i)$, and $n(i)$, respectively. Also define the mean value of an N-point discrete random variable $f(i)$ to be

$$\mathrm{E}[f(i)] = \frac{1}{N}\sum_{i=1}^{N} f(i). \tag{97}$$

Then one immediately knows that E[n]=0 and E[n^2]=ρ^2. Assuming that the target contains $L/2$ complex conjugated pole pairs, $\{(z_1, z_1^*), \ldots, (z_{L/2}, z_{L/2}^*)\}$, and using equation (92), one can express $x_t(i)$ and $x_m(i)$ as

$$x_t(i) = \sum_{k=1}^{L/2} (c_k z_k^i + c_k^* (z_k^*)^i). \tag{98}$$

$$x_m(i) = x_t(i) + n(i), \tag{99}$$

where i=1, 2, ..., N. The predicted waveform, $x_t(i)$ calculated from the predictor defined in equation (94) can then be expressed as

$$x_p(i) = x_t(i) - \sum_{k=1}^{L} a_k n(i-k), \quad i=1,2,...,N, \tag{100}$$

where $\{a_k\}$ are the coefficients of the characteristic polynomial defined in equation (93). The correlation coefficient, ρ, can then be obtained using equation (95) and the following relations:

$$|z_k^i| = 1 \tag{101}$$

$$i \neq j,\ \mathrm{E}[n(i)n(j)] = 0, \tag{102}$$

$$k \neq l,\ \mathrm{E}[z_k^i z_l^i] = 0, \tag{103}$$

$$\mathrm{E}[z_k^i (z_l^*)^i] = 0, \tag{104}$$

$$\mathrm{E}[n(i)n(i)] = \sigma^2, \tag{105}$$

$$\mathrm{E}[z_k^i (z_k^*)^i] = 1. \tag{106}$$

After some manipulation, the final correlation coefficient is

$$\rho = \frac{4\sum_{p=1}^{Lf2} |c_p|^2}{4\sum_{p=1}^{Lf2} |c_p|^2 + \sigma^2\left(1+\sum_{p=1}^{L} a_k^2\right)} \tag{107}$$

For a noise-free situation, $\sigma^2=0$, ρ equals 1, and perfect discrimination is obtained.

The same waveform, as shown in Figure 119 in the presence of different levels of random white noise, is used to study the effect of noise on target discrimination using the correlator defined previously. The numerical results are plotted in Figure 120. The numerical result shows that the presence of white noise deteriorates the discrimination ability significantly. Therefore a noise reduction process should be applied before the discrimination process. Note that the correlation coefficient is calculated for different sampling rates shown on the horizontal axis. For low sampling rates, the mean value calculation approximated by equation (97) has not converged.

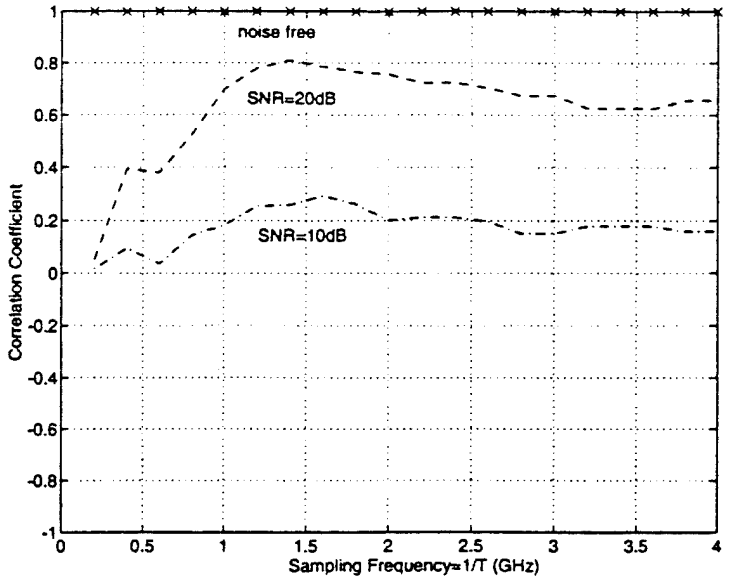

Figure 120 Discrimination determination in the presence of random white noise.

Choice of Sampling/Prediction Period, T

In a previous section, it was assumed implicitly that the data were sampled and predicted using the proper time step, T. In equation (95) the correlation coefficient, ρ, has been defined as a function of T, however, it is obvious that the sampling period T will affect the correlation coefficient. The choice of T is very important to ensure the optimum performance of the correlator and hence make a correct discrimination.

We will start our analysis with the two examples shown in Figure 121 where the CNR's of the desired waveform matches the CNR's of the measured data. For simplicity, only a single resonance is used in each case. The sampling/prediction rate varies from 250 MHz to 8000 MHz for both cases. Also note that, a noise-free environment will be assumed hereafter unless otherwise stated.

First of all, in order to represent the information contained in the waveform without distortion, the sampling rate, $f_t=1/T$, must satisfy the Nyquist sampling criteria set by the maximum frequency contained in the ''measured'' waveform. If the data are sampled and predicted at a rate lower than the minimum sampling rate, aliasing will occur in the frequency spectrum and the resonance information will be distorted. The minimum

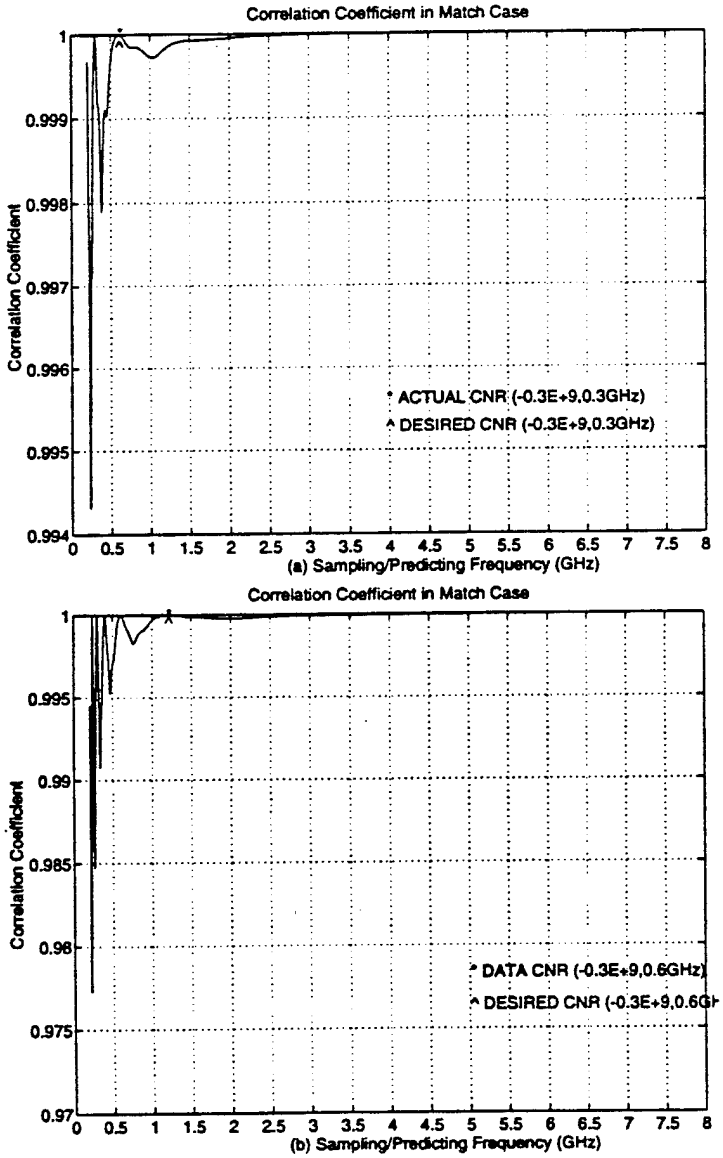

Figure 121 The correlation coefficient of a single target discrimination for different sampling/predicting period, T. (a) resonance frequency=0.3 GHz, (b) resonance frequency=0.6 GHz.

sampling/prediction rate set by the resonance contained in the measured data (''*'' mark) and the desired resonance (''^'' mark) are the same and is 0.6 GHz for case (a) and 1.2 GHz for case (b). To the left of the ''*'' mark, ρ oscillates rapidly and one should not use under-sampled data for discrimination. It is interesting to find that $\rho=1$ right at the mark position for both cases. For frequencies greater than f_t (over-sampled), ρ deviates from 1 and then rises monotonically to unity for the highly over-sampled situation. For the highly over-sampling case, Δt becomes very small and thus the poles in the complex Z-plane are separated by a very small angle, $f\Delta t$ (degrees), where f is the natural resonance frequency contained in the waveform. This concept is illustrated in Figure 122. Also note that all the poles move toward the $z=1$ point as the sampling rate keeps increasing. This movement results in an unresolvable situation using the correlator and the value of ρ will approach 1. This ambiguity is due to the resolution limitations of the chosen correlator, as will be discussed. Therefore, the highly over-sampled region in Figure 122 should also be avoided for discrimination. It is important to note that although the value of ρ varies even for this matched discrimination, the global minimum values are still very close to 1! The following two examples will allow us to study the mismatched or incoherent situation when the measured data does not contain the desired resonances.

Figure 123 (a) and (b) plot ρ as a function of sampling/predicting rate for false target discrimination. The minimum rate set by the desired target resonance frequency and by the actual resonance contained in the measured data is again marked by ''^'' and ''*'', respectively. At the ''*'' positions, ρ has reached its global minimum value for both cases. However, the minimum values may be different and are functions of the signal amplitude, degree of coherence, length of data used in summation, and other variables to be explored. At the position marked ''^'' ρ reveals its local minimum for each case. Some other local minima do appear in both cases but they have not been found useful in the current target discrimination process. In real applications, the resonances contained in the measured time-domain data are usually unknown but the desired resonances are usually known *a priori* in the searching and discrimination process.

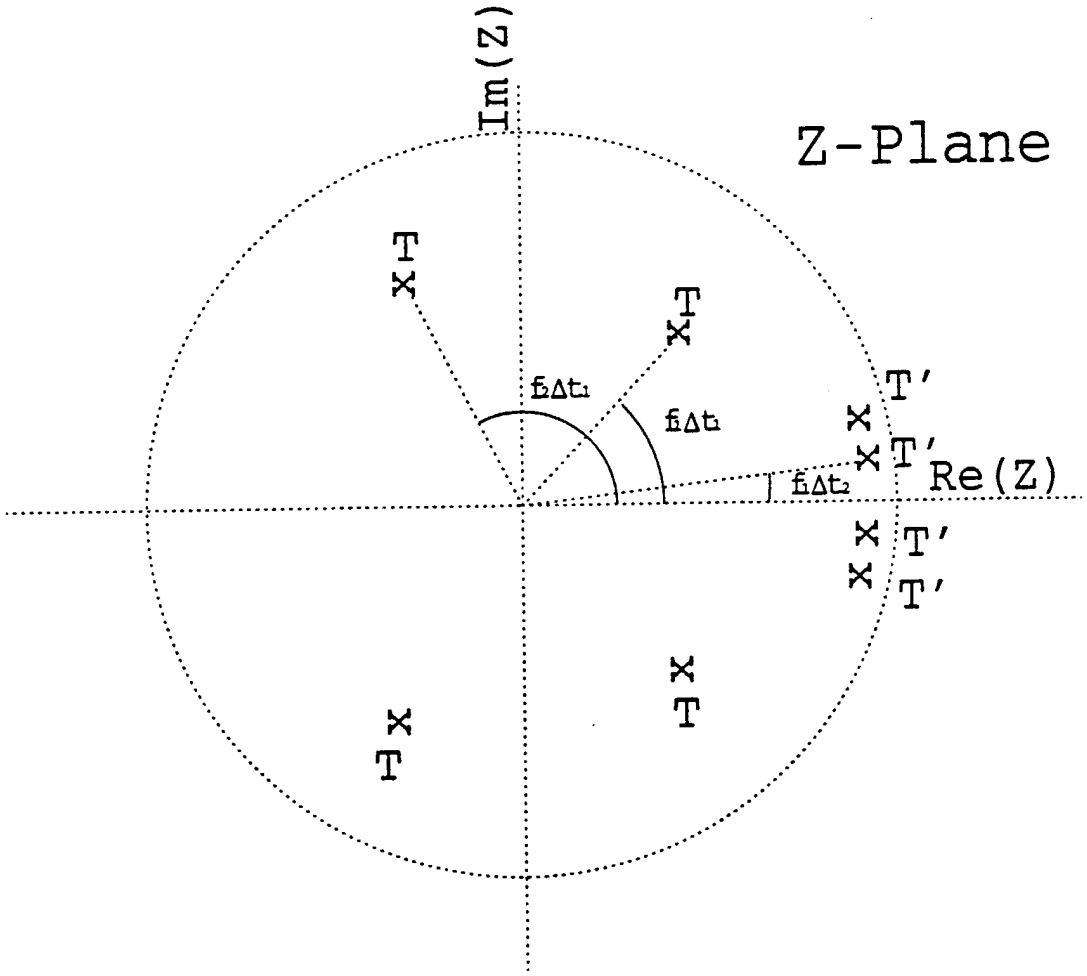

Figure 122 The movement of pole positions in the complex Z-plane for different sampling rates.

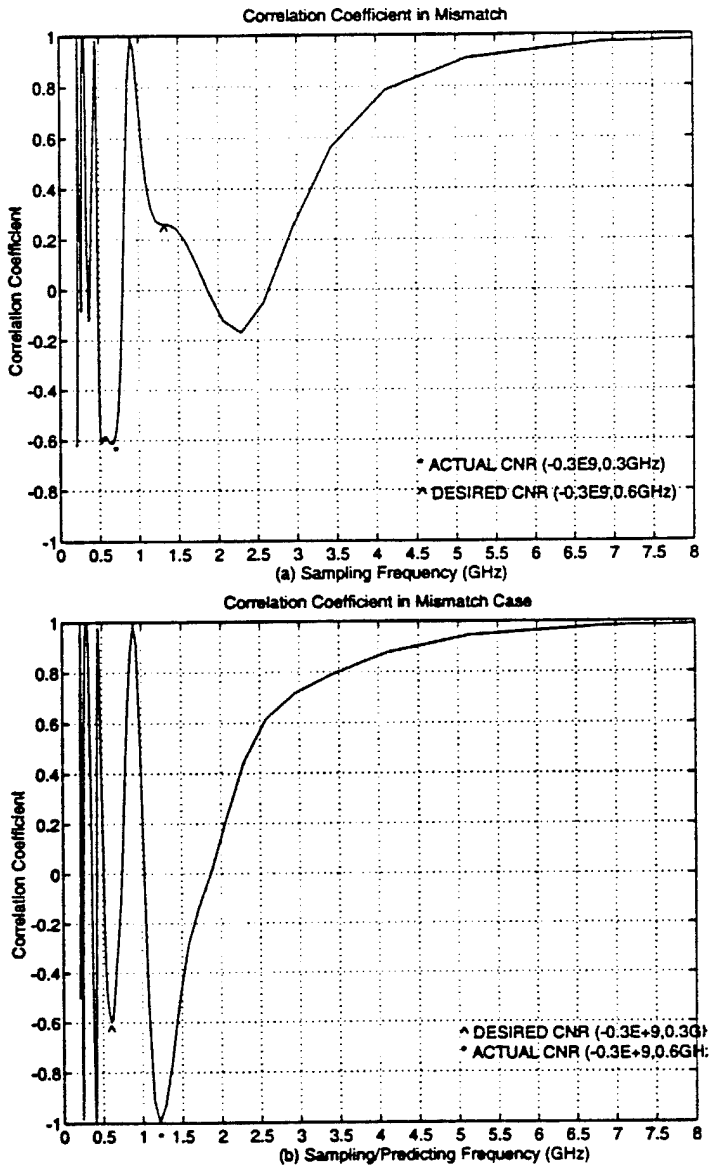

Figure 123 The correlation coefficient for incoherent target discrimination for different sampling/predicting periods, T. The measured and desired CNR in the second quadrature of complex frequency plane are also shown in parentheses.

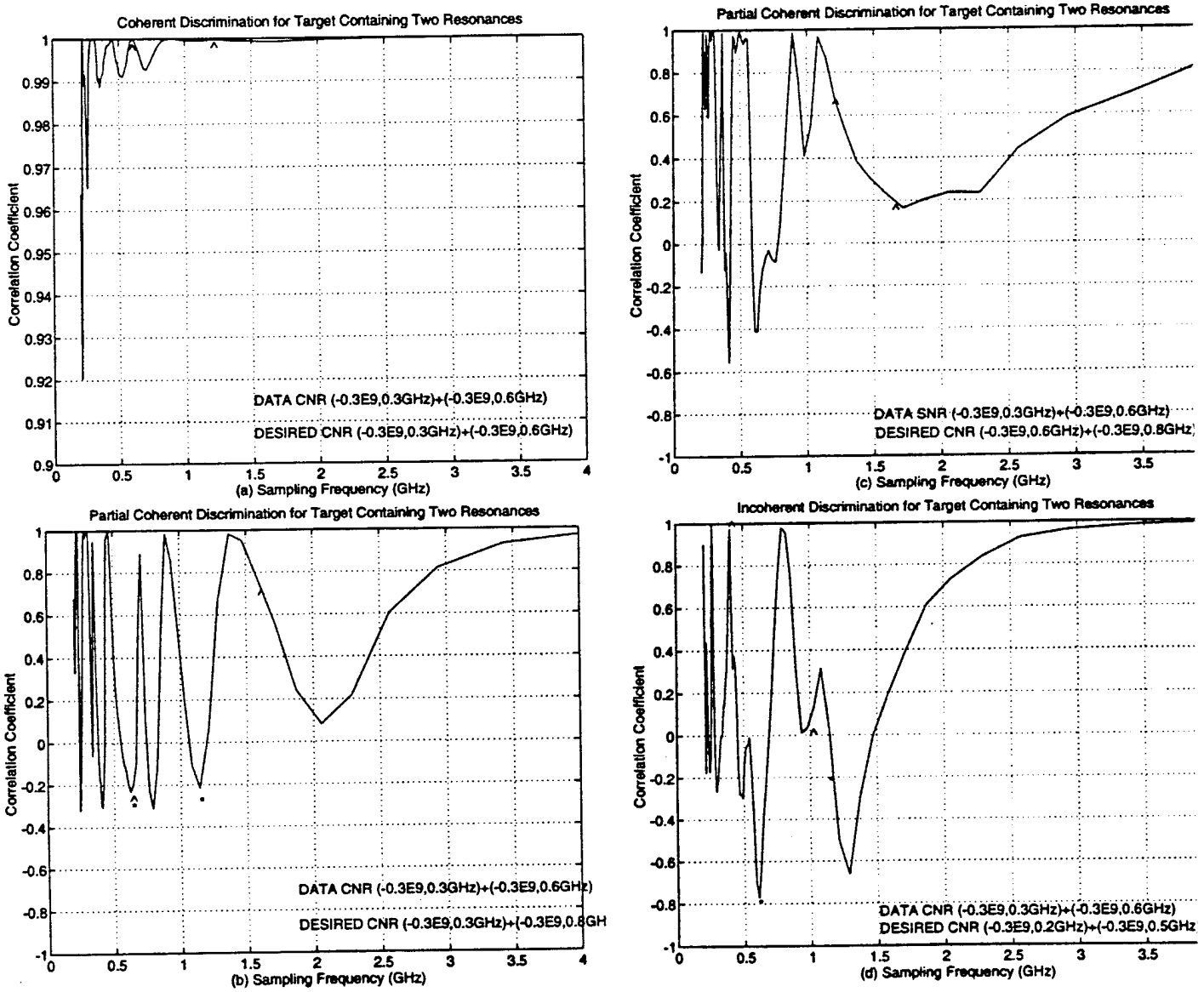

Figure 124 The correlation coefficient for target discrimination with two resonances. The measured and desired CNR's in the second quadrant of complex frequency plane are also shown in the parentheses.

Next, we will consider the situation when the desired target contains more than one resonance. We also assume that the measured waveform contains the same number of resonances; a more complicated case will be discussed in the next Section, "Multiple Target Discrimination". Let us examine the following four cases shown in Figure 124. Note that only in case (a) are the resonances of the desired target the same as those contained in the measured waveform, thus the high correlation coefficient values obtained in this case. The minimum sampling rates for each resonance of the desired target are also marked with "^". Note how ρ is close to 1 at both mark positions!

For the other cases (b) and (c), the desired target and the measured waveform have only one common resonance. One can observe the large oscillation in the calculated coefficient for each case. If we focus our attention on the coefficients calculated at the sampling/predicting rate marked by "^" and pick the minimum between them, one will get a value much less than 1 (e.g. (b) $\rho_{\min}\hat{} \approx$ -0.22, (c) $\rho_{\min}\hat{} \approx$ -0.20).

In the last case, the target and the measured data do not have any common resonance and one can find that (b) $\rho_{\min}\hat{} \approx 0.05$, which is again is much less than 1!

From the above observations, the following steps can be used with the correlator for target discrimination. It should be noted that these rules apply only to the "*N*-to-*N*" case where both the desired target and the measured data contain the same number of resonances. The rules are

1. set the limits of the sampling/predicting rate to be twice each resonance frequency of the desired target,

2. calculate the correlation coefficients for each different sampling/predicting rate chosen in the previous step and pick the minimum value among these coefficients,

3. set a threshold value, ρ_t, such that $\rho > \rho_t$ confirms the presence of the target.

Multiple Target Environment

In this section, we will discuss the discrimination of a desired target in the presence of other undesired targets. For simplicity, a noise free situation will be assumed throughout this section. The theoretical derivation is very similar to that in the previous section with the noise, $n(i)$ replaced by the undesired target responses, $x_c(i)$. Assuming that $x_c(i)$ has the SEM type representation given below

$$x_c(i) = \sum_{k=L/2+1}^{M/2} (c_k z_k^i + c_k^*(z_k^*)^i). \tag{108}$$

where $i=1, 2, \ldots, N$ and the even number M ($>L$) is the total number of complex poles contained in the data, the total measured waveform is then

$$x_m(i) = x_t(i) + x_c(i) = \sum_{k=1}^{L/2} (c_k z_k^i + c_k^*(z_k^*)^i) + \sum_{k=L/2+1}^{M/2} (c_k z_k^i + c_k^*(z_k^*)^i). \tag{109}$$

The poles in the set $\{(z_1, z_1^*), \ldots, (z_{L/2}, z_{L/2}^*)\}$ correspond to the poles of the desired target whereas the poles in the set $\{(z_{L/2+1}, z_{L/2+1}^*), \ldots, (z_{M/2}, z_{M/2}^*)\}$ correspond to the poles from the undesired targets. Because the desired target is the same as before $\{a_1, \ldots, a_L\}$ are still the same real coefficients of the characteristic equations with the roots corresponding to the desired target's poles and

$$-\sum_{k=1}^{L} a_k z_p = 1, \quad \text{for } p=1, 2, \cdots, L/2. \tag{110}$$

The predicted waveform, x_p, can then be found to be

$$x_p(i) = x_t(i) - \sum_{k=L/2+1}^{M/2} (c_k z_k^i \sum_{l=1}^{L} a_l z_k^{-l} + c_k^*(z_k^*)^i \sum_{l=1}^{L} a_l (z_k^*)^{-l}). \tag{111}$$

Note that the relations listed in equation (101) still hold for all the poles. It is not hard to show that the resultant correlation coefficient is

$$\rho = \frac{2\sum_{p=1}^{L/2} |c_p|^2 + \sum_{p=L/2+1}^{M/2} |c_p|^2 (\beta_p + \beta_p^*)}{2\sum_{p=1}^{L/2} |c_p|^2 + \sum_{p=L/2+1}^{M/2} |c_p|^2 (1 + |\beta_p|^2)}, \tag{112}$$

where

$$\beta_p = -\sum_{k=1}^{L} a_k z_p^{-k}. \tag{113}$$

Because

$$|1 - \beta_p|^2 \geq 0, \tag{114}$$

then

$$1 + |\beta_p|^2 \geq \beta_p + \beta_p^* . \tag{115}$$

That is, $\rho \leq 1$ in equation (112). The equality occurs at $\beta_p = 1$, which from equation (113) shows that the extra poles also satisfy the forward prediction equation obtained from the desired poles. This, in turns, implies the $M=L$ situation. From (112), one can clearly see that the presence of other resonances may significantly reduce ρ from unity and thus degrade the ability to discriminate the target. If the signal strength of the extra resonances is weak, it is still possible to perform the target discrimination but with lower sensitivity. This fact is further illustrated by the example shown in Figure 125, in which the resonance (-0.3E+9, 0.3 GHz) was to be discriminated in the presence of other resonances. The other resonances are (-0.3E+9, 0.6 GHz) (dashed line) and (-0.3E+9, 0.1 GHz) + (-0.3E+9, 0.7 GHz) (dash-dot line). The value of ρ at 0.6 GHz sampling/predicting rate is only about 0.05, which is likely to be below the threshold and the target will not be detected.

Resolution and Sensitivity

In practical applications, the waveform can neither be measured nor processed without any error. The measurement error will result in pole position errors in the complex frequency plane, or Z-plane. Therefore, it is necessary to know how this kind of error will affect target discrimination performance. It is more convenient to study this in the complex Z-plane because the frequency is normalized to the sampling rates. The amplitude and frequency variations in the waveform are related to the radial length and the angle of the complex pole on the Z-plane. For simplicity, the radial length error and the angle error of the pole position will be treated as independent variables and discussed separately. Figure 126 (a) plots the degradation of correlation due to the frequency error (or angle error). If the discrimination threshold is set at 0.9, then the allowance for frequency error is approximately ± 20 percent!. It is interesting to see that at ± 30 degree angle error the correlation coefficient is zero. Therefore the width of the peak is about 60 degrees. This plot indicates that the correlator is not so sensitive and the discrimination resolution is not very high. This plot is particularly helpful in choosing the threshold level. Figure 126 (b) plots the

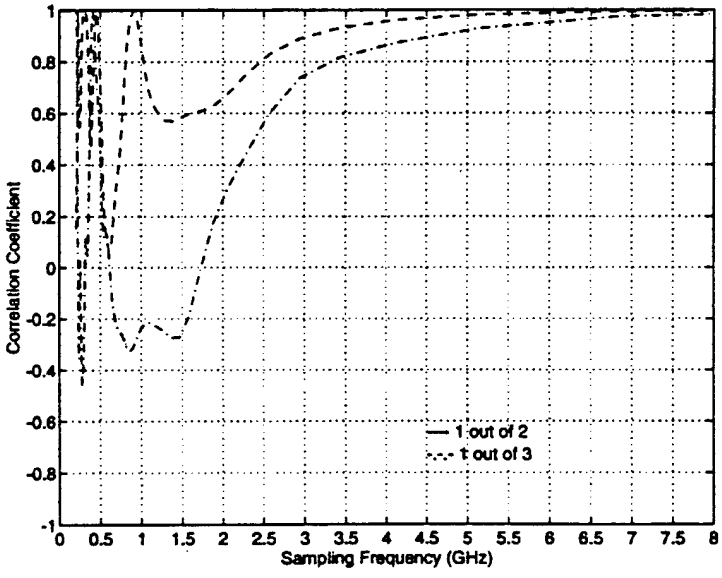

Figure 125 The degradation of correlation coefficient caused by the existence of other resonances.

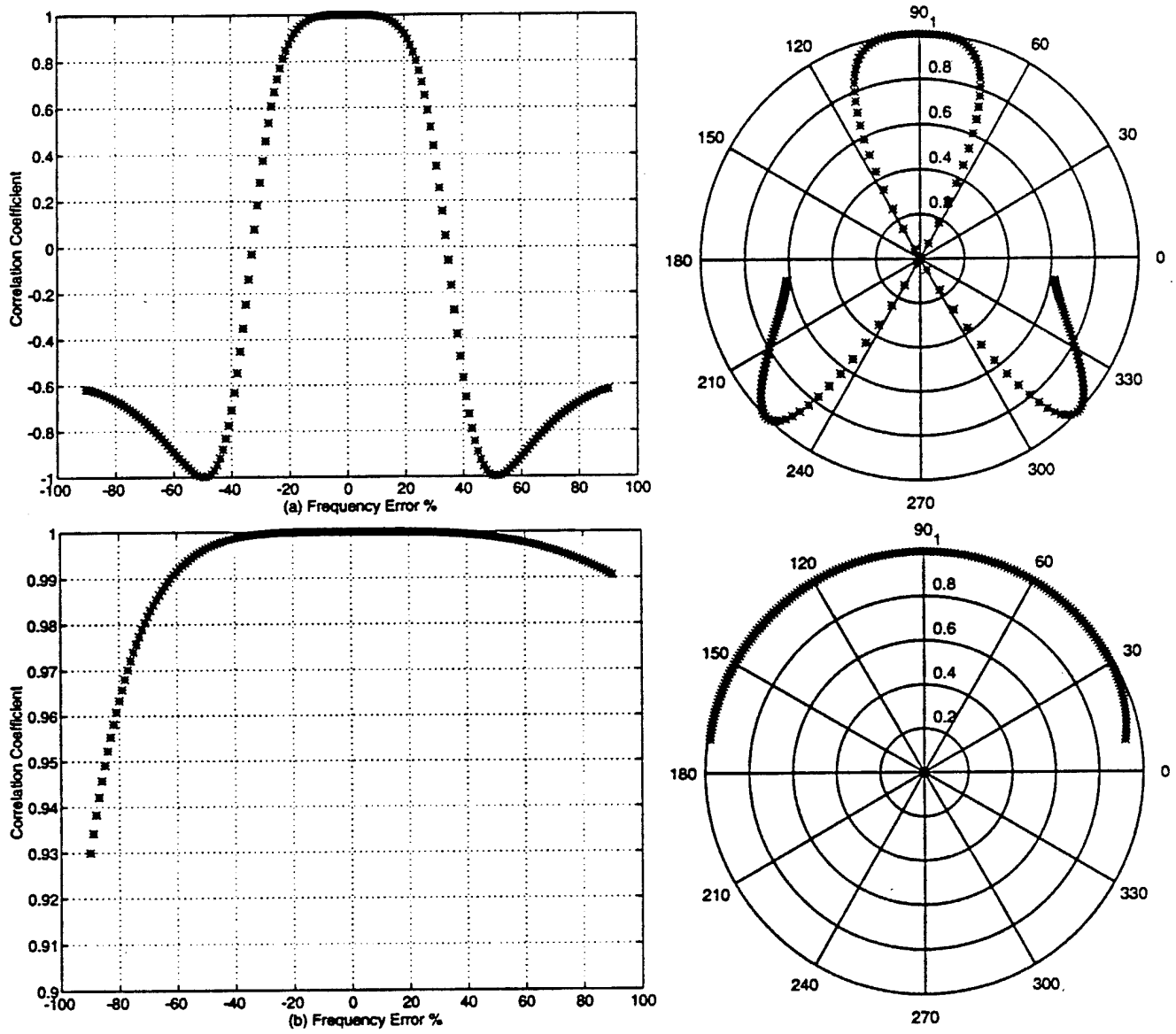

Figure 126 Calculated correlation coefficient with (a) frequency error in rectangular and polar form, (b) attenuation factor in these forms. The data are sampled and predicted at minimum rates.

degradation of correlation due to amplitude (or radial length) error. It is found that this type of correlator is very insensitive to amplitude variation. This observation confirms again the previous comment that this type of correlator is basically a coherent detector that does not use the amplitude information in performing the discrimination.

Examples from Real Measurements

In this section, real measurement data will be used as an example of target discrimination using the previous prediction/correlation technique. The data sets were measured using the system developed by ElectroScience Lab. Some of the system specifications are listed below:

1. Antenna: Loaded 1 foot Crossed-Dipole Antenna
2. Source: 60 Volts, 1 ns pulse
3. Data Collection System: Tektronix Sampling Scope, Personal Computer, A/D and D/A Interface

The target is located in air at a distance of 1 foot from the antenna. The normally incident backscattered field was measured. The measured time-domain waveform was pre-processed to remove the DC component and reduce the random noise as suggested in Section B. This processing was accomplished by autocorrelating the measured data. Four examples are given here. In the first three examples, a 2 foot metal pipe with 3/4 inch diameter is to be discriminated from the measured data from 1 foot, 2 foot, and 3 foot metal pipes with the same diameter. The pre-processed waveforms and the calculated correlation coefficients are plotted in Figure 127. The correlation coefficients at the optimum sampling/predicting rate are approximately -0.2, 0.99, and 0.65, respectively. For a discrimination threshold set at 0.9, the 2 foot pipe was successfully discriminated from among the three cases. In this example, only the first dominate pole of the 2 foot pipe, calculated using the Moment Method, is used for discrimination. It is also recalled from the previous section that this example belongs to the "1 to 1" case.

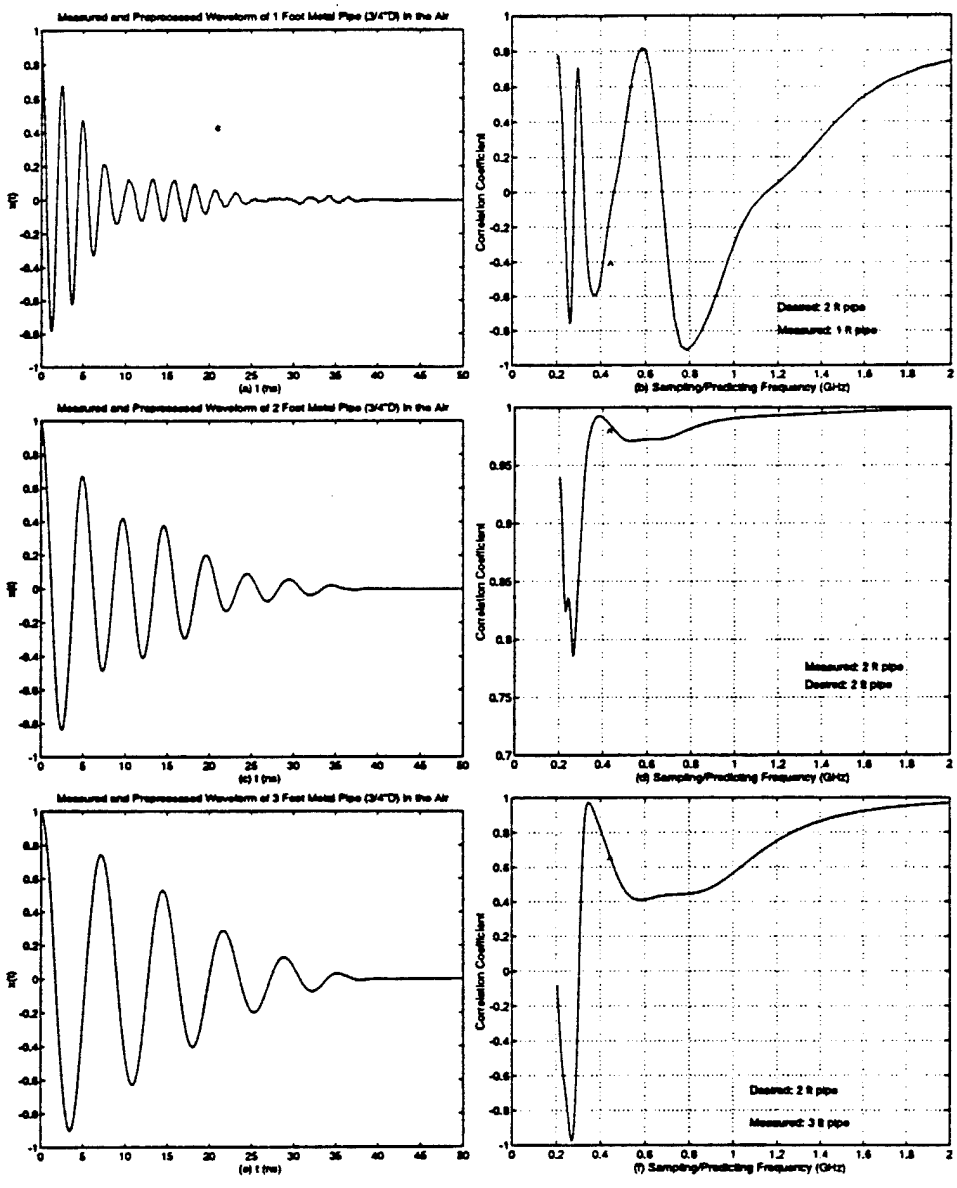

Figure 127 Measured waveforms and correlation coefficients of 1 foot [(a),(b)], 2 foot [(c),(d)], and 3 foot [(e),(f)] pipes.

Another interesting example is to discriminate a 3 foot metal pipe with a 3/4 inch diameter. The measured data is the response of a 3 foot inert ordnance item shown in Figure 128. The waveform and the correlation coefficient are plotted in Figure 129 (a) and (b). The correlation coefficient is about 0.85, which is high enough to be identified as the desired 3 foot pipe if the threshold is set at a lower value. This example indicates that the choice of threshold values plays a very important role in determining the discrimination sensitivity and the false alarm rate. This issue will be pursued in future work.

Summary

A technique using a correlator and a predictor has been introduced to perform target identification or discrimination from the knowledge of the CNR's of the desired target. Examples have been given to show that this technique can successfully discriminate the desired target from others. The existence of random noise has been shown to degrade discrimination performance and the effects of noise must be reduced through data pre-processing. It was also shown that this technique is very insensitive to amplitude variation, which may become a problem when large number of targets are to be discriminated and higher resolution is required. A complex frequency domain technique, which uses the pole positions, is under study to improve the resolution. The limitations due to the existence of other targets have also been discussed. More measured data need to be processed to study false alarm rate problems.

6.4 Summary

In this section, we discussed the usage of the SVD Prony's method as a technique to find the CNR's from GPR radar signals for target discrimination purposes. This study has provided a better understanding of the processing limits as well as techniques leading to the improvement of the stability and accuracy of extracted CNR's. It was found that the residue magnitude provides an efficient way of estimating the number of CNR's for SNRs greater than 10 dB. If one can predict the number of CNR's using other information such as target

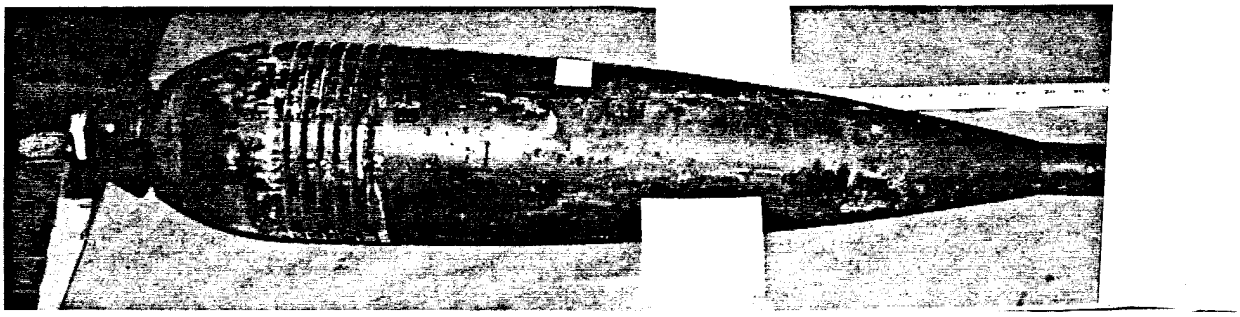

Figure 128 Photograph of Inert 2082

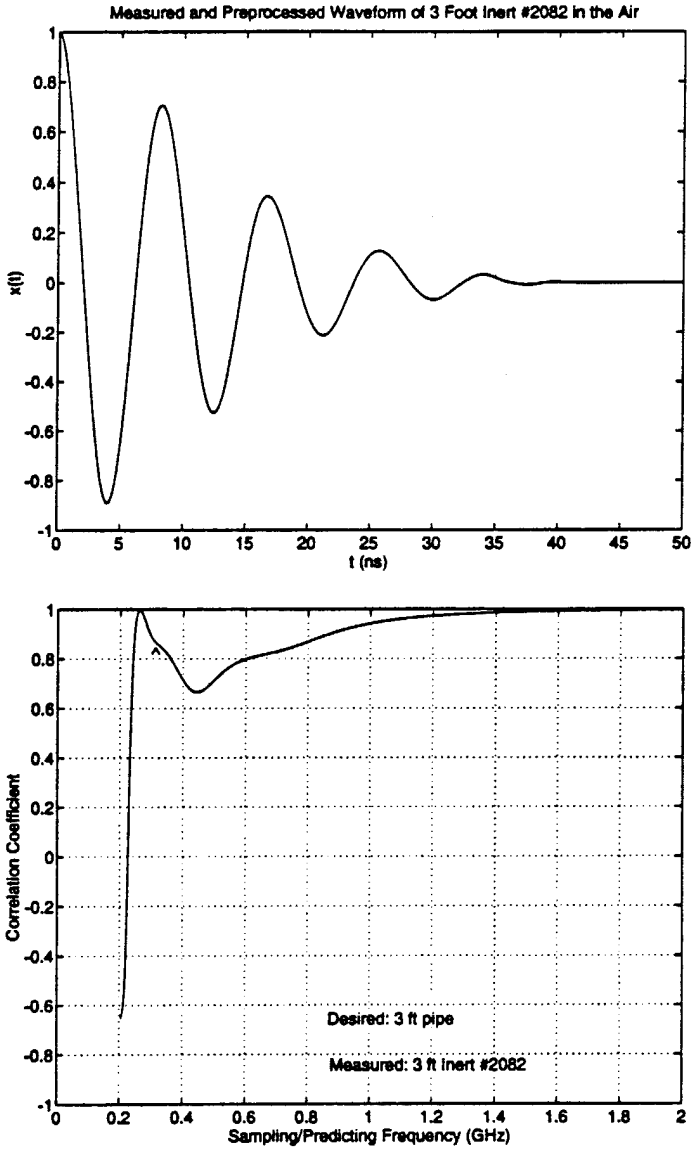

Figure 129 Measured waveforms and correlation coefficients of Inert 2082. The desired target is the 3 foot pipe.

dimensions and system bandwidth, then one can also greatly improve the processing accuracy by choosing the proper number of principle eigenvectors in applying the SVD Prony's method. It was also found that accurate CNR's can be obtained for signal-to-noise ratios as low as 5 dB by averaging. Clearly, the trade-off will be the need for more data memory and sampling time. It has been shown that when the signal contains clutter objects, such as non-resonant signals and multiple delayed resonances from different parts of the target or from undesired scatterers, the whole signal can no longer be described by the model and will cause large errors if the processing is applied blindly. This issue has been found to a major problem in data obtained from GPR's. Two techniques, the running window and resonance reduction methods, provide significant improvement for signals containing multiple delayed resonances.

A time-domain target discrimination technique using the predictor and correlator developed earlier at ESL has been reexamined. It has been shown in both calculated and measured examples that this technique provides accurate discrimination of desired targets when properly applied. However, it was found that the technique does not have good frequency resolution (or angle resolution in *the* Z-plane) and is very insensitive to the damping factor. For some applications, such as GPR, where only a few resonance frequencies are of interest and the damping factors are unstable, this might be an appropriate technique. For high resolution applications where many targets are to be discriminated, direct comparison of poles may be preferable. An experimental technique which uses the reciprocal of the pole distance has been examined.

6.5 References for Resonance Extraction Section

[1] D.A. Hill and E.M. Kennaugh, "Electromagnetic scattering concepts applied to the detection of targets near the ground.," Ph.D. Dissertation, (report 2971-1), ElectroScience Laboratory, The Ohio State University, Columbus, 1970.

[2] C.E. Baum, "On the singularity expansion method for the solution of electromagnetic interaction problems," Tech. Rep. Note 88, Air Force Weapons Laboratory, Interaction Note, December 1971.

[3] L. Marin and R.W. Latham, "Representation of transient scattered fields in terms of free oscillations of bodies," *Proc. IEEE,* vol. 53, pp. 640-641, May 1972.

[4] M.L. Van Blaricum and R. Mittra, "A technique for extraction the poles and residues of a system directly from its transient response," *IEEE Trans. Antennas Propagat.*, vol. AP-23, pp. 777-781, Nov. 1975.

[5] A.J. Poggio, M.L. Van Blaricum, and R. Mittra, "Evaluation of a processing technique for transient data," *IEEE Trans. Antennas Propagat.*, vol. AP26, pp. 174-182, Jan. 1978.

[6] M.L. Van Blaricum and R. Mittra, "Problems and solutions associated with Prony's method for processing transient data," *IEEE Trans. Antennas Propagat.*, vol. AP-26, pp. 174-182, Jan. 1978.

[7] F.M. Tesche, "On the analysis of scattering and antenna problems using the singularity expansion technique," *IEEE Trans. Antennas Propagat.*, vol. AP-21, pp. 53-61, Jan. 1973.

[8] M.S. Corrington, "Simplified calculation of transient response," *Proc. IEEE,* vol. 53, pp. 287-292, March 1965.

[9] A.J. Berni, "Target identification be natural resonance estimation," *IEEE Trans. Aerospace and Electronic Systems,* vol. AES-ll, pp. 147-154, March 1975.

[10] D.L. Moffatt and R.K. Mains, "Detection and discrimination of radar targets," *IEEE Trans. Antennas Propagat.*, vol. AP-23, pp. 358-367, May 1975.

[11] D.L. Moffatt and C.W. Chuang, "Natural resonances of radar targets via Prony's Method and Target Discrimination," *IEEE Trans. Aerospace and Electronic Systems.*, vol. AES-12, No.S, pp. 583-589, Sep. 1976.

[12] D.L. Moffatt and K.A. Shubert, "Natural Resonances via Rational Approximations," *IEEE Trans. Antennas Propagat.*, vol. AP-25, pp. 657-660, Sep. 1977.

[13] D.L. Moffatt, L.C. Chan, and L. Peters, "A characterization of sub6urface radar targets," *IEEE Trans. Antennas Propagat.*, vol. AP-67, pp. 991-1000, July 1979.

[14] D.L. Moffatt, L.C. Chan and L. Peters, "Subsurface radar target imaging estimates," *IEEE Trans. Antennas Propagat.*, vol. AP-29, pp. 413-417, Mar. 1981.

[15] D.L. Moffatt, L.C. Chan, and L. Peters, "Improved performance of a subsurface target identification system through antenna design.," *IEEE Trans. Antennas Propagat.*, vol. AP-29, No.2, pp. 307-311, Mar. 1981.

[16] C.E. Baum, "The SEM representation of scattering from perfectly conducting targets in simple lossy media," Tech. Rep. Note 492, Phillips Laboratory, Interaction Note, Apr. 1993.

[17] M.A. Morgan, "Singularity Expansion Representations of Fields and Currents in Transient Scattering," *IEEE Trans. Antennas Propagat.*, vol. AP-32, pp. 466473, May 1984.

[18] C.C. Chen, J.D. Young, L. Peters, and F. Paynter, "Radar Signature Measurements of Buried, Unexploded Ordnance Targets," technique report 727388-2, ElectroScience Lab., The Ohio State University, Columbus, Feb. 1994.

[19] R. Prony, "Essai experimental et analytique, etc.,," *Paris J. I'Ecole Poltechnique,* pp. 24-76, 1795.

[20] S.M. Kay, *Modern spectral estimation.* New Jersey: Prentice-Hall, 1988.

[21] S.L. Marple, *Digital spectral analysis with applications.* New Jersey: Prentice-Hall, 1987.

[22] R. Carriere and R.L. Moses, "High resolution radar target modeling using a modified Prony Estimator," *IEEE Trans. Antennas Propagat.*, vol. AP-40, pp. 13-18, Jan. 1992.

[23] W.M. Steedly and R.L. Moses, "The Cramer-Rao bound for pole and amplitude coefficient estimates of damped exponential signals in noise," *IEEE Trans. Antennas Propagat.*, vol. AP-41, pp. 1305-1318, Mar. 1993.

[24] H. Akaike, "Power spectrum estimation through autoregression model fitting," *Ann. Inst. Stat. Math.*, vol. 21, pp. 407-419, 1969.

[25] H. Akaike, "A new look at the statistical model identification," *IEEE Trans. Autom. Control,* vol. AC-19, pp. 716-723, Dec. 1974.

[26] E. Parzen, "Some recent advances in time series modeling," *IEEE Trans. Autom. Control,* vol. AC-19, pp. 723-730, Dec. 1974.

[27] T.J. Ulrych and R.W. Clayton, "Time series modeling and maximum entropy," *Phys. Earth Planet. Inter.*, vol. 12, pp. 188-220, August 1976.

[28] V.F. Pisarenko, "The retrieval of harmonics from a covariance function," *Geophys I. Roy. Astron. Soc.*, vol. 33, pp. 247-266.

[29] A.K. Dominek, H.T. Shamansky, and L. Peters, "Electromagnetic scattering by a straight thin wire," *IEEE Trans. Antennas Propagat.*, vol. AP-37, pp. 1019-1025, Aug. 1989.

7.0 Receiver Design

7.1 Radar Architecture

The architecture of the radar has been one of the main concerns of this program. The radar used will be an ultra wideband (UWB) radar with frequency content between 50 and 500 MHz. Two phenomena drive this use of a wide frequency range. First, we must stay fairly low in radar frequency because, in general, the lower the frequency, the lower the propagation loss in the ground medium. The advantage of including higher frequency energy is that resolution in range (depth in the ground) increases with bandwidth. Because ground is dispersive in nature, the high frequency energy is attenuated more than the low frequency energy; resolution decreases for deeper targets. In general, larger ordnance items are deeper so the loss is less critical. The second reason for employing this wide bandwidth comes from the target discrimination procedure we use. The discrimination method is based on the complex natural resonances of the inert targets. The imaginary part of the complex frequency corresponds to the resonance frequency associated with the size and geometry of the target. Because of the large variation in size of the candidate ordnance items, the frequency content must also be wide.

Two categories of systems that are potential targets are time-domain systems and frequency-domain systems. Because of Fourier theory, the two systems can be mathematically equivalent if the time-domain pulse being used has frequency content equal to that of the frequency-domain system. A Fourier transform from time to frequency domain or an inverse Fourier transform from frequency to time domain shows the systems equivalent. However, the hardware implementation of the two systems can be very different because of available technologies and real-world implications of things like the radio frequency (RF) environment at the GPR site. A critical part of this program is deciding if a time-domain, short-pulse system or a frequency-domain step-chirped system is best for this application.

Table 8 Time Domain/Frequency Domain Trade-Offs.

Frequency Domain (Step-Chirped) System	
Advantages:	1. Can use low-sampling rate, high-dynamic range A/D's (14-16 bits) 2. Can skip or shift frequencies to avoid interference sources 3. Can tailor spectrum as desired 4. Switchable antennas can be used 5. Can use high average transmitter power
Disadvantages:	1. No clutter spreading in time which would allow a percentage of the clutter to be gated out 2. High-speed operation requires fast switching transmitter (and local oscillator) and antenna 3. Cannot use time sensitivity control 4. Results in frequency domain require processing to convert to time domain 5. Use of switchable antennas requires conversion of data during post-processing
Time Domain (Pulsed) System	
Advantages:	1. Transmitter relatively simple 2. Can range gate to reduce surface clutter 3. Can use time sensitivity control 4. Time domain output ready for processing
Disadvantages:	1. High dynamic range receivers difficult and expensive to implement 2. Must receive radio frequency interference with signal 3. Low average power with present technology

Table 8 presents some of the advantages and disadvantages of the frequency-domain and time-domain architectures. The frequency-domain architecture relies on a step-chirped transmitter and local oscillator to output pulsed CW signals at a number of frequency steps (120-512) between 50 and 500 MHz. The receiver uses the local oscillator signal, filters, and mixers to receive and store the scattered signal. A high-dynamic range analog-to-digital converter (A/D) can be used. Dynamic range is of critical importance because of the high field levels returned from the earth's surface and the relatively low fields returned from the buried UXO targets. Radio frequency interference from television, radio, and other sources

can be a difficult problem. With the step-chirped system, we can program the radar to step around problem frequencies and later fill in the missing information with interpolated data. We can also use an active matching network on the antenna to improve its characteristics over the wide frequency band of interest. The main problem with a step-chirped system is the time required to step through the entire frequency band. The required stepping time for the ESL step-chirped system was significantly decreased during the course of this effort (through efforts on another contract). This radar was ultimately selected as the receiver of choice on this program because of its increased speed, high dynamic range, and versatility. It is the fastest system that is available without a significant hardware development project. The implication of using a system slightly slower than preferred is in the time required to scan a given land parcel. We believe that the path chosen by NAVEODTECHDIV, namely, to not fund a hardware development program but rely on this radar, represents the path with the least risk while still achieving a reasonable scan rate.

A system based on an impulse with frequency content between 50 and 500 MHz also enjoys many advantages. The limiting factor in such a time-domain system is dynamic range in the receiver. GPR systems have been built exploiting sampling oscilloscopes as receivers but they are too slow in nature to be seriously considered in an airborne application. A sampling oscilloscope builds up the points in the received waveform by storing a single point for each transmitted pulse; a received waveform with 512 points, for example, requires 512 pulses to be completed. Averaging many waveforms is therefore prohibitively time consuming. The other type of time-domain receiver often employed with time-domain GPR systems is referred to as a transient digitizer. This instrument is capable of recording the received energy from each pulse transmitted. One pulse generates one received waveform. The main limitation of this system is dynamic range. Digitizers based on scan converters or fast A/D converters are generally limited to 8 bits of dynamic range. The dynamic range can be improved through averaging but a price is then paid in speed. A time domain system is also inherently susceptible to RFI because the receiver allows all energy between 50 and 500 MHz into its front end.

Another approach is the hybrid system, where the system transmits a time-domain pulse but the receiver works in the frequency domain. Such an architecture allows use of slower, higher-dynamic range A/D's. This type of system can be made more immune to RFI.

7.2 System Dynamic Range

Because of the critical importance of system dynamic range in determining our ability to detect targets of interest, we feel it is very important to make sure that all people involved with the system development understand this characteristic. Dynamic range is a dimensionless ratio of two quantities, usually voltage. It is generally expressed in terms of dB, i.e., twenty times the common logarithm (base 10) of a voltage ratio or ten times the common logarithm of a power ratio. In the GPR receiver context, the dynamic range represents the ratio of the largest voltage that can be received without distortion to the smallest voltage that can be measured. In a digital system, such as the GPR receiver envisioned on this effort, the largest voltage that can be measured without distortion is one that barely toggles the most significant bit (MSB) of the A/D converter. The smallest signal that can be measured is one that toggles the least significant bit (LSB) of the A/D. An 8-bit A/D can represent 2^8 (256) distinct values. One bit must be used as a sign bit, however, so the ratio of largest to smallest numbers available becomes $2^{(8-1)}=2^7$. The single-sample dynamic range of this A/D is then

$$\text{Dyanmic Range} \equiv 20\log_{10}(2^{(8-1)}/1) = 20\log_{10}(128/1) = 42.14 \text{ dB}. \qquad \textbf{(116)}$$

Similar calculations show that a 12-bit A/D has 66.2 dB of dynamic range and a 16-bit A/D has 90.3 dB of dynamic range. Actual A/D's will probably provide somewhat less in effective dynamic range because of hardware issues in building sample-and-hold circuits and A/D's. However, the numbers quoted above are guidelines that can be used to compare between different A/D's.

The designer cannot allow a signal with a voltage larger than one that would toggle the MSB because the output of the A/D would be, in effect, a chopped-off, distorted, version of the analog waveform. Such a signal would be problematical if a discrete Fourier transform of the data stream was calculated. The chopped-off waveform would indicate the presence of frequency components that were not present in the analog waveform. The transform operation has to describe this distorted time-domain waveform that now possesses a severe discontinuity in one or more derivatives. High frequency components will be indicated that may not be present in the same strength in the analog waveform.

Similarly, no signal will be detected if it does not toggle the LSB. If the desired signal does not toggle at least the LSB, no amount of signal processing will recover it from the digitized data; the signal is, in fact, not present in the digitized data. If it toggles the LSB but is buried in noise or interference of some kind, it becomes possible, at least, for some signal processing technique to pull it out of the data.

Having a large dynamic range is crucial to the success of the Airborne GPR system because of losses due to propagation in the ground and because of the large reflection-like scattering from the air/earth interface. The receiver gain for a given pulse must be set so that the amplitude of the signal reflected from the ground is less than that for a signal that toggles the MSB. This condition must be met by the Airborne GPR. The smallest scattered signal that can be recovered from a UXO target must be no more than 42 dB less than the surface signal in the case of an 8-bit A/D receiver. It can be 66 dB or 90 dB less than the surface signal in the case of 12-bit and 16-bit A/D's, respectively. One can see that more system gain will not solve the problem because more gain also amplifies the surface return.

Several means of increasing the effective dynamic range are possible in the Airborne GPR context. With ground-based GPR systems, ESL has in the past used antennas that minimize the surface return. If the antennas reduce the surface return 10 dB by virtue of their geometry, a kind of analog signal processing, has taken place and the gain can be increased by 10 dB allowing targets 10 dB below previous levels to be detected. One can

recover 10 dB in this way only if the surface return is reduced 10 dB and the return from the target is not reduced. Another way of increasing the dynamic range is possible if a sampling oscilloscope architecture is used and the gain of the system is increased as the waveform propagates through the ground. This technique is often referred to as a gain-slope, where the gain changes with time, which in effect changes the gain with depth.

We may not be able to use a sampling oscilloscope in the airborne GPR, however. A sampling oscilloscope operates in the time domain by sampling one *point* on the received waveform for each *pulse* transmitted. A received waveform is constructed from N received pulses that are sampled and digitized such that they represent subsequent points in time differing by a fixed time increment, Δt. Using the gain slope concept, the gain is set to some low value until the return from the ground (received first in time) is recorded. Once this large amplitude signal is received and the A/D is not saturated, the gain can be increased for points which correspond to signals returned from objects below the surface. Because the losses in the ground increase nearly linearly with increasing depth, the gain can be increased linearly in time. In this way, a UXO target whose signal is more than 42 dB below the ground return can be recovered. Unfortunately, a sampling scope-based system does not have sufficient dynamic range for use on a helicopter system.

A third way to increase the effective dynamic range is to use coherent integration, which is essentially what the SAR process is doing. Figure 129A on page 205A illustrates the dynamic range achieved by coherent processing as a function of the number of samples processed.

7.3 Brassboard Prototype Receiver

Considerable effort has been extended deciding on a radar system that we could fly in a helicopter by mid-1995. Time-domain systems were ruled out because of dynamic range and/or RFI rejection limitations. It appears that a frequency-domain (step-chirped) system offers the highest probability of success in the short term. The stepped-chirp system has a

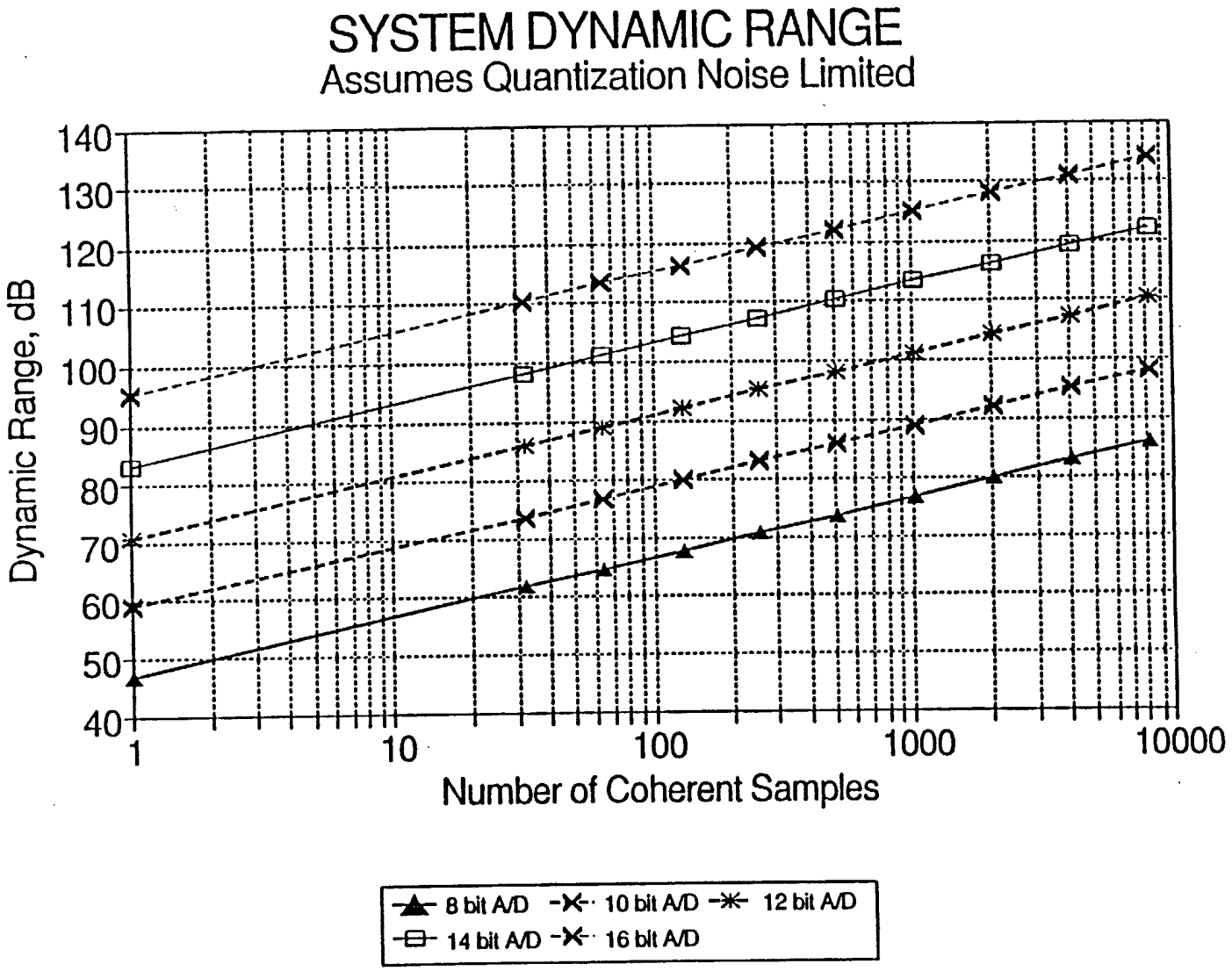

Figure 129a. Graph of Increase in Dynamic Range versus Number of Coherent Samples for Five A/D Converters

much lower peak power than the time-domain while having a higher average power. ESL uses a custom-built system that can take about 1 waveform every 4 seconds (700 frequency samples per waveform) with either 16 or 128 samples being averaged at each frequency step. Figure 130 shows the implementation. Basically two coherently coupled sources are required, one for transmission and one to provide a mixing signal. The transmitted signal is not pulse-modulated. The system is fully CW (not FMCW); the transmitter and the receiver are "on" at all times. The system is referred to as being step-chirped because it moves the source to a given frequency, takes 16 or 28 data points, and then moves to the next frequency. The received signal passes through attenuators, amplifiers, mixers, and filters until a 10 kHz wide signal centered at 100 kHz is passed to sample-and-hold circuits and digitized by 16-bit analog to digital converters. Summing and several other operations take place in the DSP box before 24-bit integers are passed to a computer. Much of the receiver architecture is based on the Hewlett-Packard 8510 network analyzer. While this design provides many of the required components, much work remains to be done. For example, GPS and/or gyro systems need to be integrated to insure accurate helicopter position knowledge for each chirp. Certainly antennas and processors need to be evaluated. It is anticipated that little information will be available in real time for this preliminary prototype. Significant post-processing will be required. We believe that this configuration will supply the sort of information we need to design, build, and test the final prototype.

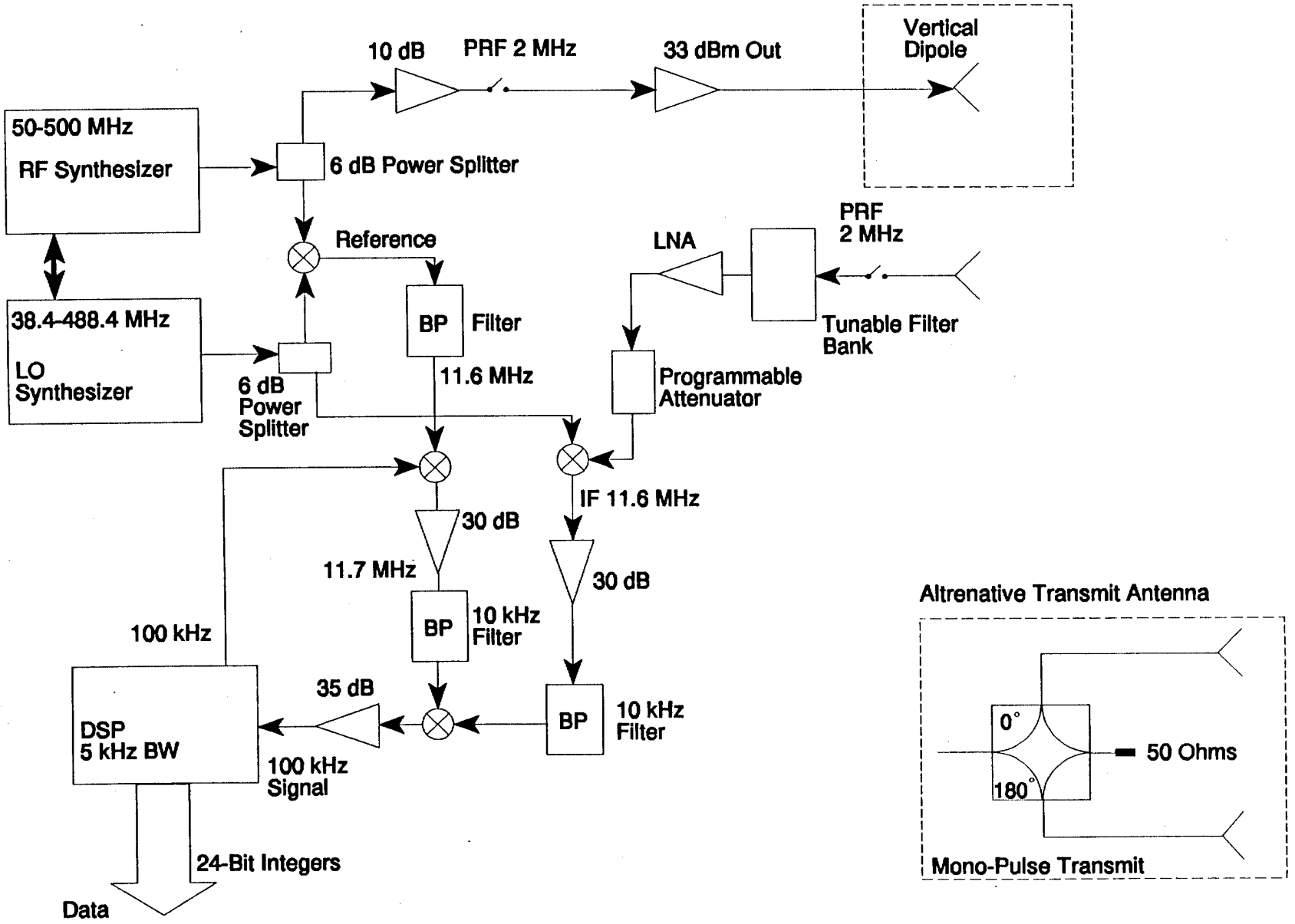

Figure 130 Block diagram of the preliminary prototype.

7.4 Final Receiver Prototype Candidates

Several candidate systems were considered for this application. We include information on all of the candidates. A final decision was not made because the second phase was not to involve fabricating a receiver. If, in the future, it again becomes necessary to choose the final version, the decision should be made based on the technology available at that point in time.

Step-Chirped System. The first candidate is very similar to the brassboard receiver (described on page 205) except the synthesizers step much faster in time. In this new configuration, only a few samples are taken at each frequency step to allow the decreased chirp time. The brassboard prototype will acquire the either 16 or 128 samples because we are using an existing system. The averaging of 16 or 128 waveforms helps with noise performance, which was important in its original application but is of less importance in the

Table 9 Step-Chirped Receiver Parts List.

DESCRIPTION	QTY	PRICE (EA)	VENDOR
Watkins-Johnson Synthesizer (WJ-45120)	2	$75,000.00	Watkins-Johnson
Power Splitter 5-500 MHz (ZFSC-2-1)	3	$ 44.95	Mini-Circuits
Double-Balance Mixer 5-500 MHz (MD-143)	5	$ 40.00	ANZAC
Low Power Amp 5-1000 MHz (AMC-182)	3	$ 289.00	ANZAC
Attenuator (P442L)	2	$ 807.39	J&B Eng. Sales
RF Switch 4 μs switch time (ZMSW-1111)	2	$ 69.95	Mini-Circuits
RF Power Amp 1-1000 MHz @ 10 W	1	$ 9300.00	Amplifier Research
Low Noise Amp 50-500 MHz (AMC-182)	1	$ 289.00	ANZAC
High Pass Filter (BHP-100)	1	$ 36.95	Mini-Circuits
A/D Converters 500 kHz 16 Bit (ADS-930MC)	2	$ 494.00	DATEL
PC/AT Single i860 (FT860/2-AT-16-1)	2	$10,795.00	ALACRON
Quadrature Hybrid 2-32 MHz (JH-6-4)	1	$ 324.00	ANZAC
Software Products FT200 ALIX 68K	1	$ 500.00	ALACRON
Compilers SUN OS Compiler (AL-F77-SV)	1	$ 4,095.00	ALACRON
Development Tools Vector Library	1	$ 995.00	ALACRON
Bandpass Filter 500 kHz BW (NBP-10.7)	3	$ 18.95	Mini-Circuits
TOTAL COST	**$190,797.38**		

airborne GPR clutter-limited problem. Table 9 provides a parts list with cost estimates for this architecture.

Frequency-Domain Receiver One candidate for the final prototype receiver is similar to the microwave channelized receiver shown in Figure 131. In this example, which was designed to receive energy between 3.5 and 4.5 GHz, the RF energy enters through a low-noise amplifier and passes to a "channel dropping" filter. This filter divides the energy between five contiguous bands, each of which comprise another low-noise amplifier, a band-pass filter, a mixer that moves the energy to an intermediate frequency, an I/Q mixer, and two 200 MHz analog-to-digital (A/D) converters. The basic function of the receiver is to digitize a 1 GHz bandwidth using slower A/D converters with 8 bits of dynamic range. A similar frequency domain receiver in this program would digitize 450 MHz bandwidth and mix it down to forty-five 10 MHz-wide channels that could be digitized by 10 MHz 14 bit A/D's. Such a receiver would be capable of real-time data acquisition, to 14 bits of resolution, of the entire 50 to 500 MHz band. This receiver will afford sufficient dynamic range and the ability to continuously record received time-domain waveforms in real time. Of course, such a receiver presents significant implementation difficulties. The most challenging aspect is designing and implementing the contiguous channel-dropping filters. Such filters are difficult to build for several reasons plus their behavior when input with out-of-band energy can change dramatically with frequency. At Battelle, we spent two years investigating such microwave receivers for electronic warfare applications under IR&D funds. The conclusion of our study was that a different architecture should be used, namely, the Time-Domain Receiver described in the next paragraph. Table 10 provides a parts list with cost estimates for the Frequency-Domain Receiver.

Time-Domain Receiver. At present, the time-domain receiver architecture shown in Figure 132 is the leading candidate for the final prototype. This configuration represents a Battelle-proprietary receiver that was designed and analyzed in detail as part of a Battelle IR&D program. As with the frequency-domain receiver described in the previous paragraph, the basic concept is to use 14-bit, 10 MHz A/D converters to sample a 450 MHz band of

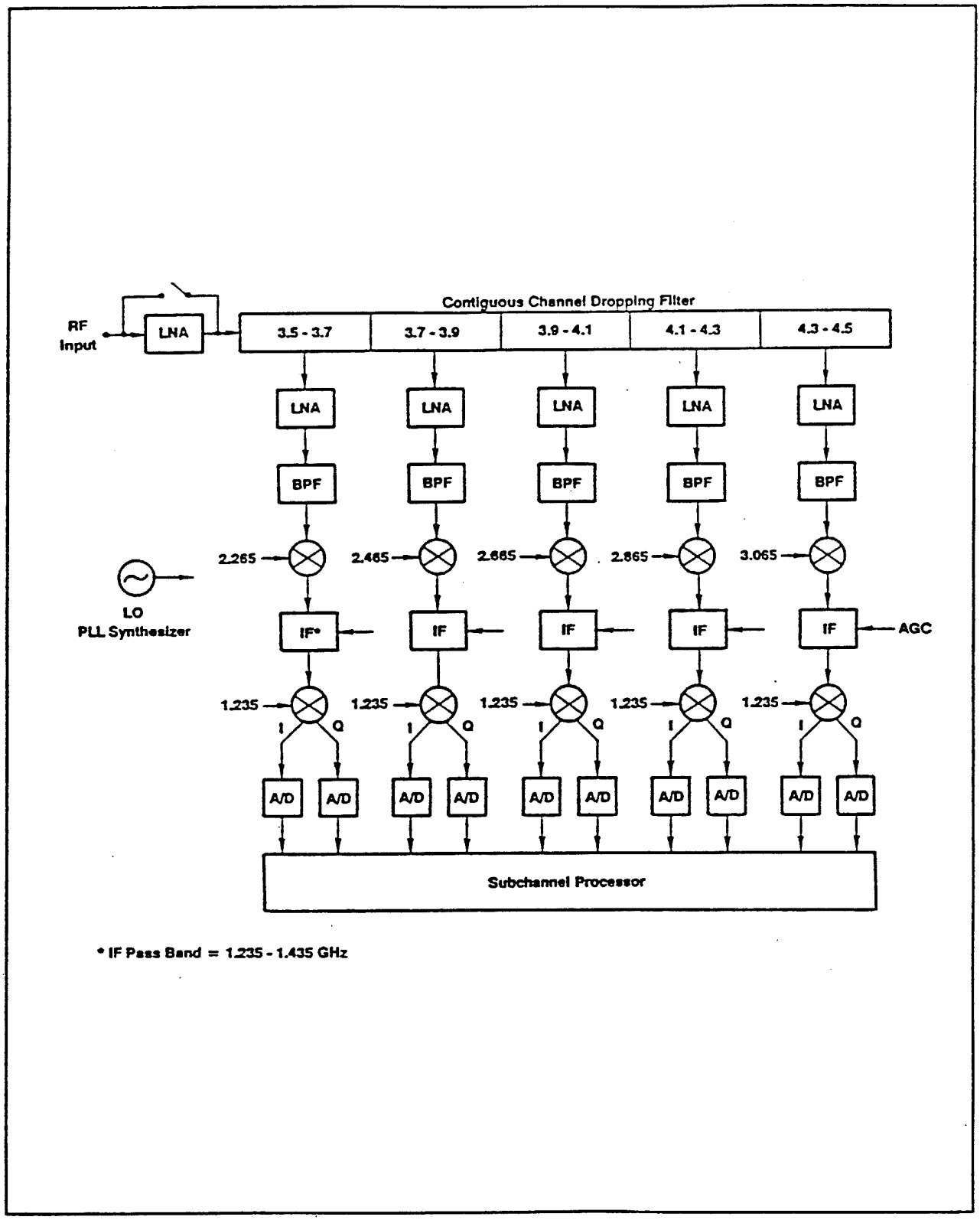

Figure 131 Architecture of a microwave channelized receiver

Table 10 Frequency Domain Receiver Parts List.

DESCRIPTION	QTY	PRICE (EA)	VENDOR
Mixers Broadband (MD-139)	90	$ 85.00	ANZAC
Bandpass Filter 50-500 MHz (PHP-100)	2	$ 14.95	Mini-Circuits
RF Switch 2 μs switch time (VSW-250DR)	1	$ 42.95	Mini-Circuits
Low Noise Amp 50-500 MHz (AM-182)	2	$ 192.00	ANZAC
Attenuator (P242L)	1	$ 628.44	J&B Eng. Sales
RF Amp 5-200 MHz (AM-138)	45	$ 192.00	ANZAC
RF Amp 100-600 MHz (AM-191)	44	$ 196.00	ANZAC
Crystal Oscillator 10 MHz (XC321)	2	$ 8.55	Digi-Key
A/D Converter 10 MHz @ 14 Bit (ADS-945)	90	$ 900.00	DATEL
Buffer Amp 20 MHz BW (HFA1135IP)	90	$ 4.12	Newark
PC/AT Single i860XP (FT860/2-AT-16-1)	2	$10,795.00	ALACRON
Quadrature Hybrid 20-200 MHz (JH-131)	30	$ 216.00	ANZAC
Quadrature Hybrid 135-350 MHz (JH-136)	30	$ 76.00	ANZAC
Quadrature Hybrid 250-500 MHz (JH-139)	30	$ 76.00	ANZAC
Software Products FT200 ALIX 68K	1	$ 500.00	ALACRON
Compilers SUN OS Compiler (AL-F77-SV)	1	$ 4,095.00	ALACRON
Development Tools Vector Library	1	$ 995.00	ALACRON
TOTAL COST	**$145,607.19**		

data. This time domain receiver requires the use of in-phase and quadrature-phase (I/Q) processing in order to realize the full 450 MHz bandwidth when sampling every two nanoseconds. Sampling at this rate with two linearly independent data streams yields the full 450 MHz bandwidth. As the signal moves along the tapped delay line (2 ns between samples), the sample and holds are clocked at a 10 MHz rate. The A/D converters then sense a sample every 100 ns. The 14-bit value is passed to buffers. The stored signal is in the buffers with the earliest data point in buffer 45, the next in buffer 44, etc. The computer can later assemble the waveform in the correct order because the sampling system is coherent in its operation. It is imperative that the sample and hold circuits possess the full 450 MHz bandwidth or they cannot respond to the waveform that is changing very quickly in time.

While this architecture seems to hold the most promise as of now, it offers significant challenges and will be expensive. We continue to evaluate other possibilities in the design phase program. Table 11 provides a parts list with cost estimates for the Time-Domain Receiver.

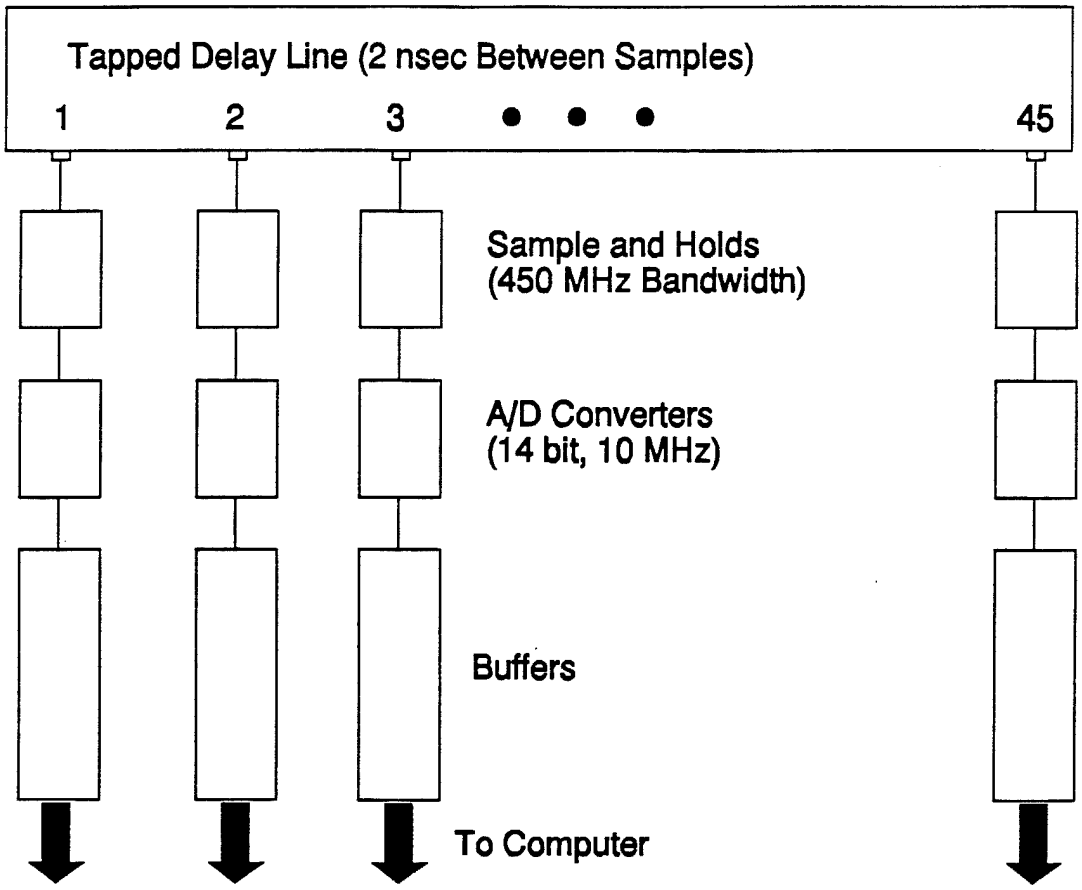

Figure 132 Tapped-delay line time-domain receiver architecture. Two systems are required, one for the I (In-Phase) channel and one for the Q (Quadrature-Phase) channel.

7.5 Conclusion

We believe the Time-Domain receiver is the leading candidate for this application. At present time, however, this receiver does not exist as any more than a preliminary design. In the follow-on effort to this program, NAVEODTECHDIV chose not to take the risk of fabricating this receiver but instead rely on the ESL step-chirped radar. Battelle concurs with this decision. If the step-chirped system demonstration shows this UXO detection system to be successful, Battelle may recommend to the Government, at that time, that this faster system be reconsidered. Unfortunately, the step-chirped system is the most expensive

Table 11 Time Multiplex Receiver Parts List.

DESCRIPTION	QTY	PRICE (EA)	VENDOR
A/D Converter 10 MHz @ 14 Bit (ADS-945)	90	$ 900.00	DATEL
Bandpass Filter 50-500 MHz (PHP-100)	2	$ 14.95	Mini-Circuits
Low Noise Amp 50-500 MHz (AM-182)	90	$ 192.00	ANZAC
RF Switch 2 μs switch time (VSW-250DR)	1	$ 42.95	Mini-Circuits
Crystal Oscillator 10 MHz (XC321)	1	$ 8.55	Digi-Key
Buffer Amp 20 MHz BW (HFA1135IP)	90	$ 4.12	Newark
Attenuator (P242L)	1	$ 628.44	J&B Eng. Sales
PC/AT Single i860XP (FT860/2-AT-16-1)	2	$10,795.00	ALACRON
Quadrature Hybrid 7-14 MHz (JH-113)	1	$ 49.00	ANZAC
Delay Lines 400 ns delay (TK5318-ND)	88	$ 15.71	Digi-Key
Software Products FT200 ALIX 68K	1	$ 500.00	ALACRON
Compilers SUN OS Compiler (AL-F77-SV)	1	$ 4,095.00	ALACRON
Development Tools Vector Library	1	$ 995.00	ALACRON
TOTAL COST	**$127,972.12**		

of the candidates considered. However, one can see from Table 9 that $150,000 of the $190,000 expense is for the two Watkins-Johnson synthesizers. The price of these synthesizers will drop. We should also be able to identify synthesizers with slightly less performance but with significantly less cost. A reasonable compromise might be to purchase the less expensive synthesizers.

8.0 Positioning and Navigation

While developing a positioning and navigation system is not part of the present contract, the use of such a system is critical to the success of the synthetic aperture radar processing and to the ability to specify the location of ordnance items once they are detected. With this requirement in mind, we have been considering positioning and navigation options and have gained an understanding of the limitations involved. We have done some work with the Global Positioning System for positioning information on a related program involving a ground-based GPR system for buried ordnance detection. Much of the information generated for that program naturally transfers to this program. We are also performing some planning for the second phase of this airborne GPR program. We have discussed the requirements with The Ohio State University Center for Mapping and asked them to conceive a system that would meet our requirements.

The Center for Mapping, in a second phase, will develop a positioning system and a moving map display for the helicopter pilot based on the Global Positioning System. The SAR processing drives the position accuracy requirements, which are currently estimated to be about 10 cm with about 20 updates per second. Such accuracy is possible with differential GPS, a system in which two GPS receivers are required. One receiver is at a fixed position, within a few miles of the area being surveyed. Its position must be known very precisely via one of several positioning methods. The other receiver and antenna are aboard the helicopter. The fixed receiver acquires the same satellite data as the helicopter receiver, with the satellites data's inherent system errors (Selective Availability, Anti-Spoofing, etc.). Because the position of the fixed receiver is known to 10 cm accuracy, the system errors can be removed and the position of the helicopter can be found via a radio link between the receivers and via data processing. This positioning information can be found in approximately 1 second intervals using off-the-shelf GPS technology. It is not known at this

time what the true update rate requirements of the GPS system are; once they are determined, the update limits of the GPS system can be determined. An inertial measurement unit (IMU) may be required to insure the required high update rates. The IMU data will be used to specify location information between the one second updates of the differential GPS.

Navigation of the helicopter to locations dictated by the SAR process is also required. Again, the GPS system can be used with a moving map display for the pilot indicating the helicopter's present location and what the pre-determined path is. The update rates and accuracies are less stringent, both in terms of accuracy and update rates, than those for the positioning system. Once those requirements have been determined, they can be factored into the requirements for the moving map display. It is anticipated that the differential GPS positioning system data can be used as input to the moving map display computer.

Figure 133 shows the initial design provided by the Center for Mapping. Although this Figure was generated under another program, it is included here for informational purposes. A parts list for this system is provided in Table 12.

As part of the demonstration at Jefferson Proving Ground, the Center for Mapping provided a GPS system for our cherry-picker airborne GPR. The result of this work was not useful because harmonic energy from the radar interfered with the GPS receiver. An analysis of the errors is included in Appendix B. The radar will be modified in 1995 to skip past the problem frequencies and/or suppress this harmonic energy.

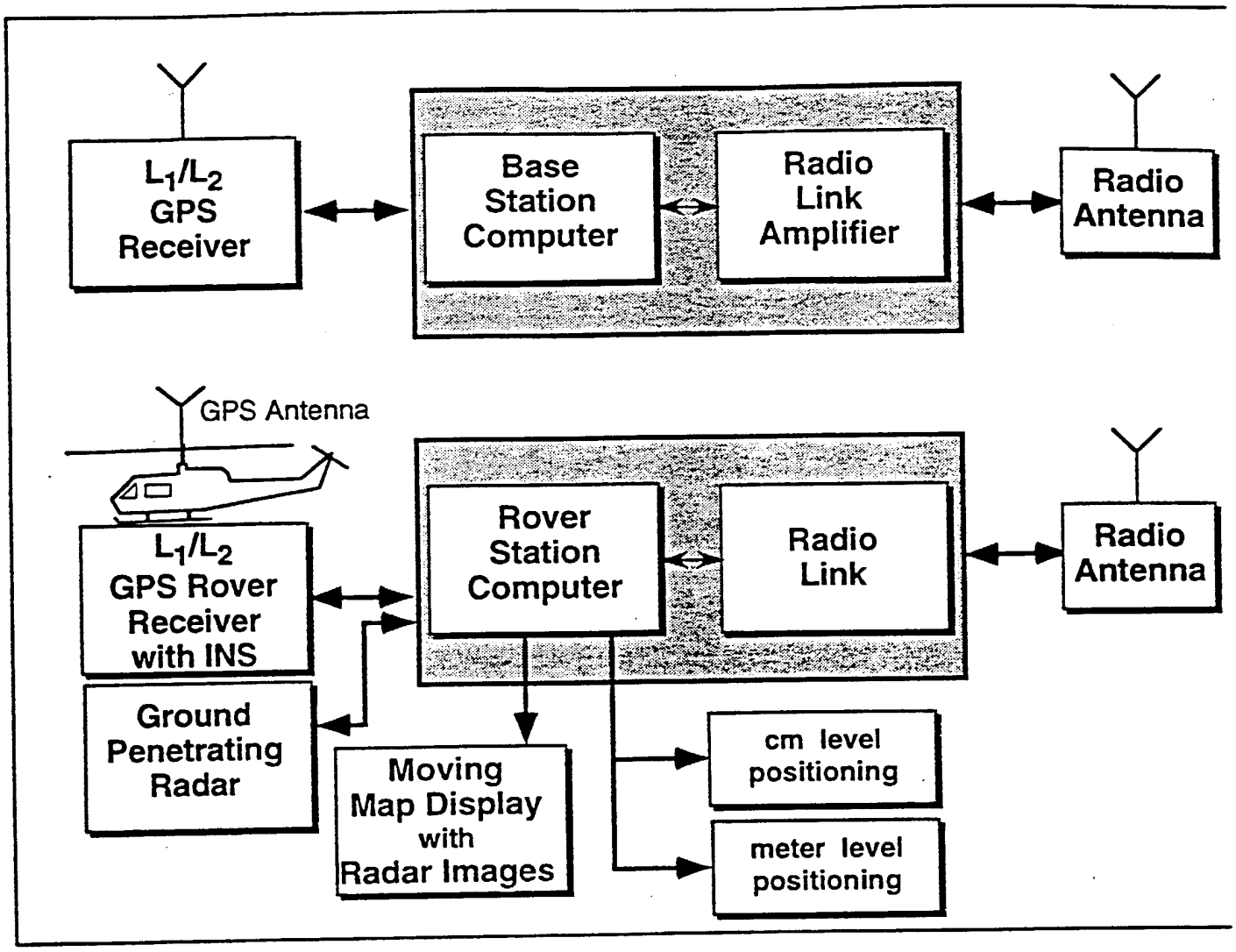

Figure 133 Airborne-Based Real-Time cm-Level GPS Positioning and Navigation System.

Table 12 Position Location and Navigation Parts List.

GPS and Navigation Equipment	
Quantity	Description
	GPS System (either Allen Osborne & Associates or Trimble Navigation)
2	Dual-Frequency GPS Receivers
1	Geodetic Ground Plane Antenna or Choke-Ring Antenna
1	Airplane Antenna
2	Power Crest Instruments RDDR-96 Radio Modem (Transmitter with Power Amplifier)
	Inertial Measurement Unit
1	Litton LN-201 AMR AAM IMU Guidance System 6 inch by 2.9 inches
	Moving Map Display Software
1	Blue Marble GeoGraphics MapTracker Moving Map Display

9.0 RF Safety Levels

We must be aware of any potential safety problems with regard to radio frequency (RF) safety levels. We have examined two information sources and will probably order a third. One source discusses some of the biological issues[1] in general; it also provides a list of appropriate documents. Another more useful source, was provided by a hardware vendor in the form of a pamphlet[2]. This pamphlet included a plot of safety levels versus frequency as recommended by the American National Standards Institute (ANSI). This plot is included as Figure 134. The full standard is also available from ANSI[3].

In order to see how the airborne GPR might fit within these standards, we went through an approximate calculation for an impulse system and a stepped-chirp frequency domain system. They must be calculated separately because they have very different sources. For the time domain system, we considered a 1 MW transmitter with a 2 ns pulse transmitting 60 pulses per second. The peak power is high with this system but because of the extremely low duty cycle, the average power is only 120 mW. The power density in mW per square centimeter, shown as the abscissa in Figure 134, implies that the calculation must be made as a function of range. A sphere 10 m from the antenna has a surface area of about 1257 m^2 which implies a power density 10 m from the antenna of about $9.55 \cdot 10^{-6}$ mW/cm^2. This result holds for an isotropic antenna. The antennas used in this program will have maximum gains similar to those of a half-wave dipole, which has a gain

---

1 S. Bren and D. Hadlock, "Health Concerns of Non-Ionizing Radiation," EMC Test & Design, August, 1993, pp. 53-57.

2 "Pocket Guide to Non-Ionizing Radiation," General Microwave, Amityville NY, 1992.

3 "Electromagnetic Fields, Safety Levels with Respect to Human Exposure to Radio Frequency," ANSI/IEEE C95.1-1992.

of 1.8 dBi (1.8 dB more gain than an isotropic antenna). Considering a maximum gain of 4 dBi, the power density in the main lobe, 10 m from the antenna will be about $2.4 \cdot 10^{-5}$ mW/cm^2. From these approximations it is clear that we will be well below the safety levels shown in the Figure. One must also consider the fields inside the helicopter which will be about 1 m from the antenna. A sphere 1 m in radius has a surface area of about 12.6 m^2. The power density on this sphere is about 0.0024 mW/cm^2. This value is plotted in Figure 134. The value is well below the indicated safety levels. From these calculations it appears that power density levels are well below safety levels in the main beam when the antenna is 10 m or more above the ground. Levels inside the helicopter may be higher because of the proximity of the antenna. If peak power was a consideration rather than average power, the projected levels would be considerably higher. We might recommend that the helicopter doors be closed during operation of the radar. Levels inside the helicopter should be measured to insure safe operation.

For a frequency domain step-chirped system, the average power will be about 10 W (higher powers could be used but the source would then interfere with other receivers in the area). For a 10 W transmitter with an 80 percent duty cycle, the average transmitted power is 8 W. The power density 10 m from the 4 dBi gain antenna is about 0.0016 mW/cm^2. This value is significantly below the safety levels. The power density at distance 1 m from the antenna is about 0.16 mW/cm^2. This value is shown in Figure 134. For this frequency-domain system, the peak power and the average power are nearly equal. Table 13 summarizes the data.

The danger from non-ionizing radiation is believed to be, at the present time, due to thermal effects such as those exploited in a microwave oven. Hence, these standards are written to average power considerations. It is not clear from current research that other mechanisms might not also constitute health risks. We believe that keeping the helicopter doors closed and not energizing the radar until we are at least 10 m off the ground will effectively minimize any potential health risk.

Table 13 Estimated Power Density Levels for Time Domain and Frequency Domain GPR's.

	Power Density (mW/cm^2)	
	Range = 1 m	Range = 10 m
Time Domain Pulsed System	0.0024	0.000024
Frequency Domain Step-Chirped System	0.16	0.0016

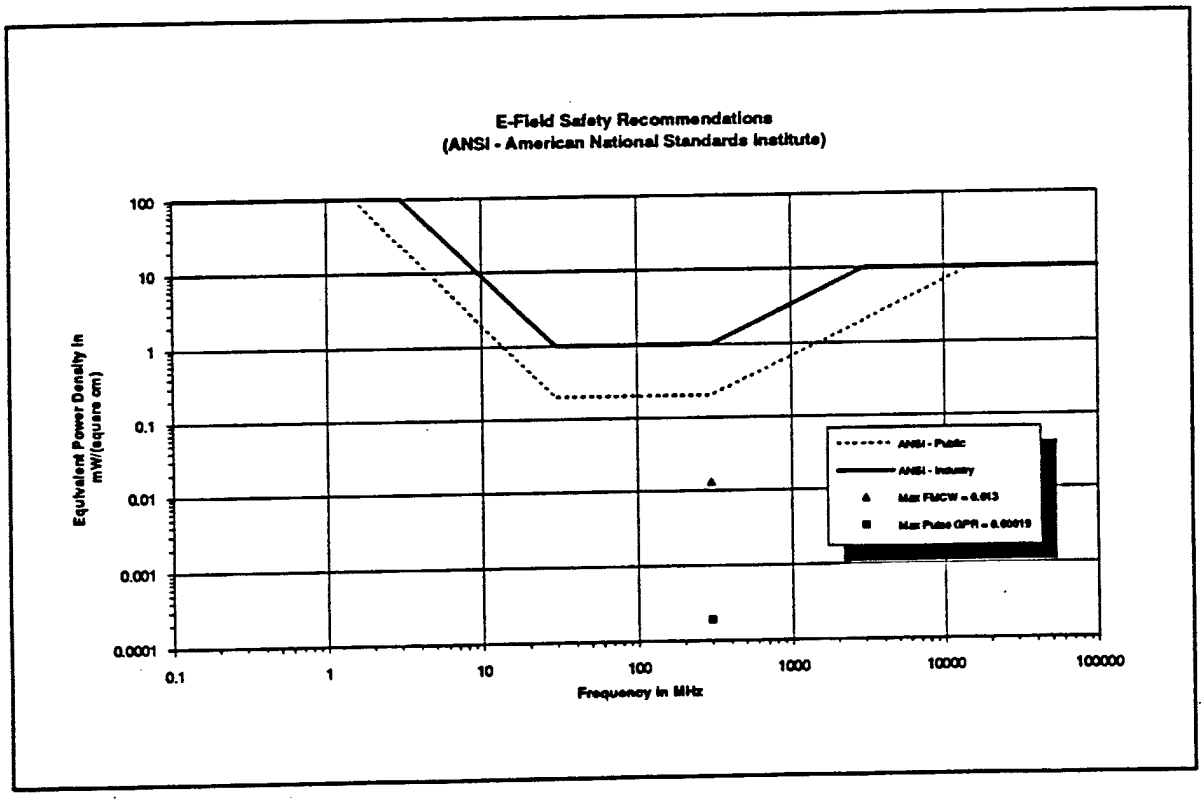

Figure 134 ANSI E-field safety levels.

10.0 Literature Review

One task in this Program was to perform a literature review of world-wide efforts in GPR in order to assess the value of any new information. We performed searches of computer data bases, compiled articles and books available to us, and discussed some recent GPR work with individuals involved. In the final evaluation, we were not able to find much useful data on GPR that was not already part of the knowledge database of the Battelle and ESL staff members involved in this project. We continue to monitor GPR-related literature for current articles that may benefit this program. The papers being referenced in this section are compiled in at the end of this section, beginning on page 235.

10.1 GPR Subjects Papers

1993 Airborne GPR Test Trials. We became aware of an airborne GPR/foliage penetration system evaluation that was held in Yuma, Arizona in the summer of 1993. Dr. Serpeil Ayasli of Lincoln Laboratory is the leader of a team evaluating the results. She said that they were just beginning to evaluate the data as of September 1993. She thought the results would first be reported through conference papers and later through formal reports. She agreed to share Lincoln Lab data with us. She presented a paper on their results at the Unexploded Ordnance Detection and Range-Remediation Conference in Golden Colorado in May 1994.

Lee (1994), presents surface to underground loss models derived from the 1993 Yuma GPR experiment, as well as some clutter data for the 100-500 MHz region and depression angles from 30° to 60°.

Time-Frequency Distributions. Three articles are included that discuss time-frequency distributions [Cohen (1989), Moghaddar (1993), Hlawatsch (1992)]. The Cohen and Hlawatsch papers are tutorials and reviews of general distributions. The Moghaddar article applies a single time-frequency distribution (the running window or short time Fourier transform) to an electromagnetic scattering application and is more useful for specific information of interest to the GPR application. From Moghaddar, the running window Fourier transform (RWFT) of $S(\Omega)$ is given by

$$\mathrm{RWFT}_s(t,\omega) = \int_{-\infty}^{\infty} S(\Omega)W(\omega-\Omega)e^{i\Omega t}d\Omega \tag{119}$$

where $W(\omega)$ is a window function. Moghaddar uses the Kaiser-Bessel window function. A similar expression can be found that processes time domain data. From equation (119) one can see that the RWFT is a surface above the time and frequency axes. Using the plot of the RWFT one can see changes in frequency as a function of time. Moghaddar includes several examples for scattering from an open-ended circular cavity. This structure is highly resonant, as are our UXO targets, and several resonances are easily identified that were not obvious in either the time-domain or frequency-domain plots of the scattered signal.

Other time-frequency distributions such as wavelet transforms, Wigner distributions, and ambiguity functions, can be used to give insight into aspects of physical behavior. The running window Fourier transform and wavelet transforms are linear operations and operate on voltages or currents. Wigner distributions and ambiguity functions operate on power or energy and are therefore quadratic in nature. The Wigner distribution can be given as

$$\mathrm{WD}_s(t,\omega) = \int_{-\infty}^{\infty} S(\omega+\frac{\Omega}{2})S^*(\omega-\frac{\Omega}{2})e^{i\Omega t}d\Omega \tag{120}$$

where the asterisk denotes the complex conjugation operation. The Wigner distribution is optimum in some sense but the quadratic nature of the distribution implies that cross-product terms are present in the distribution. For physical situations where the cross-product terms

are obvious, they can be removed. When they are not obvious in the distribution, they make interpretation much more challenging.

Time-Domain Antenna Characterization. Allen, et al., (1993) proposes definitions for characteristic properties of wide-bandwidth antennas because the frequency-domain definitions are useful and intuitive only at a single frequency. The proposed definitions include directivity, fidelity, radiation resistance, effective area, gain, efficiency antenna factor, effective height, and others. Some of the definitions are a function of the shape of the transmitted signal in the time domain.

Wideband Antennas. One of Prof. Harmuth's papers on wideband antennas is included in the list [Harmuth and Mohamed (1992)]. Over the years he and his colleagues have published theoretical analysis based on so-called "non-sinusoidal functions." We did not think the antenna discussed in this paper was useful to this program.

Complex Resonances. The Interaction Note [Baum (1993)] presents equations for determining the complex natural resonances of a scattering target when the target is immersed in a non-free space medium. The equations were discussed on page 18 and results for measured targets are presented in Table 1.

Airborne GPR Systems. One paper [Cameron (1993)] discusses the author's FM-CW radar that operates between 250 to 750 MHz. They talk a lot about their antennas (each a conical helix) that will not go as low in frequency as we want to go. They also use GPS. They record onto VHS tape and generate color-coded images. They use a precision radar altimeter to know height above ground. Their testing was done in the Mohave desert. They have had encouraging results but do not seem to do any target discrimination.

Land-Mine Applications. One paper [Roy, et al. (1990)] summarizes work using L-band (1.55 GHz, 10 nsec) and S-band (3.5 GHz, 1 nsec) radars. Because it is a land mine application they are not worried about extensive propagation loss. They used SAR with

1 transmitter and 5 receivers arrayed orthogonal to direction of propagation. Their output was images in the 3.5 GHz case. Output was waveforms in the 1.55 GHz case - claimed to detect mines but had no data on false alarms. The computer programs in back may be useful as check against our codes and approaches.

Another paper [Graham (1991)] summarizes work at 3.5 GHz on land mines. They use an extended linear array and synthetic beam-forming. The output is in the form of images. Nothing is relevant to our effort.

Ground-Based Detection Systems. One paper [Sandness and Bennett (1992)] talks about the remotely controlled vehicle (RCS) they will build for cleaning DOE sites. It will have magnetometers on-board and will have to minimize ferrous metals. PNL is developing the GPR. Other sensors (chemical, biological., etc.) may also be used but they will not be on at the same time. The vehicle has six wheels and a generator to supply power to the instrumentation. It minimizes the use of steel due to the magnetometers. They use an RF ethernet link back to the controlling station. This vehicle does exist and has undergone limited testing but the DOE program funding the work is currently on hold.

ESL Papers. Several of the papers summarize results of work performed at ESL in the last 20 years. The results of these papers provide the basic knowledge base that we use in all our activities. These papers include [Caldecott, et al, (1988), Chan et al, (1979), Chan et al, (1981), Mains and Moffatt (1974), Moghaddar and Walton, (1993), Peters, et al, (1992), Poirier (1993), Volakis and Peters (1983)].

GPR Hardware. One paper [Fenner (1992)] was one of those presented at the Government workshop on GPR at Vicksburg in 1992 [Butler (1992)]. Most of the papers are represented by one page abstracts. This paper, by GSSI representatives provides some detail on work they are doing to increase bandwidth using new transmitters and antennas but no details as to the nature of either are provided. It was very unclear what they were trying to accomplish. Two plots showed that a bigger aperture decreased the beamwidth. They keep

talking about an optimized frequency helping their process (instead of increased bandwidth). We did not find the information to be relevant.

A paper by Ralston (1993) describes a methodology for system performance comparison of ultra-wideband radars implemented as either impulse or stepped-chirp systems. All current GPR systems fit one of these categories.

Foreign UWB Radar Systems for Subsurface Applications. We found many foreign wideband or UWB systems in our literature search that were primarily designed for geophysical or subsurface applications. Some of these systems are currently being used for non-destructive testing of concrete structures and highways, mine detection, resource mapping, and foliage penetration. Research in subsurface impulse radar is aimed at target detection and identification.

In addition to the systems mentioned here, many countries are buying commercial U.S. GPR systems such as the Subsurface Interface Radar (SIR) manufactured by Geophysical Survey Systems Incorporated (GSSI) to make measurements. Many have also built custom systems around U.S. manufactured network analyzers such as the Hewlett-Packard Model 8510 Network Analyzer.

CARABAS. The Swedish National Defense Research Establishment has developed a UWB airborne radar, named Coherent All Radio Band Sensing (CARABAS) [Nordwall (1993), Hellstan (1992)]. If CARABAS is successful, applications for CARABAS may include military surveillance, civilian remote sensing, environmental mapping, and sea ice thickness measurement. CARABAS is a low frequency UWB synthetic aperture radar (SAR). It operates at low frequencies (20-90 MHz) in order to penetrate foliage and ground. The low frequency was determined by the noise environment (radio frequency interference) and the maximum practical length of the antenna. The high frequency was determined by the absolute bandwidth, SAR swath width, available transmission power, and data storage capacity.

CARABAS is a diffraction limited SAR. A SAR with a geometric resolution less than or equal to a wavelength, as set by the Rayleigh limit, produces speckle free radar images. A large relative bandwidth is required to achieve diffraction limited SAR. Increasing the bandwidth, complicates the SAR processing. A deterministic SAR processing scheme is used. CARABAS is restricted by the requirement that the length of the synthetic aperture must equal the surveillance range.

The CARABAS antennas are two broad band thick dipoles positioned on either side of the center of the aircraft. The dipoles are actually flexible sacks several meters long attached to the tail of the aircraft which are inflated with ram air when the aircraft is airborne.

CARABAS is currently limited by the state of the art of A/D converters and data storage systems. It requires a very large dynamic range to overcome the interference of airborne HF radar. Hellsten states that the most efficient use of transmitted energy requires the sampling and data rates to be comparable with the bandwidth of the transmitted pulse. CARABAS uses signal shaping and limits the maximum range to make the instantaneous bandwidth small.

CARABAS was tested in 1992 in Sweden and the reported range is 10 km, with a resolution of 2 meters. The CARABAS system has participated several times in evaluation tests in the United States under DARPA funding. To date, hardware malfunctions have prevented valid data from being collected, so the capabilities of the CARABAS system have not been established as yet.

Multistatic Radar System. In Sweden, Ulriksen [Ulriksen (1992)] has developed a five channel, computer controlled, multistatic, wideband impulse radar. The system uses five antennas mounted near the rear bumper of a van for ground penetrating radar. The antennas' boresight direction is parallel to the normal to the surface to eliminate the horizontal range component from the data. The five antennas are arranged in the form of a push-broom scanner to increase the area covered. Data is acquired from the antennas in parallel and the

image is generated by the movement of the vehicle. The antenna transmission is synchronized to avoid interference between adjacent antennas. This system has been used to survey roads, bridges, and earth dams. The van can be driven at 100 km/hr, taking data at 1 meter intervals.

ERA Technology. An overview of UWB radar technical developments at ERA Technology Ltd. Leatherhead Surrey, United Kingdom during the early to mid 1980's towards a ground penetrating radar has been published by ERA staff [Chignall et al, (1988)]. ERA has designed and developed resistively loaded monopole and dipole antennas for ground penetrating radar for use close to the ground. They have used crossed, resistively loaded dipoles to find buried plastic objects and resistively loaded monopoles in narrow boreholes. A time-domain pulsed system was chosen in order to try to separate the low target signal from the much larger clutter signal. A pulse is transmitted many times and the received signal is sampled once per transmitted pulse. Many transmitted pulses are used to build up the received waveform. PRFs of up to 1 MHz have been used. ERAs pulse generators use an avalanche transistor as a fast switch to trigger the pulse. The receiver consists of a nondispersive, ultrawideband amplifier (20 kHz to 7 GHz) and a commercial sampling head. ERA has investigated various methods of signal processing, including simple energy detection and extraction of the complex natural resonances of the targets using Prony's Method.

ERA has also developed low cost impulse generators for use in ground penetrating radar systems [Daniels (1993)]. They claim the continuously resistively loaded dipole is useful in free space short range radar.

Abrahamsson, et al., have developed a ground penetrating radar using an antenna and radar unit designed by ERA Technology and a 486 computer mounted on a jeep [Abrahmson (1992)]. The pulse width is 1 ns, the pulse repetition frequency is 250 kHz, and the peak power is 50 W. The transmit and receive antennas are crossed-dipoles with exponential, resistive loads. The antennas are mounted on the front of a jeep and scan across the path in

front as the jeep moves forward. The speed of the jeep is 5 km/hr. Only preliminary field tests have been performed. Some measurements were made over an archaeological site to try to locate walls. In an anechoic chamber, Abrahamsson, et al., are also measuring the impulse response of some simple objects. They hope to use the characteristic frequency signatures to identify objects. They only show data for a perfectly conducting sphere.

Danials (1994), gives a tutorial on GPR for various applications. This paper is essentially an updated an less technical version of a comprehensive summary published in 1989 (Danials, 1989).

Short Range Subsurface Radars. Several short range surface penetrating UWB radars have been developed by foreign sources. These systems are aimed at detecting defects or objects within trees or poles or behind walls or floors.

A portable impulse radar has been developed for short range, less than 2 m, penetration by researchers at both the Radio Laboratory and the Laboratory of Applied Electronics, Helsinki University of Technology, Espoo, Finland [Vainikainin (1992), Vainikainin (1989)] . A pulse length of 0.2 to 0.35 ns is used to obtain a range resolution of 3 to 5 cm in this surface penetrating radar system. This system is hand-held, low power (8 watts), and low weight (3 kg). The transmitter has two possible impulse lengths, 0.2 ns for detecting dry objects and 0.5 ns for detecting wet objects. The PRF is about 1 MHz. The antennas are modified unsymmetric TEM horns filled with a lossy dielectric (PVC). The antennas were designed to be small and reduce ringing. Frequency of operation is 1-4 GHz. The sampling-type receiver uses a schottky diode bridge as a sampling gate for a gate time of less than 0.2 ns. The noise level of the receiver is limited by the ringing of the antennas at short ranges. A single board AT-compatible computer controls the data collection and signal processing. This battery operated portable system weighs about 10 kg. The system has been used to distinguish between rotten parts of a telephone pole and the front and back edges of a pole. This radar has also been used to examine walls and floors in buildings.

Olver and Cuthbert [Olver (1988)] have described the use of frequency modulated carrier wave (FMCW) radar for short range detection of objects hidden behind walls and floors.

Subsurface Impulse Imaging Radar (SIIR). Researchers at the Changchun Institute of Geography, Academia Sinca, Chang Chun, People's Republic of China, have developed an impulse imaging radar for subsurface applications that can be dragged along the ground by hand or pulled by a truck [Junrong (1992)]. Junrong et al. have developed a Subsurface Impulse Imaging Radar (SIIR) that uses a transmitting pulse repetition frequency of 100 kHz, 5 ns pulse width, and 150 V double-direction pulse amplitude. The antenna is a bow-tie dipole style. Each dipole is a copper triangle 600 mm long, 300 mm wide, and 1 mm thick. An IBM PS/2 30 computer controls the data collection and signal processing with the help of a Z80 microprocessor. The system has been used to probe metal and non-metal pipes underground and the profile of a lake bed.

Other Foreign Subsurface Radars. Cambridge Consultants Ltd. (CCL) Cambridge, United Kingdom has developed several surface and subsurface impulse radar systems [Oswald (1988)]. CCL has developed a helicopter-mounted system for measurement of sea-ice thickness, a trolley-mounted system for surface measurements, and a borehole system for measuring mineral seam boundaries.

In the United Kingdom impulse radar is being built and tested as a means for non-destructive testing of concrete slabs and in highway construction [Baston-Pitt (1992]. Impulse radar can be used to test the density, thickness, and steel placement within the concrete. Impulse radar is routinely used to examine hidden defects within structures [Henderson (1990].

Zhang of China has also developed a carrier free impulse subsurface radar. The system uses a gaussian pulse with a pulse width of 2.6 ns, rise time of 1.9 ns, a repeating

frequency of 200 kHz, and amplitude of 100 volts to examine underground targets [Zhang (1989)].

Researchers from NTT Electrical Communications Laboratories, Nippon Telegraph and Telephone Corporation, Tokyo, Japan have developed a wideband microwave holographic method for imaging buried objects [Osumi (1989)].

Researchers at McMaster University and the Ontario Ministry of Transportation, Canada have developed an impulse radar for evaluating asphalt covered bridge decks [Chung (1992)]. A stepped-frequency ground penetrating radar has been developed by a joint Canadian and Japanese research team [Iizuka (1984)].

10.2 SAR Processing of Underground Targets

A number of recent papers have discussed SAR processing of underground target data for both two-dimensional and three-dimensional images. The emphasis in most of these papers has been on the effects of non-homogeneous ground properties on the imaging process, and methods of mitigating for unknown and variable underground wave propagation velocities (due to ground dielectric constant and loss tangent variations for GPR systems).

One should note that the so-called "migration" processing employed to generate 2-D or 3-D seismic imagery is often mathematically equivalent to 2-D or 3-D SAR processing of GPR imagery. Many recent authors have recognized this, and have written papers which apply to either seismic or GPR image processing.

Some recent papers of this nature have been several by Fisher et.al (1992) who describe 2-D reverse-time migration of impulse GPR data (a process exactly equivalent to 2-D SAR processing of down-looking GPR data).

A paper by Schleicher, et.al. (1993) describe 3-D migration for arbitrary underground velocity profiles, included variations in x, y, and z coordinates.

A paper by Lee, et.al. (1993) describes a partially coherent migration process which attempts to compensate for errors in the underground velocity model used for the processing.

A paper by Spagnolini (1993) discusses 2-D phase unwrapping and phase aliasing, a process that is required when the data sample spacing is too large relative to the target signal variations. This form of processing, for example, may be required for the track-to-track processing of the airborne GPR data to generate the 3-D imagery.

A paper by Daniels, et.al. (1993) describes 3-D GPR imaging of geophysical targets and the need for appropriate 3-D visualization software in order to correctly interpret the imagery.

A paper by Casper, et.al. (1993) describes the use of software developed for 2-D seismic migration to generate 2-D GPR imagery for a ground medium that is inhomogeneous in both depth and the along-track direction.

Roberts and Daniels (1991) describe a technique for the use of bistatic GPR data to recover the velocity versus depth profile directly from the radar data.

McCorkle and Nguyen (1994) describe a 2-D SAR imaging approach for dispersive targets, that is targets whose scattering is frequency dependent.

10.3 Symposia and Reviews

Various GPR-related symposia have been conducted recently covering a variety of subjects. Some of these are directly related to UXO and/or mine detection, others are oriented primarily toward geophysical applications, and still others toward wideband radar technology in general.

These include the EPA and Ohio State University Advanced Ground Penetrating Radar Technologies and Applications workshops held in October 1992, 1993, and 1994. Papers presented at these workshops have primarily a geophysical target orientation, although GPR technology in general is also discussed. The papers presented at these workshops are published as workshop proceedings.

The international conference on GPR held in 1990, with abstracts only published in conference proceedings. Again, these conferences are heavily oriented toward geophysical applications.

The SPIE conferences on ultra-wideband radar in 1992, ultra-high resolution radar in 1993, in 1994, and mine detection to held in April 1995. These conferences are oriented toward ultra-wideband radar technology in general including foliage penetration, GPR, mine detection, and a variety of other non-GPR applications. Most of the hardware related papers and many of the signal and data processing related papers are, however, directly relevant to GPR radar systems. Papers presented at these conferences are published by the SPIE in conference proceedings.

A conference specifically oriented toward UXO detection and range-remediation was held in May, 1994. A proceedings containing the papers presented has been published.

Several recent reviews of GPR technology have also been published. One is a general review of sensor technology for ordnance and explosive waste detection and location by JPL (1994) in which GPR's are discussed as well as a variety of other sensors.

Another is a GPR specific technology review by Lincoln Lab (1994) which reviews GPR systems, soil parameter measurements, signal processing, waveform design, phenomenology and modeling including subsurface tomography from boreholes, and some shuttle imaging radar results.

10.4 References for Literature Review

Abrahamsson, S., et al., "Development of a Ground Penetrating Radar System for Object Detection and Classification", Fourth International Conference on Ground Penetrating Radar, (Editors: P. Hanninen and S.Autio),pp.65-69, Rovaniemi, Finland, June 8-13,1992.

Allen, O.E., D.A. Hill, and A.R. Ondrejka, "Time-Domain Antenna Characterization," IEEE Trans. on Electromagnetic Compatibility, Vol. EMC-35, No. 3, pp. 339-346, August 1993.

Arioka, R., "New Underground Radar System," NTT, No-Dig 92 Conference Paper, Washington, D.C., April 1992.

Bartel, David C., and A. Becker, "Time-Domain Electromagnetic Detection of a Hidden Target", Geophysics, Vol. 53, No.4, April 1988, pp.537-545.

Baston-Pitt, J., "Computers and impulse radar in highway construction", Highways and Transportation, vol.39, no.4, pp.10-12, April 1992.

Baum, C.E., "The SEM Representation of Scattering from Perfectly Conducting Targets in Simple Lossy Media," Interaction Note 492, Phillips Laboratory, April 1993.

Bennett, S., L. Tarno, J. Butler, "Range Clearance Technology Assessment," Naval Explosive Ordnance Disposal Technology Center, prepared for U.S. Army Corps of Engineers, March 1990.

Bowders, J.J., Jr, R.M. Koerner, "Buried container detection using ground-penetrating radar", Journal of Hazardous Materials, Vol. 7, No. 1, pp. 1-17, November 1982.

Botros, Adel Z., and A. David Olver, "Analysis of Target Response of FM-CW Radar," IEEE Transaction of Antennas and Propagation, Vol. AP-34, No.4, April 1986, pp. 575-581.

Butler, D.K., "Proceedings of the Government Users Workshop on Ground Penetrating Radar Applications and Equipment 26-27 March 1992, Vicksburg, Mississippi," U.S. Army Waterways Experiment Station, December 1992. (AD-A261 873)

Caldecott, R., M. Poirier, D. Scofea, D.E. Svoboda, and A.J. Terzuoli, "Underground Mapping of Utility Lines Using Impulse Radar," IEE Proceedings, Vol. 135, Pt. F, No.4, August 1988, pp. 343-353.

Cameron, R.M., "Development and Application of Airborne Ground-Penetrating Radar for Environmental Disciplines," Ninth Thematic Conference on Geologic Remote Sensing, Pasadena, CA, February 1993.

"Carrierless Pulsed Radar System Detects Buried Plastic Pipes," The Chemical Engineer, October 1986.

Casper, D.A., et.al., "Testing a two-dimensional, seismic migration routine on ground-penetrating radar simulations", Proc. of the Second Government Workshop on GPR, Advanced Ground Penetrating Radar: Technologies and Applications, Oct. 26-28, 1993, Fawcett Center, The Ohio State University, Sponsored by U.S. Environmental Protection Agency, Region V and the Ohio State University, Oct. 1993, pp 319-336.

Chan, Luen C., David L. Moffatt, and Leon Peters, Jr., "A Characterization of Subsurface Radar Targets," Proceedings of the IEEE, Vol. 67, No. 7, July 1979, pp. 991-1000.

Chan, Luen C., Leon Peters, Jr., and David L. Moffatt, "Improved Performance of a Subsurface Radar Target Identification System Through Antenna Design", Transactions of Antennas and Propagation, Vol. AP-29, No. 2, March 1981, pp. 307-311.

Chignell, R.J., P.A. Jackson, and K. Madani, "Early Developments in Ground-Probing Radar at ERA Technology Ltd.," IEE Proceedings, Vol. 135, Pt. F, No. 4, August 1988, pp. 362-370.

Chung, T., et al., "Impulse Radar Evaluation of Asphalt-Covered Bridge Decks", IEEE Trans. on Aerospace and Electron. Sys., vol.28, pp.125-136, 1992.

Clarricoats, P.J.B., "Portable radar for the detection of buried objects," IEEE/IEE Radar-77 International Conference Proceeding, pp. 547-551, October 1977.

Cohen, L, "Time-Frequency Distributions - A Review," Proceedings of the IEEE, Vol. 77, No. 7, pp. 941-981, July 1989.

Daniels, D.J., "Developments in impulse radar technology for surface penetrating radar", IEE Colloquium on 'Antenna and Propagation Problems of Ultrawideband Radar' (Digest No. 004), pp.2/1-11, January 12, 1993.

Daniels, D.J., "Surface Penetrating Radar for Industrial and Security Applications", Microwave Journal, Dec. 1994, pp. 68-82.

Daniels, D.J., D.J. Gunton, and H.F. Scott, "Introduction to Subsurface Radar," IEE Proceedings, Vol. 135, Pt. F, No. 4, August 1988, pp. 278-320.

Daniels, J.J., et.al., "3-D GPR", Proc. of the Second Government Workshop on GPR, Advanced Ground Penetrating Radar: Technologies and Applications, Oct. 26-28, 1993, Fawcett Center, The Ohio State University, Sponsored by U.S. Environmental Protection Agency, Region V and the Ohio State University, Oct. 1993, pp 307-318.

Fenner, T.J., "Recent Advances in Subsurface Interface Radar Technology," Proceedings of the Government Users Workshop on Ground Penetrating Radar Applications and Equipment 26-27 March 1992, Vicksburg, Mississippi," U.S. Army Waterways Experiment Station, pp. 68-74, December 1992. (AD-A261 873)

Fisher, Elizabeth, George A. McMechan, and A. Peter Annan, "Acquisition and Processing of Wide-Aperture Ground-Penetrating Radar Data", Geophysics, Vol. 57, No. 3, March 1992, pp. 495-504.

Fisher, Elizabeth, George A. McMechan, A. Peter Annan, and Steve W. Cosway, "Examples of Reverse-Time Migration of Single-Channel, Ground-Penetrating Radar Profiles," Geophysics, Vol. 57, No. 4, April 1992, pp. 577-586.

Fisher, E., G.A. Mcmechan, and A.P. Annan, "Reverse Time Migration Applied to Ground Penetrating Radar," Third International Conference on Ground Penetrating Radar, U.S. Geological Survey Open-File Report 90-414, Lakewood, CO, p 25, May 1990.

Geo-Centers, Inc., "Final Technical Report - Remote Detection of Unexploded Ordnance - Ground Penetrating Radar," Report GC-TR-91-1691, prepared for Naval Explosive Ordnance Disposal Technology Center, February 1992.

Giglio, D., J.M. Ralston, and M. Braunstein, "Perspective on Underground and Obscured Target Detection and Imaging," Institute for Defense Analysis Document D-1362, prepared for ARPA, May 1993.

Graham, W.J.,"Focused Synthetic Microwave Array for Mine Detection and Imaging," Report No. TR-91-001-01 Graham Research Corp, prepared for Belvoir Research Development and Engineering Center, December 1991. (AD-A244 649)

Grosch, T.O., "Ground Penetration Radar Technology Review", Project Report GPR-1, prepared for U.S. Army Research Laboratory, Sep. 1994.

Harmuth, H.F. and N.J. Mohamed, "Large Current Radiators," IEE Proceedings Part H, Vol. 139, No. 4, pp. 358-362, August 1992.

Haykin, S., and C. Deng, "Classification of radar clutter using neural networks", IEEE Transactions on Neural Networks, Vol. 2, No. 6, pp. 589-600, November 1991.

Hellstan, H., "CARABAS--An UWB Low Frequency SAR", IEEE MTT-S International Microwave Symposium Digest, vol.3, pp. 1495-1498, June 1-5, 1992.

Henderson, D., "Use for impulse radar for the investigation of hidden features and defects in structures", British Journal of Non-Destructive Testing, vol.32, no.8, pp.405-407, August 1990.

Hipp, J.E., "Soil electromagnetic parameters as functions of frequency, soil density, and soil moisture," Proceedings of the IEEE, Vol. 62, No. 1, pp. 98-103, January 1974.

Hill, David A., "Near-Field Detection of Buried Dielectric Objects," IEEE Transactions on Geoscience and Remote Sensing, Vol. 27, No. 4, July 1989, pp. 364-368.

Hlawatsch, F., and G.F. Boudreaux-Bartels, "Linear and Quadratic Time-Frequency Signal Representations," IEEE Signal Processing Magazine, April 1992, pp. 21-67.

Holloway, A.L., N.M. Soonawala, and L.S. Collett, "Three-Dimensional Fracture Mapping in Granite Excavations Using Ground-Penetrating Radar," CIM, Vol. 79, No. 896, pp. 54-59.

Iizuka, K. and A.P. Freundorfer, "Detection of nonmetallic buried objects by a step frequency radar," Proceedings of the IEEE, Vol. 71, No. 2, pp. 276-279, February 1983.

Iizuka, K. and P. Freundorfer, et al., "Step-Frequency Radar", J. Appl. Phys., vol.56, pp. 2572-2583, 1984.

Imai, T., Tl Sakayama, and T. Kanemori, "Use of ground-probing radar and resistivity surveys for archaeological investigations," Geophysics, Vol. 52, No. 2, pp. 137-150, February 1987.

Jet Propulsion Laboratory, Contributors, Peterson, J.C., et.al., "Sensor Technology Assessment for Ordnance and Explosive Waste Detection and Location", Report No. JPL D-11367 Revision A, May 12, 1994.

Junkin, G., and A.P. Anderson, "Limitations in Microwave Holographic Synthetic Aperture Imaging over a Lossy Half-Space," IEE Proceedings, Vol. 135, Pt. F, No. 4, August 1988, pp. 321-329.

Junrong, Z., L. Fengyu, W. Hongqi, C. Meng, and H. Yan, "The Development of Subsurface Impulse Imaging Radar and Its Applications", Fourth International Conference on Ground Penetrating Radar, Geological Survey of Finland, Special Paper 16, pp.71-77, June 8-13, 1992.

Lee, C.F., "Ground Penetration Radar Phenomenology Investigations", Project Report GPR-2, prepared for U.S. Army Research Laboratory, Sep. 1994.

Lee, D., et.al., "Partially coherent migration", Geophysics, Vol. 58, No. 9, Sept. 1993, pp 1301-1313.

Lerner, R. M., T.E. Landers, W.R. Zettler, J.R. Brown, "Observations and Measurements Related to the Use of Airborne UHF CW Radar for Underground Tunnel Detection," Project Report TRE-1, MIT Lincoln Laboratory, February 1983.

Li, H.J., V. Chiou, "Aerospace Target Identification-Comparison Between the Matching Score Approach and the Neural Network Approach," Journal of Electromagnetic Waves and Applications,Volume 7, No. 6, pp. 873, 1993.

Lucius, J.E. G.R. Olhoeft, and S.K. Duke, ed., "Third International Conference on Ground Penetrating Radar," U.S. Geological Survey Open-File Report 90-414, Lakewood, CO, May 1990.

Mains, R.K., and D.L. Moffatt, "Complex Natural Resonances of an Object in Detection and Discrimination," Technical Report 3424-1, The Ohio State University ElectroScience Laboratory, June 1974.

Maloney, J.G. and G.S. Smith, "A Study of Transient Radiation from the Wu-King Resistive Monopole - FDTD Analysis and Experimental Measurements," IEEE Trans. on Antennas and Propagation, Vol. 41, No. 5, pp. 668-676, May 1993.

McCorkle, J. and Nguyen, L., "Focusing of Dispersive Targets Using Synthetic Aperture Radar", Report No. ARL-TR-305, Aug. 1994.

Michiguchi, Yoshihiro, Kazuo Hiramoto, Masatsugi Nishi, Toshihide Ootaka, and Masumi Okada, "Advanced Subsurface Radar System for Imaging Buried Pipes," IEEE Transactions on Geoscience and Remote Sensing, Vol. 26, No. 6, November 1988, pp. 733-739.

Michiguchi, Y., K. Hiramoto, N. Masatsugu, F. Takahashi, T. Ohtaka, and M. Okada, "Development of Signal Processing Method for Imaging Buried Pipes," IEEE Trans. on Geoscience and Remote Sensing, Vol. GE-25, No. 1, January 1987, pp. 11-15.

Moghaddar, A. and E.K. Walton, "Time-Frequency Distribution Analysis of Scattering from Waveguide Cavities," IEEE Trans. on Antennas and Propagation, Vol. AP-41, No. 5, May 1993, pp. 677-680.

Nordwall, B.D., "Swedish-Developed Radar to Penetrate Foliage, Ground," Aviation Week & Space Technology, Volume 138, pp. 53-53, January 1993.

Olver, A.D., and L.G. Cuthbert, "FMCW Radar for Hidden Object Detection," IEE Proceedings, Vol. 135, Pt. F, No. 4, August 1988, pp. 354-361.

Osumi, N., and K. Ueno, "Detection of Buried Plant," IEE Proceedings, Vol. 135, Pt. F, No. 4, August 1988, pp. 330-342.

Oswald, G.K.A., "Geophysical Radar Design," IEE Proceedings, Vol. 135, Pt. F, No. 4, August 1988, pp. 371-379.

Peters, L., Jr., M. Poirier, and M. Barnes, "General Ground Penetrating Radar (GPR) Concepts," Proceedings of the Fourth International Conference on Ground Penetrating Radar, Rovaniemi, Finland, p. 7-12, June 1992.

Poirier, Michael, "Advanced Ground Penetrating Radar", The Ohio State University ElectroScience Laboratory Technical Note, 1993.

Ralston, J.M., "System Analysis of Ultrawideband Instrumentation Radars: Impulse Versus Stepped-Chirp Approaches," R.S. Vickers, Editor, Proc. of SPIE 1875, pp. 114-123, 1993.

Roberts, R.L, et.al, "Analysis of the effectiveness of velocity-depth inversion using bistatic GPR data collected over targets of different sizes, shapes, and orientations", Proc. of the Second Government Workshop on GPR, Advanced Ground Penetrating Radar: Technologies and Applications, Oct. 26-28, 1993, Fawcett Center, The Ohio State University, Sponsored by U.S. Environmental Protection Agency, Region V and the Ohio State University, Oct. 1993, pp 83-99.

Robertson, Richard, "UNDEX Site Survey Report," Naval Explosive Ordnance Disposal Technology Center report prepared for Toxic and Hazardous Material Agency, September 1991.

Rocca, F. C. Cafforio, and C. Prati, "Synthetic Aperture Radar - - A New Application for Wave Equation Technique," Geophysical Prospecting, V. 37, 1989, pp. 809-830.

Roy, S., R.S. Berkowitz, W.J. Graham, and D. Carlson, "Applications of Subsurface Radar for Mine Detection," University of Pennsylvania, prepared for U.S. Army Research Office, December 1990. (AD-A234 847)

Rutt, D.R., "Use of an Ultrawideband Synthetic Aperture Radar Technique for Buried Mine Detection," R.S. Vickers, Editor, Proc. of SPIE 1875, pp. 68-76, 1993.

Sandness, G.A. and D.W. Bennett, "A Remote Characterization System for Subsurface Mapping of Buried Waste Sites," Technical Note, Pacific Northwest Laboratory (DOE-Battelle), 1992.

Schleicher, et.al., "2-D true-amplitude finite-offset migration", Geophysics, Vol. 58, No. 8, Aug. 1993, pp 1112-1126.

Schutz, A.E., "Practical Radar Applications to Real World Locating Problems History," Geophysical Survey Systems, Inc., 1990 Plastic Pipe Detection Conference, May, 1990.

Sheen, D.R., S.C. Wei, T.B. Lewis, S.R. De Graaf, "Ultrawide-Bandwidth Polarimetric SAR Imagery of Foliage-Obscured Objects," R.S. Vickers, Editor, Proc. of SPIE 1875, pp. 106-113, 1993.

Smith, Glenn S., "Summary Report: Workshop on New Directions for Electromagnetic Detection of Non-Metallic Mines," June 23-26, 1992, Research Triangle Park, NC.

Smith, Glenn S. and Waymond R. Scott, Jr., "A Scale Model for Studying Ground Penetrating Radars", IEEE Transactions on Geoscience and Remote Sensing, No. 27, No. 4, July 1989, pp. 358-363.

Smith, C. Ray, and Paul M. Goggans, "Radar Target Identification," IEEE Antennas and Propagation Magazine, Vol. 35, No. 2, April 1993, p.27-38.

Spagnolini, U., "2-D phase unwrapping and phase aliasing", Geophysics, Vol. 58, No. 9, Sept. 1992, pp 1324-1334.

Suzuki,Tsutomu and Ikuo Arai, "Advance on Underground Radars", IEICE Transactions, Vol. E 74, No. 2, February 1991, p.289-294.

Ulriksen, P., "Multistatic radar system - MRS", Fourth International Conference on Ground Penetrating Radar, Geological Survey of Finland, Special Paper 16, pp.57-63, June 8-13, 1992.

Ursin, B., "Review of Elastic and Electromagnetic Wave Propagation in Horizontally Layered Media," Geophysics, Vol. 48, 1983, pp. 1063-1081.

Vainikainen, P., M. Tiuri, V. Knotra, M. Saarikoski, E. Nyfors, and R. Salminen, "High-resolution portable impulse radar", Conference Proceedings - European Microwave Conference, no. 19, pp.1091-1095, September 407, 1989.

Vainikainen, P., M. Tiuri, V. Kontra, and E. Nyfors, "Portable Short Range Subsurface Radar", Fourth International Conference on Ground Penetrating Radar, Geological Survey of Finland, Special Paper 16, pp.29-33, June 8-13, 1992.

Vellidis, G., M.C. Smith, D.L. Thomas, and L.E. Asmussen, "Detecting Wetting Front Movement in A Sandy Soil with Ground-Penetrating Radar," Transactions of the American

Society of Agricultural Engineers (ASAE), Vol. 33, No. 6, November-December 1990, pp. 1867-1874.

Volakis, John L., and Leon Peters, Jr., "Improved Identification of Underground Targets Using Video Pulse Radars by Elimination of Undesired Natural Resonances", IEEE Transactions on Antennas and Propagation, Vol. AP-31, No. 2, March 1983, pp. 334-340.

"Workshop on Noninvasive Geophysical Site Characterization", Private Communication from the Los Alamos National Laboratory.

Zhang, H., "Detection of the underground target by carrier, free impulse subsurface radar", Sichuan Daxue Xuebao (Journal of Sichuan University Natural Science Edition) (SCTHA), vol.26, no. 4, pp.501-504, June 9, 1989.

11.0 Airborne Platform

During the course of this effort, several airborne platform candidates have been considered. The most viable candidate continues to be a helicopter because of its large payload capacity, on-board power, and position control. The other candidates considered include a hot air balloon, a dirigible, and a cherry-picker. These options are discussed briefly below. The platform of choice is the UH-1 helicopter. Others are seriously considered only as test platforms.

11.1 UH-1 Helicopter

During May and June 1994 we had discussions with the Ohio Air National Guard about the possibility of using one of their helicopters as a test vehicle. We talked with Lt. Col. Lynn Coriell, the head of the Ohio Air National Guard (ANG) and Major Craig Ceneskie, the flight operations officer. They were both extremely cooperative. We visited Rickenbacker Air National Guard Base near Columbus, visited with the Army pilots stationed there, and viewed the UH-1 helicopter. The pilots were enthusiastic about participating in the program because it would be a break from their usual jobs as pilot trainers.

We met with the ANG in February 1995 on another program. Craig Ceneskie is now Lt. Col. Ceneskie and is the commander of the ANG. He remain extremely cooperative. We are working with the ANG to get mounting details arranged and initial flight tests scheduled. Everyone at the ANG is anxious to help us in this effort.

The aircraft themselves seem to be sufficiently large to house the electronics we anticipate using. The on-board electric power seemed adequate but without knowing the equipment we would use, we cannot finalize that arrangement. The National Guard furnished us with an operations manual that specifies flight profiles, weights, and available

power. The Guard must approve a long vertical dipole antenna,. These helicopters have an alternative strut structure that is four feet high. This strut provides an extra measure of versatility. We are not sure what kinds of approvals we need to obtain to mount an antenna structure below the aircraft. A line drawing of the helicopter is shown in Figure 135.

11.2 Hot Air Balloon

As an alternative aircraft for testing, we have been in communication with Col. Steve Watson at Hill Air Force Base in Utah. His unit performs atmospheric experiments using a hot air balloon with a 600 pound load limit. Col. Watson is interested in participating in our program. Generally, they hang a generator below the balloon basket. Because of our relatively low altitude requirements, we could possibly run an extension cord to the basket. Our antenna would be mounted below the balloon. They control the balloon position by tethering it above a truck that is driven slowly.

11.3 Dirigible

We are aware of a dirigible (self-powered) similar to the commercial blimps frequently used by television for coverage of sporting events. Such a self-controlled platform could be useful to us for testing without the expense and difficulties involved with using a helicopter. As of December 1994, we are still attempting to obtain more information on this platform. This platform is being considered as a test platform and not the final platform of choice.

11.4 Cherry-Picker

In a separately-funded but related effort, Battelle and ESL personnel participated in the UXO detection and remediation demonstrations at Jefferson Proving Ground in September 1994. We employed a step-chirped radar that will probably be used in the airborne system. Because of time and budget limitations, we were not able to use a helicopter. Instead, we employed a 14 ton, self-propelled cherry-picker capable of raising

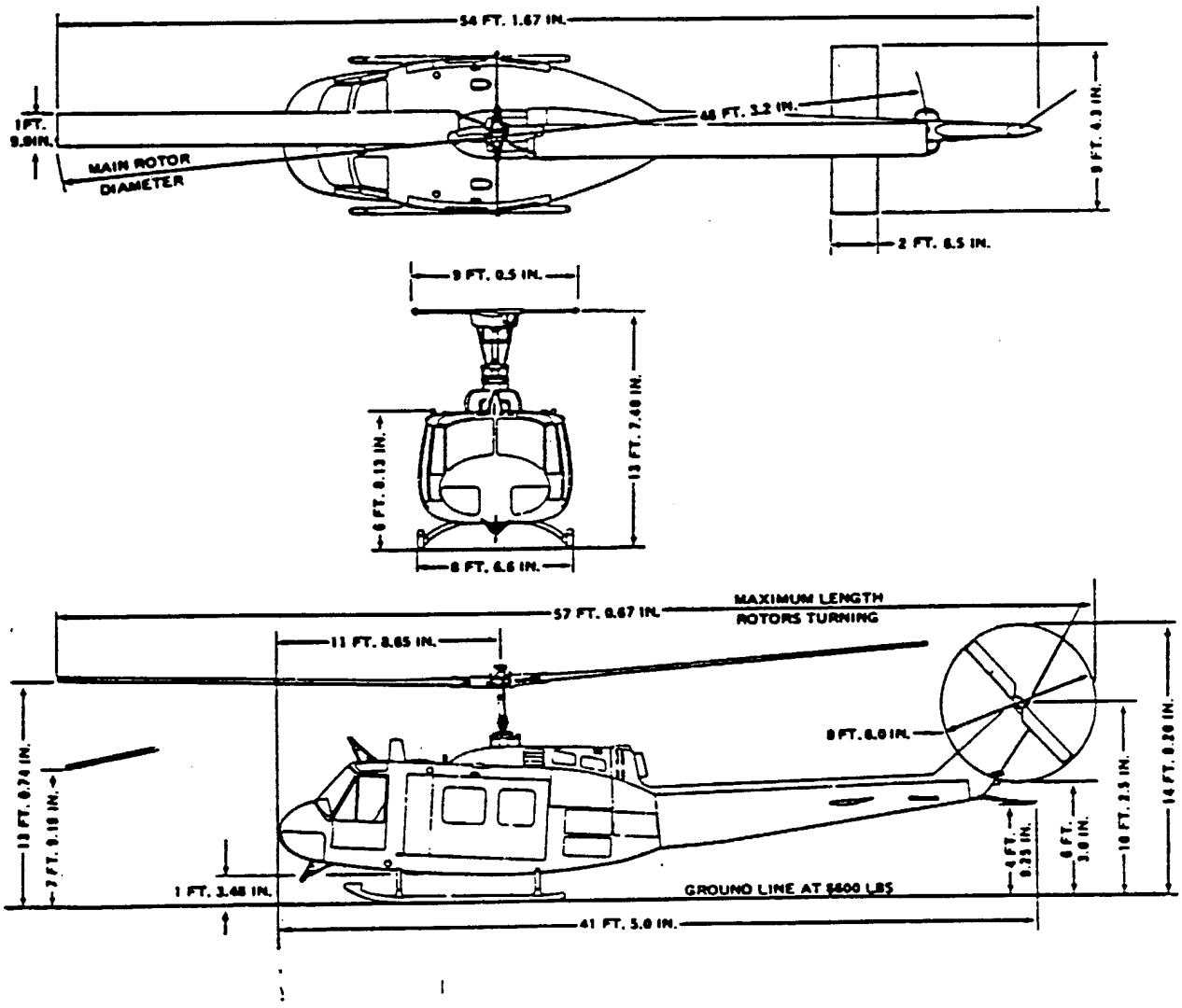

Figure 135 Line drawing of the UH-1 helicopter.

our antennas to 66 feet above the surface. The equipment was driven down a road adjacent to the 80 acre airborne test site. Figure 136 shows the antennas that were mounted on the cherry-picker bucket. These antennas were built by ESL for foliage penetration efforts. Their nominal response is between 100 and 700 MHz. Figure 137 shows the equipment being driven down the road with the antennas 60 feet high. The white trailer behind the cherry-picker housed the computers and most of the radar. We are still processing the results. We captured data with the antennas at 40, 50, and 60 feet above the surface. We believe that our experiences at this demonstration will reap significant benefits for this program.

The antennas, shown in Figure 136, cannot be helicopter mounted, but they provided practical experience with the operation of such a system to obtain real data.

We operated this radar with a high resolution GPS unit mounted on the bucket with the radar antennas, in order to find the precise location of the antennas as the system moved down the road. We found that harmonics of the transmitted signal were interfering with the GPS system about half the time (depending on exact position of the relay satellites). Thus, we see a need for tracking filters on the radar transmitter as well as on the receiver. During the next phase of this effort, we have plans to purchase and install such tracking filters. An analysis of the GPS problems are included in Appendix B of this document.

The sensitivity of the system was sufficient for targets on or near the surface at ranges less than 1000 feet. Future systems with more transmit power, and with additional filtering on the receiver, will allow for sensing at greater distances and with greater target depth.

The system, as implemented, still created some interference at TV broadcast frequencies. A revised system control program, which turns off **both** the transmitter and the receiver in those bands, will be used in the future to alleviate this problem. This revised system will be used in the second phase of this program.

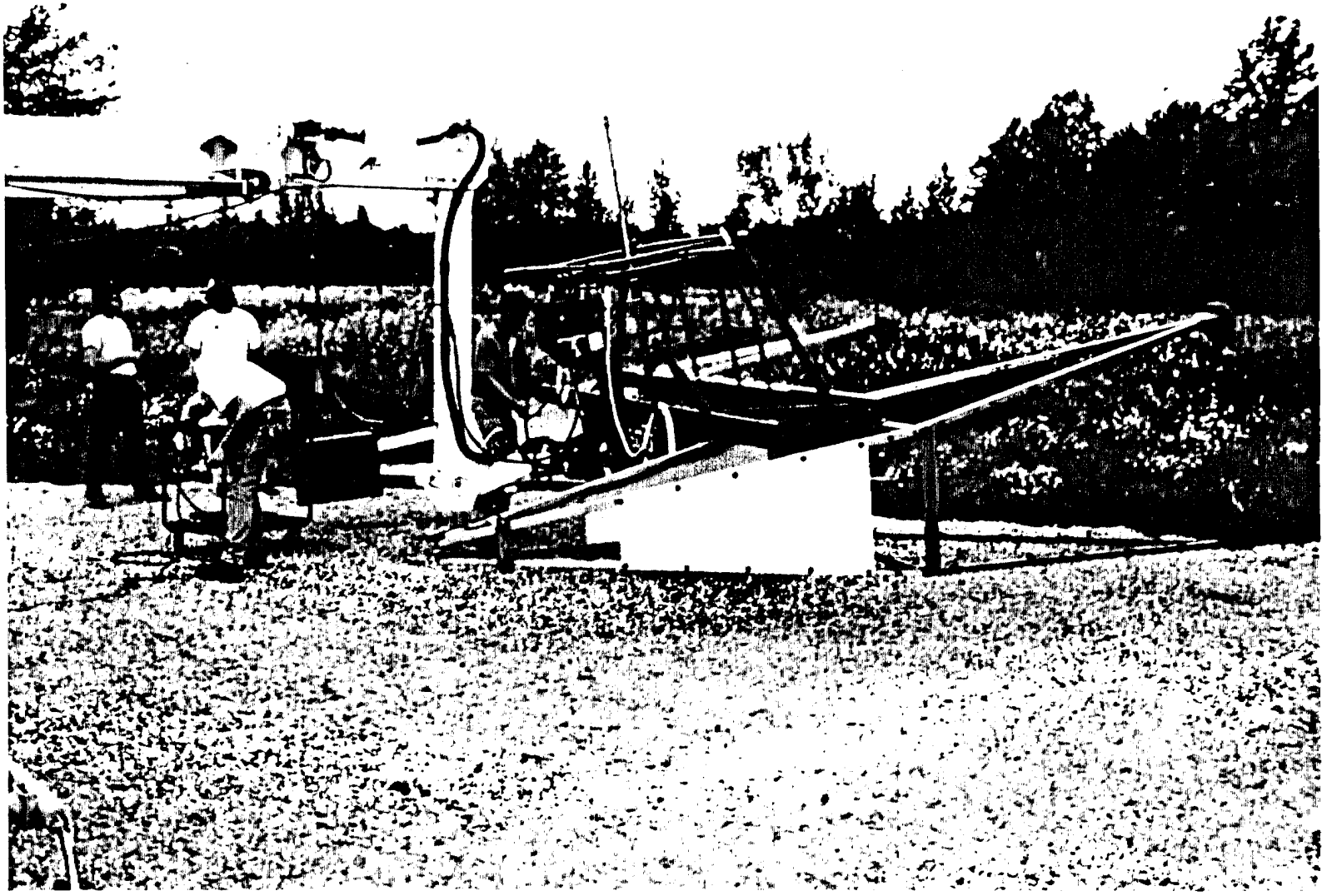

Figure 136 The antennas mounted on the cherry-picker bucket at Jefferson Proving Ground.

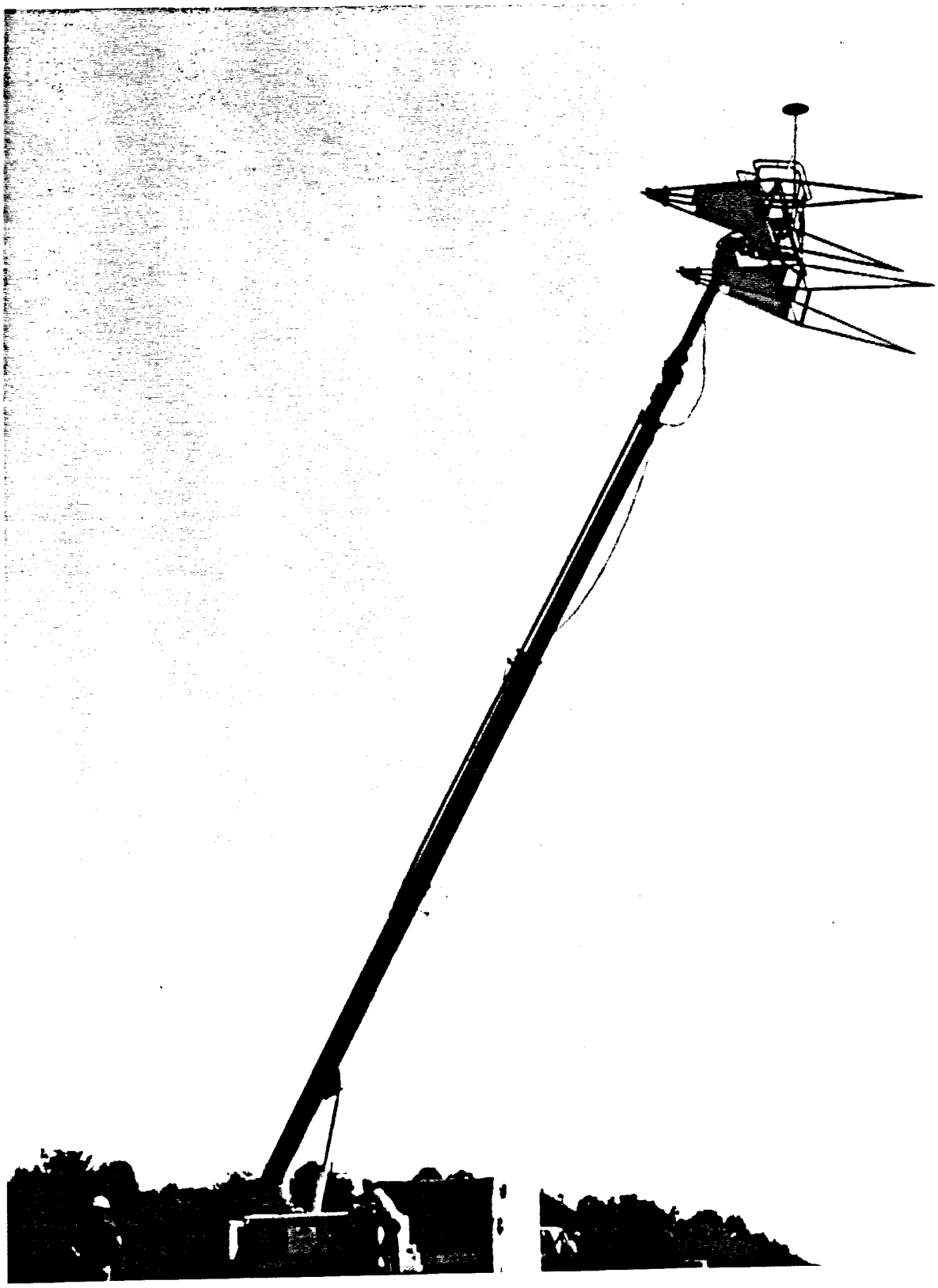

Figure 137 The cherry-picker extended to 60 feet above the surface at the Jefferson Proving Ground demo. The saucer-shaped GPS antenna is on a pole above the bucket.

12.0 Summary

This report contains results of this two-year study in which Battelle and The Ohio State University ElectroScience Laboratory investigated nearly every anticipated aspect of flying an airborne ground penetrating radar built for the purpose of detecting buried unexploded ordnance. The main areas of work included a literature search, a trade-off study of radar architectures, modeling of synthetic aperture radar processing for this application, an examination of antenna candidates, and an investigation of potential improvements to the complex natural resonance target identification technique. ESL also did extensive testing on inert ordnance items provided by NAVEODTECHDIV.

During this study we identified and concentrated on the seven critical technologies necessary for a successful system. These technologies are listed in Table 14.

We remain convinced that an airborne GPR can successfully locate buried ordnance. Table 15 provides a list of the obstacles necessary for a successful system and our approach to overcoming those obstacles.

The program changed course away from spending effort on the design of receivers because the second phase would concentrate on demonstrating technology. There are currently no plans to build receivers. Still, the results of the design efforts are included in this report.

We have continued to keep on top of the latest hardware developments with some notable advances in pulsed sources and analog-to-digital converters. We have examined the time domain/frequency domain question from several points of view and continue to evaluate the receiver architecture in light of these studies and potential new hardware.

Table 14 Technologies Critical to the Success of Airborne GPR.

Technologies Critical to a Successful Airborne GPR for UXO Detection	
Target/Clutter Discrimination	The ability to discriminate between clutter and targets is essential to providing an acceptable false alarm rate. This requirement is fundamental to the design (it drives the frequency requirements) and cannot be added later.
3-D SAR Processing	3-D SAR Processing serves three purposes. It decreases resolution cell size to increase probability of separating clutter and targets into separate cells. It provides more accurate target position information. It decreases the effects of RFI.
High Update-Rate Differential GPS	GPS position information to 10 cm accuracy is required with update rates of about 20 per second. This information at this high rate is necessary for proper SAR processing in a moving aircraft. The high-accuracy GPS data also allows precise target positioning information.
Ultrawide Bandwidth (50 MHz to 1 GHz)	Wide bandwidth provides range resolution into the ground and allows the complex natural resonances of different size targets to be used as discriminants. The use of energy down to 50 MHz allows reasonable penetration into many types of soil.
Receiver Speed	This requirement is a result of using a moving aircraft and the requirement for clearing large amounts of land in minimal time. A frequency-domain system must be able to step in frequency very fast with a high data rate receiving system. Similarly, a high PRF impulse source with a high throughput receiver is essential.
Adaptive Processing for Inhomogeneous Soils	Variation of ground dielectric constants and loss with both depth and location can result in the inability to correctly focus buried targets by SAR processing. Processing methods capable of compensating for this issue are required.
High Dynamic Range Analog-to-Digital Converters	A high dynamic range A/D is required (14-16 bits is the current estimate) because of low-level return from buried targets in the presence of the high surface return. The dynamic range requirement is not independent of the receiver speed requirement. Both capabilities must be present.
Analog Signal Processing Antenna	The antenna can help in reducing the surface return from directly below the aircraft and in reducing the RFI level.

We have been communicating with The Ohio State University Center for Mapping about global positioning system information that will be necessary for both the short-term and

Table 15 Obstacles to the Airborne GPR Solution.

Obstacle	Details	Solution
Instrumenting Helicopter	No team experience with interference, vibration, EMI environment, etc aboard helicopter.	Will work with experienced groups, use proper mounting techniques
GPR Interference with GPS	Do not know if our high power GPR signals will interfere with sensitive GPS receivers.	GPS operates at higher frequencies. Will skip problem frequencies where harmonics cause problems.
RFI	Radio frequency interference in our frequency band causes significant problems especially if we use a time domain receiver.	Can skip over problem frequencies with a frequency domain system. Antenna configuration and SAR processing will reduce RFI's effects.
Dynamic Range Requirements Challenging	Because of the anticipated large return from the surface and the anticipated small return from buried ordnance items, we require a large but not yet quantified dynamic range.	System dynamic range is one of the primary drivers in the evaluation of candidate receiver architectures. Must go with frequency domain system.
Surface Return	No researchers have quantified the range of amplitudes that we can expect at our frequencies.	Obtained some data during 1994 JPG trials but more data necessary.
Large Relative Surface Return	Cannot quantify surface return amplitude at this time but we know that it must be minimized.	Antenna configuration can reduce specular return from directly below the aircraft, generally the worst case.
Receiver Speed	Currently used stepped chirp systems slow, transient digitizer have slow throughput rates.	Receiver speed is a primary driver of radar architecture. We know which candidate's technology can be pushed.
Unanticipated Problems with Airborne GPR	When we go airborne, we know that some unanticipated problems will arise.	Early in Phase 2, we should build and test a short-term brassboard prototype in a helicopter before we make the decision on the final configuration.
Ground Effects	Refraction effects from high dielectric constants and losses cause problems. Soil inhomogeneities cause problems	Must choose proper antenna geometry and go to higher powers for some soils. Examine adaptive processing techniques to compensate for this problem using seismology techniques.
Clutter	The surface and other objects in the ground will limit our detection. We will be clutter-limited and not noise-limited. Need to separate target-like clutter from UXO targets.	SAR processing will help separate UXO targets and clutter into distinct resolution cells. Resolution voxel size determined by synthetic aperture size and returned signal bandwidth. CNR techniques will also decrease clutter effects.

long-term demonstration systems. They were funded on a separate effort to evaluate potentially useful navigation systems. The results of their efforts are included in this report.

We feel confident that our approach to this difficult problem is sound and that our focused and deliberate investigation provides the path with the highest probability of success. We are on schedule with the results that were planned in the earliest stage of the program. While significant obstacles are present, we anticipate them, we feel that we understand their implications, and we see solutions to the problems they represent.

The selection of an appropriate antenna type and polarization remains a very complex issue. In addition to minimizing the antenna ringing and maximizing the efficiency by appropriate antenna configurations and matching, several systems issues are driven by the antenna type used. These issues involve the achievable system dynamic range, the efficacy and sub-clutter visibility attainable by SAR processing, and the detection probabilities of specific UXO targets.

There are two dominant and, unfortunately, conflicting requirements driving the antenna choice. One requirement is the large surface clutter return from directly below the vehicle. It is desirable to reduce this clutter return as much as possible prior to digitizing the received data. This requirement leads to consideration of antennas such as vertically polarized, horizontal monopulse, horizontal crossed dipoles, etc. All of these antennas generate a null directly below the aircraft, thus reducing the surface clutter and improving the available system dynamic range. The second dominant factor influencing the antenna choice is the refraction associated with the air-ground interface. Energy incident on the ground from the entire upper hemisphere is refracted into a conical region about the vertical with a half-angle of 19° (or less depending upon the ground dielectric constant). Similarly, energy scattered from an underground target that lies outside this 19° vertically-centered cone, is simply reflected back into the ground at the ground-air interface and never returns to the receiver. As a result of this refraction, from the viewpoint of maximizing the effective aperture and the resultant sub-clutter visibility and target resolution attainable by SAR processing, it is desirable to have the maximum energy from the antenna directed primarily

downward rather than to the side. For an antenna with a beam maximum at a large angle from the vertical, data collected over a large aperture in space may not result in useful imagery when SAR processed, if the angular range over which the target is viewed in the soil is compressed to a few degrees near the outer edge of the refraction cone.

Analytical trade-offs of these factors have been made. However, due to the lack of viable data on the surface clutter magnitude, surface roughness effects (on both the surface clutter and the refraction), and the effects of airborne platform angular motions, experimental data will be required to resolve these issues.

As of the writing of this report at the end of this Phase 1 effort, Phase 2 is beginning. Under this second phase, we will be instrumenting a helicopter with the GPR and GPS systems and taking GPR data from the airborne platform. Because of the previously-mentioned lack of data on surface clutter effects and because of other issues, we will also perform the following tasks

1. Fly both vertical polarization and horizontal polarization antennas over known subsurface calibration targets, to resolve antenna and look-angle issues.

2. Collect surface clutter data using both polarizations, over the frequency range of interest.

3. Examine ways to eliminate transmit/receive antenna coupling for the ESL radar (i.e., long pulse, etc.).

4. Examine ways to increase the ESL radar data rates.

While we have not resolved all of the issues associated with our primary task, we are measurably closer to achieving a useful airborne system. We look forward to the second phase of this program and the challenges it presents.

13.0 Appendices

13.1 Appendix A: Numerical Modeling of UXO's and CNR Extraction

In this appendix, theoretical results based on the numerical modeled UXO's are presented. The backscattered fields from these UXO's, calculated assuming plane-wave incidence are then calculated in free space using moment method code for bodies with symmetry of revolution. The impulse responses are then obtained by applying the inverse Fourier transform to the frequency-domain data. These time-domain data sets are then processed using the CNR extracting algorithm discussed in Section 6.0 to find the CNR's for each UXO. All the non-conjugated CNR's and insignificant CNR's below the chosen threshold have been removed.

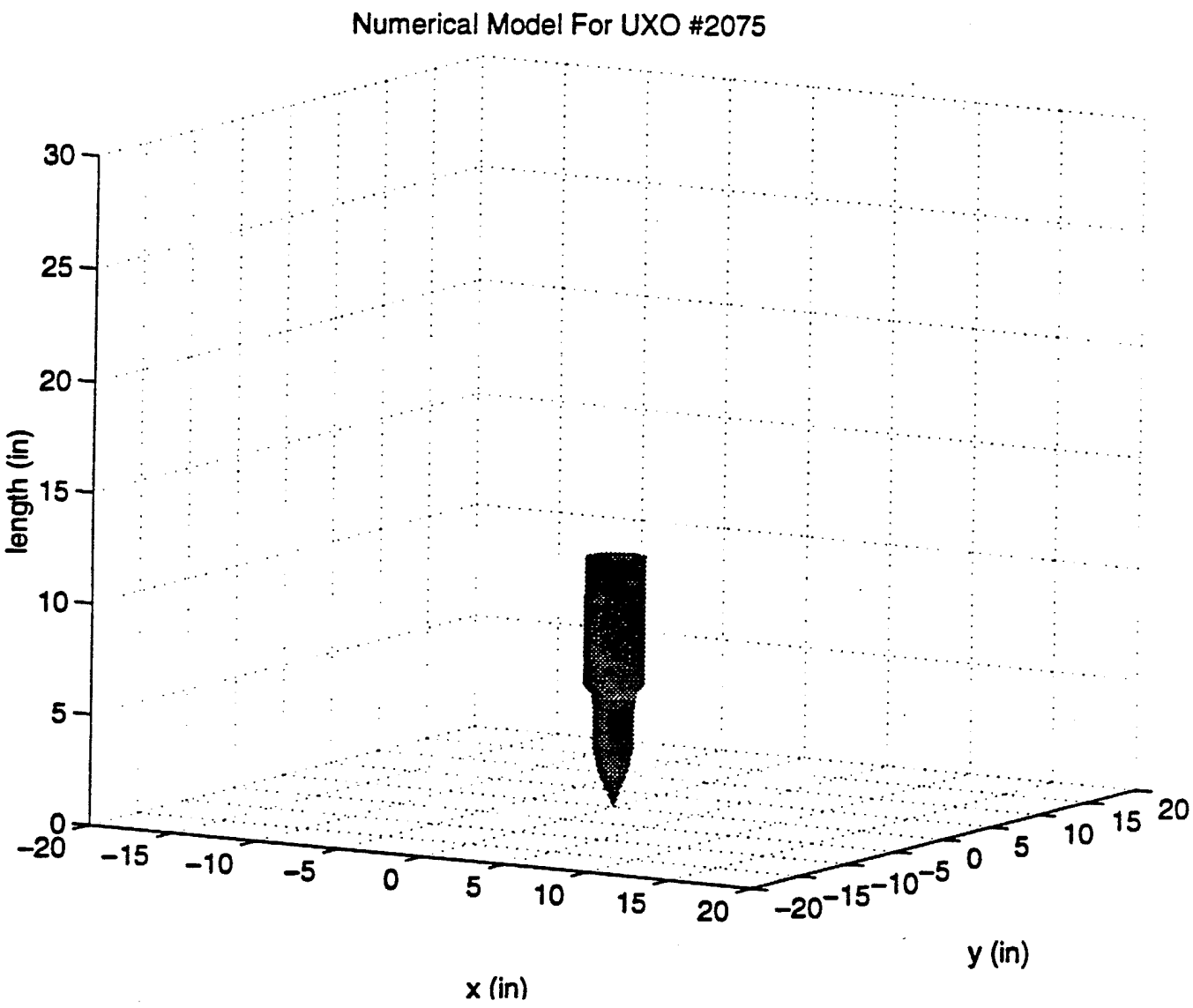
Numerical Model For UXO #2075
length (in)
30
25
20
15
10
5
0
−20
−15
−10
−5
0
5
10
15
20
x (in)
−20
−15
−10
−5
0
5
10
15
20
y (in)

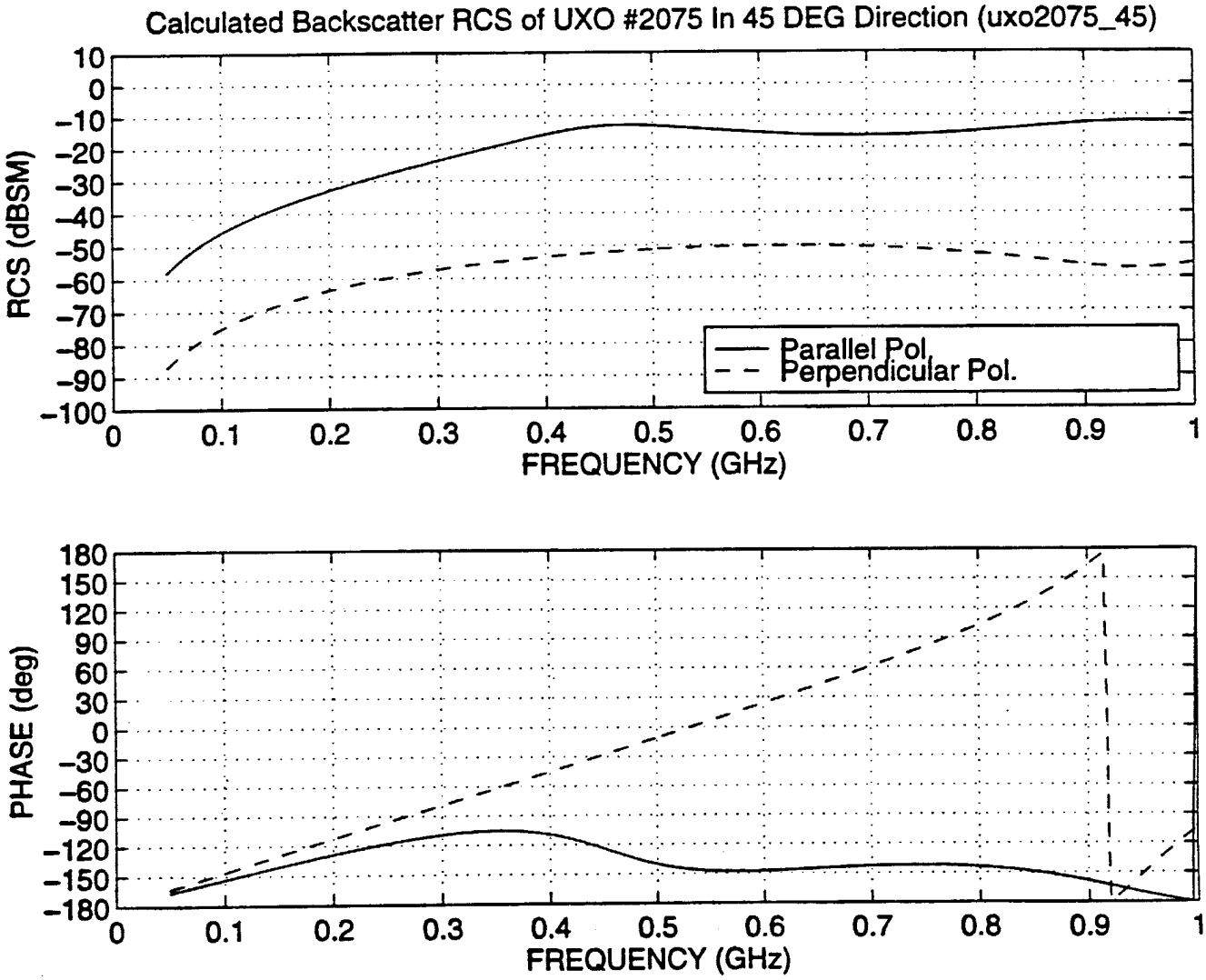
Calculated Backscatter RCS of UXO #2075 In 45 DEG Direction (uxo2075_45)
RCS (dBSM)
10
0
-10
-20
-30
-40
-50
-60
-70
-80
-90
-100
0
0.1
0.2
0.3
0.4
0.5
0.6
0.7
0.8
0.9
1
FREQUENCY (GHz)
Parallel Pol.
Perpendicular Pol.
PHASE (deg)
180
150
120
90
60
30
0
-30
-60
-90
-120
-150
-180
0
0.1
0.2
0.3
0.4
0.5
0.6
0.7
0.8
0.9
1
FREQUENCY (GHz)

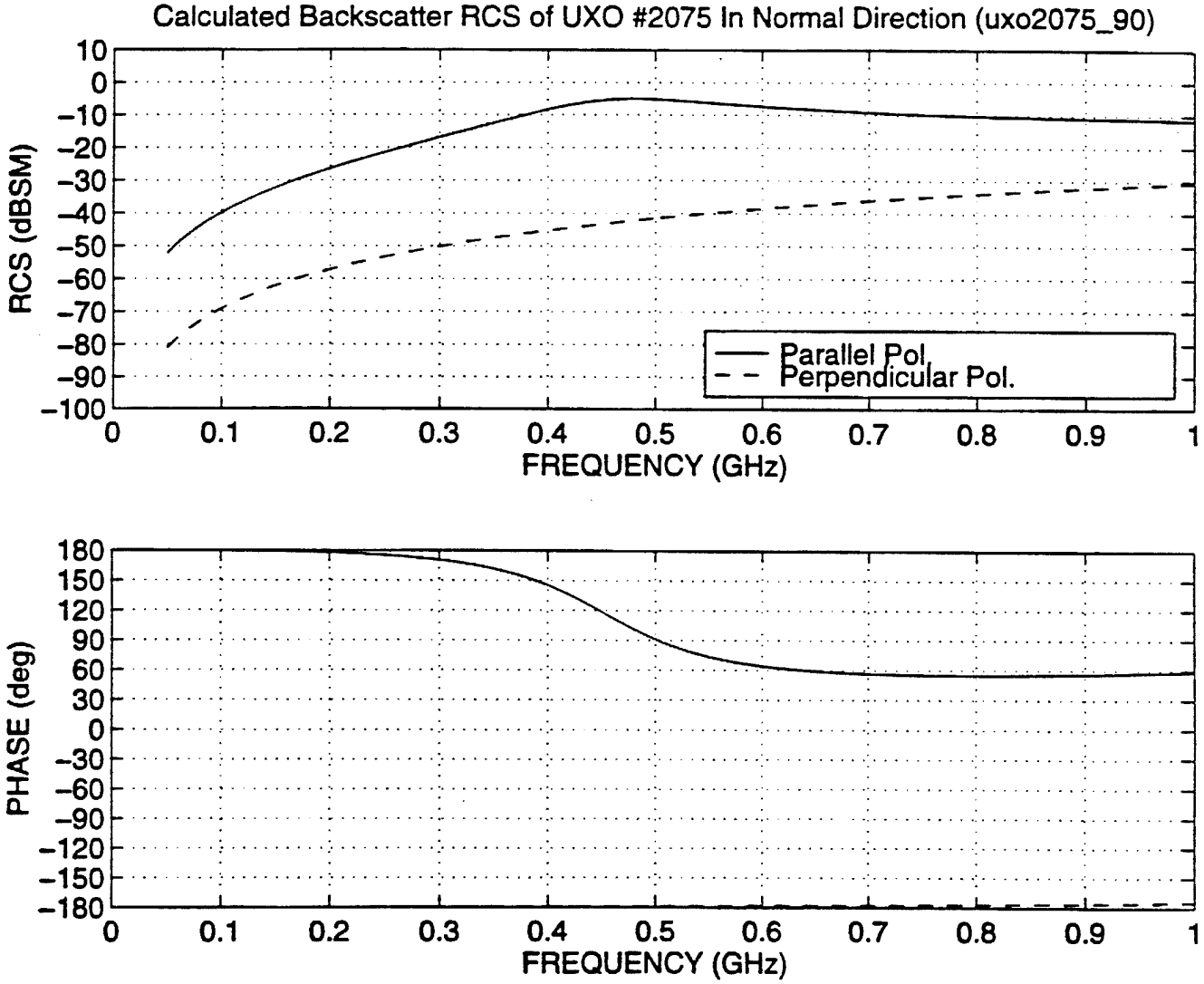
Calculated Backscatter RCS of UXO #2075 In Normal Direction (uxo2075_90)
RCS (dBSM)
10
0
-10
-20
-30
-40
-50
-60
-70
-80
-90
-100
0
0.1
0.2
0.3
0.4
0.5
0.6
0.7
0.8
0.9
1
FREQUENCY (GHz)
Parallel Pol.
Perpendicular Pol.
PHASE (deg)
180
150
120
90
60
30
0
-30
-60
-90
-120
-150
-180
0
0.1
0.2
0.3
0.4
0.5
0.6
0.7
0.8
0.9
1
FREQUENCY (GHz)

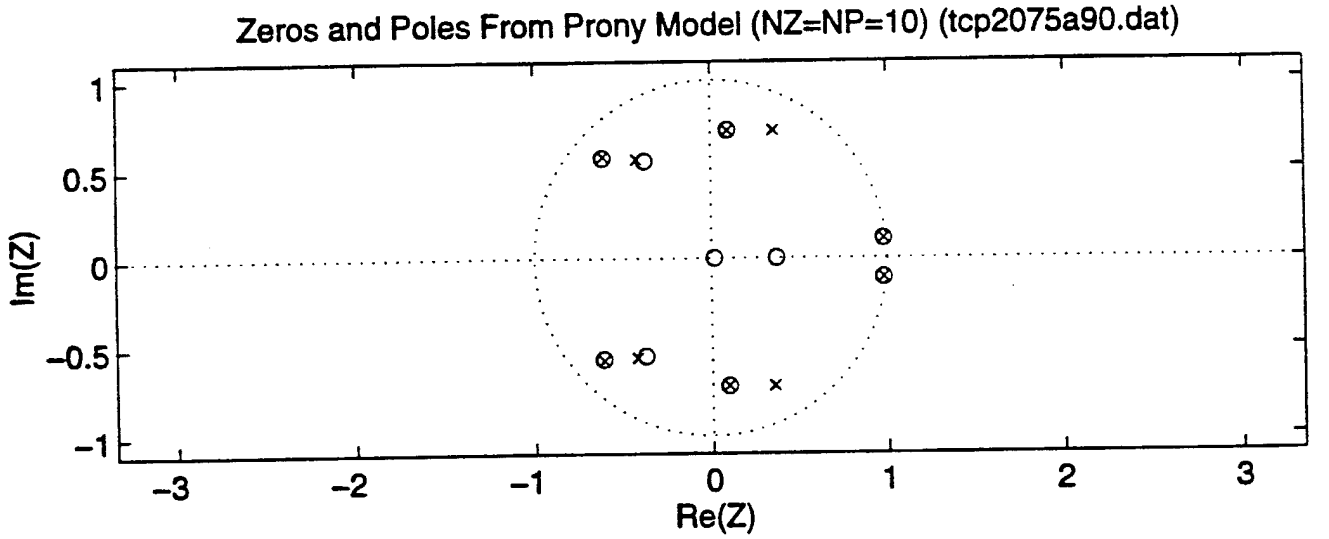
Zeros and Poles From Prony Model (NZ=NP=10) (tcp2075a90.dat)
Im(Z)
Re(Z)
1
0.5
0
−0.5
−1
−3
−2
−1
0
1
2
3

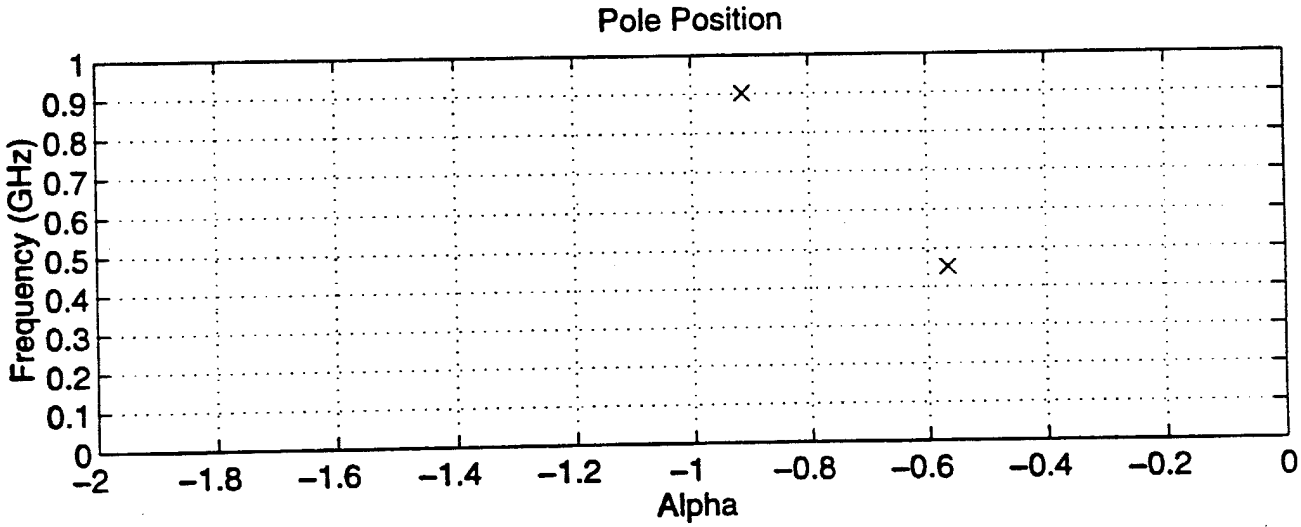
Pole Position
Frequency (GHz)
Alpha
1
0.9
0.8
0.7
0.6
0.5
0.4
0.3
0.2
0.1
0
−2
−1.8
−1.6
−1.4
−1.2
−1
−0.8
−0.6
−0.4
−0.2
0

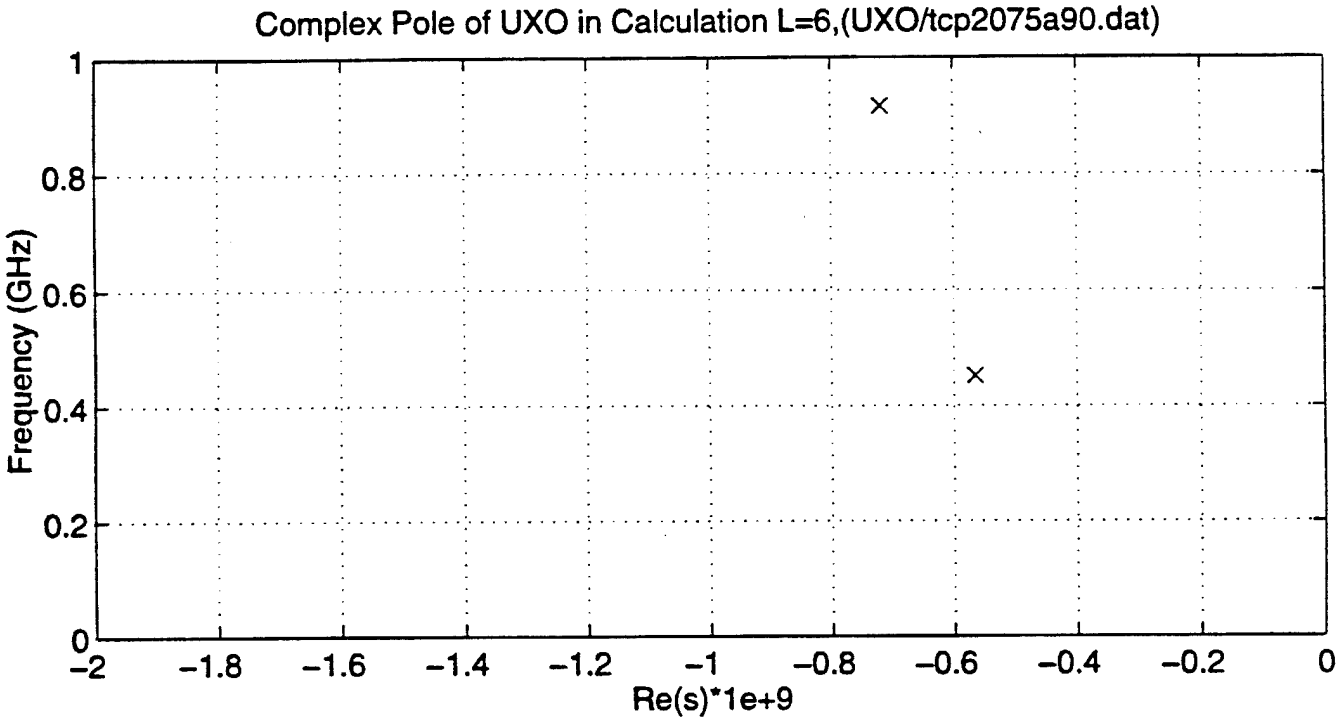
Complex Pole of UXO in Calculation L=6,(UXO/tcp2075a90.dat)
Frequency (GHz)
1
0.8
0.6
0.4
0.2
0
−2
−1.8
−1.6
−1.4
−1.2
−1
−0.8
−0.6
−0.4
−0.2
0
Re(s)*1e+9

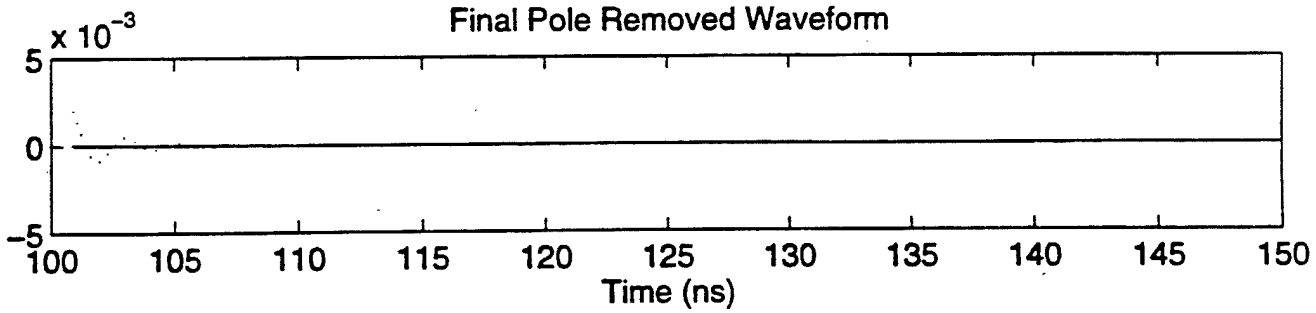
Final Pole Removed Waveform
x 10^-3
5
0
−5
100
105
110
115
120
125
130
135
140
145
150
Time (ns)

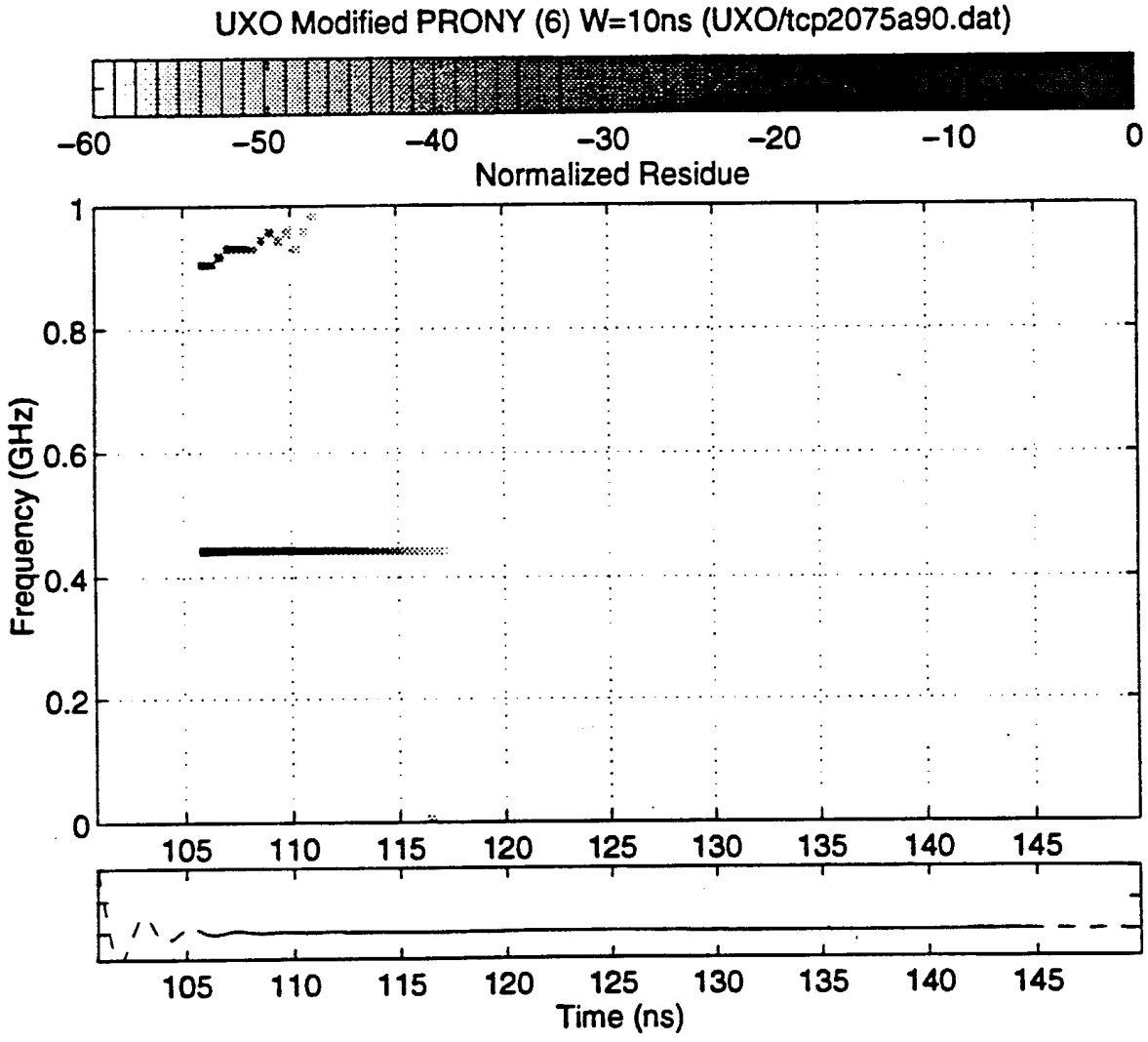
UXO Modified PRONY (6) W=10ns (UXO/tcp2075a90.dat)
−60
−50
−40
−30
−20
−10
0
Normalized Residue
Frequency (GHz)
1
0.8
0.6
0.4
0.2
0
105
110
115
120
125
130
135
140
145
Time (ns)

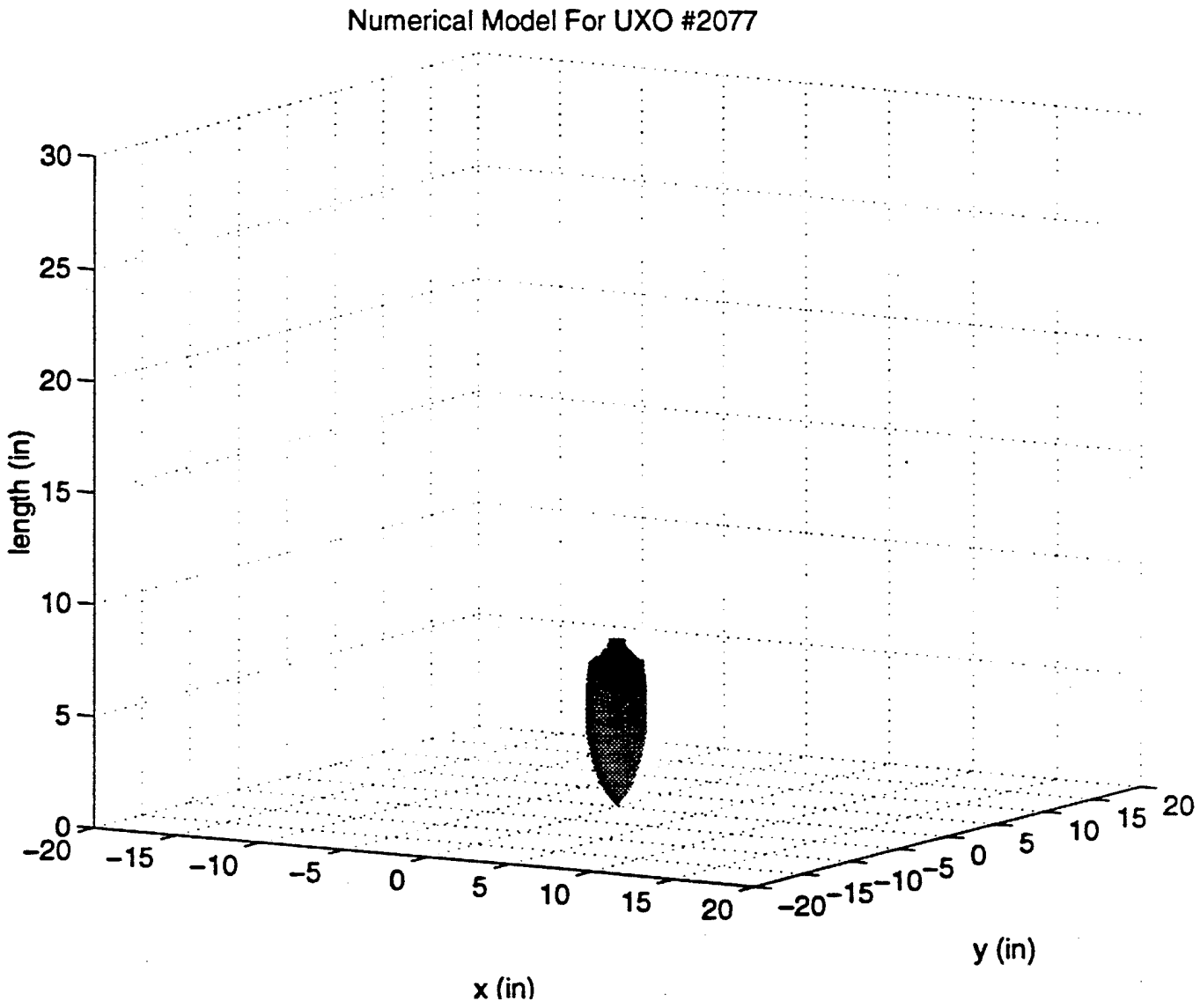
Numerical Model For UXO #2077
30
25
20
15
10
5
0
length (in)
−20
−15
−10
−5
0
5
10
15
20
x (in)
−20
−15
−10
−5
0
5
10
15
20
y (in)

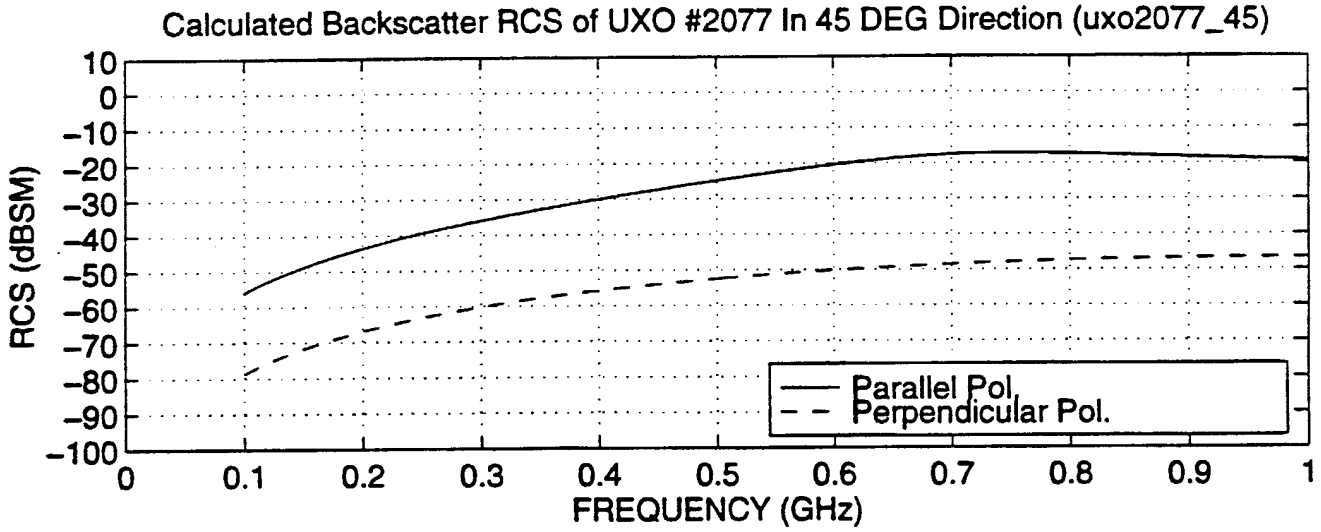
Calculated Backscatter RCS of UXO #2077 In 45 DEG Direction (uxo2077_45)
RCS (dBSM)
10
0
-10
-20
-30
-40
-50
-60
-70
-80
-90
-100
0
0.1
0.2
0.3
0.4
0.5
0.6
0.7
0.8
0.9
1
FREQUENCY (GHz)
Parallel Pol.
Perpendicular Pol.

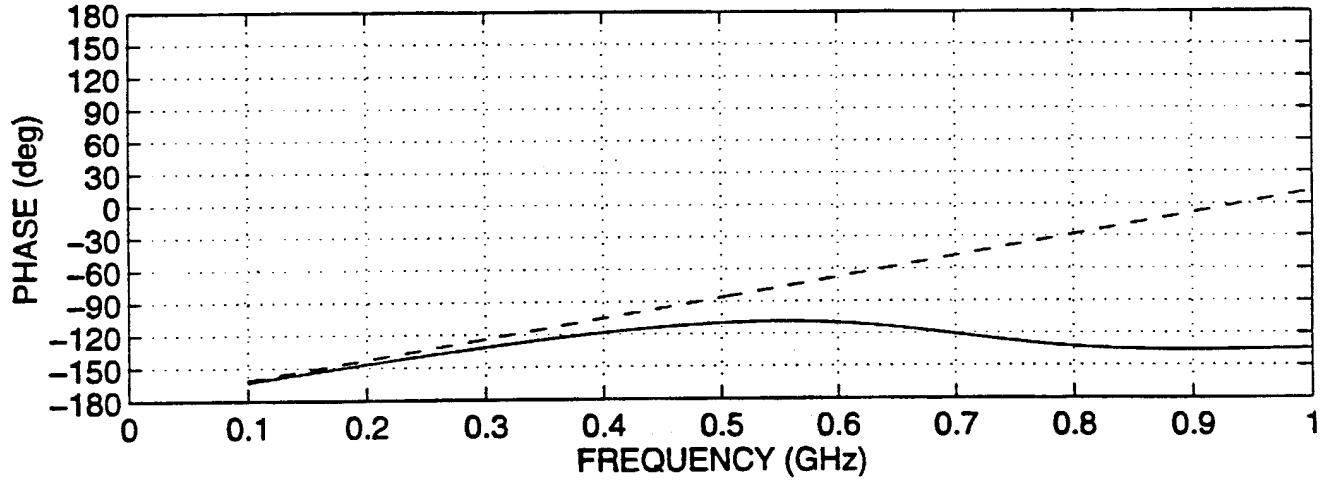
PHASE (deg)
180
150
120
90
60
30
0
-30
-60
-90
-120
-150
-180
0
0.1
0.2
0.3
0.4
0.5
0.6
0.7
0.8
0.9
1
FREQUENCY (GHz)

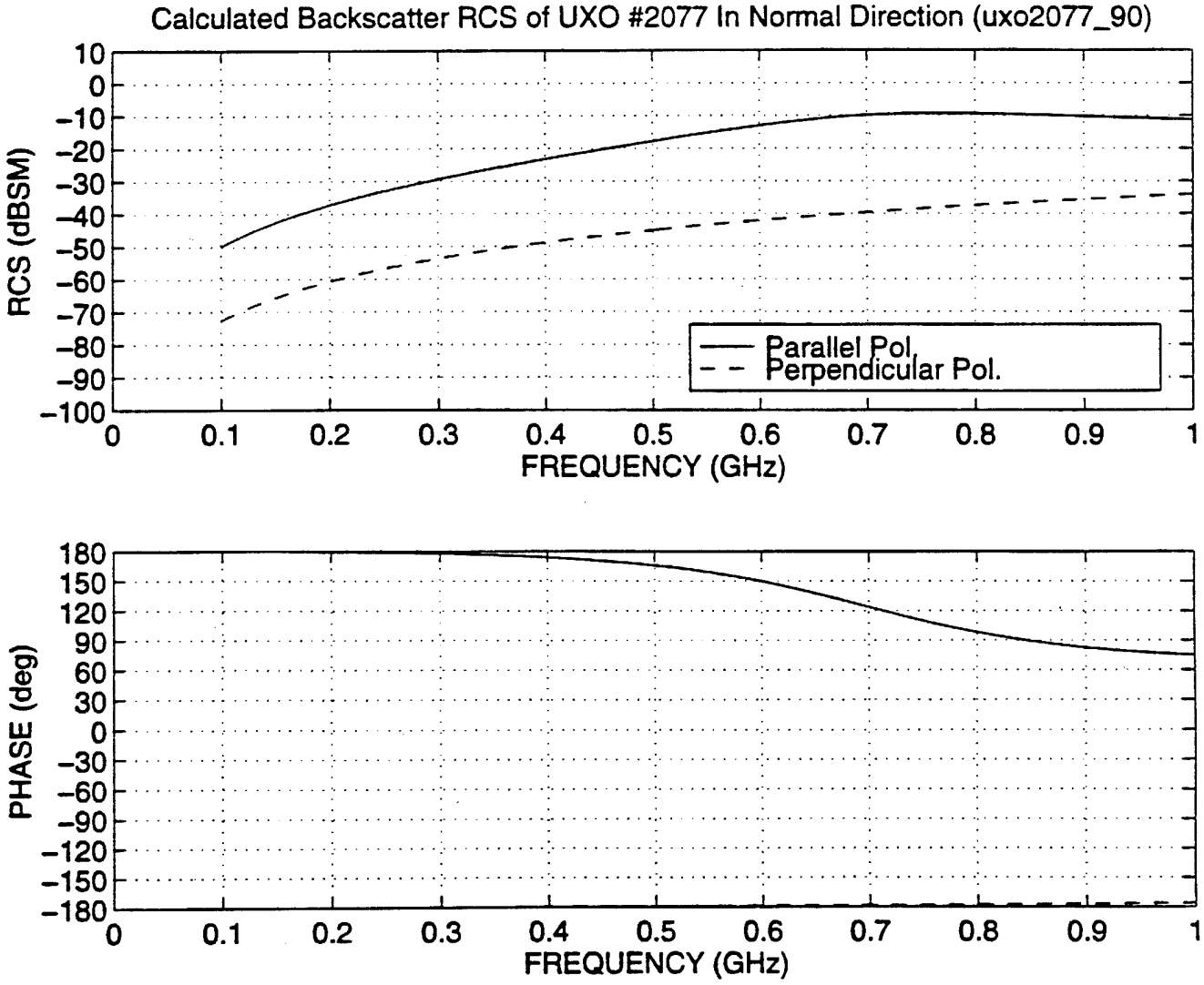
Calculated Backscatter RCS of UXO #2077 In Normal Direction (uxo2077_90)
RCS (dBSM)
10
0
-10
-20
-30
-40
-50
-60
-70
-80
-90
-100
0
0.1
0.2
0.3
0.4
0.5
0.6
0.7
0.8
0.9
1
FREQUENCY (GHz)
Parallel Pol.
Perpendicular Pol.
PHASE (deg)
180
150
120
90
60
30
0
-30
-60
-90
-120
-150
-180
0
0.1
0.2
0.3
0.4
0.5
0.6
0.7
0.8
0.9
1
FREQUENCY (GHz)

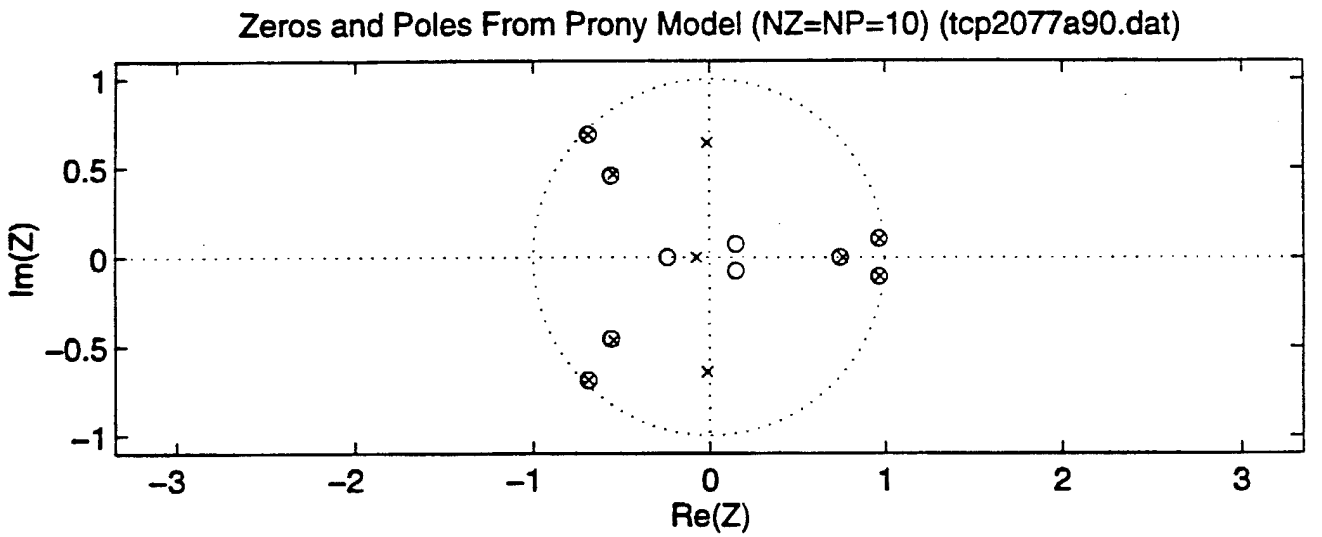
Zeros and Poles From Prony Model (NZ=NP=10) (tcp2077a90.dat)
Im(Z)
Re(Z)
1
0.5
0
−0.5
−1
−3
−2
−1
0
1
2
3

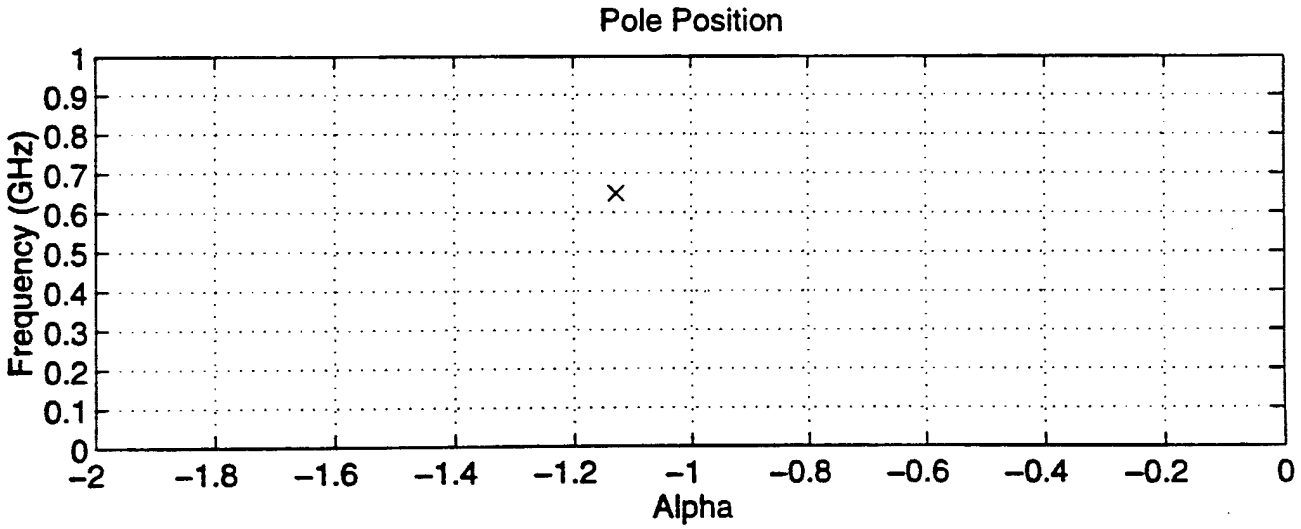
Pole Position
Frequency (GHz)
Alpha
1
0.9
0.8
0.7
0.6
0.5
0.4
0.3
0.2
0.1
0
−2
−1.8
−1.6
−1.4
−1.2
−1
−0.8
−0.6
−0.4
−0.2
0

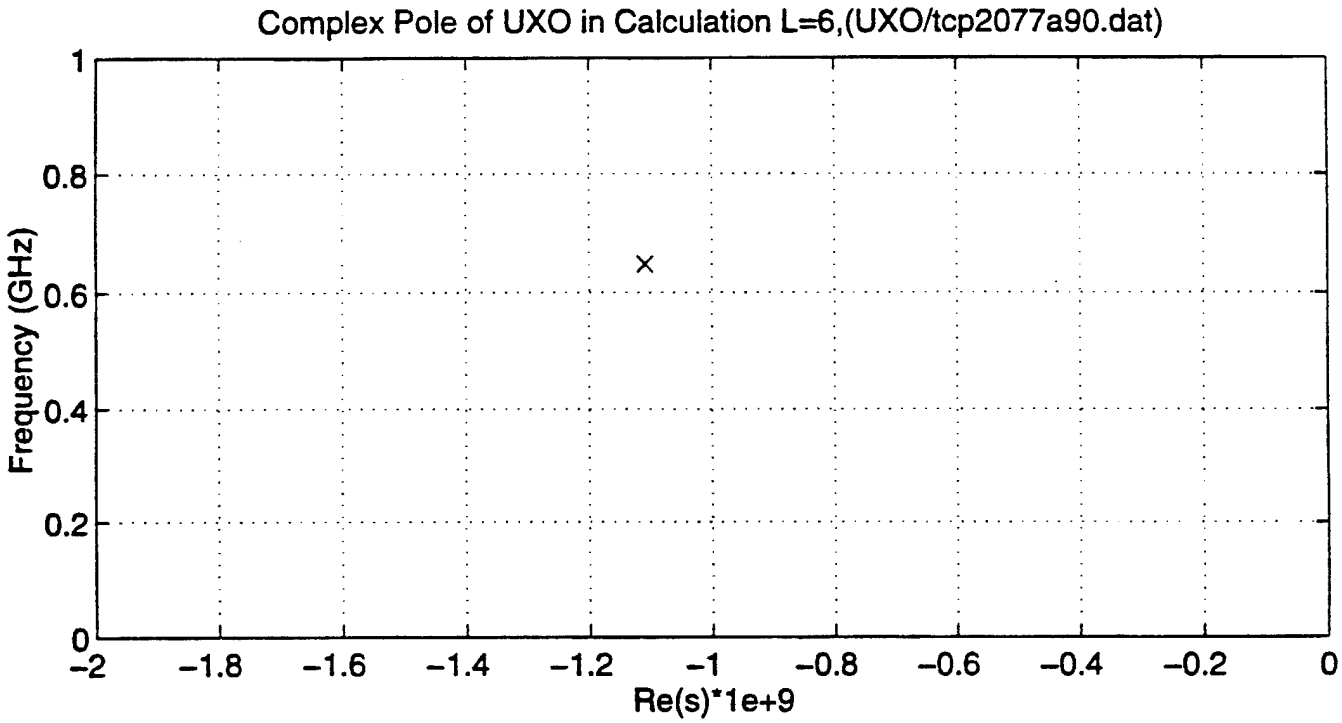
Complex Pole of UXO in Calculation L=6,(UXO/tcp2077a90.dat)
Frequency (GHz)
1
0.8
0.6
0.4
0.2
0
−2
−1.8
−1.6
−1.4
−1.2
−1
−0.8
−0.6
−0.4
−0.2
0
Re(s)*1e+9

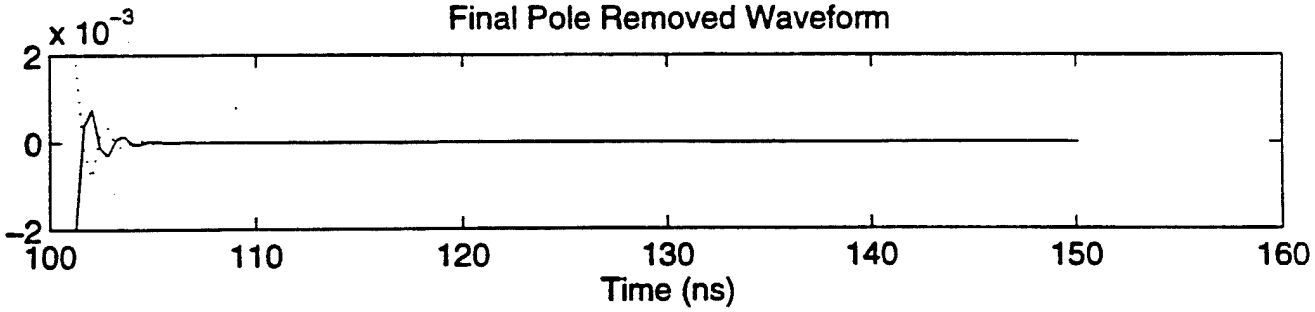
Final Pole Removed Waveform
x 10^-3
2
0
−2
100
110
120
130
140
150
160
Time (ns)

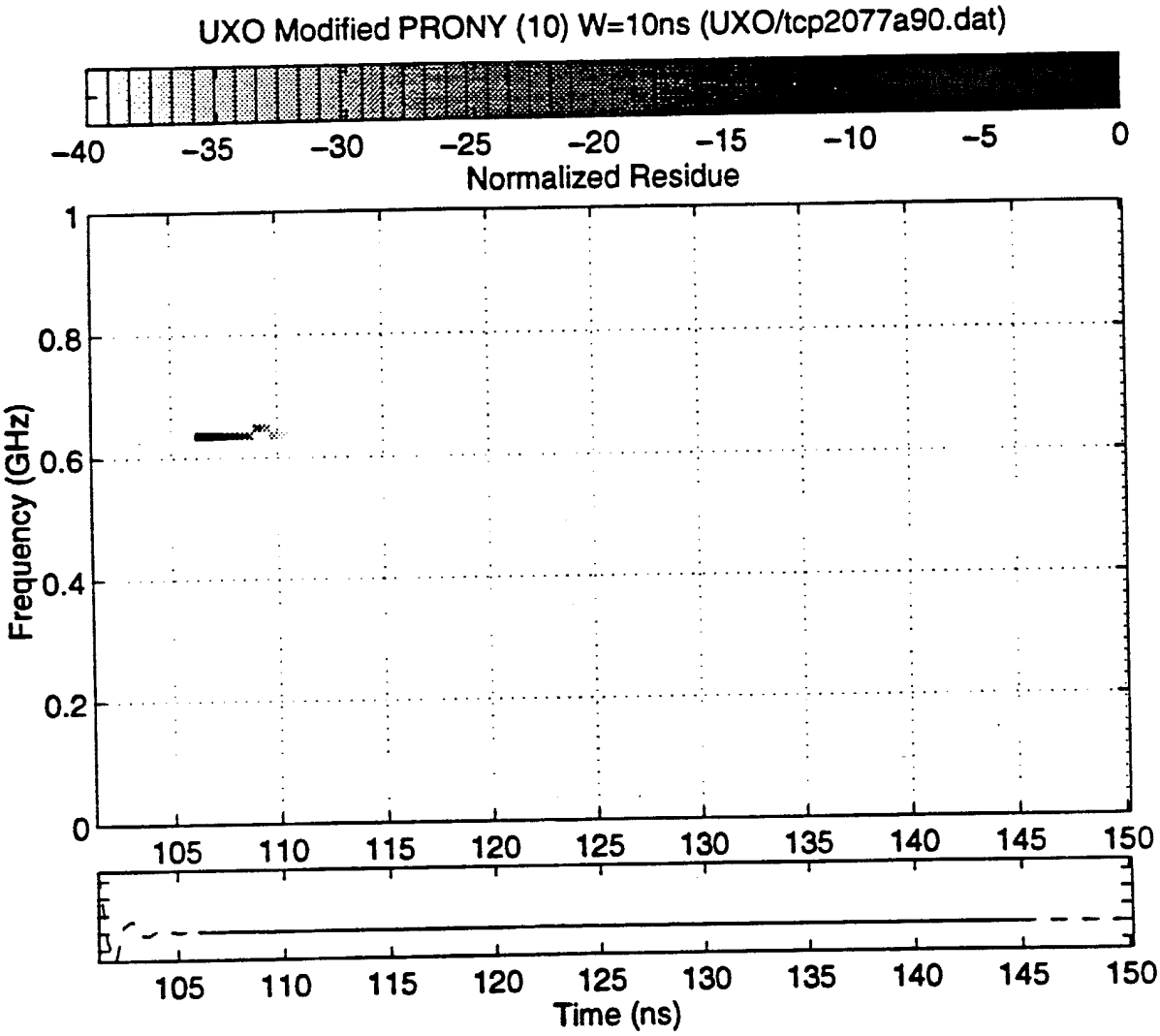
UXO Modified PRONY (10) W=10ns (UXO/tcp2077a90.dat)
−40
−35
−30
−25
−20
−15
−10
−5
0
Normalized Residue
1
0.8
0.6
0.4
0.2
0
Frequency (GHz)
105
110
115
120
125
130
135
140
145
150
Time (ns)

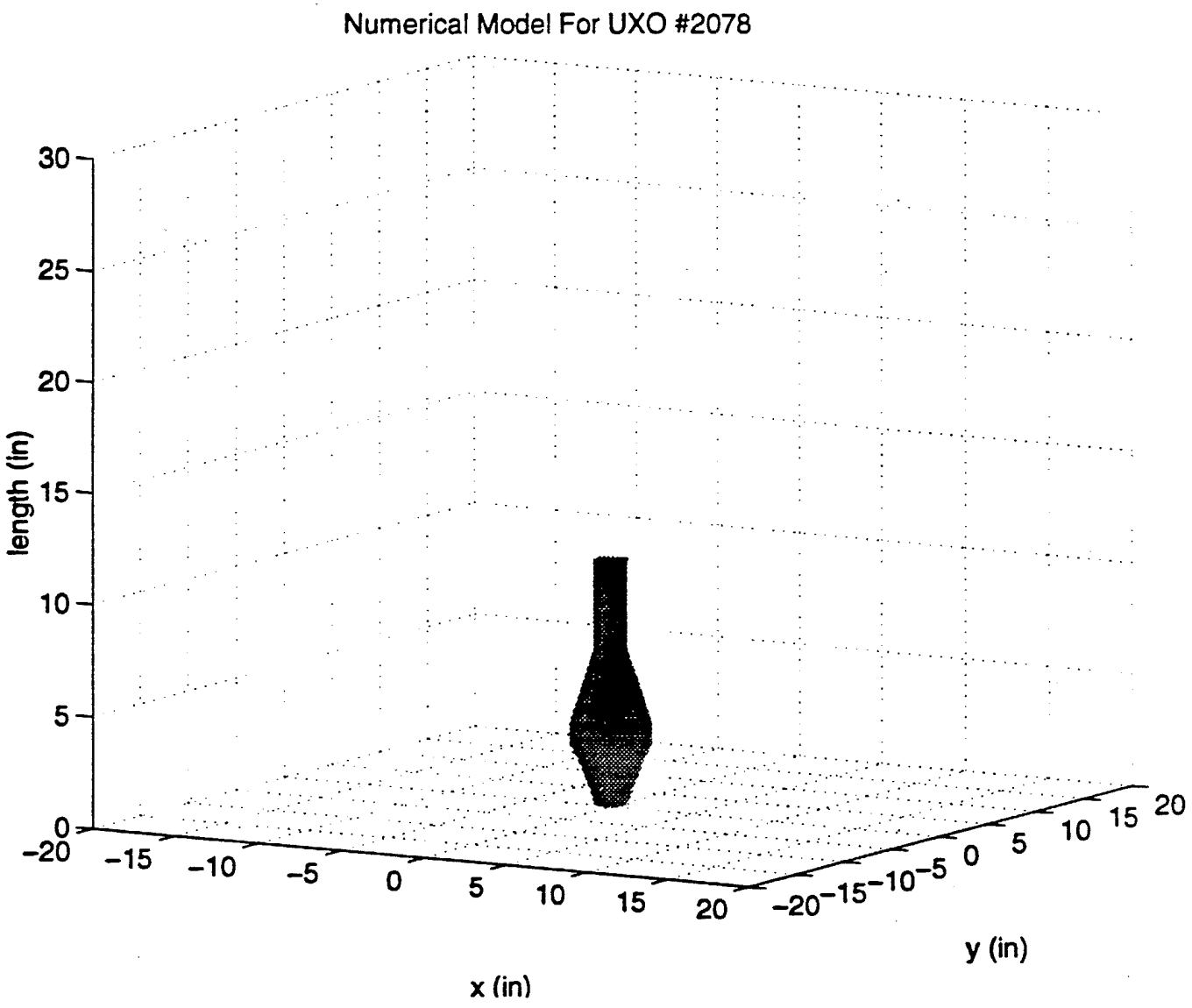
Numerical Model For UXO #2078
length (in)
30
25
20
15
10
5
0
-20
-15
-10
-5
0
5
10
15
20
x (in)
-20
-15
-10
-5
0
5
10
15
20
y (in)

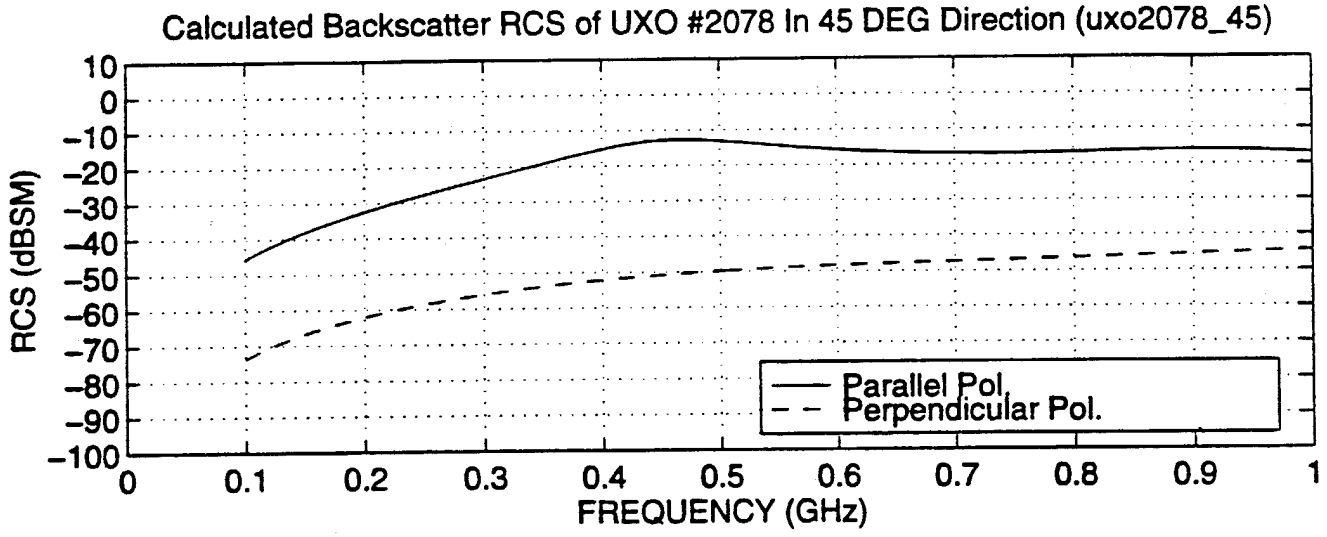
Calculated Backscatter RCS of UXO #2078 In 45 DEG Direction (uxo2078_45)
RCS (dBSM)
10
0
-10
-20
-30
-40
-50
-60
-70
-80
-90
-100
0
0.1
0.2
0.3
0.4
0.5
0.6
0.7
0.8
0.9
1
FREQUENCY (GHz)
Parallel Pol.
Perpendicular Pol.

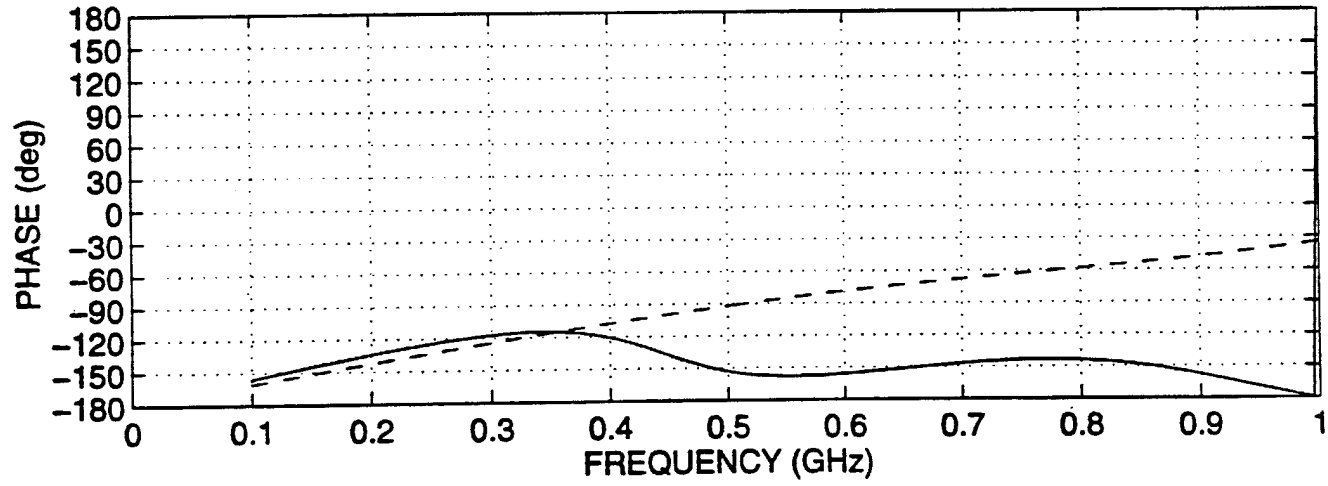
PHASE (deg)
180
150
120
90
60
30
0
-30
-60
-90
-120
-150
-180
0
0.1
0.2
0.3
0.4
0.5
0.6
0.7
0.8
0.9
1
FREQUENCY (GHz)

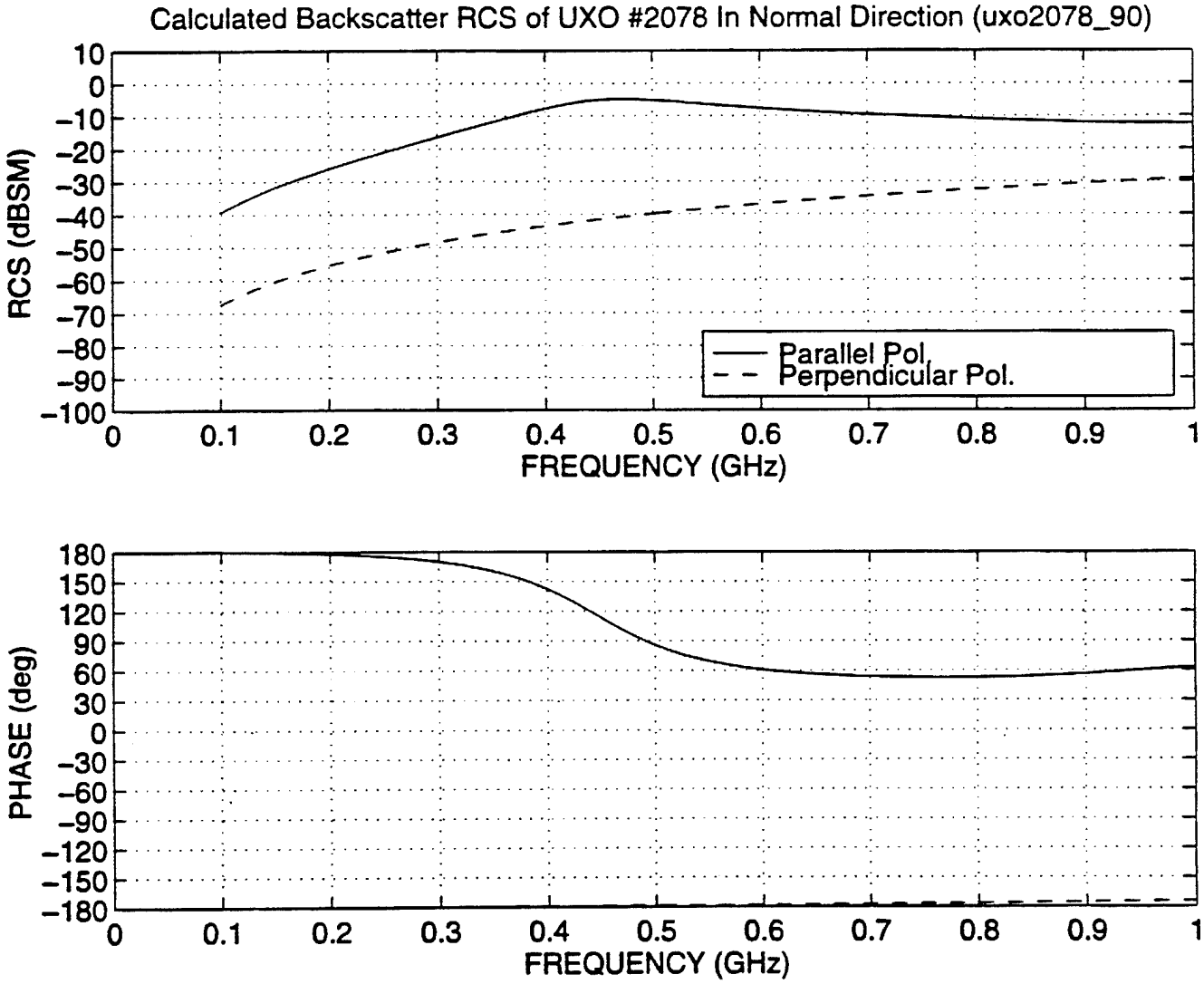
Calculated Backscatter RCS of UXO #2078 In Normal Direction (uxo2078_90)
RCS (dBSM)
10
0
-10
-20
-30
-40
-50
-60
-70
-80
-90
-100
0
0.1
0.2
0.3
0.4
0.5
0.6
0.7
0.8
0.9
1
FREQUENCY (GHz)
Parallel Pol.
Perpendicular Pol.
PHASE (deg)
180
150
120
90
60
30
0
-30
-60
-90
-120
-150
-180
0
0.1
0.2
0.3
0.4
0.5
0.6
0.7
0.8
0.9
1
FREQUENCY (GHz)

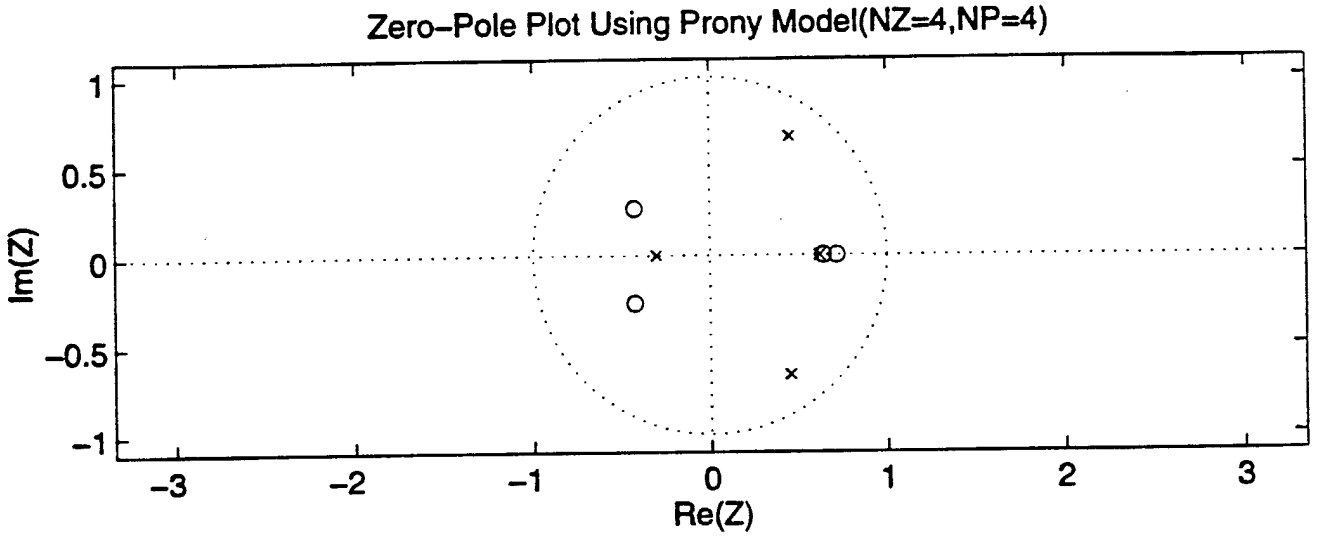
Zero–Pole Plot Using Prony Model(NZ=4,NP=4)
Im(Z)
Re(Z)
1
0.5
0
−0.5
−1
−3
−2
−1
0
1
2
3

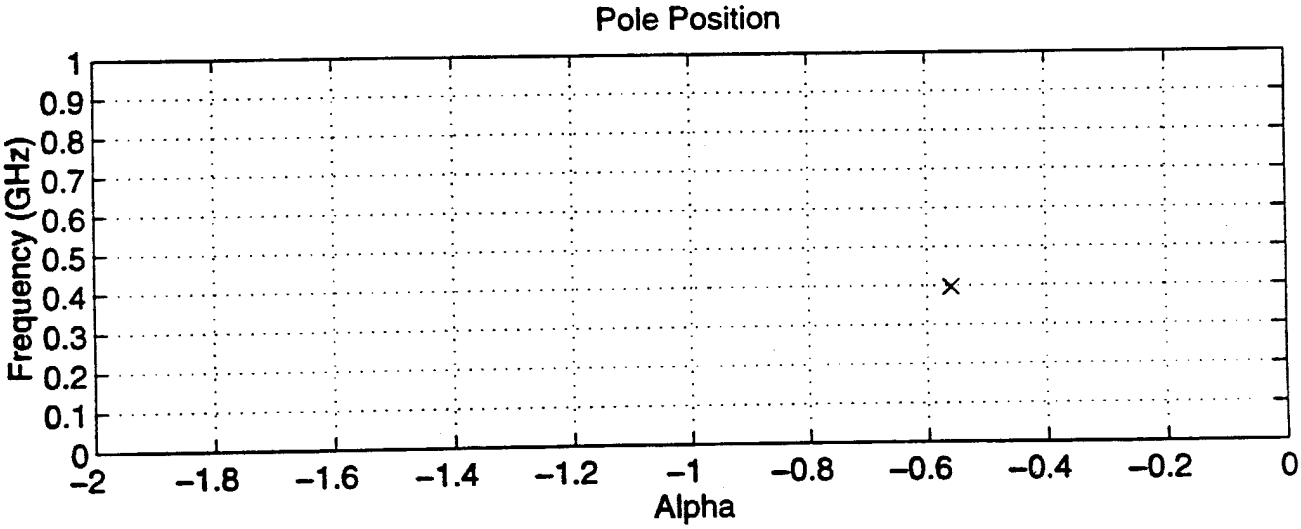
Pole Position
Frequency (GHz)
Alpha
1
0.9
0.8
0.7
0.6
0.5
0.4
0.3
0.2
0.1
0
−2
−1.8
−1.6
−1.4
−1.2
−1
−0.8
−0.6
−0.4
−0.2
0

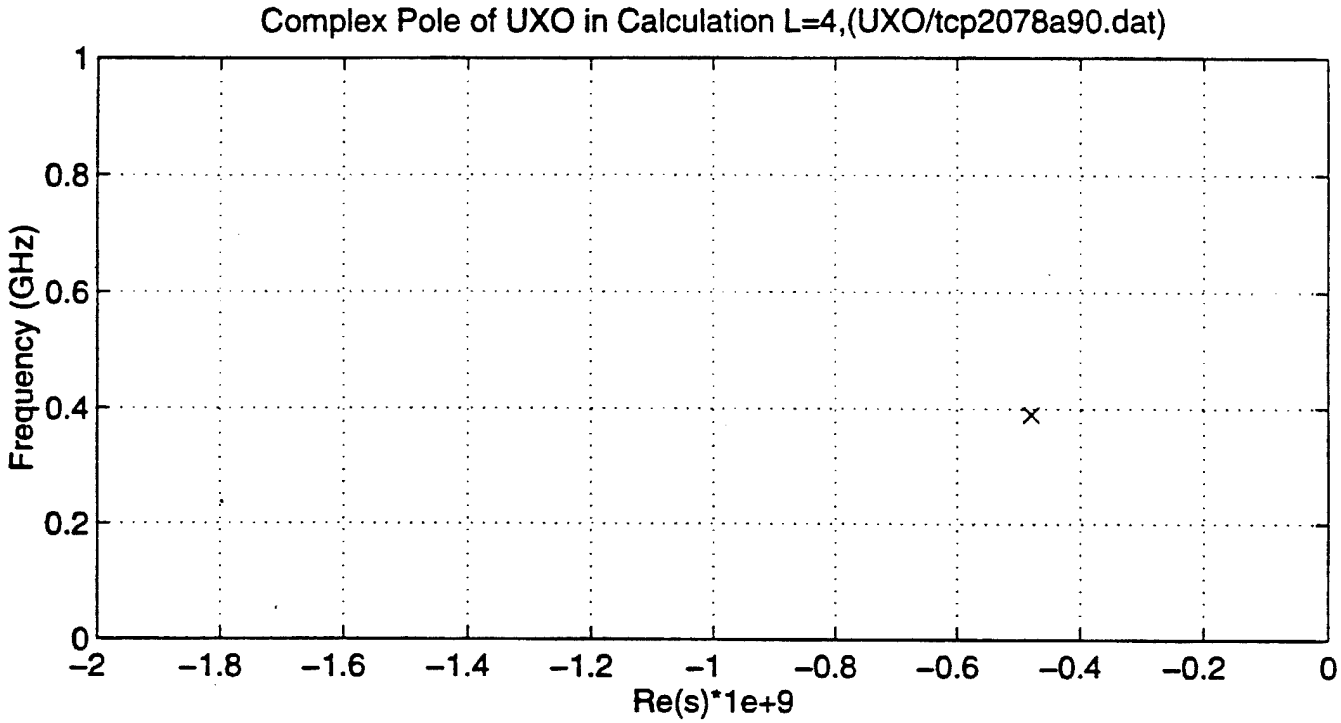
Complex Pole of UXO in Calculation L=4,(UXO/tcp2078a90.dat)
Frequency (GHz)
1
0.8
0.6
0.4
0.2
0
−2
−1.8
−1.6
−1.4
−1.2
−1
−0.8
−0.6
−0.4
−0.2
0
Re(s)*1e+9

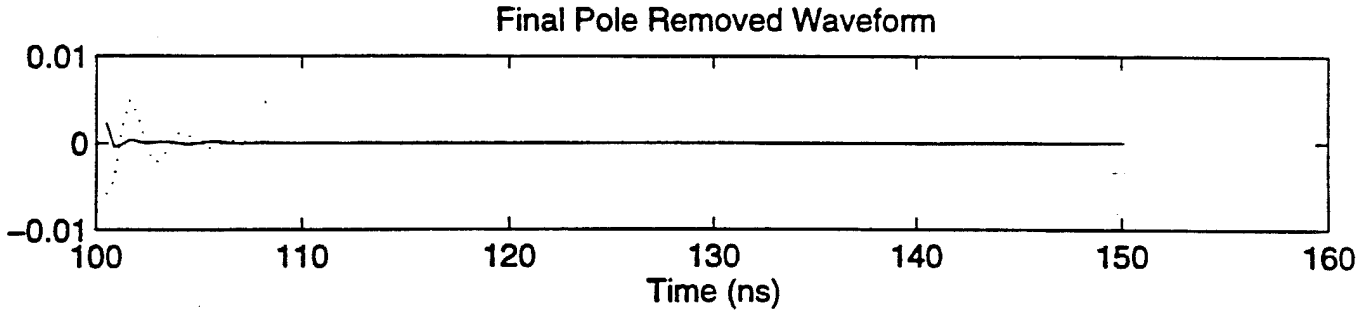
Final Pole Removed Waveform
0.01
0
−0.01
100
110
120
130
140
150
160
Time (ns)

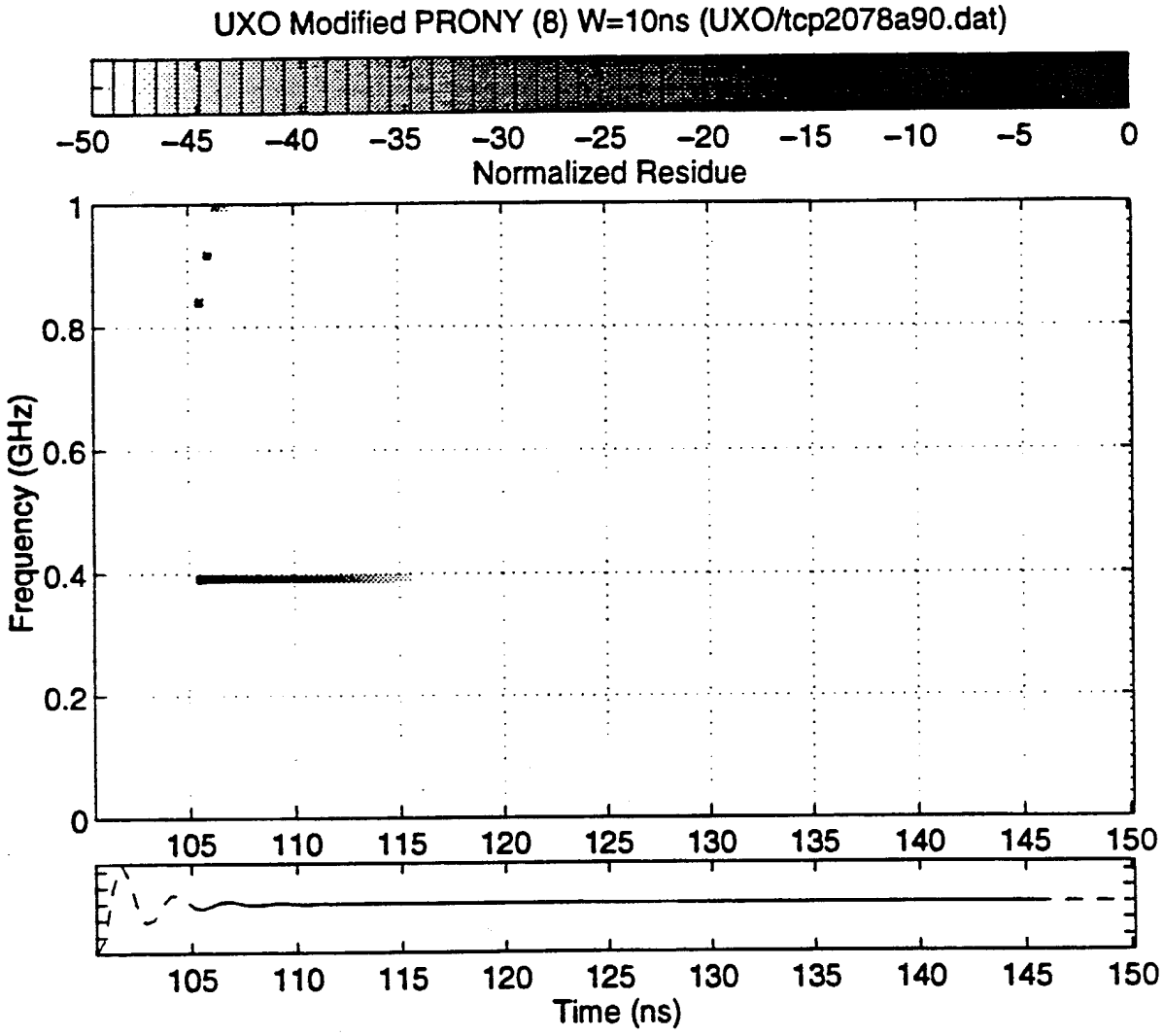
UXO Modified PRONY (8) W=10ns (UXO/tcp2078a90.dat)
−50 −45 −40 −35 −30 −25 −20 −15 −10 −5 0
Normalized Residue
Frequency (GHz)
1
0.8
0.6
0.4
0.2
0
105 110 115 120 125 130 135 140 145 150
105 110 115 120 125 130 135 140 145 150
Time (ns)

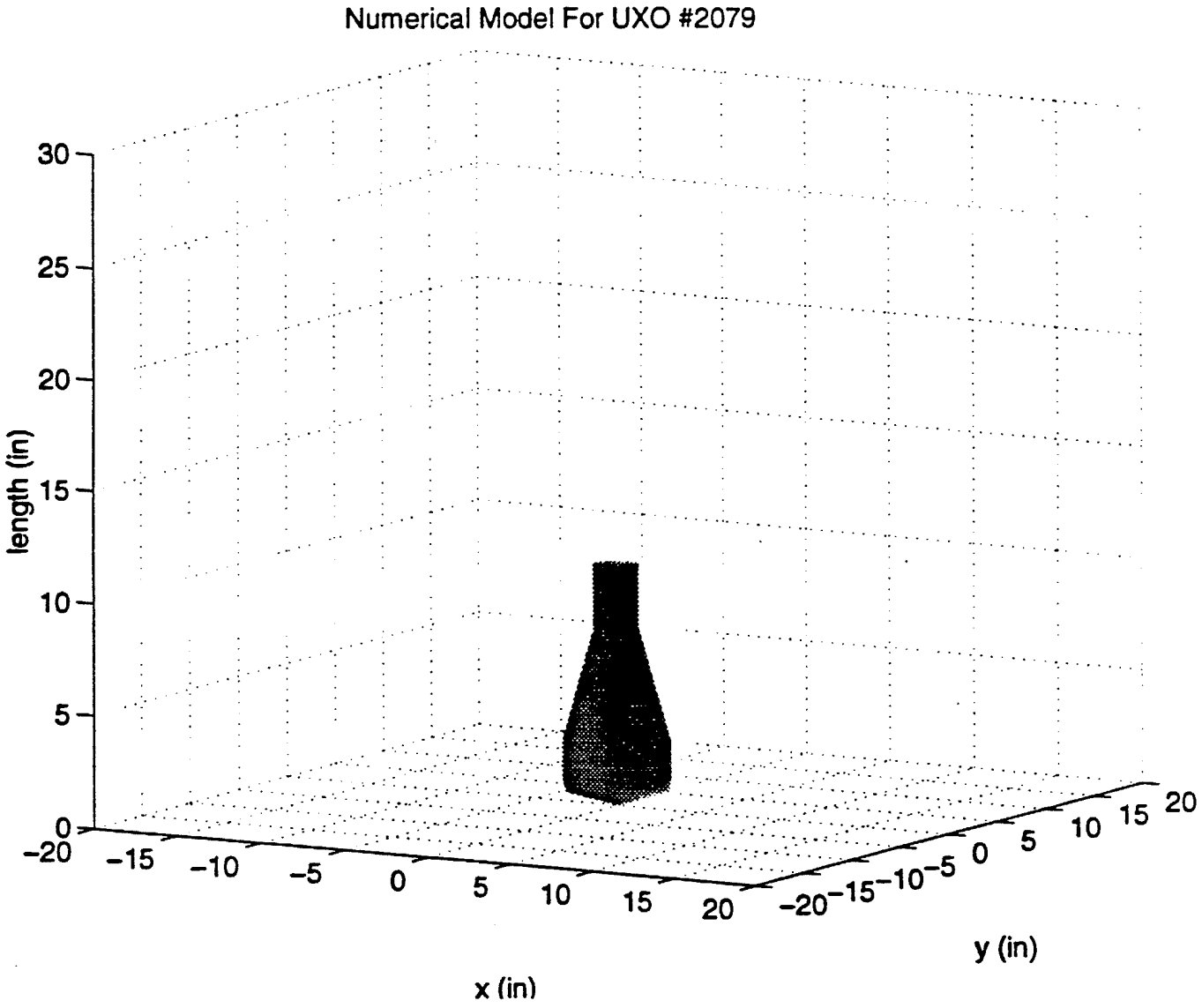
Numerical Model For UXO #2079
length (in)
30
25
20
15
10
5
0
−20
−15
−10
−5
0
5
10
15
20
x (in)
−20
−15
−10
−5
0
5
10
15
20
y (in)

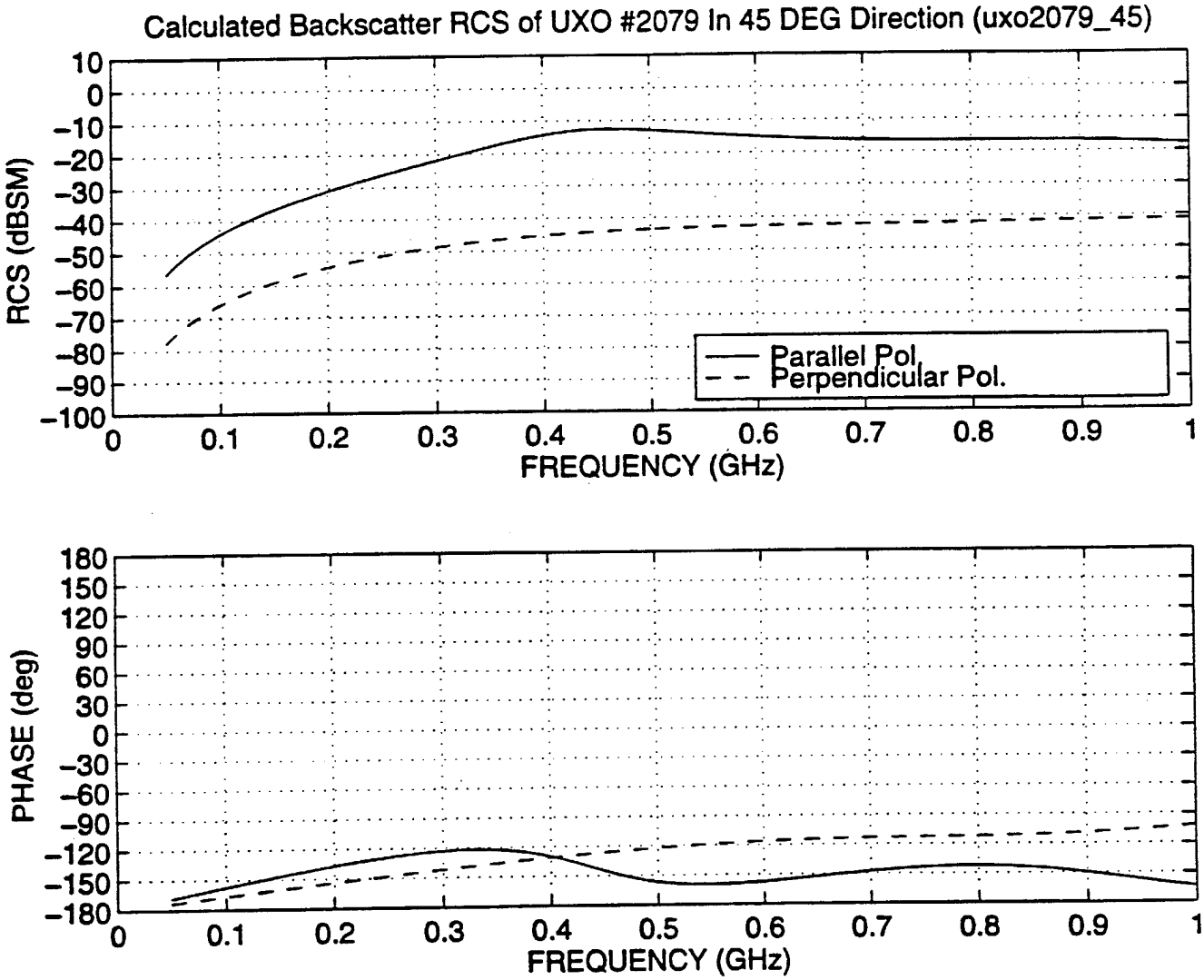
Calculated Backscatter RCS of UXO #2079 In 45 DEG Direction (uxo2079_45)
RCS (dBSM)
10
0
-10
-20
-30
-40
-50
-60
-70
-80
-90
-100
0
0.1
0.2
0.3
0.4
0.5
0.6
0.7
0.8
0.9
1
FREQUENCY (GHz)
Parallel Pol.
Perpendicular Pol.
PHASE (deg)
180
150
120
90
60
30
0
-30
-60
-90
-120
-150
-180
0
0.1
0.2
0.3
0.4
0.5
0.6
0.7
0.8
0.9
1
FREQUENCY (GHz)

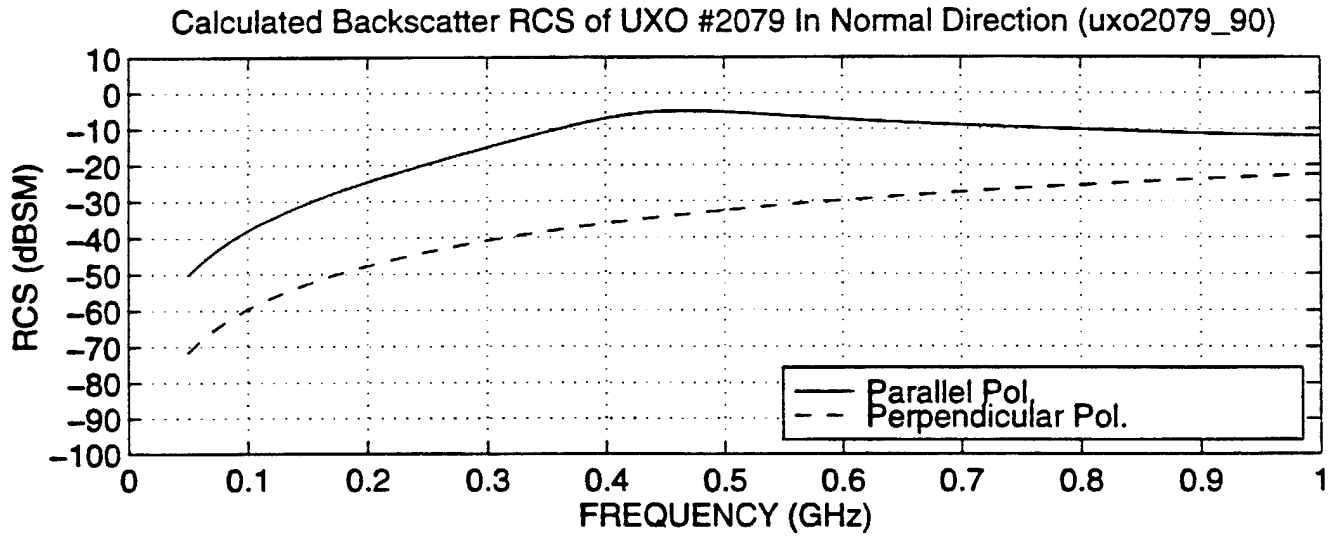
Calculated Backscatter RCS of UXO #2079 In Normal Direction (uxo2079_90)
RCS (dBSM)
10
0
-10
-20
-30
-40
-50
-60
-70
-80
-90
-100
0
0.1
0.2
0.3
0.4
0.5
0.6
0.7
0.8
0.9
1
FREQUENCY (GHz)
Parallel Pol.
Perpendicular Pol.

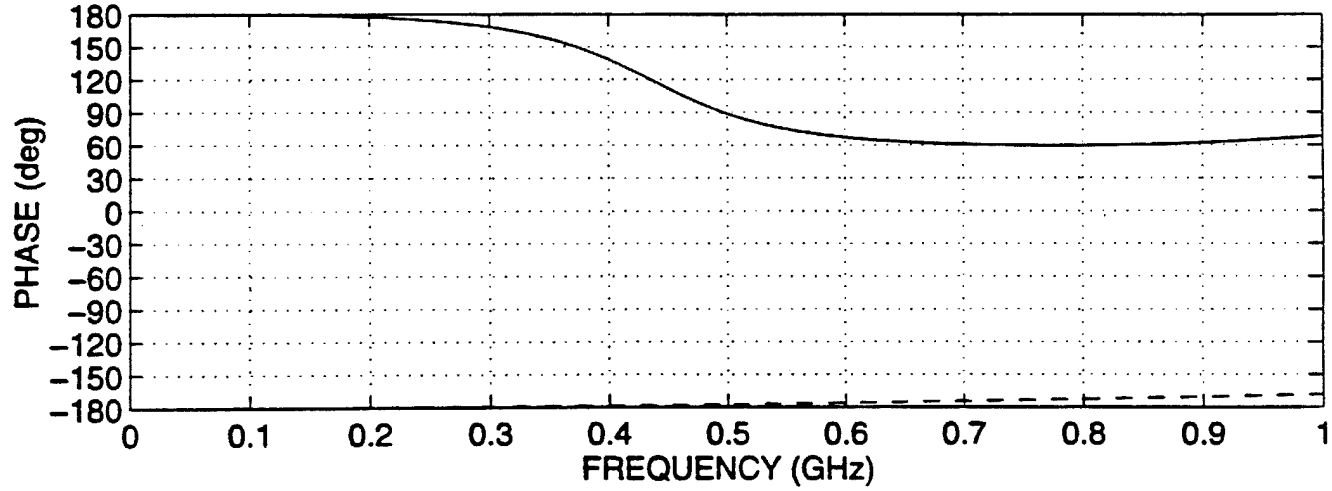
PHASE (deg)
180
150
120
90
60
30
0
-30
-60
-90
-120
-150
-180
0
0.1
0.2
0.3
0.4
0.5
0.6
0.7
0.8
0.9
1
FREQUENCY (GHz)

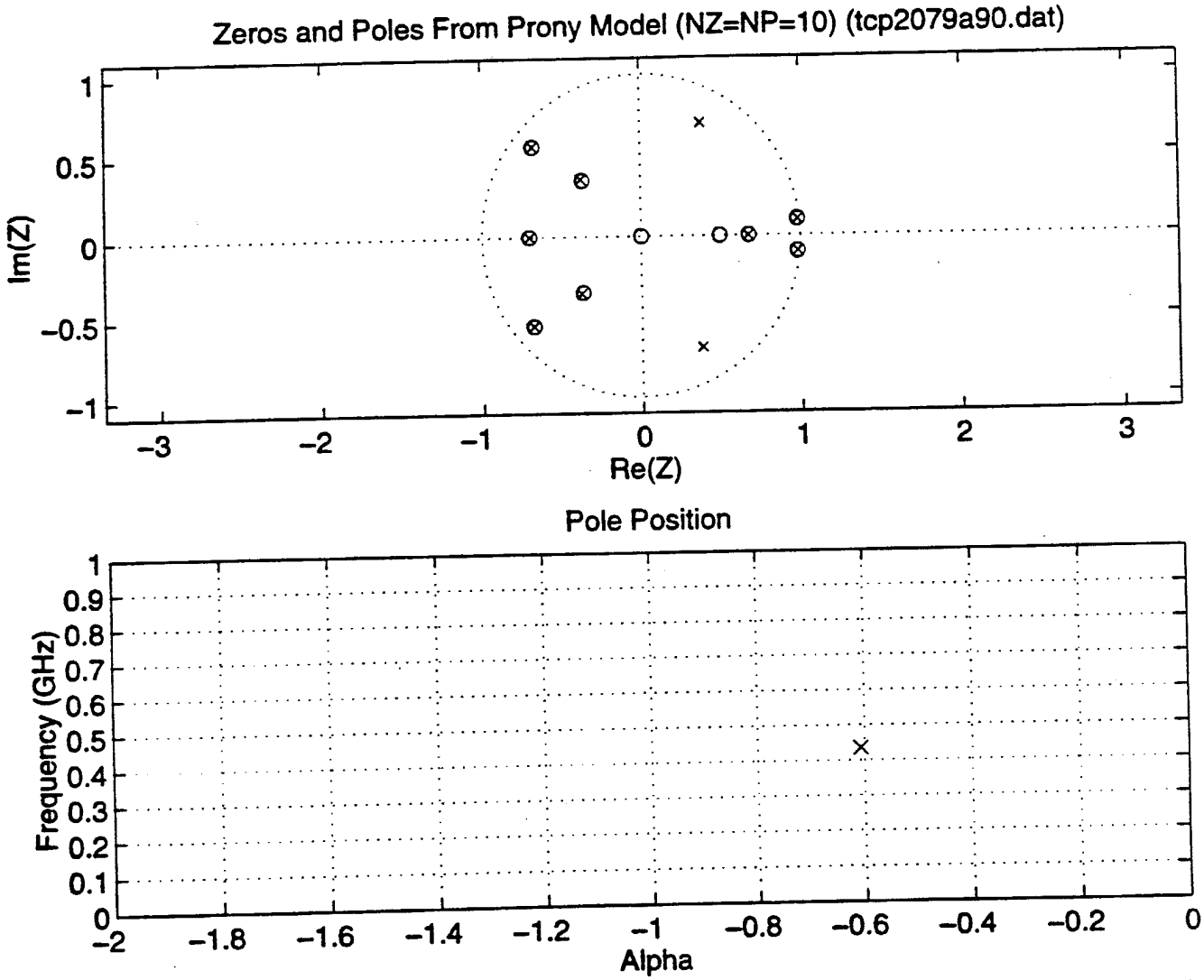
Zeros and Poles From Prony Model (NZ=NP=10) (tcp2079a90.dat)
Im(Z)
Re(Z)
1
0.5
0
−0.5
−1
−3
−2
−1
0
1
2
3

Pole Position
Frequency (GHz)
Alpha
1
0.9
0.8
0.7
0.6
0.5
0.4
0.3
0.2
0.1
0
−2
−1.8
−1.6
−1.4
−1.2
−1
−0.8
−0.6
−0.4
−0.2
0

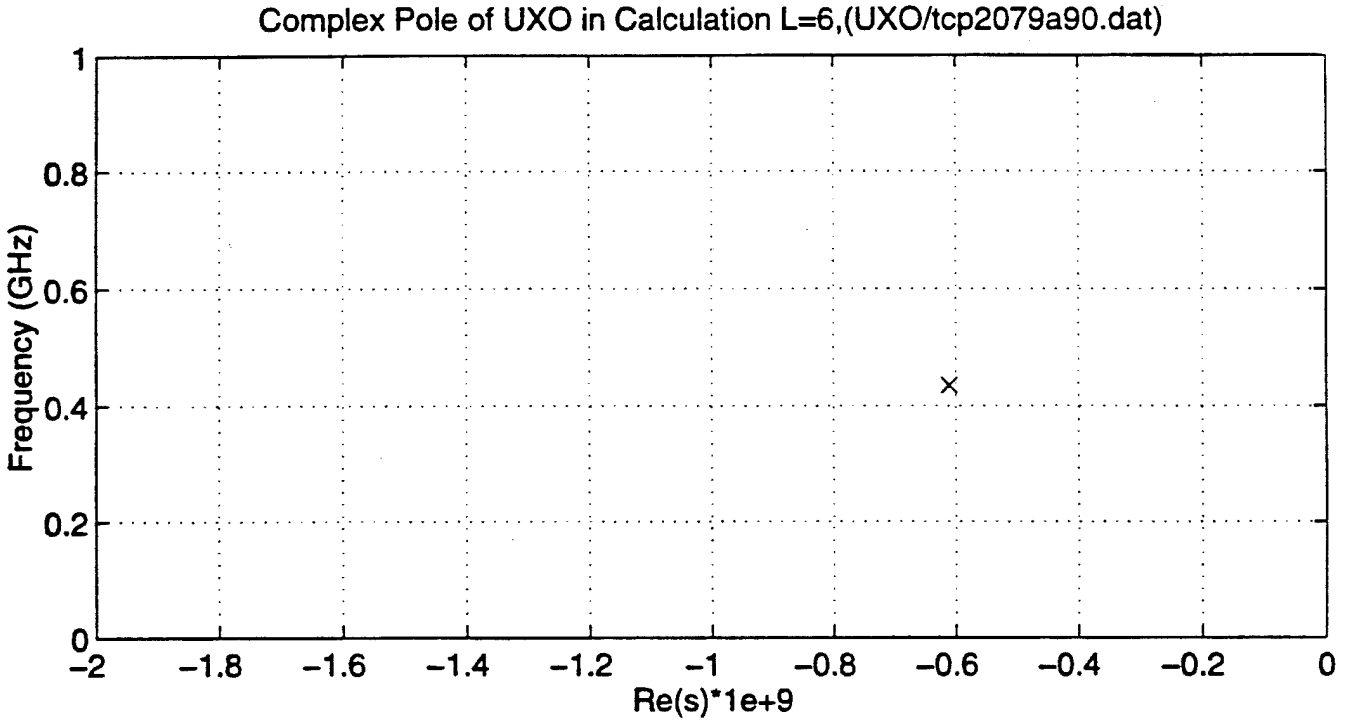
Complex Pole of UXO in Calculation L=6,(UXO/tcp2079a90.dat)
Frequency (GHz)
1
0.8
0.6
0.4
0.2
0
−2
−1.8
−1.6
−1.4
−1.2
−1
−0.8
−0.6
−0.4
−0.2
0
Re(s)*1e+9

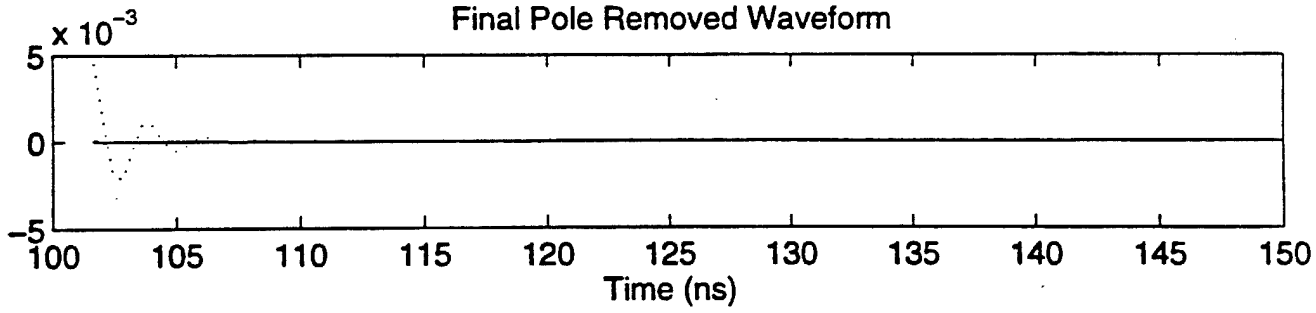
Final Pole Removed Waveform
x 10^-3
5
0
−5
100
105
110
115
120
125
130
135
140
145
150
Time (ns)

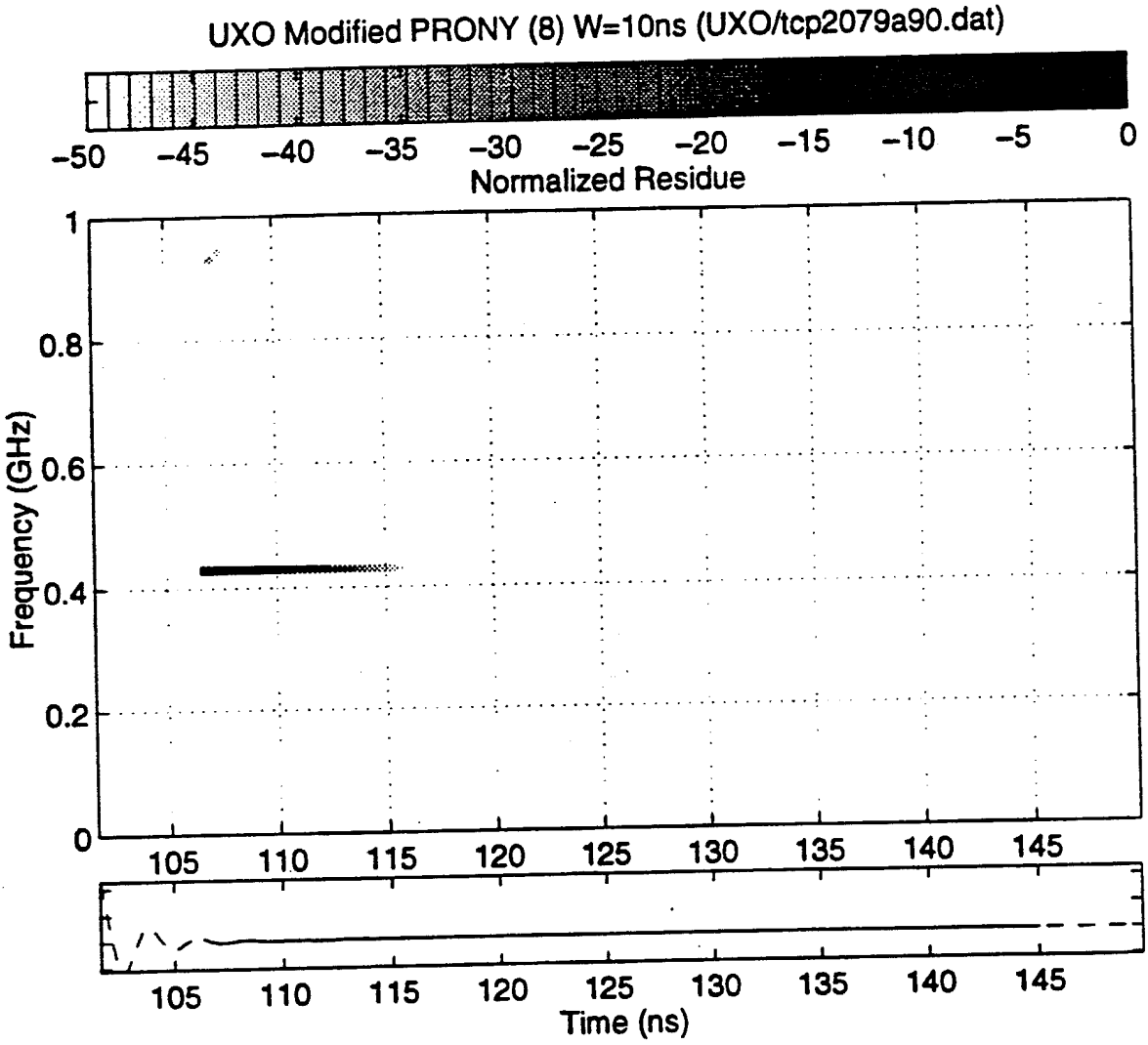
UXO Modified PRONY (8) W=10ns (UXO/tcp2079a90.dat)
−50 −45 −40 −35 −30 −25 −20 −15 −10 −5 0
Normalized Residue
Frequency (GHz)
1
0.8
0.6
0.4
0.2
0
105 110 115 120 125 130 135 140 145
105 110 115 120 125 130 135 140 145
Time (ns)

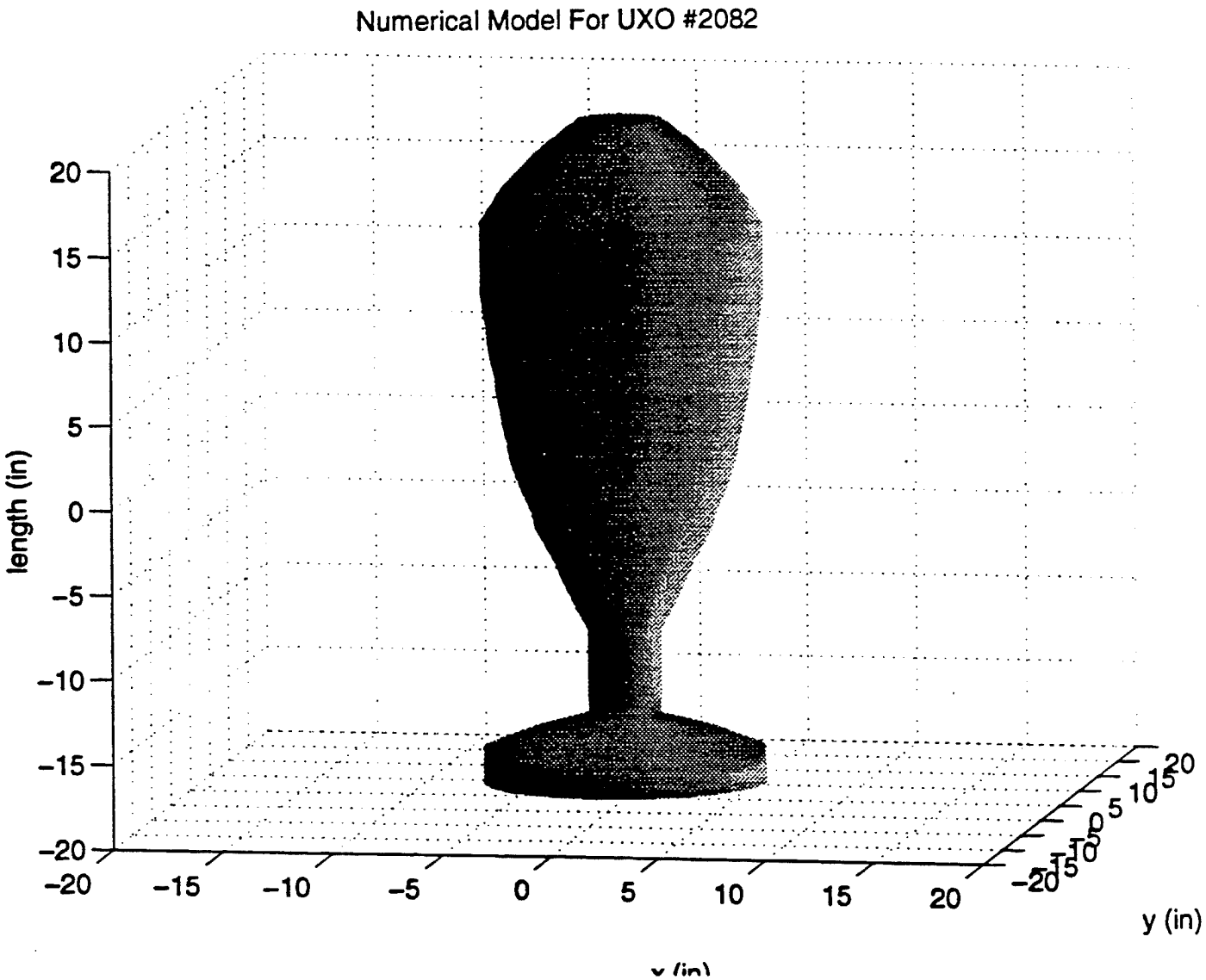
Numerical Model For UXO #2082
length (in)
20
15
10
5
0
−5
−10
−15
−20
−20
−15
−10
−5
0
5
10
15
20
y (in)

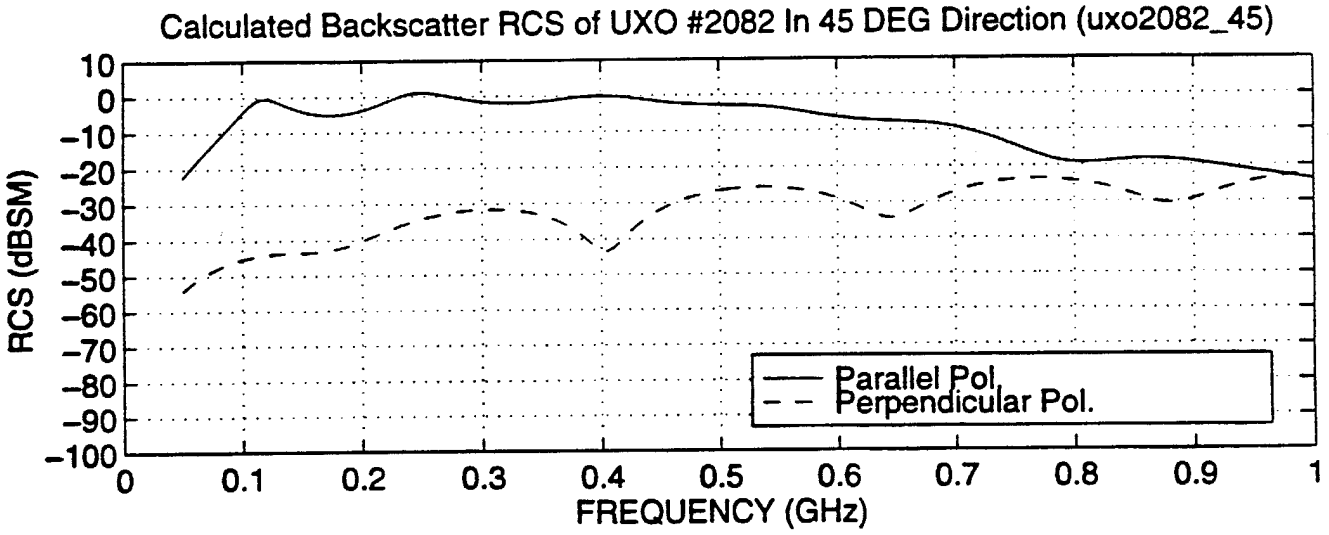
Calculated Backscatter RCS of UXO #2082 In 45 DEG Direction (uxo2082_45)
RCS (dBSM)
10
0
-10
-20
-30
-40
-50
-60
-70
-80
-90
-100
0
0.1
0.2
0.3
0.4
0.5
0.6
0.7
0.8
0.9
1
FREQUENCY (GHz)
Parallel Pol.
Perpendicular Pol.

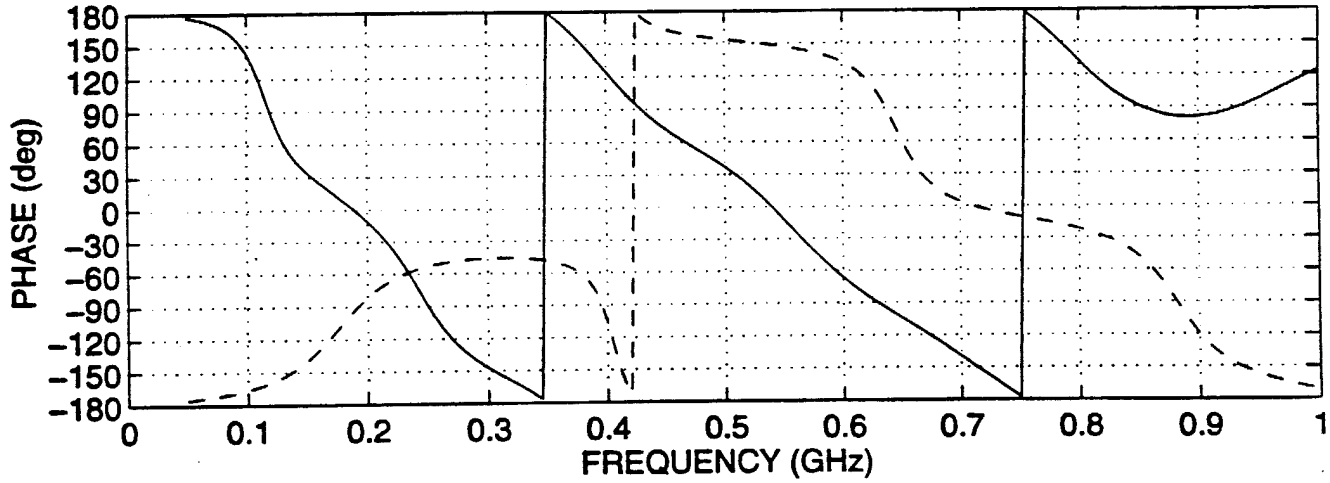
PHASE (deg)
180
150
120
90
60
30
0
-30
-60
-90
-120
-150
-180
0
0.1
0.2
0.3
0.4
0.5
0.6
0.7
0.8
0.9
1
FREQUENCY (GHz)

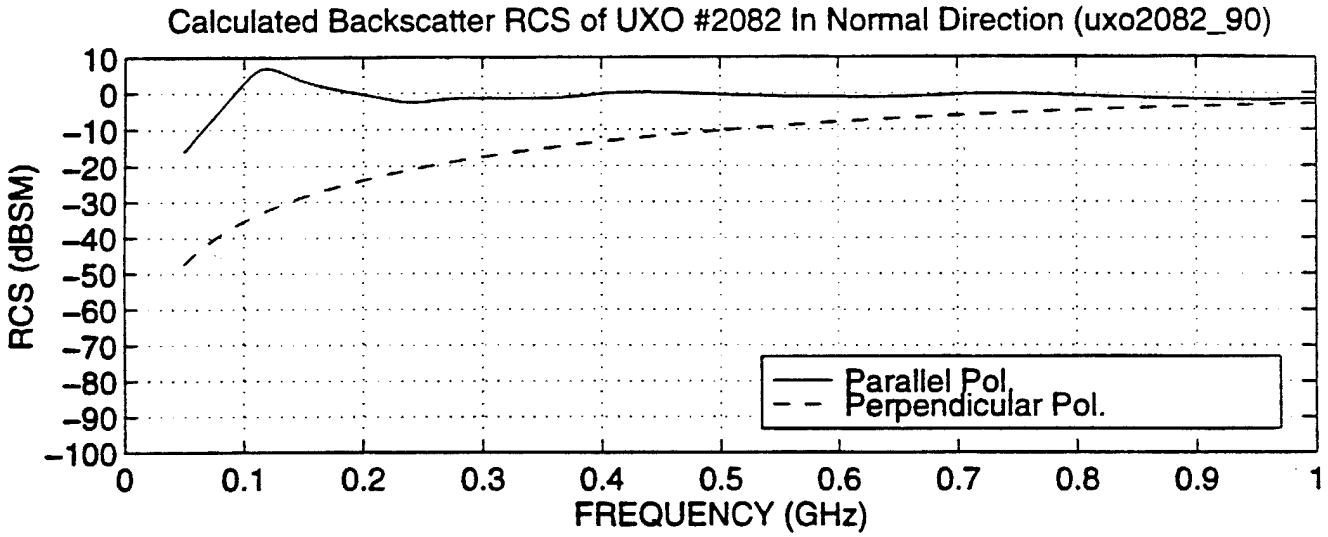
Calculated Backscatter RCS of UXO #2082 In Normal Direction (uxo2082_90)
RCS (dBSM)
10
0
-10
-20
-30
-40
-50
-60
-70
-80
-90
-100
0
0.1
0.2
0.3
0.4
0.5
0.6
0.7
0.8
0.9
1
FREQUENCY (GHz)
Parallel Pol.
Perpendicular Pol.

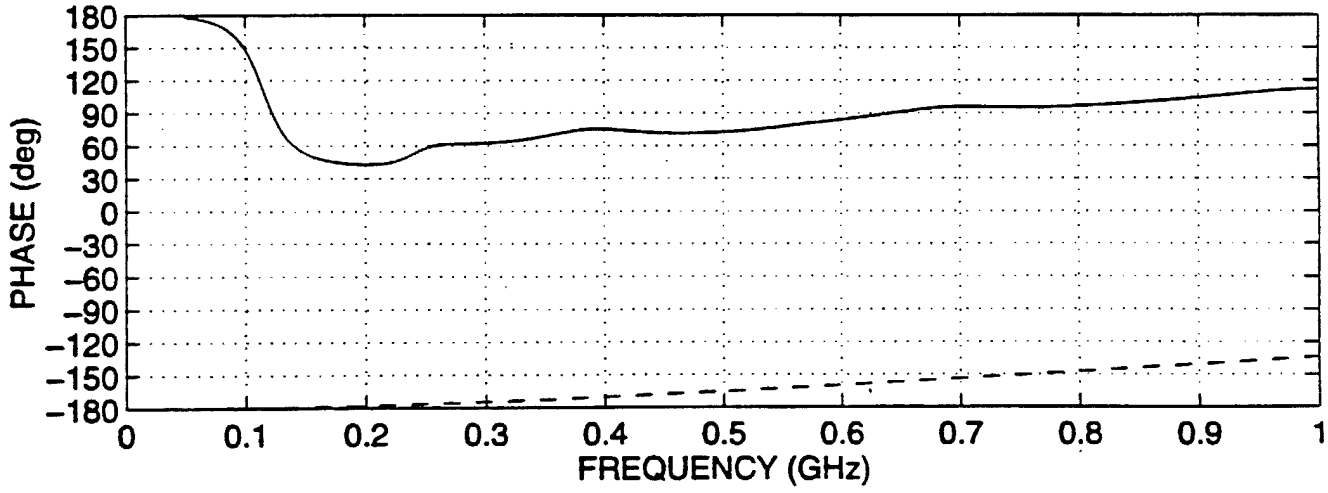
PHASE (deg)
180
150
120
90
60
30
0
-30
-60
-90
-120
-150
-180
0
0.1
0.2
0.3
0.4
0.5
0.6
0.7
0.8
0.9
1
FREQUENCY (GHz)

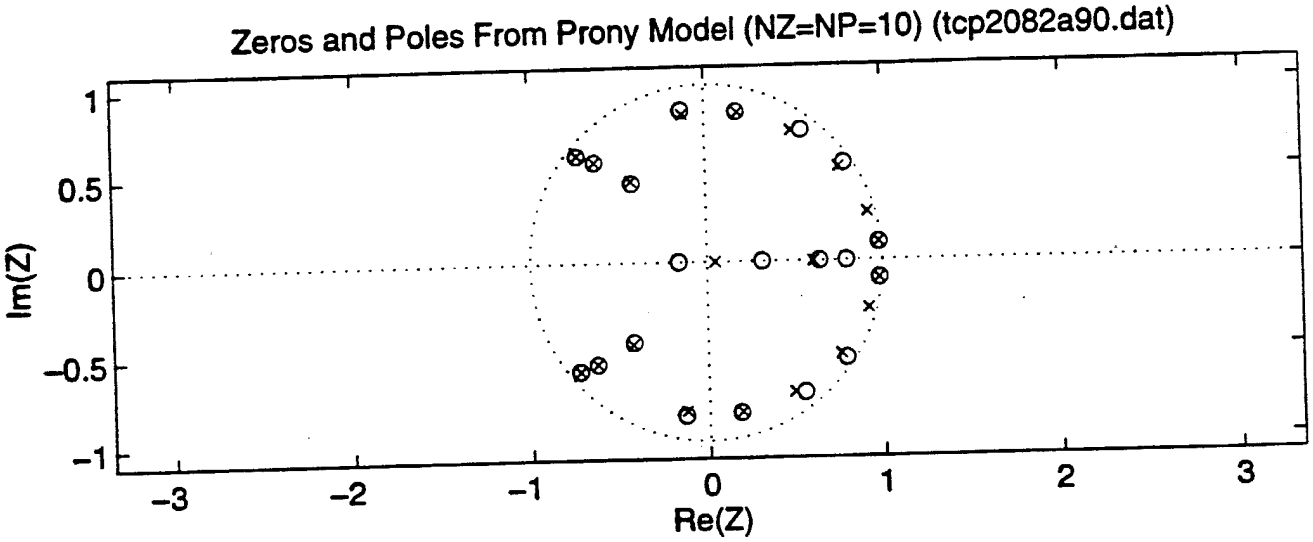
Zeros and Poles From Prony Model (NZ=NP=10) (tcp2082a90.dat)
Im(Z)
Re(Z)
1
0.5
0
−0.5
−1
−3
−2
−1
0
1
2
3

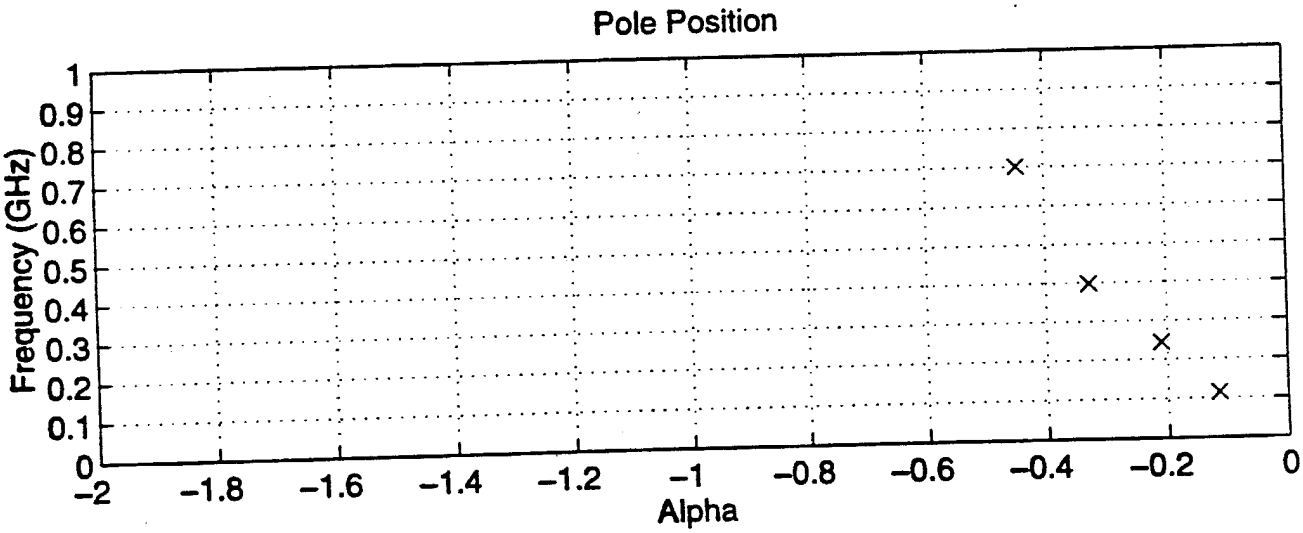
Pole Position
Frequency (GHz)
Alpha
1
0.9
0.8
0.7
0.6
0.5
0.4
0.3
0.2
0.1
0
−2
−1.8
−1.6
−1.4
−1.2
−1
−0.8
−0.6
−0.4
−0.2
0

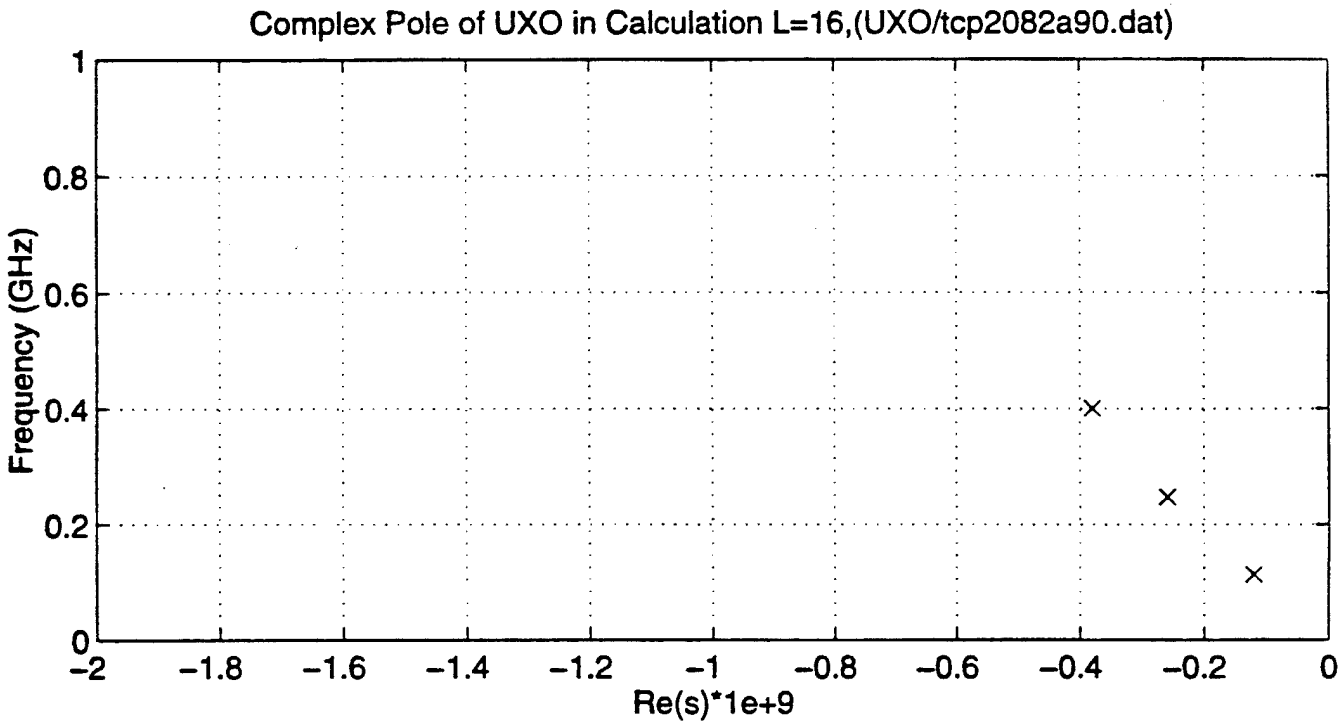
Complex Pole of UXO in Calculation L=16,(UXO/tcp2082a90.dat)
Frequency (GHz)
1
0.8
0.6
0.4
0.2
0
−2
−1.8
−1.6
−1.4
−1.2
−1
−0.8
−0.6
−0.4
−0.2
0
Re(s)*1e+9

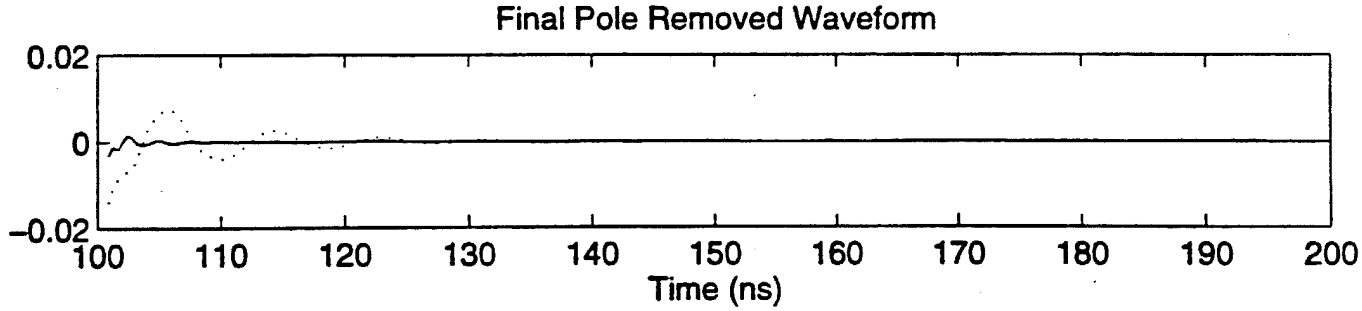
Final Pole Removed Waveform
0.02
0
−0.02
100
110
120
130
140
150
160
170
180
190
200
Time (ns)

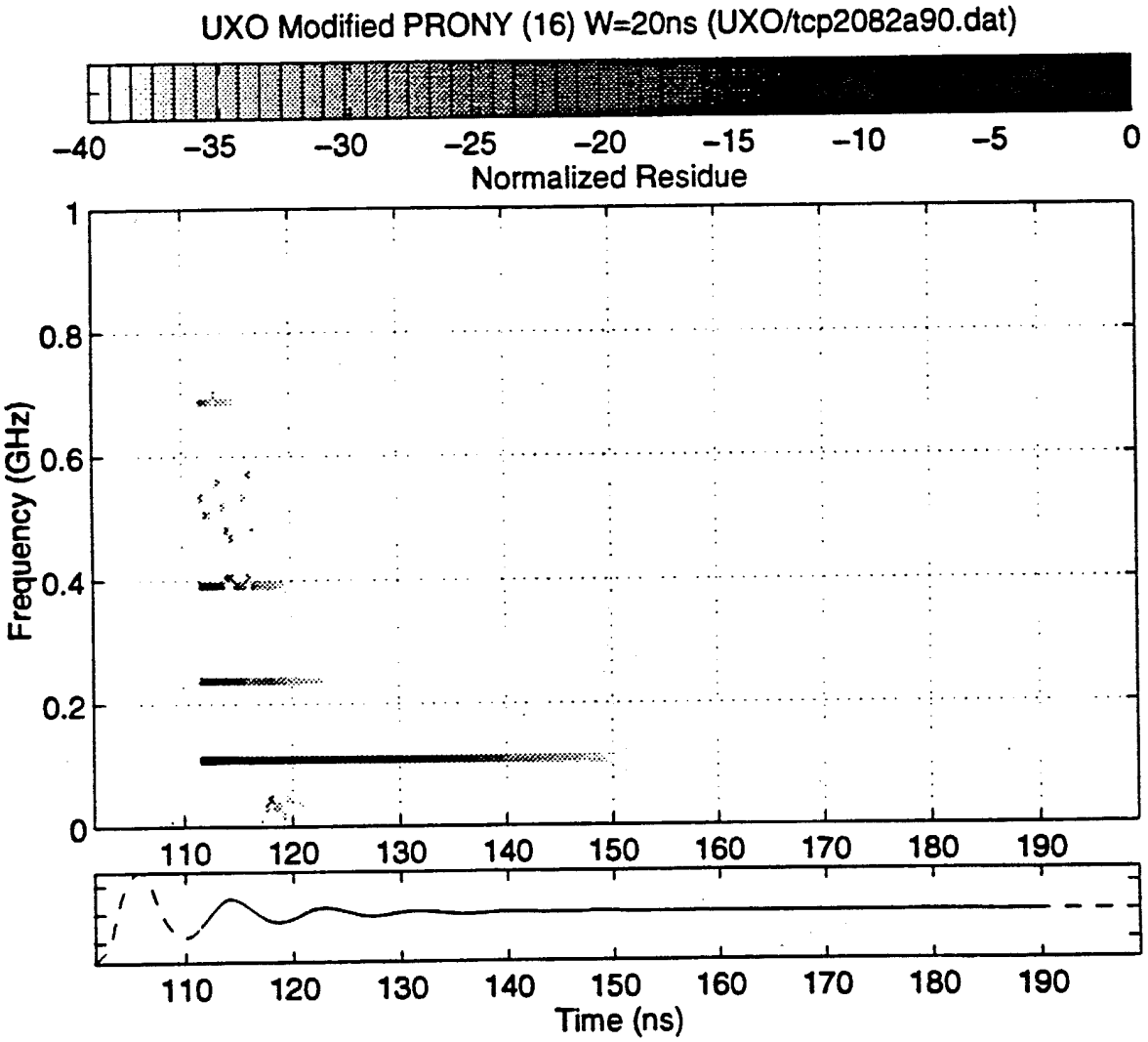
UXO Modified PRONY (16) W=20ns (UXO/tcp2082a90.dat)
−40
−35
−30
−25
−20
−15
−10
−5
0
Normalized Residue
Frequency (GHz)
1
0.8
0.6
0.4
0.2
0
110
120
130
140
150
160
170
180
190
Time (ns)

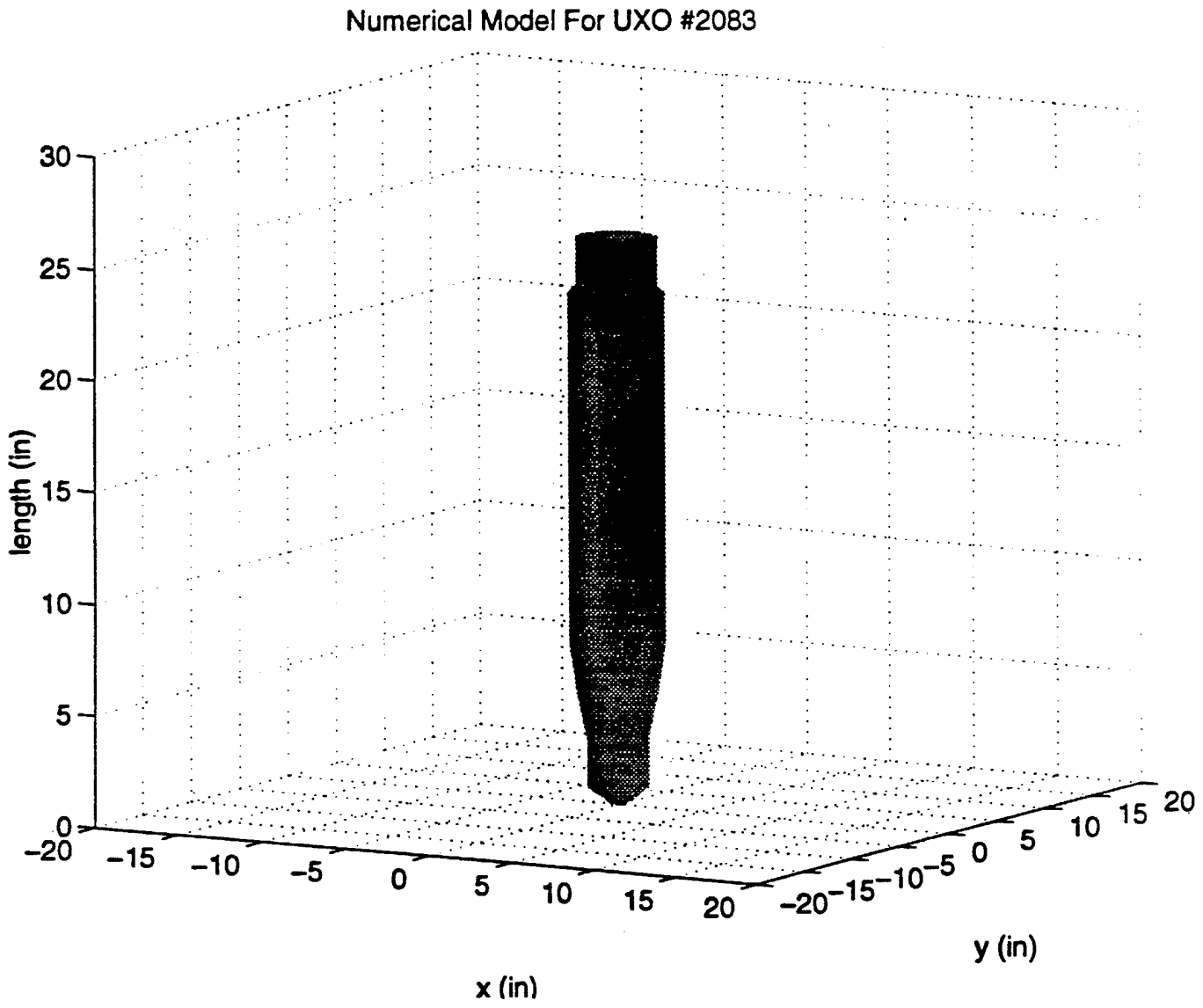
Numerical Model For UXO #2083
30
25
20
15
10
5
0
length (in)
−20
−15
−10
−5
0
5
10
15
20
x (in)
−20
−15
−10
−5
0
5
10
15
20
y (in)

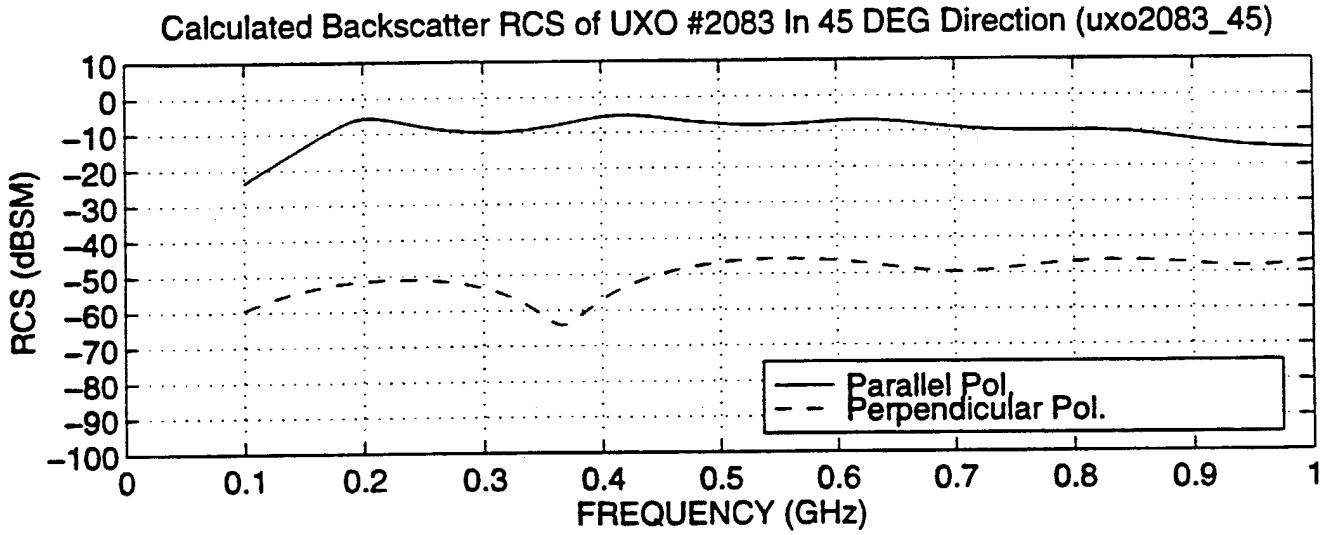
Calculated Backscatter RCS of UXO #2083 In 45 DEG Direction (uxo2083_45)
RCS (dBSM)
10
0
-10
-20
-30
-40
-50
-60
-70
-80
-90
-100
0
0.1
0.2
0.3
0.4
0.5
0.6
0.7
0.8
0.9
1
FREQUENCY (GHz)
Parallel Pol.
Perpendicular Pol.

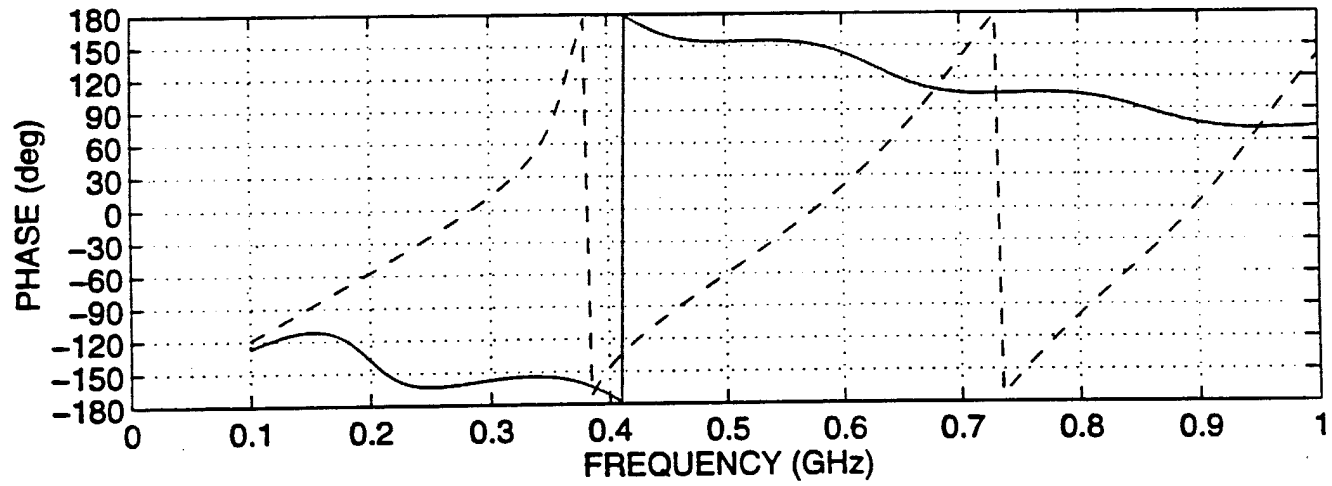
PHASE (deg)
180
150
120
90
60
30
0
-30
-60
-90
-120
-150
-180
0
0.1
0.2
0.3
0.4
0.5
0.6
0.7
0.8
0.9
1
FREQUENCY (GHz)

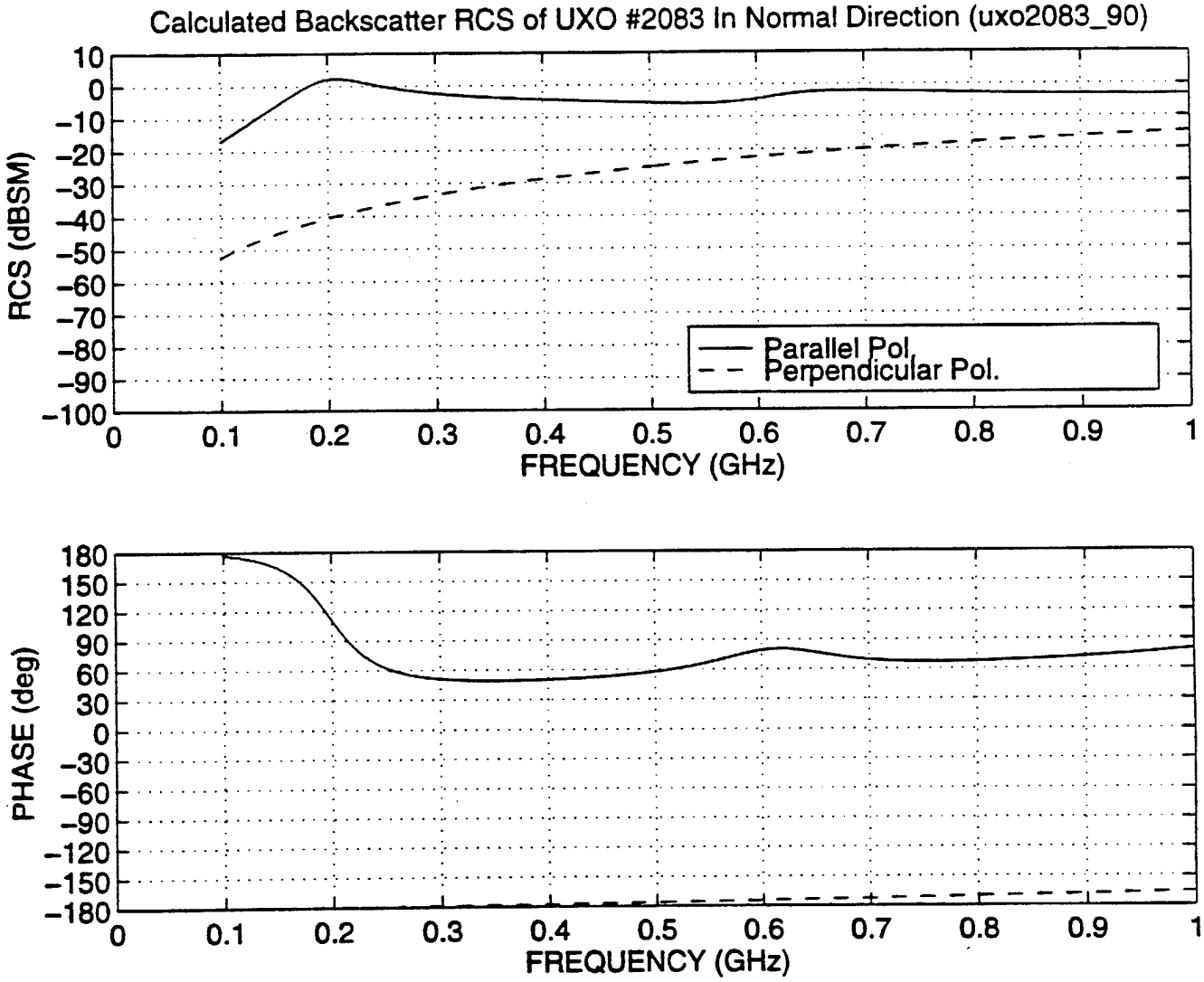
Calculated Backscatter RCS of UXO #2083 In Normal Direction (uxo2083_90)
RCS (dBSM)
10
0
-10
-20
-30
-40
-50
-60
-70
-80
-90
-100
0
0.1
0.2
0.3
0.4
0.5
0.6
0.7
0.8
0.9
1
FREQUENCY (GHz)
Parallel Pol.
Perpendicular Pol.
PHASE (deg)
180
150
120
90
60
30
0
-30
-60
-90
-120
-150
-180
0
0.1
0.2
0.3
0.4
0.5
0.6
0.7
0.8
0.9
1
FREQUENCY (GHz)

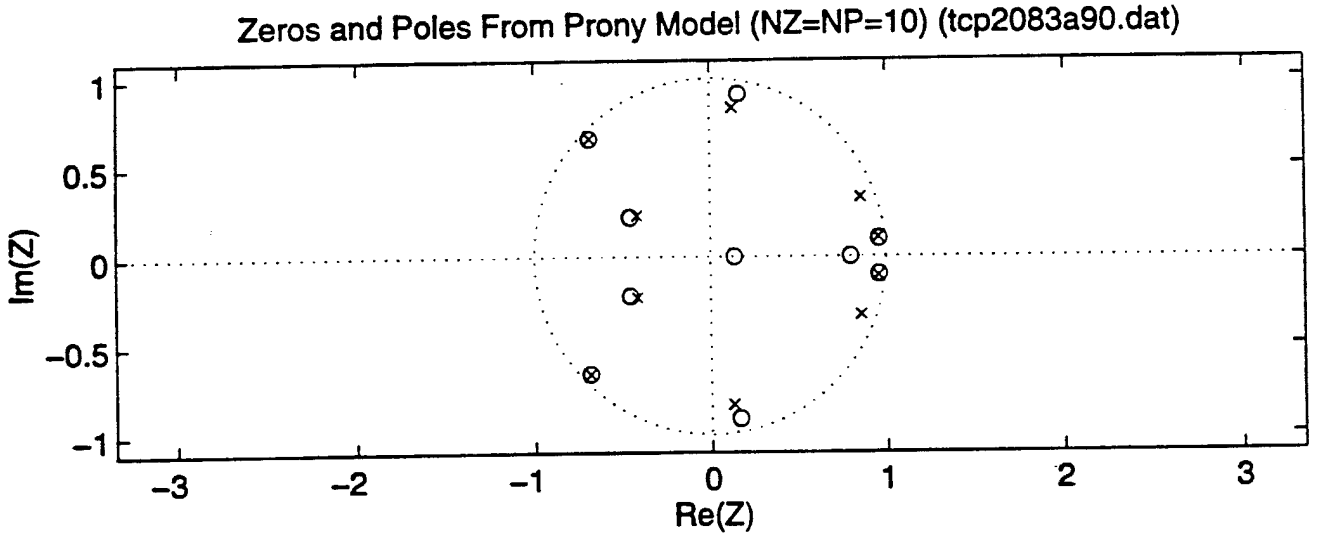
Zeros and Poles From Prony Model (NZ=NP=10) (tcp2083a90.dat)
Im(Z)
Re(Z)
1
0.5
0
−0.5
−1
−3
−2
−1
0
1
2
3

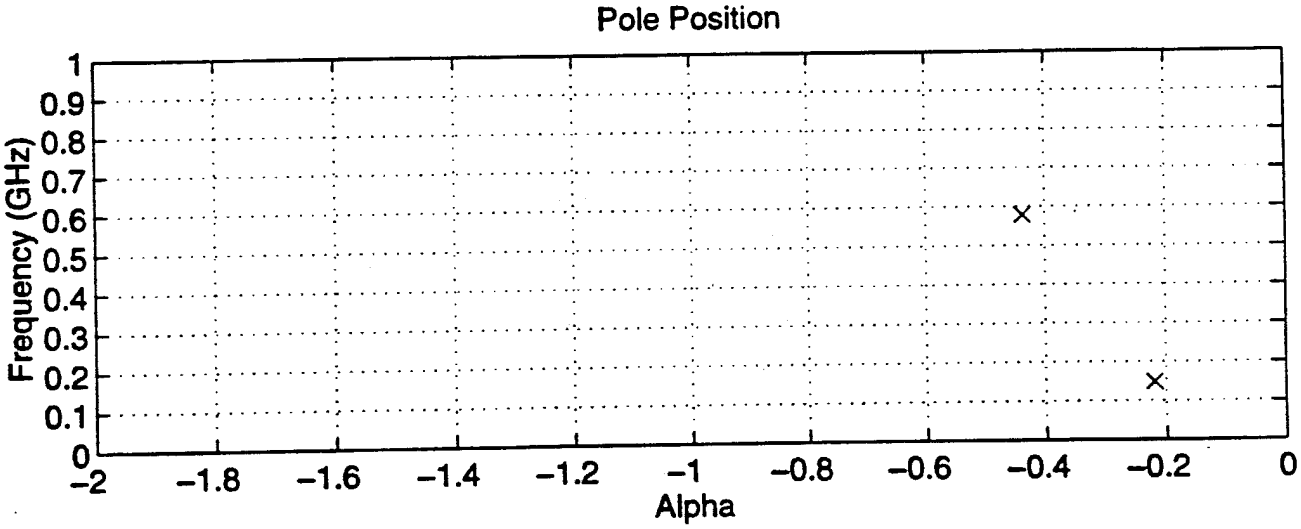
Pole Position
Frequency (GHz)
Alpha
1
0.9
0.8
0.7
0.6
0.5
0.4
0.3
0.2
0.1
0
−2
−1.8
−1.6
−1.4
−1.2
−1
−0.8
−0.6
−0.4
−0.2
0

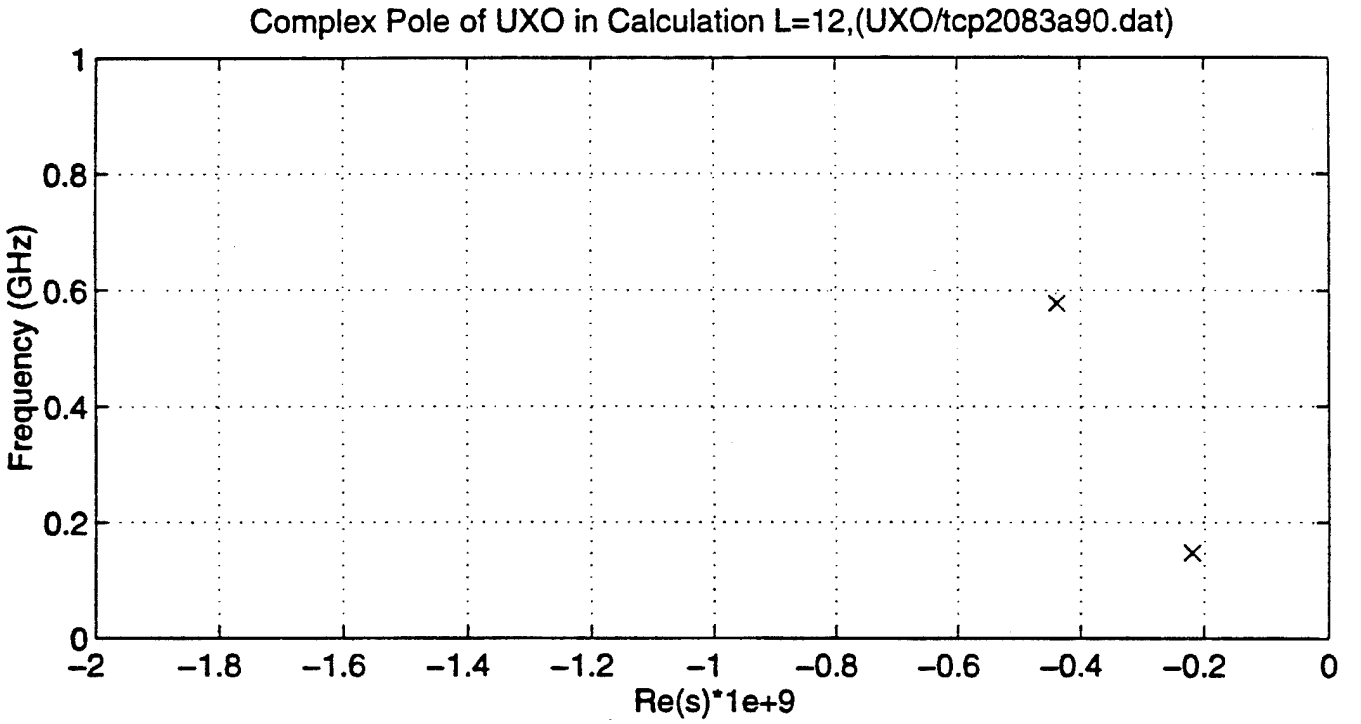
Complex Pole of UXO in Calculation L=12,(UXO/tcp2083a90.dat)
Frequency (GHz)
1
0.8
0.6
0.4
0.2
0
−2
−1.8
−1.6
−1.4
−1.2
−1
−0.8
−0.6
−0.4
−0.2
0
Re(s)*1e+9

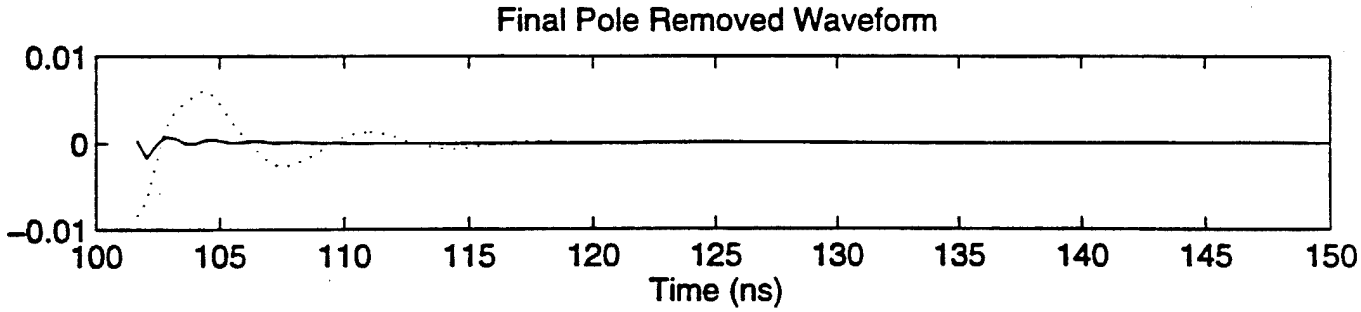
Final Pole Removed Waveform
0.01
0
−0.01
100
105
110
115
120
125
130
135
140
145
150
Time (ns)

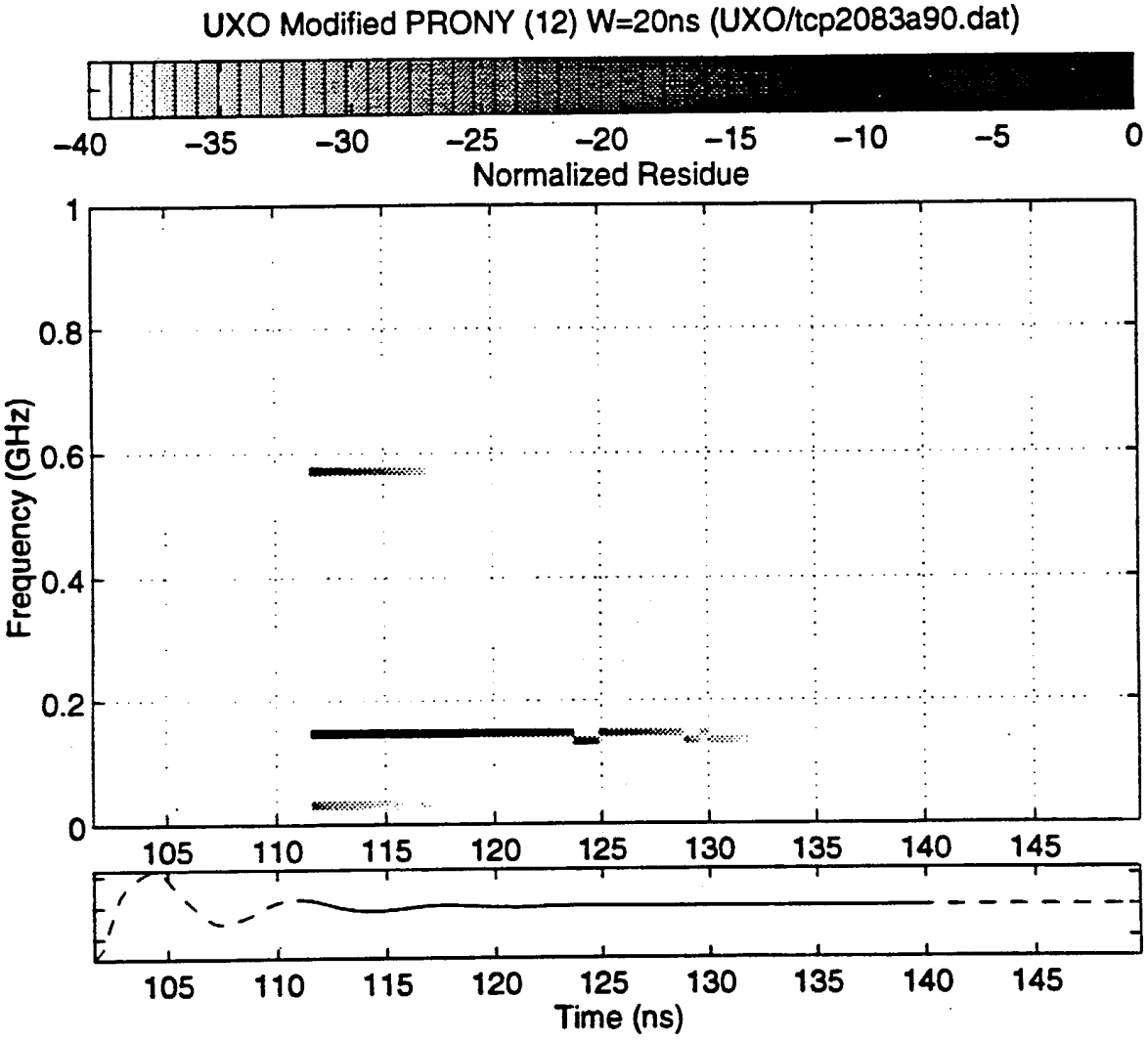
UXO Modified PRONY (12) W=20ns (UXO/tcp2083a90.dat)
−40
−35
−30
−25
−20
−15
−10
−5
0
Normalized Residue
Frequency (GHz)
1
0.8
0.6
0.4
0.2
0
105
110
115
120
125
130
135
140
145
Time (ns)

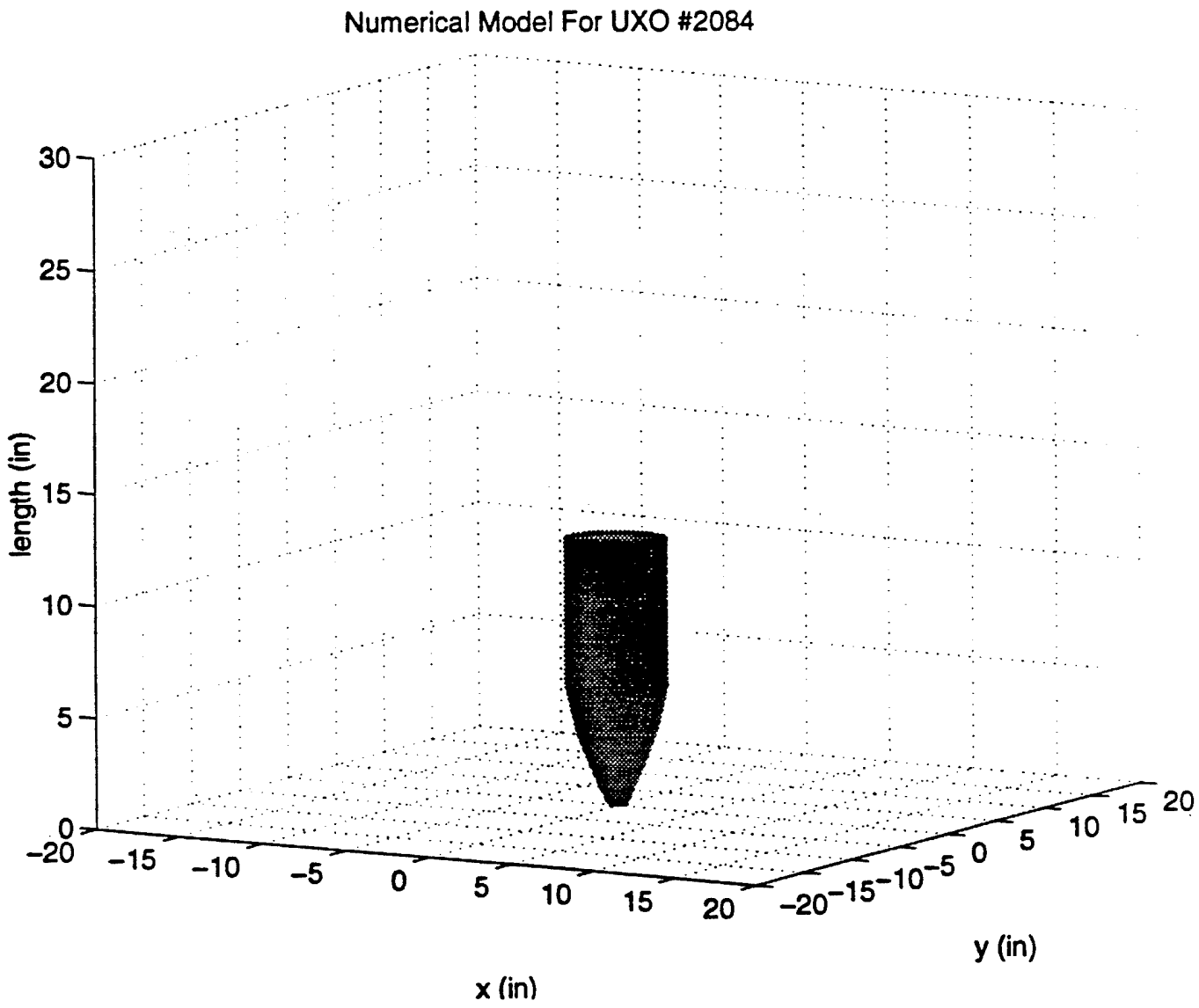
Numerical Model For UXO #2084
length (in)
30
25
20
15
10
5
0
−20
−15
−10
−5
0
5
10
15
20
x (in)
−20
−15
−10
−5
0
5
10
15
20
y (in)

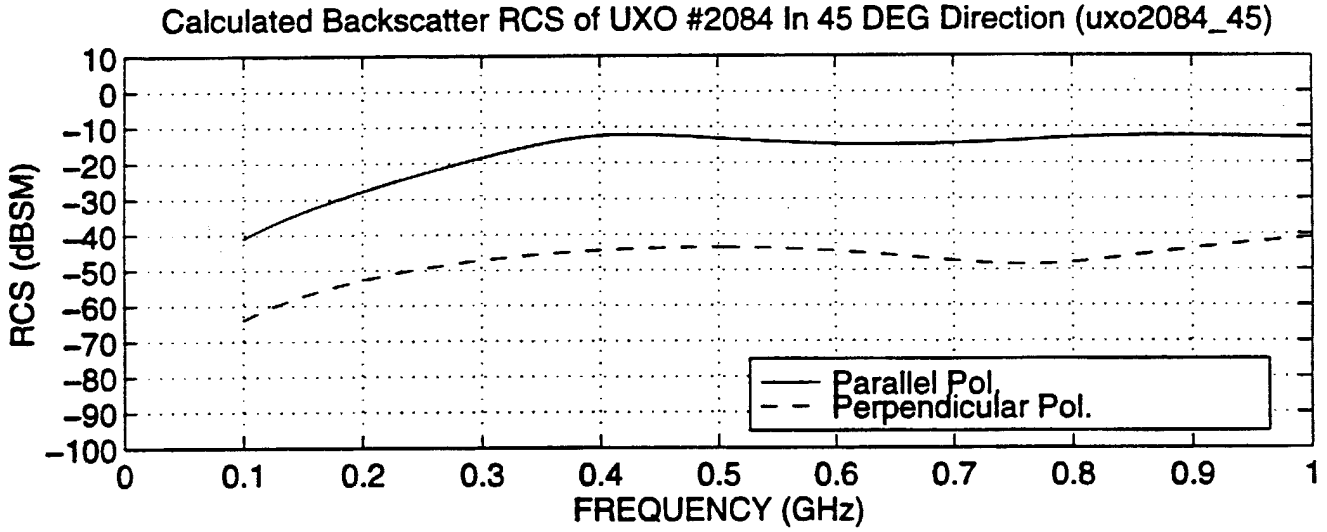
Calculated Backscatter RCS of UXO #2084 In 45 DEG Direction (uxo2084_45)
RCS (dBSM)
10
0
-10
-20
-30
-40
-50
-60
-70
-80
-90
-100
0
0.1
0.2
0.3
0.4
0.5
0.6
0.7
0.8
0.9
1
FREQUENCY (GHz)
Parallel Pol.
Perpendicular Pol.

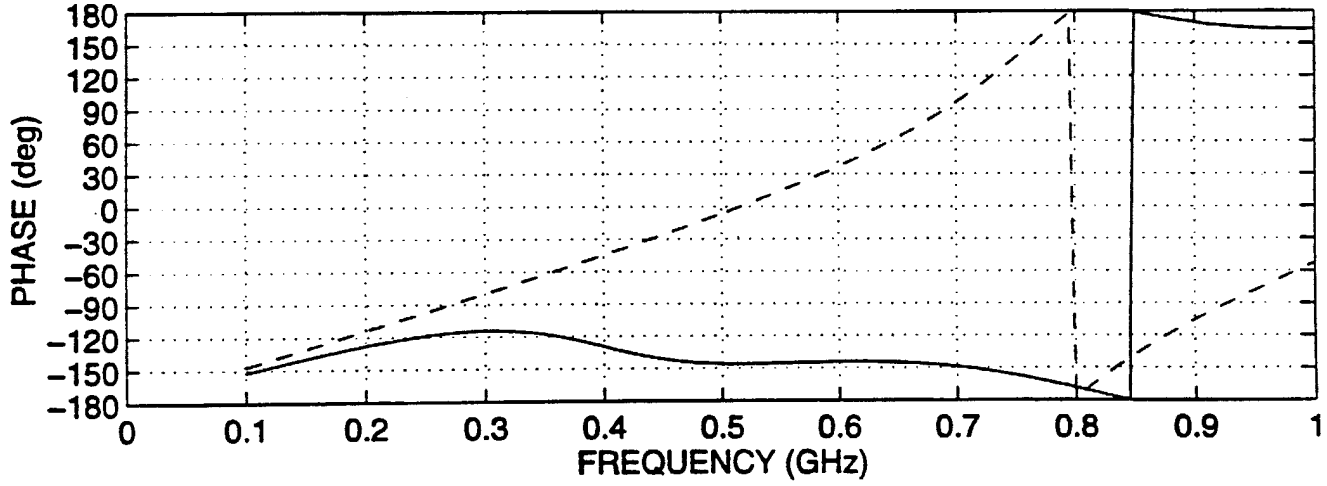
PHASE (deg)
180
150
120
90
60
30
0
-30
-60
-90
-120
-150
-180
0
0.1
0.2
0.3
0.4
0.5
0.6
0.7
0.8
0.9
1
FREQUENCY (GHz)

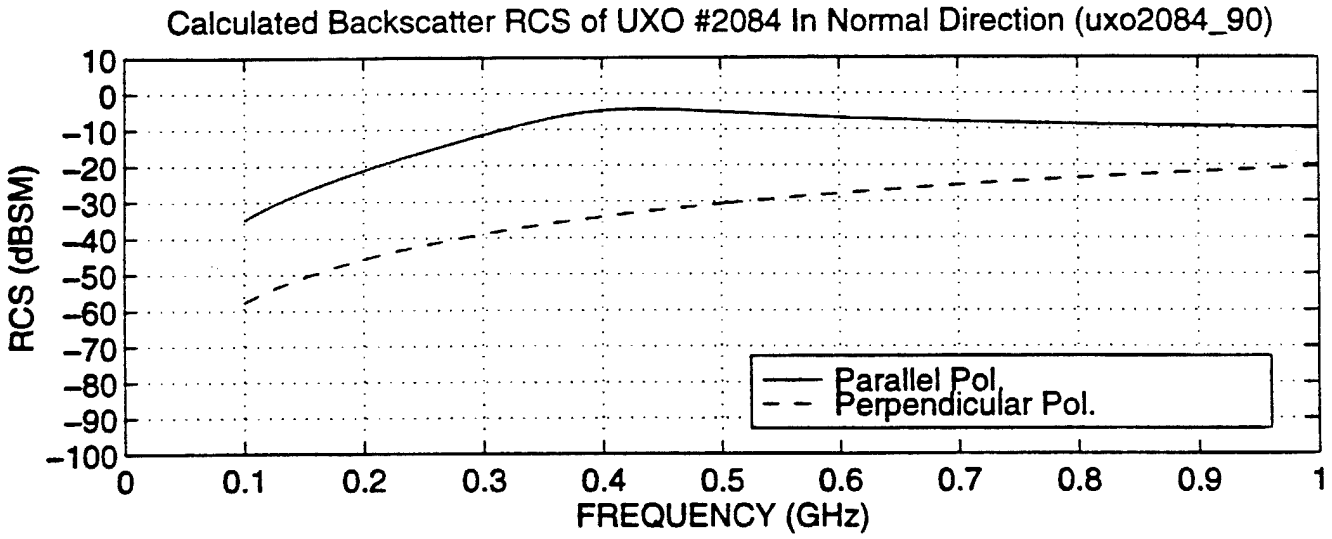
Calculated Backscatter RCS of UXO #2084 In Normal Direction (uxo2084_90)
RCS (dBSM)
10
0
-10
-20
-30
-40
-50
-60
-70
-80
-90
-100
0
0.1
0.2
0.3
0.4
0.5
0.6
0.7
0.8
0.9
1
FREQUENCY (GHz)
Parallel Pol.
Perpendicular Pol.

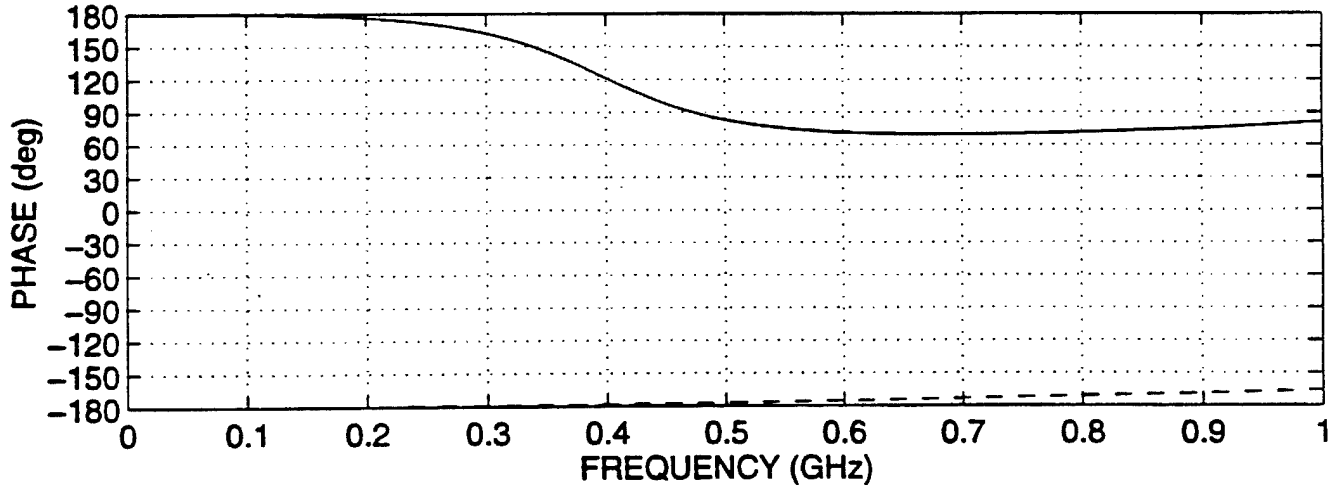
PHASE (deg)
180
150
120
90
60
30
0
-30
-60
-90
-120
-150
-180
0
0.1
0.2
0.3
0.4
0.5
0.6
0.7
0.8
0.9
1
FREQUENCY (GHz)

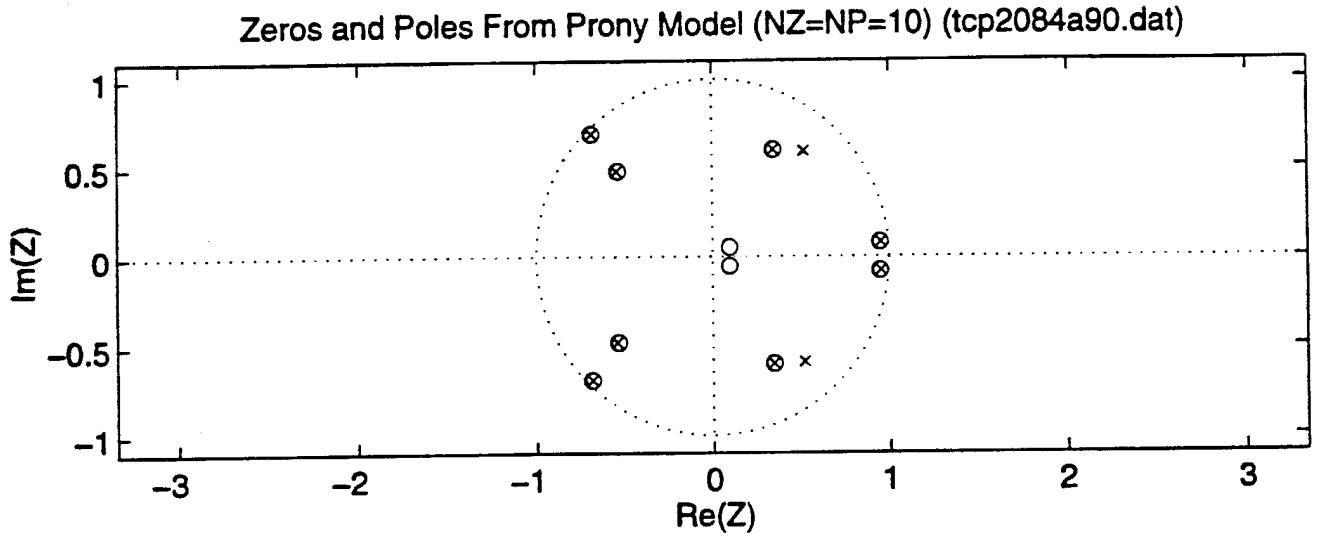
Zeros and Poles From Prony Model (NZ=NP=10) (tcp2084a90.dat)
Im(Z)
Re(Z)
1
0.5
0
−0.5
−1
−3
−2
−1
0
1
2
3

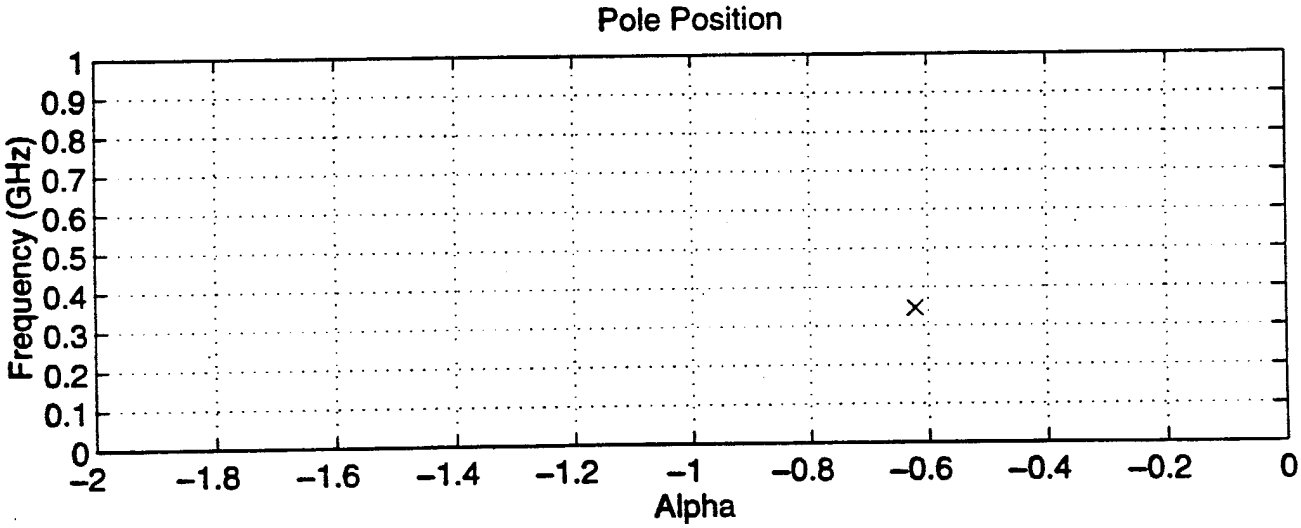
Pole Position
Frequency (GHz)
Alpha
1
0.9
0.8
0.7
0.6
0.5
0.4
0.3
0.2
0.1
0
−2
−1.8
−1.6
−1.4
−1.2
−1
−0.8
−0.6
−0.4
−0.2
0

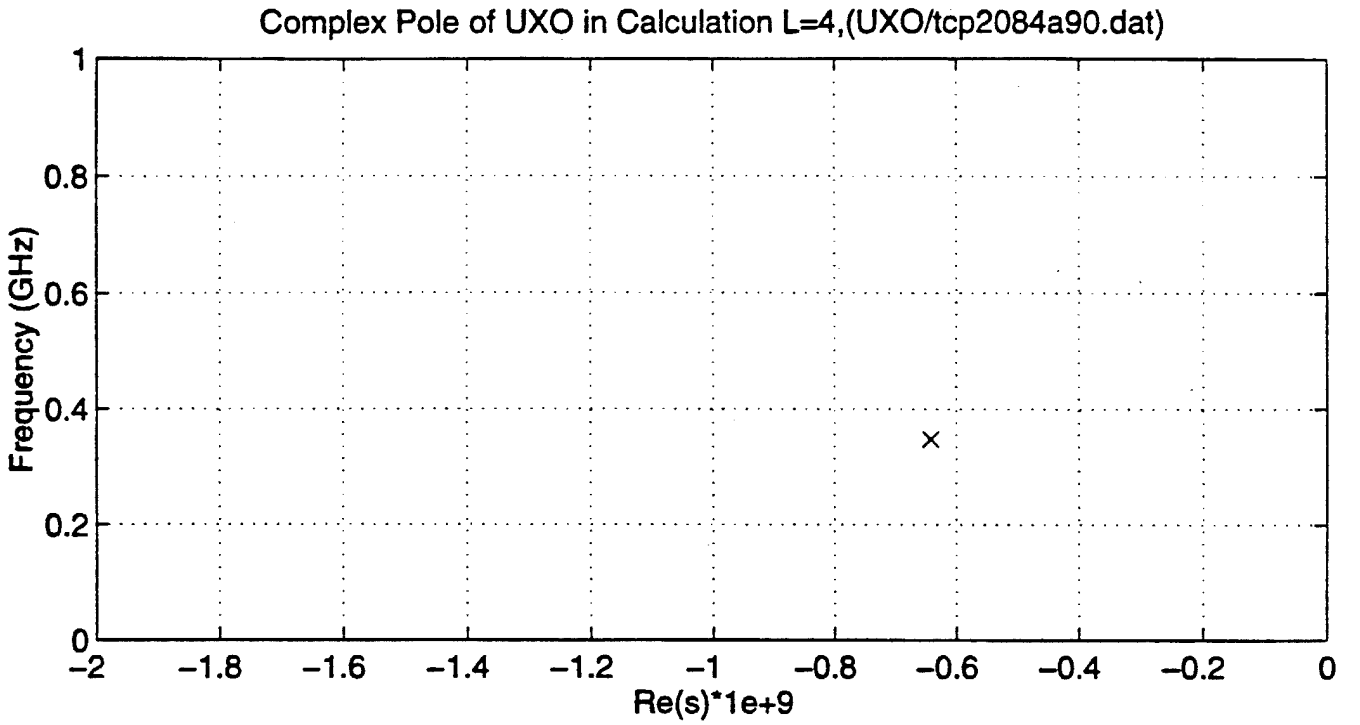
Complex Pole of UXO in Calculation L=4,(UXO/tcp2084a90.dat)
Frequency (GHz)
1
0.8
0.6
0.4
0.2
0
−2
−1.8
−1.6
−1.4
−1.2
−1
−0.8
−0.6
−0.4
−0.2
0
Re(s)*1e+9

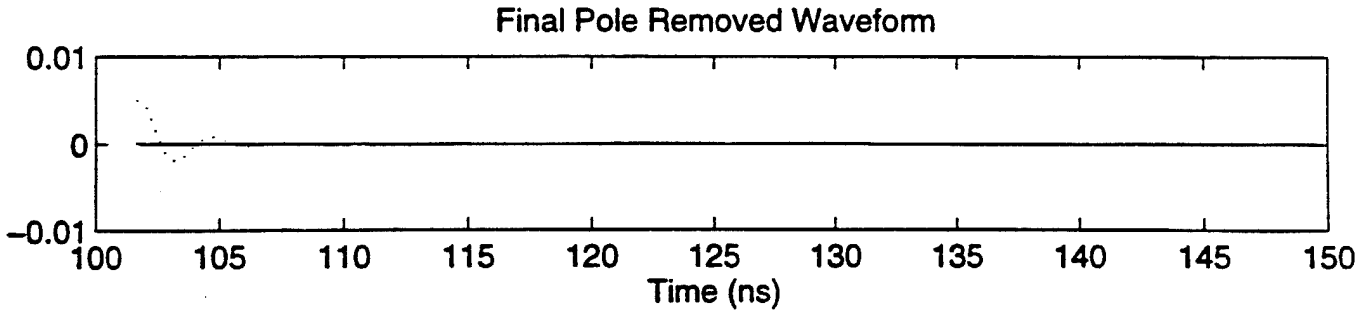
Final Pole Removed Waveform
0.01
0
−0.01
100
105
110
115
120
125
130
135
140
145
150
Time (ns)

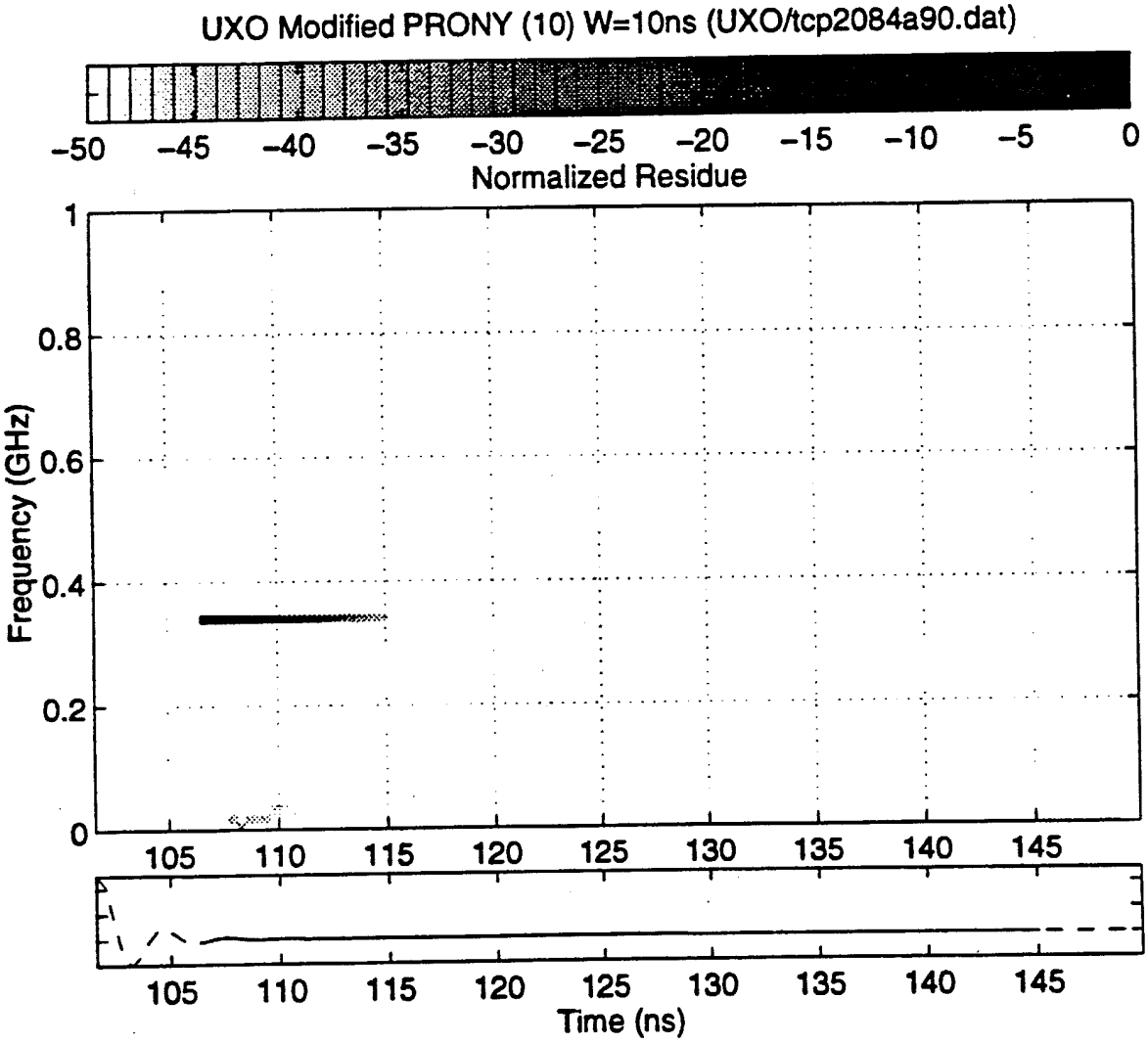
UXO Modified PRONY (10) W=10ns (UXO/tcp2084a90.dat)
−50 −45 −40 −35 −30 −25 −20 −15 −10 −5 0
Normalized Residue
Frequency (GHz)
1
0.8
0.6
0.4
0.2
0
105 110 115 120 125 130 135 140 145
105 110 115 120 125 130 135 140 145
Time (ns)

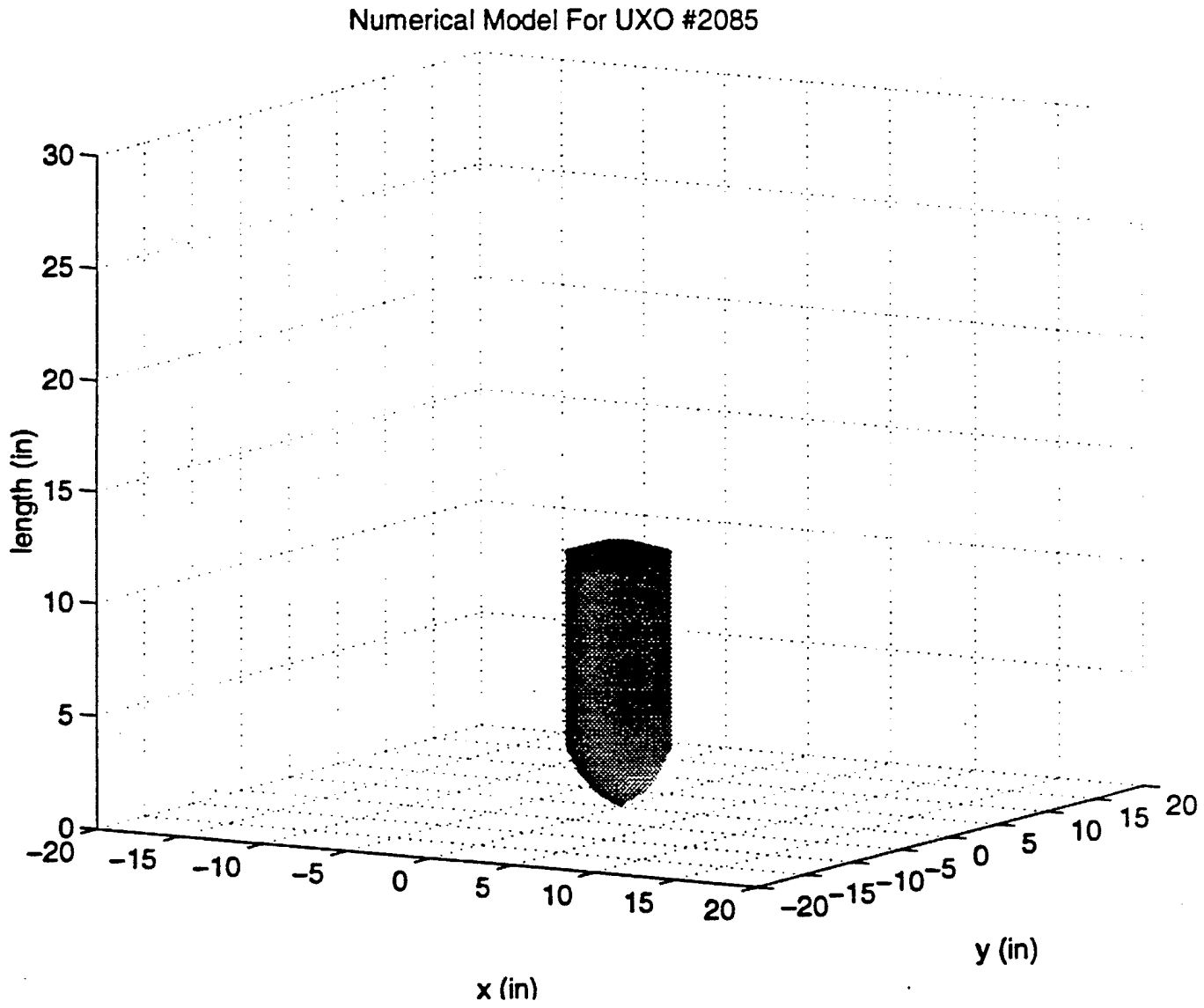
Numerical Model For UXO #2085
length (in)
30
25
20
15
10
5
0
−20
−15
−10
−5
0
5
10
15
20
x (in)
−20
−15
−10
−5
0
5
10
15
20
y (in)

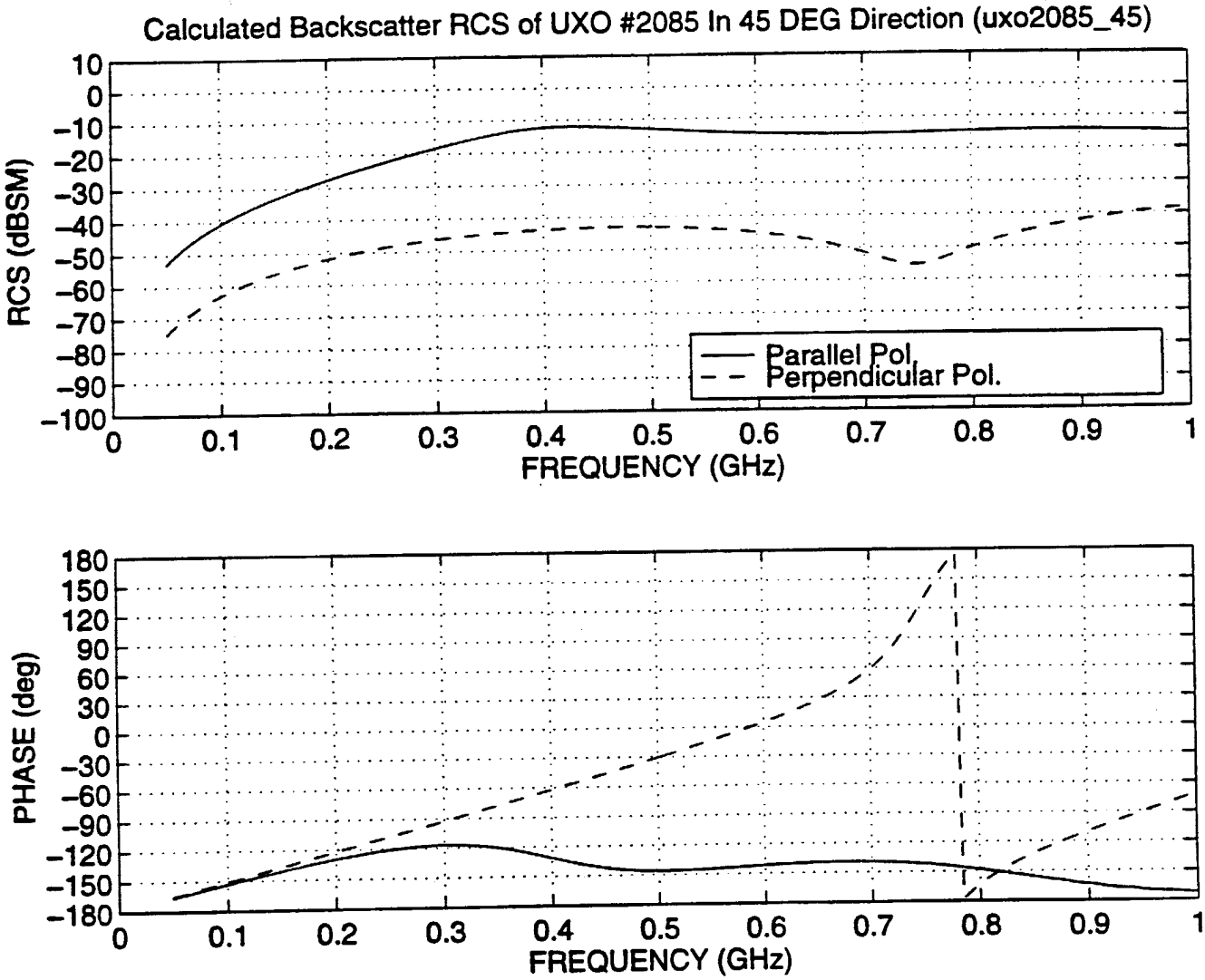
Calculated Backscatter RCS of UXO #2085 In 45 DEG Direction (uxo2085_45)
RCS (dBSM)
10
0
-10
-20
-30
-40
-50
-60
-70
-80
-90
-100
0
0.1
0.2
0.3
0.4
0.5
0.6
0.7
0.8
0.9
1
FREQUENCY (GHz)
Parallel Pol.
Perpendicular Pol.
PHASE (deg)
180
150
120
90
60
30
0
-30
-60
-90
-120
-150
-180
0
0.1
0.2
0.3
0.4
0.5
0.6
0.7
0.8
0.9
1
FREQUENCY (GHz)

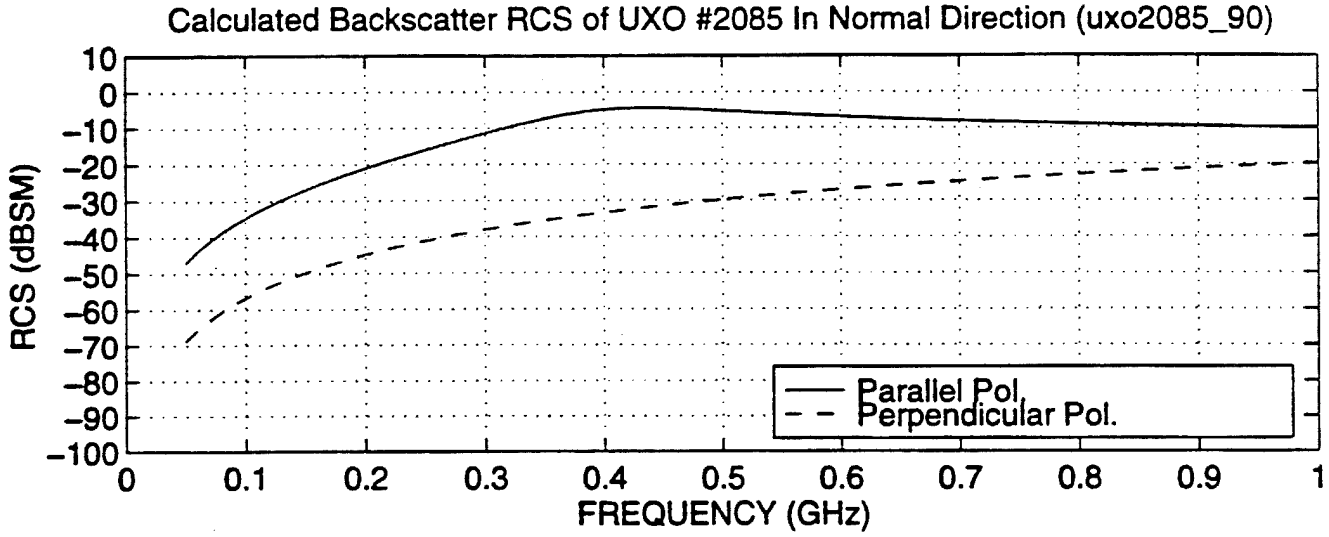
Calculated Backscatter RCS of UXO #2085 In Normal Direction (uxo2085_90)
RCS (dBSM)
10
0
-10
-20
-30
-40
-50
-60
-70
-80
-90
-100
0
0.1
0.2
0.3
0.4
0.5
0.6
0.7
0.8
0.9
1
FREQUENCY (GHz)
Parallel Pol.
Perpendicular Pol.

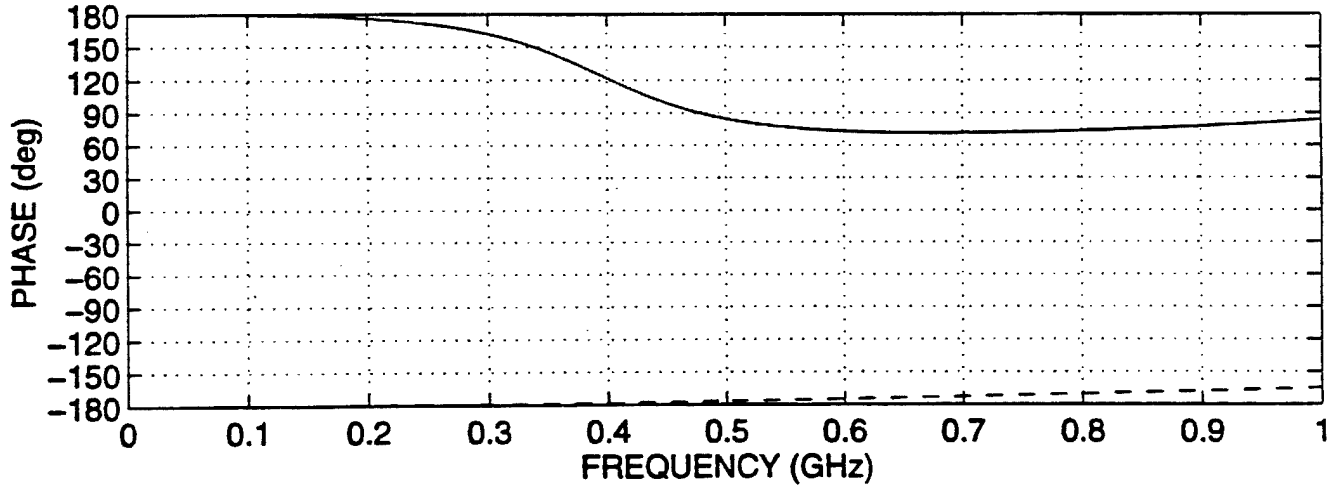
PHASE (deg)
180
150
120
90
60
30
0
-30
-60
-90
-120
-150
-180
0
0.1
0.2
0.3
0.4
0.5
0.6
0.7
0.8
0.9
1
FREQUENCY (GHz)

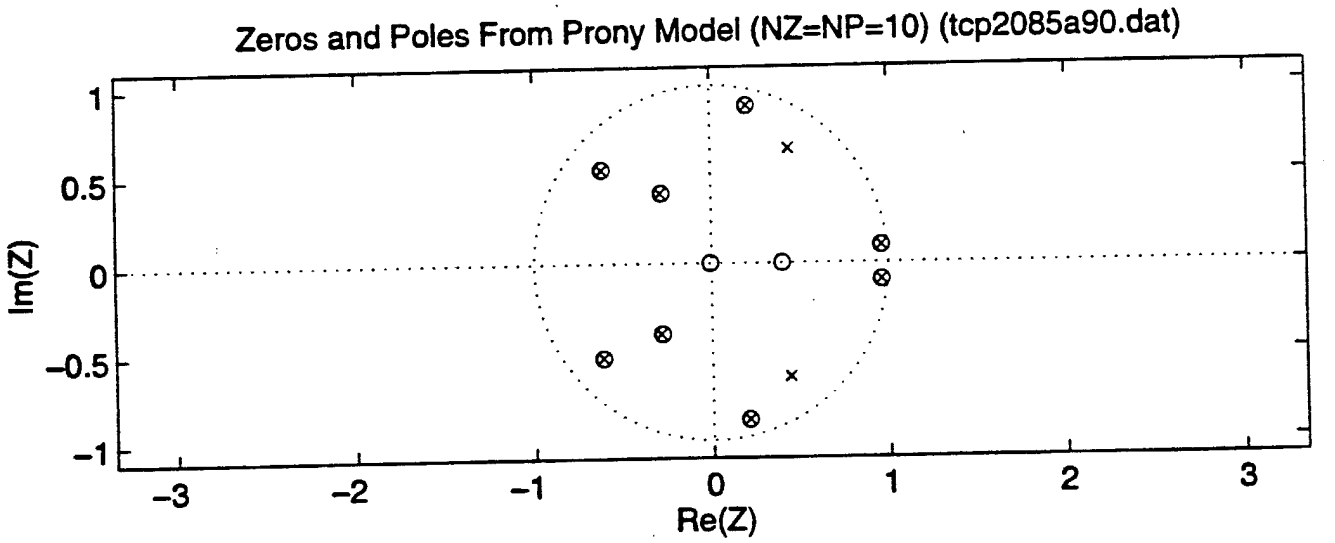
Zeros and Poles From Prony Model (NZ=NP=10) (tcp2085a90.dat)
Im(Z)
Re(Z)
1
0.5
0
−0.5
−1
−3
−2
−1
0
1
2
3

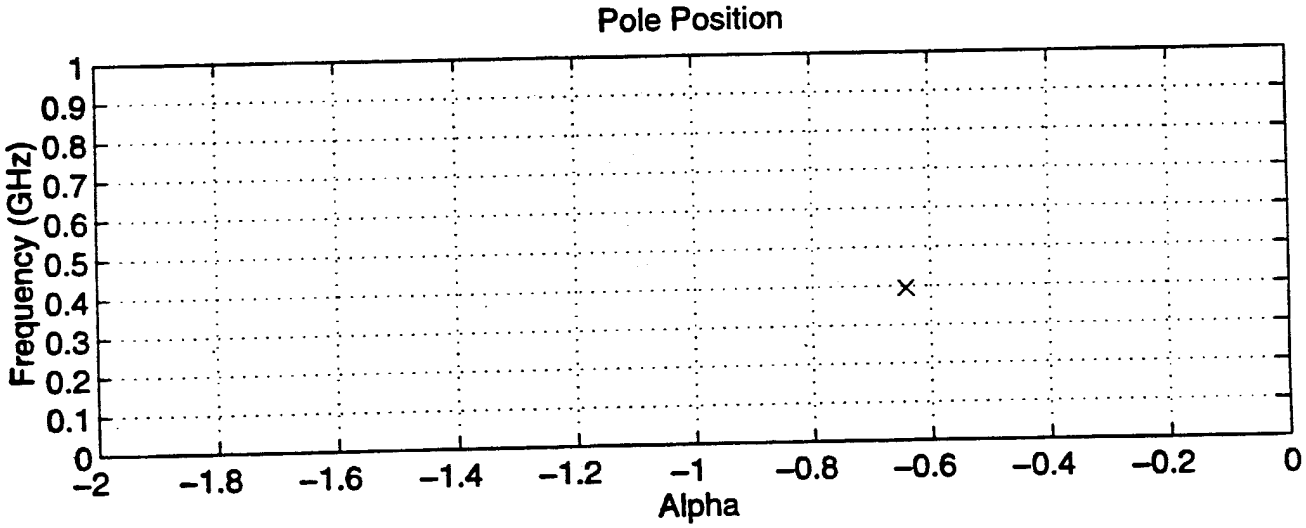
Pole Position
Frequency (GHz)
Alpha
1
0.9
0.8
0.7
0.6
0.5
0.4
0.3
0.2
0.1
0
−2
−1.8
−1.6
−1.4
−1.2
−1
−0.8
−0.6
−0.4
−0.2
0

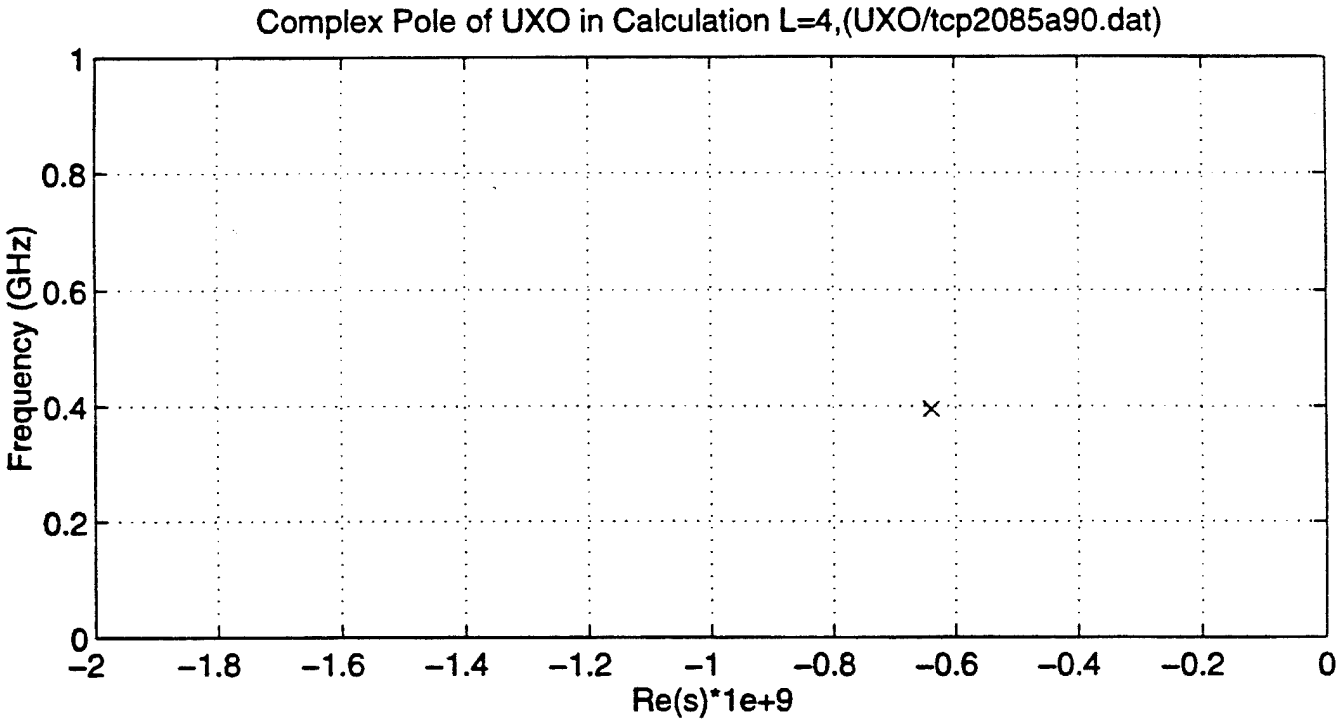
Complex Pole of UXO in Calculation L=4,(UXO/tcp2085a90.dat)
Frequency (GHz)
1
0.8
0.6
0.4
0.2
0
−2
−1.8
−1.6
−1.4
−1.2
−1
−0.8
−0.6
−0.4
−0.2
0
Re(s)*1e+9

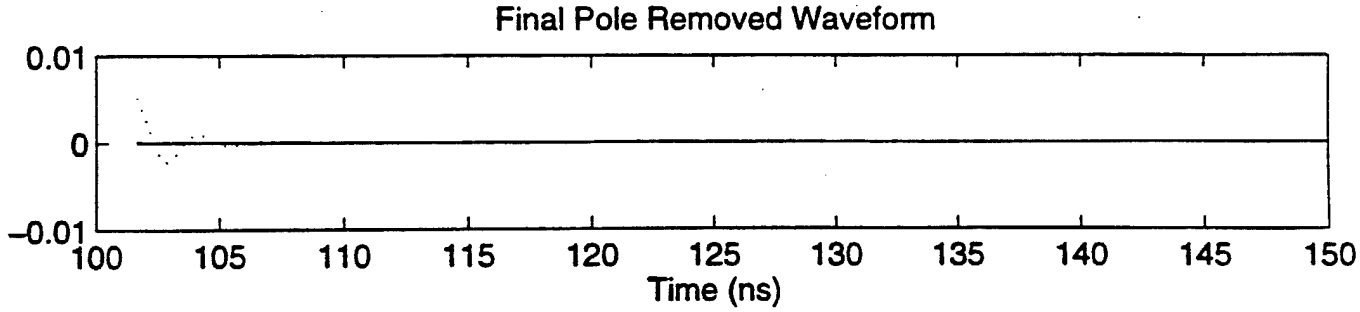
Final Pole Removed Waveform
0.01
0
−0.01
100
105
110
115
120
125
130
135
140
145
150
Time (ns)

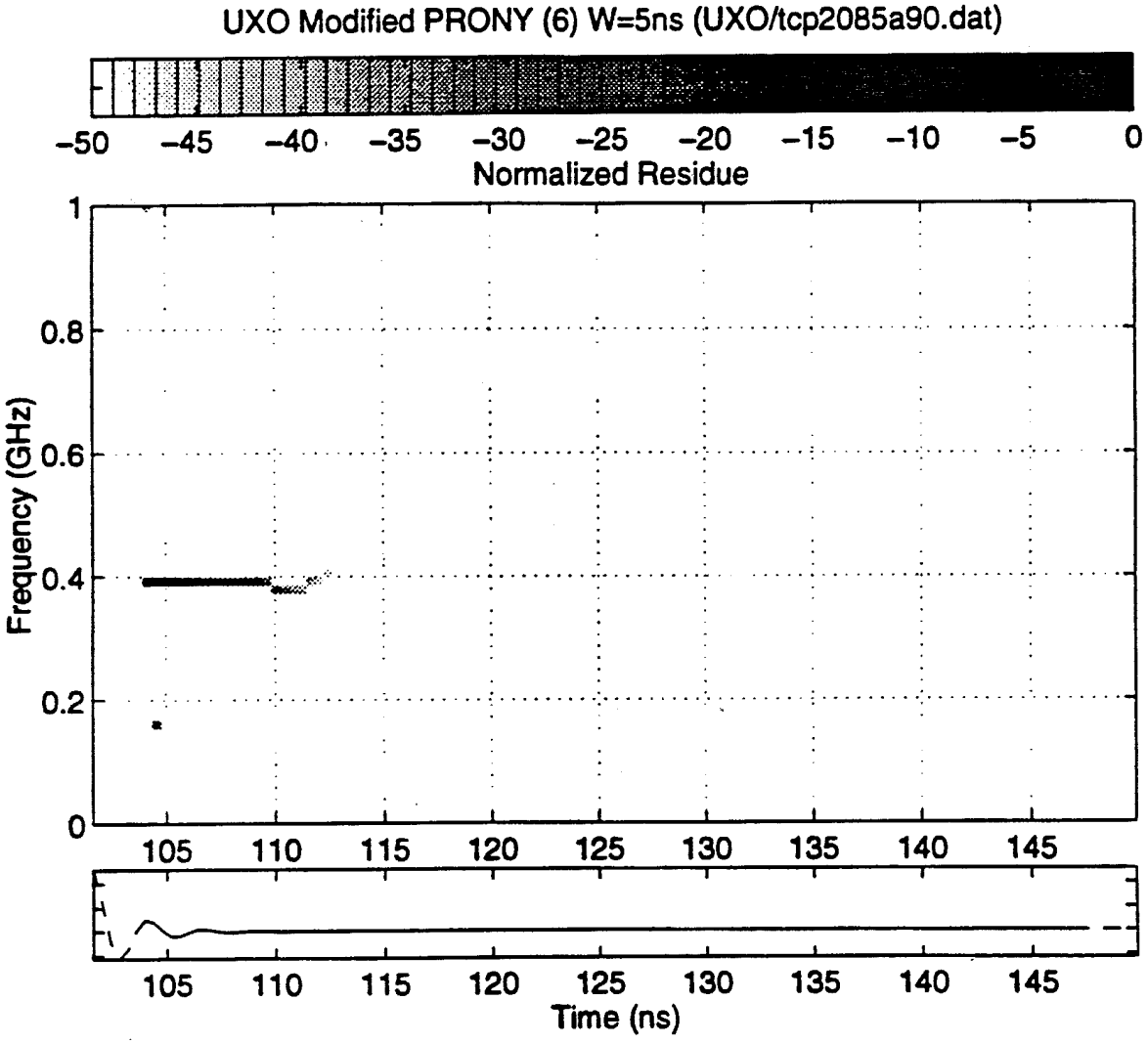
UXO Modified PRONY (6) W=5ns (UXO/tcp2085a90.dat)
−50 −45 −40 −35 −30 −25 −20 −15 −10 −5 0
Normalized Residue
Frequency (GHz)
1
0.8
0.6
0.4
0.2
0
105 110 115 120 125 130 135 140 145
105 110 115 120 125 130 135 140 145
Time (ns)

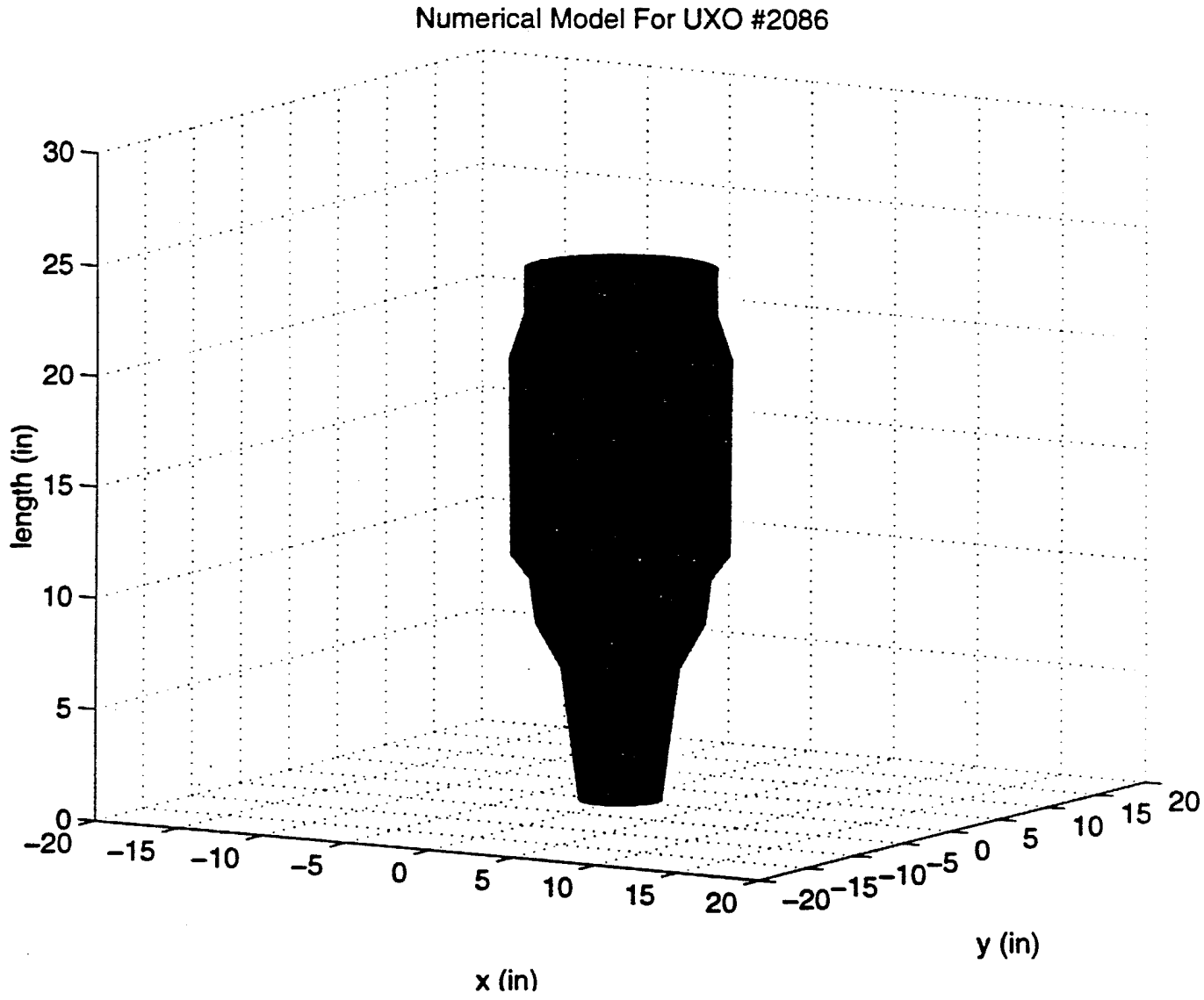
Numerical Model For UXO #2086
length (in)
30
25
20
15
10
5
0
−20
−15
−10
−5
0
5
10
15
20
x (in)
−20
−15
−10
−5
0
5
10
15
20
y (in)

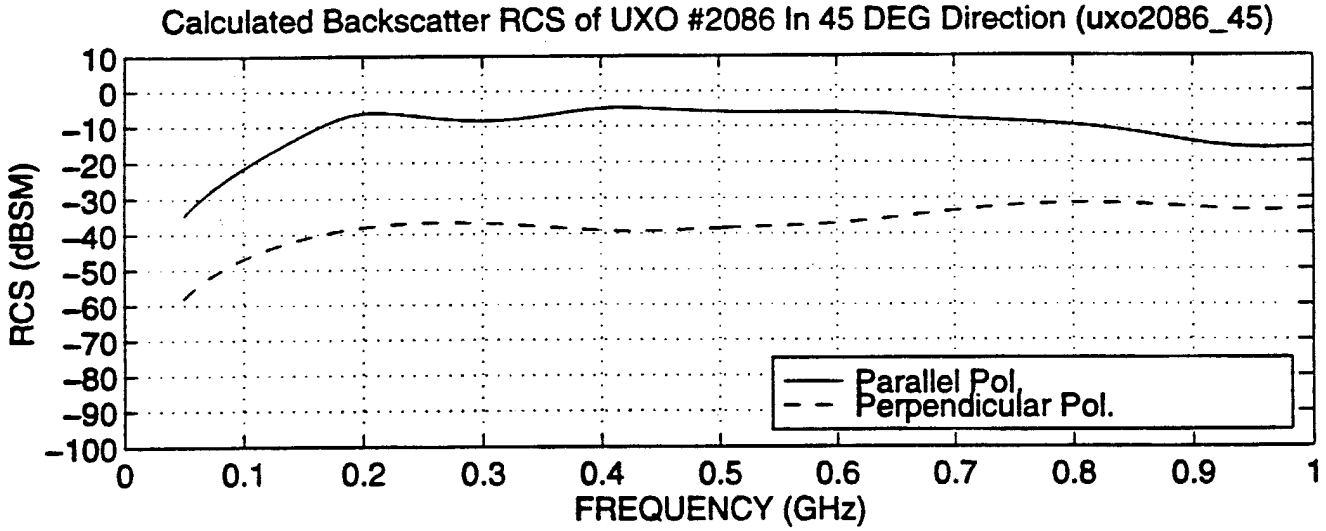
Calculated Backscatter RCS of UXO #2086 In 45 DEG Direction (uxo2086_45)
RCS (dBSM)
10
0
-10
-20
-30
-40
-50
-60
-70
-80
-90
-100
0
0.1
0.2
0.3
0.4
0.5
0.6
0.7
0.8
0.9
1
FREQUENCY (GHz)
Parallel Pol.
Perpendicular Pol.

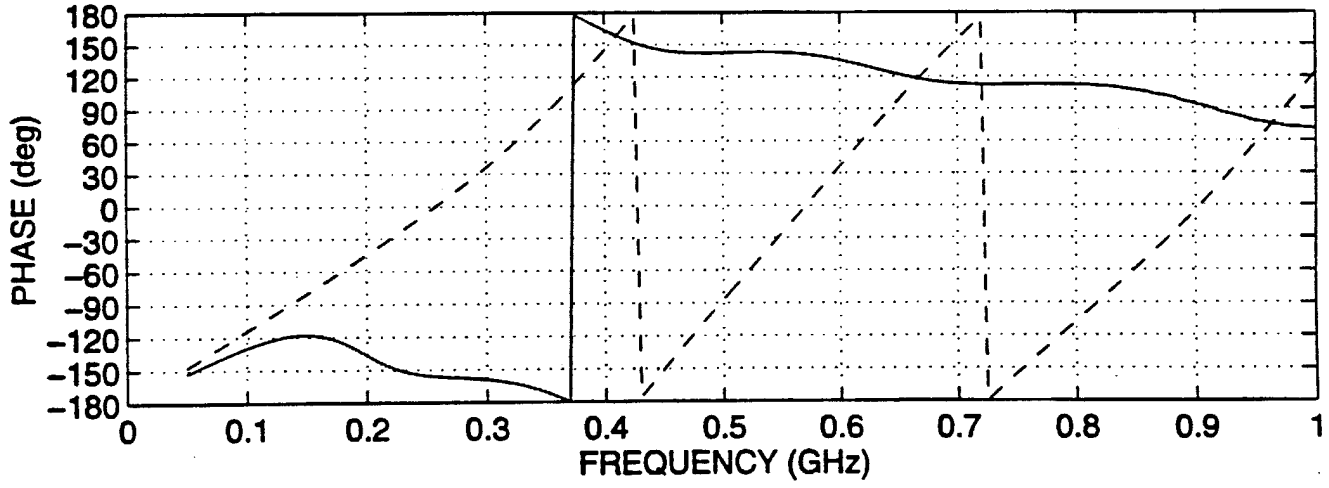
PHASE (deg)
180
150
120
90
60
30
0
-30
-60
-90
-120
-150
-180
0
0.1
0.2
0.3
0.4
0.5
0.6
0.7
0.8
0.9
1
FREQUENCY (GHz)

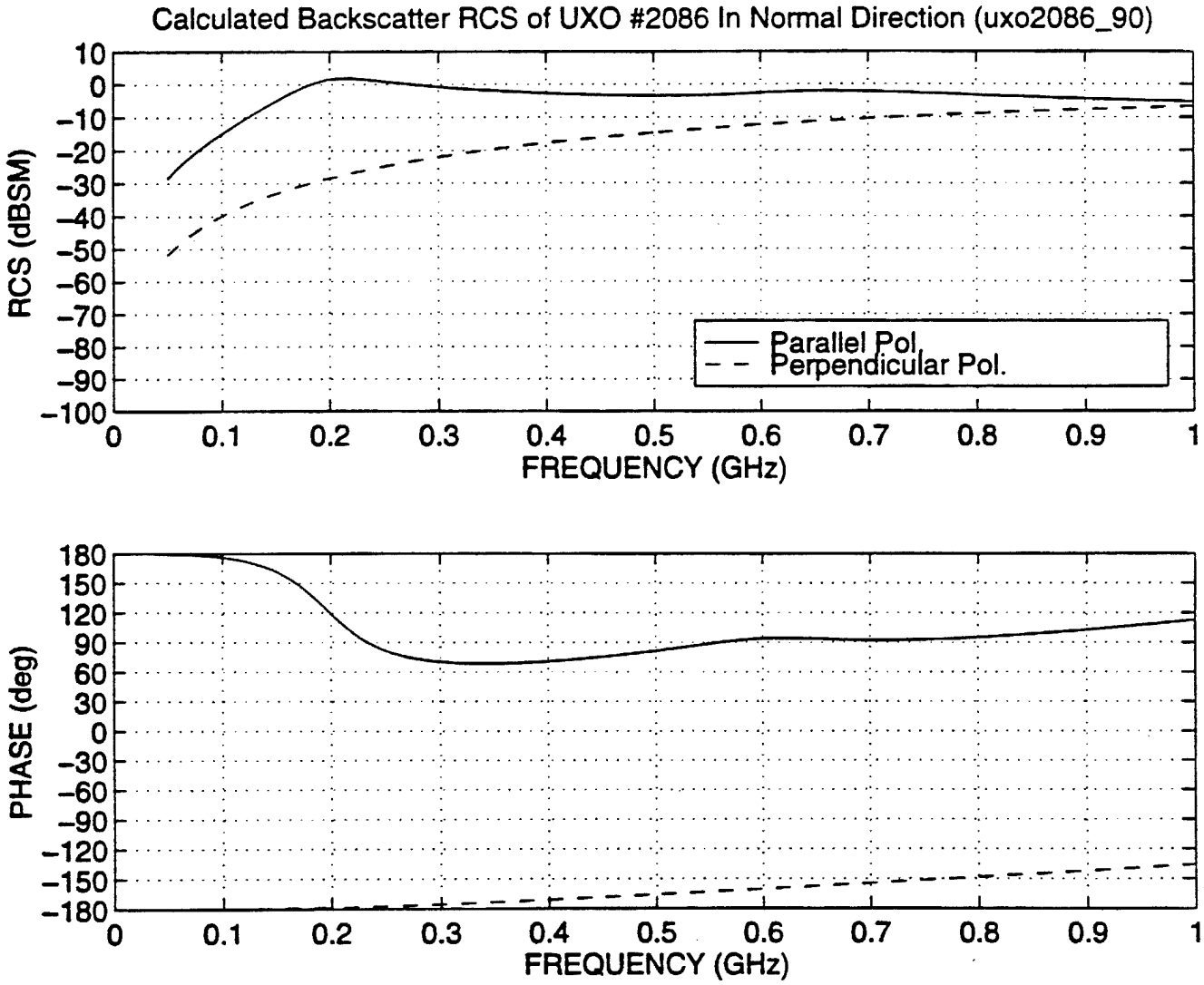
Calculated Backscatter RCS of UXO #2086 In Normal Direction (uxo2086_90)
RCS (dBSM)
10
0
-10
-20
-30
-40
-50
-60
-70
-80
-90
-100
0
0.1
0.2
0.3
0.4
0.5
0.6
0.7
0.8
0.9
1
FREQUENCY (GHz)
Parallel Pol.
Perpendicular Pol.
PHASE (deg)
180
150
120
90
60
30
0
-30
-60
-90
-120
-150
-180
0
0.1
0.2
0.3
0.4
0.5
0.6
0.7
0.8
0.9
1
FREQUENCY (GHz)

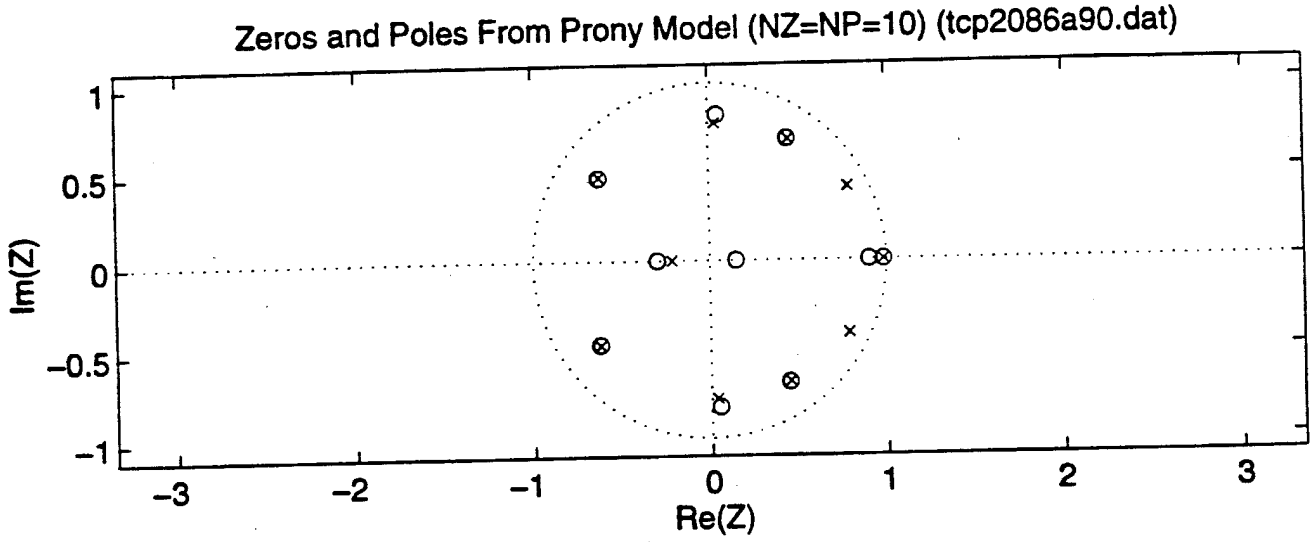
Zeros and Poles From Prony Model (NZ=NP=10) (tcp2086a90.dat)
Im(Z)
Re(Z)
1
0.5
0
−0.5
−1
−3
−2
−1
0
1
2
3

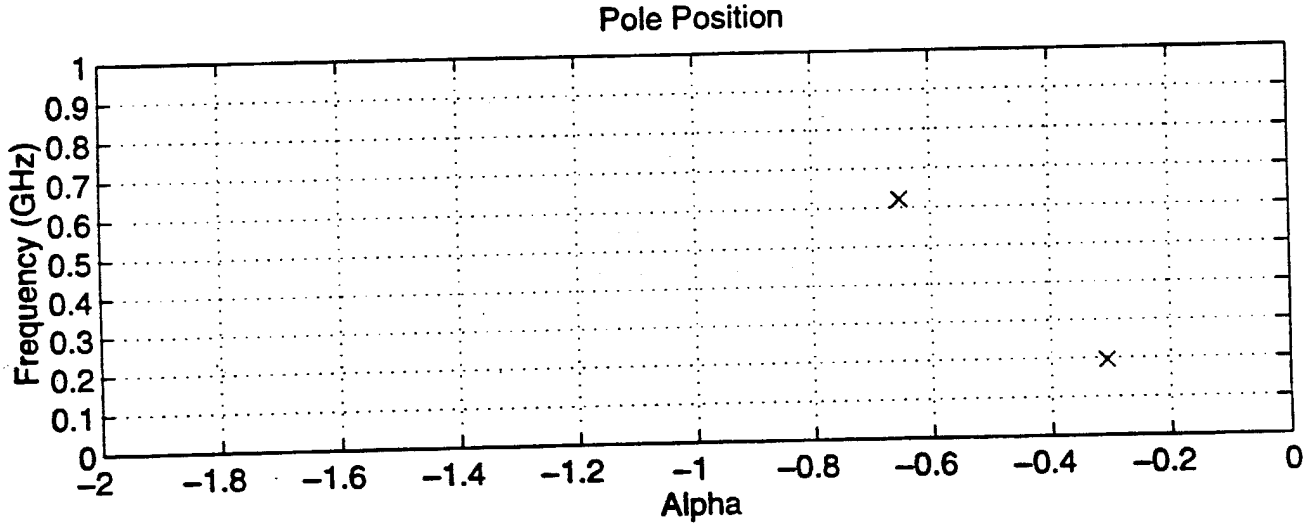
Pole Position
Frequency (GHz)
Alpha
1
0.9
0.8
0.7
0.6
0.5
0.4
0.3
0.2
0.1
0
−2
−1.8
−1.6
−1.4
−1.2
−1
−0.8
−0.6
−0.4
−0.2
0

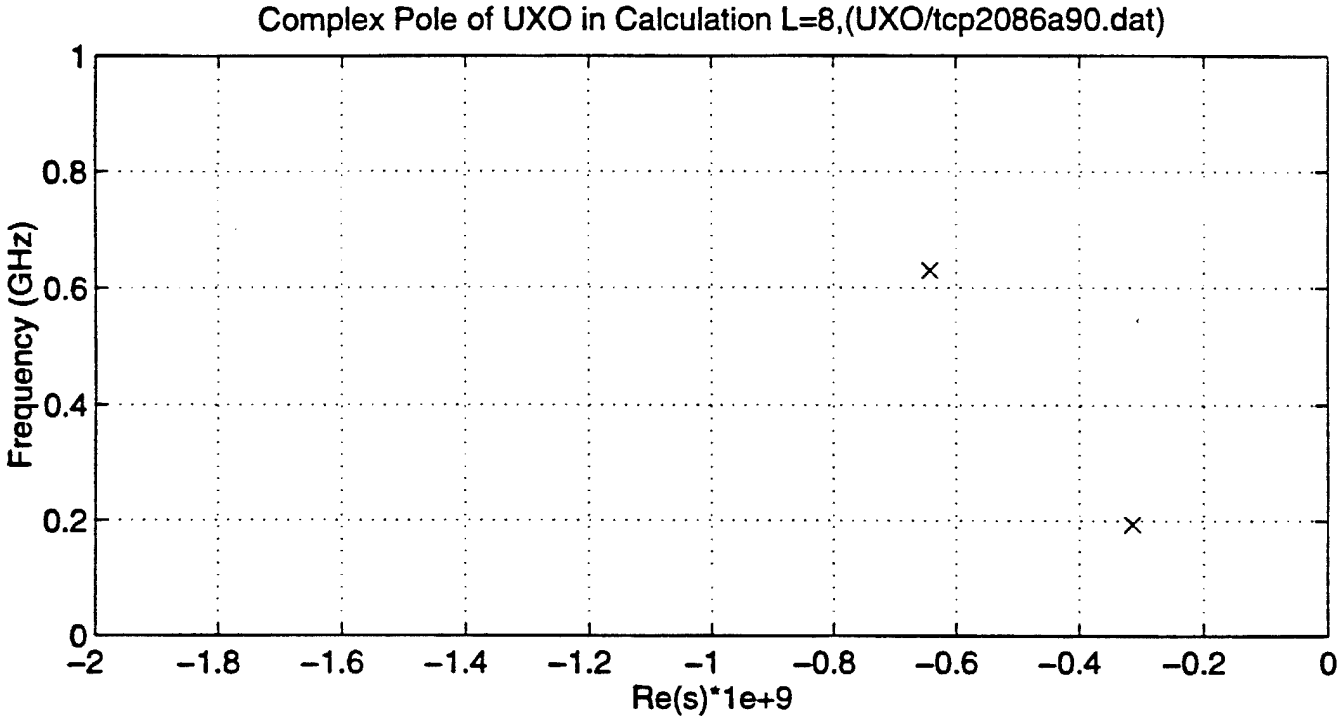
Complex Pole of UXO in Calculation L=8,(UXO/tcp2086a90.dat)
Frequency (GHz)
1
0.8
0.6
0.4
0.2
0
−2
−1.8
−1.6
−1.4
−1.2
−1
−0.8
−0.6
−0.4
−0.2
0
Re(s)*1e+9

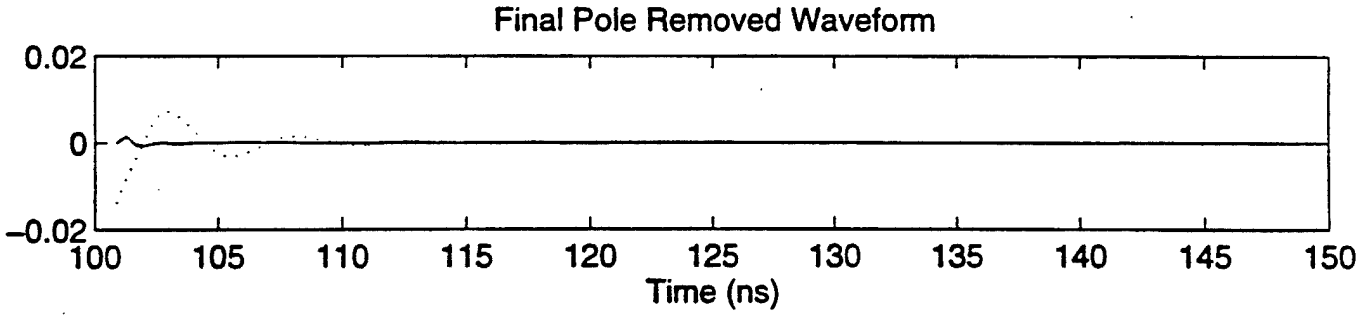
Final Pole Removed Waveform
0.02
0
−0.02
100
105
110
115
120
125
130
135
140
145
150
Time (ns)

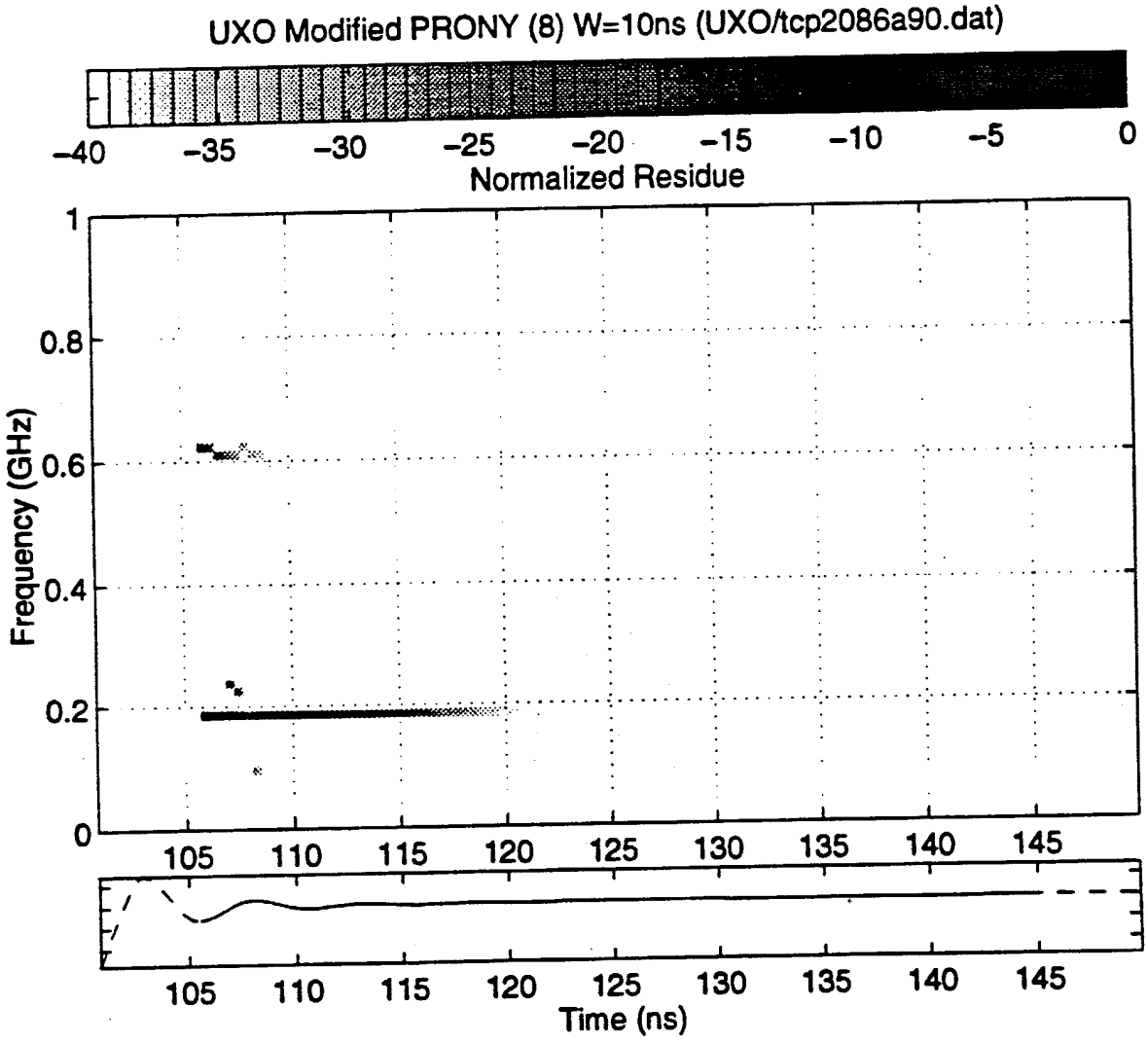
UXO Modified PRONY (8) W=10ns (UXO/tcp2086a90.dat)
−40
−35
−30
−25
−20
−15
−10
−5
0
Normalized Residue
Frequency (GHz)
1
0.8
0.6
0.4
0.2
0
105
110
115
120
125
130
135
140
145
Time (ns)

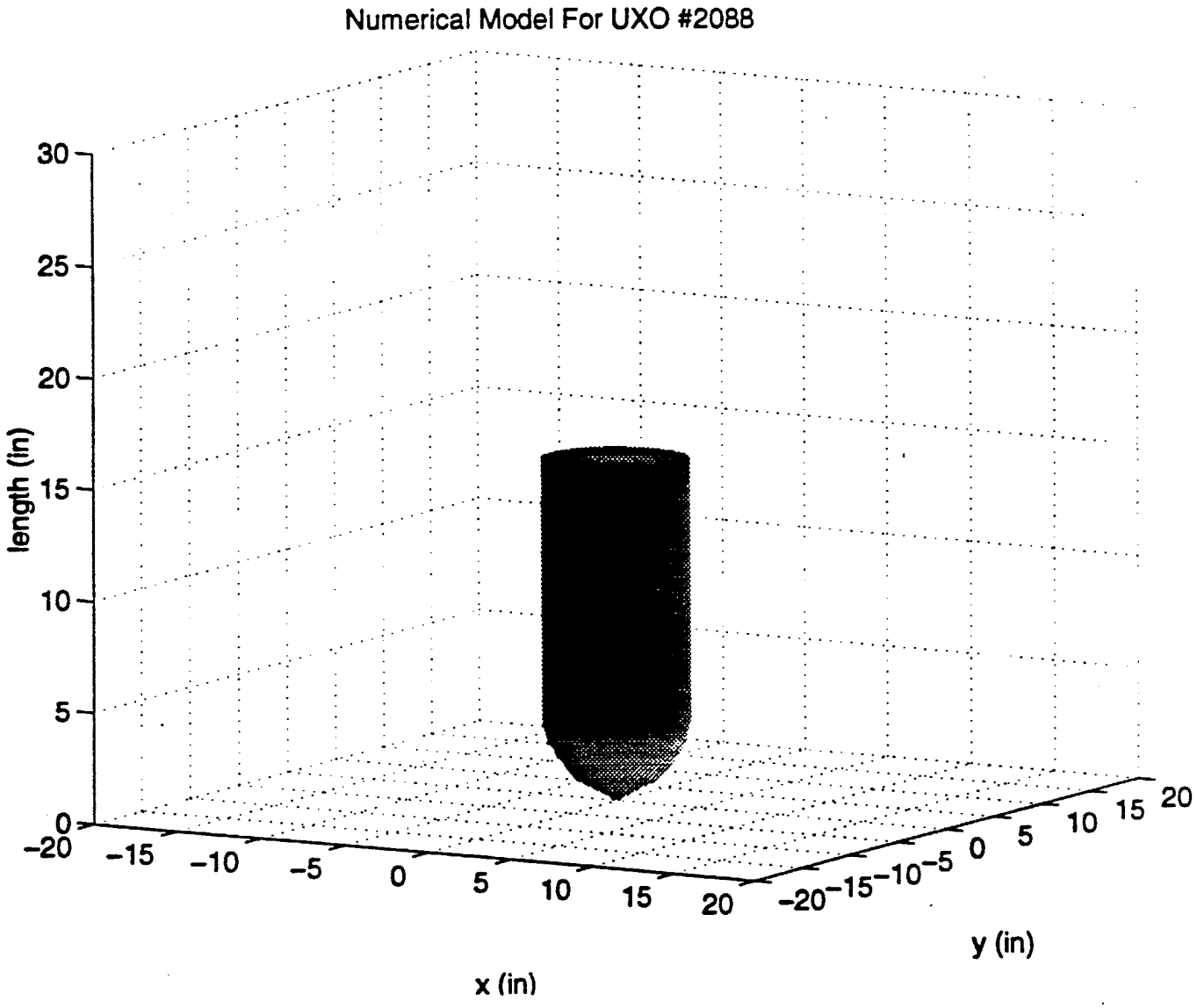
Numerical Model For UXO #2088
length (in)
30
25
20
15
10
5
0
-20
-15
-10
-5
0
5
10
15
20
x (in)
-20
-15
-10
-5
0
5
10
15
20
y (in)

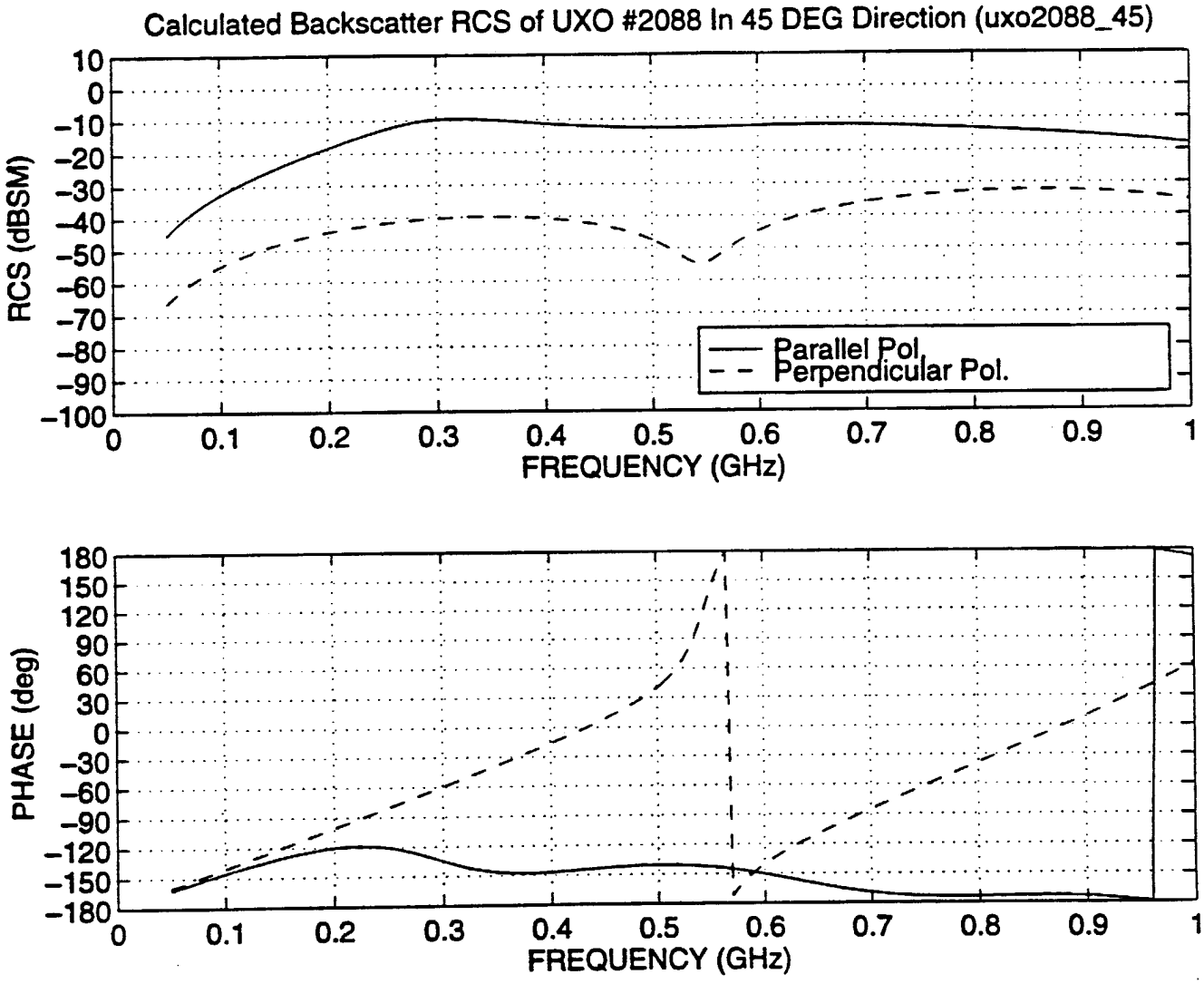
Calculated Backscatter RCS of UXO #2088 In 45 DEG Direction (uxo2088_45)
RCS (dBSM)
10
0
-10
-20
-30
-40
-50
-60
-70
-80
-90
-100
0
0.1
0.2
0.3
0.4
0.5
0.6
0.7
0.8
0.9
1
FREQUENCY (GHz)
Parallel Pol.
Perpendicular Pol.
PHASE (deg)
180
150
120
90
60
30
0
-30
-60
-90
-120
-150
-180
0
0.1
0.2
0.3
0.4
0.5
0.6
0.7
0.8
0.9
1
FREQUENCY (GHz)

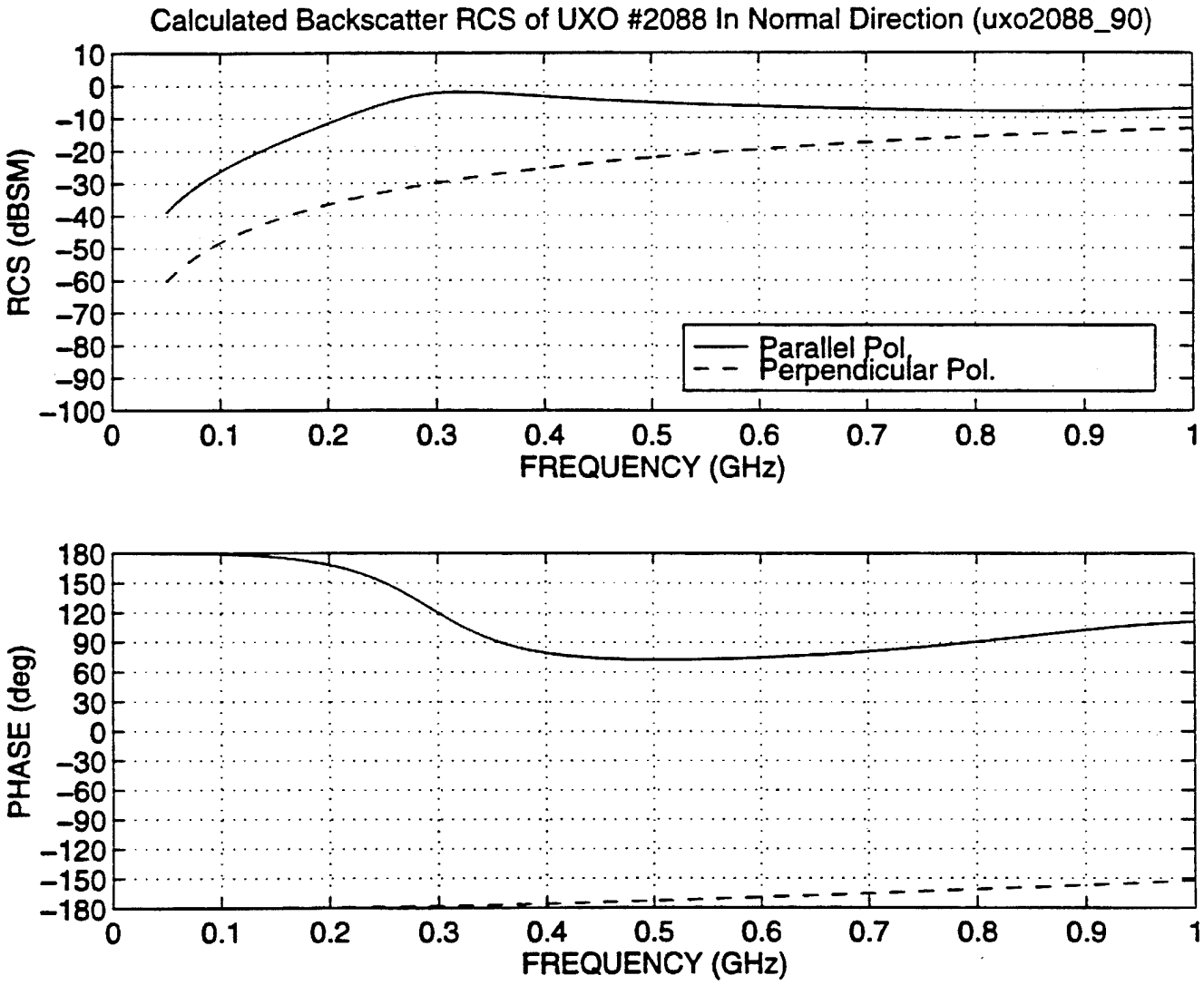
Calculated Backscatter RCS of UXO #2088 In Normal Direction (uxo2088_90)
RCS (dBSM)
10
0
-10
-20
-30
-40
-50
-60
-70
-80
-90
-100
0
0.1
0.2
0.3
0.4
0.5
0.6
0.7
0.8
0.9
1
FREQUENCY (GHz)
Parallel Pol.
Perpendicular Pol.
PHASE (deg)
180
150
120
90
60
30
0
-30
-60
-90
-120
-150
-180
0
0.1
0.2
0.3
0.4
0.5
0.6
0.7
0.8
0.9
1
FREQUENCY (GHz)

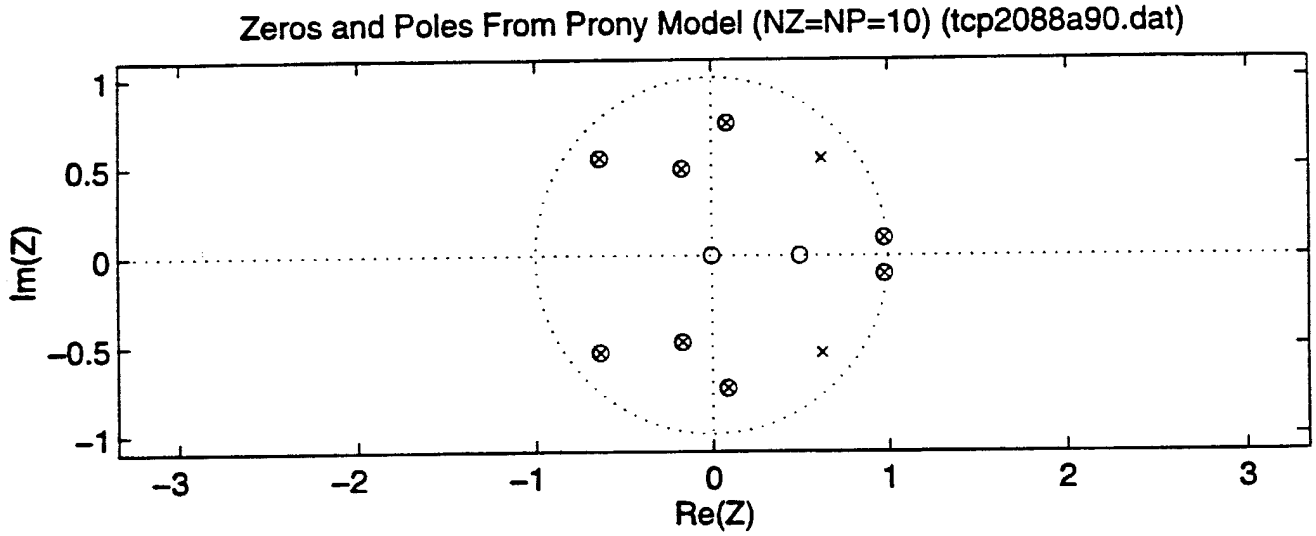
Zeros and Poles From Prony Model (NZ=NP=10) (tcp2088a90.dat)
Im(Z)
Re(Z)
1
0.5
0
−0.5
−1
−3
−2
−1
0
1
2
3

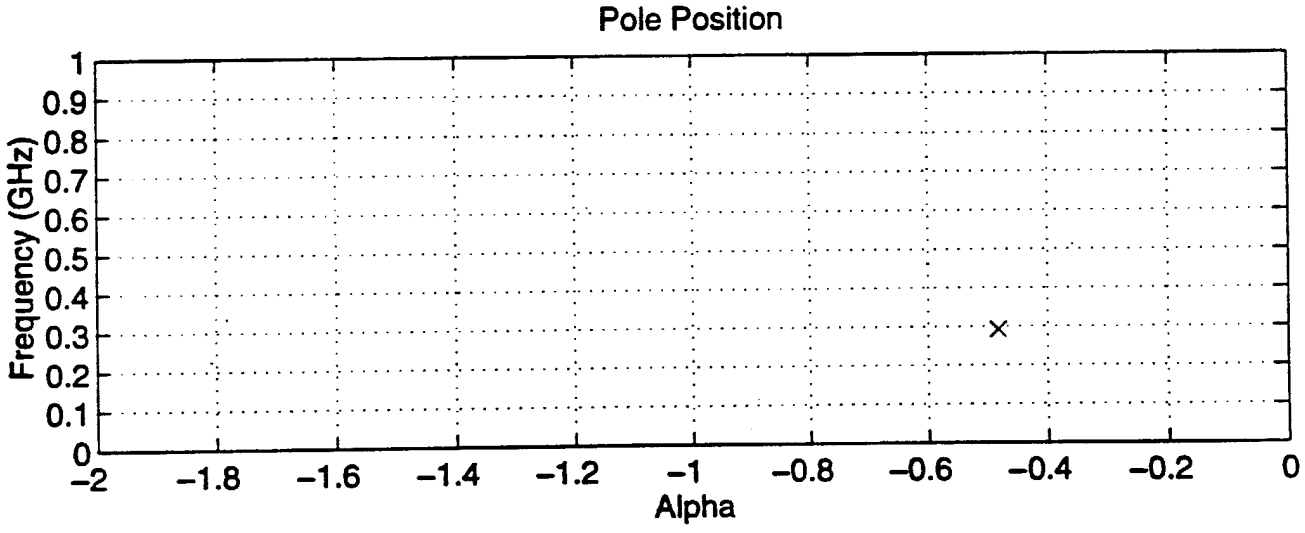
Pole Position
Frequency (GHz)
Alpha
1
0.9
0.8
0.7
0.6
0.5
0.4
0.3
0.2
0.1
0
−2
−1.8
−1.6
−1.4
−1.2
−1
−0.8
−0.6
−0.4
−0.2
0

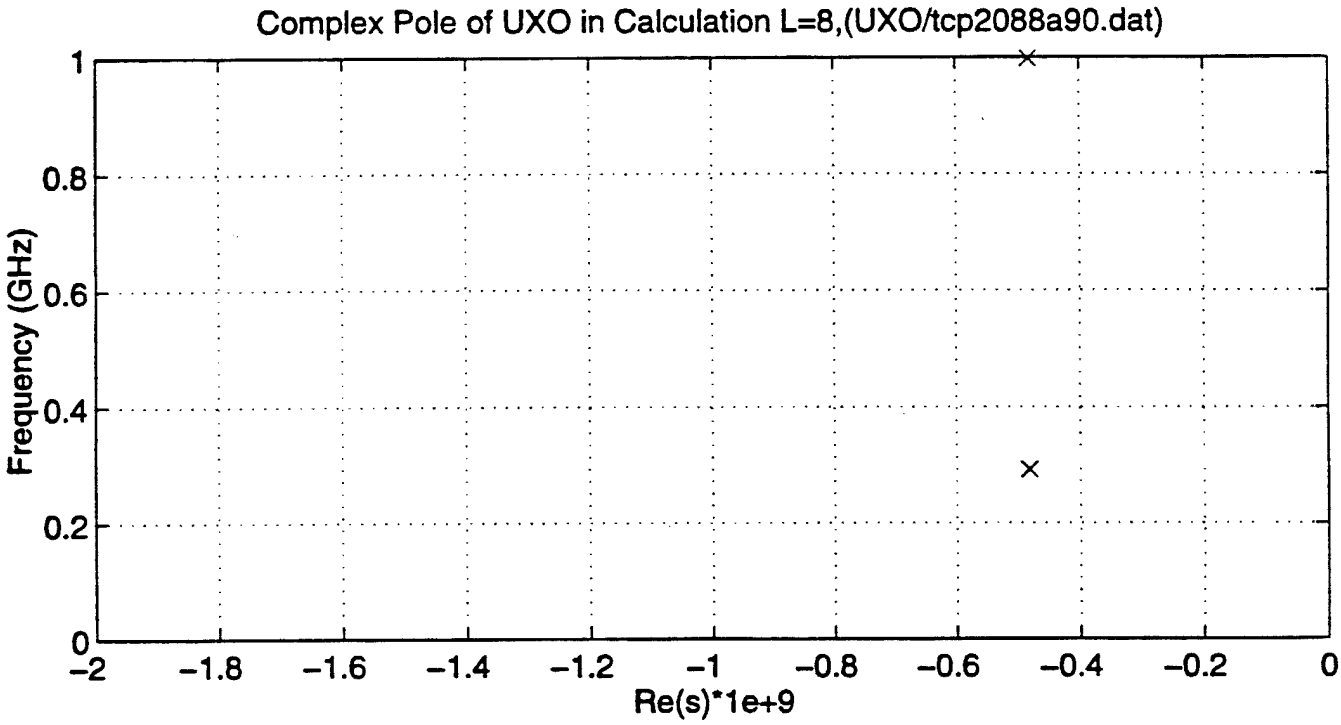
Complex Pole of UXO in Calculation L=8,(UXO/tcp2088a90.dat)
Frequency (GHz)
1
0.8
0.6
0.4
0.2
0
−2
−1.8
−1.6
−1.4
−1.2
−1
−0.8
−0.6
−0.4
−0.2
0
Re(s)*1e+9

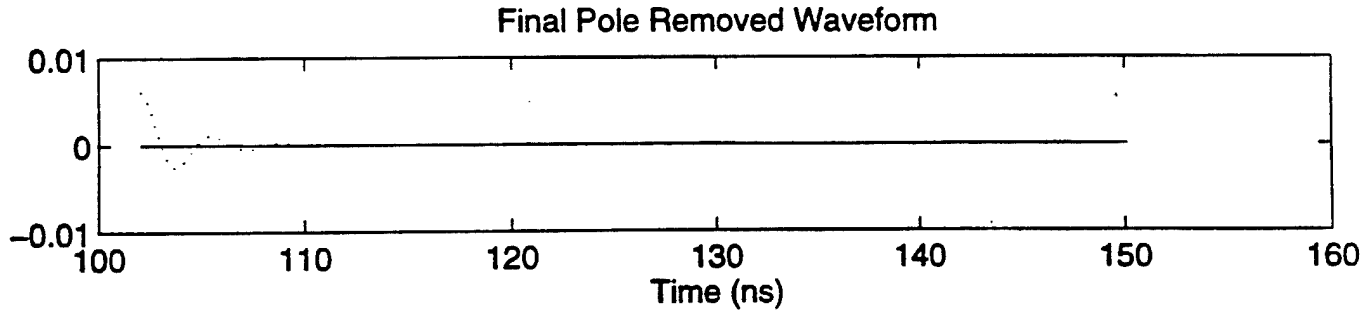
Final Pole Removed Waveform
0.01
0
−0.01
100
110
120
130
140
150
160
Time (ns)

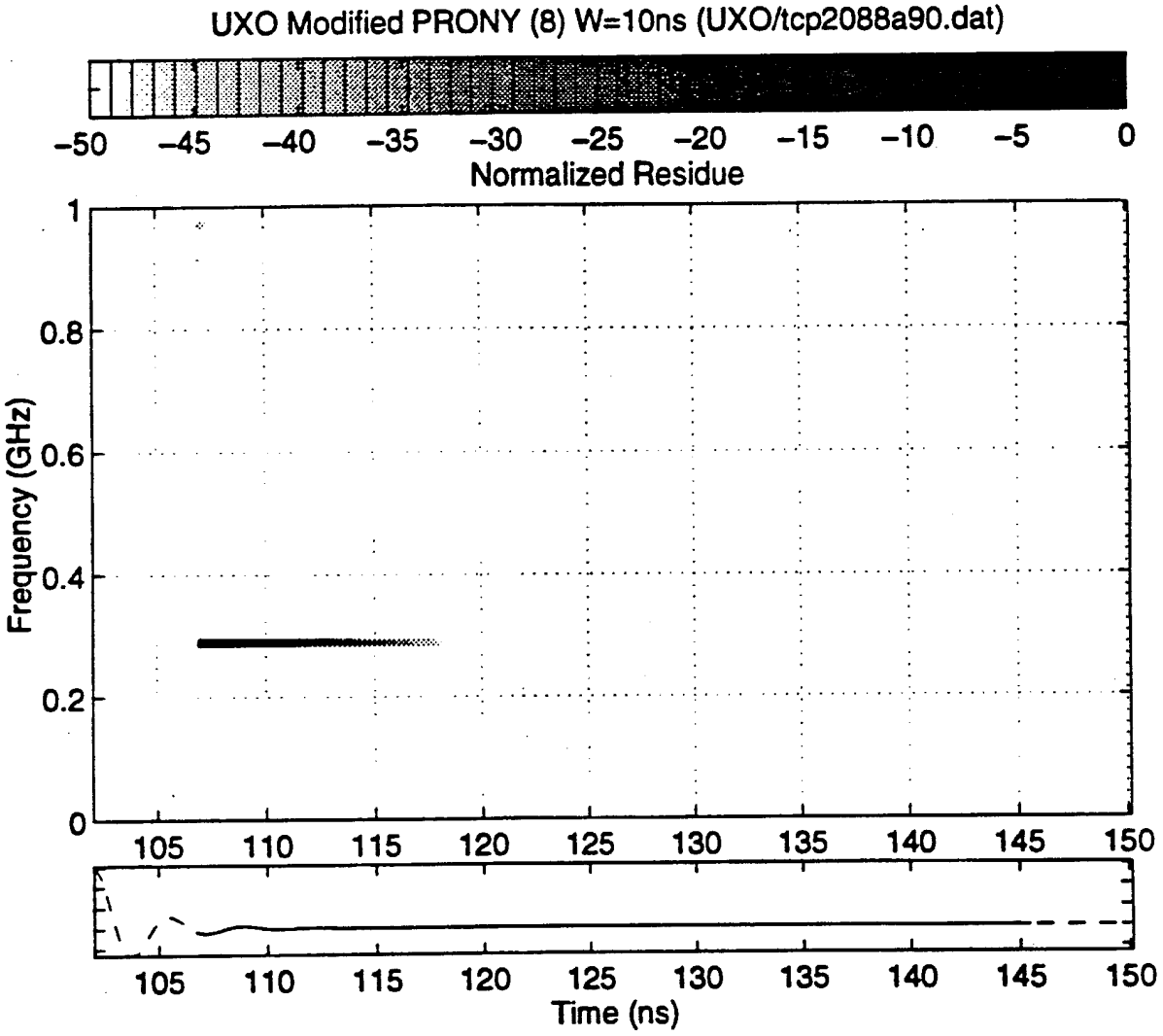
UXO Modified PRONY (8) W=10ns (UXO/tcp2088a90.dat)
−50 −45 −40 −35 −30 −25 −20 −15 −10 −5 0
Normalized Residue
Frequency (GHz)
1
0.8
0.6
0.4
0.2
0
105 110 115 120 125 130 135 140 145 150
105 110 115 120 125 130 135 140 145 150
Time (ns)

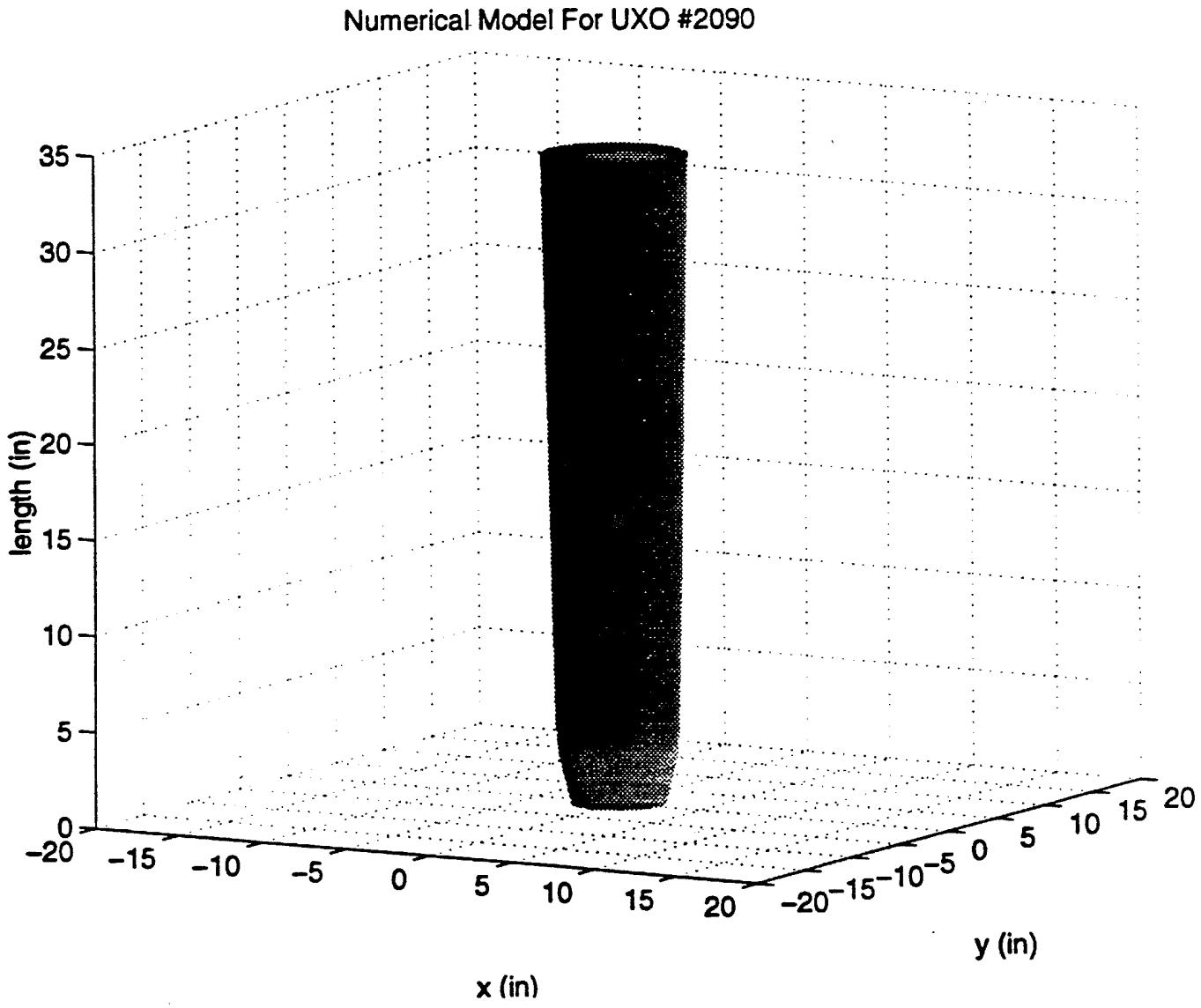
Numerical Model For UXO #2090
length (in)
35
30
25
20
15
10
5
0
-20
-15
-10
-5
0
5
10
15
20
x (in)
-20
-15
-10
-5
0
5
10
15
20
y (in)

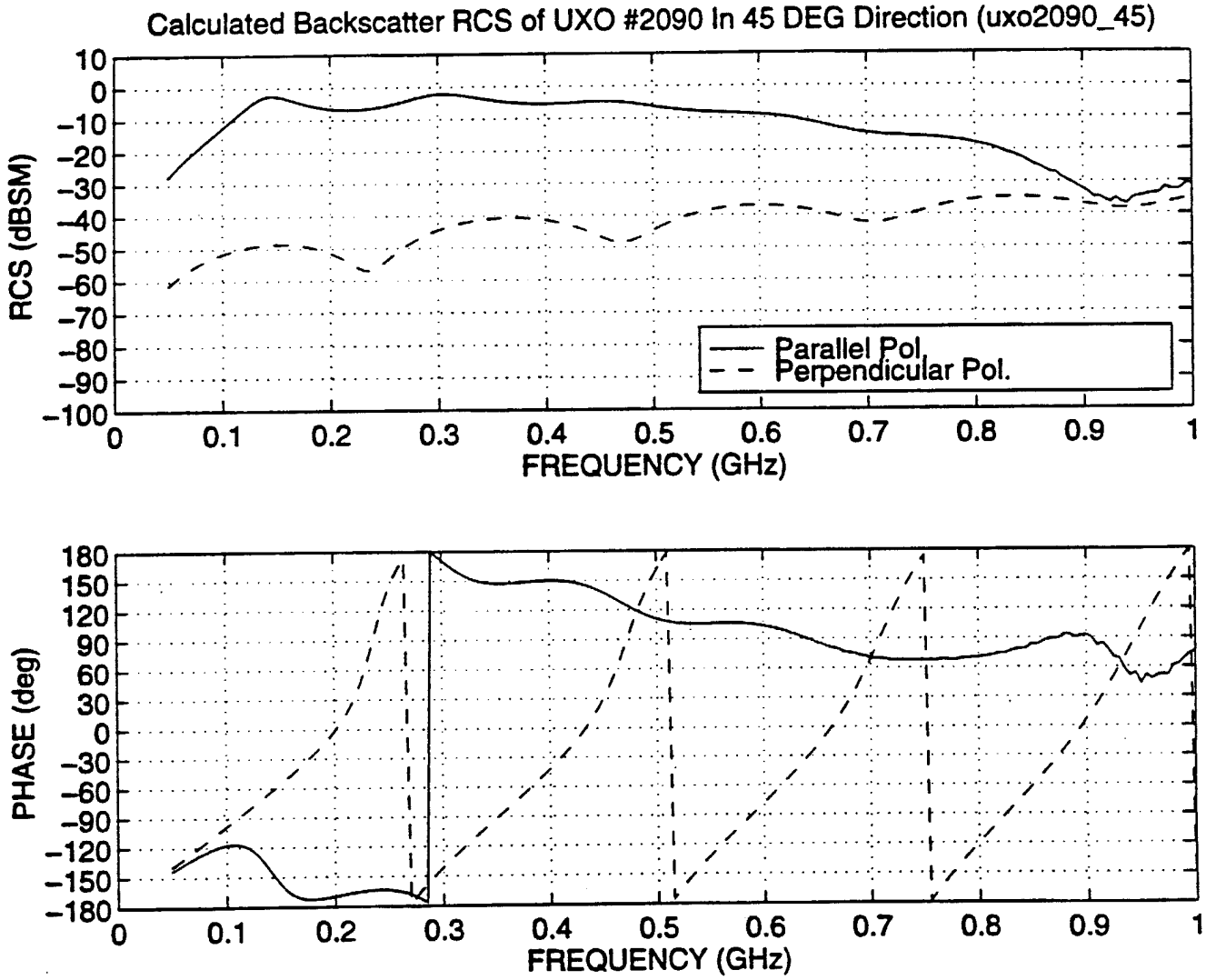
Calculated Backscatter RCS of UXO #2090 In 45 DEG Direction (uxo2090_45)
RCS (dBSM)
10
0
-10
-20
-30
-40
-50
-60
-70
-80
-90
-100
0
0.1
0.2
0.3
0.4
0.5
0.6
0.7
0.8
0.9
1
FREQUENCY (GHz)
Parallel Pol.
Perpendicular Pol.
PHASE (deg)
180
150
120
90
60
30
0
-30
-60
-90
-120
-150
-180
0
0.1
0.2
0.3
0.4
0.5
0.6
0.7
0.8
0.9
1
FREQUENCY (GHz)

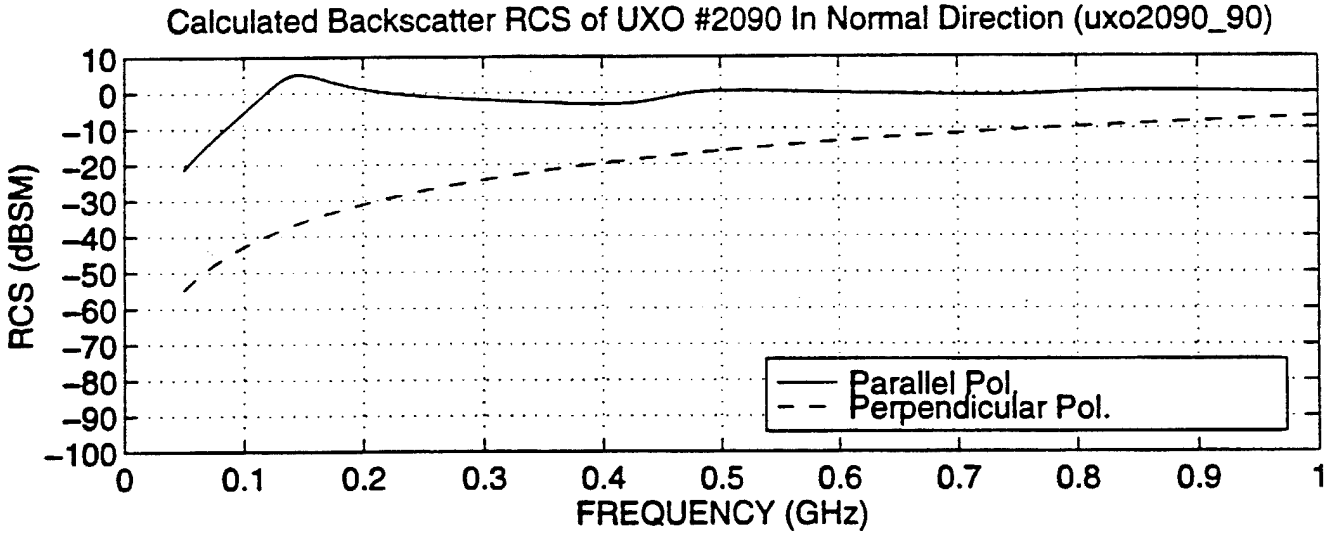
Calculated Backscatter RCS of UXO #2090 In Normal Direction (uxo2090_90)
RCS (dBSM)
10
0
-10
-20
-30
-40
-50
-60
-70
-80
-90
-100
0
0.1
0.2
0.3
0.4
0.5
0.6
0.7
0.8
0.9
1
FREQUENCY (GHz)
Parallel Pol.
Perpendicular Pol.

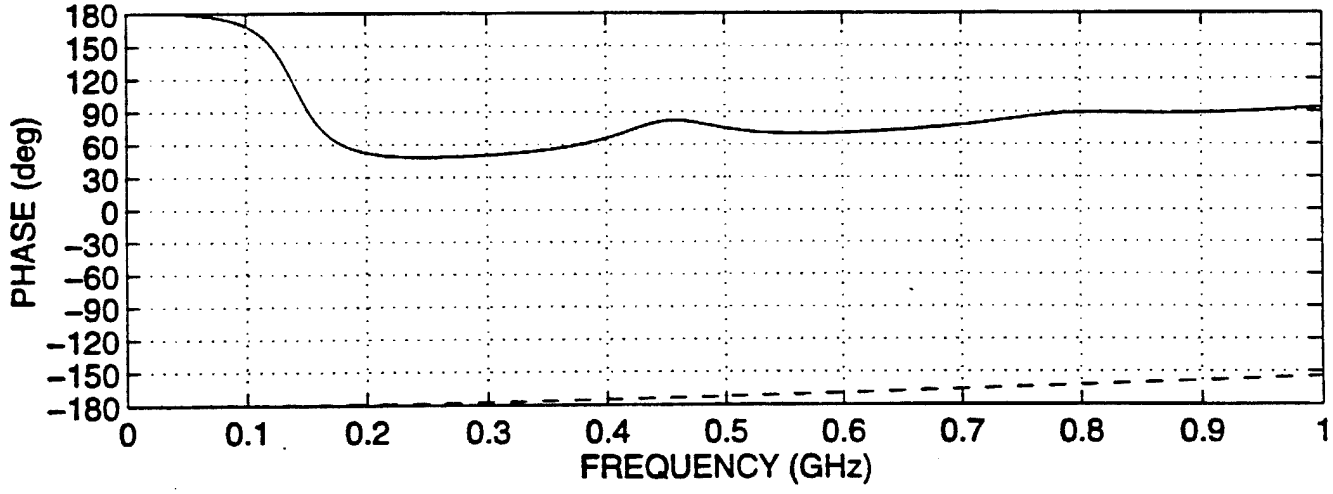
PHASE (deg)
180
150
120
90
60
30
0
-30
-60
-90
-120
-150
-180
0
0.1
0.2
0.3
0.4
0.5
0.6
0.7
0.8
0.9
1
FREQUENCY (GHz)

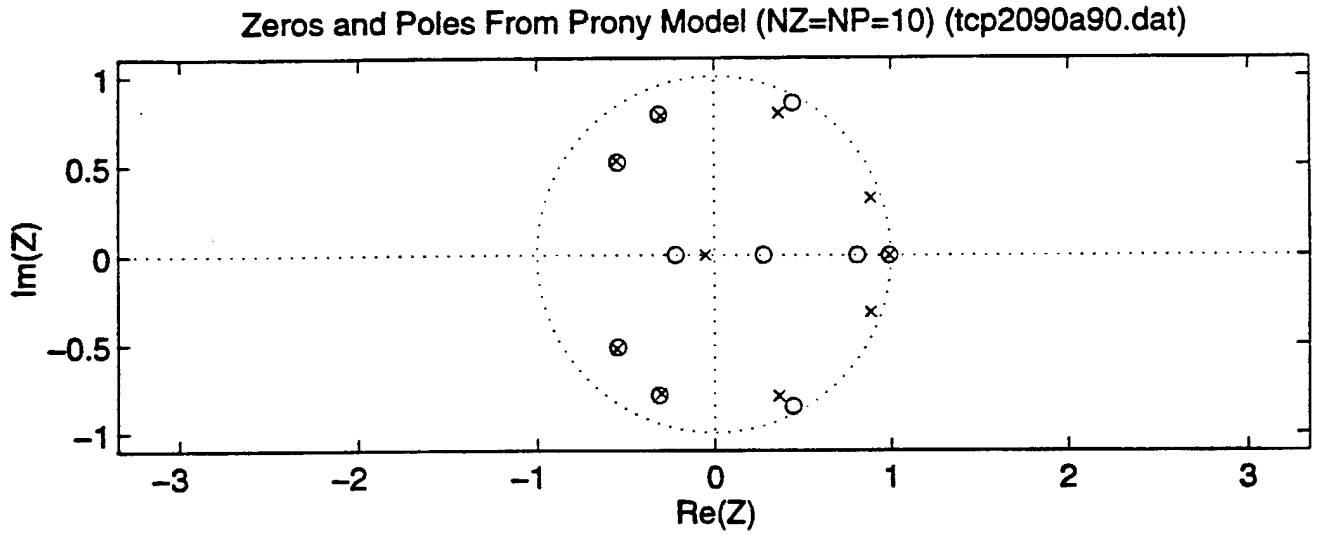
Zeros and Poles From Prony Model (NZ=NP=10) (tcp2090a90.dat)
Im(Z)
Re(Z)
1
0.5
0
−0.5
−1
−3
−2
−1
0
1
2
3

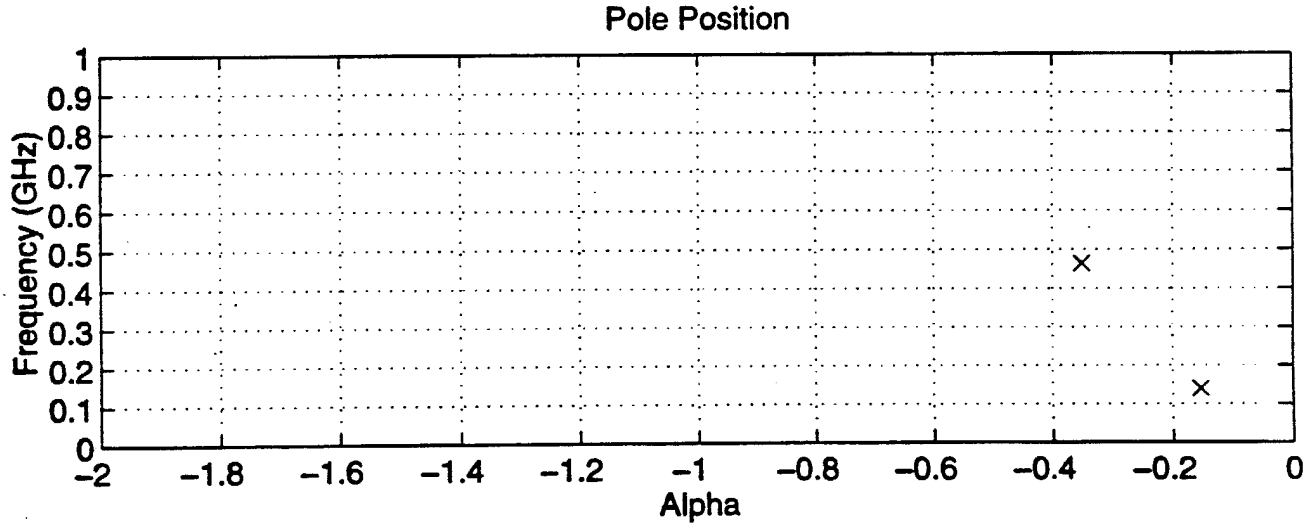
Pole Position
Frequency (GHz)
Alpha
1
0.9
0.8
0.7
0.6
0.5
0.4
0.3
0.2
0.1
0
−2
−1.8
−1.6
−1.4
−1.2
−1
−0.8
−0.6
−0.4
−0.2
0

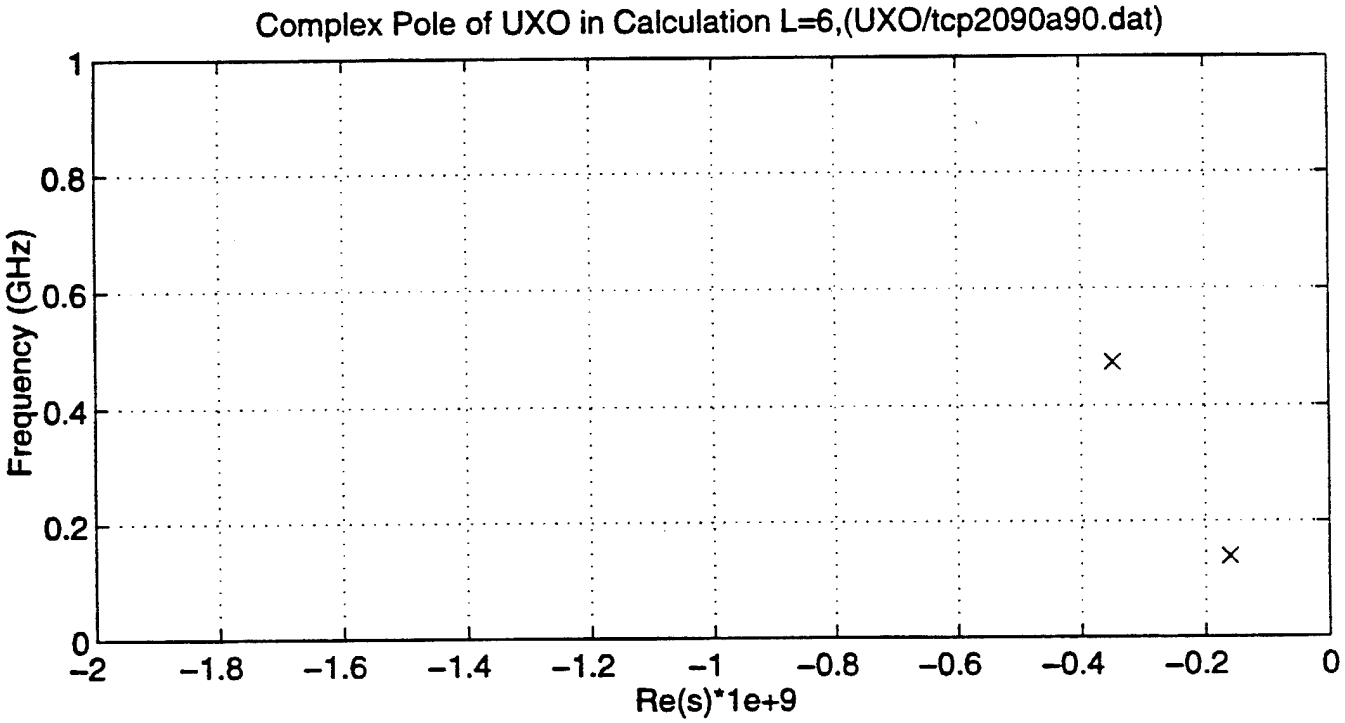
Complex Pole of UXO in Calculation L=6,(UXO/tcp2090a90.dat)
Frequency (GHz)
1
0.8
0.6
0.4
0.2
0
−2
−1.8
−1.6
−1.4
−1.2
−1
−0.8
−0.6
−0.4
−0.2
0
Re(s)*1e+9

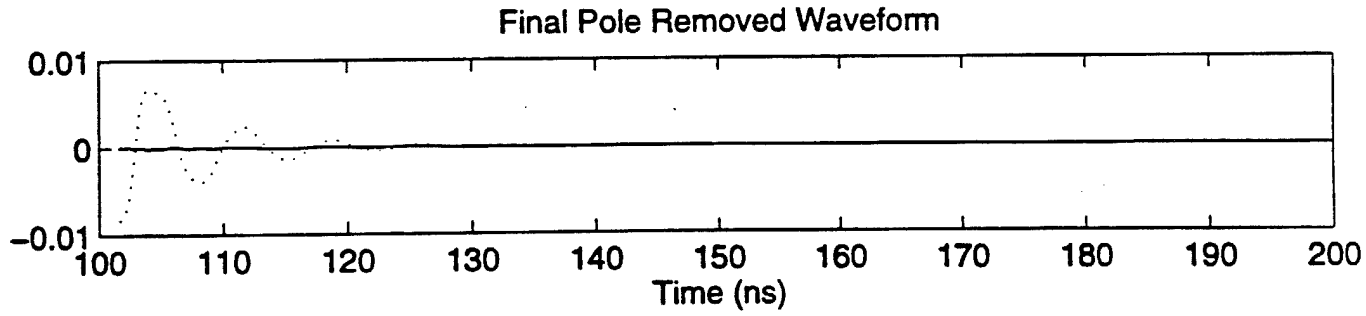
Final Pole Removed Waveform
0.01
0
−0.01
100
110
120
130
140
150
160
170
180
190
200
Time (ns)

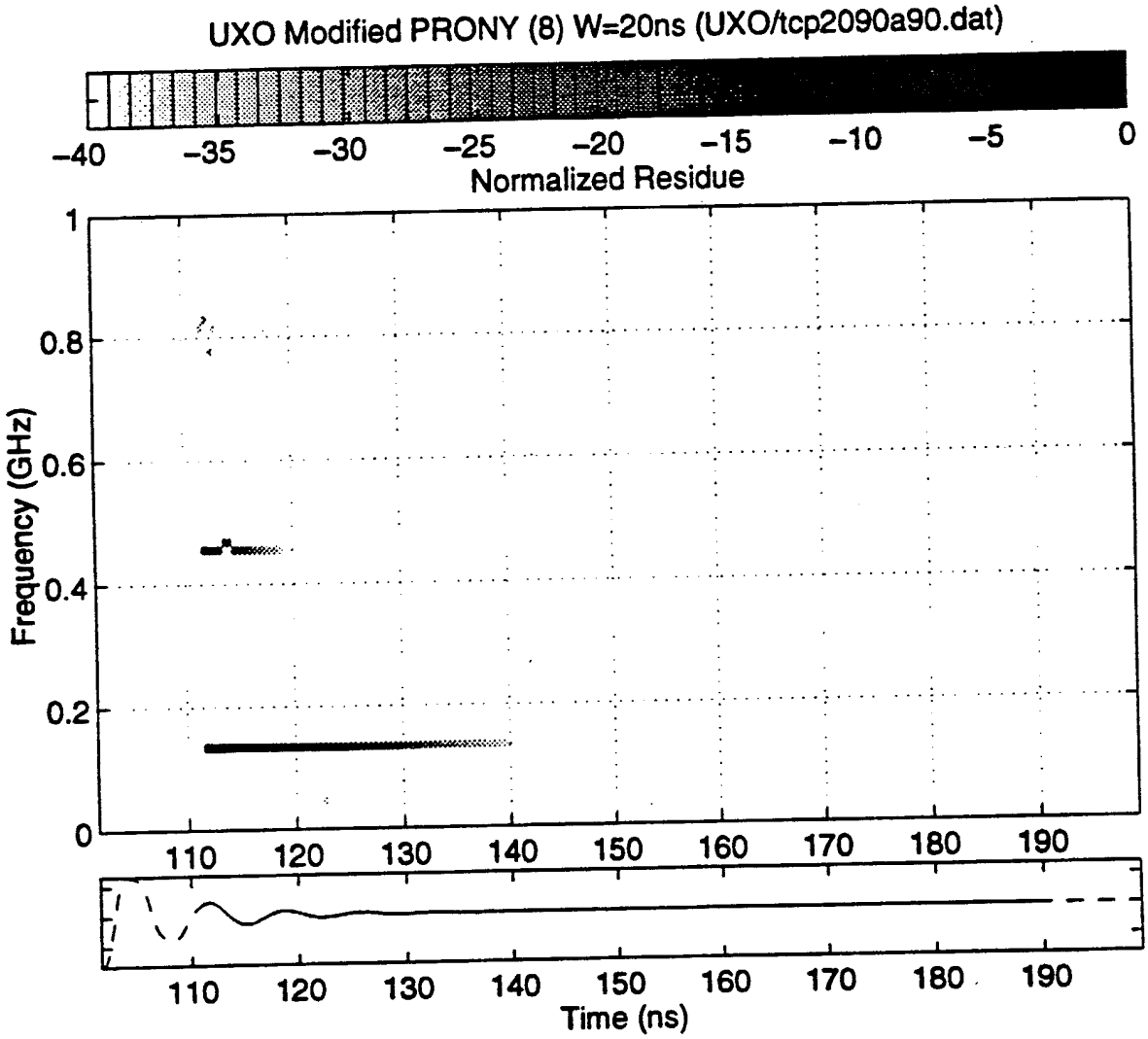
UXO Modified PRONY (8) W=20ns (UXO/tcp2090a90.dat)
−40
−35
−30
−25
−20
−15
−10
−5
0
Normalized Residue
Frequency (GHz)
1
0.8
0.6
0.4
0.2
0
110
120
130
140
150
160
170
180
190
Time (ns)

13.2 GPS Error Analysis

GPS Positioning and GPR Interference during the GPS/GPR airborne experiments at Jefferson Proving Ground.

Differential GPS data was collected for approximately 12 hours over two days (09/19/94, 09/20/94). The data was collected at a 1 Hz rate as the vehicle on which the GPR was mounted was moving at approximately 0.27 ft/sec. This data was processed using CFM GPS software to determine the vehicle's motion. The requirement is for ~0.07m positioning of the GPR in quasi real-time. The data discussed here is for the last 3.5 hour period on 09/20/94.

The GPS satellites transmit signals at two frequencies, L1 and L2. Very accurate (cm-level) differential positioning can be achieved with only a few epochs of data using double difference widelane observables (L1-L2) from the L1 and L2 carrier phase observations for epochs when four or more satellites are available. The GPS receiver tracks the L1 signal more easily than the lower power L2 signal. If only L1 data is available, it is more difficult and takes longer (5-15 minutes), to determine the carrier phase ambiguities required for very accurate differential processing. If L1 and L2 data is available for at least four satellites, very accurate positioning can be achieved in quasi real-time, within a few epochs of data.

Figure 1 shows the motion of the satellites during the time of the experiment. The concentric circles represent the constant elevations, 0, 30, 60 and 90 degrees, and the azimuth is indicated circularly about the center of the graph. Only satellites with an elevation > 5 degrees are indicated on this graph as those with elevations < 5 degrees are excluded from the processing. The signals from low elevation satellites have relatively large errors as the signals travel larger distances through the troposphere and ionosphere. From Figure 1 it can be seen that, at any time during the experiment, 6-8 satellites have elevations > 30 degrees. This is sufficient in order to obtain high accuracy GPS results.

The quality of the GPS data collected during this experiment was unexpectedly poor. For a large number of the epochs throughout the duration of the experiment, the L2 data and, in many cases, even the L1 data, is missing. For many epochs, even though 6-8 satellites are available, less than four have L2 data and the accurate widelane processing cannot be performed. The data was processed on the basis of the L1 data, as described below.

Figures 2 and 3 show the variation in the PDOP during the time of the experiment. The PDOP relates to the geometry of the satellites and varies in a regular fashion as this geometry changes. Figure 2 shows the expected PDOP calculated from the satellite orbits. Figure 3 shows the PDOP calculated from the satellites used in the processing, i.e., those satellites for which L1 data is available. The spikes in Figure 3 occur when satellites are missing L1 data and the geometry of the satellites used in the processing has been altered. This PDOP can be compared with the output of the processing to determine the affect of missing L1 data.

Figures 4 through 12 show the results of processing using only the available L1 data for the 3.5 hour period at the end of the data collection on 09/20/94.

Figures 4, 5, 6 show the change in position (velocity) between consecutive epochs for the east, north and up directions. For epochs for which less than four satellites have L1 data, the velocity was not computed and 1e+20 substituted for velocity in the velocity data file. These missing velocities appear as pairs of clipped vertical lines in the plots. It can be seen that there are many epochs for which less than four satellites are available.

Comparing the velocities in Figures 4, 5, 6 with the PDOP in Figure 3, it can be seen that the velocity values are incorrect when there is a spike in the PDOP. So, low accuracy measurements of velocity are removed by rejecting velocities for which the PDOP is > 2.5. The velocity for these epochs and for the epochs with less than four satellites with L1 data are estimated by linear interpolation. The results of these are shown in Figures 7, 8, 9. In these plots, the velocity measurements are much less noisy.

The corresponding distances moved by the vehicle in the east, north and up directions, derived by integrating the velocities in the corresponding directions, were plotted in Figures 10, 11, 12. These show the general motion of the vehicle from its initial stationary position. The time at which the motion starts can be seen as the time at which the distance changes and at which the velocity in the north direction (Figure 8) changes.

The interruption of the L1 signal is caused by interference with the signal from the GPR. The GPS frequencies are L1 at 1575.42 MHz and L2 at 1227.6 MHz. The GPS signals are within +/- 10 MHz of the third harmonics of the GPR transmission. This interference is dependent only on the direction of the GPR signal in relation to the GPS signal and can interfere with signals from high elevation satellites, for which the GPS data should otherwise be of good quality. The GPR was transmitting in the East-West direction and, examining the GPS data from the receiver mounted with the GPR data, satellites 16 and 17 moving from West to East (see Figure 1) lose their L1 and L2 data more often than other satellites. A more detailed analysis of the GPR antenna pattern and its relation to the direction of the satellites which have been interfered with, will provide additional insight into the GPS/GPR interference.

The plots in Figures 7 through 12 show that an average velocity and corresponding distance can be determined despite the noise in the data. This is not adequate to provide high accuracy results. In order to achieve high accuracy positioning, the GPR should be equipped with filters to eliminate the interfering frequencies.

Date: 1994/ 9/20
Location:
Lat: 38:52:46.30 N Lon: 85:22:33.00 W

Time Zone: Greenwich Std Time
Local Time - GMT = -0.00 Mask: 05(deg)

>>> Satelite Sky Plot <<<

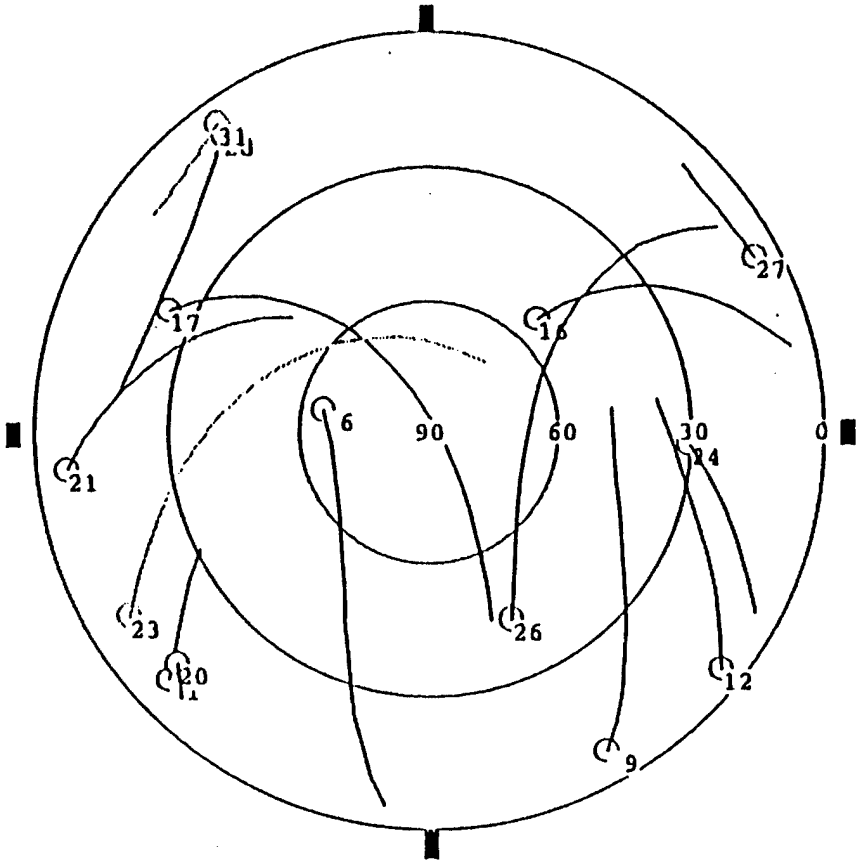

Figure 1 GPS satellite trajectories

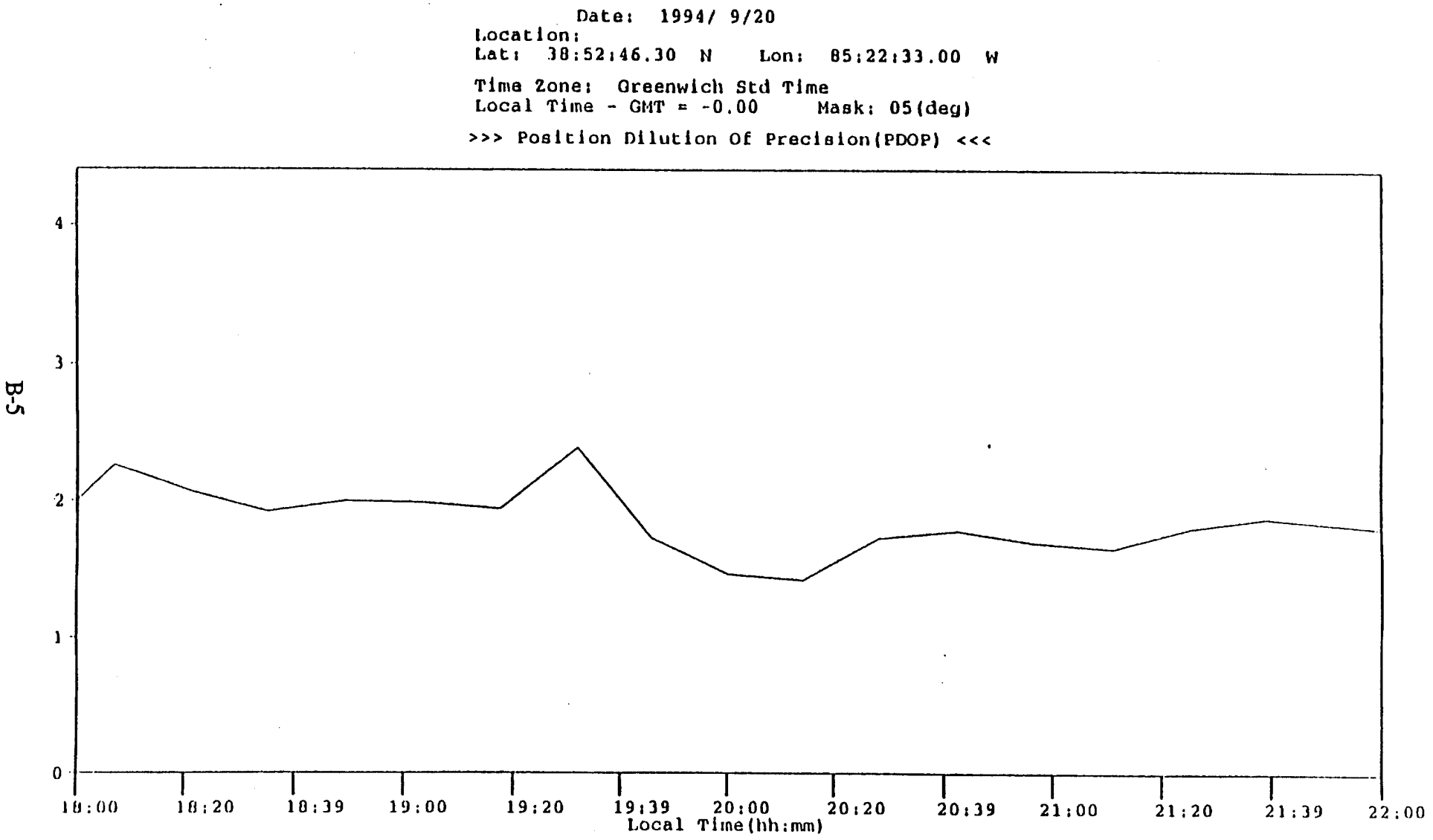

Figure 2 PDOP for GPS satellites

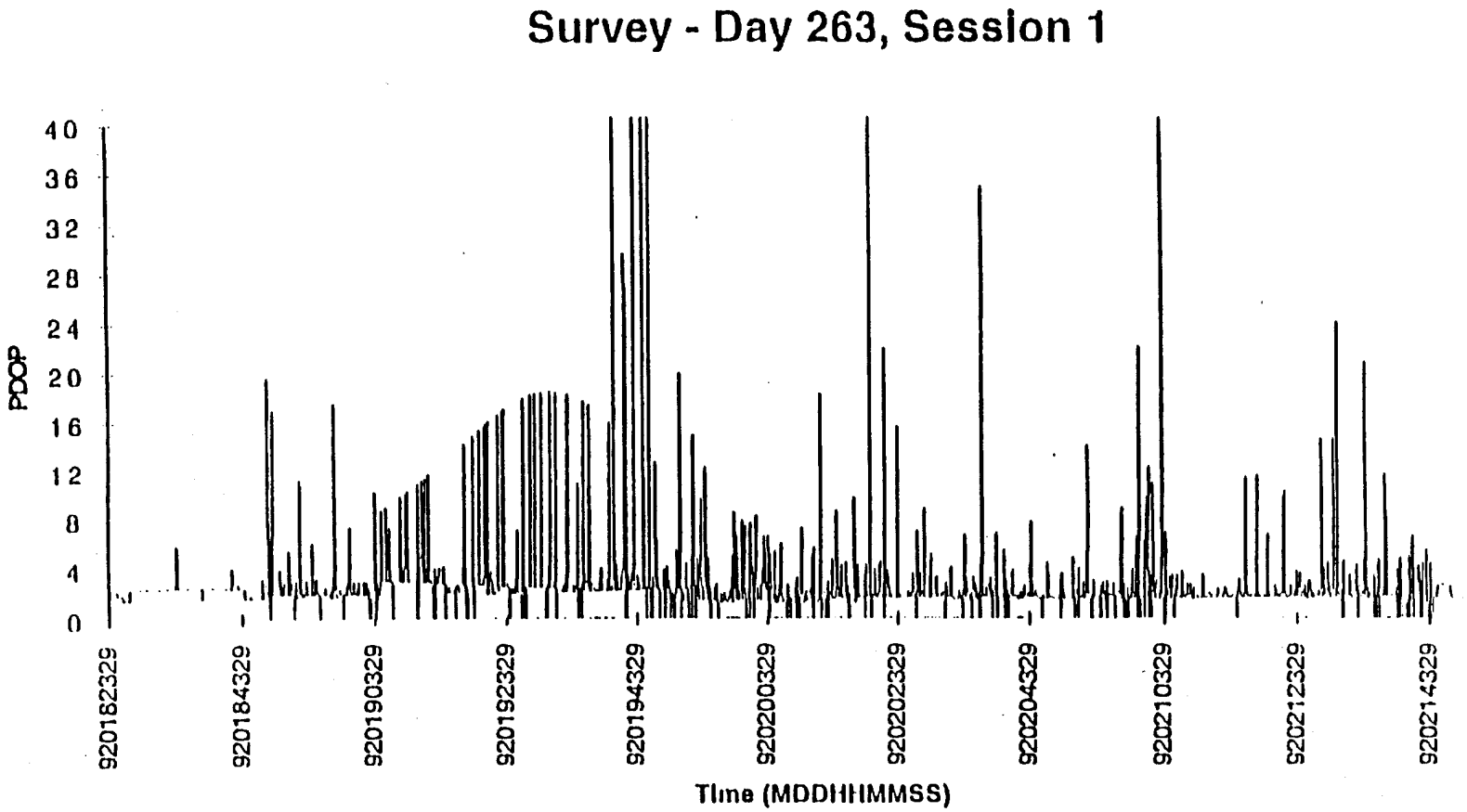

Figure 3 PDOP for GPS satellites with L1 data

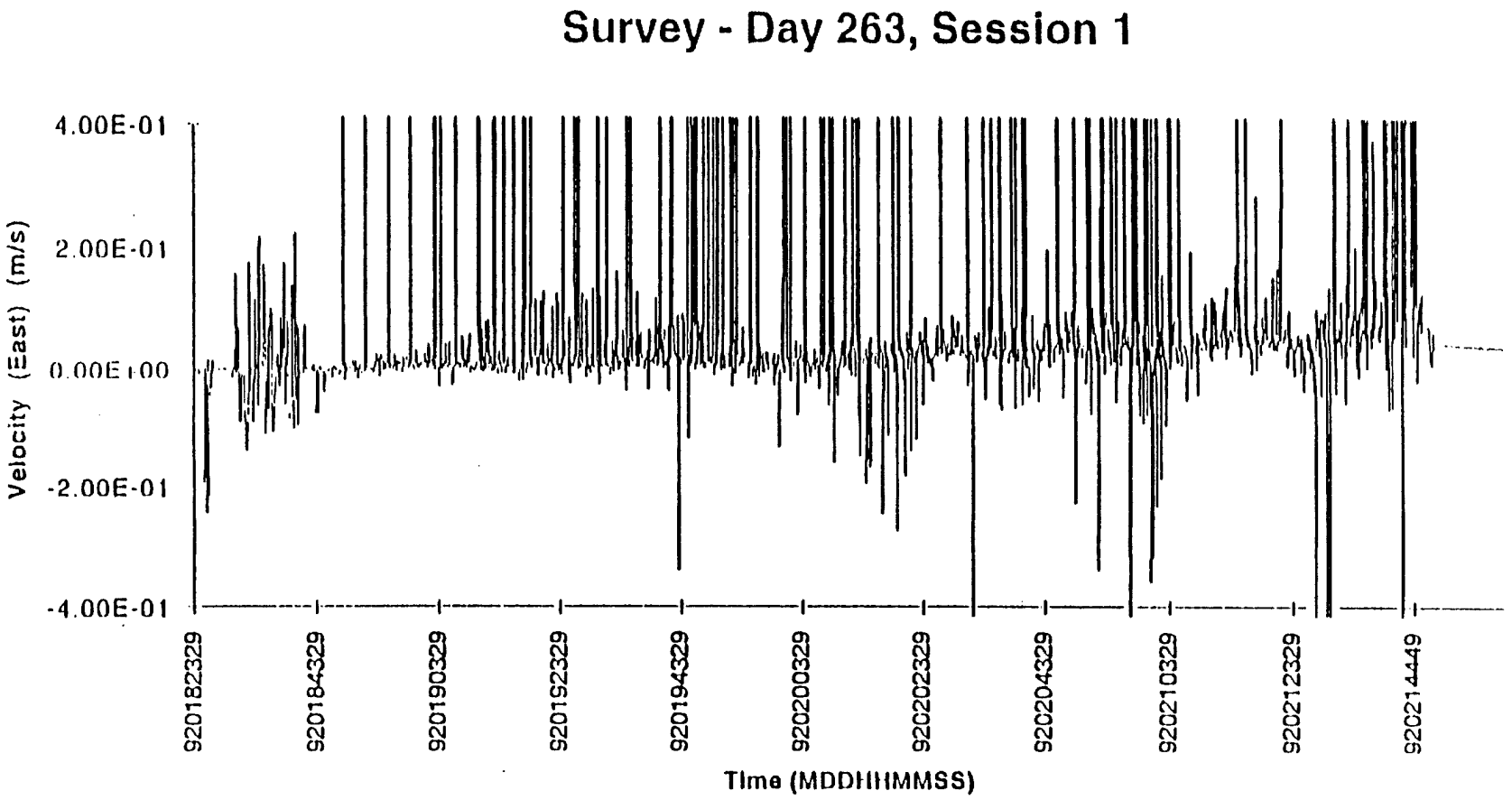

Figure 4 Velocity (East)

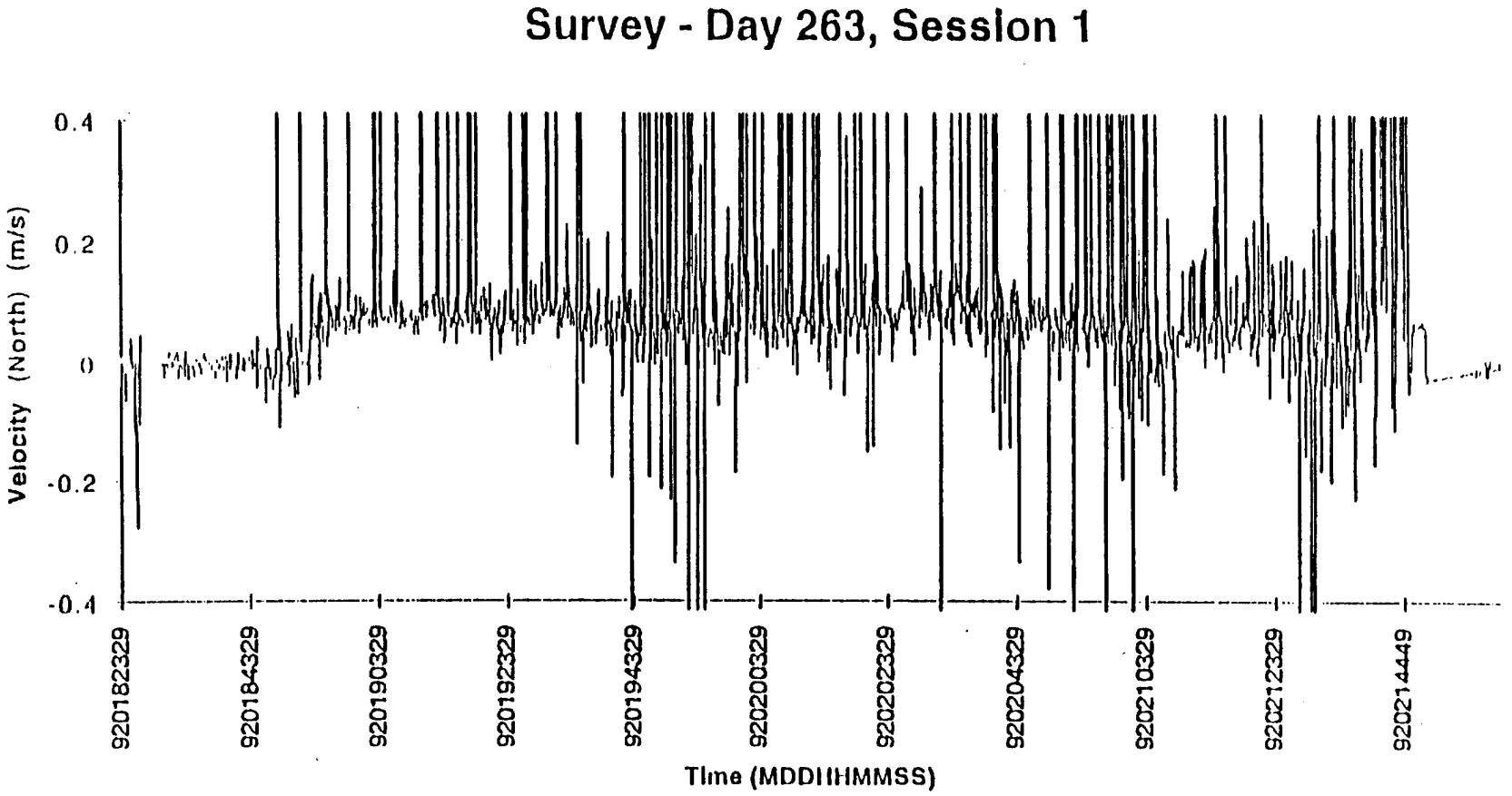

Figure 5 Velocity (North)

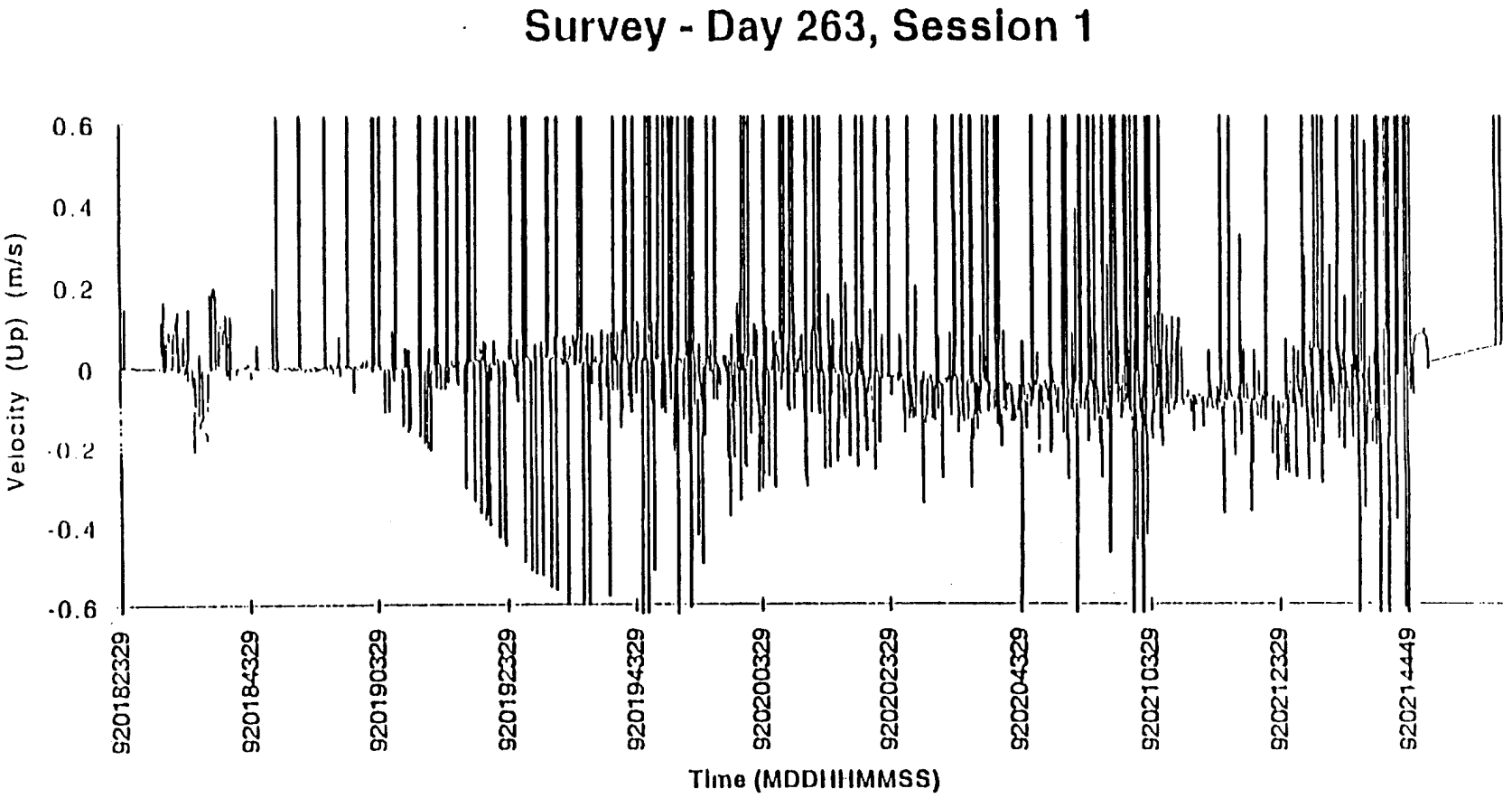

Figure 6 Velocity (Up)

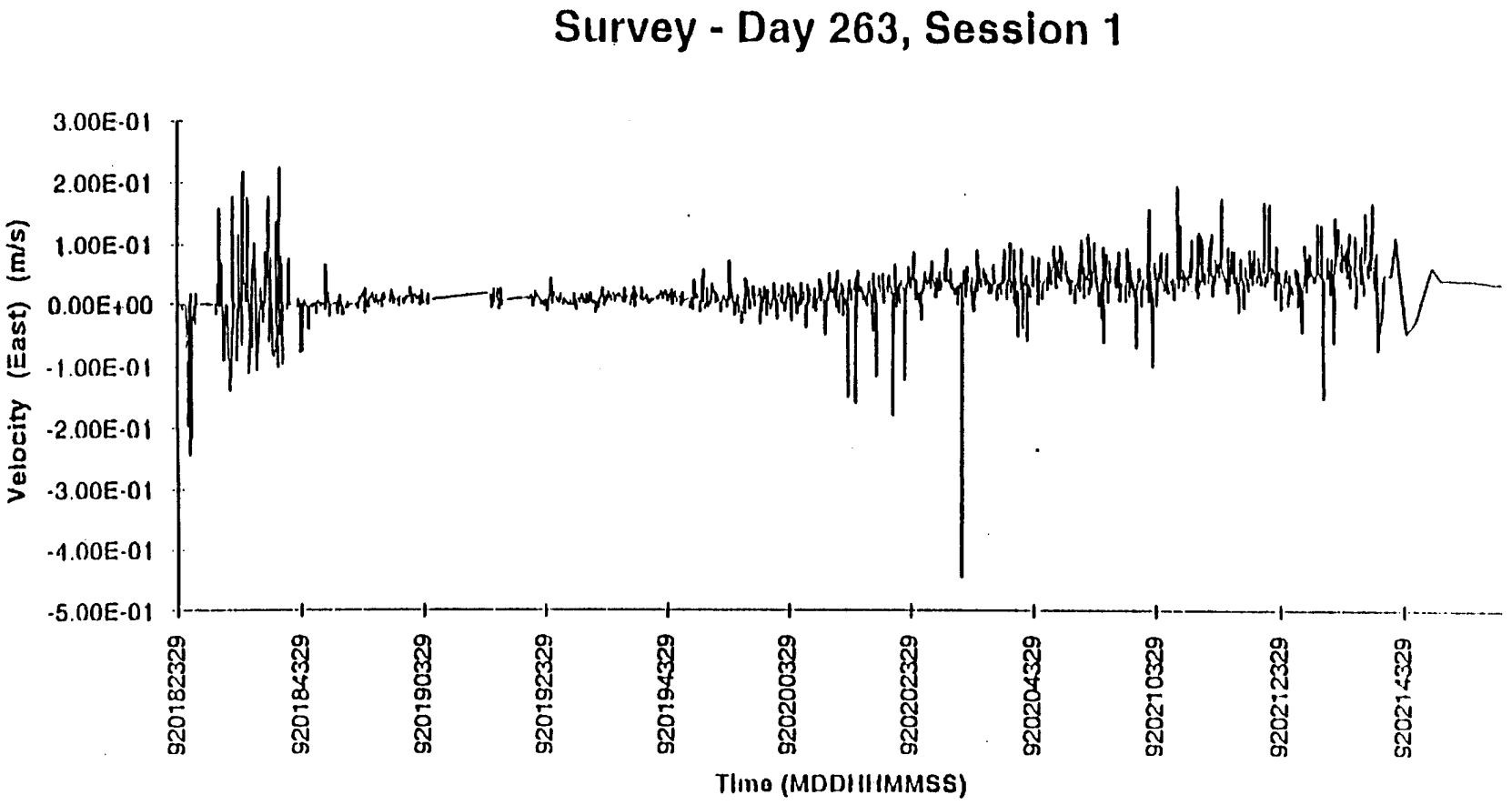

Figure 7 Velocity (East) - Interpolated

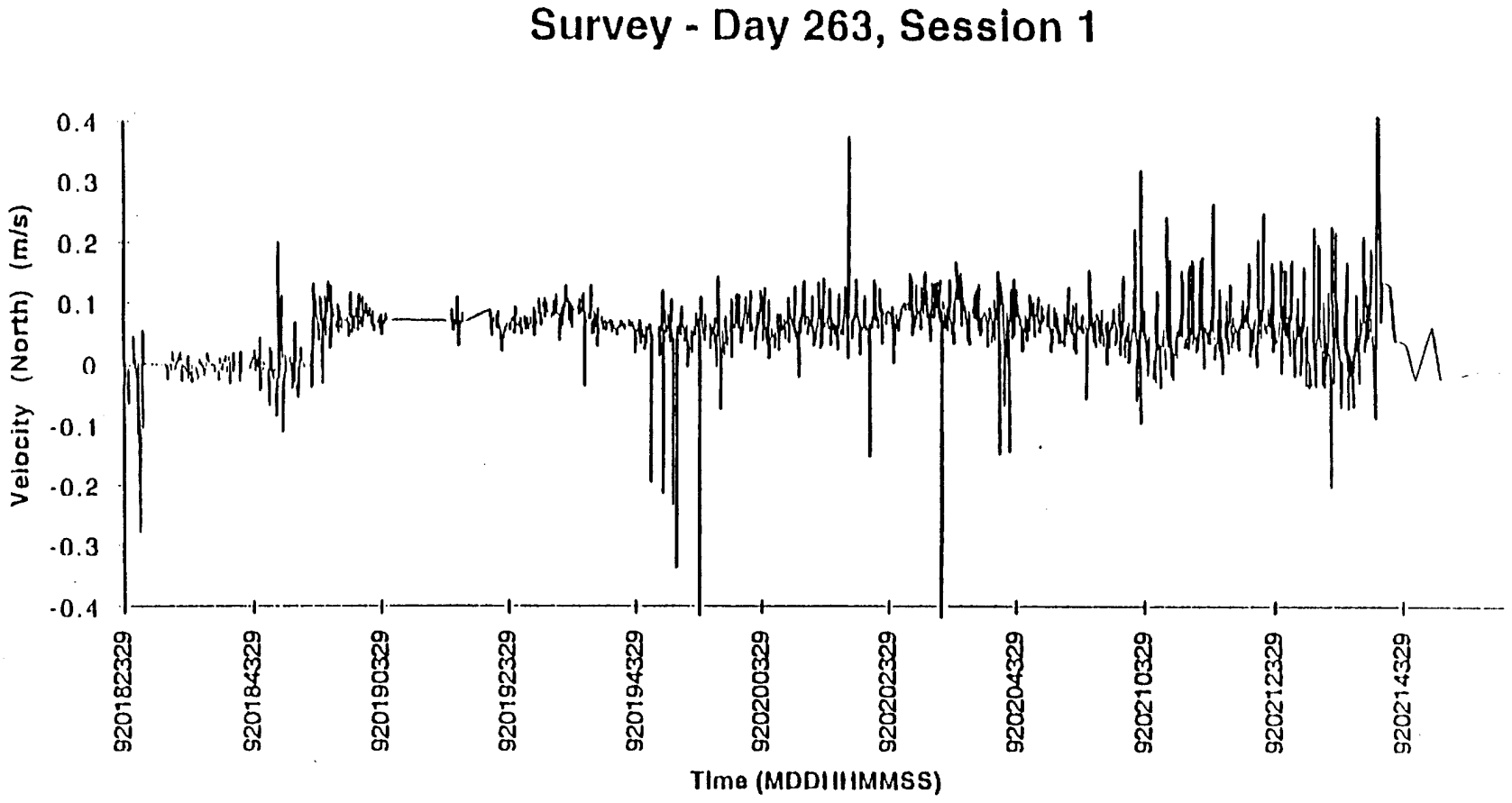

Figure 8 Velocity (North) - Interpolated

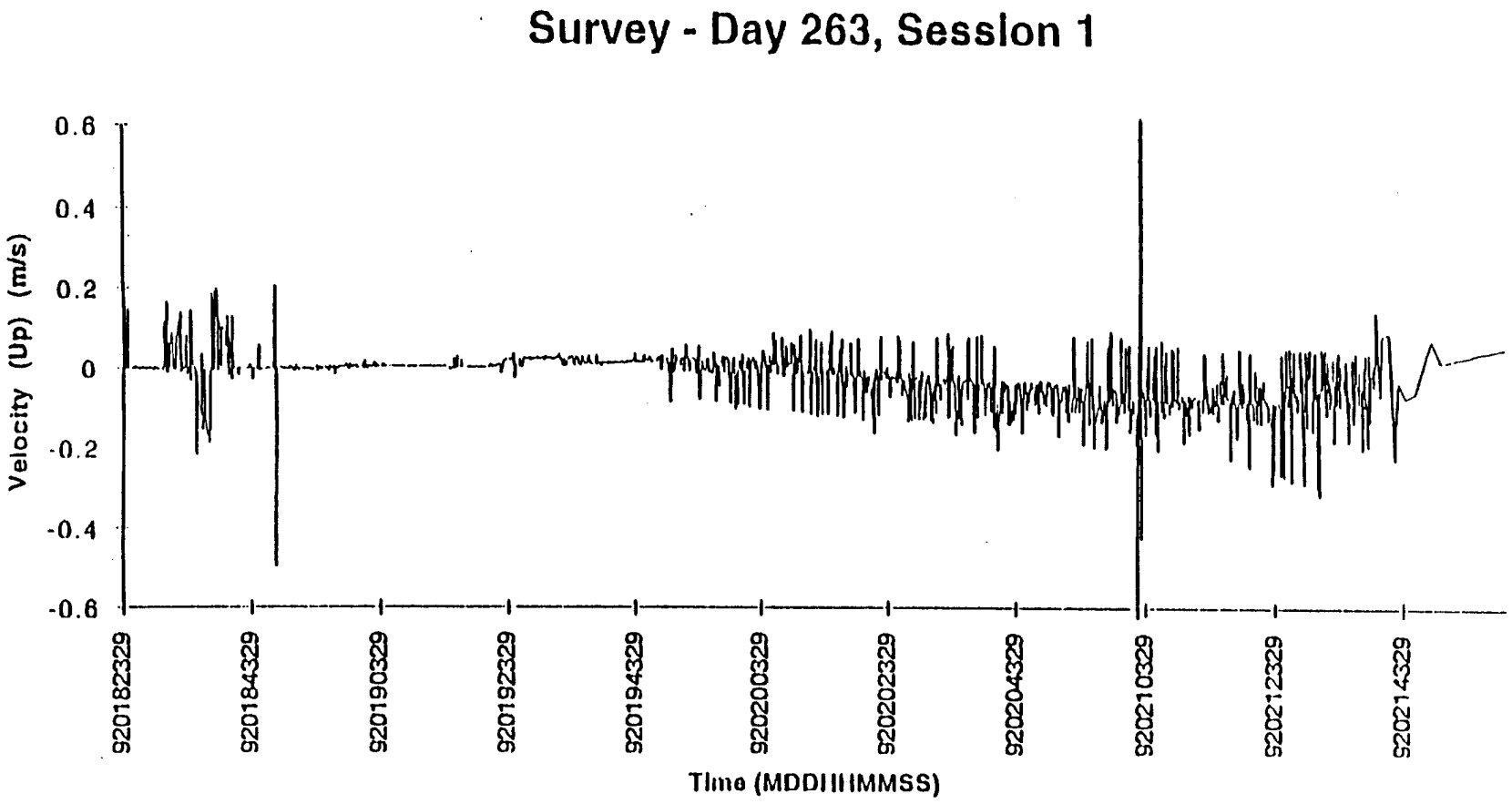

Figure 9 Velocity (Up) - Interpolated

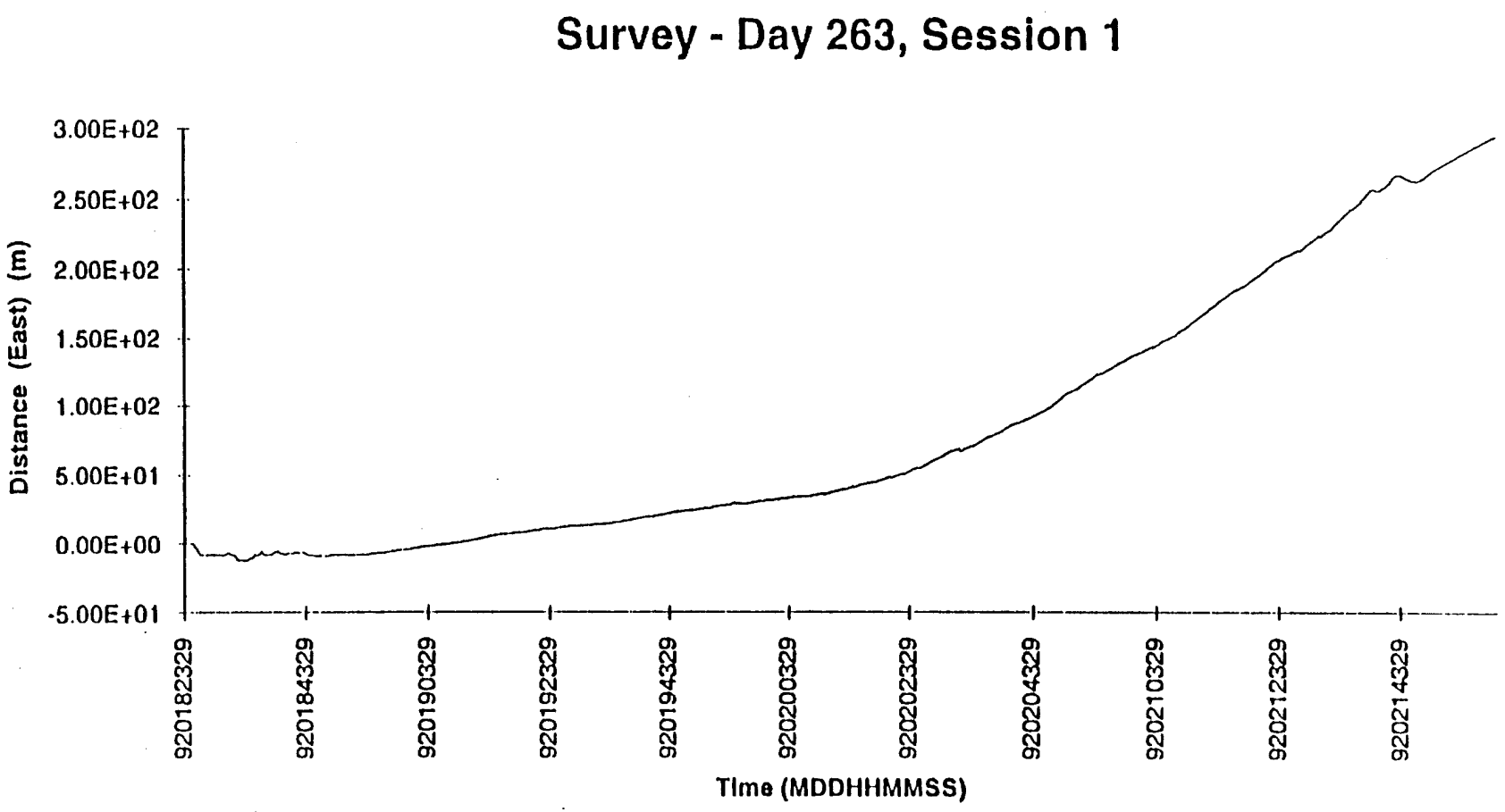

Figure 10 Distance (East)

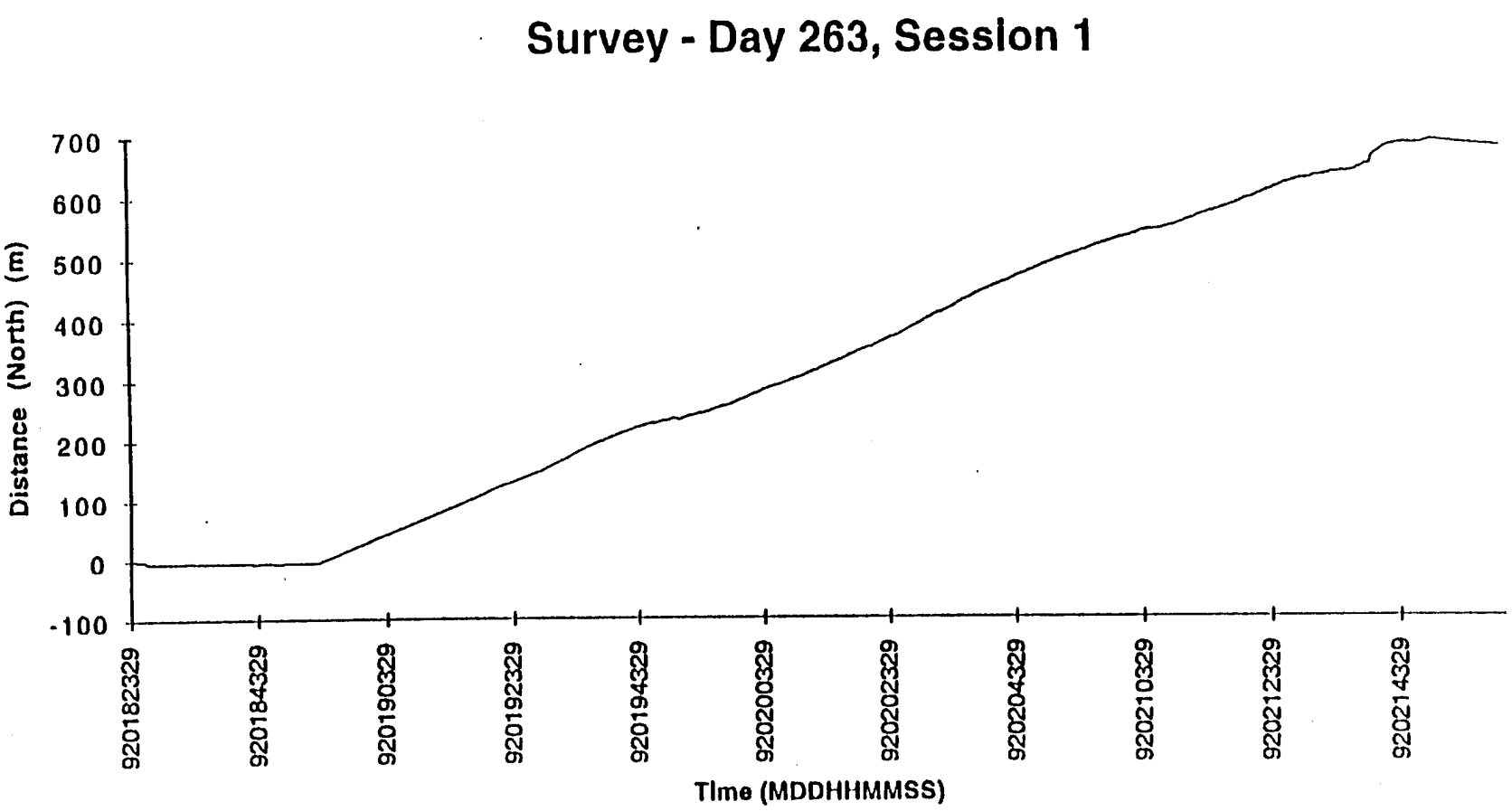

Figure 11 Distance (North)

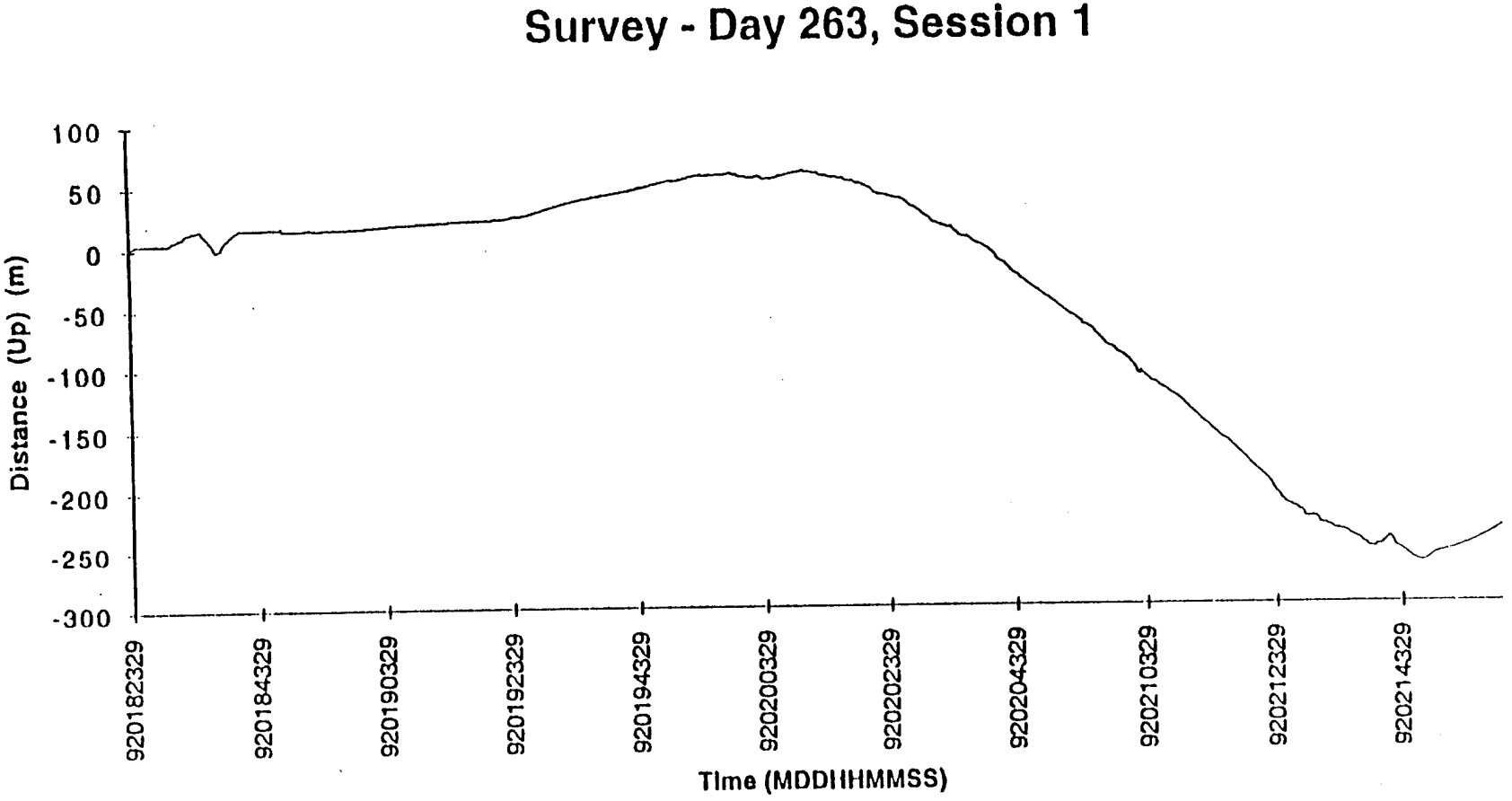

Figure 12 Distance (Up)